A STUDY OF THE STRUCTURE, EVOLUTION AND OBSERVATION OF HORIZONTAL BRANCH STARS

by

Benjamin Dorman
B.A., Trinity College, Cambridge, 1983
Certificate of Advanced Study in Mathematics,
Trinity College, Cambridge, 1984
M.Sc., Queen's University, 1986

ACCEPTED
FACULTY OF GRADUATE STUDIES
DEAN
DATE 1990-11-08

A Dissertation submitted in partial fulfillment of the
of the requirements for the degree of
DOCTOR OF PHILOSOPHY
in the Department of Physics and Astronomy
We accept this dissertation as conforming
to the required standard

Dr. D.A. VandenBerg, Supervisor (Department of Physics and Astronomy)

Dr. F.D.A. Hartwick, Departmental Member (Dept. of Physics and Astronomy)

Dr. C.D. Scarfe, Departmental Member (Department of Physics and Astronomy)

Dr. K.R. Dixon, Outside Member (Department of Chemistry)

Dr. P. van den Driessche, Outside Member (Department of Mathematics)

Dr. A.V. Sweigart, External Examiner (NASA — Goddard Space Flight Center)

University of Victoria

September 1990

Supervisor: Professor Don A. VandenBerg

ABSTRACT

This dissertation presents a detailed study of many aspects of the Horizontal Branch (HB) phase of stellar evolution. A classical technique of stellar structure analysis is summarized, and applied to Zero-Age Horizontal Branch (ZAHB) models. The chief conclusions from this work are firstly, that the total mass of the envelope sensitively affects the luminosity of the hydrogen-burning shell and the equilbrium of the helium-rich core. Secondly, the rapid progression of models across the Hertzsprung-Russell diagram with decreasing mass is the result of important changes in the hydrostatic structure of the stars. Thirdly, the luminosity-metallicity relationship of the Zero Age models results from the change in the core equilibrium luminosity with the CNO abundance of the shell region, together with the decrease in stellar mass at fixed effective temperature. The change in the mass-temperature relation with CNO is found to be the most important determining factor in the Horizontal Branch stellar distribution, and therefore is the most appropriate 'first parameter' for HB morphology. The evolution of the stars is then considered, and the analysis of the interior structures provides a reclassification of HB track morphology into three categories, depending on whether the model contains an outer convection zone or a radiative outer envelope, and on the luminosity of the hydrogen-burning shell. Lastly, the question of the formation of red-giant stars is considered; the general conclusions of this part of the study support the arguments presented by Yahil and van den Horn (1985).

Next, the evolution of the convective core of HB stars is reviewed, together with a detailed account of the numerical techniques developed for modelling semi-

convection. The problems associated with the late phase of HB evolution are also discussed. A brief review of the physical inputs and numerical methods used in the interior is presented, focussing on the calculation and implementation of the Equation of State. The calculations performed for this study are then presented in detail. The effects of oxygen enhancement on zero-age sequences are illustrated for a range in metallicity, and theoretical relations between luminosity and metallicity for the ZAHBs are demonstrated. The evolutionary tracks computed are illustrated and summarized in extensive tabulations in the Appendices.

The final chapter reproduces previously published studies of globular clusters. The first of these investigates the globular cluster NGC104 (47 Tucanae). By fitting the theoretical models to recent CCD photometry of the cluster, it was found that its initial helium content must have been close to 24% by mass. In addition, the best fits show that models for [Fe/H] $= -0.65$ provide an excellent match to the horizontal branch, if $(m - M)_V \approx 13.44$, and thereby yield consistency over the entire color-magnitude diagram of the cluster. The second study presents an investigation of the horizontal branch of M15. Detailed matches of our theoretical sequences to the cluster observations indicate that high envelope helium abundances are incompatible with the observed morphology. It is found that there is a clear preference for values of $0.21 \lesssim Y \lesssim 0.25$, independent of the value of [O/Fe]. The precision of the method is reduced by uncertainties in the observations and in the available synthetic temperature–bolometric-correction relations. The oxygen-enhanced zero-age HB models are found to have a period-colour relationship which is almost identical to that of their scaled-solar counterparts, but they reduce significantly the predicted double-mode variable masses. Importantly, it is found that, for reasonable assumptions about the reddening to M15, there is no discrepancy between the predicted and observed periods for the RR Lyrae variables. However, the period shift between M3 and M15 can be explained by canonical models only if the helium abundance in both clusters is low ($Y_{HB} \sim 0.21$), and the bulk of the

RR Lyrae star population in M15 is at late stages of evolution. These conclusions are reconsidered in the light of the new calculations presented here.

Examiners:

Dr. D.A. VandenBerg

Dr. F.D.A. Hartwick

Dr. C.D. Scarfe

Dr. K.R. Dixon

Dr. P. van den Driessche

Dr. A. V. Sweigart

Table of Contents

List of Tables

List of Figures

Acknowledgements

It is difficult in a few short lines to acknowledge all of the help and support I have received over the past four years without seeming insincere, but I will try. My first thanks go to my wife Catriona and my step-daughter Tara, not only for their day to day love and support but also for making this endeavour seem worthwhile. Many thanks go to my parents-in-law, Dr. Alan and Mrs. Christine Johnson, for much support throughout the summer in so many ways, and without whom we would have been living on solid air. My thanks go also to the Community of the University of Victoria, which has given me many experiences and opportunities to grow in these years. Many thanks go to the secretaries of the Physics and Astronomy Department (Lorraine Charron, Carolyn Swayze, Laurie Newby, Alison Marchant, Josie Gelling and Lorene Dingman) for much helpful assistance. Thanks are also due to Melvin Klassen and other members of the University of Victoria Computing services.

On the academic side, I owe a great debt to my supervisor, Don VandenBerg, for pointing me in the right directions and making sure I stayed on course. His great insight into the important problems of the comparison of theory and observation, and rigorous, careful work on stellar interiors have earned my sincere respect and admiration, which is of course shared by the entire astronomical community. My thanks go also to Young-Wook Lee for his contribution to the last chapter of this work, and for many useful discussions. I would also like to acknowledge useful discussions with Alan Irwin and Allen Sweigart. Thanks are due finally to Brian Pedersen for useful discussions, and for being good-natured enough occasionally to do tedious tasks which I couldn't face myself.

Dedication

I would like to dedicate this thesis to the memory of the great sages of Judaism, whose thoughts formulated my approach to life:

[יד] הוּא הָיָה אוֹמֵר: אִם אֵין אֲנִי לִי, מִי לִי? וּכְשֶׁאֲנִי לְעַצְמִי, מָה אֲנִי?
וְאִם לֹא עַכְשָׁו, אֵימָתַי?

" He [Rav Hillel] used to say:

If I am not for myself, then who is for me?

But if I am only for myself, then what am I ?

And if not now, then when ?"

[א] **בֶּן זוֹמָא** אוֹמֵר: אֵיזֶהוּ חָכָם? הַלּוֹמֵד מִכָּל אָדָם, שֶׁנֶּאֱמַר: ,,מִכָּל מְלַמְּדַי הִשְׂכַּלְתִּי.״[3] אֵיזֶהוּ גִבּוֹר? הַכּוֹבֵשׁ אֶת יִצְרוֹ, שֶׁנֶּאֱמַר: ,,טוֹב אֶרֶךְ אַפַּיִם מִגִּבּוֹר, וּמֹשֵׁל בְּרוּחוֹ מִלֹּכֵד עִיר.״[4] אֵיזֶהוּ עָשִׁיר? הַשָּׂמֵחַ בְּחֶלְקוֹ, שֶׁנֶּאֱמַר: ,,יְגִיעַ כַּפֶּיךָ כִּי תֹאכֵל אַשְׁרֶיךָ וְטוֹב לָךְ.״[5] ,,אַשְׁרֶיךָ״ — בָּעוֹלָם הַזֶּה, ,,וְטוֹב לָךְ״ — לָעוֹלָם הַבָּא. אֵיזֶהוּ מְכֻבָּד? הַמְכַבֵּד אֶת הַבְּרִיּוֹת, שֶׁנֶּאֱמַר: ,,כִּי מְכַבְּדַי אֲכַבֵּד, וּבֹזַי יֵקָלּוּ.״[6]

"Ben Zoma said:

Who is wise? The one who learns from every person...

...Who is honoured? The one who honours all creatures"

Chapter 1 Introduction

Globular clusters, stellar associations containing $10^5 - 10^6$ solar masses, provide an excellent framework for the study of stellar evolution as they comprise vast numbers of stars which are of homogeneous compositions and which are isochronous in formation. Variances between their properties as apparent from their colour-magnitude (CM) diagrams may be understood by generating models of stars of similar composition and age, thus eliminating two key parameters which differentiate stellar objects. Models of stars of different mass and therefore at various stages of evolution may be used in the construction of isochrones, which have shown notable success in duplicating the cluster CM observations of main sequence and giant-branch stars (VandenBerg & Bell 1985; Hesser *et al.* 1987). Another prominent feature of many globular cluster CM diagrams is a 'horizontal' sequence, which may extend from a point close to or abutting the giant branch, to a location in colour corresponding to surface temperatures greater than 20,000 K.

The subject of this dissertation is the structure and evolution of these Horizontal Branch stars, and the understanding which may be gained from the application of theoretical horizontal-branch evolutionary sequences to globular clusters. As is widely known, horizontal branch tracks display a variety and subtlety which is arguably greater than for any other phase of evolution. The excellent agreement between the gross properties of low-mass stellar models having helium-burning cores and hydrogen burning shells with observations of clusters provides irrefutable evidence of the nature of this phase of evolution. For the metal-poor clusters of the Galactic Halo, as well as the more metal-rich Disk clusters, detailed modelling of the Horizontal Branch can provide insight into a number of interesting questions concerned with the chemical evolution of the galaxy, and indirectly the distance scale and age of the universe.

Across the *HR* diagram lies a strip in which stars are unstable to relatively large-amplitude radial pulsations, and the intersection of this strip with the Horizontal Branch is referred to as the RR Lyrae gap, containing variable stars whose archetype is the 9th magnitude field star RR Lyrae. These variables have periods of under one day. This "instability strip" itself is a region containing stars in which the ionization zone caused by $He\,II$ is deep enough to drive a significant amount of outlying material into pulsation (Zhevakin 1953, Cox 1963), but not so deep as to be incapable of overcoming the inertia of those outer layers.

Horizontal Branches of different clusters vary from blue, with all stars to the left of the instability strip, to red, with all objects comprising a clump adjacent to the red giant branch. The various observed horizontal branch morphologies have been classified in a variety of ways. For example, the Dickens type (Dickens 1972) classifies HBs into seven categories, from I (blue) to VII (red), or by the Mironov index (Mironov 1972), based upon the ratio $B/(B+R)$ where B and R are the numbers, respectively, of horizontal branch stars to the blue and to the red of the instability strip. Recently, a third classification, using the ratio $(B-R)/(B+V+R)$ has been introduced by Lee (1989). In this classification, R represents the numbers of RR Lyrae variables, and this index has the advantage of being sensitive to the presence of the variable stars.

Various observations have helped both to simplify and to complicate the theoretical expectations from the horizontal branch phase. Examples of the former are the observational constraints on the Universal helium abundance, thought to be primordial in origin. In the latter category are the observed variation in horizontal branch morphology, and the discovery of significant heavy-element abundance variations in globular cluster stars.

Since the late 1960's, refinements of the theory of primordial nucleosynthesis have been fully absorbed into stellar evolution calculations, and observations of

galactic and extragalactic nebulae have constrained expectations of the helium abundance (Y) of stars. It has therefore been possible to limit a very important parameter which is known to influence profoundly the relative strength of the two energy sources in these stars (see Rood 1970). The lower bound which exists to the fraction of helium in all matter so far observed is taken as a firm indicator of its primordial origin. While matter in the solar neighborhood is expected to be contaminated by enrichment through stellar nucleosynthesis, relatively unevolved, metal-poor objects – or objects such as globular clusters whose stellar population formed early in the history of the galaxy – may be used to constrain the amount of helium formed cosmologically. For some time, studies of gaseous nebulae in blue compact galaxies have yielded the lowest estimates, and the currently accepted values are in the range 23 -24 % by mass (*e.g.,* Pagel, Terlevich, and Melnick 1986). As far as the study of Galactic stellar evolution is concerned, constraints on globular cluster helium abundance have been made theoretically using the R-method (Iben 1968; Buzzoni *et al.* 1983). However, the well-known strong dependence of the horizontal branch width on helium abundance (Sweigart and Gross 1976; Sweigart 1987; Lee and Demarque 1990) suggests that sufficiently accurate photometric data can be used with evolutionary sequences to provide estimates of the helium abundance for globular clusters. The advantage of this technique over the R-method is that, when it can be applied, it provides *necessary* conditions on Y. However, both of these methods depend critically on theoretical HB evolution.

It was originally thought that the ratio of heavy-element abundances of stars was similar to that found in the sun. Recently, much attention has focussed on stellar abundances, showing that globular clusters have not been subject to the same chemical history as the galactic disk. In particular, massive stars which live briefly, and whose detonation early in galactic history is apparently responsible for high abundances of carbon, oxygen and the α-nuclei (such as calcium, magnesium,

silicon, and sulphur), are adduced to explain relative abundance peaks in these elements. While the study of globular cluster elemental content is far from totally explicable by current theory, these observed phenomena can do much to refine the stellar evolution models and add to the predictive power of the theory.

A much-researched question concerns the famous 'second parameter problem' (*e.g.*, see Hartwick 1968), which is the unknown cause of the diversity in the morphology of horizontal branches among clusters with apparently similar metallicity (the latter being the "first parameter"). The importance of this problem is somewhat enhanced by the fact that it is prevalent in the outer Galactic Halo, indicating that its solution may contain important information about Galactic Evolution. The variation of pulsational properties of RR Lyrae stars with cluster parameters, referred to as the Oosterhoff effect, has also been the cause of some debate: globular clusters have been divided into the two Oosterhoff groups, in which the mean period of fundamental pulsators $< P_{ab} > \sim 0.55$ days for Oo I, and 0.65 days for Oo II (Oosterhoff 1939). This problem has resurfaced over the last eight years as the Sandage Period-Shift effect, which is an apparent correlation of RR Lyrae periods with cluster metallicity (Sandage 1982a, 1990b) in a manner which is difficult to reconcile with the theoretical calculations.

This study focusses on three issues in the structure and evolution of the horizontal branch phase, which together makes up a comprehensive review of this particular field of research. In the chapters on stellar structure, the previous literature on the subject is reviewed, paying tribute in particular to the early work by John Faulkner, Icko Iben, and Robert Rood (see references in §2.1) who first identified that the nature of stars located on the observed 'horizontal branch' was, in fact, that described above; they described qualitatively the major features of HB stellar evolution, up to the 'second' (or 'asymptotic') giant branch, where inert carbon-oxygen cores are enclosed by helium and hydrogen-burning shells. In this work, the hydrostatic structure of HB stars is analyzed using the mathematics of

polytropes (Chandrasekhar 1939) in an attempt to add rigour to this understanding. Insight into this phase of evolution can, additionally, aid in the understanding of the evolution of the earlier red-giant epoch. The principal conclusion from the first part of the study, which explicitly portrays the variations in interior stellar structure with mass, is that the luminosity of the hydrogen burning shell is of signal importance in determining the location of an initial Zero-Age Horizontal Branch (hereafter ZAHB) model on the HR diagram. The variation across the HB is the result of the adjustment, at thermal and hydrostatic equilibrium, of the stellar interior to a greater or lesser burning strength. After establishing this result, the sensitivity of horizontal branch interiors to various input parameters (helium abundance, heavier element mix, total mass, and core mass) is discussed. The evolution of HB stars is then investigated in detail, and the evolution of the stellar interior is used to provide an explanation for the shape of the evolutionary tracks. These results are summarized by classifying the HB morphology. A discussion of hydrostatic structure at late evolutionary times shows that stars entering the AGB phase of evolution have similar interiors to red-giants, as can be expected but as has not been previously shown explicitly. In the process, the question of why stars become red giants is discussed, including a critical review of recent literature on this subject.

In chapter 3, the equilibrium of the convective core is reviewed. The basic problem under discussion was first researched by Schwarzschild and Härm (1958) in the context of massive stars, but for helium burning stars the problem was noted somewhat later, by Schwarzschild (1970), Paczyński (1970), and by Robertson and Faulkner (Faulkner 1971; Robertson and Faulkner 1972). The problem arises because the convective core undergoes expansion early in its evolution, but the usual stability criteria do not permit this expansion to continue after the core has grown significantly without the creation of a partial mixing zone. A numerical mixing routine for 'semiconvection' has been developed for this study, and the discussion

in chapter 3 describes its implementation in detail. Unfortunately, however, the continuation of the semiconvection assumption to later epochs in the evolution leads to severe numerical problems. The late-time behaviour of HB evolutionary tracks has become a source of some controversy. Most computer programmes (Castellani *et al.* 1985, Lattanzio 1986, and Sweigart 1990) designed to model the phase immediately prior to central helium exhaustion have produced results referred to as 'breathing pulses', in which a converged model shows a sharp increase in core helium abundance. The controversy arises as to whether these events are 'real' (occur in real stars) or are numerical artefacts. This question is reviewed here by illustrating the behaviour of the core physical variables throughout evolution, and the discussion favours the idea that the pulses are artificial.

In chapter 4, the physical inputs to the computer programme are discussed, together with a brief explanation of other numerical techniques used by or developed for this study. These include a discussion of the procedures used for producing ZAHB models as well as a discussion of the equation of state and the interpolation methods necessary for the use of tabulated equation of state data in a stellar evolution code. A brief summary of the physical inputs adopted in the stellar interior is also included, and the variations in the evolutionary tracks caused by different assumptions about the interior physics are illustrated. The implementation of the stellar evolution code, which has proved very successful in simplifying the mechanics of producing a large number of calculations, is also described.

Chapter 5 contains the major results of the calculations to be presented. These calculations span the range of metallicities appropriate to globular clusters. The features of the new grid of calculations are the adoption of enhanced oxygen abundance, and the incorporation of non-ideal effects into the equation of state for the stellar material in the deep interior. For each metallicity, an oxygen enhancement has been used which is roughly the mean of current estimates for the

observed value of [O/Fe] in clusters. The equation of state adopted was the one recently tabulated by Straniero (1988) for high temperatures: it includes non-ideal effects that appear to be important for carbon and oxygen at temperatures and pressures appropriate to the cores of HB stars. In addition, the core masses and hydrogen shell chemical profiles adopted are consistent with precursor red-giant models, which were evolved to the tip of the giant branch by VandenBerg (1990). In the first part of this section, the discussion focusses on zero age sequences and their implications for globular clusters. Additional ZAHBs illustrate the range of uncertainty in derived cluster parameters which arises from composition determinations. In particular, the oxygen enhanced sequences are compared with their scaled solar counterparts. The second part deals with evolutionary sequences for each composition in the grid. A feature of these calculations is that they have been extended beyond the era of helium exhaustion to the lower regions of the AGB. Since the major features of the evolution are discussed in chapter 2 and elsewhere in the literature, the main object of this section is to illustrate the evolutionary tracks in the observational plane.

Finally, chapter 6 contains detailed studies of two clusters, 47 Tucanae and M15. Each of the sections have been previously accepted for publication (Dorman, VandenBerg and Laskarides 1989, hereafter DVL; Dorman, Lee and VandenBerg 1991)[1] In both of these studies, the object was to show that matching the observed HB morphology accurately with theoretical calculations is a viable technique for deriving cluster composition parameters. In the case of the metal-rich cluster 47 Tuc, in which recent CCD photometry was available, firm conclusions were possible concerning the cluster helium content. The second study, of the very metal-weak cluster M15, was performed with the intention of constraining the cluster helium

---

[1] *For each of these studies, the precursor giant-branch models were computed by D.A. VandenBerg. For the M15 study, Synthetic Horizontal Branches were contributed by Young-Wook Lee.*

abundance, and attempting to show the effect of adopting enhancements in the oxygen abundance. As well, since the RR Lyrae stars in M15 have been the focus of much attention, the study also deals extensively with the properties of the variable stars. A point that is particularly stressed is the necessity for the stellar properties which are implied by both pulsation theory and evolution theory to be consistent with each other and with the observations.

Chapter 2 On the Structure of Horizontal Branch Stars

2.1 Introduction and Historical Review

It was Faulkner (1966) who first firmly established that stellar models with helium burning cores and hydrogen shells of varying relative strengths could explain the sequence of observed stars which were nearly constant in magnitude despite a very wide range in colour index. An important issue that was resolved in this paper was the question of core-envelope interaction during the helium flash. This work established that a high degree of mixing between the two zones was inconsistent with the observations. Models which were homogenized during the flash would reappear on the helium-rich main sequence which lies parallel and to the left of the hydrogen burning population where the vast majority of stars are to be found. This introduced a very crucial simplification in the theory of the horizontal branch which allowed the extension of stellar modelling to this later phase of evolution. The $(B-V)$ colour index of the Horizontal Branch (hereafter abbreviated to HB) stars appeared to have a value with a well-defined maximum which was a function of their heavy element abundance. Equivalently, the gap between the reddest horizontal branch stars and the red giant branch was observed to vary inversely with metallicity. Following this, in early studies of the evolution of the HB stars, Iben and Faulkner (1968), and Rood and Iben (1968), showed how this phase of evolution could be used to derive very important information about the Galactic globular cluster system, including its age and helium abundance. Both of these questions have great relevance to the age of the Universe and to the details of its early history.

Following these studies, more extensive grids of initial models and evolutionary sequences were published by Rood (1970) and Iben and Rood (1970, hereafter IR70). The second of these papers provided a grid of horizontal branch calculations for a range in helium abundance (denoted by the symbol Y) and 'metallicity'

(the sum of the abundances of all elements heavier than helium) which is represented by the symbol Z. The sensitivity of HB models to composition and other parameters found by Faulkner (1966) was verified by these calculations, which were performed with more complete descriptions of the interior physics. Rood (1970) described how the luminosity of the models varied with the mass of the helium-rich core (M_c), the total mass (M_*), and with the composition parameters (Y and Z), noting in particular how the hydrogen-burning shell luminosity varied with Y. The extreme sensitivity of the energy balance between the core and shell burning regimes to practically every parameter affecting stellar structure was already becoming clear. These models were used by IR70 to illustrate most of the major features of horizontal branch evolution — with the important exception of the core expansion problem dealt with more extensively in chapter 3. In doing so, Iben and Rood described most of the features of HB evolution whose explanation is the subject of a major part of this current study. In particular, they noted that (i) the shape of the evolutionary sequences was due to the changing strength of the hydrogen and helium burning energy sources (ii) the appearance of globular cluster horizontal branches necessitated mass loss at or near the helium flash and (iii) the asymptotic giant branch (AGB) was the phase of evolution following helium exhaustion at the centre of the stars. Whilst the HB models spanned a large temperature range, the first associations of very blue helium burning models with the observed population of O and B subdwarfs seem to have been made by Caloi (1972) and Faulkner (1972).

It was realized by a number of researchers (Schwarzschild 1970; Paczyński 1970; Castellani, Giannone, and Renzini 1971a,b) that the 'expanding core' phenomenon, found in models of very massive stars, would also occur for helium-burning stars, although for different reasons. Robertson and Faulkner (1972) first developed an algorithm for dealing with semiconvection in this case, and it was adopted by Sweigart and Gross (1974) in a comprehensive study of the evolution

of a single model. Later, extensive grids by Sweigart and Gross (1976, hereafter SG76) and Sweigart (1987, hereafter S87) became the standard work on the subject.

The dependence of double-energy-source models upon the significant parameters of Stellar Evolution Theory as mentioned above has attracted a relatively small number of theoretical studies, of which the first and perhaps most extensive appeared in the early seventies. In a series of papers, D. Lauterborn and S. Refsdal, together with several collaborators (Refsdal and Weigert 1970; Lauterborn, Refsdal and Weigert 1971a,b; Lauterborn, Refsdal and Stabell 1972), investigated the interiors of stars which derived their energy sources from hydrogen shell burning, later concentrating on objects which also had significant helium core burning luminosity. The first of these papers introduced an analytical technique which was generalized for the case of central energy production. They defined three regimes for core helium burning stars, of which the lower branch, with relatively thin hydrogen-rich envelopes, assuming that the core mass was approximately one-half solar, corresponded to the observed location of the HB. The latter two of these papers concentrated on the blueward loops in the HR diagram found both for HB model sequences and for their high-mass counterparts, which become Cepheid variables as they cross the instability strip.

In principle (see Chapter 6), when theoretical sequences are applied to real stellar systems, the range of parameters can be constrained in a variety of ways. The total mass is bounded above only by the age of the cluster, which determines the mass of stars reaching the tip of the red giant branch (to a good approximation the same as that of the turnoff stars). The core masses are constrained theoretically by a couple of factors. Firstly, there is a minimum core size which is necessary for the helium flash to occur (Refsdal and Weigert 1970). Secondly, as the star proceeds up the red giant branch, neutrino losses by plasma, photodisintegration, and pair-creation processes remove energy from the core, delaying the onset of

the flash by reducing the rise with evolution of the central temperature. Such processes, along with others which delay the helium flash (such as rotation), allow the size of the helium rich core to grow. Neglecting these processes bounds the core mass at the helium flash from below (for a given set of physical assumptions — *i.e.*, nuclear reaction rates, equation of state, and opacities etc). As will be seen later, the importance of these factors can be constrained by observation. As far as the abundances are concerned, there are at least three separate factors: the helium abundance of the envelope, the abundances of the catalyst elements for hydrogen burning (carbon, nitrogen, and oxygen, hereafter CNO), and the abundance of elements which liberate free electrons for opacity processes — such as sodium, calcium, magnesium, silicon, and sulphur (referred to as the α nuclei) and relatively abundant heavy elements such as iron. Abundances of these elements are constrained by observation and predicted theoretically by Galactic chemical evolution models (*e.g.*, Matteucci 1987). In summary, the range of colours spanned by observed horizontal branches renders the total mass of horizontal branch stars a parameter which is virtually free of constraints, and can in principle be found for each cluster by detailed matching if the composition can be determined to some degree of precision.

In the rest of this chapter, the object is to re-examine the effect of each theoretical parameter on the structure and evolution of the horizontal branch stellar models. A classical stellar structure technique (composite polytropes) is adopted, in order to show clearly how the variations in interior configurations explain the behaviour of zero-age models. Many of the main conclusions of this discussion have been noted previously; however, the object of this section is to demonstrate a theoretical basis which unites the various phenomena which HB stars demonstrate. Some matters, particularly the rôle played by relative abundances of the CNO group of elements and the other 'heavy' elements have been subject to debate, with opposite conclusions appearing in a few papers in the literature (Hartwick

and VandenBerg 1973a; Castellani and Tornambé 1977; Bencivenni *et al.* 1989). The effects of variations in the total mass are investigated, and the results are used to show that the response of the hydrogen shell to differing circumstances is the most important determining factor for the variations in ZAHB structure and *HR* diagram location. An understanding of the dependencies which give rise to this sensitivity is also helpful for explaining the response of the star to variations in other parameters. The discussion then turns to the behaviour of stellar evolutionary sequences with evolution. Using illustrations of the changes in hydrostatic structure, density and radius with time, a pattern emerges which explains the direction of evolution of model sequences on the HR diagram. Finally, since the range of the calculations performed for this study includes the early AGB phase, an investigation of the issue of red-giant formation is undertaken, which includes a critical review of recent studies of this question.

2.2 A Summary of the Mathematics of Polytropes.

The analysis of HB structural variations begins with a condensed summary of the properties of polytropes, in order to provide the necessary theoretical framework. It will be shown that identification of the character of the solution to the stellar structure equations in terms of composite polytropes can explain the equilibrium configuration in a very natural manner.

Polytropes are defined by solutions to the Lane-Emden equation (Lane 1869; Emden 1907), which is written in the form

$$\frac{1}{\xi^2}\frac{d}{d\xi}\left(\xi^2\frac{d\theta}{d\xi}\right) = -\theta^n. \tag{2.1}$$

together with the boundary conditions

$$\theta(\xi = 0) = 1;\ \theta'(\xi = 0) = 0. \tag{2.2}$$

This is derived from the equations of stellar structure involving hydrostatic equilibrium and mass conservation (in spherical symmetry), together with a relation for the equation of state of the form

$$P(r) = \mathcal{K}\rho(r)^{1+1/n} \tag{2.3}$$

where $P(r), \rho(r)$ are the total pressure and density in the sphere at radius r, and n is a real constant taken here to be greater than unity[1]. $\mathcal{K}$ is a constant of proportionality which labels polytropics of fixed index n (see Chandrasekhar 1939, Chapter 2). The symbols ξ and θ are the transformed radius and density given by

[1] *Solutions are, however, possible for smaller values of n; as mentioned below, for $n = 0$ (constant pressure) and $n = 1$ the solutions have closed form. It the latter case, the Lane-Emden equation is linear.*

$$r = a\xi, \tag{2.4}$$

$$\rho = \rho_c \theta^n, \tag{2.5}$$

where a is a constant

$$a = \left(\frac{(n+1)K}{4\pi G} \rho_c^{1/n-1} \right), \tag{2.6}$$

and for central density ρ_c. Hence the point $\xi = 0$ (referred to below as the origin) is identified with the centre of the polytrope, and the point $\xi_1 : \theta(\xi_1) = 0$ is associated with its outer radius.

It must be stressed that except for fully convective gas spheres, such as very low mass stars or models of stars in the process of contraction to the main-sequence, realistic stellar models cannot be described by simple polytropes (*i.e.*, with n constant). This is because they obey the full set of coupled differential equations which also include the energy conservation equation and a radiative transfer law. In addition, a fixed power of n ($= 1.5$) describes the equation of state only for fully ionized or non-relativistically degenerate gases, or alternatively for radiation-dominated or relativistically degenerate gases ($n = 3$). In physical situations, the index n varies as a function of radius, and the physical inputs to the problem (equation of state, opacity function, and nuclear energy generation rates) determine the local 'polytropic index', through the other equations of structure. Further, whereas spherically symmetric stars in hydrostatic equilibrium must necessarily follow the solutions of (2.1) for some value of n, some parts of the star can be described by solutions which are irregular, in the sense that they satisfy boundary conditions distinct from those given by (2.2).

It is easy to prove the following theorem (Fowler 1930):

Homology Theorem: The solutions to (2.1) obeying the conditions (2.2) form a homologous family. *That is, if $\theta(\xi)$ is a solution, then $A^{2/(n-1)}\theta(A\xi)$ is also a solution, for an arbitrary constant A. Further, all solutions with θ finite at the origin also satisfy $\theta' = 0$ at the origin.*

Thus, for fixed n, the members of this homologous family comprise all possible solutions to (2.1) with θ finite at the origin. The solution family is denoted $\{\theta_n(\xi)\}$, and its members are referred to as E-solutions; in the cases $n = 0$, 1 and 5, the E-solutions have closed form. As an example of two homologous solutions, one can cite the case of two gas spheres with different composition, obeying the relation (2.3) for some n. A second example is a set of gas spheres with different masses, again with n fixed.

In order to relate the discussion more easily to stellar interiors, it is convenient to transform the Lane-Emden equation into one of first order. That this is possible is clear from the homology theorem, since one constant of integration can be used to determine the scale A. For brevity and relevance, the range of n is restricted to $n < 5$ (in what follows), since, except for isothermal cores, burning shells, and ionization zones, this is the range of values most usually encountered in stellar interiors. [2]

The theorems which are summarized below are proved by referring the equation (2.1) to the (y, z) plane (Emden 1907), referred to below as the Emden plane. This transformation is included for completeness, and also because it is easiest to demonstrate the existence and nature of a singular point of the equation. Taking $\xi = \exp(-t)$, and setting

$$z = \xi^{\overline{\omega}}\theta, \tag{2.7}$$

[2] *N.B. isothermal structures have $P \propto \rho$; in the isothermal limit, $n \to \infty$.*

$$y = \frac{dz}{dt}, \tag{2.8}$$

where $\overline{\omega} = 2/(n-1)$, one obtains the transformed equation

$$y\frac{dy}{dz} + (2\overline{\omega} - 1)y + \overline{\omega}(\overline{\omega} - 1)z + z^{2/\overline{\omega}+1} = 0. \tag{2.9}$$

Both equations (2.1) and (2.9) are singular are the point $\xi = 0$, which corresponds to the origin $(y, z) = (0, 0)$ of the transformed plane. However, the E-solutions are regular at this point. For $n \leq 3$, the origin of the Emden plane is also encountered by a set of "irregular solutions", called the M-solutions, [3] for which $\theta \to \infty$ as $\xi \to 0$. Further, for $n > 3$, it is apparent on inspection that there exists a second singular solution, with constant z, *i.e.*,

$$z_s = [\overline{\omega}(1 - \overline{\omega})]^{\overline{\omega}/2}$$

or

$$z_s = \left(2\frac{(n-3)}{(n-1)^2}\right)^{1/(n-1)}, \tag{2.10}$$

for which θ has a power law behaviour close to the centre. It will be seen later that there exist infinitely many such solutions, which are analogues of the irregular solutions which pass through the origin if $n \leq 3$. The interested reader is referred to Chandrasekhar's (1939) monograph, and the paper by Hopf (1931), for diagrams of the appearance of solutions in the Emden plane.

A more insightful transformation, perhaps, is given by the (U,V) plane, which has also been used directly in calculating numerical models (Schwarzschild, Howard and Härm 1957; Schwarzschild 1958). Let

[3] *Historical aside: the names E- , M- and F- solution pay tribute to the research by Emden, Milne, and Fowler who investigated these equations in detail.*

$$U = -\frac{\xi\theta^n}{d\theta/d\xi} \tag{2.11}$$

$$V = -\frac{\xi d\theta/d\xi}{(n+1)\theta}. \tag{2.12}$$

These coordinates are related to the variables of stellar structure by

$$U = \frac{d\log M}{d\log r} = \frac{4\pi r^3\rho}{M} = 3\rho/\overline{\rho}, \tag{2.13}$$

where $\overline{\rho}$ is the mean density within the sphere of radius r, and

$$V = -\frac{d\log P}{d\log r} = \frac{GM\rho}{rP}. \tag{2.14}$$

(Compare Schwarzschild 1958 and Chandrasekhar 1939: the latter defines V slightly differently). It is easily seen that $(U,V) \to (3,0)$ as $\xi \to 0$, and that, as the surface is attained ($\rho \to 0$), the value of U drops toward zero whilst V must become very large. E-solutions on the (U,V) plane are plotted in Figure 2-2-1 , for values of n between 1.5 and 5.

After some manipulation, one obtains equations for the variables U and V as functions of ξ, as follows:

$$\frac{1}{U}\frac{dU}{d\xi} = -\frac{1}{\xi}(U + nV/(n+1) - 3) \tag{2.15}$$

$$\frac{1}{V}\frac{dV}{d\xi} = \frac{1}{\xi}(U + V/(n+1) - 1), \tag{2.16}$$

from which the (U,V) plane trajectories can be described by the differential equation

$$\frac{U}{V}\frac{dV}{dU} = -\frac{U + V/(n+1) - 1}{U + nV/(n+1) - 3}. \tag{2.17}$$

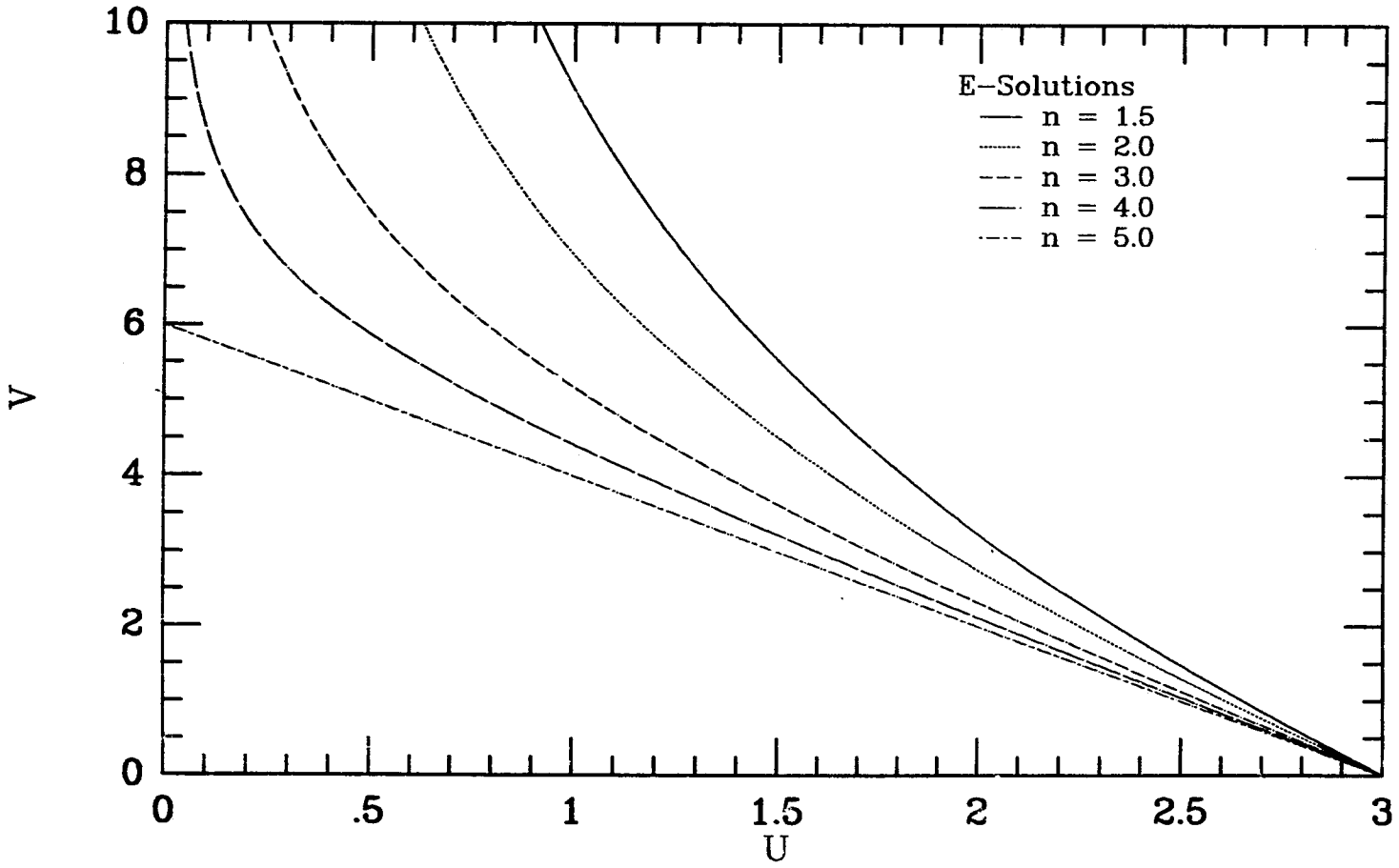

Fig. 2–2–1: E–solutions to the Lane–Emden equation plotted in the $U - V$ plane, for polytropic index n equal to 1.5, 2, 3, 4 and 5.

As discussed by Yahil and van den Horn (1985, hereafter YvdH), the topology of the (U, V) plane can be understood by noting the sign of the derivative (2.17) of solution curves, in regions bounded by the straight lines on which the right hand sides of (2.15) and (2.16) vanish. These lines intersect outside the physical range for $n < 3$, on the V-axis for $n = 3$, and at the point

$$(U_s, V_s) = \left(\frac{(n-3)}{(n-1)}, \frac{2(n+1)}{(n-1)}\right) \tag{2.18}$$

for $n > 3$, which corresponds to the singular point $(0, z_s)$ in the Emden plane. Thus, the singular-point solutions are associated with diverging θ as $\xi \to 0$, and cannot represent the structure of stars close to the core. As n varies, the locus of the singular point is given by

$$V_s = 4 - 2U_s \qquad (0 \leq U_s \leq 1/2). \tag{2.19}$$

By considering the behaviour of the solutions to (2.9) as they approach the singular points $(y, z) = (0, 0)$ and $(z_s, 0)$, and by noting the constraints that are placed upon solution curves by the coordinate derivatives y' and z', it is possible to prove additional theorems which classify the solutions to (2.1) (see Fowler 1930, Hopf 1931, Milne 1931; 1932, and Chandrasekhar 1939). Together with the results mentioned above, these can be summarized as follows:

The solutions to the Lane-Emden equation (2.1), for a given n, can be classified into three types:

(i) The homologous family $\{\theta_n(\xi)\}$ is the E-solution, which is finite at the origin $\xi = 0$ and takes a maximum value at that point. This solution is unique, apart from an arbitrary scaling factor.

The E-solution defines a critical curve in either the Emden, or the (U, V) plane, which divides the space of possible solutions into regions containing the two solution types described below. For example, if ξ_1 is such that

$\theta(\xi_1) = 0$ lies on an E-solution, then if $\xi_2 < \xi_1$ and some function $\phi(\xi)$, satisfying (2.1) has a zero $\phi(\xi_2) = 0$, then ϕ is an M-solution, as described in (ii). If $\xi_3 > \xi_1$ is such that $\eta(\xi_3) = 0$ and η is a solution of (2.1), then η is an F-solution, as described in (iii).

(ii) The M-solutions, whose properties vary considerably with n:

(a) $\theta \to \infty$ at the origin, with $\theta' \to -\infty$.

(b) On the Emden plane, the solutions lie wholly within the E-solution curve, and lie in the region between the positive U, V axes and the E-solution curve on the (U, V) plane.

(c) For $1 < n \leq 3$, the solutions tend to the origin on the (y, z) plane with $\xi \to 0$, and to the point $(n+1, 0)$ on the (U, V) plane.

(d) The behaviour of the solutions for $3 < n < 5$ is different, depending on whether n is less than, or greater than, a value $n^* = (11 + 8\sqrt{2})/7$. This arises from the solutions to (2.9) for $z \sim z_s + z_1, z_1 \ll 1$, which can be exponential or oscillatory. For $3 < n < 5$, the solutions tend, as $\xi \to 0$, to the singular point $(z_s, 0)$ on the Emden plane, and to $(U_s, V_s) = ((n-3)/(n-1), 2(n+1)/(n-1))$ on the (U, V) plane. For $n < n^*$, the solutions tend to the singular point exponentially, whereas for $n^* < n < 5$, the solution curves spiral around it. The solution is determined by initial conditions (*i.e.*, the value of ξ_0 such that $\theta(\xi_0) = 0$), so that there are infinitely many solutions which converge to this point.

(iii) The F-solutions, which have the following properties for each fixed value of n:

(a) There exists a finite value of $\xi > 0$, ξ_1, say, with $\theta(\xi_1) = 0$, $\theta'(\xi_1) > 0$, and at least one further value $\xi_2 > \xi_1$ such that $\theta(\xi_2) = 0$.

(b) The F-solutions lie wholly outside the corresponding E-solution in (y, z) coordinates, and wholly above the E-solution on the (U, V) plane.

All three solution classes arise in realistic stellar models, which are composite polytropes. The solution close to the centre is necessarily an E-solution; in the particular case of horizontal-branch models, which have central convection zones, the structure is close to that of a polytrope with index 1.5. In regions where radiation pressure and non-ideal corrections can be neglected, the polytropic index is related to the stellar structure variables by

$$\nabla = \frac{d\log T}{d\log P} \approx \frac{1}{(n+1)}, \tag{2.20}$$

and so takes a value close to 1.5 in a central convection zone. As the effective gradient becomes controlled by the radiative transfer equation, the value of ∇ decreases and n increases. However, as pointed out by Russell (1931), the E-solutions for a lower value of n lie outside those of higher n. Thus, the solution curve which is followed by a model with n increasing outward from the centre necessarily becomes an F-solution when the index changes. Conversely, if n were to decrease outward from the centre (for example, as occurs in a model with radiative core and a convective envelope), the solution curves smoothly match central E-solutions with outer M-solutions.

The (U, V) plane solutions for stellar interiors have been discussed in the last few years by YvdH and by Applegate (1988). However, the diversity of possible trajectory curves have not been fully appreciated by these authors, as will now be demonstrated. Two sets of M-solutions, for $n = 2.9$ and $n = 4.2$, are shown in Figures 2-2-2 and 2-2-3 . These figures illustrate curves for varying initial conditions, which correspond to different values of ξ at the outer boundary, which is attained as $(U, V) \rightarrow (0, \infty)$. Also shown are the 'cut lines' on which the derivatives of U and V with respect to the radius variable change sign. Thick arrows denote the sense in which the solution in each regime travels toward the outer boundary. In the diagrams and in the text that follows, the symbols dU, dV represent the derivatives $dU/d\xi$ and $dV/d\xi$. For the lower value of n, there is

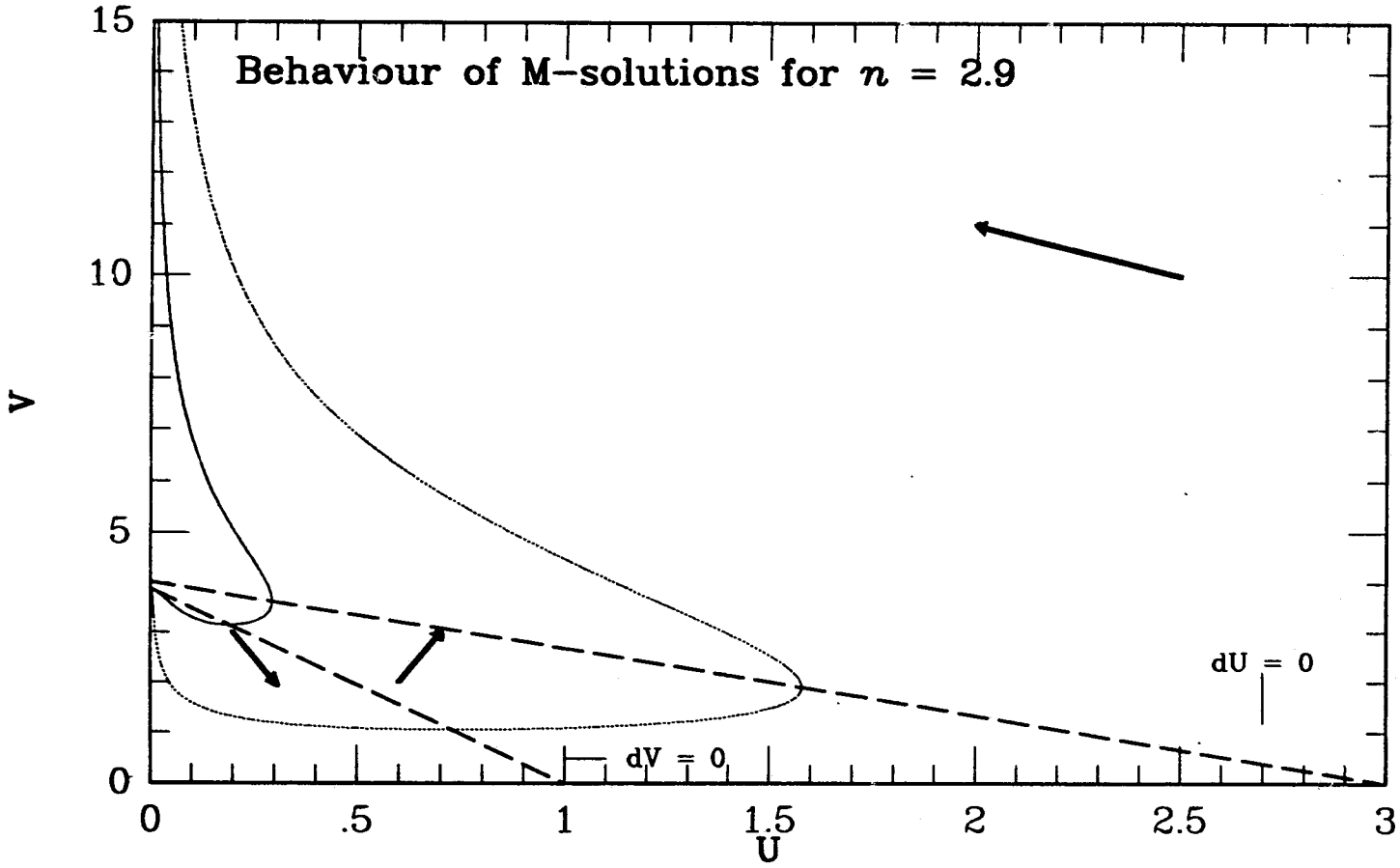

Fig. 2–2–2: M–solutions for n = 2.9. Both curves have the same value of the scaled radius variable ξ at the outer boundary, $\xi_0 = 4$, and $V_i = 20$. Solid curve: $U_i = 0.005$. Dotted curve: $U_i = 0.03$.

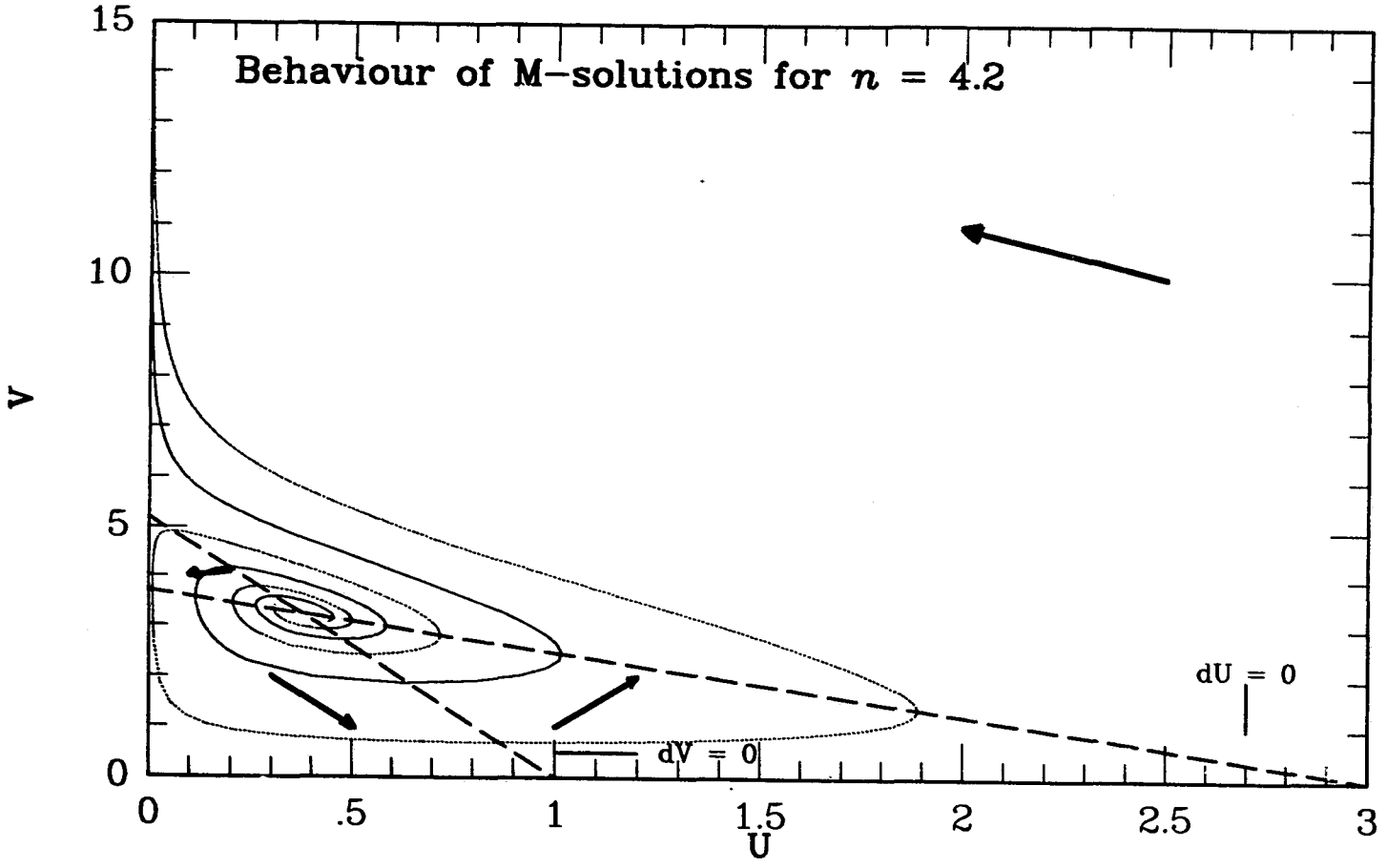

Fig. 2–2–3: M–solutions for $n = 4.2$. The solid curve has $(\xi_0, U_i, V_i) = (4, 0.0001, 20)$, and the dotted curve has $(\xi_0, U_i, V_i) = (7, 0.001, 8)$.

no singular point in the positive (physical) quadrant of the (U, V) plane, and thus no regime in which $dU < 0$ and $dV < 0$. The solution curves here show how the sensitivity to boundary values can produce solutions which, although apparently very similar at each boundary, can be strongly divergent within the physical range of the solution. A fuller discussion of these papers is provided in §2.5.v, where the early evolution on the Asymptotic Giant Branch is studied.

So far, this discussion is valid for homogeneous stellar models. Horizontal branch stars (and red-giant stars) contain a zone in which the composition profile is nearly discontinuous, separating the helium-rich core and the hydrogen-rich envelope. Further, as will be seen, variation in the strength of the hydrogen-burning source at the base of the hydrogen-rich envelope can produce important changes in the solution. At such a chemical discontinuity, the structure variables $(R, L, P, T; M)$ are continuous, so that [4]

$$\left[\frac{d\log T}{d\log P}\right]_{int} = 0. \tag{2.21}$$

but the density is not, as can be most easily appreciated by reference to the ideal gas law. That is, if P and T are continuous, then

$$[\rho/\mu]_{int} = 0,$$

so that, as μ decreases in passing from heavier to lighter material, both U and V are displaced toward the origin. If the discontinuity is sufficient to force the solution curve across the critical E-solution at the appropriate local value of n, then the structure in the outer part of the star will be described by an M-solution. After such a sharp decrease in U and V, the nature of the solution immediately

[4] *The large square brackets denote the change in the enclosed quantity across a discontinuity. The subscript int will refer to the value of a quantity at the upper edge of the discontinuity.*

exterior to the inhomogeneous region will depend on two factors: firstly, the local value of n in that region, and secondly, whether the exterior solution matches the interior solution on the upper or lower part of the 'loop' which is described by any of the curves exemplified in Figures 2-2-2 and 2-2-3. That is, if the match in the (U, V) plane occurs at a point below the line where dU vanishes, then the solution will describe a loop in the plane. Thus the line $dU = 0$ represents a cut in the (U, V) plane for any value of n; for fixed n, and *for some choice of boundary conditions* (U_i, V_i) , the interior and exterior solutions will match below the cut line [5].

In the next section, these theoretical considerations will be applied to realistic stellar models. It will be shown how, for horizontal branch interiors, the hydrogen burning shell determines the matching condition between the composite solutions which apply in the inner and outer part of the star.

---

[5] *The numerical solutions plotted in (2-2-2) and (2-2-3) have been generated by assuming pairs of values* (U_i, V_i) *such that* $U \sim 0$ *and* $V \sim 20$. *The larger values of* U_i *are of order* 10^{-2}; *the resulting solution curves correspond to choices of the outer radius variable* ξ_0 *which are closer to the value at the boundary of the critical E-solution curve. As* $\xi_0 \rightarrow \xi_1 : \theta_n(\xi_1) = 0$, *the M-solutions turn into the E-solution.*

2.3 On the Variation of Zero Age Models with Mass

2.3.i The polytropic structure of ZAHB models

The object of this section is to show how the hydrostatic structure of the outer layers of the helium core region of horizontal branch stars react to varying hydrogen shell strengths, using the theory summarized in the previous section. In particular, it is demonstrated that models of red horizontal branch stars have solution curves which contain loops in the (U, V) plane. Further, the 'horizontal' morphology of this phase of evolution (*i.e.*, the shape of the sequence formed by models of decreasing envelope mass, every other parameter being held constant) arises from the rapid changes across models of differing mass of the polytropic index at the core-shell interface. These changes occur as the matching between core and envelope solutions switches from being below to above the cut line described in the previous section. In the following section, the effects of different parameters on the magnitude of the hydrogen shell burning source will be investigated.

The first task is show that different HB model structures appear in the framework of the composite polytropic models discussed earlier. In order to do this, ZAHB models have been constructed with very high resolution through the shell-burning region (see discussion in chapter 4). Zero-age models are chosen because they contain only one chemical discontinuity, which greatly simplifies this analysis.

A set of models of fixed composition ($Y_{HB} = 0.246$, [Fe/H] $= -2.26$, [O/Fe] $= 0.75$) has been chosen from those available. Figure 2-3-1 shows the (U, V) plane trajectories for masses $M = 0.90, 0.78, 0.72, 0.68, 0.62$ and $0.54\ M_{\odot}$. The E-solutions for various values of n are superimposed upon these graphs. Figure 2-3-2 shows an expanded view of the region of the (U, V) plane which corresponds to the outer part of the hydrogen-burning shell. In Figure 2-3-3 , the $(\log P, \log T)$ plane for these models is illustrated. These figures are extremely important, because they show unambiguously that the core structure is significantly affected by the

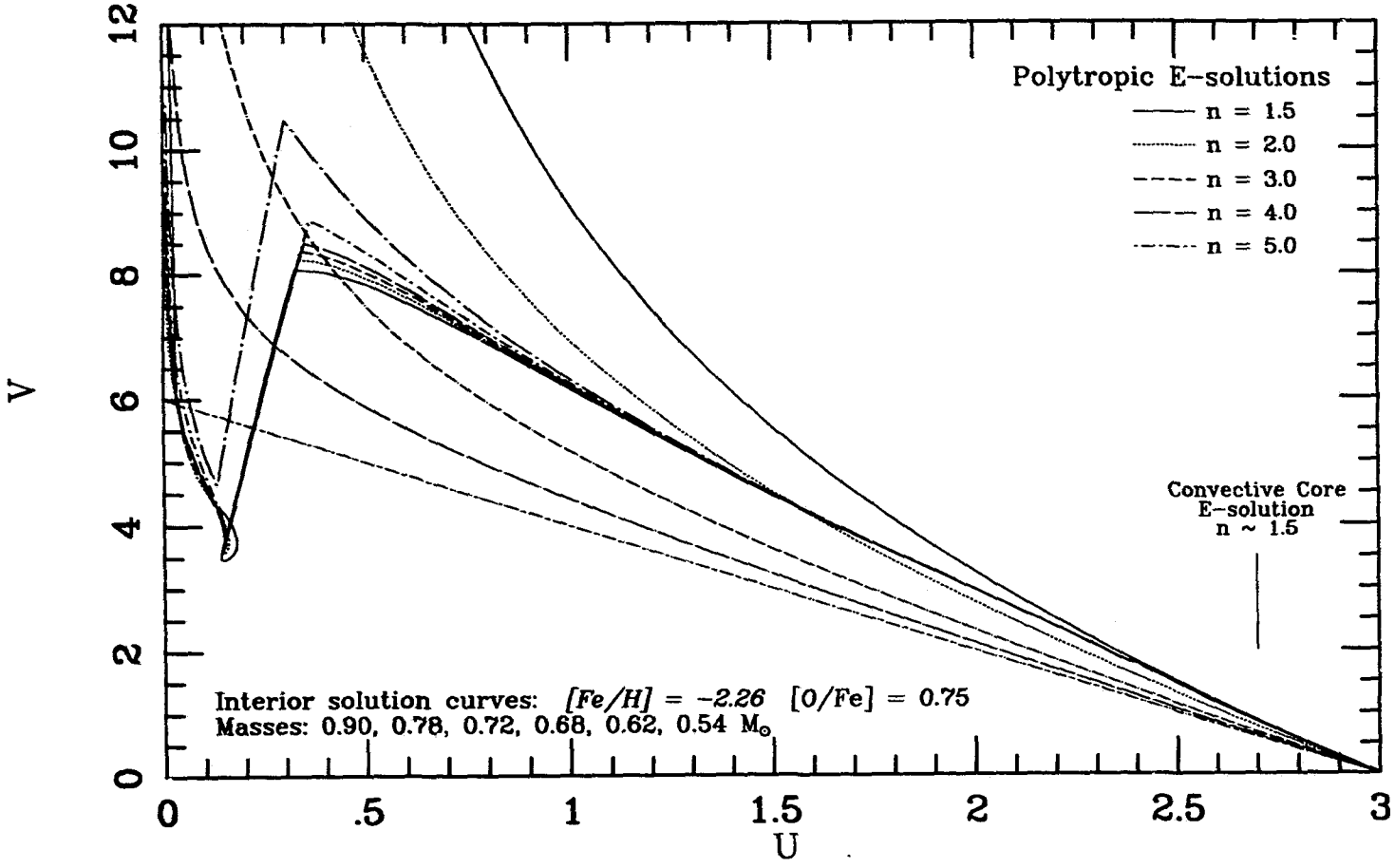

Fig. 2–3–1: *U–V* plane trajectories for ZAHB stellar models, plotted with the polytrope solutions of 2–2–1. The models have $Y_{HB} = 0.246$, [Fe/H] = –2.26, [O/Fe] = 0.75. The masses of the unlabelled solution curves, in solar units, are 0.90 (solid curve), 0.78 (dotted curve), 0.72 (short dash curve), 0.68 (long dash curve), 0.62 (short dash–dot curve), and 0.54 (long dash–dot curve).

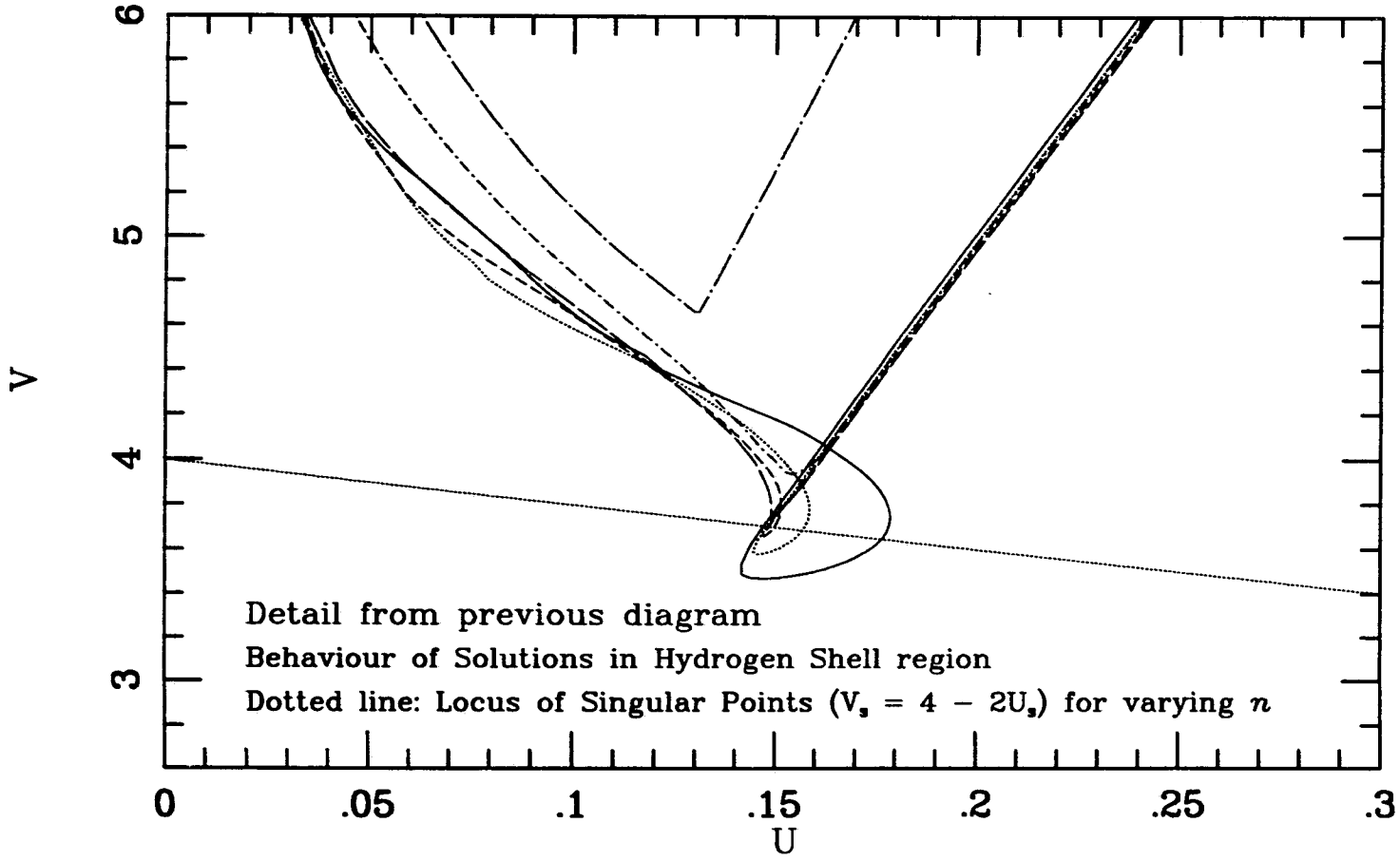

Fig. 2–3–2: Expanded view of the previous diagram. The region above the shell source is shown. The straight line marks the locus of singular points for varying n, $V_s = 4 - 2U_s$.

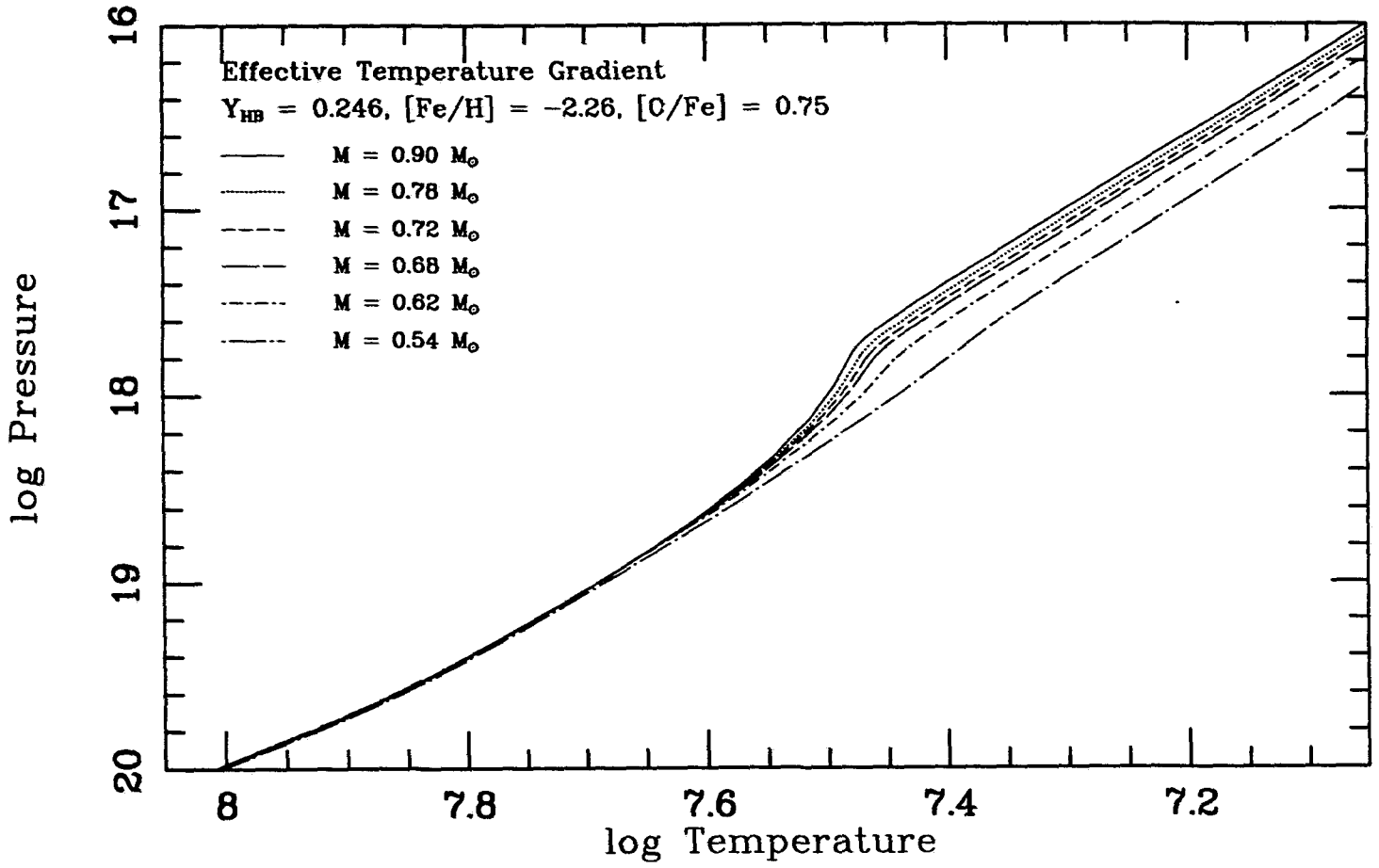

Fig. 2–3–3: The Temperature–Pressure relationship for the models shown in Figure 2–3–1. The change in slope of the curves decreases with mass, and occurs immediately below the core–envelope interface region.

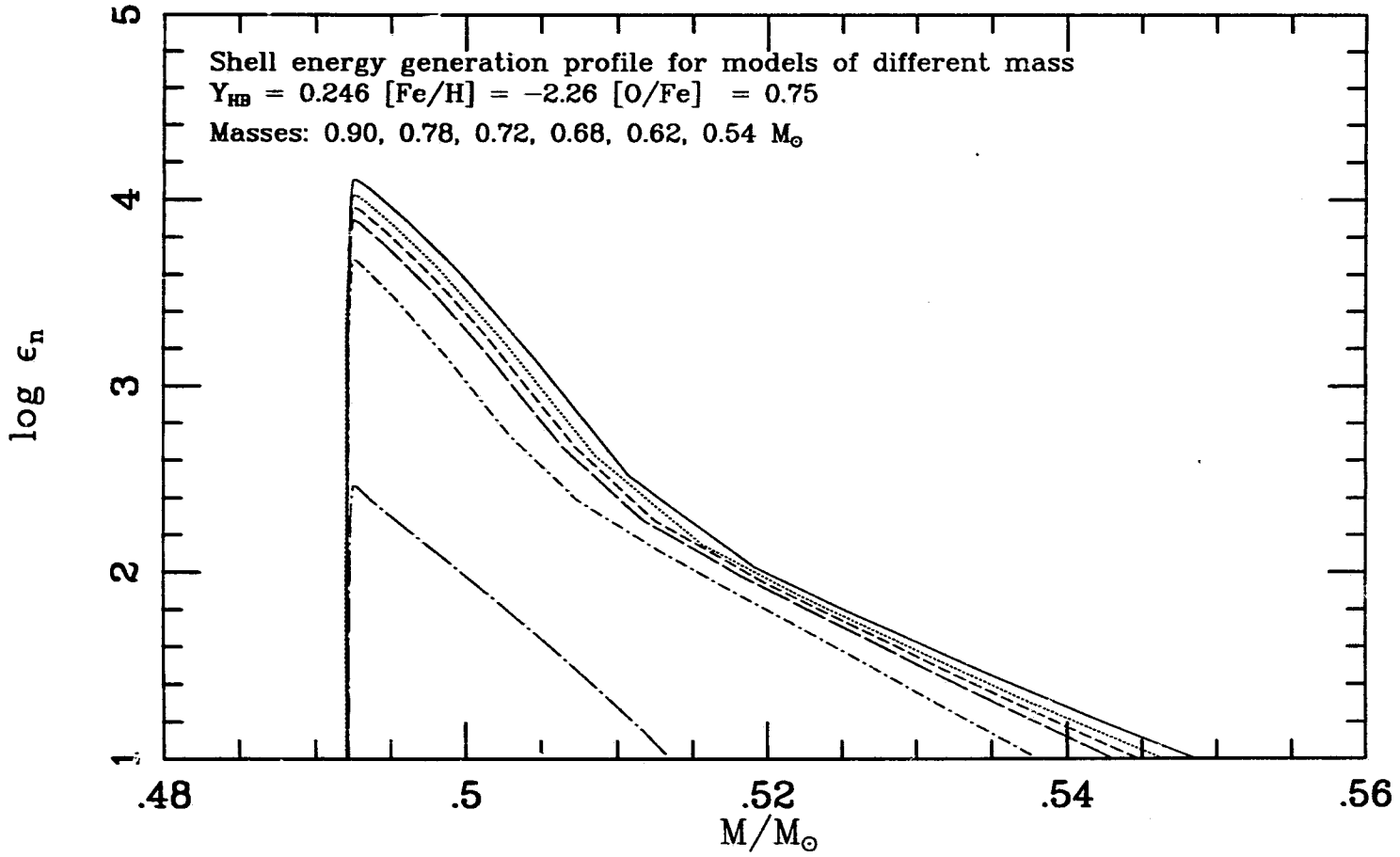

Fig. 2–3–4: The rate of energy generation in the hydrogen burning shell for the models show in Figure 2–3–1.

hydrogen shell source. The pronounced change in slope of these curves for the more massive models occurs *below* the interface between the helium-rich core and the hydrogen-rich envelope. The change in the slope decreases with the mass of the envelope, and this provides the key to understanding the complexity of horizontal branch models. Figure 2-3-4 shows the energy generation profile for the shell sources of these models, illustrating the run of nuclear energy released against mass.

Table 2-3-1: Zero Age Horizontal Branch: Bulk properties
$Y = 0.247$, $Z = 0.0001$, [O/Fe] $= 0.75$, $M_c = 0.4923$

$M/M_\odot$	$\log L/L_\odot$	$\log T_{eff}$	$\log R_s$	$\log g_s$	$\log T_c$	$\log \rho_c$
0.5400	1.3083	4.2691	10.4851	4.8851	8.0726	4.2737
0.5600	1.3523	4.2194	10.6066	4.6579	8.0734	4.2669
0.5800	1.4119	4.1693	10.7365	4.4134	8.0738	4.2632
0.6200	1.5352	4.0549	11.0270	3.8613	8.0739	4.2623
0.6400	1.5808	3.9964	11.1667	3.5957	8.0738	4.2629
0.6600	1.6162	3.9413	11.2946	3.3532	8.0738	4.2634
0.6800	1.6447	3.8891	11.4133	3.1288	8.0737	4.2640
0.7000	1.6677	3.8412	11.5206	2.9268	8.0736	4.2645
0.7200	1.6870	3.7984	11.6158	2.7486	8.0736	4.2649
0.7400	1.7033	3.7714	11.6780	2.6361	8.0735	4.2654
0.7800	1.7298	3.7531	11.7279	2.5592	8.0735	4.2660
0.9000	1.7862	3.7404	11.7815	2.5141	8.0732	4.2678
1.0000	1.8224	3.7369	11.8067	2.5096	8.0731	4.2689
1.1000	1.8556	3.7365	11.8239	2.5165	8.0730	4.2702
1.2000	1.8883	3.7377	11.8378	2.5264	8.0728	4.2714
1.3000	1.9216	3.7404	11.8491	2.5386	8.0727	4.2727
1.4000	1.9564	3.7437	11.8599	2.5493	8.0725	4.2741
1.5000	1.9928	3.7493	11.8669	2.5651	8.0724	4.2756

Table (2-3-1) lists the important properties of a set of ZAHB models which are used in this section as examples. In this table, the first two columns give the mass and luminosity of the star both in solar units (all tabulated quantities, apart

from the first column are logarithmic). The third, fourth and fifth column list the effective temperature (K), radius (cm), and surface gravity (cm s^{-2}), whilst the last two give the central temperature (K) and density (g cm^{-2}).

Tables (2-3-2 a to d) represent 'case studies' for four of the solutions, at 0.90, 0.72, 0.68, and 0.54 $M_{\odot}$, with values of the physical variables of interest for the region enclosing the core-shell interface and the 'loop' illustrated in Figures 2-3-1 and 2-3-2. In the first column, the mass coordinate in solar units is listed; the second and third columns give, respectively the logarithm of the pressure and temperature variables in the appropriate cgs units. The fourth column contains the value of n, as calculated from the equilibrium temperature gradient ∇ at that point in the star. The next two columns list U and V, whilst the final two give the logarithm of the density, and the hydrogen mass fraction.

Figure 2-3-1 illustrates the whole stellar interior. The most obvious features of this diagram are the 'regular' interior solutions seen as U decreases from its central value of 3, the discontinuous region which corresponds to the point where the chemical composition is changing rapidly, and the small loops present for the more massive stars. All of the curves are close to the $n = 1.5$ polytropic structure within the convective core region; indeed, the solutions are very similar for the range $3 \geq U \gtrsim 1.5$. Also, for each curve, n increases outward from the convective core, varying slowly, so the models become composite F-solution curves as n increases.

For the more massive models, n reaches very large values in the outer parts of the core. As mentioned above, this represents a very important change in the hydrostatic structure of the core, as can clearly be seen in Fig. 2-3-1, resulting from a significant drop in the temperature gradient (*cf.* Fig. 2-3-3, and Table 2-3-1a: recall that steep gradients correspond to low values of $n \propto 1/\nabla - 1$). This is caused by the bright burning source, which acts to resist and therefore reduce

Table 2-3-2: Stellar Profile above Helium-Rich Core

(a) Mass = 0.90 $M_\odot$ Y_{HB} = 0.246 [Fe/H] = −2.26 [O/Fe] = 0.75

$M_r/M_\odot$	log P	log T	n	U	V	log ρ	X
0.7167	14.1864	6.6076	3.2266	0.1658	4.0301	−0.5713	0.754
0.7070	14.3273	6.6410	3.2105	0.1688	3.9921	−0.4639	0.754
0.6849	14.6453	6.7170	3.1489	0.1745	3.9076	−0.2218	0.754
0.6635	14.9476	6.7905	3.0901	0.1778	3.8272	0.0071	0.754
0.6407	15.2688	6.8694	3.0566	0.1789	3.7468	0.2493	0.754
0.6205	15.5578	6.9408	3.0429	0.1782	3.6834	0.4670	0.754
0.6091	15.7244	6.9821	3.0331	0.1770	3.6503	0.5923	0.754
0.5890	16.0259	7.0571	3.0123	0.1735	3.5970	0.8187	0.754
0.5787	16.1848	7.0968	3.0033	0.1710	3.5723	0.9380	0.754
0.5705	16.3153	7.1294	2.9951	0.1687	3.5533	1.0358	0.754
0.5515	16.6285	7.2079	2.9935	0.1620	3.5097	1.2695	0.754
0.5345	16.9283	7.2829	3.0051	0.1550	3.4843	1.4940	0.754
0.5191	17.2200	7.3556	3.0265	0.1479	3.4711	1.7128	0.753
0.5107	17.3879	7.3972	3.0624	0.1442	3.4742	1.8399	0.752
0.5045	17.5172	7.4286	3.1979	0.1419	3.4885	1.9390	0.746
0.4997	17.6200	7.4522	3.6231	0.1418	3.5359	2.0226	0.732
0.4962	17.6969	7.4675	4.5800	0.1442	3.6219	2.0914	0.709
0.4939	17.7485	7.4758	6.3399	0.1477	3.7149	2.1421	0.687
0.4936	17.7548	7.4766	6.7125	0.1483	3.7284	2.1485	0.684
0.4933	17.7611	7.4774	7.1461	0.1488	3.7422	2.1549	0.681
0.4930	17.7674	7.4781	7.6564	0.1494	3.7564	2.1614	0.678
0.4927	17.7741	7.4789	8.3269	0.1504	3.7798	2.1693	0.673
0.4926	17.7762	7.4791	8.6324	0.1529	3.8418	2.1780	0.653
0.4925	17.7782	7.4793	8.9532	0.1555	3.9055	2.1868	0.633
0.4924	17.7815	7.4796	181	0.1823	4.5767	2.2582	0.453
0.4923	17.7827	7.4797	11.079	0.2105	5.2790	2.3213	0.312
0.4922	17.7859	7.4800	13.039	0.3019	7.5474	2.4793	0.038
0.4919	17.7918	7.4804	12.829	0.3255	8.0749	2.5140	0.000
0.4889	17.8559	7.4853	11.135	0.3550	8.0717	2.5728	0.000
0.4727	18.1296	7.5145	6.5839	0.5045	7.8328	2.8137	0.000

the temperature gradient in this region. As the luminosity of the model increases outward with the energy production, the temperature gradient must steepen in order to be able to carry the increased flux, and as the luminosity variable L_r

Table 2-3-2 (continued)

(b) Mass = 0.72 $M_\odot$ Y_{HB} = 0.246 [Fe/H] = −2.26 [O/Fe] = 0.75

$M_r/M_\odot$	log P	log T	n	U	V	log ρ	X
0.5948	15.7202	6.9649	3.0929	0.1445	4.0429	0.6056	0.754
0.5809	16.0010	7.0338	3.0680	0.1484	3.9600	0.8175	0.754
0.5674	16.2678	7.0996	3.0452	0.1508	3.8874	1.0184	0.754
0.5535	16.5427	7.1677	3.0306	0.1518	3.8147	1.2245	0.754
0.5392	16.8261	7.2380	3.0334	0.1514	3.7503	1.4369	0.754
0.5260	17.0918	7.3039	3.0427	0.1500	3.7016	1.6363	0.753
0.5199	17.2170	7.3348	3.0513	0.1492	3.6841	1.7306	0.753
0.5126	17.3682	7.3721	3.0732	0.1482	3.6689	1.8450	0.753
0.5073	17.4798	7.3994	3.1200	0.1474	3.6598	1.9296	0.751
0.5014	17.6063	7.4295	3.3464	0.1472	3.6683	2.0276	0.744
0.4980	17.6805	7.4459	3.7815	0.1486	3.7050	2.0890	0.732
0.4948	17.7491	7.4590	4.8323	0.1516	3.7755	2.1501	0.714
0.4932	17.7845	7.4646	6.0903	0.1543	3.8327	2.1842	0.701
0.4929	17.7900	7.4654	6.3829	0.1548	3.8444	2.1898	0.699
0.4927	17.7944	7.4660	6.6888	0.1569	3.8937	2.1988	0.683
0.4925	17.7989	7.4665	7.0239	0.1590	3.9443	2.2079	0.668
0.4925	17.8005	7.4667	7.3205	0.1663	4.1235	2.2285	0.613
0.4924	17.8019	7.4669	7.6983	0.1781	4.4146	2.2592	0.533
0.4924	17.8024	7.4669	7.8518	0.1835	4.5479	2.2725	0.500
0.4923	17.8032	7.4670	8.2687	0.2003	4.9607	2.3110	0.408
0.4923	17.8043	7.4671	8.8717	0.2288	5.6624	2.3693	0.283
0.4923	17.8047	7.4672	9.1440	0.2436	6.0281	2.3969	0.229
0.4922	17.8053	7.4672	9.5070	0.2660	6.5770	2.4352	0.160
0.4922	17.8064	7.4673	10.002	0.3027	7.4756	2.4919	0.068
0.4919	17.8128	7.4679	9.9824	0.3421	8.3770	2.5471	0.000
0.4894	17.8653	7.4729	8.9756	0.3669	8.3498	2.5942	0.000
0.4820	18.0015	7.4883	6.9807	0.4377	8.2145	2.7134	0.000
0.4725	18.1477	7.5086	5.5626	0.5239	7.9682	2.8371	0.000

increases rapidly, n decreases sharply back towards the range of values necessary for structures with finite radii. In the (U, V) plane diagrams used here and later, the point where the solution trajectory resumes smooth behaviour corresponds to the point at which the composition attains its (homogeneous) outer envelope

Table 2-3-2 (continued)

(c) Mass = 0.68 $M_\odot$ Y_{HB} = 0.246 [Fe/H] = −2.26 [O/Fe] = 0.75

$M_r/M_\odot$	$\log P$	$\log T$	n	U	V	$\log \rho$	X
0.5715	16.1222	7.0562	3.0765	0.1410	4.0833	0.9164	0.754
0.5603	16.3647	7.1158	3.0511	0.1447	4.0041	1.0989	0.754
0.5481	16.6242	7.1800	3.0450	0.1473	3.9215	1.2935	0.754
0.5356	16.8872	7.2451	3.0472	0.1488	3.8518	1.4910	0.754
0.5239	17.1318	7.3055	3.0557	0.1492	3.7958	1.6748	0.753
0.5182	17.2539	7.3355	3.0647	0.1493	3.7741	1.7669	0.753
0.5118	17.3899	7.3689	3.0867	0.1493	3.7538	1.8699	0.753
0.5065	17.5036	7.3966	3.1375	0.1491	3.7392	1.9560	0.751
0.5013	17.6147	7.4230	3.3209	0.1495	3.7395	2.0419	0.745
0.4946	17.7610	7.4537	4.7069	0.1541	3.8296	2.1656	0.719
0.4933	17.7883	7.4582	5.5113	0.1560	3.8665	2.1910	0.711
0.4927	17.8022	7.4603	6.1306	0.1574	3.8963	2.2053	0.704
0.4925	17.8075	7.4610	6.6352	0.1679	4.1509	2.2369	0.625
0.4924	17.8086	7.4611	6.9169	0.1780	4.4010	2.2632	0.555
0.4923	17.8107	7.4614	7.7722	0.2181	5.3843	2.3525	0.344
0.4922	17.8139	7.4617	9.1617	0.3216	7.9125	2.5225	0.041
0.4919	17.8196	7.4623	8.9753	0.3486	8.5101	2.5594	0.000
0.4836	17.9800	7.4807	6.7070	0.4294	8.3449	2.6997	0.000
0.4746	18.1229	7.5011	5.4145	0.5120	8.0911	2.8200	0.000

value. The brighter shells are, for fixed composition, wider in extent, and thus the gradient continues to steepen outward of the core-shell interface for a greater range in mass. As a result n reaches lower values and the solution possesses a small loop in the (U, V) plane as will be discussed below. As the shell strength increases further, the loop increases in size and contains progressively more mass, and the distribution of material in the envelope region above the shell is considerably modified.

It has been shown above that a necessary and sufficient condition for the existence of a loop is that the solution curve must have $dU > 0$ in a region where the

Table 2-3-2 (continued)

(d) Mass = 0.54 $M_\odot$ Y_{HB} = 0.243 [Fe/H] = −2.26 [O/Fe] = 0.75

$M_r/M_\odot$	$\log P$	$\log T$	n	U	V	$\log \rho$	X
0.5284	15.9595	6.9622	3.2080	0.0600	6.0770	0.8481	0.754
0.5245	16.2486	7.0312	3.1687	0.0716	5.7567	1.0680	0.754
0.5180	16.6293	7.1230	3.1441	0.0876	5.3756	1.3560	0.754
0.5139	16.8265	7.1706	3.1487	0.0962	5.2007	1.5049	0.754
0.5047	17.2059	7.2620	3.1515	0.1129	4.9090	1.7919	0.753
0.4992	17.4011	7.3090	3.1660	0.1215	4.7813	1.9401	0.753
0.4939	17.5756	7.3508	3.1969	0.1290	4.6732	2.0724	0.752
0.4932	17.5968	7.3558	3.2050	0.1299	4.6602	2.0885	0.752
0.4926	17.6166	7.3605	3.2360	0.1324	4.7056	2.1087	0.736
0.4925	17.6208	7.3615	3.2951	0.1371	4.8622	2.1264	0.692
0.4925	17.6216	7.3617	3.3259	0.1396	4.9488	2.1347	0.669
0.4924	17.6245	7.3624	3.5419	0.1587	5.6155	2.1920	0.517
0.4923	17.6253	7.3625	3.6429	0.1688	5.9687	2.2193	0.451
0.4923	17.6278	7.3631	4.0291	0.2168	7.6448	2.3289	0.220
0.4922	17.6291	7.3633	4.2003	0.2456	8.6478	2.3836	0.124
0.4921	17.6316	7.3638	4.3721	0.2850	10.000	2.4490	0.025
0.4919	17.6389	7.3652	4.1721	0.3017	10.467	2.4757	0.000
0.4883	17.7413	7.3855	3.9034	0.3420	10.123	2.5568	0.000
0.4784	17.9617	7.4324	3.5405	0.4428	9.3313	2.7280	0.000
0.4732	18.0557	7.4534	3.4401	0.4920	8.9787	2.7998	0.000

composition is homogeneous. For this reason, the line $dU = 0$ is referred to below as *the* cut line in the (U, V) plane. This criterion is obviously strongly dependent on the value of n, n_{int}, at the point (U_{int}, V_{int}) where the solution resumes smooth behaviour. Consider the possible solution trajectories as a function of n at this point. The simplest case is where $n_{int} < 3$. Then there exists a loop if and only if the point lies below the cut. If $n_{int} > 3$, then there are two possibilities: If it is close to 3, the singular point lies close to the V-axis, and the solution crosses the line $dU = 0$ before $dV = 0$. The locus of the singular points (2.19) has some utility

here; for small enough n_{int} [6] a loop occurs if and only if this line is traversed. This is the case for all the solutions plotted in 2-3-2 and 2-3-5. For much larger n_{int}, *i.e.*, for values closer to 3.5, the solution may cross the line $dV = 0$ first, in which case it will begin to spiral toward the V-axis, but if the change in n as the solution continues its path is not too rapid, it will then enter the region $dU > 0$, and so contain a loop.

For zero age sequences, then, there exists some value of the total mass for which models with redder colours possess (U, V) plane loops. In the models studied here, the loop appears between 0.68 and 0.70 $M_{\odot}$ and attains significant size for a mass of about 0.72 $M_{\odot}$. In this mass range, the models cross the entire temperature range of the RR Lyrae instability strip (see chap. 4). In other words, this most 'horizontal' part of the HB, marked by a rapid relocation of models to the red with mass, is caused by a important structural change within the stars. It is *precisely* where the density distribution changes significantly in the region just above the shell source, forcing the outer layers of the star to lower densities, temperatures and thus redder colours[7]. As the solution curves move away from the cut line with decreasing mass, the corresponding models move rapidly to higher surface temperatures. The low luminosity, combined with high temperatures, indicates that these objects have relatively small radii; models evolving from red to blue must also suffer envelope contraction. The total stellar luminosity is bounded below by the core luminosity, which is maintained (to order of magnitude) even by the least massive objects modelled here. In this way, the mass luminosity relationship for HB stars changes slope blueward of the point in the sequence where the loops vanish.

This variation in solution type occurs across the horizontal branch for each

---

[6] *i.e.*, n_{int} *is such that* $U_{int} > U_s(n_{int})$.

[7] *The terms 'red' and 'low temperature' will often be used interchangeably throughout this study; similarly 'blue' and 'high temperature'.*

fixed composition, but the (U, V) solution curves are too complex in general to provide insight in the differences caused by varying abundances. It is already clear that, even at fixed Z, each solution is subject to strong variations in the run of n. Secondly, for fixed polytropic index, variations in the outer boundary conditions to the solution can produce a wide variety of possible structures (recall Figs 2-2-2 and 2-2-3). For the cores, the situation is much less complex; the models have similiar solutions in the convective core, and the structure of their outer layers depends on the hydrogen-shell strength, as described above. However, using knowledge gained from other phases of stellar evolution it is possible to predict the sense of the changes which will result from varying metallicity. These predictions may be confirmed by the inspection of stellar interior profiles in appropriate co-ordinates.

The data presented in Tables (2-3-2) show how the structure of model envelopes responds to the presence of varying hydrogen shell strength. The first Table, 2-3-2a, gives data for a model at the red end of the HB, containing a significant loop where n reaches a value just below 3. Note that the cut line moves upward in the plane with decreasing n. For the data given in Table (2-3-2b), location of the loop can be determined graphically by reference to equation (2.19); since the loop is very small, the solution curve only marginally crosses the cut. Therefore its lowest point at approximately $(U, V) \sim (0.148, 3.706)$ implies that the local index is $n_{eff} \sim 3.35$, an estimate which agrees very well with the value in Table 2-3-2b at the appropriate point. Finally, in the very low mass model presented in Table (2-3-2d), the shell region lies well away from the cut lines for the appropriate values of n, which experiences only relatively small changes. The temperature gradient in the outer part of the core is hardly modified by the shell source, and the value of $\log T_{int}$ is consequently much lower. It is clear also that the outer boundary condition ($U \to 0, V \to \infty$ as $M \to M_*$), together with the hydrostatic equilibrium condition, places a severe constraint on the hydrogen shell burning strength. If the envelope is too thin, then it is not possible to produce

a strong nuclear energy zone and satisfy the outer boundary conditions, as there is not enough mass inside the star. Indeed, for the lowest mass illustrated here, the effect of the burning shell upon the interior structure is almost negligible, generating under one percent of the total stellar luminosity. It appears that the sensitivity of the solution to the total mass of the star directly corresponds to the dependence of the matching condition on the outer boundary values for idealized solutions (*i.e.*, those with fixed n). The models which have strongly radiative envelopes have relatively high surface densities and pressures, and thus correspond to solutions with large boundary values of U. But these solutions, if carried inward, have very large (U, V) plane loops, which, as discussed in more detail below, must contain large quantities of mass. Hence, the solutions must match above the cut. A corollary to this statement is, that if the envelope is sufficiently massive, such solutions (with large U_i, V_i) may exist.

From the definition of U, it is seen that the looping behaviour implies an inflection point in the density distribution. U stays relatively large, and V relatively small in the region of the loop, so that the density decreases less rapidly with decreasing pressure. It can be seen from Table (2-3-2a) that the loop, with a relatively large value of n, contains a large amount of mass, and that the solution proceeding to the boundary at large V and small U begins its ascent at lower temperature and density than is the case for models without the loop. This guarantees a tenuous outer zone; as the opacity rises rapidly with decreasing temperature here, a point is reached where the outermost material becomes convective, conforming to an M-solution with index $n = 1.5$.

For larger masses, the shell increases in strength and width, the core-envelope interface region becomes more nearly isothermal, and the width of the loop increases and contains more mass. As a result, the temperatures and densities attained at the outer boundary are both reduced, which forces a surface convection zone if the temperatures reached are sufficiently low. Towards the surface,

the opacity rises sharply as the metal ionization zones are reached, and n falls rapidly to its adiabatic value. Since the temperature gradient in the envelope is approximately fixed where adiabatic convection takes place, the value of T_{eff} becomes a function of the convective zone depth, which is a relatively weak function of mass.

For still higher masses, the movement of the model in the HR diagram back to the blue results from changes in the opacity in the upper part of the envelope, which are in turn the result of changes in the gradient throughout the hydrogen rich layers. The shell temperature increases steadily with mass, and the gradient also becomes steeper with the increase in luminosity. A point is reached where the temperature in a high opacity region rises, rather than falls, with increased mass. This results in a smaller convection zone depth. It has previously been shown that models with $M \gtrsim 1\,M_{\odot}$ begin their core-helium-burning evolution at locations which lie above the HB, forming a sequence of objects which increase in temperature with mass: this is regime III defined by Lauterborn, Refsdal and Stabell (1972).

Figure 2-3-5 illustrates a set of such models, with masses between 1.00 and 1.50 $M_{\odot}$. The larger loops have very thick shells in which n holds a constant, relatively low value, and the temperature gradient in the envelope is steeper throughout. The inner boundary of the convection zone moves outward with mass, and the surface temperature slowly increases. With more of the energy being produced by the hydrogen shell, the core luminosity decreases in absolute size with increasing mass. This diagram also implies that the existence of a loop in the (U, V) plane may not necessarily give rise to a distended convective envelope, if the envelope mass is sufficiently great; the existence of blue giants undergoing central helium burning (*cf.* Weiss 1989) may provide such an example. However, the work of YvdH shows that even for models as massive as 5 $M_{\odot}$, the loop may grow to contain enough mass to force the outer layers into convection as the evolution

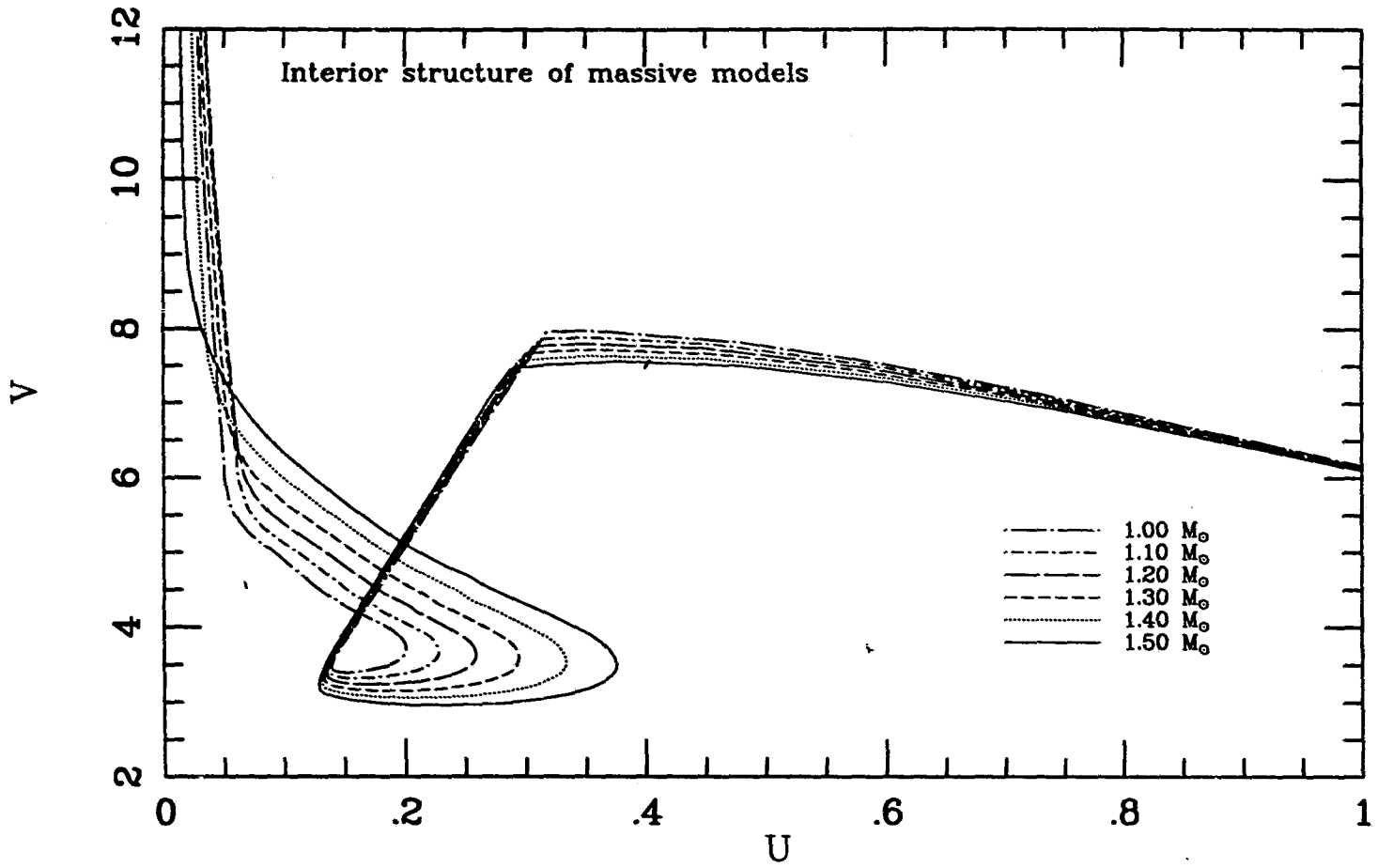

Fig. 2–3–5: *U–V* plane trajectories for models with higher masses. The composition and core mass parameters of these models are similar to those plotted in 2–3–1, but the masses are 0.90, 1.00, 1.10, 1.20, 1.30, 1.40 and 1.50 Mo.

proceeds.

The difference in gradients in the outer part of the core forces a higher temperature at the interface for the more massive models, and a very slight increase in the radius implying a lower value of ρ_{int}. The dependence of core strength on the equilibrium configuration of the outer core is evidenced by the fact that the core luminosity peaks in the 'horizontal' part of the sequence. As the shell sources (and the models) become brighter with increasing mass, the core luminosity drops slightly, due to a small decrease in the central temperature, mitigated by a slight increase in central density; this effect continues at least through the entire mass range illustrated by Figure 2-3-5. But the effect is slight; as the shell-burning strength changes by orders of magnitude across the mass sequence, the core luminosity varies by at most 20%.

In sum, the dependences appear to be:

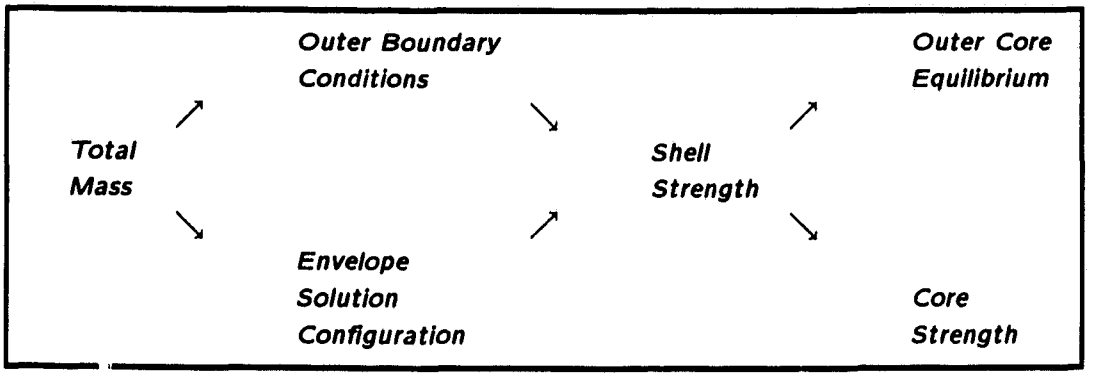

Models which reach the limit at which outer convective zones are dictated by the hydrostatic equilibrium condition are often referred to as lying on a Hayashi sequence (Hayashi 1966a). The location of such a sequence is a function of the interior conditions, which are different for pre-main-sequence, giant branch and horizontal branch stars. In the study of YvdH, using models published in the literature by Iben and others, it was shown how the ascent up the giant branch was characterised by the development of the loop in the (U, V) plane of increasing

width as both the luminosity increased, and the temperature gradient in the core became progressively more shallow. The size of the loop grows with evolution on the giant branch, and appears to be related most strongly to the strength of the shell (see also Applegate 1988).

It must be stressed that the appearance of the models on the (U, V) plane, which is probably the most direct measure of structural changes within the stellar interior, strongly indicates that the interaction between the core and the envelope is of primary importance. Many previous analyses treated these two zones as separate, and have demonstrated the existence of loops in the HR diagram as a function of evolution, by consideration of variations in core mass and radius. The series of papers by Lauterborn *et al.* considered the problem of fitting massive helium cores of differing mass and radii, with and without significant interior burning, to hydrogen burning envelopes. Their attempts to parametrize the model behaviour from the core properties failed in the case where central helium burning is significant and the mass of the envelope is smaller than that of the core (*i.e.*, for their 'Regime I' Horizontal Branch models as opposed to the Regime III objects). However, their hypothesis, that the core and envelope may be treated independently, fails to describe the core-envelope interaction which explains the changes in solution with mass. The early studies of evolution were also executed before the phenomenon of semiconvection was incorporated into the models. Core evolution will be later shown to be important for the core-envelope interaction, too, but in different ways from compositional changes.

The central thesis of this section may be summarized by saying that, for each fixed composition, the outer boundary condition imposed by the total stellar mass alters the hydrostatic structure of the star, modulating the strength of the hydrogen burning shell. This phenomenon by itself is independent of composition and core mass. However, as the parameters are varied, the structure of models at fixed mass is sensitively affected by the run of the polytropic index in the envelope

(clearly affected by the opacity κ), by the core mass (variation of which changes the envelope mass) and by the helium abundance. The effects of these changes are now considered in more detail.

2.4 Variations in ZAHB parameters

2.4.i Introduction

As far as the composition is concerned, there are clearly three separate parameters which must be considered. Firstly, variations in the helium abundance, at fixed metallicity, cause direct modification of the mean weight of the envelope μ, and therefore in the size of the discontinuity in ρ, U and V at the core-shell interface. Secondly, the strength and width of the hydrogen burning shell are modified by the abundance of the catalyst elements carbon, nitrogen and oxygen. It will be shown below how an increased quantity of CNO catalyst elements serves to reduce the hydrogen burning shell temperature, thus altering the entire interior configuration of the star. Thirdly, it has been seen how the structural configuration is dependent on the run of the radiative gradient in the envelope, which is a function of the opacity. Thus, as the fraction of heavy elements present is increased, both the fall in envelope temperatures and the increased abundance of larger ions will raise the opacity coefficient κ. It is well-known that adopting higher model core masses results in brighter ZAHB sequences, however the cause of this is not completely straightforward. In particular, for a model of given mass, changing M_c results generally in a model which is significantly bluer, but changes little in luminosity unless the hydrogen shell source is dominant. This observation is not new (compare calculations from SG76 at $M_c = 0.475$ with those at 0.525 at similar masses), but has received relatively little attention.

2.4.ii On the Effects of Varying CNO, Metallicity, and Opacity.

The question of oxygen abundances on the horizontal branch has a great deal of importance for the understanding of globular clusters, for which there is mounting evidence of greater than solar CNO abundance ratios. As previous studies have shown (*e.g.,* Castellani and Tornambè 1977), and as will be emphasized here, enrichment of the CNO group elements changes the energy balance in the

double-energy source Horizontal Branch models, and therefore sensitively affects the mass of RR Lyrae variable stars[8].

To understand the response of HB stars to heavy element abundance changes, it is helpful to separate those factors which affect the energy generation from those which affect the opacity. In order to do this, interior profiles of a set of stellar models at fixed mass (0.72 $M_\odot$) have been constructed. The calculations presented here are as follows: zero-age horizontal branch sequences with scaled-solar element mixes in the opacity table for: (i) $Z = 0.0001$ ([Fe/H] $= -2.26$); (ii) a test sequence which utilizes the same opacity table as in (i) but with an oxygen overabundance [O/Fe] $= 0.75$, all other elements taking the scaled-solar abundance at that metallicity; (iii) a sequence with the same oxygen overabundance as (ii) in both the opacity and composition, and (iv) a sequence with $Z = 0.0004$ ([Fe/H] $= -1.66$) which has similar number abundance of CNO elements to (ii) and (iii). In each case, $Y \approx 0.245$, and the core mass is 0.492 $M_\odot$.

Figure 2-4-1 shows the energy generation profile of the hydrogen burning shell for models from each sequence. The logarithm of ϵ_n, the nuclear energy generated per gram, is plotted against the mass coordinate. It is clear that at fixed mass, the models with similar CNO abundance have very similar hydrogen shell luminosity, differing from each by at most 1%. Figure 2-4-2 illustrates the run of opacity against temperature. The edge of the helium core appears as a sharp discontinuity in the opacity. It is seen that this occurs at a higher temperature in the lower metallicity scaled-solar model. Comparing the opacity curves of the test and oxygen-rich models, it is seen that the latter has a localized peak in opacity at

[8] *Parts of this section have been submitted to the proceedings of the "Confrontation between Stellar Evolution and Pulsation" conference, Bologna (Dorman 1990). This version of that submission revises some of its conclusions, and extends its range to the study of variations in metal abundance. The original version of this section will appear in Dorman, Lee and VandenBerg (1991).*

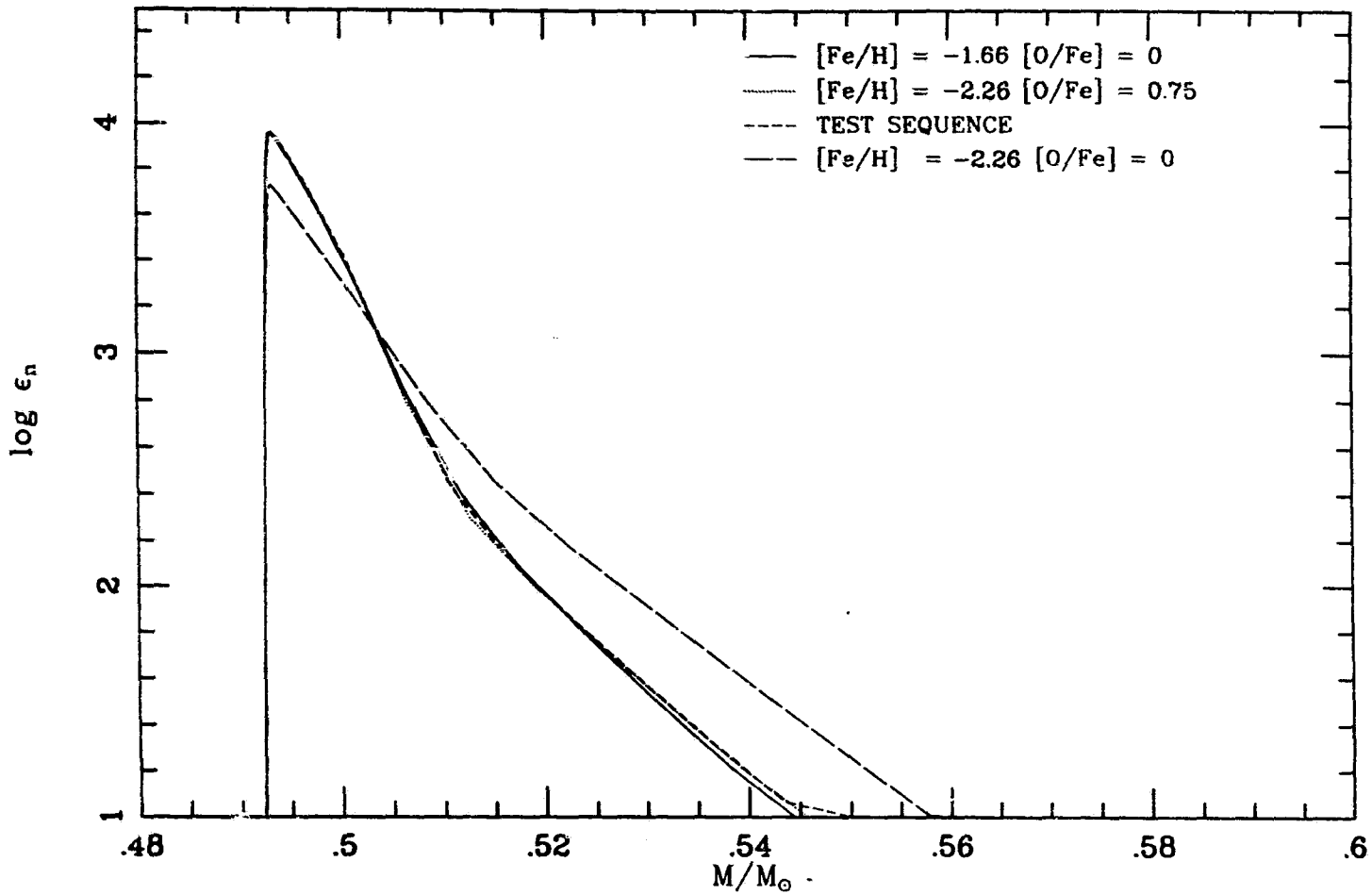

Fig. 2–4–1: Interior profile of log ϵ_n against mass for models with M* = 0.72 Mo. Solid line: Scaled solar sequence with [Fe/H] = –1.66. Dotted line: Oxygen–Enhanced sequence with [Fe/H] = –2.26, [O/Fe] = 0.75. Short dashes: Test sequence with scaled–solar opacities for [Fe/H] = –2.26 and with enhanced oxygen composition as for dotted line. Long dashes: Scaled–solar sequence with [Fe/H] = –2.26.

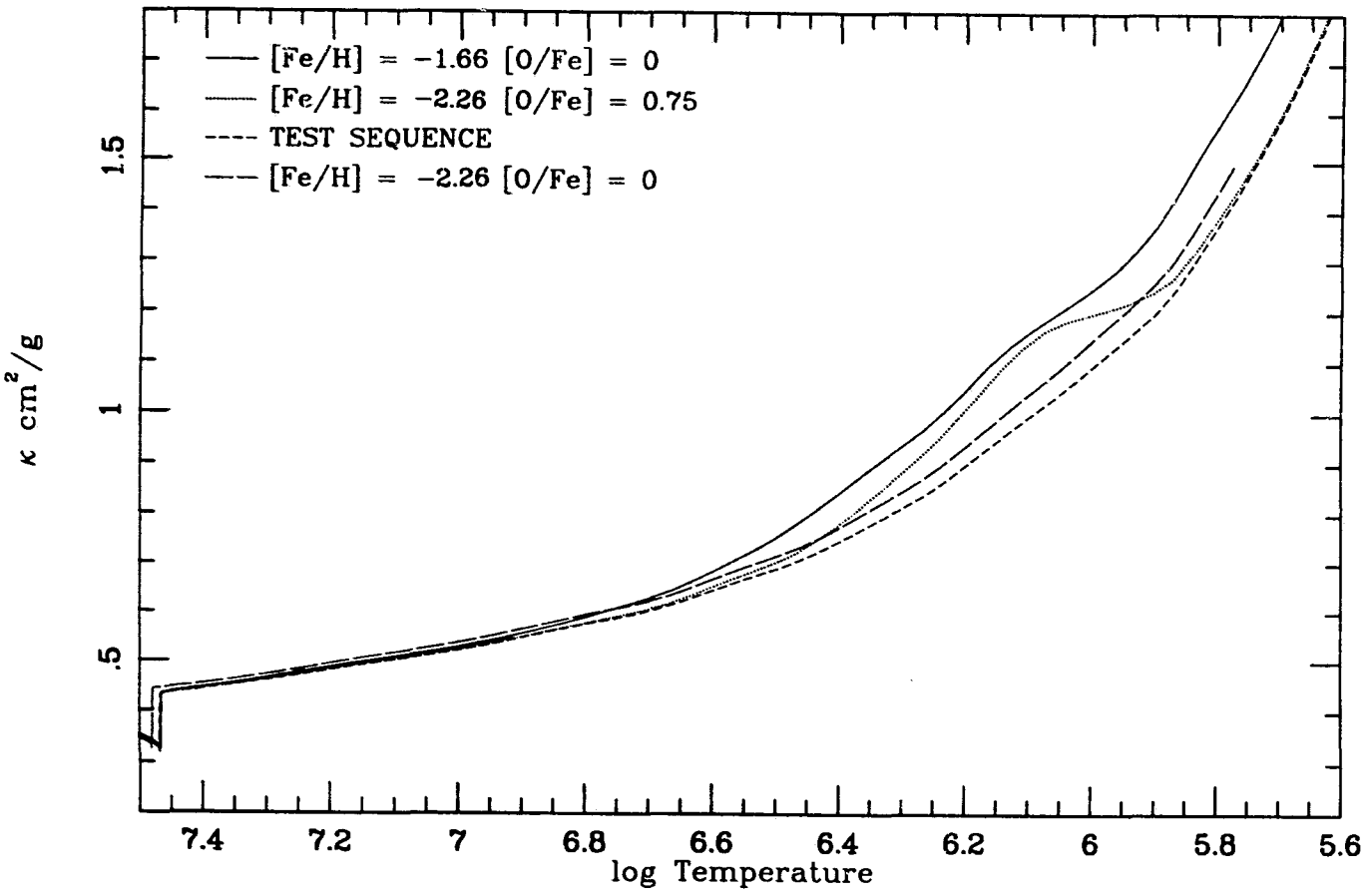

Fig. 2–4–2: As for Figure 2–4–1, but with the opacity coefficient κ plotted against the logarithm of the temperature, T.

a temperatures of around 10^6 K. Apart from this phenomenon, the changes in the interior opacity result from the alteration in T, as opposed to those resulting from the changes in composition. It is crucial to realize that the change in temperature resulting from increased oxygen modifies the structure of the entire star, and thus the model with lower oxygen content has a hotter core which produces a larger fraction of the luminosity. In other words, it appears that the CNO abundance can regulate the core luminosity, whilst the metal opacity affects the energy produced by the shell.

These points can be amplified further by considering a range of oxygen enhancement. Firstly, Figure 2-4-3 illustrates the change in the shell energy generation profile with changing [O/Fe]. In this diagram, $\log \epsilon_n$ is plotted against $\log T$. In the following diagram, Figure 2-4-4 , the luminosity coordinate is plotted against mass. In each case, the models shown have mass $0.90 M_\odot$, and again, the core mass is about 0.492. The energy-temperature plot shows that increases in the oxygen abundance progressively lowers the burning temperature. Also, as [O/Fe] increases, the shell width is seen to decrease, as significant energy production takes place only above $\log T \sim 7.2$. The luminosity-mass plot shows how the central temperature is regulated by the shell burning equilibrium. As the shell temperature falls, the central temperature is also reduced. However, the shell energy generation increases by a greater amount as a result of the increased abundance of CNO catalysts. Thus, the balance of energy production is shifted towards shell burning, and the ZAHB sequence minimum temperature is lower. As the mass of the models is decreased, the shell decreases in luminosity without significant change in the core luminosity, so that the ZAHB sequences with higher [O/Fe] will cross the instability strip at lower magnitude.

Figure 2-4-5 shows the ZAHBs constructed with the scaled-solar, [O/Fe] = 0.75 and the test sequences. Sequence A is markedly different from the others; in the sequences with higher oxygen content, the mass at which convective envelopes

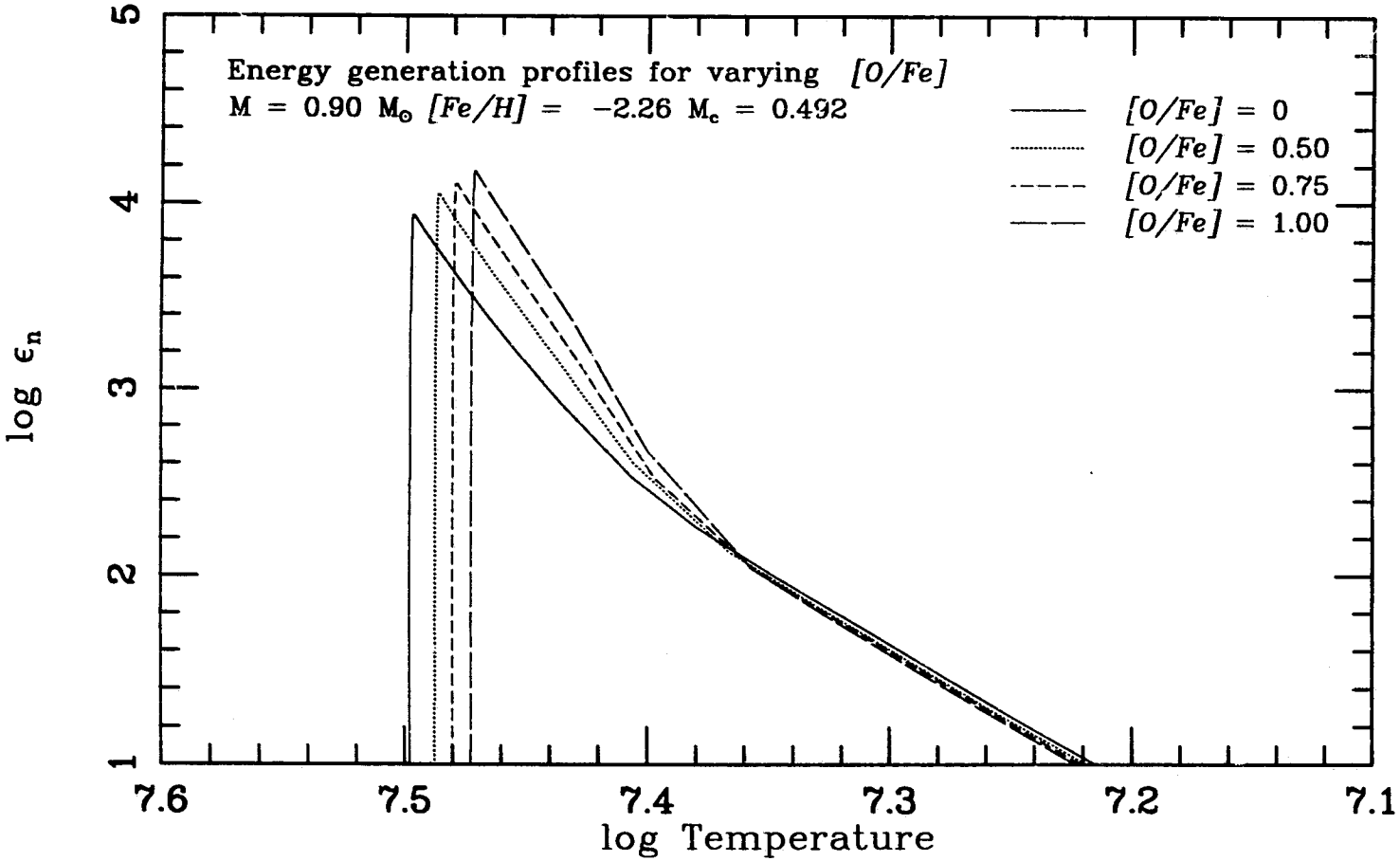

Fig. 2–4–3: Changes is shell energy generation profiles resulting from different oxygen abundances. In this diagram log ϵ_n is plotted against log T, illustrating the change in temperature of the burning shell with oxygen abundance. Solid curve: [O/Fe] = 0. Dotted curve: [O/Fe] = 0.50. Short dashes: [O/Fe] = 0.75. Long Dashes: [O/Fe] = 1.0.

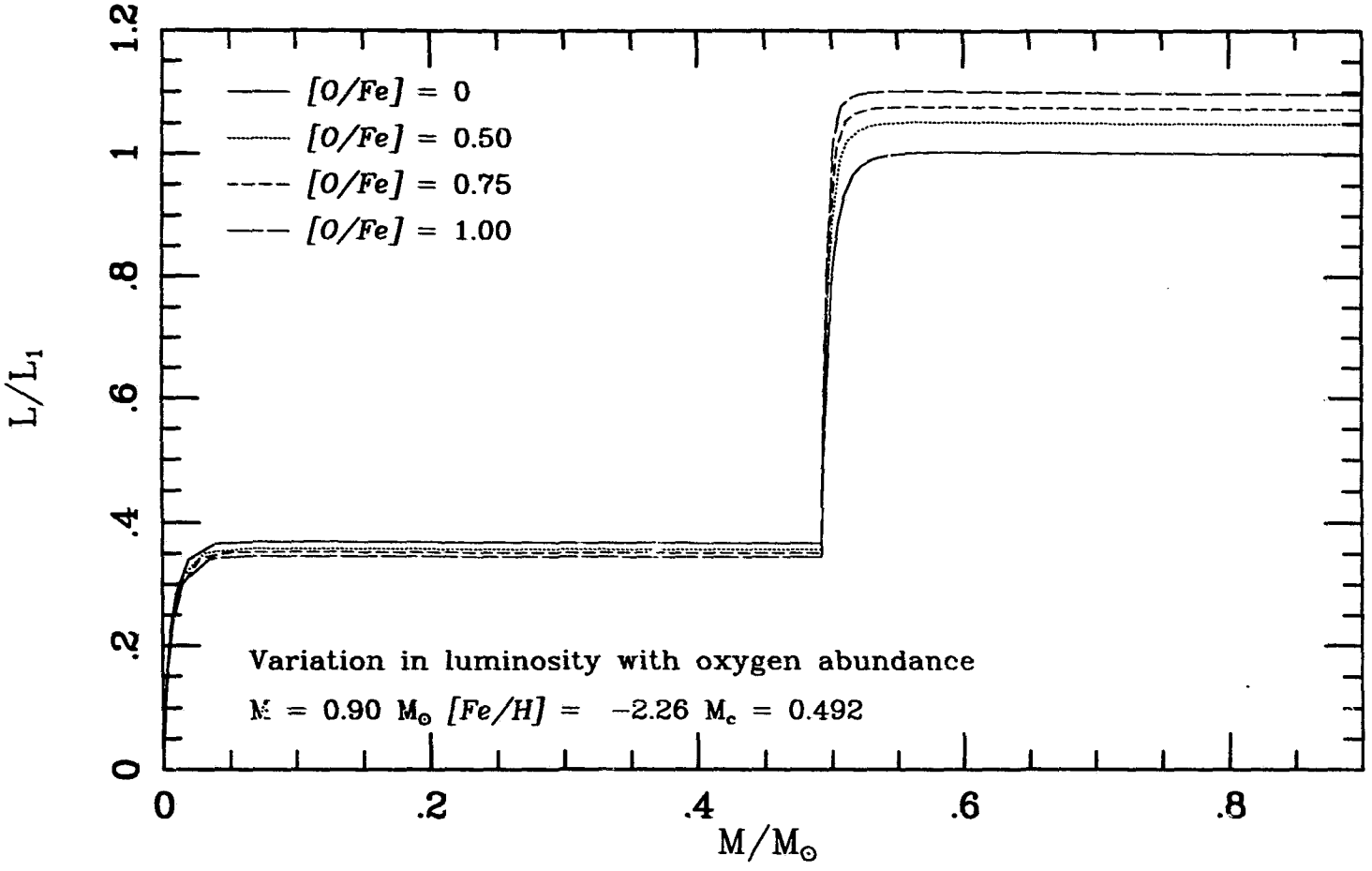

Fig. 2–4–4: As for Figure 2–4–3, but with the luminosity profile plotted against mass. The ordinate (L/L_1) is the luminosity variable normalized to unity at the total luminosity of the scaled–solar model.

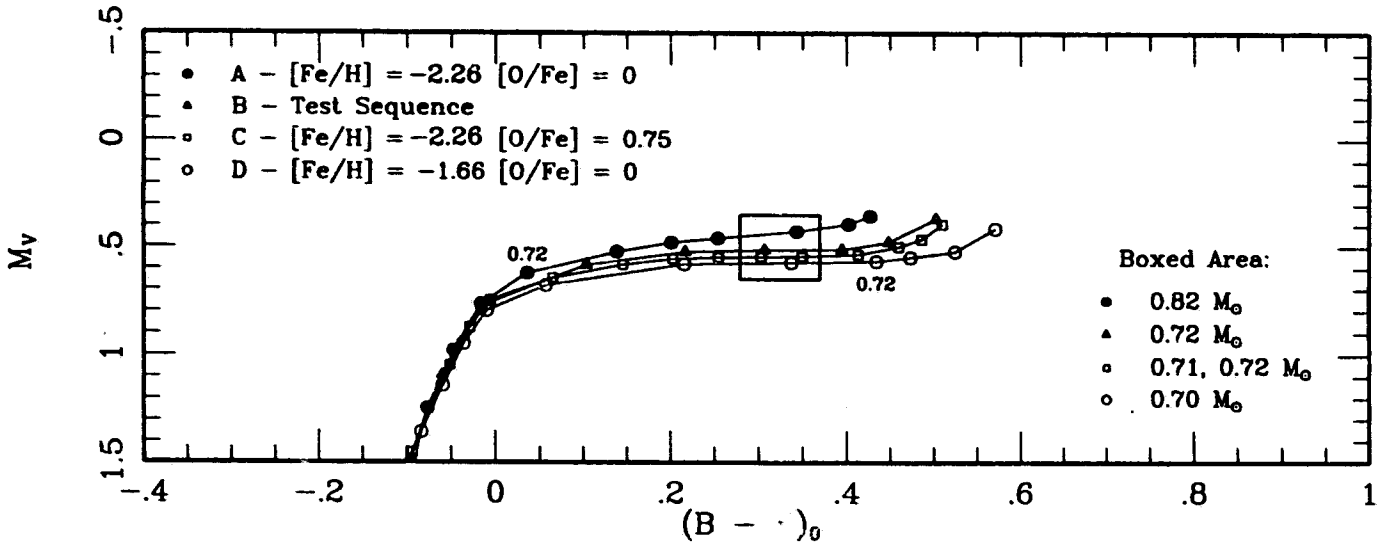

Fig. 2–4–5: Zero Age Horizontal Branches constructed from models with the compositions used for Figures 2–4–1 and 2–4–2. The range of masses of models plotted is the same in each sequence.

appear is less than the mass of stars which are presently reaching the tip of the red giant branch, for current estimates of globular cluster ages. Sequence D extends furthest to the red, owing to greater atmospheric line-blanketing in the models. Importantly, it is apparent that the mass of models at fixed colour (the boxed area marks out, approximately, the part of the instability strip occupied by fundamental mode pulsators) has only a small dependence on the metal opacity, but is very sensitive to the oxygen abundance. That is, the incorporation of oxygen enhancement (if indeed this is present in globular clusters) in the determination of evolutionary masses for RR Lyrae variables is of paramount importance.

Recently, Iglesias, Rogers and Wilson (1990)[9] have stated that metal opacities are significantly underestimated by the Los Alamos calculations in a range of temperature around $\log T \approx 5.4$. The major difference between the test sequence and the high [O/Fe] models is an opacity peak through a narrow range of temperature, albeit one which is higher than that suggested by these authors. Nevertheless, the effect on stellar parameters may be similar in kind to that indicated by Figure 2-4-2. Within the range of temperature spanned by the opacity peak, the models of sequence C have, compared to sequence B, a steeper temperature gradient (leading to a lower T_{eff}) and a reduction in the density (leading to a larger radius). The effect on the structure, therefore, depends on the height of the opacity peak, and its range of applicability in temperature. The former, at least, will increase with metallicity, so that the resultant changes in luminosity should produce a steepening of the theoretical period-metallicity relationship towards values suggested by Sandage (1982a), with predictions for variable masses changing little. As a second point, the comparison between sequences B and D stresses the fact that the relationship between mass and metallicity almost disappears altogether if the

[9] *Similar results to these are promised by Mihalas (1990, address to Bologna conference and private communication) and Seaton from the 'opacity project' (Seaton 1987), currently in its late stages.*

CNO abundance is held approximately constant.

In the next diagrams, the effects of increased metallicity are studied. Figure 2-4-6 shows the shell burning profiles for a range of metallicities from [Fe/H] $= -2.26$ to -0.47. The models plotted in this and the following figure have scaled-solar abundances, and a core mass $M_c = 0.499\ M_\odot$. This first plot is visually very similar to Fig 2-4-3, suggesting that it is indeed the CNO component of the heavy-element abundance which causes the change in shell temperature. Figure 2-4-7 shows the run of luminosity L in the interior. These curves have been normalized such that the most metal-poor sequence has $L = 1$. In this set of models, the central temperature peaks for metallicity [Fe/H] $= -1.78$, and the model with the highest luminosity is that at [Fe/H] $= -1.48$[10]. The shell luminosity attains a maximum value, and then declines; the shell energy production rate does not increase with further increase in CNO, but the burning temperature, and thus the width of the burning region, continues to drop with increased CNO fraction. The luminosity profile curves in the region of the shell, as a consequence of the shell narrowing, bend more abruptly as the metallicity increases.

The increase in opacity with metallicity has predictable effects on the outer structure of the envelope. The temperature gradient steepens at lower temperatures, so that the outer convection zone, where present, penetrates to deeper levels. As a result, the effective temperatures of the models are reduced, and cool extreme of the HB is considerably redder. This last factor is reinforced by the increase in atmospheric line-blocking with metallicity. Finally, as the mass is continuously decreased at fixed composition, the interior structure is changed so as to reduce the convection zone depth, and the mass at which the instability strip is reached can be as low as $0.58 - 0.60 M_\odot$ where the oxygen abundance is as high as $[O/H] \sim -0.25$. Of course, clusters with very high metallicity are not observed

[10] *This more complex behaviour may be caused by the adopted variation in Y with* [Fe/H].

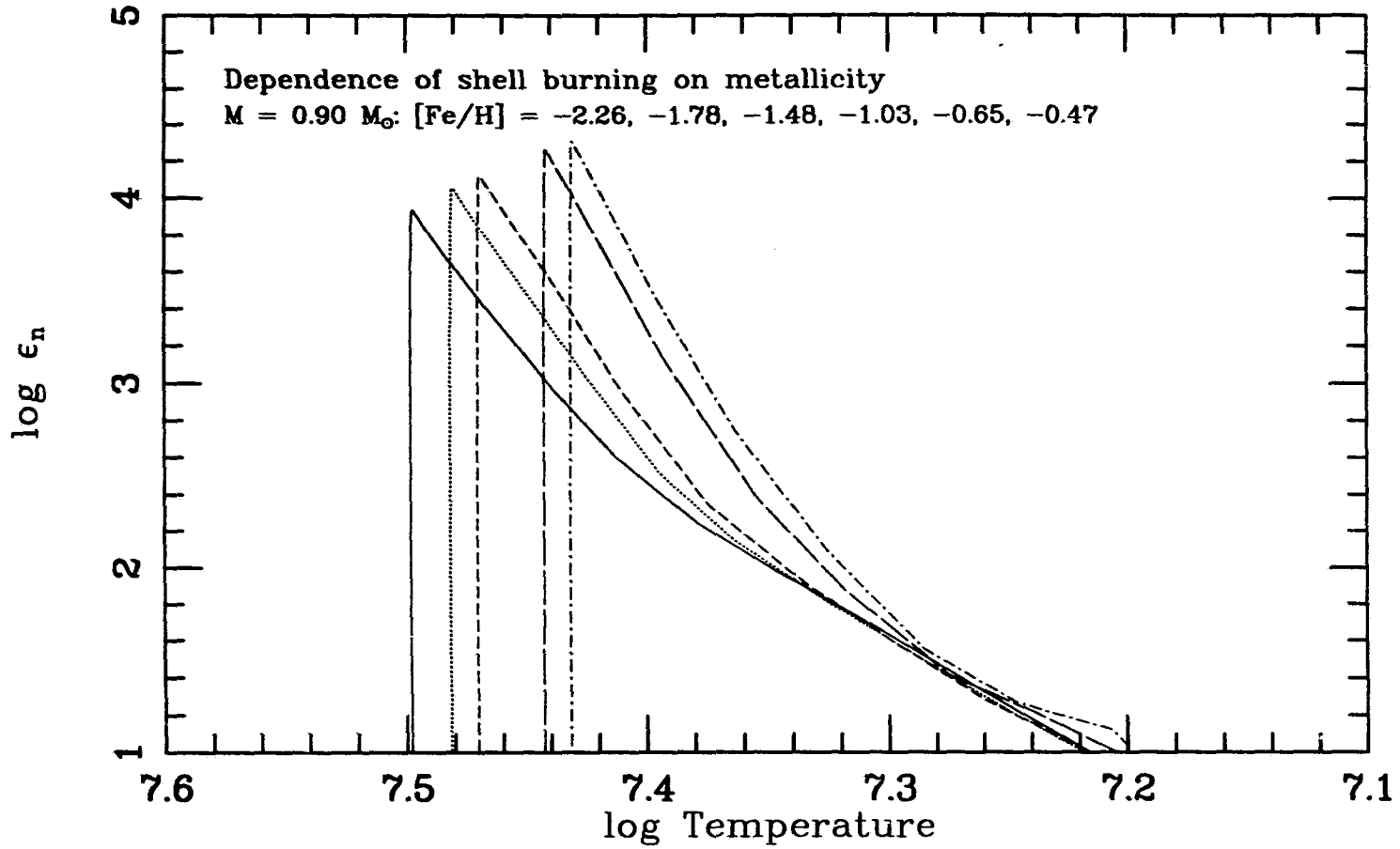

Fig 2–4–6: Interior profile of log ϵ_n versus log T for models of varying metallicity. The curves shown are (left to right) [Fe/H] = –2.26, –1.78, –1.48, –0.78 and –0.47, with scaled solar abundances. In each case (M_*, M_c) = (0.90, 0.499) $M_\odot$.

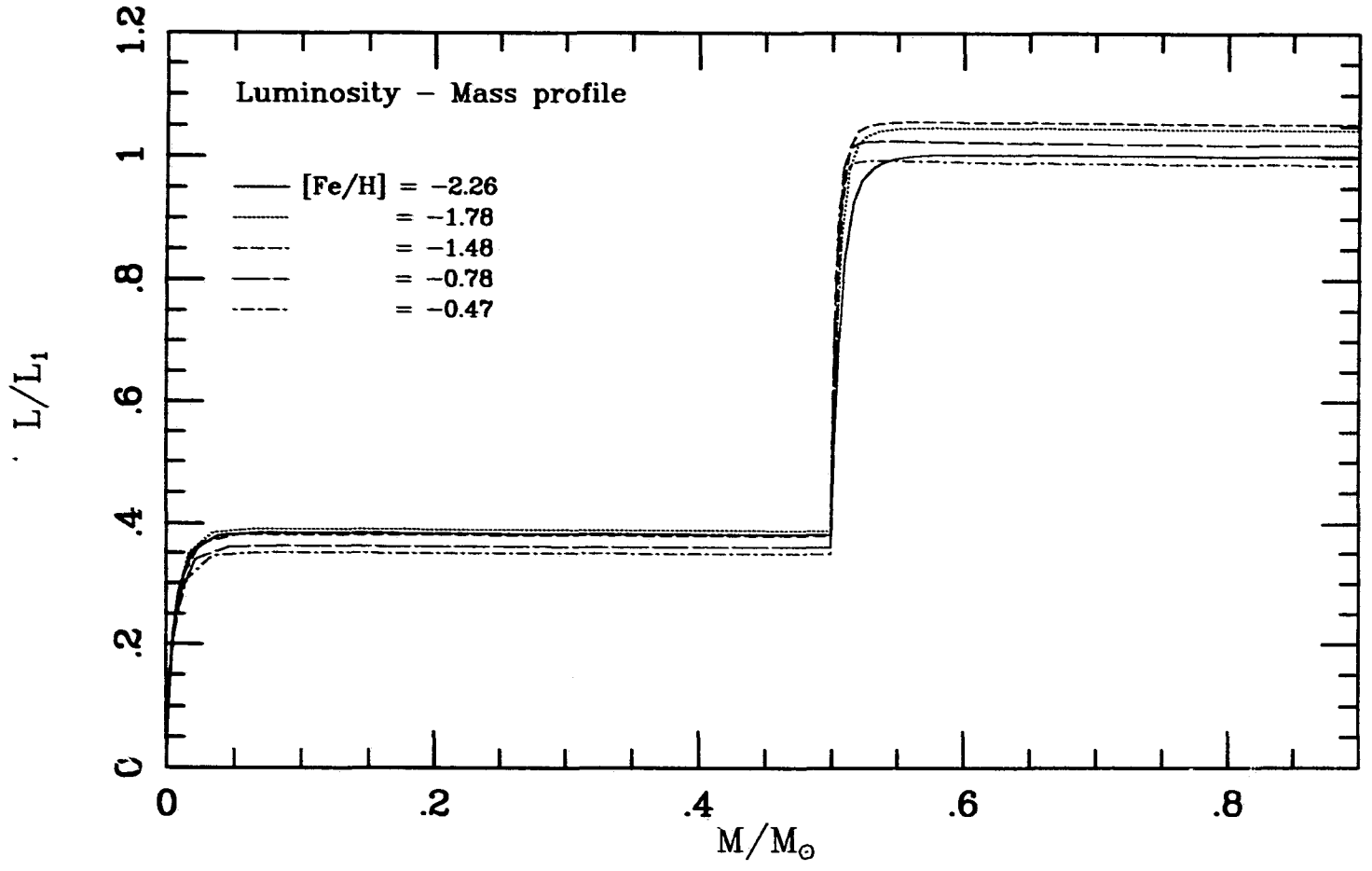

Fig. 2–4–7: As for Figure 2–4–6, but with luminosity plotted against mass.

with significant instability strip populations, but these comments may be relevant to consideration of the masses of field RR Lyrae stars.

One important omission from this study is the effect of overabundant α-nuclei. These are expected to be greater than the scaled-solar proportion as they are also produced by massive supernovae; however detailed modelling of stars with $[Ca, Si, Mg ... etc/Fe] > 0$ awaits appropriate atmospheric models and synthetic colours. It is expected that higher abundance of these elements will affect the line-blanketing of the models, moving the model to the red. In addition, the higher envelope opacities should adjust the shell luminosity downward. It is not clear in advance how different models with enhanced α-nuclei as well as enhanced CNO abundance will differ from scaled-solar models computed with higher iron-peak elements (*i.e.*, higher [Fe/H]). However, models with a range of primordial abundances variations may well serve to elucidate problems in cluster metallicity calibration, especially since elements such as calcium are often used as metallicity indicators for RR Lyrae variables.

It should also be pointed out that the core masses of metal-rich HB stars are predicted to be smaller, thus further reducing the luminosities of these objects. The precise relationship between luminosity and metallicity is the subject of a great deal of controversy amongst observers, and the steepness of the slope of this relationship has been determined observationally by several methods, utilizing, for example, fits to globular cluster colour magnitude diagrams (*e.g.*, Buonanno *et al.* 1990), or applying Baade-Wesselink methods (Liu and Janes 1990) to their RR Lyrae variables. The above discussion suggests that the relationship should be non-linear even over the range of metallicities spanned by globular clusters for which the instability strip is populated; however, the available data for globular clusters and for field RR Lyrae stars are usually fitted to a straight line. Similar comments to these have been made by Castellani, Chieffi and Pulone (1990), for very similar reasons; the relationship between ZAHB luminosity in the instability strip for

high metallicity is very different from that for low metallicity. To complicate the issue further, recall that the examples used in this discussion are for high mass objects lying at the red end of the instability strip; in fact ZAHB models lie in the instability strip only if the hydrogen shell is considerably weaker and the model mass smaller (the relationship is usually sought at a fixed effective temperature appropriate to the centre of the instability strip — see §6.2). But that mass is a strong function of $[O/H]$, and also depends significantly on M_c; thus the relationship is very model-dependent. Notwithstanding these theoretical difficulties, the relationship indicated by the grid of models presented in this study will be derived in Chapter 5.

2.4.iii Sensitivity to envelope helium abundance

The chief variation in the structure caused by changes in the envelope helium abundance are in the size of the discontinuity at the core-envelope interface. Figure 2-4-8 shows models with $(M_*, M_c) = (0.90, 0.499)$ for $Y \sim 0.28, 0.25$ and 0.21. The structure of the envelope as marked by the (U, V) plane curves above the chemical discontinuity is obvious; no other parameter has such little effect on the underlying mass distribution. Also, this structural similarity is not a function of metallicity; it holds for a large range in metal abundance. The major difference between the models is the shallower temperature gradient close to the core-shell interface. The more rapid change in chemistry required in the lower helium models has the effect of steepening the temperature gradient in the outer part of the core, thus producing lower temperatures in the shell. The magnitude of this shift is $\Delta \log T / \Delta Y \sim 0.01/0.035$.

The lower the value of Y, the larger is the chemical discontinuity; hence the temperature must fall further in order to meet the core boundary condition. The high sensitivity of the nuclear reactions to changes in T results in a large difference in the total luminosity; whilst the core luminosity varies little

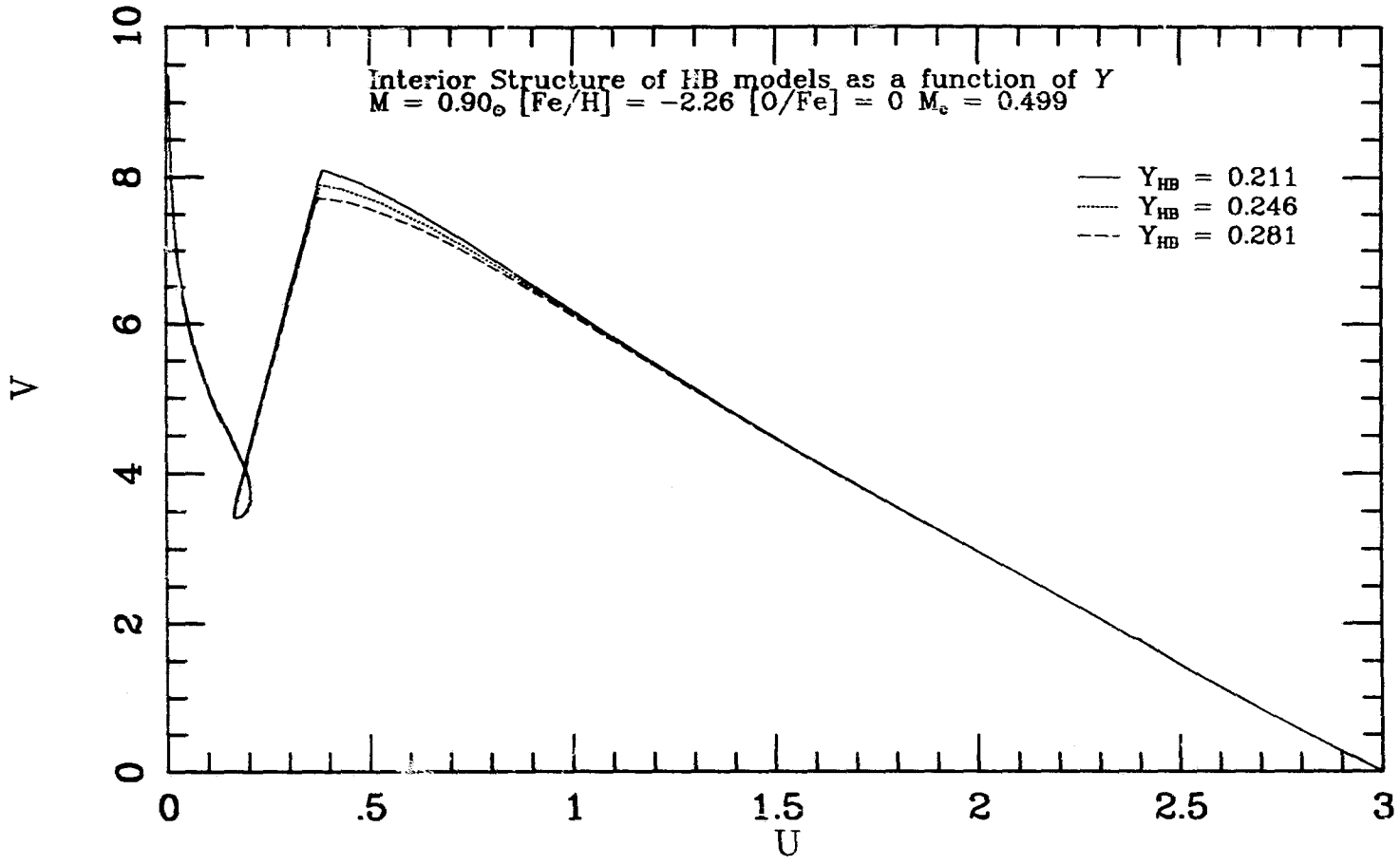

Fig. 2–4–8: (U,V) plane curves for models of varying *Y*. Each curve represents a model with (M_*, M_c) = (0.90, 0.499) $M_\odot$, and [Fe/H] = –2.26. The values of *Y* are (top to bottom) Y_{HB} = 0.21, 0.25 and 0.28.

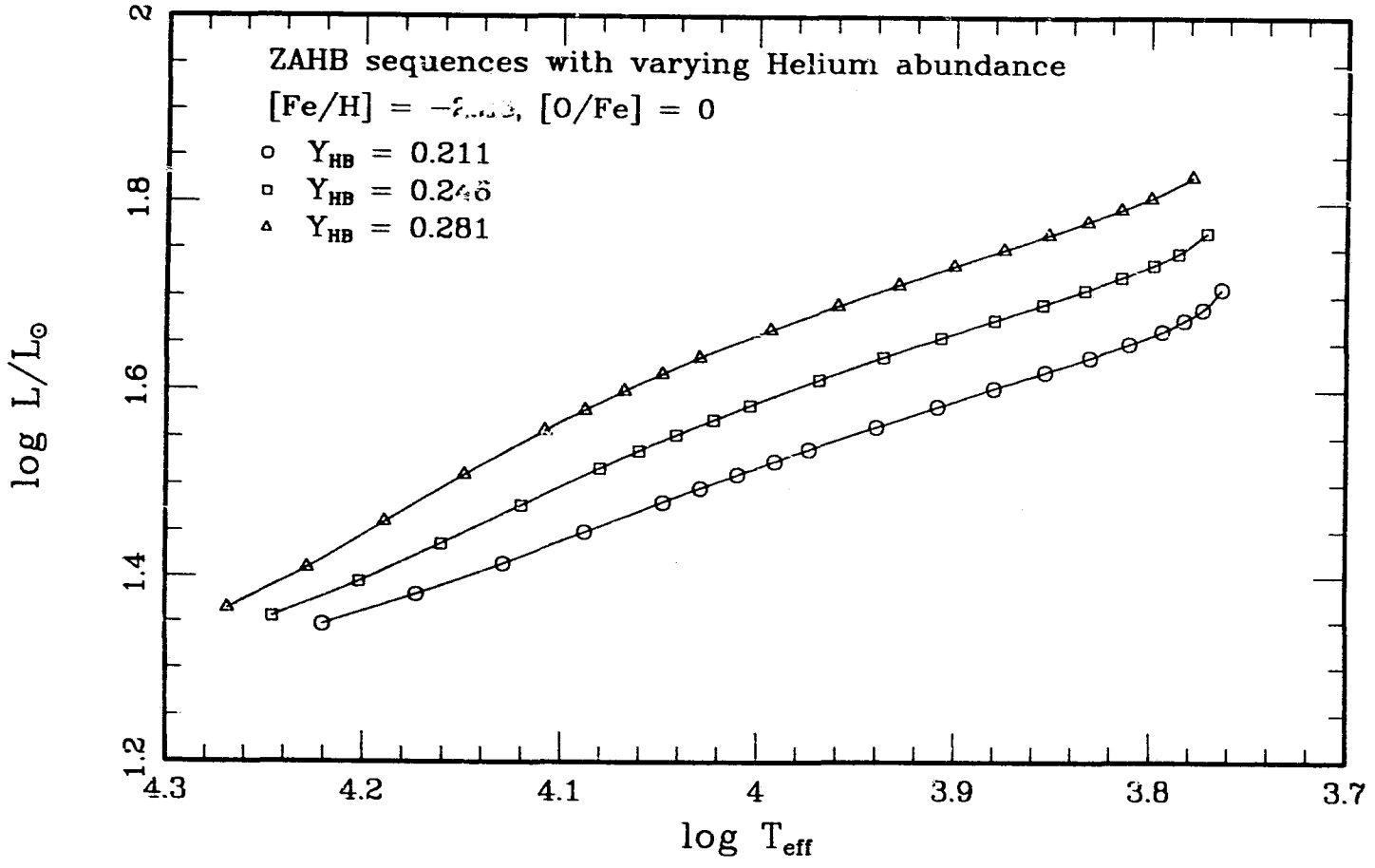

Fig. 2–4–9: ZAHB sequences for models with the helium abundances used for Figure 2–4–8, and with [Fe/H] = –2.26, [O/Fe] = 0. Triangles: $Y = 0.28$. Squares: $Y = 0.25$. Circles: $Y = 0.21$.

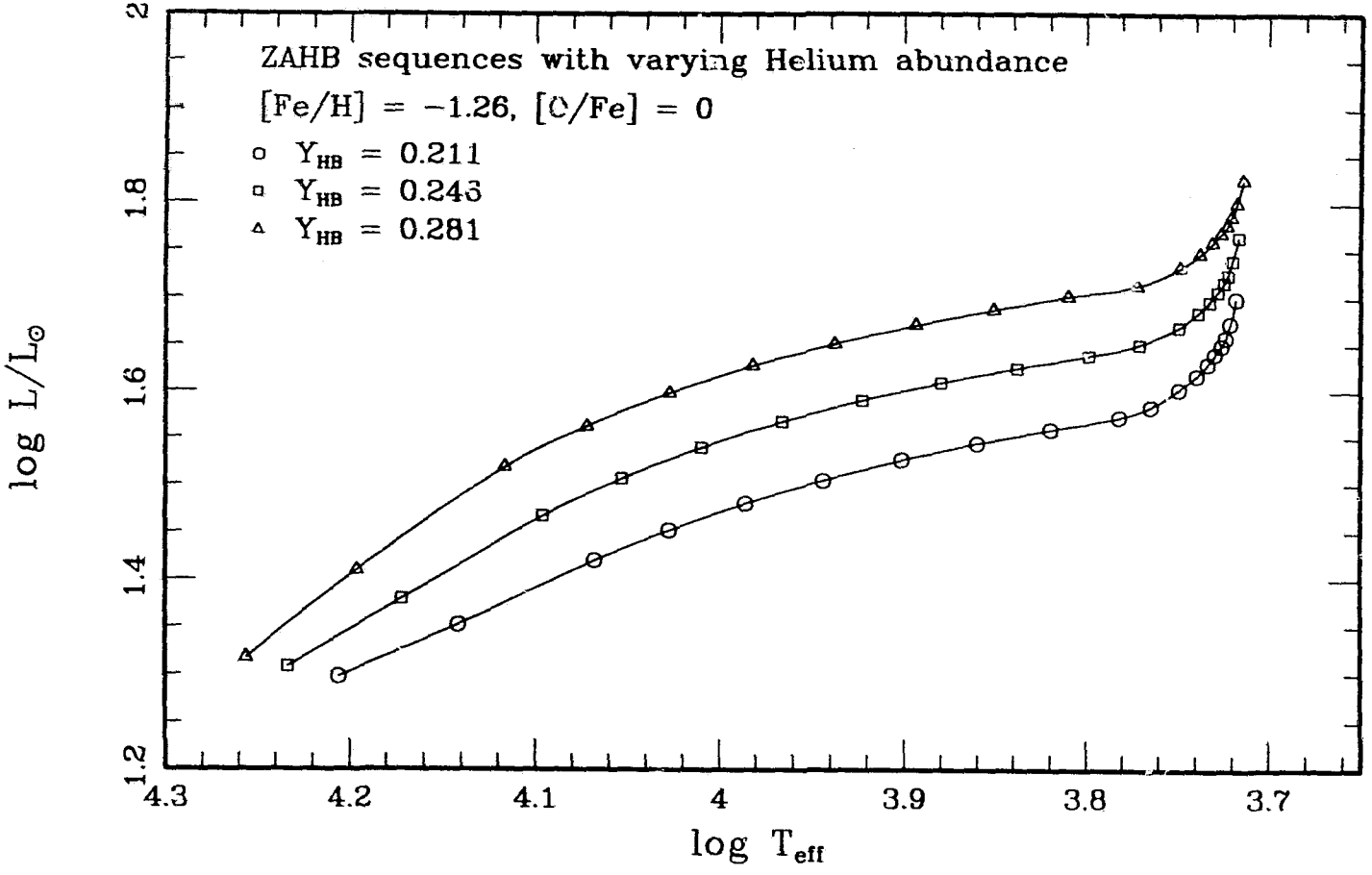

Fig. 2–4–10: ZAHB sequences for models with the helium abundances used for Figure 2–4–8 and 2–4–9, but with [Fe/H] = –1.26, [O/Fe] = 0. Triangles: $Y = 0.28$. Squares: $Y = 0.25$. Circles: $Y = 0.21$.

with Y, the shell brightness changes in these models by nearly 40%. According to the theory presented in §2.3, the small shift in envelope temperatures should produce a small shift to higher effective temperatures for models lying redward of the instability strip (region where the (U,V) plane loop vanishes) and a larger shift in that direction for lower masses. The near-homologous nature of the envelopes illustrated here indicates that the difference in the envelope temperatures, while regulating shell luminosity, produces little effect on the envelope opacities which determine the radiative gradient. Figures 2-4-9 and 2-4-10 show the effect on the ZAHB of changes in Y, at [Fe/H] $= -2.26$ and -1.26. These sequences have been constructed so that each contains models of the same masses; the core mass is the same for all models plotted here. All of the predicted features are present in these sequences; in particular, the near-invariance of model masses to Y at a given $\log T_{eff}$ is a natural consequence of the theory. This is also apparent in the model calculations presented in SG76 and S87. Major changes do occur in the evolutionary tracks because the shell luminosity at the ZAHB is depressed, and because the shell burning luminosity is constrained by the envelope helium abundance during the entire evolution.

An important implication of the near-invariance of HB envelopes to helium abundance can be drawn from the fact that it is apparently the magnitude of the chemical discontinuity at the core-shell interface, rather than the mean molecular weight of the entire envelope, that changes the evolutionary characteristics of the stars. In particular it is the composition in the burning shell which is responsible for the behaviour associated with high Y. Since the energy generation peak moves outward with evolution by only a few hundredths of a solar mass during the entire evolution to the base of the AGB, the insensitivity of the structure implies that the atmospheric abundance, as determined indirectly from pulsational calculations, provides little evidence for the interior helium abundance of the envelope. Most

pulsational calculations for the RR Lyrae stars (Cox 1987; Kovács 1985) have been conducted with a value of Y close to 0.30, which is difficult to reconcile with the resulting morphology of the horizontal branch (see Chap. 6). Although this is apparently more the result of 'historical' choices of parameters rather than of theoretical constraints, Cox (1987) has claimed that stable double-mode RR Lyrae pulsators, which exist in significant numbers in M15 (see Bingham *et al.* 1984), can only exist if Y is about this high. Since the comparison of theory with observation prefers values of Y less than 0.25 for the interior of the star, this would require an enhanced helium abundance in the pulsation zone (which contains very little mass). However, there is no known mechanism which would enhance Y to this extent if indeed primordial abundances are lower.

2.4.iv Sensitivity to core mass changes

Figure 2-4-11 shows three ZAHB sequences, with composition (Y_{HB}, [Fe/H], [O/Fe]) = $(0.246, -2.26, 0.75)$, for models with core masses which are increased (triangles) and decreased (open circles) by 0.01 $M_\odot$ from the value in Table (2-3-1). The masses plotted in each case are the same, 0.90, 0.82, 0.78, 0.74, 0.70, 0.66, 0.64, 0.62, 0.58 and 0.56 $M_\odot$. Again, plotting similar masses in each sequence allows the detection of an important subtle feature in the models. Namely, that the predominant effect of the core mass difference is one of colour, rather than luminosity, for the bulk of the models.

The effects of increasing the core mass are twofold; firstly, the central temperature is increased, and secondly, the shell temperature is reduced. The first of these effects raises the core luminosity, and the second reduces the shell luminosity. Further, the reduction in the *envelope mass* produces an effect similar to that seen earlier in the reduction of the *total mass*. That is, when the (U, V) plane loop is no longer present, the models are relocated rapidly to the blue with decreasing mass. If the decrease in the shell luminosity is similar in magnitude to the increase

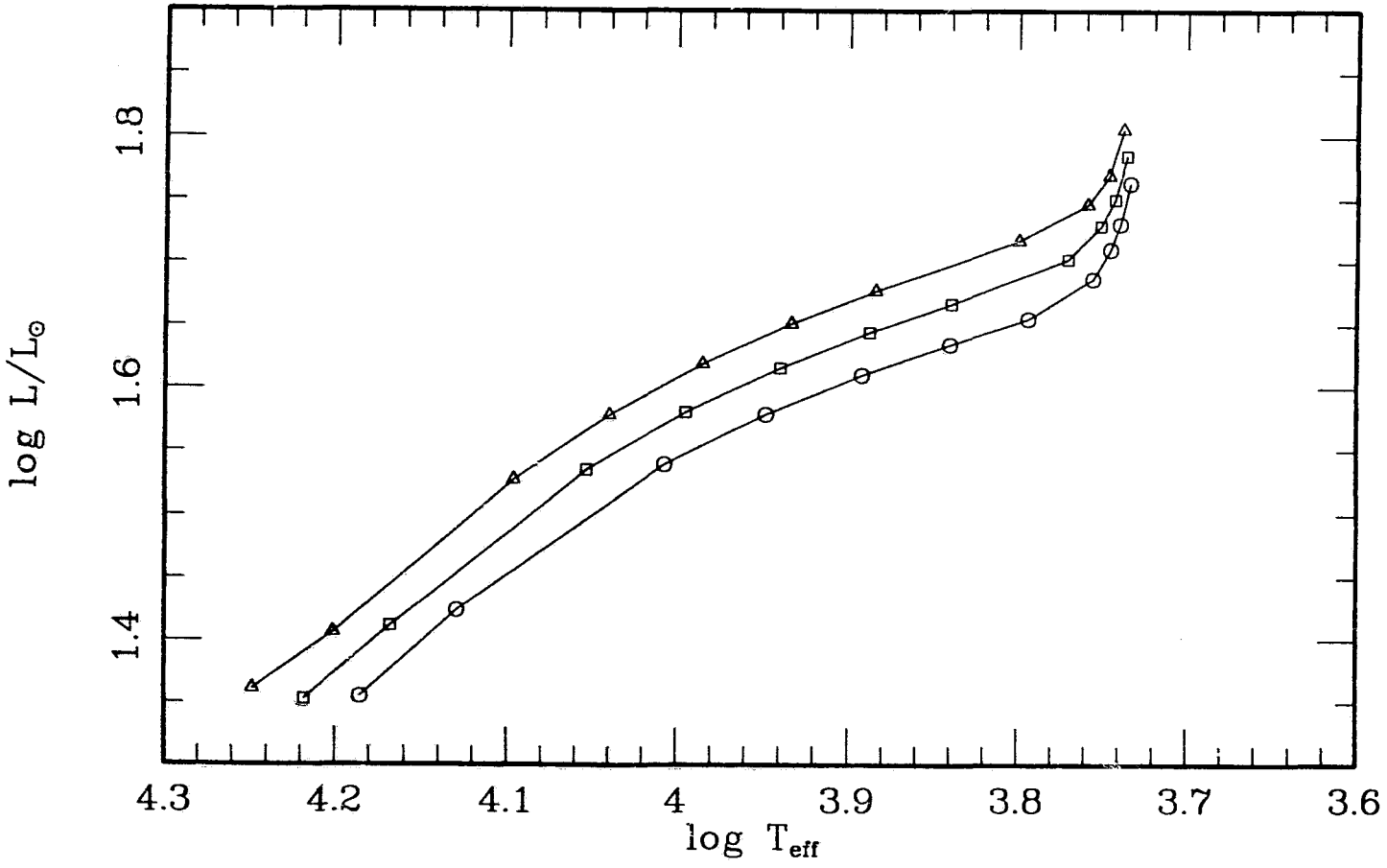

Fig. 2–4–11: The effect of core mass variations on the ZAHB. For each sequence of models, $Y_{HB} = 0.246$, [Fe/H] = –2.26, [O/Fe] = 0.75. The masses shown are 0.90, 0.82, 0.78, 0.74, 0.70 (0.02) 0.62, 0.58 and 0.54 M_o. Triangles: $M_c = 0.502$. Squares: $M_c = 0.492$. Circles: $M_c = 0.482$.

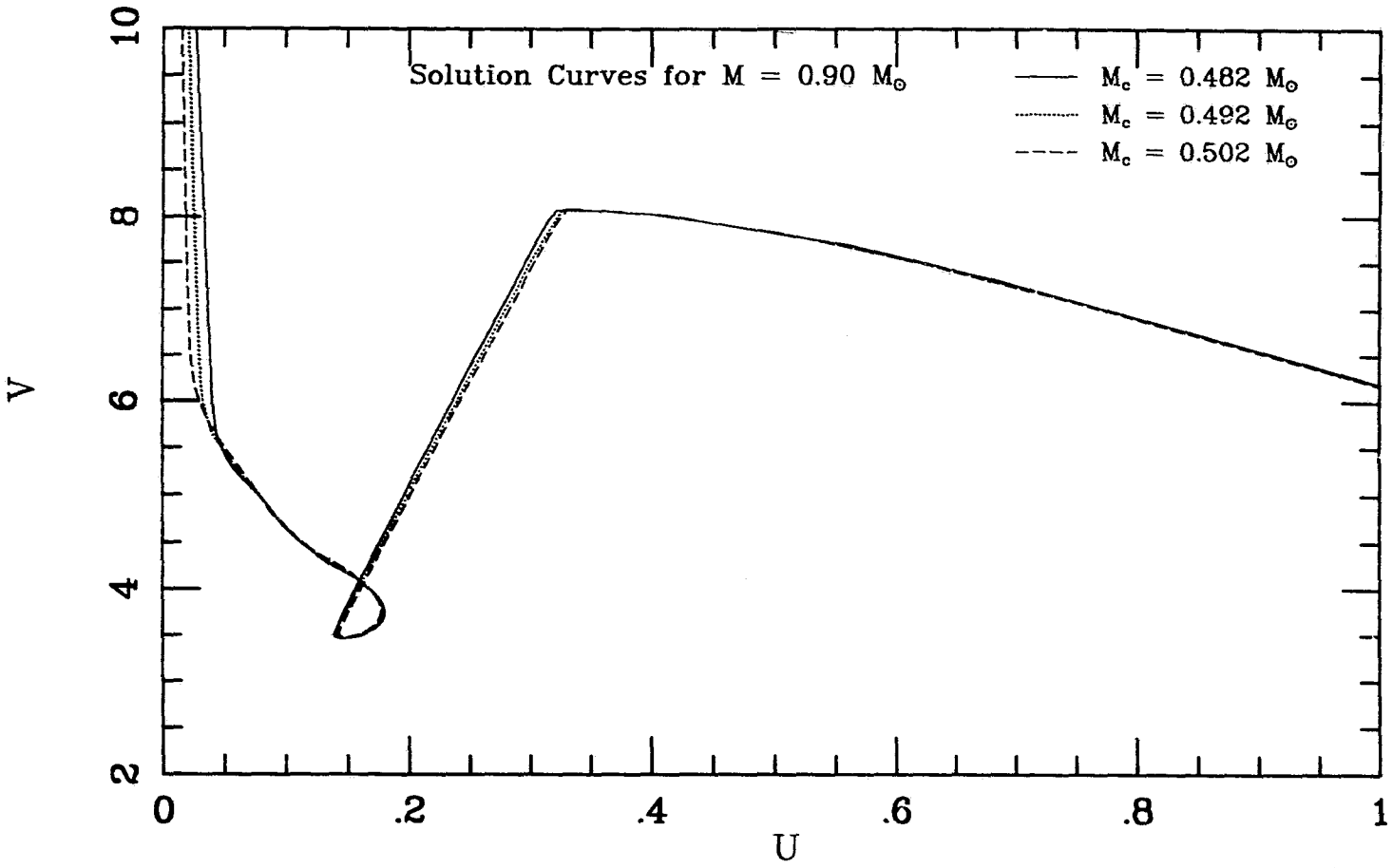

Fig. 2–4–12: *(U, V)* plane curves for models from the sequences plotted in the previous diagram. In this plot, each curve represents a model of 0.90 $M_\odot$. Dashed curve: $M_c = 0.502$. Dotted curve: $M_c = 0.492$. Solid curve: $M_c = 0.482$.

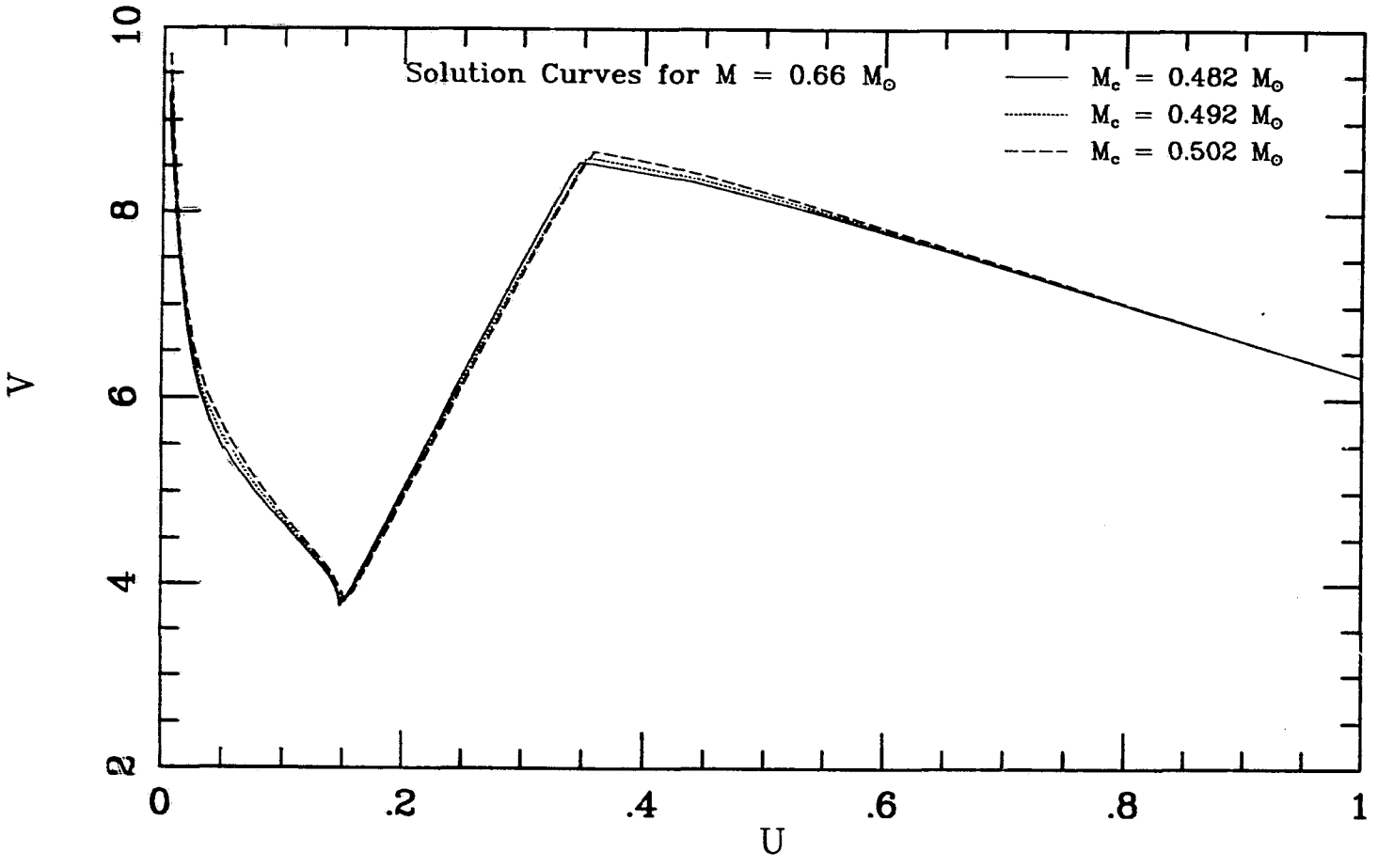

Fig. 2–4–13: As for Figure 2–4–12, but with models of total mass 0.66 Mo.

in core luminosity, then the effect of the core mass change will be most striking in colour, rather than magnitude. At the red end of the HB, the shell luminosity is less sensitive to small changes in the shell temperature; the structure adjusts to a smaller envelope by reducing the depth of the outer convection zone, and thus moves very slightly to the blue. Figure 2-4-12 shows the (U,V) plane solutions for models with $M_* = 0.90 M_\odot$. The model cores have the same structure; however, it is the outermost curve (solid line) which corresponds to the model with the smallest M_c. Thus, as long as the shell luminosity is roughly fixed by the surface conditions, the core structure is homologous, with the larger cores possessing a lower mean density. In contrast, the outermost core layers of the 0.66 $M_\odot$ models (Figure 2-4-13) are progressively steeper, implying greater difference in the shell temperature. The explanation of this behaviour is not entirely straightforward. It is well-known that for *isothermal* cores the central temperature is approximately proportional to the core radius, and despite the fact that the cores illustrated here are far from being isothermal, this same behaviour is demonstrated (the larger-mass cores are also larger in size). These comments emphasize the difficult in interpreting results for non-idealized stellar structure problems.

Nevertheless, the overall visual impression one obtains from Figure 2-4-11 is that the ZAHB luminosity increases with M_c. Theoretical uncertainties in the values of M_c derived from red-giant evolution can therefore cause significant uncertainties in the apparent brightness of the ZAHB. In these models, a variation of 0.01 $M_\odot$ in the adopted value of the core mass produces a change of about 0.08 in the visual magnitude V in the vicinity of the instability strip. Currently, calculations of red-giant models for similar main-sequence composition (VandenBerg 1990, S87) produce excellent agreement in core mass values, which differ by far less than this amount [11]. Of course it should be added that the core masses used

[11] *Indeed, for one particular choice of parameters ($Y_{MS} = 0.20$, $Z = 0.0001$), the core mass values derived by Sweigart (1987) and VandenBerg (1990) differ by one*

here are derived from canonical evolutionary sequences, in which stellar rotation is neglected, and such possibilities as WIMPs (Weakly Interacting Massive Particles; see Faulkner and Gilliland 1985) are ignored. The uncertainty in the core mass value is therefore deper dent on the reliability of the adopted neutrino energy loss rates and the 'safety' of the canonical assumptions.

ten-thousandth of a solar mass!

2.5 On the Evolution of Horizontal Branch Stars

2.5.i Introduction

This section begins by presenting a picture of the physical processes which give rise to the shape of evolutionary sequences on the HR diagram. This scenario is later discussed in some detail, and illustrated by showing the run of interior variables within evolving models. Early investigations of Horizontal Branch evolution (IR70, Lauterborn *et al.* 1972, Fricke and Strittmatter 1972) were carried out before the convective core expansion problem[12] was investigated in HB models. With semiconvection, the temperature gradient is forced to be equal to the adiabatic gradient in a steadily growing region, so that the central E-solution is followed outward to progressively larger values of the mass co-ordinate. At the same time, the composition discontinuity at the edge of the semiconvection zone grows in size. However, the qualitative features of evolution, described by IR70, are the same as those found here. The core behaviour as a function of time is qualitatively similar for any choice of envelope mass or composition, although the size of the convective core and semiconvective zone does depend on envelope mass and composition. A thorough discussion of the evolution of the core is contained in the next chapter, and here attention turns to (re-) classifying the morphology of the evolutionary tracks according to the time variation in the hydrogen shell and in the core behaviour.

As the evolution of HB stars proceeds, their HR diagram behaviour must depend on the response of the shell source to the evolution of the core. The preceding

[12] *N.B. An ambiguity arises at this point. The 'core expansion problem' discussed in the next section refers to the growth of the inner part of the core in the mass co-ordinate, i.e., in a Lagrangian framework. In this chapter, 'expanding core' strictly refers to changes in radius of the entire helium-rich central region.*

discussion (§2.3) has shown that it is the envelope mass which largely determines the effective temperature of the model, whilst the core luminosity bounds the model luminosity from below. The existence of the hydrogen shell source adds to the evolutionary behaviour a further complication, that, as Cox and Giuli (1968, §26.4d), put it "the shell source is situated approximately at a node of the mass motions of the various layers". This is sometimes known as the 'mirror principle'. The physical reason for this tendency is the extreme temperature sensitivity of nuclear reactions, and the requirement of thermal equilibrium implies that the shell temperature cannot change too rapidly with time. Stein (1966) shows that, given certain conditions, the direction of mass motion is reversed at a shell source. In the model calculations performed for this study, it is found that this result holds true for sufficiently bright hydrogen-burning shells.

In order to clarify the following discussion it is helpful to anticipate the results of the calculations to be presented in Chapter 5 by illustrating the HB track morphologies for a range of stellar masses. Evolutionary tracks for a range of masses are shown in Figure 2-5-1 in order to illustrate the different types. The parameters for these tracks are (Y_{HB}, M_c, [Fe/H], [O/Fe]) = (0.246, 0.490, −2.03, 0.66). In the classification to be presented below, model sequences are divided into three categories. The first type refers to sequences which can evolve strongly to the blue during evolution, the width spanned in colour or temperature range being greater for greater envelope mass. Examples are tracks for 0.62 through to 0.70 $M_\odot$. The second category contains those sequences which are characterized by outer convection zones. These sequences are generally brighter than the part of the ZAHB that runs through the instability strip, and may evolve weakly to the blue, or, for sufficiently high mass, evolve almost vertically in the colour magnitude diagram ($M \gtrsim 0.74 M_\odot$). The third category consists of models which evolve redward and upward in the HR diagram, and is exemplified by the tracks with $M \lesssim 0.6 M_\odot$. Of course, the mass range for each class is a function of composition,

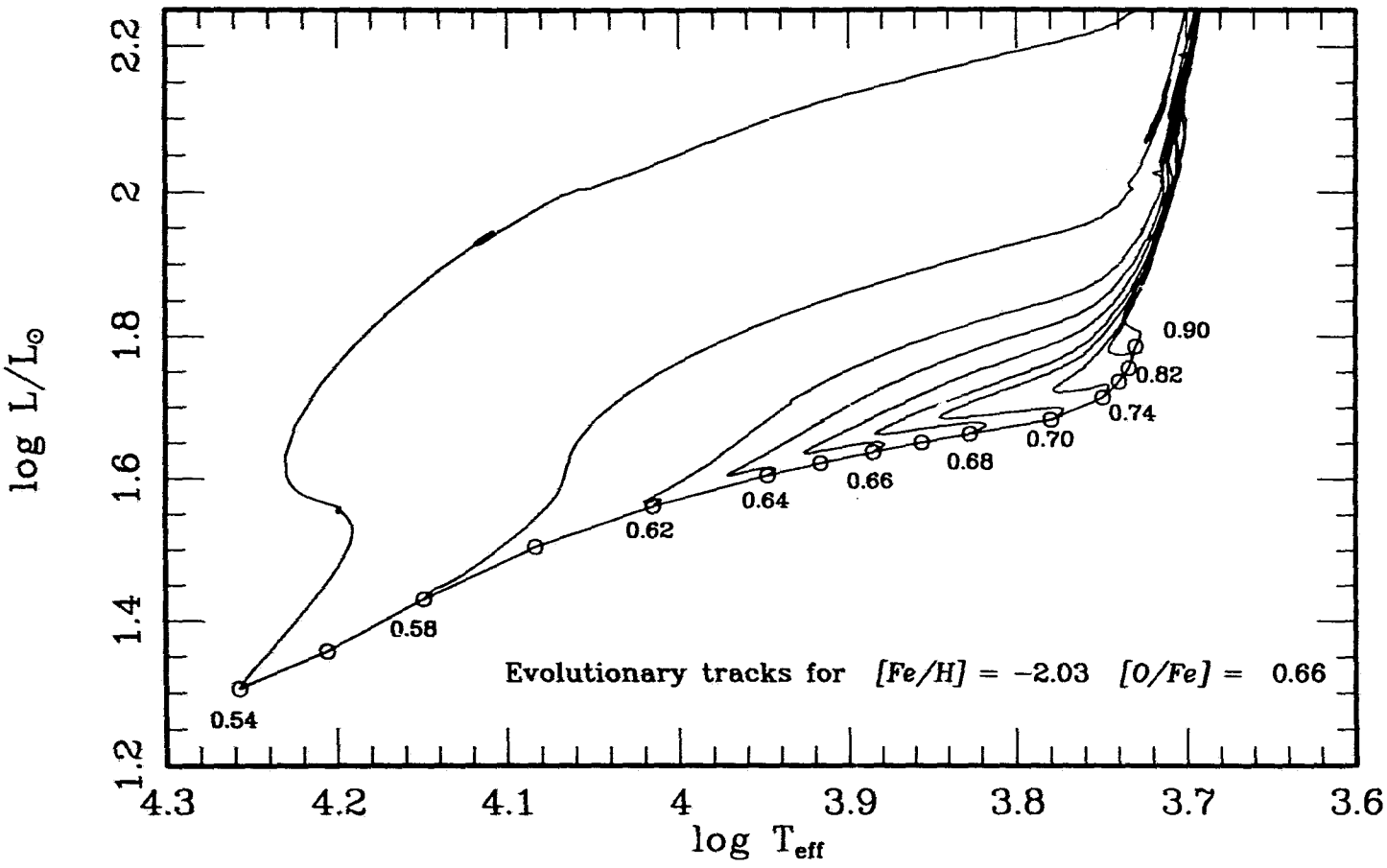

Fig. 2–5–1: Evolutionary sequences for models with parameters (Y_{HB}, M_c, [Fe/H], [O/Fe]) = (0.246, 0.490, –2.03, 0.66). Individual tracks sre labelled by their total masses in solar units.

and the transition between different types is not sharp.

Section 2.5.ii considers the evolution of the core with time and its effect on the shell. Section 2.5.iii deals with the evolution of the hydrogen burning shell, demonstrating the importance of 'shell relaxation' to the sequence morphology. Section 2.5.iv then considers the later stages of horizontal branch evolution, and §2.5.v deals with the early part of the AGB, demonstrating the structural changes which appear with giant evolution. Finally, the results of this section are drawn together in a summary and explanation of horizontal branch track morphology.

2.5.ii An Overview of Core Evolution

In the initial stages of central helium burning on the horizontal branch, the core has an tendency to expand (in contrast, hydrogen burning stars contract throughout their evolution). This has been noted earlier by Hayashi (1966b) and Hofmeister, Kippenhahn, and Weigert (1966). Figure 2-5-2 shows the change in radius from a stage close to the ZAHB to that just after the central density minimum is reached. The model has mass 0.70 $M_\odot$, and the turning points in the surface temperature and central density are virtually coincident. In this plot, the model radius variable has been normalized so that the value R_1 of the radius variable at the surface of the model corresponding to the solid curve is equal to unity. This first model is computed at $t - t_{ZAHB} \sim 2.5$ Myr. This tendency to expand is counteracted in the outer layers of the core by the requirement that the radius of the burning shell be fixed, as is evident from the the 'node' in the mass motion at the shell location. Note that the value of M_c (defined as the mass lying inside the shell at which the hydrogen burning is maximum), increases from its ZAHB value of 0.490 to about 0.505 during the time period depicted here.

The core expansion is broken at some point in the evolution, being replaced by a contraction which grows in rapidity as the helium in the centre is depleted. As has been reported in earlier work (IR70), this occurs when the central helium

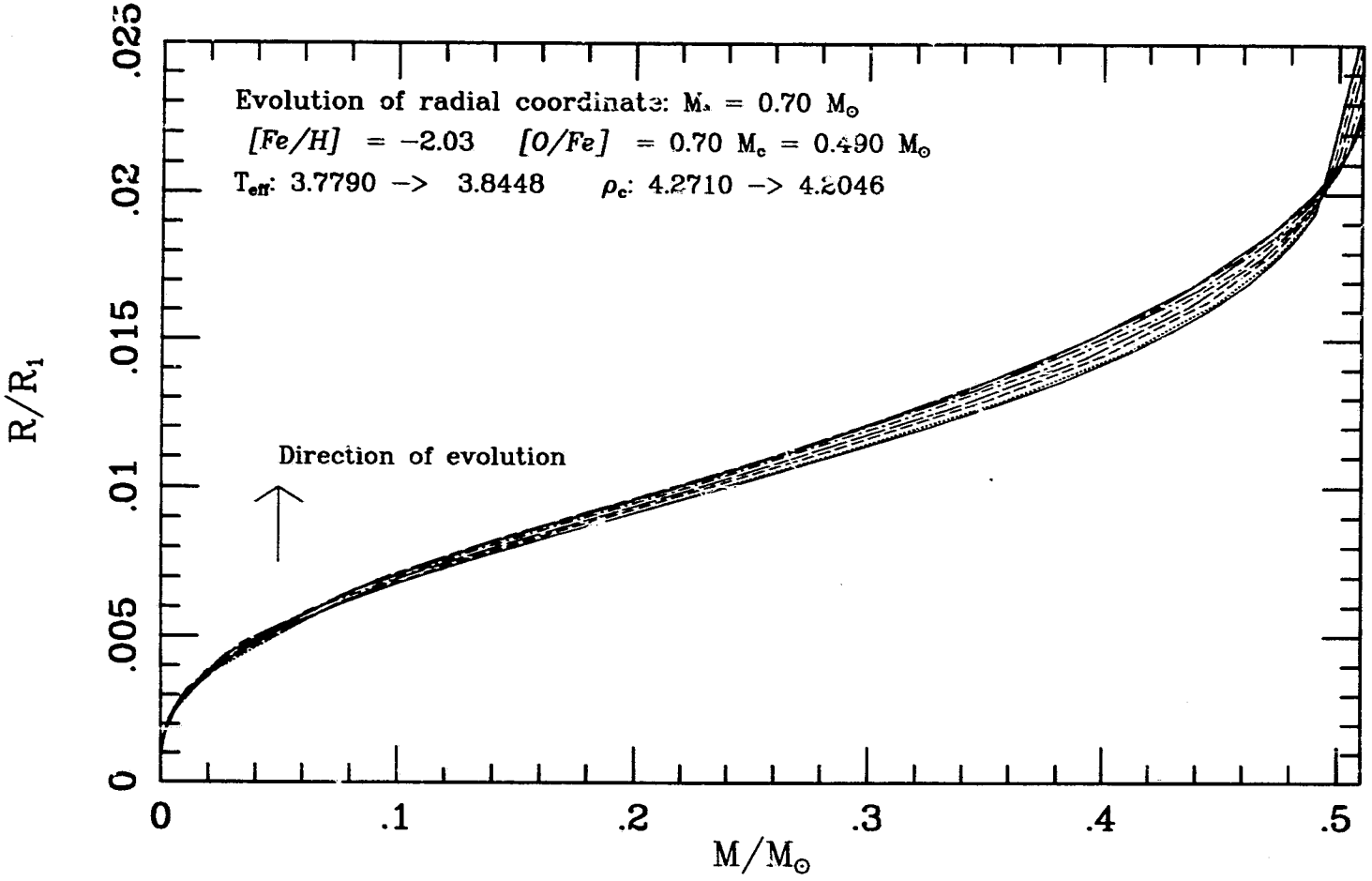

Fig. 2–5–2: The evolution of the radius variable interior to the core for the model with mass 0.70 Mo. The interior profiles are plotted for models close to the ZAHB to a point close to the central density minimum.

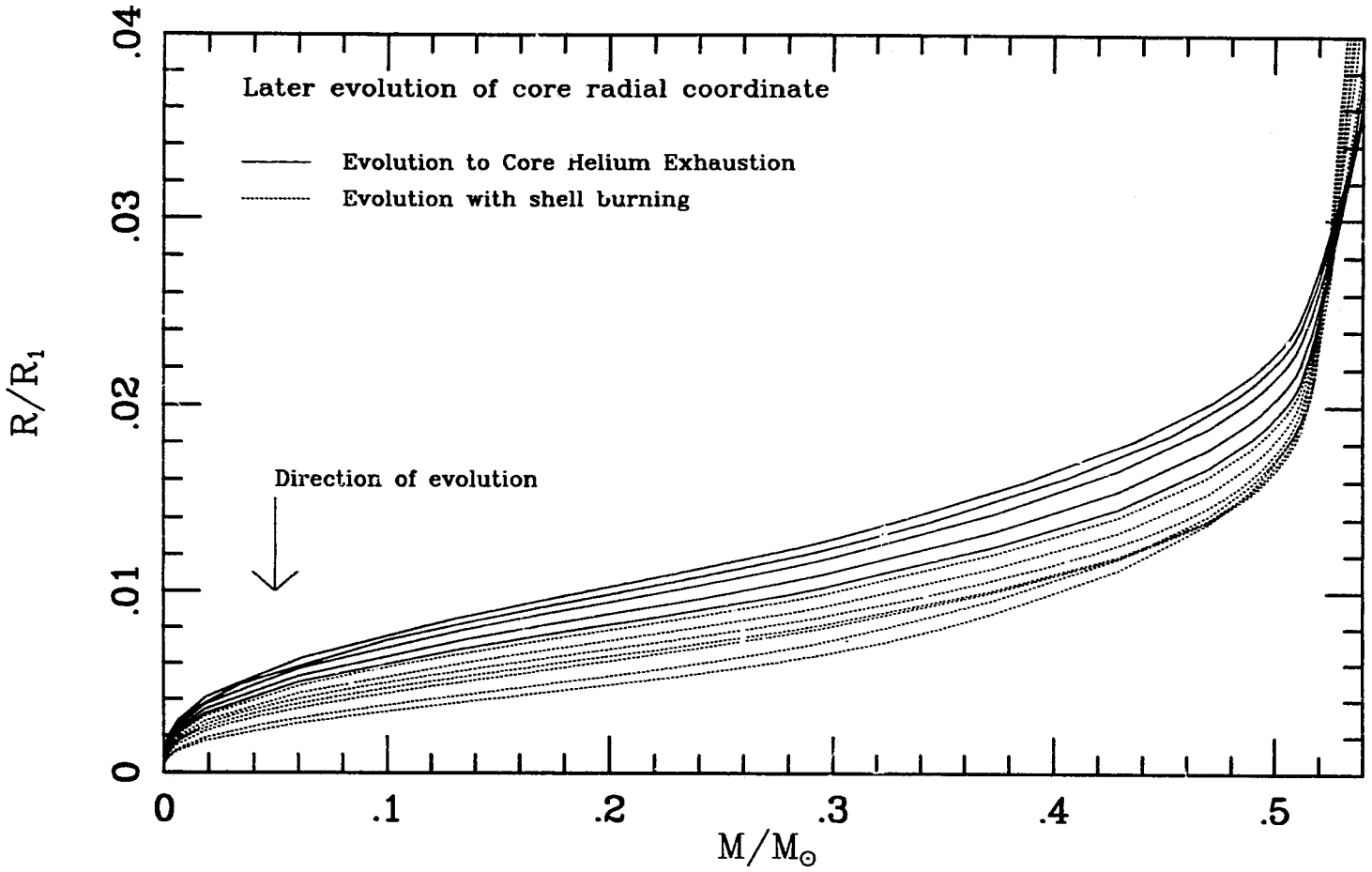

Fig. 2–5–3: As for Figure 2–5–3, but from models later in the evolution.

abundance is still relatively large. Fig 2-5-3 shows the later phases of evolution for this sequence. These model profiles are again normalized to the radius of the solid curve, and the direction in which evolution proceeds is reversed in both the core and the shell.

The evolutionary tracks computed for this study show that the end of the 'expansion' phase and the bluest point on the evolutionary tracks (if this is defined), are distinct events. Define these two points in time by the symbols t_ρ, when the minimum central density is achieved, and t_T, where the maximum surface temperature is reached. A point t_ρ can be defined for every sequence computed, and so must be a feature of HB evolution. However, t_T is obviously not defined for every sequence. Using the computations, it may be observed that, to within numerical uncertainties (caused by discrete timesteps etc.), $Y_c(t_\rho)$ is a decreasing function of mass, for masses in the range $0.54 < M/M_\odot < 0.90$, and takes values between about 0.42 and 0.32. Secondly, $Y_c(t_T)$, where it is defined, also decreases with mass until it is, again to with numerical uncertainty, closely coincident with t_ρ. If t_T were much greater than t_ρ it would mean that both the envelope and core would be contracting, in contradiction to requirement of thermal equilibrium for the shell.

To test the origin of the initial core expansion, an evolutionary sequence was constructed with $M = 0.54 M_\odot$, $M_c = 0.535 M_\odot$. For this sequence, the hydrogen burning luminosity is almost negligible; however, even for this sequence, the core expands initially. In fact, apart from a relocation outward of the density discontinuity, the structure of models of this sequence in the (U, V) is almost identical to that of their counterpart discussed below with smaller core masses. Further, pure helium stellar models contract throughout evolution in the same fashion as for hydrogen burning main sequence stars (Hartwick and VandenBerg 1973b). It is unclear exactly why the presence of the chemical discontinuity forces an initial core expansion. It might be surmised that this is a continuation of the

expansion which results from the lifting of the core degeneracy after the helium flash, and therefore stems from the imposed initial conditions of the evolution. Indeed, the core does become less degenerate in the early part of the evolution, but it continues to do so for a time after the core starts to contract again. Another possibility is that the initial expansion of the core is the result of its response to the abrupt change in chemical discontinuity at its outer boundary, which ensures that the density in the outer layers of the core must fall as the mean weight per particle increases in the central convective region. As will be seen later, the effect of the shell, if sufficiently bright, is both to smooth out and to move the chemical discontinuity. In this case, the requirement that the burning shell stays approximately fixed in radius leads to a modification of the density of the outer core layers.

2.5.iii The Evolution of the Hydrogen Shell

As originally determined by Faulkner (1966), observations of HB stars in globular clusters are best explained if the helium flash results in negligible mixing between the helium-rich core and the envelope. This being the case, it seems reasonable to adopt for the ZAHB models a hydrogen composition profile above the boundary of the helium core which is similar to that found at the tip of the giant branch (but see §4.2). However, the hydrogen shell burning characteristics of horizontal branch evolution are very different from the thin shell which provides the luminosity for red giants. In red giants, the shell is very thin because the temperature is much higher than in the burning shells of HB stars. This is, in turn, a consequence of the fact that the cores of RGB models are far denser[13].

Thus in the initial phase, lasting up to 20 Myr, the shell moves from its initial

[13] *It is possible to show, that in the case of an isothermal core, that the temperature at its outer boundary is approximately proportional to the radius at fixed core mass (cf. Stein 1966; Cox and Giuli 1968, §23.6c; see also Schönberg and Chandrasekhar 1942)*

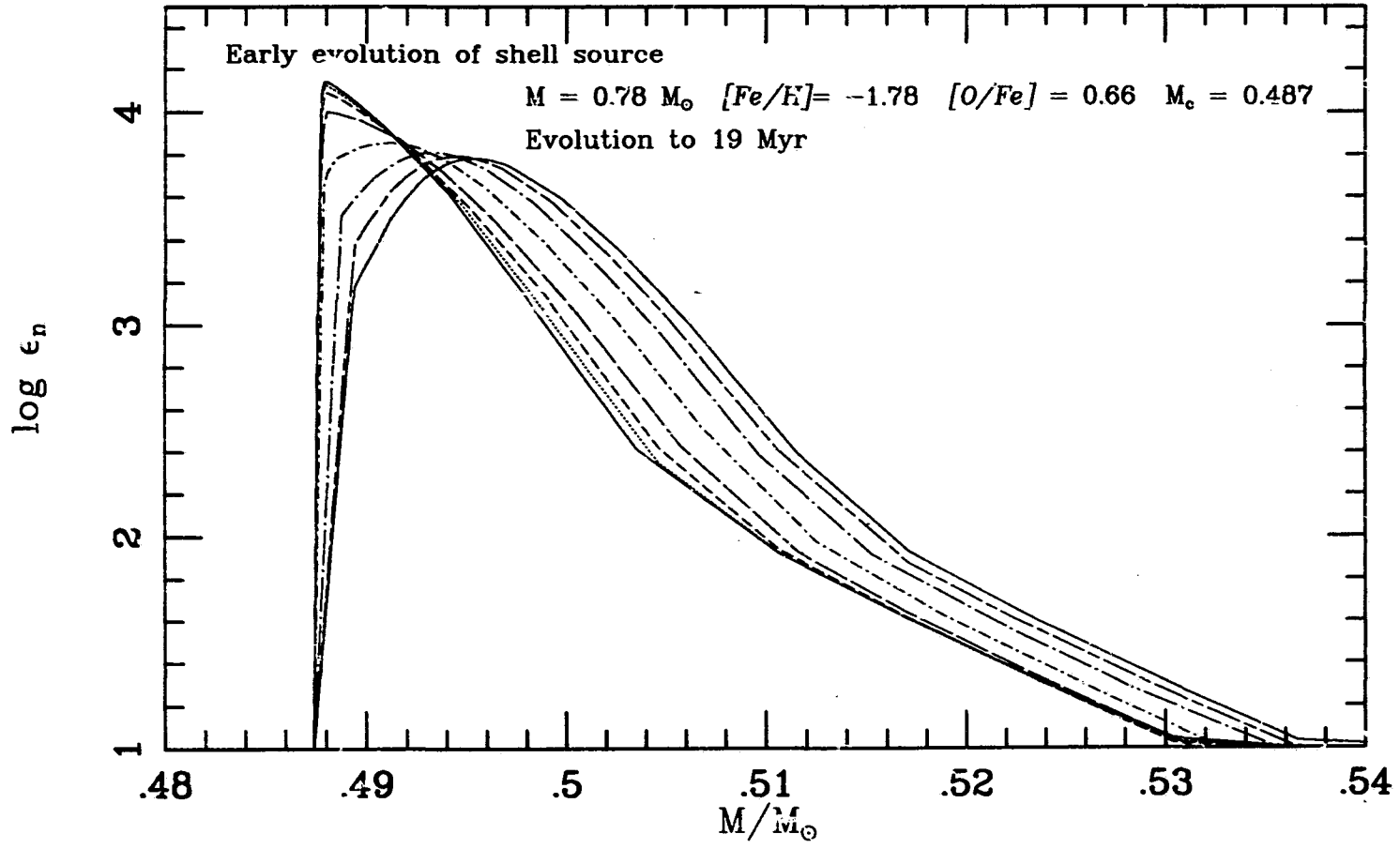

Fig. 2–5–4: Evolution of Hydrogen Shell during the shell relaxation phase of evolution, for a model with mass 0.70 Mo. The evolution of the shell proceeds from the 'sawtooth' shaped curve on the left towards the right.

'sawtooth' energy generation profile, to a configuration whose power output is more symmetrical, as shown in Figure 2-5-4 . The equilibrium shape of the energy generation profile is reached when all of the hydrogen in the narrow red-giant shell-burning region is converted to helium, and the peak of the energy output moves to a point where the hydrogen abundance is much greater. If the burning zone develops its full width, then although its intensity decreases with time it is sufficiently powerful to consume small but significant amounts of hydrogen, and so moves outward with evolution.

In the absence of a significant effect on the structure caused by the shell source, the temperature at the core boundary falls as the core expands. The shell does not relax, in the easily identifiable sense described above, but grows dimmer with time as the temperature falls with the expansion of the core. The early evolution of the shell in such a case is depicted in Figure 2-5-5 . Although the peak burning rate actually increases slightly, the overall shell width decreases (this occurs because of the cutoff temperature of the nuclear reactions - see §2.4). In this case, the shell stays virtually at the same mass location until very late in the evolution. In a sense, one can think of sequences with this kind of shell evolution, which are followed by the very lowest HB star masses, as being comprised of an extended shell relaxation phase, briefly reaching the blueward/redward evolution pattern displayed by more massive models very near to helium core exhaustion. At very late stages of evolution, the core energy production is all but extinguished, so that the hydrogen shell must supply nearly all of the stellar luminosity. Hence the relaxation 'eventually' occurs if the model does not evolve directly to the white dwarf region of the HR diagram.

To follow the evolution of different types of sequence towards core exhaustion, it is instructive to view the development with time of the (U, V) plane trajectories taken by the interior structure. From the investigation of Zero Age models above, it is seen that the magnitude of the shell significantly alters the equilibrium of the

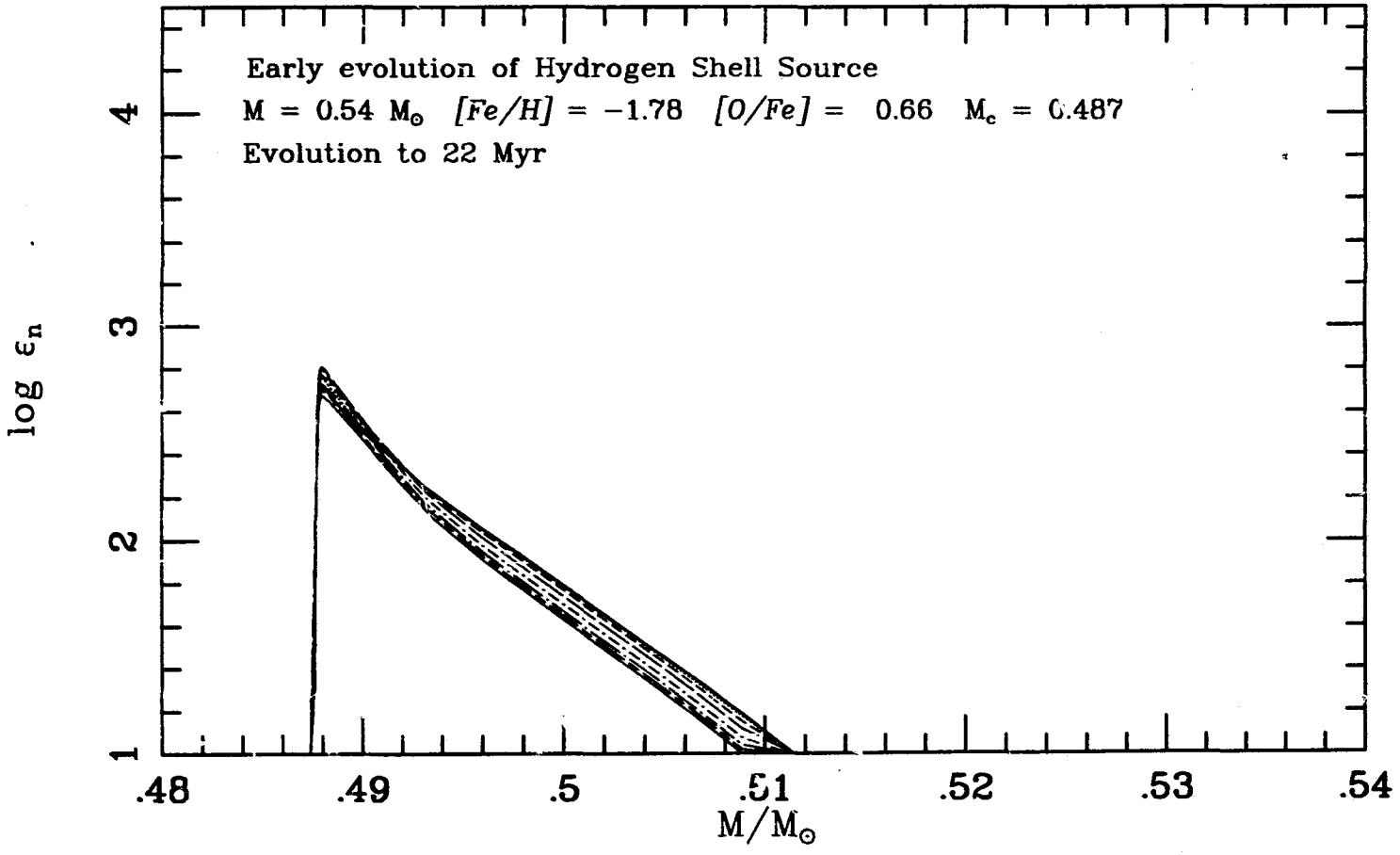

Fig. 2–5–5: As for Figure 2–5–4, but for a lower mass model, 0.54 $M_{\odot}$, plotted to the same scale as the previous graph. The shell evolution proceeds to the right as in the previous figure, but is very weak in comparison.

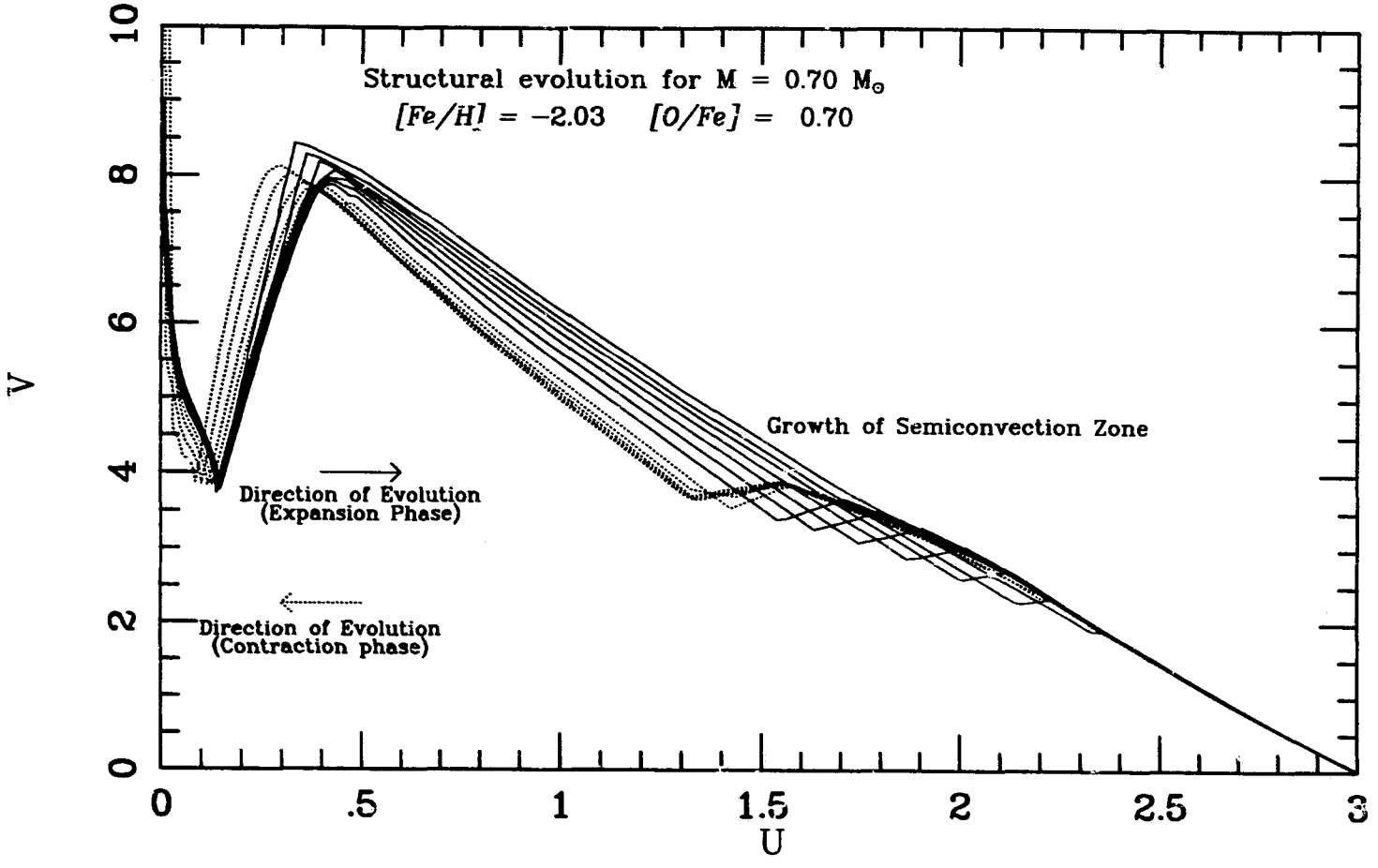

Fig. 2–5–6: The evolution of the interior structure of the 0.70 Mo model from the ZAHB to core exhaustion. The solid curves are taken from the early phase (blueward evolution), and the dotted curves from the redward evolving phase.

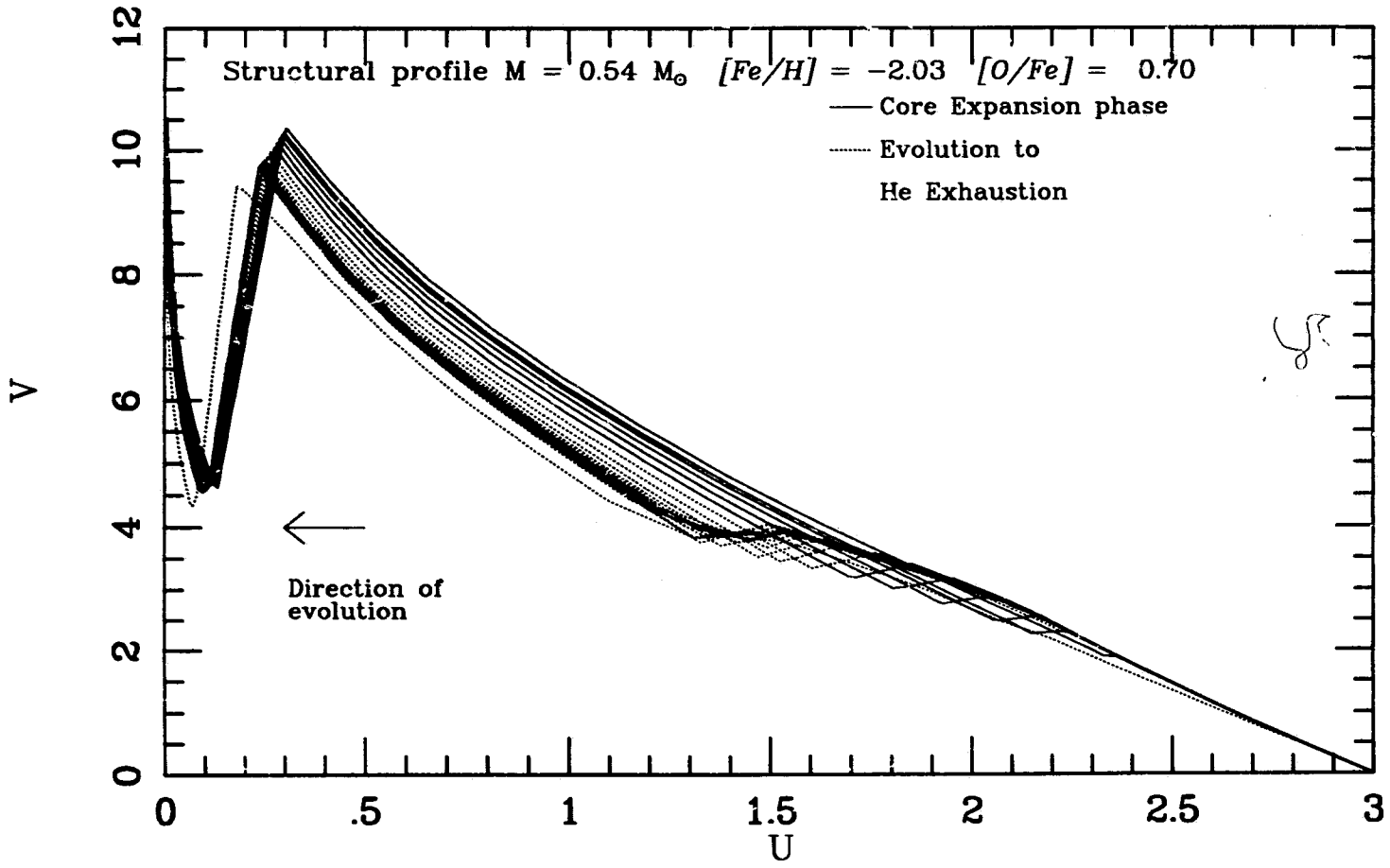

Fig. 2–5–7: As for figure 2–5–6, but for the model of mass 0.54 Mo.

outer core layers. Since the shell luminosity changes significantly with evolution, the structure of the outer core layers is modified accordingly. Figure 2-5-6 shows the evolution of the interior structure on the (U, V) plane from the ZAHB to helium exhaustion (defined as the point where $Y_c < 10^{-4}$). The growth of the semiconvection zone is marked to the right of the figure; the effect on the structure of the growing chemical discontinuity at its outer edge can be seen. At the core-shell interface, the (U, V) curves become smoother after the shell has relaxed. The direction of evolution during the core expansion phase is down and to the right, and this is reversed when the minimum core density is reached. In contrast, the evolution shown on Figure 2-5-7 , for the $0.54M_\odot$ model, shows a continuous direction of (U, V) evolution.

This increase in U for the more massive models is tantamount to an increase in relative central concentration, and given the expansion of the inner core layers, this appears somewhat paradoxical. In order to illustrate these effects, consider Figure 2-5-8 (for $0.54M_\odot$) and 2-5-9 (for $0.70M_\odot$), which show the evolution of the density profile in the outer part of the core. The lower mass model has a core which expands in radius throughout the early phase of evolution. The density and temperature in the shell decrease with time as the core expands, and the model evolves continuously to the red. In contrast, the evolution of the density profile of the more massive star contains a node (*i.e.*, a point where the density is fixed). The composition discontinuity at the core edge is smoothed out and moved outward, and the density in the outer layers of the core actually grows. After relaxation, the shell moves slowly outward as the hydrogen is consumed, and, because its radius is approximately fixed, the temperature drops and the shell dims. According to the reasoning given in §2.3, this decrease in shell luminosity results in a steepening of the gradients in the outer layers of the core, which is *exactly* the physical circumstance which allows the radius of the shell to remain roughly constant. Furthermore, the envelope density is also increased, implying

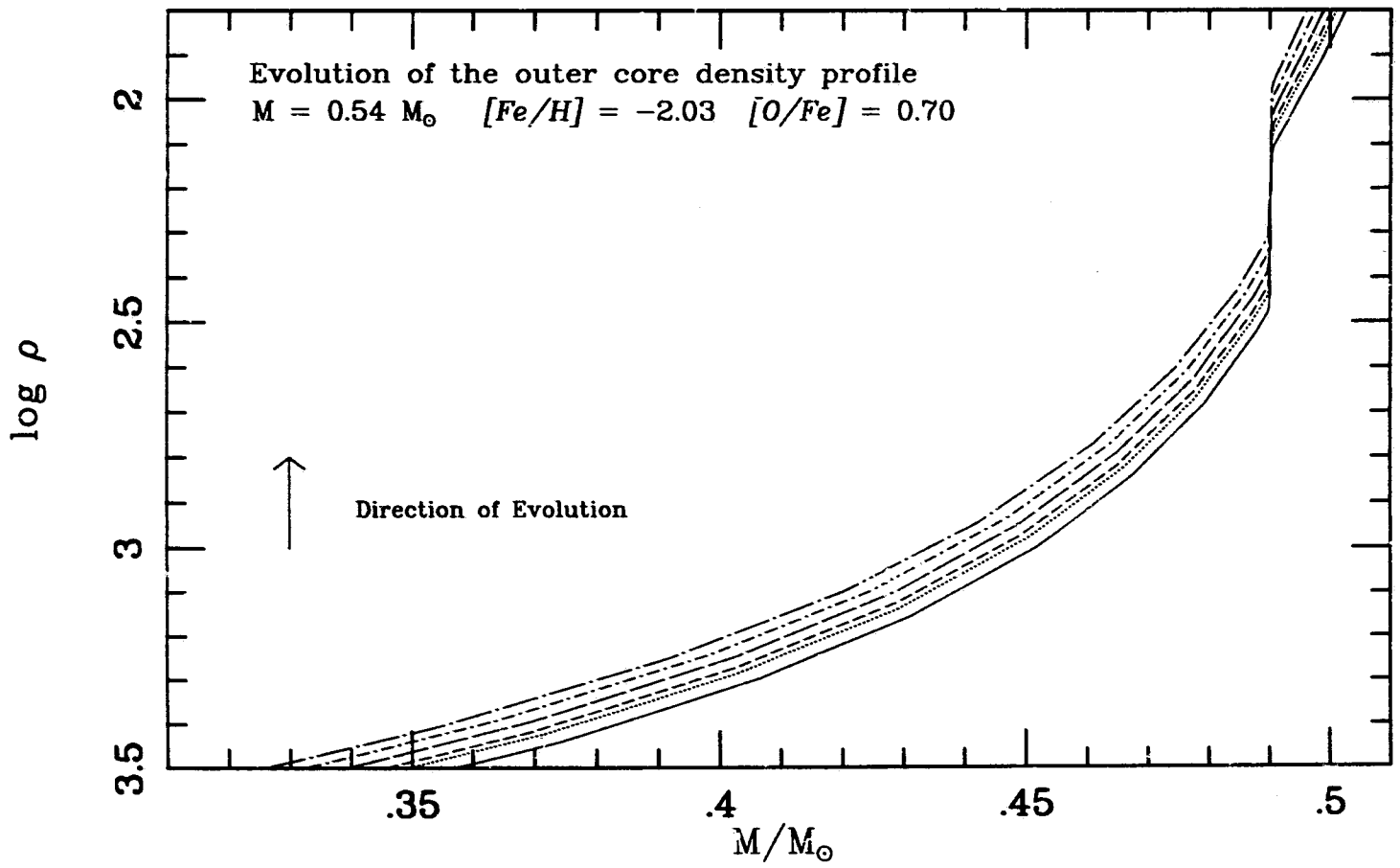

Fig. 2–5–8: The evolution of the density in the core for the model of mass 0.54 Mo, up to the point t_r. The direction of evolution is denoted on the left by an arrow.

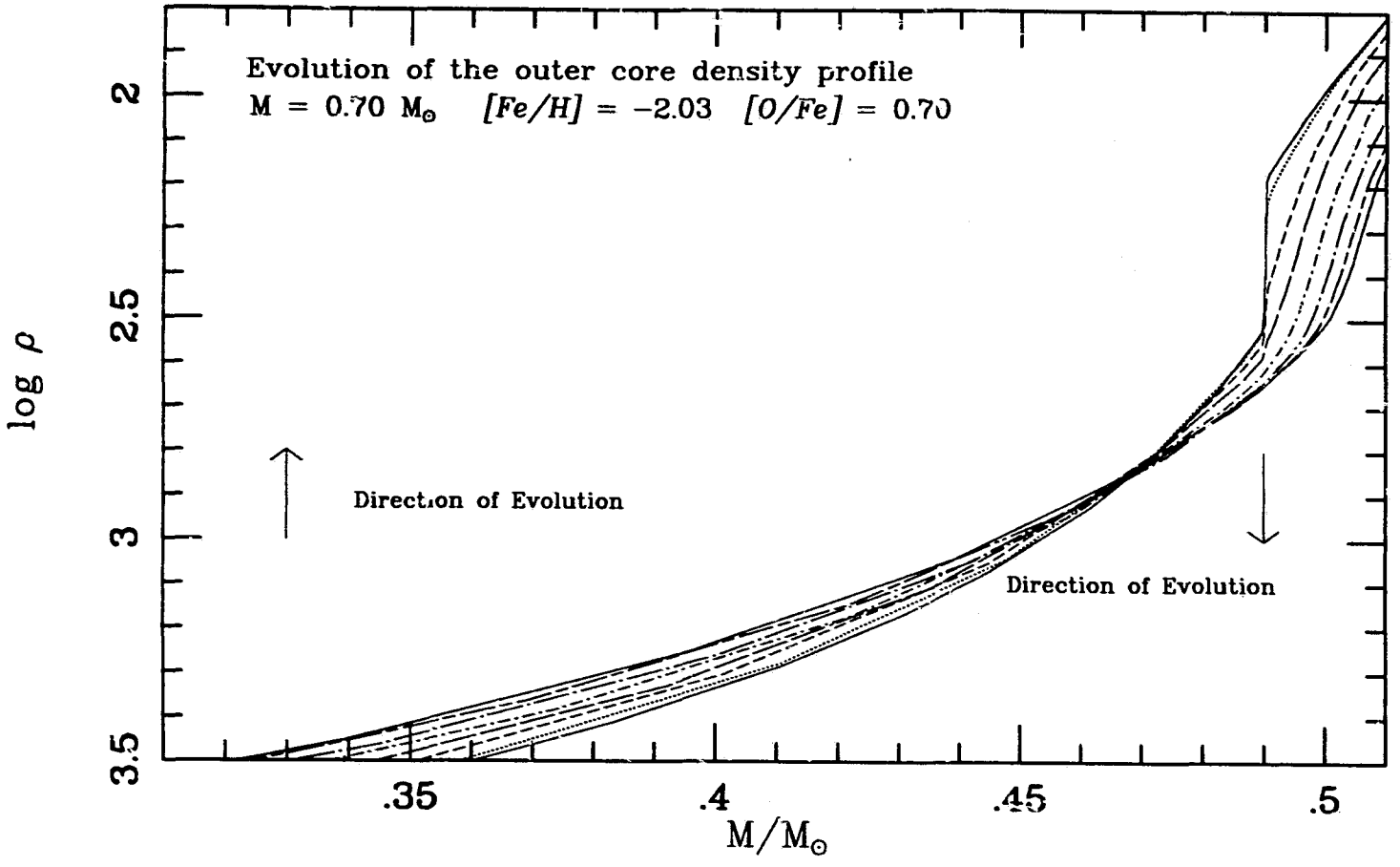

Fig. 2–5–9: As for fig 2- 5–8, but for a model of mass 0.70 Mo. In this case, the direction of evolution is different in the outer layers, as denoted by arrows to the extreme left and right of the diagram.

contraction and therefore blueward motion in the HR diagram. As the model mass is continuously decreased, the node in the density moves toward the core-shell interface. The density evolution in the layers above it weakens, and therefore the blueward motion also shrinks in colour width. When, for sufficiently low mass, the nodal point reaches the chemical discontinuity, the structure of the core becomes that of the lower mass models seen in Figure 2-3-1, and it changes with evolution in the fashion seen in Figure 2-5-7. On the other hand, as the envelope mass is increased, the shell source becomes brighter and the outer layers of the envelope become convective. The increase in envelope density with evolution redistributes the mass inward, and as a consequence, less mass is contained in the convective zone. The outer boundary is then attained at a higher temperature, since the effective temperature is a decreasing function of the convection zone. However, since this change in envelope structure is weaker than for radiative envelopes, the result is a slower blueward evolution; for sufficiently large envelope masses, the change in T_{eff} can be almost non-existent.

Thus an understanding of the intricacies of the core and shell evolution has lead to an explanation of the morphology of HB sequences in the HR diagram. The resulting sequence topologies are summarized in the last part of this section.

2.5.iv The Evolution to the Asymptotic Giant Branch

For those sequences with relaxed shells at the time when the core starts to contract, the evolutionary behaviour is similar. The core contraction is obviously related to central helium depletion, as pointed out by IR70. They noted that the dependence of the triple-α reaction on the third power of the helium content made it much more sensitive to abundance than the hydrogen burning rates. The high temperature sensitivity of the helium burning reactions implies that the central temperature will rise but slowly with the mean molecular weight. Since the central conditions of ZAHB models do not vary greatly with mass, the decrease

in $Y_c(t_\rho)$ with mass must result from the difference in core evolution discussed in the previous section. The rate of central temperature increase escalates with decreasing helium abundance, and this drives the rate of evolution of the star on the colour-magnitude diagram. The maximum rate of evolution is governed by the thermal timescale, which is attained when the helium content of the core drops to zero.

For the faint blue HB models, the contraction also increases the shell reaction rates. As a result, the burning profile at last attains its equilibrium shape and the track begins to evolve to the blue, turning back toward the red and the AGB as the helium supply is finally exhausted. Figure 2-5-10 shows the evolution of the shell burning profile in such a case; the expansion, contraction and exhaustion/shell burning phases are indicated. After the core stops expanding, the burning shell is driven to higher temperatures, until finally it becomes bright enough to smooth out the chemical discontinuity at the core edge. Evolution then proceeds to the blue until the core contraction brightens the shell sufficiently to enforce steeper temperature and mass gradients in the outer layers of the envelope. At this point, the evolution reverses direction back to lower temperatures. Provided no mass loss takes place, the lower limit to asymptotic giant masses is set only by the ability of the shell to support the star while the core burning switches from the centre to a second shell.

As the central fuel source becomes close to being exhausted, the core helium/carbon burning is almost completely quenched; the strong contraction at the centre contributes an amount of energy which is similar in magnitude to the nuclear sources. The region just above the hydrogen shell is simultaneously involved in a rapid expansion (this corresponds to the development of the loop in the (U, V) plane, as will be seen presently), which is powered by the increasing shell luminosity. Following this, the star moves on the HR diagram at a rate governed by the thermal timescale. The helium core luminosity begins to decrease rapidly,

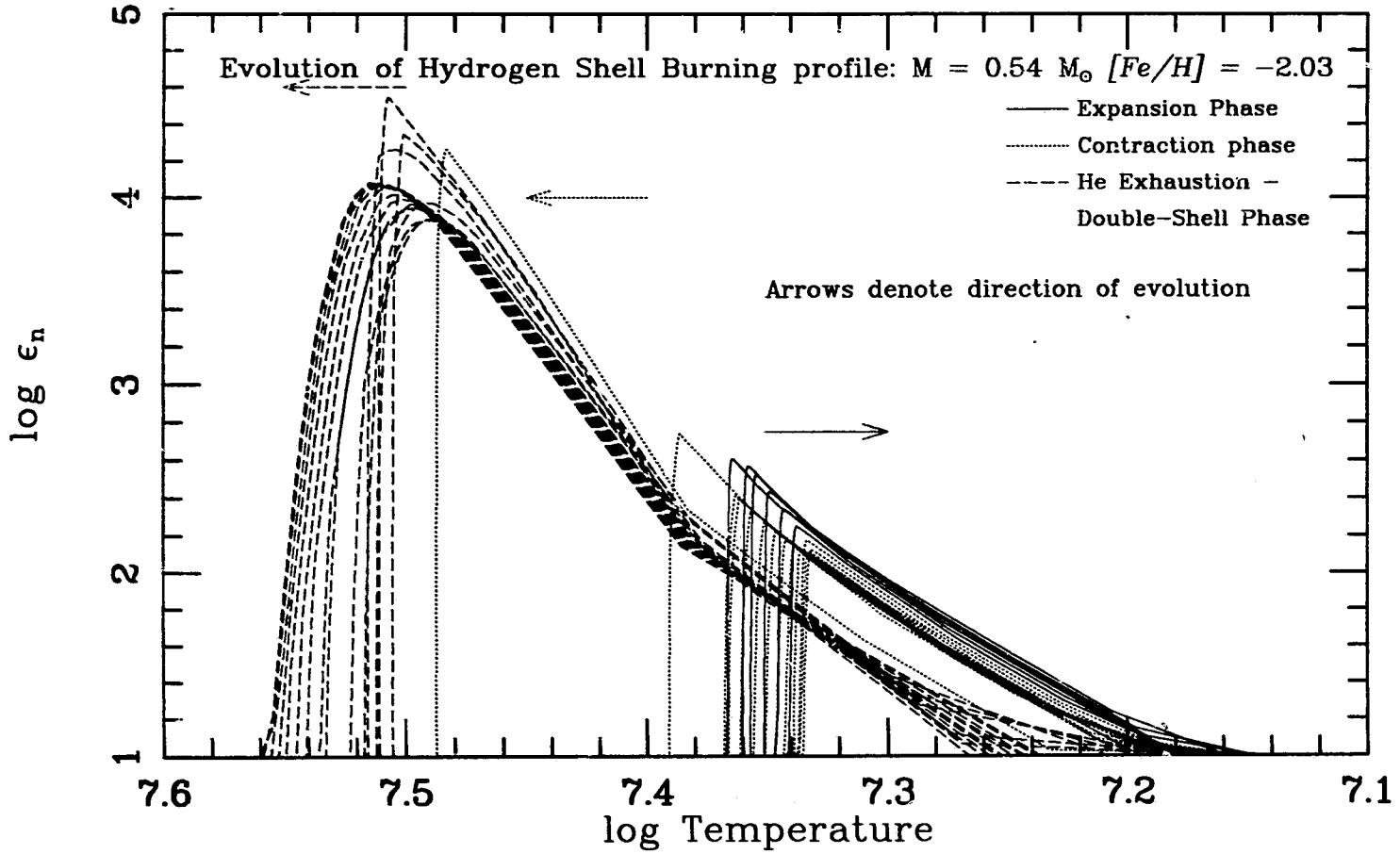

Fig. 2–5–10: The shell energy generation profile for the model with mass 0.54 Mo. The phases of expansion, contraction, and shell burning are plotted with solid, dotted and dashed curves respectively.

and the contracting core generates thermal energy equal to about 40 - 45% of the total power output. At this time the contraction leads to a very rapid rise in the shell luminosity, which can produce up to 70 - 75 % of the power output of the star. The increased flux steepens the temperature gradient, and develops a steadily larger convective envelope; the excess energy goes into expanding the region immediately above the shell. Although models with convective envelopes are extensive, it is interesting to note that the material in the outer convection zone is not in motion; it is the region where the gradients are changing rapidly which expands. The drop in temperature which accompanies this change forces the convection zone boundary downward as the material becomes more opaque. This process is equivalent to the formation of a red giant, and the reasons why the structure responds in this fashion are discussed more fully in the next section.

2.5.v Early AGB Evolution and the formation of giant stars.

The calculations performed for this study have been terminated at a fixed luminosity given by $\log L/L_{\odot} = 2.25$. At least for masses less than $1M_{\odot}$, this limit is reached well after helium is exhausted in the core. This places within the scope of this study the phenomenon of red giant formation, discussed recently in the papers by YvdH and Applegate (1988). However, the major portion, at least in evolutionary path length if not in duration, of AGB evolution is beyond the scope of this work. In this section, the process of red giant formation is reconsidered, because this is the dominant feature of the post-exhaustion phase of evolution. The phenomenon of AGB star formation seems to have much in common with the formation of 'first branch' (hydrogen-shell) red giants, and it is interesting to look for common features within the evolution of the structure. The most important characteristic of a red giant is, of course, a distended convective envelope. There is a close association between this feature in the models and the existence of a loop in the (U, V) plane, for sufficiently small envelope masses. The obvious problem

to be faced in studying the phenomenon in this context is the fact that horizontal branch stars are already fairly large, and the massive red models start their life on the ZAHB with giant envelopes. Thus, the models evolving from the extreme blue end of the ZAHB to the AGB provide more useful examples. The $0.54M_{\odot}$ model used above has been evolved to a stage just before thermal pulsing begins ($\log L \sim 2.75$) in order to provide such an illustration.

The other feature of the early AGB is the reversal in evolutionary direction seen in most of the tracks plotted in Figure (2-5-1). This has been discussed elsewhere (*e.g.,* IR70); briefly it is due to the changeover between hydrogen and helium shell burning. The core contraction increases the hydrogen luminosity, and the helium core burning decreases. Until the shell is properly established in the region above the old convective core[14], the net result is a decrease in total luminosity. Since in the region of the core immediately above the semiconvection zone the material is partially mixed by semiconvection, this feature is modified by the mixing assumptions adopted earlier in the evolution. The evolution reverses in direction when the helium shell luminosity has increased sufficiently to compensate for the reduction in hydrogen shell power output. The helium burning shell begins to dominate the energy production and the luminosity of the star rises steadily until the the thermal pulses appear at $\log L/L_{\odot} \sim 3$.

A few papers in the last ten years have studied the question of red-giant formation (Eggleton and Faulkner 1981; Renzini 1984; YvdH; Applegate 1988), and the question itself seems to have aroused many debates and conflicting explanations. Many papers on this subject include a list of 'incorrect' explanations, which the authors have a duty to dismiss. Part of the object of this section is to show that some of these authors may have found the causes of the giant phenomenon, yet their arguments lack the necessary rigour to be conclusive.

---

14 *i.e., the zone which is bounded below by the mass coordinate at the outer boundary of the convective region at the time when convection started retreating.*

Eggleton and Faulkner (1981) suggested that the correct explanation (for the phenomenon they term "giganterithrotropism, or the tendency of stars to form red giants") was that red giants resulted from the development of a gradient in molecular weight, and the initiation of shell burning. They proposed a solution which appealed to the behaviour of simple polytropes, which exhibit large radii for value of n close to 5. They argued that the development of the molecular weight gradient (at the burning shell) and the influence of a burning shell both serve to increase the mean value of n. This conclusion is not too different from that reached here, the major difference being that simple polytropes do not provide the answer, since the value of n is raised for a very narrow region, and the gross expansion to the giant branch demonstrably does not take place where n is above 4. The argument adopted here and by YvdH appeals to the behaviour of M-solutions to the Lane Emden equation, which must be more appropriate since the chemical discontinuity at the shell forces the solution trajectories into the region of the (U, V) plane below the appropriate E-solution. More directly, M-solutions have the property to be "infinite" since although their radial variable is bounded, their central density is not. It must be stressed that each E- or M-solution represents a family of solutions whose absolute radius scale is determined by the density at its lowest point of applicability within the model [15] and the constant $\mathcal{K}$ (see §2.2). As far as the exterior solution is concerned, the initial point of the exterior solution is 'close to the centre' (Upton, Little, and Dworetsky 1968) and thus at high scaled density. If the loop is large, then the outer density attained may be very small indeed, and absolute radius scale may therefore be very great.

The paper by YvdH has already been extensively referenced above, and a search for similar features in the AGB models that they found in giant stars was an important motivator for using the methodology adopted in this entire chapter.

---

[15] *This is a generalization of the result for E-solutions, in which the scale depends on the central density.*

They give three conditions for giant star formation: (i) the presence of a condensed core; (ii) a density discontinuity in the model, such as is provided by the core-shell interface, and (iii) a zone in which the polytropic index lies between 3 and 5. They claim that the the massive increase in envelope size with evolution is the result of the index being greater than 3 (at which the solution has a power law behaviour), and crossing the cut in the (U, V) plane. All of these conditions are indeed satisfied, but their arguments are flawed for the following reasons. Firstly, the power law solution exhibited by structures with index greater than 3 is reached near the *centre*, not the *surface* of the model. The M-solutions, which are obtained if the (U, V) curve crosses the E-solution of appropriate index, have power law, exponential, or oscillatory behaviour for $n \geq 3$ near $\xi = 0$ (see §2.2), but are regular for finite values of ξ. Secondly, the 'singular point' they refer to does, of course, exist in the (U, V) plane, but the loop in the (U, V) plane is not necessarily associated with it. It is of much greater importance that, on the upper side of the density discontinuity, the trajectory lies below the cut *for the local value of* n. Thirdly, although all of the solutions do contain a shell where $n > 3$, and obey all of the other conditions, as has been seen for the very low mass models which are not giants, this is not a sufficient condition. In fact, a necessary and sufficient condition for the existence of a loop given above and in section 2.2 is precise because of the boundary conditions $(U \to 0, V \to X)$[16], which ensure that dU changes sign again before the boundary is attained.

Despite these objections, they point out the essential role that the loops in the (U, V) plane play in the production of giant envelopes (see also Upton, Little, and Dworetsky 1968). That is, the existence of the loop increases the path length of the solution trajectory in the plane. Since the density gradient is approximately constant along the curve (until the convective region is attained) the density drops

[16] *For finite surface pressure boundary conditions,* $V \to 10 - 20$ *at the outer boundary.*

to much lower values compared to a solution curve for a model of the same mass which does not contain a loop. This implies a huge increase in radius, and, as the temperature decreases, again with approximately fixed gradient, the opacity eventually rises when the ionization zones are attained. This occurs at a steadily decreasing value of the mass coordinate as the loops grow in size.

Figure 2-5-11 shows the (U, V) plane curves for the $0.54 M_{\odot}$ model from the core exhaustion point to just before the thermal pulsing era. In these curves, the direction of evolution of the point in the diagram representing the edge of the core is leftward throughout. Figure 2-5-12 shows the evolution of the nuclear energy generation with respect to the radius variable. The location of the helium shell is identifiable as a near-inflection point in the curves (see Fig. 2-5-11), which moves outward with time. The composition changes in the helium-burning zone are relatively smooth because the burning region is very thick. The evolution of the hydrogen burning shell can be seen at the peak in the curve to the left. The contraction of both shell regions occurs in such a way as to hold their densities approximately fixed. Thus, as the shells both move outward, thermal equilibrium requirements ensure that a node exists in the mass motions at the hydrogen shell, but not at the helium burning location. As the helium shell moves outward in mass, the hydrogen shell is reignited and becomes very thin owing to the increase in its temperature.

Figure 2-5-13 shows the development of the (U, V) plane loop. Inspection of the behaviour of n shows that it has a value of 3.08 ± 0.01 close to the outer edge of the hydrogen shell in all of these curves. The cut line for this value of n is shown on the graph; for the sake of illustration, the lines for 3.12 and 3.04 are also plotted to indicate the sensitivity of the cut to changes in n. Note that the loop behaviour appears only if the solution trajectory crosses the cut, as expected, and this occurs here because of the decrease with evolution in the V coordinate at the top of the shell. Further, for this value of n, the singular point lies at

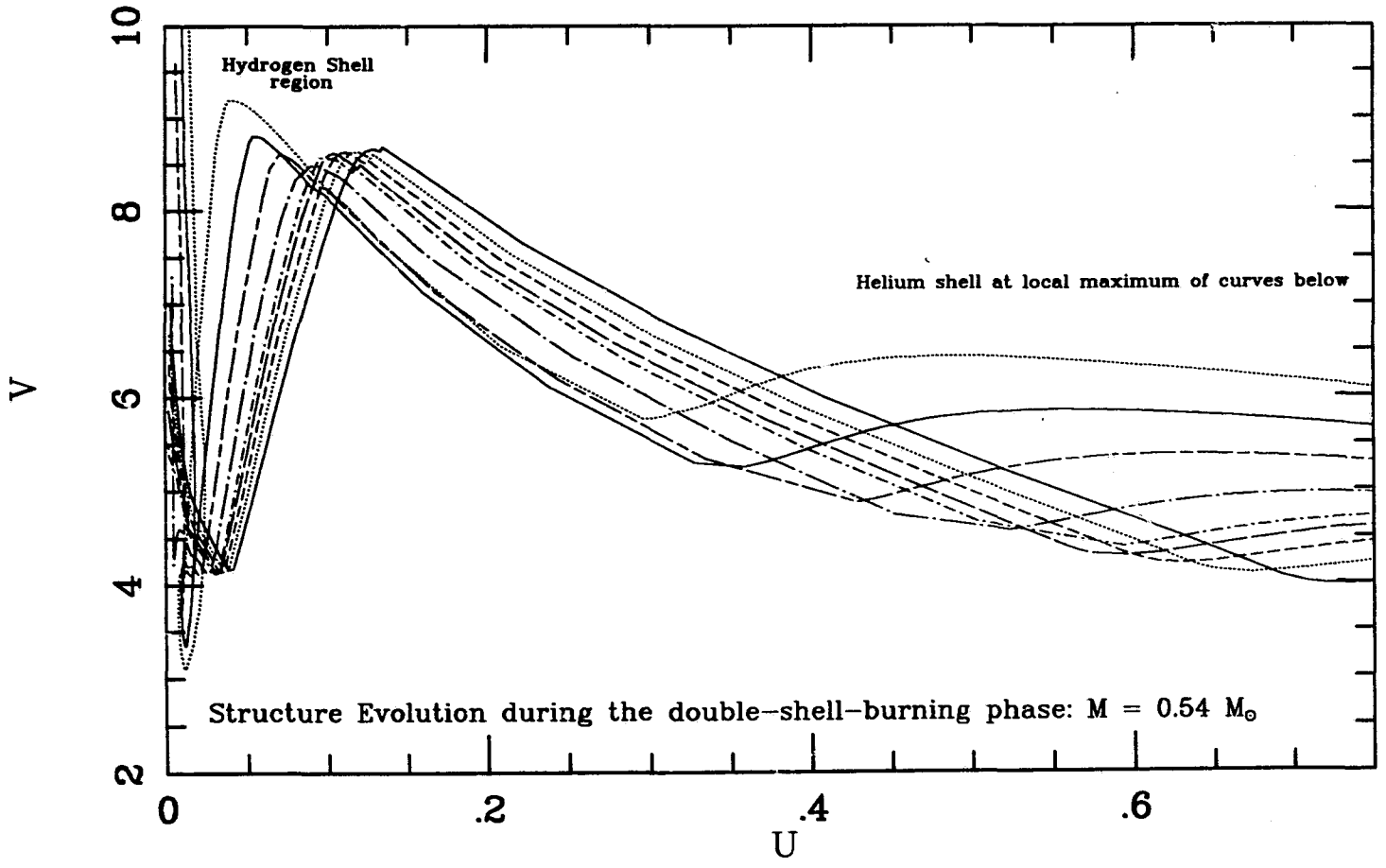

Fig. 2–5–11: *(U,V)* plane curves for the model with mass 0.54 Mo illustrated above for the evolutionary phase between core helium exhaustion and the point where log $L \sim 2.75$.

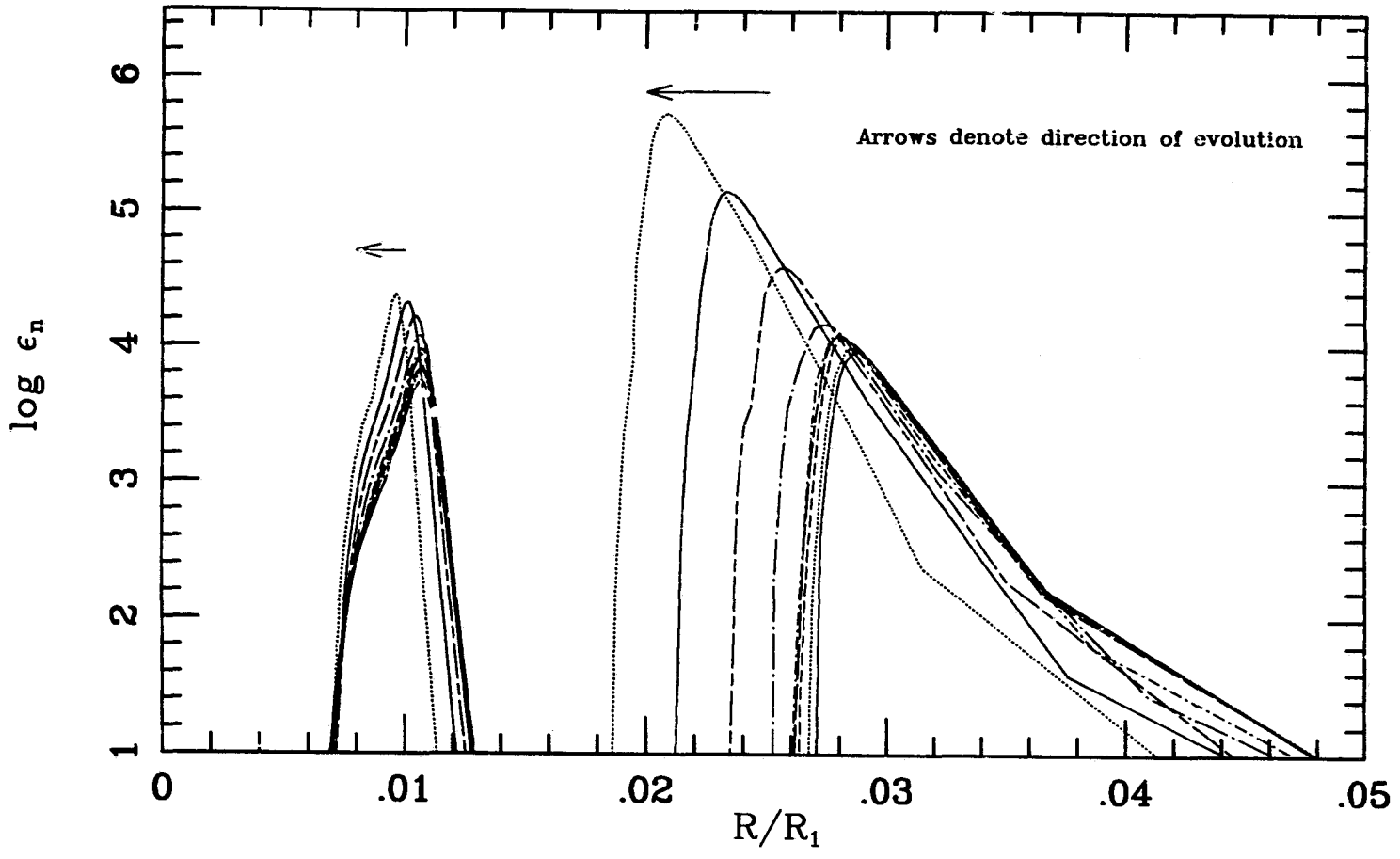

Fig. 2–5–12: Evolution of the energy generation profiles in both the hydrogen and helium burning shells for this model in the same evolutionary epoch.

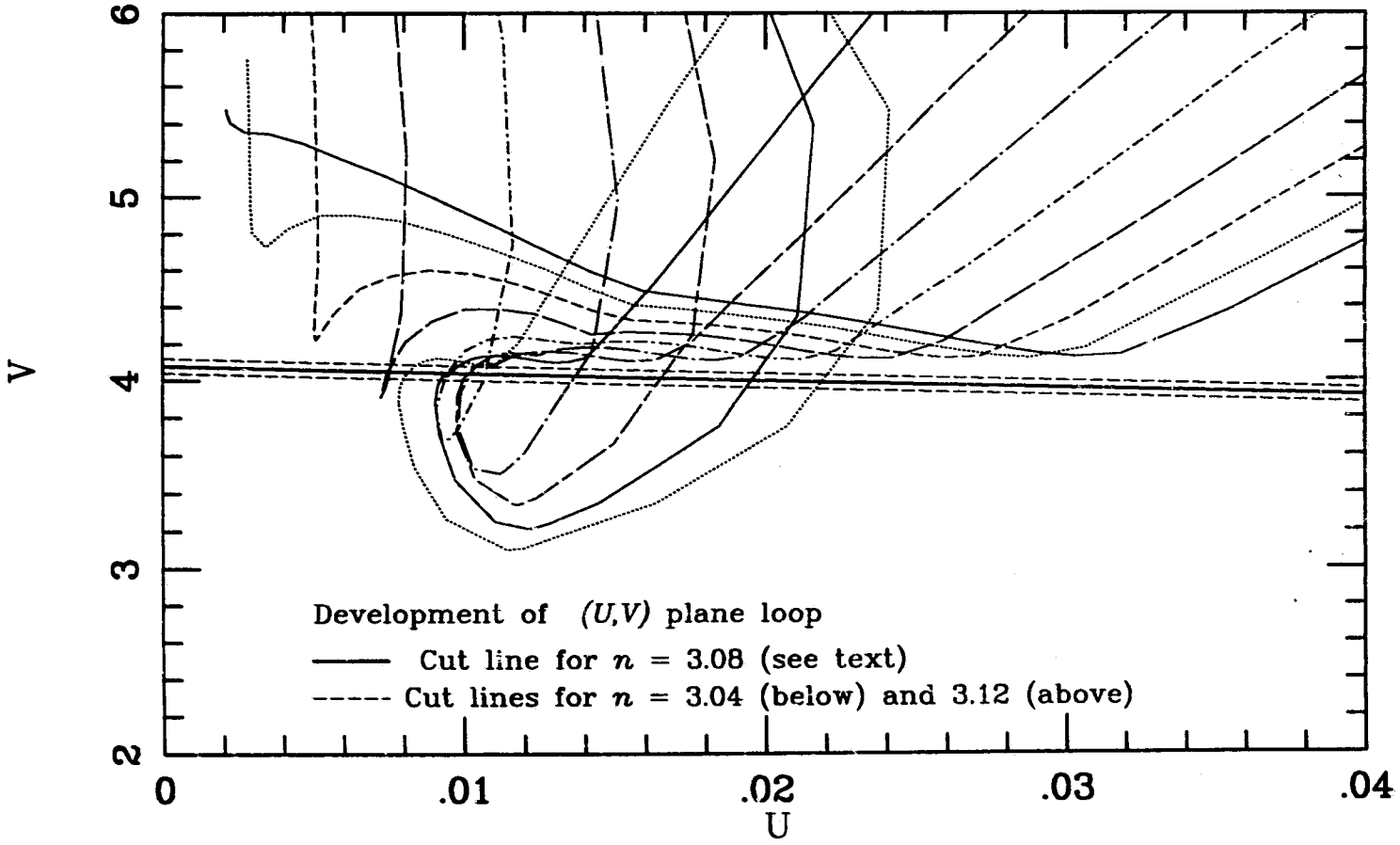

Fig. 2–5–13: The development of the loop in the *(U,V)* plane. This diagram shows the last nine curves plotted in Figure 2–5–11, together with the cut lines for values of n close to that attained above the hydrogen shell in the curves with loops.

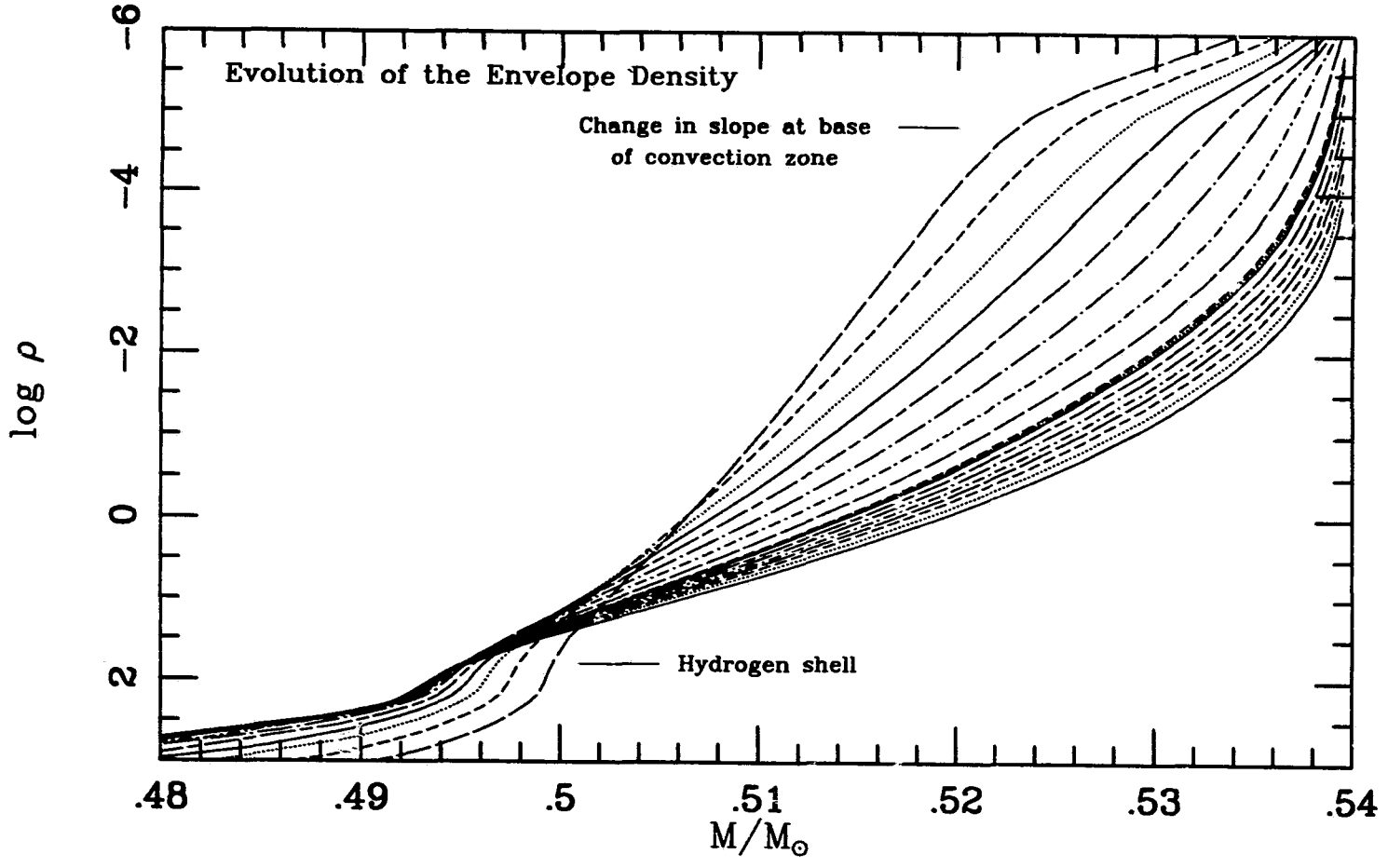

Fig. 2–5–14: The evolution of the density profile in the envelopes of the models used for Figures 2–5–11 and 2–5–12.

$U \sim 0.038$, $V \sim 3.9$, so that the loop development is not related to the existence of the singular point. The loops exist in the last six curves plotted; inspection of the envelope density profiles (Figure 2-5-14) shows that significant convection zones exist only for these models. At the onset of envelope convection, the density gradient with mass becomes appreciably shallower.

Since the hydrogen shell moves slowly in mass, and relatively rapidly inward in radius, it follows that the gravitational potential ϕ at the shell is decreasing. Since inspection of the pressure profile leads to the observation that P also varies little at the shell location, it follows that the drop in V in this part of the model must stem from the decrease in density. *In this particular case*, the additional change in ρ is provided by the narrowing of the burning shell. After the trajectory crosses the cut, the continuing evolution carries the envelope to ever lower densities. However, it must be stressed that the reasons why the solution curves cross the cut can be different in different models. The essential point, though, is that if the effects of stellar evolution are such that the structure traverses the cut line, then changes in stellar parameters can be quite rapid. For this to occur, necessary conditions are the existence of a chemical discontinuity — so that the core solutions match discontinuously with M-solutions — and a bright shell source.

Two arguments have appeared relatively recently which suggest that the red giant phenomenon results from the fact that there exists an upper limit to the luminosity which can be transmitted by a radiative envelope. Renzini (1984) points to the behaviour of the opacity derivatives in the upper part of the envelope, and predicts a 'thermal runaway', leading to massive expansion, where the derivative of luminosity with radius W changes sign (recall that the opacity and luminosity are only related in radiative regions). His arguments have, however, been extensively investigated by Weiss (1989), who concludes that the development of giant envelopes is not related to the behaviour of W: "*... W merely reflects the changes in luminosity and radius that take place [with the evolution], but does not demon-*

strate any properties of the star". Significantly, however, he notes that the region of expansion lies immediately above the shell-burning source, which is exactly the behaviour of the models demonstrated here.

Applegate (1988), on the other hand, adopts a model with a central core region which produces all of the luminosity. Then, assuming a Kramers opacity function, he integrates the structure equations at fixed luminosity, and finds that there is a maximum luminosity solution for each choice of core mass. He then shows that in such a model, the exterior polytropic index is determined by the opacity law, and that the interior solution above the core has a power law character. Note that the power law solution he derives is not related to the power law behaviour of polytropes, since for the index 3.2 he has in his model, the M-solutions are oscillatory decaying exponentials (similar to the M-solutions illustrated in Fig. 2-2-3) in the neighbourhood of the origin. In fact, for Applegate's assumptions, his maximum luminosity lies close to that found at the tip of the giant branch, long after stars become red giants. Applegate also claims that a molecular weight discontinuity is not necessary for the formation of giants. This argument can be objected to on the grounds that he has not modelled the region interior to his assumed core. Certainly his power law solution is not valid below the inner boundary of his solutions, since the density at the centre must be finite. In any case, his power law solution must be joined to an E-solution for some index n; this necessitates a discontinuity in the model's (U, V) solution, which in turn implies a discontinuous density function.

As an example of giant characteristics on the ZAHB, the $0.90\,M_\odot$ model for the most metal rich ZAHB presented here is 23 times larger but only 3 times brighter than the $0.54\,M_\odot$ model, and almost all of the additional luminosity is produced in the shell. The core radius in each case is similar, and very much smaller than the stellar radius; hence as far as the outer layers are concerned, the twin energy-producing regions are indistiguishable from a single shell source. As an

additional point, the fact that the more massive, brighter models for $M_* > 1\,M_\odot$ have smaller, rather than larger, convective zones indicates that giants can form well before the 'theoretical' maximum luminosity is reached.

2.6 Summary

This current work appears to be the first attempt at a full investigation of the hydrostatic structure of horizontal branch stars. This investigation has been made possible by the facility to depict a large range of different phenomena occuring within the models, a technique which obviously has applications to other branches of stellar evolution theory. The view taken here has been to regard the models as 'numerical experiments', observation of which can draw out features of stellar structure which have previously been difficult to understand.

The recent interest in the evolution of the HB sparked, perhaps, by the great improvement in photometry of globular clusters, plus the controversy surrounding the Sandage Period Shift Effect, has also inspired new models of HB stars which contain some discussion of their interior behaviour (Bencivenni *et al.* 1989), referring also to some of the phenomena and dependences cited here.

Earlier work on the structure of HB stars was carried out by Lauterborn *et al.* (1971a) and in Lauterborn (1973). They calculated numerical derivatives for the change in envelope parameters, and concluded that the interaction between core and envelope was negligible. Their conclusions are different from those found here because of their assumption that the core boundary pressure and temperature were expressible in terms of the core luminosity and radius. In fact, as has been shown, these latter quantities vary little with envelope or total mass, but the temperature is highly sensitive to the size of the envelope. SG76 noted explicitly that the decline in luminosity with envelope helium fraction was due to the decline in hydrogen shell burning. However, this study provides an explanation for the near-constancy of these models with varying Y at fixed mass.

A number of previous authors (IR70, SG76) have described the nature of the evolution in terms of the initial luminosity ratio between core and shell. According to such a 'classification', models with sufficiently high values of L_{He}/L_* evolve to the red, and for each composition there exists a critical mass at which this

value is attained. This analysis has attempted to provide an explanation for this empirical fact about the models, which give excellent agreement with observations of cluster horizontal branches. The association between the behaviour of high mass horizontal branch stars with very small blueward loops and the presence of convection zones was been noted by IR70 in passing, but there appears to be no other explanatory material in the literature for this phenomenon. The transition between redward evolving sequences and tracks which contain blueward loops has seemingly not previously been studied in any detail. The various possible track morphologies discussed above are summarized in a separate section below.

2.6.i Summary: Evolutionary track morphology

(i) **Hydrogen shell relaxation with radiative exterior.** The shell develops fully, and decreases in luminosity as the star evolves to the blue. The near stationary nature of the shell radius yields an increase in the outer core density, which also implies a reduction in the shell temperature and luminosity. The envelope is therefore forced into contraction; as is well known, the evolutionary sequence proceeds in this case rapidly to the blue. Since the decrease in shell luminosity is approximately equal to the increase in core luminosity, the resulting track is almost horizontal in the HR diagram. As the hydrogen shell weakens with decreasing envelope mass, the motion to the blue on the HR diagram becomes weaker until the core evolution is one of homologous expansion. In the marginal case where the density node lies on the interface between core and envelope, the model stays almost stationary on the HR diagram until the core begins to contract.

(ii) **Complete hydrogen shell relaxation with convective exterior.** Firstly, if the shell is strong enough to force a surface convection zone, the core evolution weakens it, by reducing the effective envelope mass, reducing also the convection zone depth. The resultant evolutionary track will move slowly

blueward in the HR diagram. The shell luminosity evolves very slowly downward. In this case, the increase in core luminosity may be larger than the decrease in the shell brightness, so that the track may evolve upward. Thus, for a large range in mass, metal-rich HB stars maintain deep convection zones throughout the evolution, and the result is a very red 'stubby' HB morphology. In real, metal-rich stellar systems, the range of masses of stars surviving through the helium flash is generally observed to be insufficient to populate the bluer parts of the Horizontal Branch.

(iii) **No (or 'delayed') hydrogen shell relaxation.** In this case, the helium core contributes nearly all of the luminosity, and the evolution proceeds to higher luminosities. If the shell luminosity is too small to move away from the boundary of the the ZAHB helium-rich core, the shell source weakens further with time, as the core initially expands homologously. This results in a lower shell and surface temperature, so that the evolution proceeds continuously redward.

2.6.ii Some brief suggestions for future work

Although this study is primarily theoretical in content, it is hoped that a better understanding of the physics of the horizontal branch may lead to enhanced predictive power for the observations. The complexities of the Horizontal Branch phase of evolution, as well as the availability until recently of only a very limited number of evolutionary sequences have made detailed comparisons with observation a difficult task. In particular, the sensitivity of horizontal branch models to practically every input parameter impedes the interpretation of cluster data because of the inability to interpolate between sequences of different mass and composition. As well, the morphology of the sequences itself provides some degree of difficulty. The most important example of this is in the determination of HB stellar masses through the instability strip. The shape of the evolutionary tracks

implies that a range of stellar masses will occupy lines of constant colour in a cluster colour magnitude diagram. However, the stellar distribution in mass at fixed colour depends on the assumed mass dispersion of stars arriving on the HB, the morphology of the sequences, as well as relative rates of evolution along the tracks. One important technique for dealing with this 'degeneracy' is to generate 'Synthetic Horizontal Branches' (*cf.* Rood 1973; Rood and O'Connell 1985; Lee 1989; Lee, Demarque, and Zinn 1990) from the tracks, by assuming random arrival times for the HB stars, Gaussian ZAHB mass distributions etc. Such calculations have been used with considerable success in some cases to synthesize integrated properties of cluster Horizontal Branches.

Since some of the properties of the evolution have been shown to be quantifiable, it is possible that the theoretical understanding gained here could be put to use in the calculation of more realistic synthetic sequences. The conclusion above regarding the variations in track morphology with mass may allow the definition of 'equivalent evolutionary phases' (Green, Demarque and King 1987; Bergbusch and VandenBerg 1990) on the HB. This would allow interpolation along the sequence in mass. The next step could be to attempt to include some of the effects of parameter variations within clusters. For example, the effect of a range of core masses in each cluster caused by varying rotation rates earlier in the evolution. Another possibility would be to incorporate the effects of varying CN abundances, as are being found by observers. Possibly of crucial importance, as stated earlier, is the construction of new sequences with enhanced α elements, as are also implied by observations.

Chapter 3 On The Cores of Horizontal Branch Stars

3.1 Introduction: Semiconvection and Convective Overshoot

3.1.i Nature of the problem

Historically, the problem discussed here arose with the evolution of massive stars, and was reported by Schwarzschild and Härm (1958) who found that the (U,V) matching technique for stellar models failed to produce a stellar envelope which was in radiative equilibrium above a convective core. The Schwarzschild (1906) stability criterion (*i.e.*, convection ensues wherever the radiative gradient ∇_r exceeds the adiabatic gradient ∇_{ad}), which is used to determine whether the heat transfer process is radiative or convective, may be understood by noting that the radiative transfer equation (in the diffusion approximation) defines a certain value of the temperature gradient ∇T [1] which is necessary to drive the flux outward. If this gradient is larger than the value of ∇T at which fluid may move adiabatically, the material will be forced into convection, the flux being carried by a small super-adiabaticity.

In this context, the problem arises because the adiabatic gradient decreases as a result of increased temperature and therefore radiation pressure, while the opacity in the core, due to electron scattering, is lower than that of the hydrogen rich layers immediately outside the core. The adiabatic gradient, decreasing faster than the radiative gradient, reduces the ability of the central zone to carry the flux without being driven into convection, causing core expansion (for models with weaker radiation pressure, the reduction in opacity dominates and the core contracts, leaving an inhomogeneous zone). The resulting mixing of layers above

[1] *The effective temperature gradient referred to below as* ∇_{eff}, *is actually* $\left(\partial \log T/\partial \log P\right)$; *this is equal to* $(P\hat{\mathbf{r}}.\nabla T)/(T\hat{\mathbf{r}}.\nabla \phi)$

the core inward brings more opaque material inside it, thus reinforcing rather than removing the instability. Since a partially mixed zone above the convective core restores stability, the mixing process invoked was dubbed 'semiconvection'.

For Horizontal Branch stars, the situation is reversed (Paczyński 1970). The much higher densities and pressures involved imply that radiation pressure is negligible, and plays little role in the discussion, although it does depress the value of ∇_{ad} slightly at the centre. As the evolution proceeds, carbon and later oxygen become significant components of the interior chemistry, and the free-free absorption coefficient of the larger ions produces an increase in the central opacity. Figure 3-1-1 illustrates this discussion. In this plot the opacity profile is reproduced of a 0.90 $M_{\odot}$ model with composition [Fe/H] = −2.03, [O/Fe] = 0.70, selected from those available. The curves are spaced at intervals of ten models. The curve which has the lowest opacity in the centre is the zero age model, where the entire helium-rich core is close to being homogeneous. Subsequently, the opacity in the core region rises, so that the point where the radiative gradient exceeds the adiabatic gradient moves outward from its ZAHB location. According to the Schwarzschild criterion, convection occurs below the point where these gradients cross[2]. As the star evolves, then, the medium becomes more opaque, and convection will homogenize the entire region until the opacity in the resulting mixture is low enough to admit stable radiative transfer. In Horizontal Branch stars, at least for the early part of evolution, the core boundary moves irreversibly outward. This phenomenon will be referred to as 'core expansion', in order to distinguish it

---

[2] *The debate concerning which criterion should be adopted (Schwarzschild 1906 versus Ledoux 1947) has been covered extensively elsewhere (see e.g., Spiegel 1969, Stothers 1970 and references therein) and seems to favour the former. The arguments for the Schwarzschild criterion adopt the point of view (in part verified by terrestrial observations) that the semiconvective instability is based on temperature, rather than density considerations, which is the point of view implicit here.*

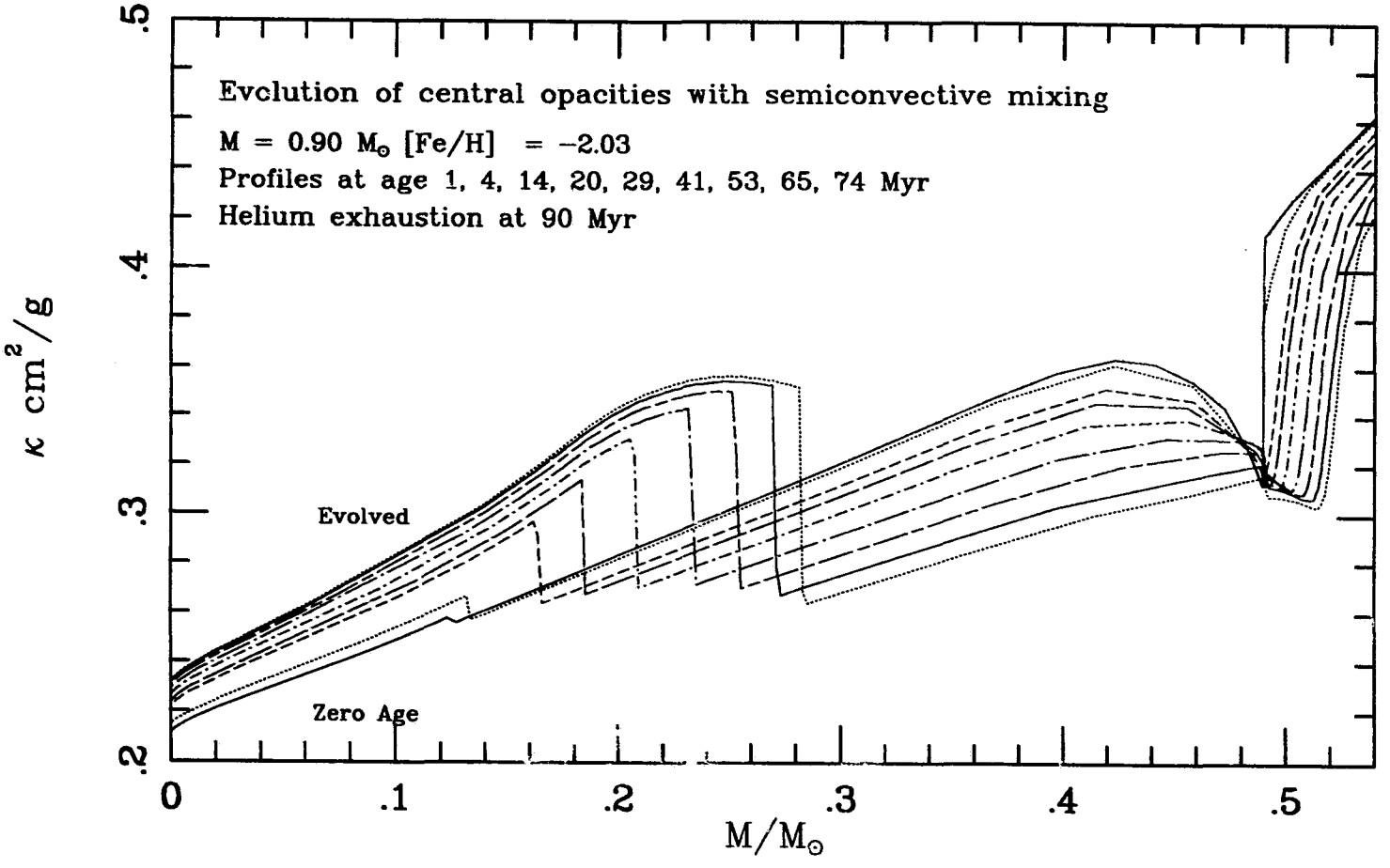

Fig. 3–1–1: Evolution of the opacity function in the central regions of a star, assuming semiconvection. The model plotted has M = 0.90 Mo, [Fe/H] = –2.03, [O/Fe] = 0.70 and Y_{HB} = 0.246.

from 'convective overshooting' as discussed below. In Figure 3-1-1 the first three curves are taken from this expansion phase.

It is clear from the diagram that if the core were to continue to expand, the decreased temperature in its outer layers would increase the opacity to such an extent that at some point, these layers would be unstable to convection under further expansion (consider the effect of extrapolating the core opacity curves outward). Thus, similar circumstances to those under which the term semiconvection was first coined arise again, namely a central convective zone whose further expansion produces further instability.

Thus, imposing the usual criterion (that the core will reach out to the point where it is no longer *accelerated* outward), implies that the core will expand with time. The core will be homogeneous in composition if the convective turnover time is much less than the evolutionary timescale, and if one can neglect any 'stratification' caused by different ionic weights of the material's constituents. Both of these are common assumptions which are easy to justify given the vigorous nature of convection.

3.1.ii Semiconvection and Convective Overshoot

Various schemes have been proposed to deal with this difficulty, which strictly speaking arises because of the simplicity of the treatment of fluid behaviours in stellar evolution codes. The complexity of modelling fluid dynamics in circumstances which are not reproducible in the laboratory (convection with free boundaries; motions possible over many scaleheights; negligible molecular viscosities), together with the complex problems of the turbulent flows usually assumed to be present in central convection, have led researchers into a number of different avenues.

In principle, the standard assumption, that convective zones end at the point where the radiative and adiabatic gradients cross, is unphysical, because the velocity of rising gas elements is non-zero at this point. In the following, the term 'convective overshooting' refers to penetration of gases into stable radiative layers. Since their motion is retarded by the temperature gradient as well as by dissipation, the existence of a zone of penetration may be similar to a 'skin depth' effect, a region where the amplitude of fluid motions decays exponentially. Convective overshooting models attempt to model this phenomenon, and some routines are based directly on variations of the stellar structure equations, together with assumptions derived from mixing length theory (see Cox and Giuli, 1968; for examples of such techniques, see Maeder 1975; Bressan *et al.* 1981; Cogan 1975). These techniques are 'ballistic', in the sense that they attempt to model the penetration of rising convective elements by estimating their velocities and accelerations. Other, more complex derivations, such as those of Cloutman (1987) and Xiong (1981, 1986) begin with the Navier-Stokes equation and attempt to solve for the convective velocity field.

Given the above definition, the overshooting region ends where the convective velocities are brought to zero by the negative acceleration of the medium. It seems clear that the overshooting does occur to some extent, but the question arises as to whether the additional mixed regions affect the evolution significantly. This question was explored by Saslaw and Schwarzschild (1965) and by Shaviv and Salpeter (1973), who came to opposite conclusions. Their arguments are important, despite the fact that the conclusions of both papers are based on model parameters which are very different from those obtained in helium burning cores. In the first of these papers, the authors carried out a perturbation analysis on the fundamental mode of convection, predicting the velocity field above the core. They showed that the extent of the overshooting region was a function of the buoyancy of the rising material (proportional to the net value of the superadiabaticity in

the core). They further investigated the expected propagation of material out from the core by overshooting over the evolutionary timescales (which are much greater than the convective timescale) and concluded that the expected extent of mixing by overshooting was still negligible. They also stated that conditions in helium-burning cores were even less favourable for convective overshooting than those burning hydrogen.

The second of these papers argued that, provided the mixing length α was a significant fraction of the pressure scaleheight $\mathcal{H}_P$, then the overshooting region would be non-negligible. Their study calculated overshooting based on both local and non-local mixing length assumptions, and their solution exhibited all of the features described above. On the illustrative assumption of $\alpha \sim 0.5\mathcal{H}_P$, they found that the material would be mixed out to $\sim 0.07\mathcal{H}_P$. However, their calculations were based on homogeneous, unevolving interior models. Further, their demonstration relies on an important undetermined parameter, the mixing length, which must be significant if the evolutionary implications are to be significant.

In the 'convective overshooting' scenario, there is a region between the point where the superadiabaticity $\Delta\nabla T = \nabla_{eff} - \nabla_{ad}$ is zero and where v_{conv} vanishes in which rising fluid elements will be cooler than their surroundings (as $\nabla_{ad} > \nabla_{eff}$). This implies a negative convective flux (see Bressan *et al.* 1981), and a radiative flux gradient which is greater than the usual definition of the radiative gradient. (Recall that ∇_r is defined to be that value of the temperature gradient required to drive the *total* flux outward; here the 'radiative' flux must compensate for the negative convective flux). The arrangement of gradients and heat fluxes should therefore be as illustrated in Figures 3-1-2 a and b respectively. In the overshooting zone, the gradient carrying radiative flux lies between the adiabatic value and that which would be obtained without overshooting. The convective flux, which is equal to the total luminosity within the convective core, falls to a value less than zero, whilst the radiative flux rises from zero to a value greater than

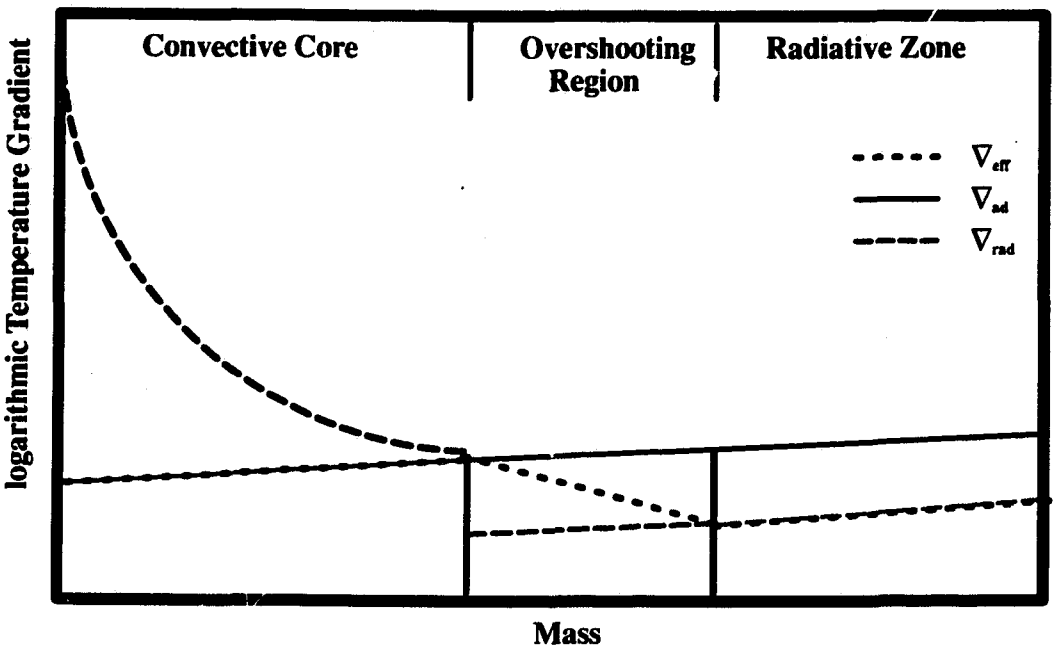

Figure 3–1–2a: The temperature gradients in a zone of convective overshoot. The effective gradient in the overshooting zone is super–radiative and subadiabatic. Elsewhere, it follows the lesser of the radiative and adiabatic gradients.

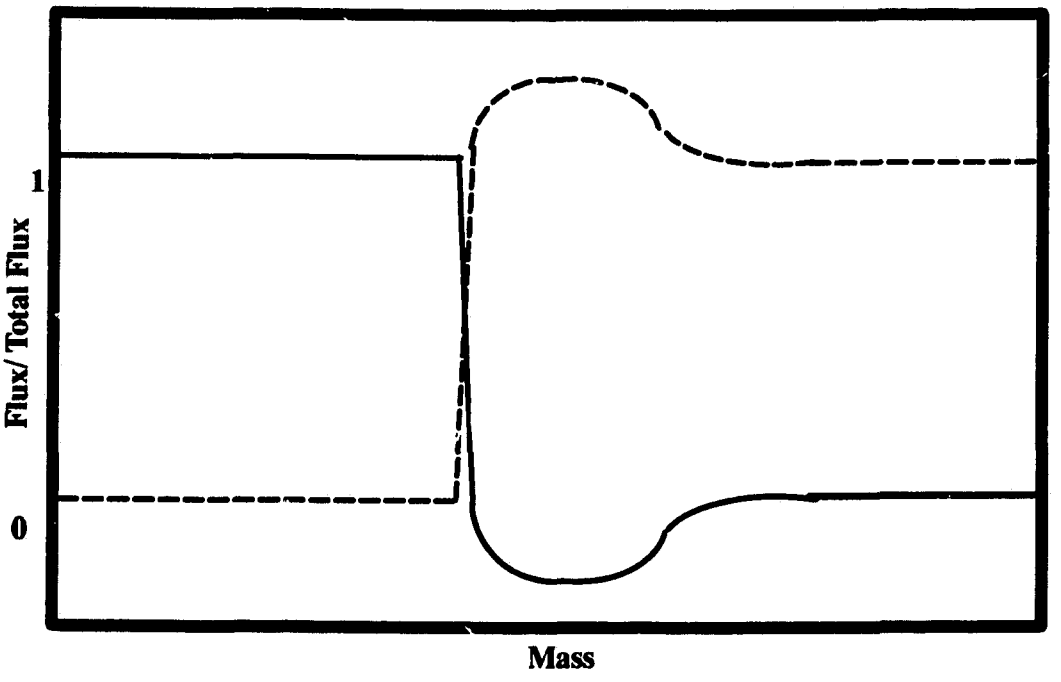

Figure 3–1–2b: Schematic of the fluxes in the convective overshooting zone, The radiative flux is indicated with a dashed line, and the convective flux with a solid line.

the total flux. At the upper boundary of the overshooting zone the convective flux must become zero and the radiative flux be equal to the total flux. It seems very likely, however, that the instability described in the previous section will appear as the core grows in size, if the entire region from the centre to the outer edge of the overshooting region is made homogeneous. This conclusion could perhaps be avoided if the overshooting distance is large enough, but too large a mixing zone raises other theoretical problems. The available calculations of core helium burning with overshooting (Bertelli *et al.* 1986), do not provide more details of their numerical procedures, but refer instead to Bressan, Bertelli and Chiosi (1981) who formulated their method for massive star evolution.

The other major issue arising from convective overshooting is that of the rate of outward motion of the core edge. An early paper, by Castellani, Giannone, and Renzini (1971a), attempted to derive a value for this quantity, but their assumptions suffer from some major inconsistencies (Renzini 1977) and their conclusions for the size of the overshooting region are somewhat difficult to accept. However, they derived a result for the rate of core expansion through overshooting of the form

$$v_p = \beta \frac{(1 - \nabla_{ad}/\nabla_{eff})}{(1 - \mu_{core}/\mu_{ext})},$$

where μ represents the mean weight per particle of the mixture, and the subscripts take their obvious meaning. They derived a value for β of around 10^{-5}, whilst Sweigart (1990) regarded it as a free parameter. For suitable values of β ($5 \times 10^{-6} \lesssim \beta \lesssim 10^{-4}$), this formula has been shown (Sweigart and Gross 1974; Sweigart 1990) to produce similar results to semiconvective techniques. This range of values gives agreement to an order of magnitude with the original determination by Castellani *et al.* of the core propagation rate. As a final note, the reader is referred to the paper by Renzini (1987), which contains a detailed discussion of the problems with many of the existing overshooting routines, and concludes that their basic problem is that hybrid methods between local and non-local mixing

theories lead to severe physical inconsistencies.

In the 'canonical semiconvection' prescription, the core expansion phase ends when further expansion of the homogenized core would result in a minimum in the radiative gradient (see Castellani, Giannone and Renzini 1971b). Referring back to Fig. 3-1-1, it is seen that the helium-rich layers above the convective core are strongly radiative, and thus there exists an intermediate composition, for every layer of the temperature stratification, which gives strict convective neutrality ($\nabla_r = \nabla_{ad}$). The curves show that, as the evolution proceeds, the opacity function within the semiconvective zone is deflected downward in its outer regions. (refer to the fifth, sixth and seventh curves in the diagram). The maximum in κ which appears later in the evolution — and is common to all of the evolutionary tracks calculated — is of critical importance, as is the fact that the core opacity increase levels off very considerably. These phenomena will be discussed in detail below. The canonical semiconvection prescription is the assumption that physical processes will act to mix the material in the proportion needed to satisfy the neutrality requirement. That is, whatever processes cause material to mix outward from the convective region, the result at the end of a timestep will be that chemical profile in which the core material is either convective or 'approximately' neutrally stable inside a radiative helium rich region. It should be stressed that a numerical routine which achieves this does not model the actual physical processes. The computer code attempts to estimate what the effect of many discrete mixing events will be at the end of a timestep of the evolution code, if this is indeed how the core mixing takes place. The timesteps used in the evolution code are much greater than any mixing timescales, and therefore the minutiae of the fluid dynamics cannot be studied in detail.

The physical process most often cited as possibly giving rise to a 'semiconvective' chemical profile is that of double-diffusion, which is interesting enough to be worth a small diversion here. Double-diffusive convection is the name given to

a class of phenomena, which are observed both in the laboratory and in nature, whereby two physical processes act to produce mixing of material (Turner 1974; Huppert 1979). These phenomena are also known as thermohaline or thermosolutal convection.

Originally, double diffusion was conceived as follows; suppose we have a tank in which warm, salty water lies on top of cold, fresh water. This situation can stay in equilibrium provided the upper layer is, despite its salinity, less dense than the lower. If a conducting pipe is inserted into the tank and cold water pumped up through it, the cool water will heat up and become less dense, and because the pipe prevents it from becoming salty, it is less dense also than its surroundings. and so continue to rise (this is called the 'salt fountain' mechanism). It was later realised that the existence of the 'pipe' was not essential. Provided that salt is transferred more slowly than heat, (or, more generally, that the mixing timescale is longer than that for heat diffusion), the mechanism would still operate. If the layers are reversed, then if a parcel of fluid rises, as it cools to the temperature of its new surroundings it loses its buoyancy and so it will be driven back downward, producing an oscillation. But a lag in temperature between the fluid and its surroundings (dependent on the conductivity) would mean than the fluid has a net buoyancy over a cycle, and thus its position, on average, would move upward. Both of the above two phenomena have in fact been observed in the laboratory and in nature. The first situation gives rise to 'salt fingers' and the second to diffusive mixing by the oscillatory motions. It is, of course, the latter process which is of interest in stellar cores. The relevance of this picture to stellar cores is questionable, though, on the grounds that, in the ocean environment, it occurs slower than any other mixing process; if the central region is turbulent, double diffusion will be swept away by vigorous fluid motions. Of course, this argument merely implies that some other mechanism will act against the chemical discontinuity which would otherwise appear at the convection boundary.

Both 'overshooting' and 'semiconvective' routines have been used to resolve the difficulty noted by Schwarzschild and Härm (1958), but it must be said that the problem is rather too complex to be dealt with properly within current stellar evolution codes[3]. If the theoretical models are to make predictions of observations, then it is highly desirable for these predictions to be as independent as possible of free parameters, and it was for this reason that the 'semiconvective' prescription was chosen for this study.

[3] *Spiegel (1979) has noted that when the problem of stellar convection is handled properly, the evolution code is likely to become a subroutine within the convection code!*

3.2 A method for the calculation of Semiconvective Mixing

In this section, the numerical mixing routine used in this study is discussed. The method used cannot be described as an 'algorithm', since it fails to be logically exhaustive, although, with slight abuse of language it will be referred to as such below for convenience. However, it is almost completely reliable until the late stages of evolution $Y_c \lesssim 0.16$, during which all such routines apparently encounter numerical difficulties. In this chapter, the evolution of the convective/semiconvective core, arising from the canonical semiconvection prescription, will be illustrated. Further, it will be shown how the convergence problems which arise at late times do so as a natural continuation of the evolution process, and suggest how they might, in principle, be overcome. A controversial question concerning late HB evolution is the appearance of 'breathing pulses' (*cf.* Lattanzio 1986), which consist of discrete mixing events which replenish the helium supply in the centre of the model. These appear in many numerical procedures (including the one described here), and it is unclear whether they are 'real' or numerical artefacts. I will argue that the evolution is unlikely to produce these events. Although it should be said that there is observational evidence which could be interpreted as supportive of their existence (see Lee 1990 and references therein), stronger evidence implies that, in general, they do not occur.

The adopted method is based upon a routine which was originally suggested in and used by Castellani, Chieffi, Puloné, and Tornambè in 1985 (hereafter CCPT) in a study of the late evolution of the Horizontal Branch phase. The idea, which is intuitively appealing, consists of mixing the core material outward until the stability of the material in the core and its surrounds obeys the semiconvection prescription. The important addition in this programme over the routine described in CCPT is one of refinement; the chemical composition in each shell is determined so that neutral stability is attained to a specified accuracy. Needless to say, the

range of desirable accuracies for such a method is bounded above by efficiency considerations and by the large uncertainties in the other quantities involved, and below by the desire for the best possible consistency with the adopted assumptions. The problem which must be faced is the interconnectedness of the changes in the temperature and the composition; neither are properly determined at the start of a new model calculation, and adjusting one affects the convergence of the other.

The 'core expansion' phase is straightforward to calculate. The initial model supplied by the initialization procedure (see chap. 4) has been computed so that the convective core boundary is marked by a meshpoint of the Henyey scheme[4]. Firstly, an iteration of the relaxation scheme (a four-dimensional Newton-Raphson technique) is executed, generating a new set of 'trial' physical variables. Programme control then passes to the semiconvection routine. A set of differential equations is solved for the new chemical composition as determined from the nucleosynthesis resulting from these trial values. The chemistry is then homogenized in the region between the centre of the model and the convective core boundary found at the last model convergence. The programme then mixes the mass shells from the centre outward until the outermost shell becomes radiative, as determined by recalculating ∇_r and ∇_{ad} for an appropriate range of meshpoints. As it mixes the material outward, vectors containing the core composition at the current ($\mathbf{X}'$) and previous mixing step ($\mathbf{X}$) are stored. For clarity, suppose the outer layers of the core become radiative when shell M is added to the convective region, with the mass shell number decreasing outward. Then the core boundary is defined to be at

---

[4] *The term meshpoint refers to a value of the independent variable (the mass co-ordinate) of the finite difference approximation used to solve the equations of stellar structure; for details of the method, see Kippenhahn et al. 1967; for its implementation here, see VandenBerg (1983). The term 'shell' will often be used to mean the zone between two adjacent meshpoints, and the shells will be enumerated by the meshpoint number at their outer edges.*

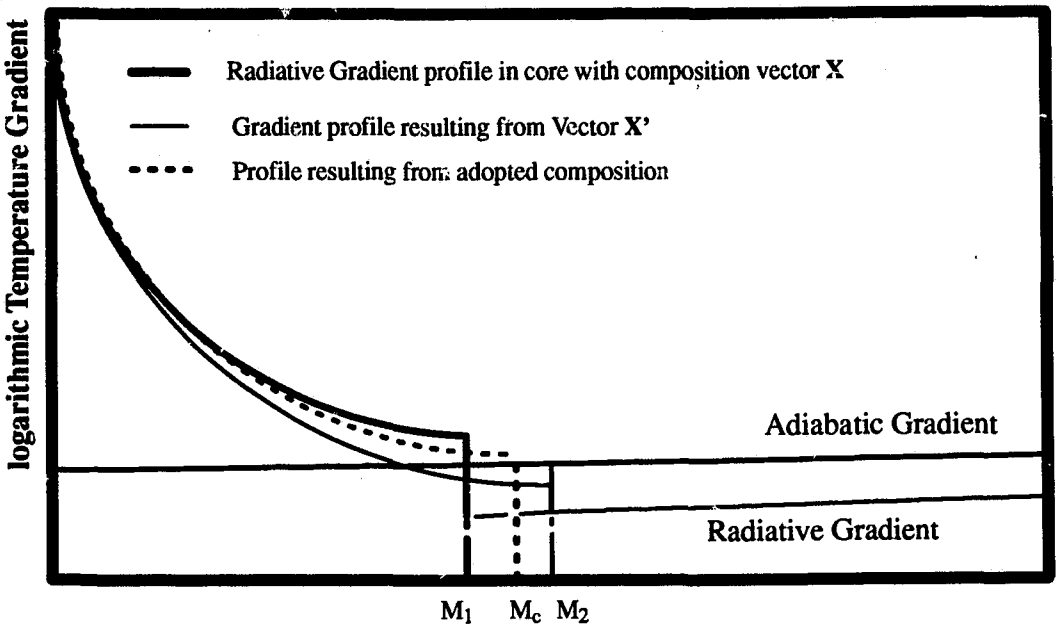

Figure 3–2–1a: Schematic illustration of the radiative and adiabatic gradients in the core during the core expansion phase.

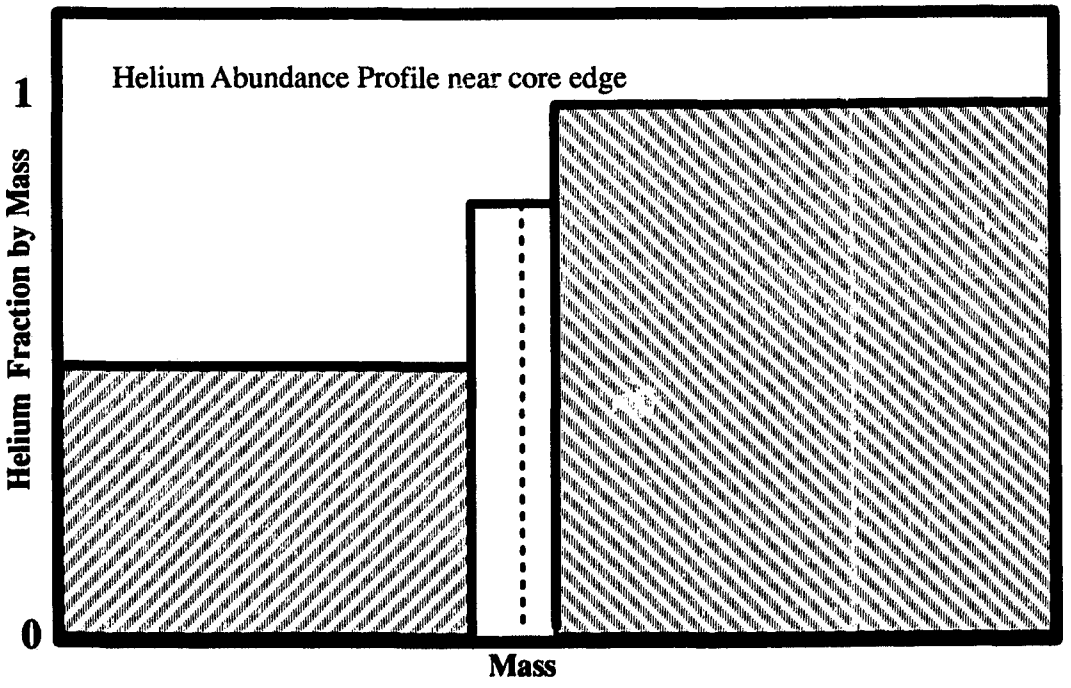

Figure 3–2–1b: Compositions of the shells in the core (left), the partially mixed shell (unshaded) and in the radiative zone,. The composition in the radiative zone is equal to the zero age composition of the helium rich region $0 < M < M_c$.

shell $M+1$, (denoted LCOMP), and the composition adopted in the core is $\mathbf{X}$. Since it is unlikely that the 'exact' boundary will again fall on a meshpoint, a further step is executed. The gradients generated at the core edge are modified by mixing part of the shell LCOMP - 1. A bisection loop is performed on this shell, until a point is found within it such that $\nabla_r/\nabla_{ad} - 1 < \epsilon$, where ϵ is the adopted numerical tolerance. The mass contained between this point ("LCOMP $- 1/2$") and LCOMP is added to the mass below LCOMP, and this value is reported as the convective core mass (see Figure 3-2-1).

Let the value of the mass coordinates at LCOMP, LCOMP $- 1/2$ and LCOMP-1, be denoted M_1, M_c and M_2. Let the composition vector interior to M_1 be denoted $\mathbf{X}$ and that between M_1 and M_2 be denoted $\tilde{\mathbf{X}}$ (which approximately equals the initial ZAHB composition). Then the output composition in the shells below LCOMP, is given by $\mathbf{X}_{new}$, and in the shell above LCOMP by $\tilde{\mathbf{X}}_{new}$, where

$$\mathbf{X}_{new} = \frac{(M_c - M_1)\tilde{\mathbf{X}} + M_1\mathbf{X}}{M_c}, \tag{3.1}$$

$$\tilde{\mathbf{X}}_{new} = \frac{(M_2 - M_c)\tilde{\mathbf{X}} + (M_c - M_1)\mathbf{X}_{new}}{M_2 - M_1}. \tag{3.2}$$

This simple method (bisection search followed by averaging) is also the major improvement made to the semiconvection part of the algorithm.

Towards the end of this expansion phase, the rate of decrease of the radiative gradient necessarily reduces, until a minimum appears in the ratio ∇_r/∇_{ad}. The onset of semiconvection produces a set of difficulties which are related to the fact that a realistic computer code must work to within numerical criteria rather than derive exact results, and the evolution in time is calculated in a discrete fashion. In particular, it is important that the timestep not be too great at this point, since otherwise the routine will 'overmix' by overestimating the central carbon

abundance. After each model has converged, the rate of change of ∇_r/∇_{ad} is computed, and if less than a given value (determined by trial) the timestep is reduced. Nevertheless, the 'overmixed' situation often arises at the end of the phase, but is dealt with (if necessary) as follows. At the first instance where the gradient ratio increases outward, the minimum thus reached is flagged by the programme. The convective core boundary is defined at the minimum, and the single shell above it `LCOMP-1` which has a higher value of ∇_r/∇_{ad} is mixed partially with the shell `LCOMP-2` in the proportion required to make it convectively neutral. Thus the semiconvection zone contains a single shell. After this model has converged, the next model may fail to detect a minimum. Semiconvection is 'switched off', and the core is extended outward again until neutrality is found. Usually, the following model then contains two or three shells in which ∇_r/∇_{ad} rises, and the semiconvection part of the routine operates normally as described below.

The criterion for the detection of a minimum in the normal case is that ∇_r/∇_{ad} rises for two consecutive shells. All of the shells which lie beyond this minimum are mixed outward to achieve neutrality; the mixing terminates at the point where the mixed material is insufficiently opaque to be convectively unstable. Until the semiconvection zone is larger than 5 meshpoints in width, its outer boundary is allowed to move in either direction. Then, during the middle phase of evolution ($Y_c \gtrsim 0.16$) the previous extent of the semiconvection zone is taken (for definiteness and stability) as an approximation to its final extent. This assumption has the disadvantage that it looks explicitly for a growing semiconvection zone.

Suppose the minimum in ∇_r/∇_{ad} occurs at shell N. The shells $N-1, N-2...$ are mixed with the shells above them until they, in turn become convectively neutral. When the shell $N-K$ is reached such that shell $N-1$ becomes radiative, the composition found by mixing the shells $N-1$ to $N-K+1$, is then adopted. Following this, a bisection search is performed on the shell $N-K$, which finds the

fraction of that shell required to make shell $N-1$ convectively neutral to within the numerical tolerance, if this is required. The composition in shell $N-K$ is then averaged as described above. The same procedure is then executed, starting with shell $N-2$, then $N-3$, and so on. The mixing terminates when it is only necessary to mix a shell, $N-J$, say, with a fraction of the shell above it, and this shell becomes the outer extent of the new semiconvection zone, denoted M_{sc} at meshpoint LSEMI. More formally this may be stated as follows:

For each $i < i_s$ there is a k_i with $k_i \geq 1$ such that when shells $\{N-i,\ N-i-1...\}$ are mixed together, either

(a) The value of ∇_r/∇_{ad} at meshpoint $N-i$ is > 1 when the shell $N-k_i$ is added, and < 1 when the next shell $N-(k_i+1)$ is mixed, or

(b) $\nabla_r/\nabla_{ad} < 1$, in which case $k_i \equiv i$.

The extent of the semiconvection zone is given by that value of i, i_s, such that

$$k_{i_s} = \max\{k_i : i < i_s\}, \text{ with}$$
$$k_{i_s} = i_s + 1$$

In the above notation, $J = i_s$, and $K-1 = k_i$ for each shell in the semiconvection zone. In case (a), if $\nabla_r/\nabla_{ad} > 1+\epsilon$ on adding shell k_i, then the bisection algorithm is used to find the fraction of the shell $N-(k_i+1)$ needed to bring the ratio down into the range of tolerance, by constructing trial compositions and checking the gradient in shell $N-i$. Case (b) arises mainly during the iteration process in the main semiconvective phase (rather than at the iteration at which convergence is attained). A schematic flow diagram for this subroutine is given in Figure 3-2-2 .

During the middle to late part of the evolution (*i.e.*, from the onset of semiconvection) the chemical and physical variables converge to a consistent profile, with a quasi-static convective core size defined by $\{M_{cc} : \nabla_r/\nabla_{ad}(M) > 1+\epsilon$ for all $M < M_{cc},\}$, and *growing* semiconvection region with $\{1-\epsilon < \nabla_r/\nabla_{ad}(M) < 1+\epsilon$

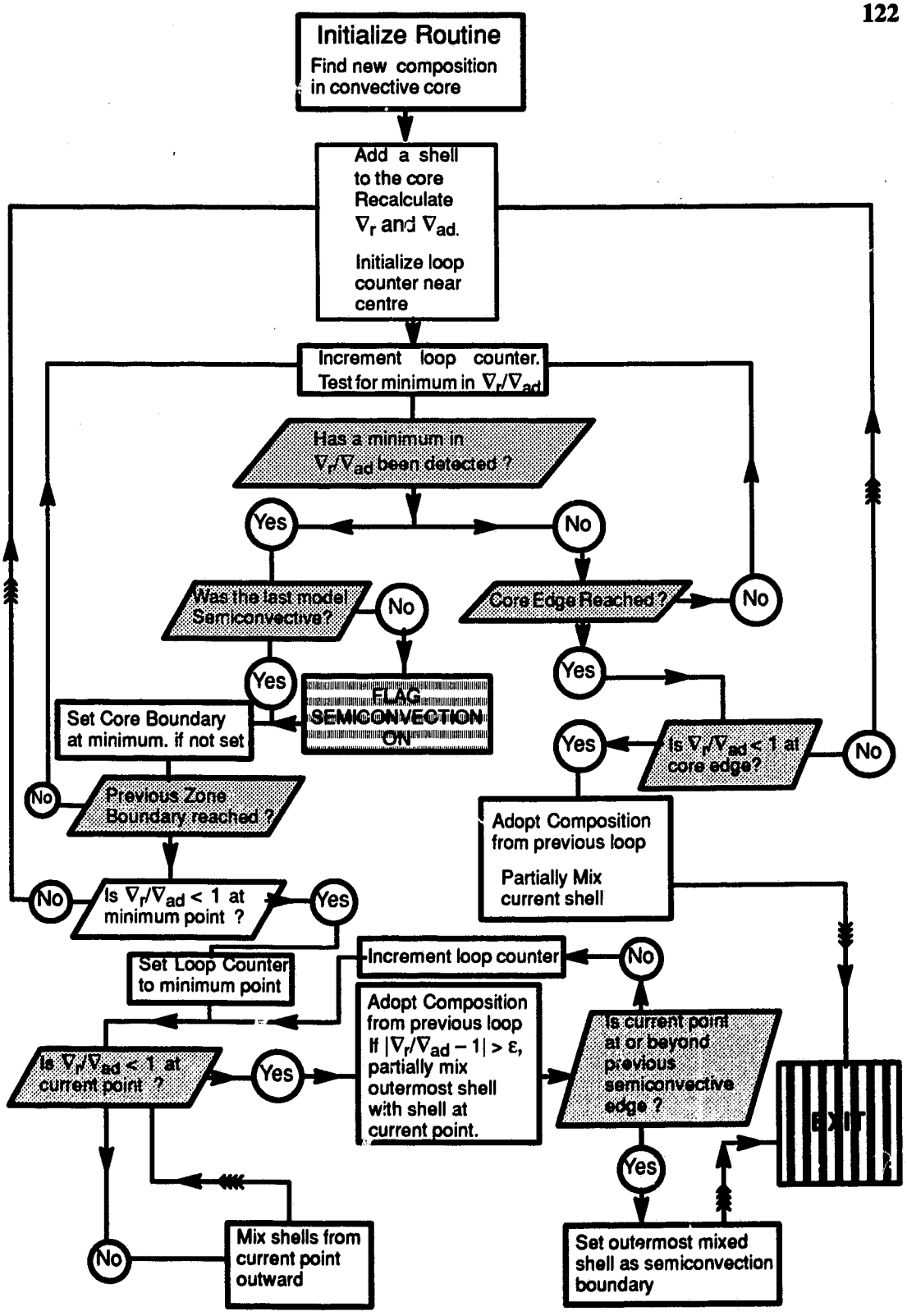

Figure 3–2–2: Schematic Flow Chart for Semiconvection Routine

for all $M_{cc} < M < M_{sc}\}$, where M_{sc} is the mass coordinate at the outer boundary of the semiconvective zone. An experiment was also conducted in which this requirement was relaxed. The core behaved very similarly to the case with this restriction, except that its size became even more unstable late in the evolution. ϵ represents, again, the numerical tolerance criterion used in the program for the allowed average deviation from convective neutrality of the material in the semiconvection zone. The chemical profile is deemed to have converged if

$$\frac{1}{J-1}\sum_{i=N-1}^{N-J}(1-\nabla_r(i)/\nabla_{ad}(i)) < \epsilon.$$

In single precision arithmetic, the composition variables (*i.e.*, ^4He, ^{12}C, ^{13}C, ^{14}N and ^{16}O) are determined with $\epsilon = 5\,\mathrm{x}\,10^{-4}$. However, the mean deviation from neutrality at convergence is often ten times smaller than this number.

3.2.i Notes on the convergence of the method.

This method effectively 'flattens' the rising gradient profile, but at some large cost in recalculation of opacities, and of the equation of state variables ρ and ∇_{ad}, especially since the mesh spacing must be fine and the semiconvective zone is large towards later times. Taking the worst possible case, suppose there are S shells in the semiconvective region. Then the gradients must be recalculated $(S-1)+(S-2)+...+1 = \frac{1}{2}S(S-1)$ times. The iterations of the programme can slow down dramatically as a result. During the iteration process, a major difficulty arises because of the effect of composition changes on the temperature profile, which has a large influence on the radiative gradients because the large power dependence of the latter on temperature. At the first iteration, the temperature is underestimated, so that the mixing routine produces a more extensive semiconvective zone. The enhanced helium fuel in the centre so generated tends to predict

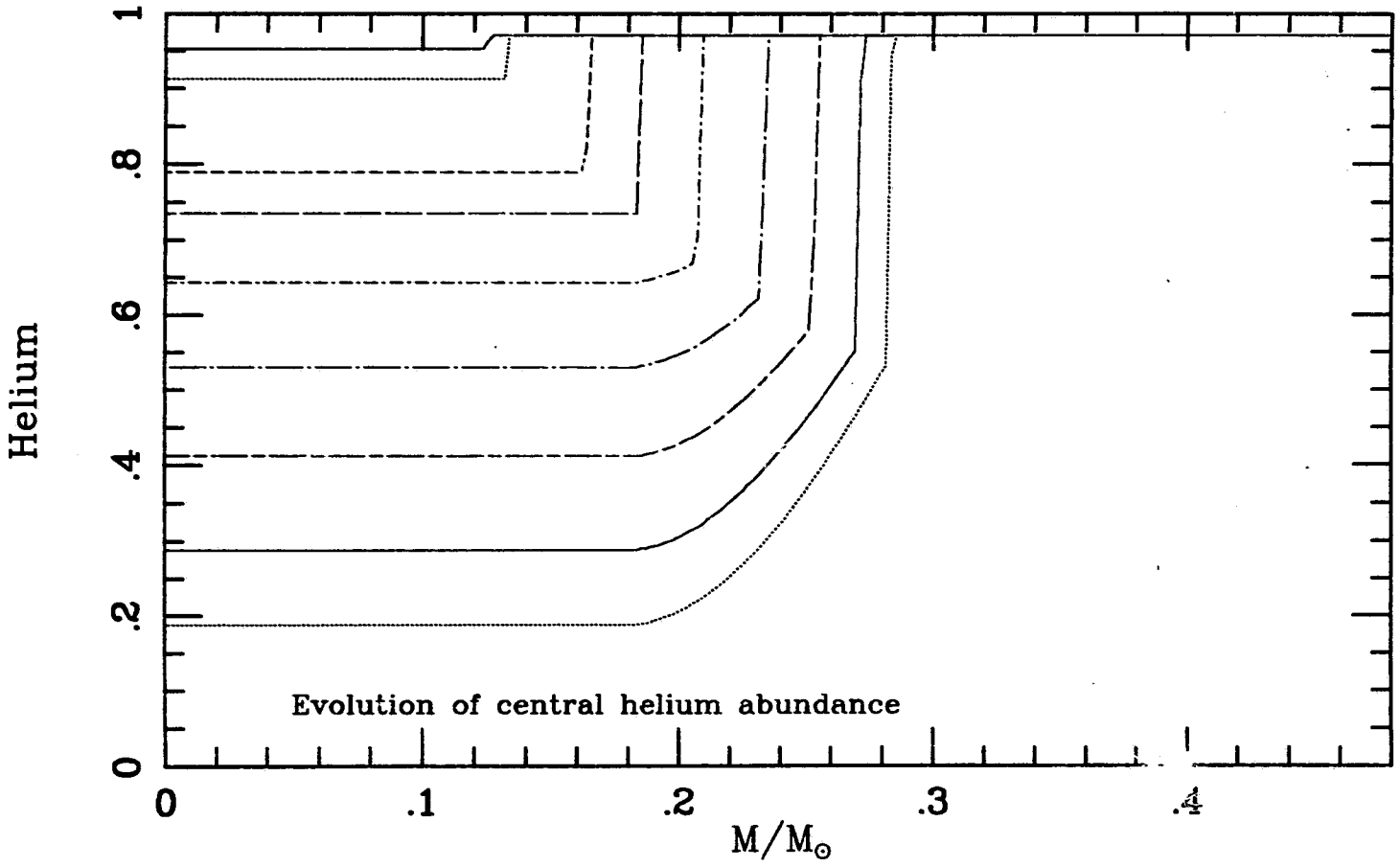

Fig. 3–2–3: Helium abundance profile during the main part of evolution with semiconvection, plotted for the model illustrated in Figure 3–1–1.

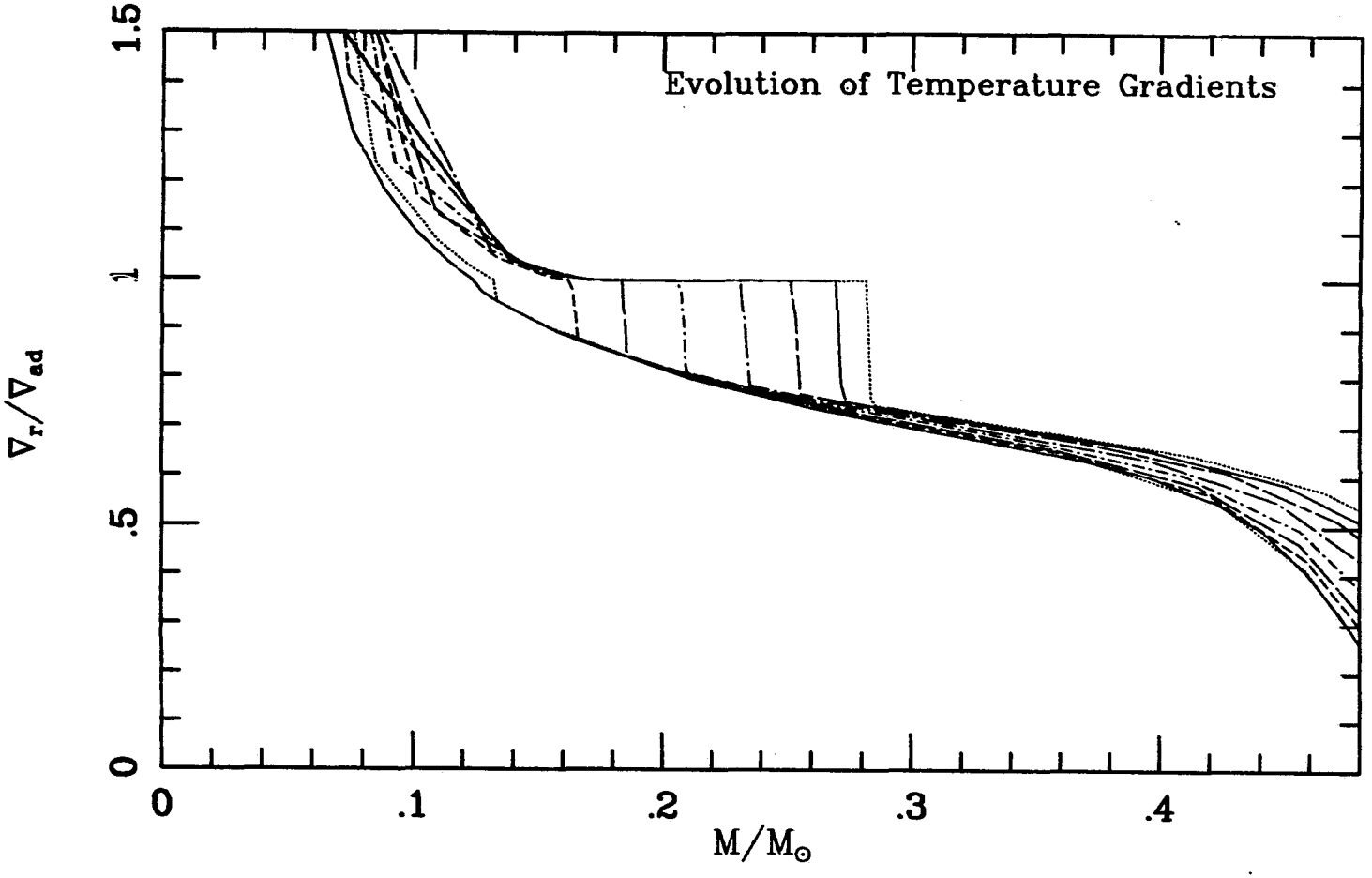

Fig. 3–2–4: Evolution of the temperature gradient during the main part of evolution with semiconvection, again plotted for the model illustrated in Figure 3–1–1.

a relatively high temperature in the next iteration. As a result, the opacity of the material is sufficiently reduced to render the outer part of the previous extent of the semiconvection zone radiative. In this case, the mixing routine need not move through all the shells in the zone. It appears that the programme described above is successful largely because the effect of temperature on opacity, and composition on temperature, eventually converge to a configuration which is consistent with the canonical semiconvection prescription. The programme converges in around 4-6 iterations in the early phase of semiconvection, and 9-12 iterations toward the end of the middle phase. In order to improve convergence at a cost in speed of execution, the proportion of the Henyey corrections applied at each iteration is steadily reduced during semiconvection. Typical results for the helium profile during the middle phase of evolution and the gradient ratios are illustrated in Figs. 3-2-3 and 3-2-4 , drawn from the same model as that used for Fig. 3-1-1. Indeed, Figure 3-2-3 is strikingly similar to Figure 2 of Sweigart and Demarque (1972). For all models, the initial core mass was $\sim 0.11 \pm 0.01 M_{\odot}$, and the expansion phase lasted for $\sim 18 - 22 \times 10^6$ years, when the core contained $\sim 0.170 \pm 0.005 M_{\odot}$. At this point, the central helium abundance was $\sim 0.73 \pm 0.01$ by mass. The routine produces very similar results to the Robertson-Faulkner method used by Sweigart and Gross (1976) and Sweigart (1987). That method estimates the helium abundance required to achieve convective neutrality by calculating opacity derivatives with respect to composition. Since the opacity is actually a function of two independent composition variables (because of the presence of $^{12}C(\alpha,\gamma)^{16}O$ burning), an assumption must be made about the ratio of carbon to oxygen in the semiconvective zone, usually that it is constant throughout (Sweigart and Gross 1974). However, if the process involved in semiconvection is, in fact, diffusive, it is quite probable that the oxygen component of the composition behaves quite differently from the carbon. Although this could be included in a crude fashion within the method used here, this has so far not been tried.

Despite the fact that the convergence properties of the physical variables with the chemistry are rather difficult to manage, the routine actually does behave very predictably during most of the lifetime of the star. The necessity for fixing a chemical profile consistent with the assumptions delays the convergence of the physical variables; in particular, the quadratic convergence rate of the Newton-Raphson iteration scheme is lost. For example, if the programme adopts, on convergence, the composition profile generated after the first iteration, the result is invariably a massive expansion of both the convective and semiconvective regions.

The mixing routine also stores for its internal use another interesting mass coordinate. Figure 3-2-5 a shows the gradient profile which arises after the physical variables have been modified by the Henyey mesh, but before the mixing step has been applied. The value of the mass at which the radiative gradient peaks is denoted M_{trap}. For the initial phase of semiconvection ($0.60 \lesssim Y_c \lesssim 0.72$), $M_{trap} \approx M_c$, but as the evolution proceeds, M_{trap} ceases to move outward, as illustrated in Fig. 3-2-5b. In a typical case, on convergence M_{trap} attains a maximum value of $\approx 0.22 \pm 0.01\, M_\odot$. As the evolution proceeds, this point starts to move back towards the centre despite a growing semiconvection zone. The cause for this behaviour is related to the appearance of a local maximum in the opacity which appears after the semiconvective zone becomes sufficiently large. The abundance vector required to give neutral convective stability is a function of the temperature. The radiative gradient within a particular model is approximately proportional to $\kappa/(MT^{3/2})$ (the flux being fixed within the semiconvection zone, and the pressure being related to the opacity by the adiabatic gradient). As the semiconvection zone grows in size, a point is reached where the outward temperature decrease, rather than increasing opacity, controls the increase in the radiative gradient at its outer extreme, and the abundance vector required to give neutrality changes rapidly with increasing mass coordinate (note the change in the slope of the helium profile in Fig 3-2-3). Note also that the semiconvection zone almost stops growing

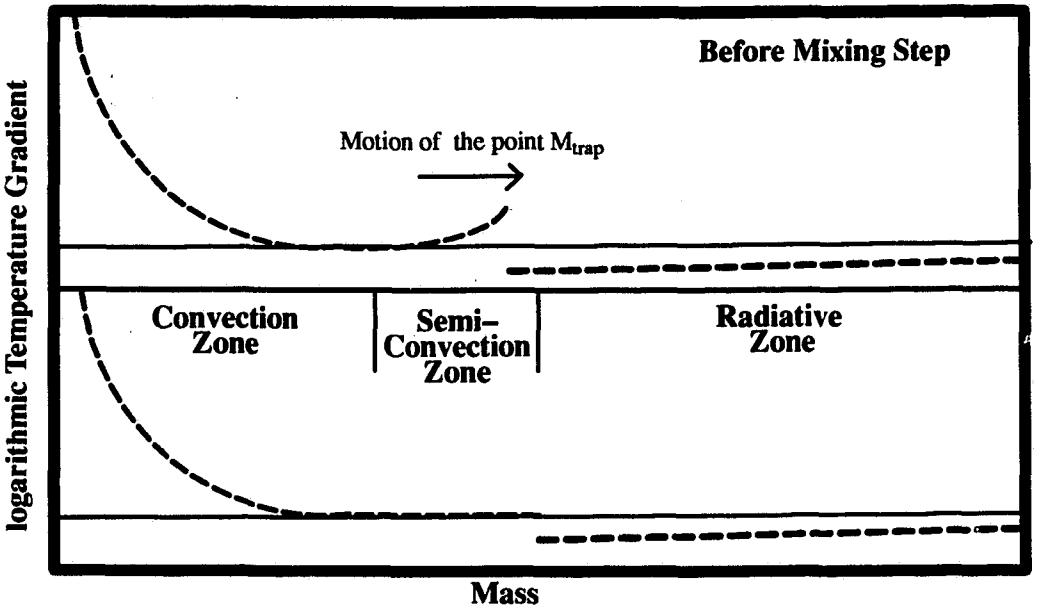

Figure 3–2–5a: Gradients before and after the semiconvection routine is applied, from a model early in the semiconvective phase. As before, ∇_{rad} and ∇_{ad} are indicated with dashed and solid lines respectively.

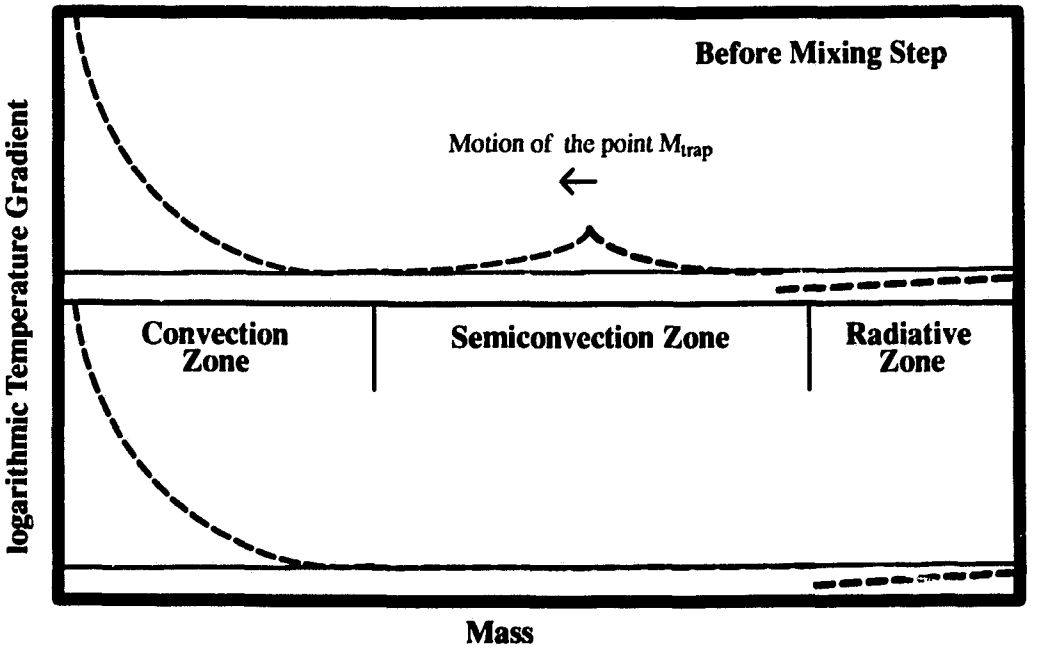

Figure 3–2–5b: Gradient profiles in a model taken late in the semiconvection phase. The arrow indicates the motion of the point M_{trap} described in the text.

during the later part of the evolution.

The programming of this algorithm requires some precise handling of details across subroutines in the stellar evolution code; in particular, the method depends on a fine mesh spacing in and above an expanding semiconvection zone. The subroutine which accomplishes this task, based upon the **SELECT** routine in a 1986 version of the VandenBerg (1983) stellar evolution code, works by producing a function which f which depends upon the differences in various physical quantities between adjacent meshpoints. The total number of shells in the model is fixed, and meshpoints are added(deleted) where f exceeds (falls below) a given range of values. Subsequent to this, the new mesh is augmented by a fine-spacing zone, centred at the convective core boundary. Below this point, the meshpoints are spaced apart by a fraction of a pressure scaleheight. Above it, they are spaced apart by a fixed value of the mass. The values adopted are 0.015 $\mathcal{H}_P$ spacing below the core boundary, and 0.002 $M_\odot$ above it. Some trial and error has, naturally, been involved in finding a sufficiently fine spacing. Originally, a spacing proportional to the total mass of the star was used, as suggested by Lattanzio (1986); it was found, however, that the lower mass objects with finer spacing converged more easily. Since the semiconvective zones are in any case similar in size irrespective of the mass, it was decided to reduce the spacing in all of the models. The shell routine is made aware of the location of the semiconvective zone boundary **LSEMI**, if present, and the number of shells within the zone **LSEMIC**. As the latter rises, mass shells are redistributed into the semiconvective region; the total number of shells is allowed to vary, currently between about 480 and 520. Also, the region in which fine spacing is applied extends to 10 shells above the current value of **LSEMI**, to allow for expansion during the model. As the fine spacing region is centred on a point within the mesh which moves occasionally, some interpolation method must be used to recreate the composition profile when the value of M_{cc} changes. Again, after some experimentation with spline interpolation,

a simple linear scheme was found to be the most reliable.

To a lesser extent, the timestep routine is also important, but this is true only at the stage of onset of semiconvective instability and at very late evolution. It is difficult to derive working criteria for setting timesteps which are small enough to avoid the 'overmixing' difficulty, at both of these phases of evolution. Setting too small a timestep is also found to cause convergence difficulties.

3.2.ii The Late Evolutionary Phase

As first noted by IR70, the triple-α process initiates a contraction of the core as the helium supply becomes depleted, which causes an escalation of the rate at which the central temperature rises (see Figure 3-2-6). The $^{12}C(\alpha,\gamma)^{16}O$ reaction becomes a more important source of energy, but does not dominate the nuclear processes until very late in the evolution. This reaction rate actually is about a factor of 100 faster than the triple-α process, for temperatures in the range $8.05 < \log T < 8.20$, but is dependent on a smaller power of the density. To understand the behaviour of the core at late times, the following features should be noted. Firstly, the radiative gradient (and the opacity) depend on a negative power of the temperature. Consequently, if the composition were fixed, the opacity and radiative gradient profiles would both fall with increasing central temperature. Secondly, because the temperature decreases outward, the outer layers of the core region are more prone to be convective, again at fixed composition. Thirdly, an increase in the carbon and oxygen abundance at fixed temperature serves to increase the opacity. Finally, the rapid temperature rise at late times is due to the contraction of the core in response to the scarcity of helium. Thus the situation which arises is one where the rising temperature acts against the convective instability.

The stellar evolution programme was found to suffer from severe convergence difficulties, usually after $Y_c < 0.20$. The code itself failed to meet the joint conver-

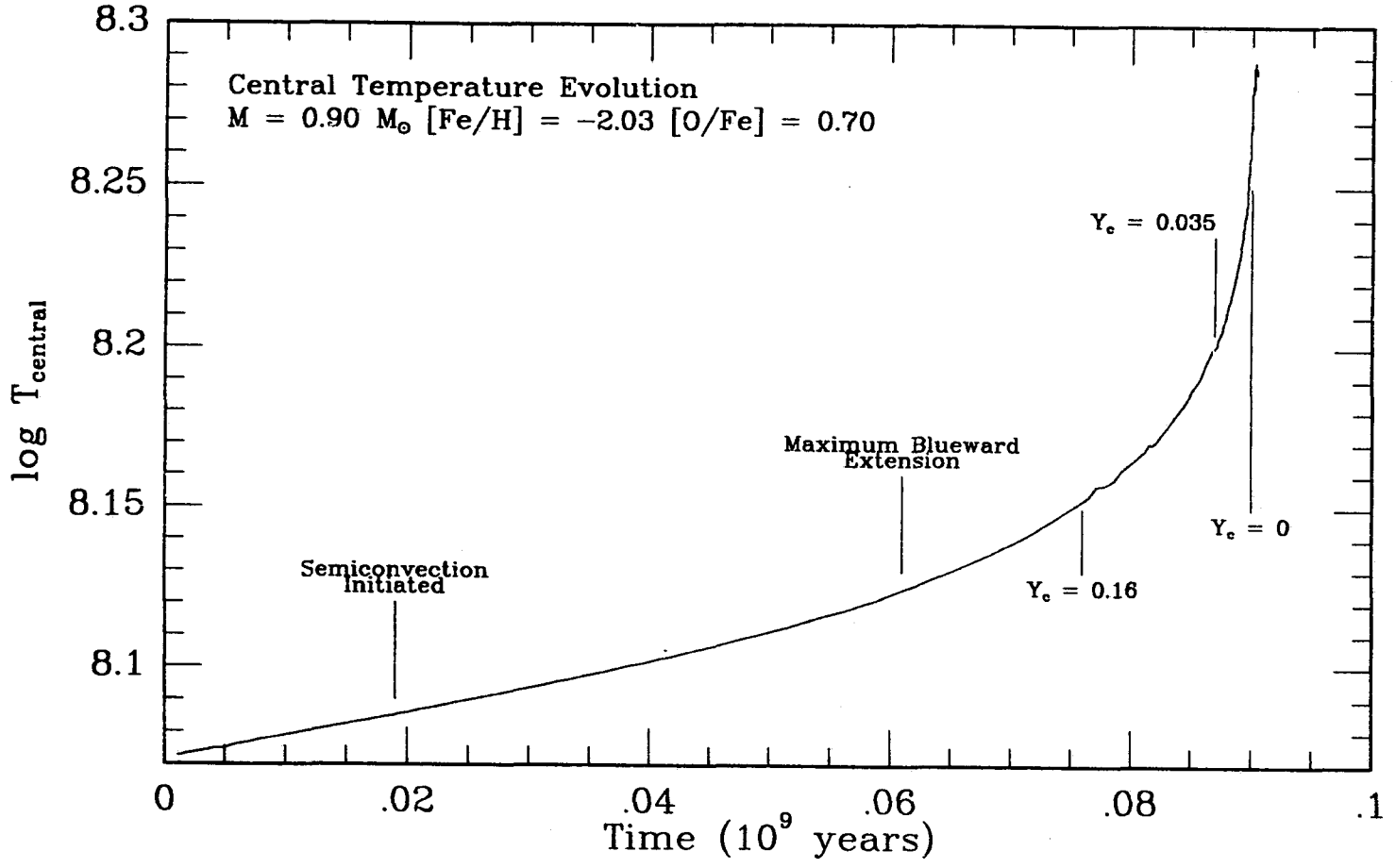

Fig. 3–2–6: The evolution of the central temperature, T_c, as a function of time. The points on the curve where the semiconvection algorithm changes its mode of operation are indicated.

gence conditions, and the calculation was therefore automatically terminated. In such a case it was often found that the physical variables continued to converge until the Henyey corrections became very small indeed, whilst the average deviation from neutrality of the semiconvective region remained large. Another possibility which arose was that semiconvective zone of larger mass extent was attained to high accuracy, but the physical variables did not converge. These observations can be summarized by saying that in the case of failure, the semiconvection routine failed to determine a point M_{trap}, close to the value found for the previous model.

In one instance where the physical variables converged properly, inspection of the final model showed that, in the semiconvective region, the innermost part was neutral, whereas the outer part of the zone had values of ∇_r significantly lower (*i.e.*, $\sim 0.980 - 0.997\nabla_{ad}$). Inspection of the differences in the variables between the two last models indicated that it was, indeed, the rising temperature (causing a drop in the opacity) which was responsible for the failure of the semiconvective zone convergence. An obvious solution to this convergence difficulty would be for the routine to mix a larger amount of helium into the semiconvective region; however, this should not occur if the outer shells of the semiconvection zone are stable to convection. In other words, the programme could find no solution with a semiconvective zone of the same size or greater. The other reason for convergence failure (failure of Henyey convergence) indicates a severe overmixing, which can usually be solved by reducing the timestep. In one such case, both the convective and semiconvective regions expanded by about 0.03 - 0.04 $M_{\odot}$. This latter instance looks very similar to the 'breathing pulse' effect referred to by CCPT and Lattanzio (1986). In several cases during the computation of the model grid listed in Appendix B, a model did manage to converge with an enriched core region. An example of such a sequence is illustrated and discussed below.

In order to improve the reliability of the routine, it was decided to relax the criterion for convergence in the semiconvective zone, for $Y_c \lesssim 0.16$. If convergence

fails more than once in the same model before this point is reached, then the following procedure is also initiated. The mixing routine is called at each iteration until the physical variables converge to a mean error which is an order of magnitude higher than the convergence criterion accepted for a model[5]. In subsequent iterations, the chemical profile outside the convective core is held fixed until the model reaches convergence, when the mixing routine is called a final time. This releases the semiconvection convergence criterion for the model, whilst still attempting to follow the iteration of the physical variables with the composition. In practise, the resulting composition profiles are generally radiative (with $\nabla_r \gtrsim 0.99$) in their outer layers, and sometimes no less accurate than earlier in the evolution. The resulting higher range of acceptable chemical profiles now allows the central helium to stay constant or rise slightly between two consecutive models, where the average deviation from neutrality is less in the following model than in the preceding. These instances differ from 'true' breathing pulses in that the central temperature continues to rise through them. As evolution proceeds toward helium exhaustion, the approach introduces deviations from neutrality within the semiconvective region of order 1% (to a maximum of about 4%) despite rapidly rising temperatures.

Figures 3-2-7 and 3-2-8 illustrate, respectively, the opacity and gradient profile at later evolutionary phases than those shown in Figures 3-1-1 and 3-2-3, and represent sample output from this phase of evolution (top three curves) and the later, exhaustion phase discussed in chapter 5. The uppermost sequence in Fig. 3-2-7 shows the opacity profile at age 81 Myr. The curve has lost the smooth shape which is attained when neutrally-stable semiconvective profiles are computed accurately; however, the interesting feature of this plot is the *reduction*

[5] *The usual convergence criterion adopted for the Henyey mesh is that* $\overline{\delta} < 5 \times 10^{-5}$, *where* $\overline{\delta}$ *is the mean value of the differences between the Henyey corrections at consecutive iterations.*

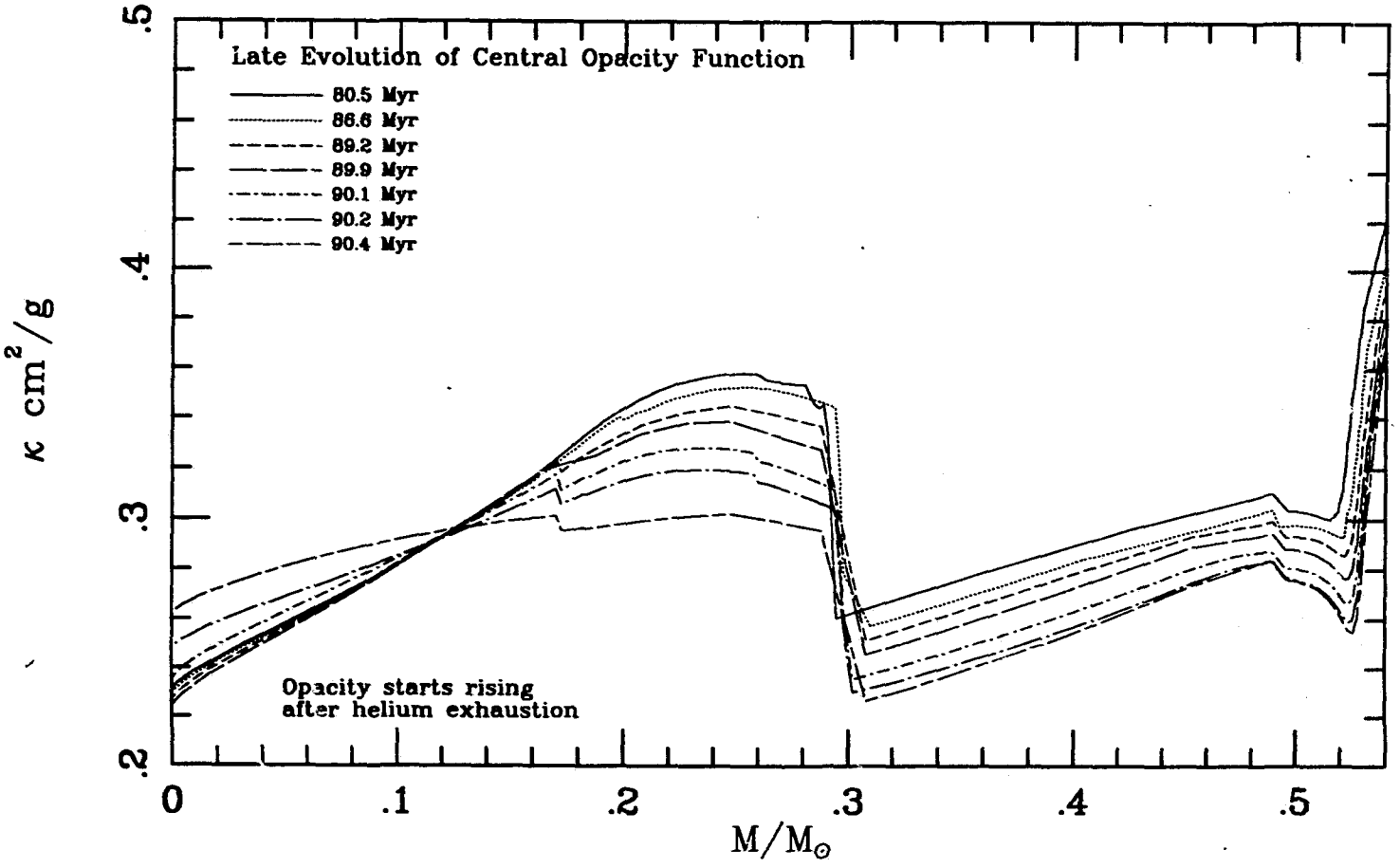

Fig. 3–2–7: As for 3–1–1, but showing the evolution from the the last curve plotted in that diagram to beyond central helium exhaustion.

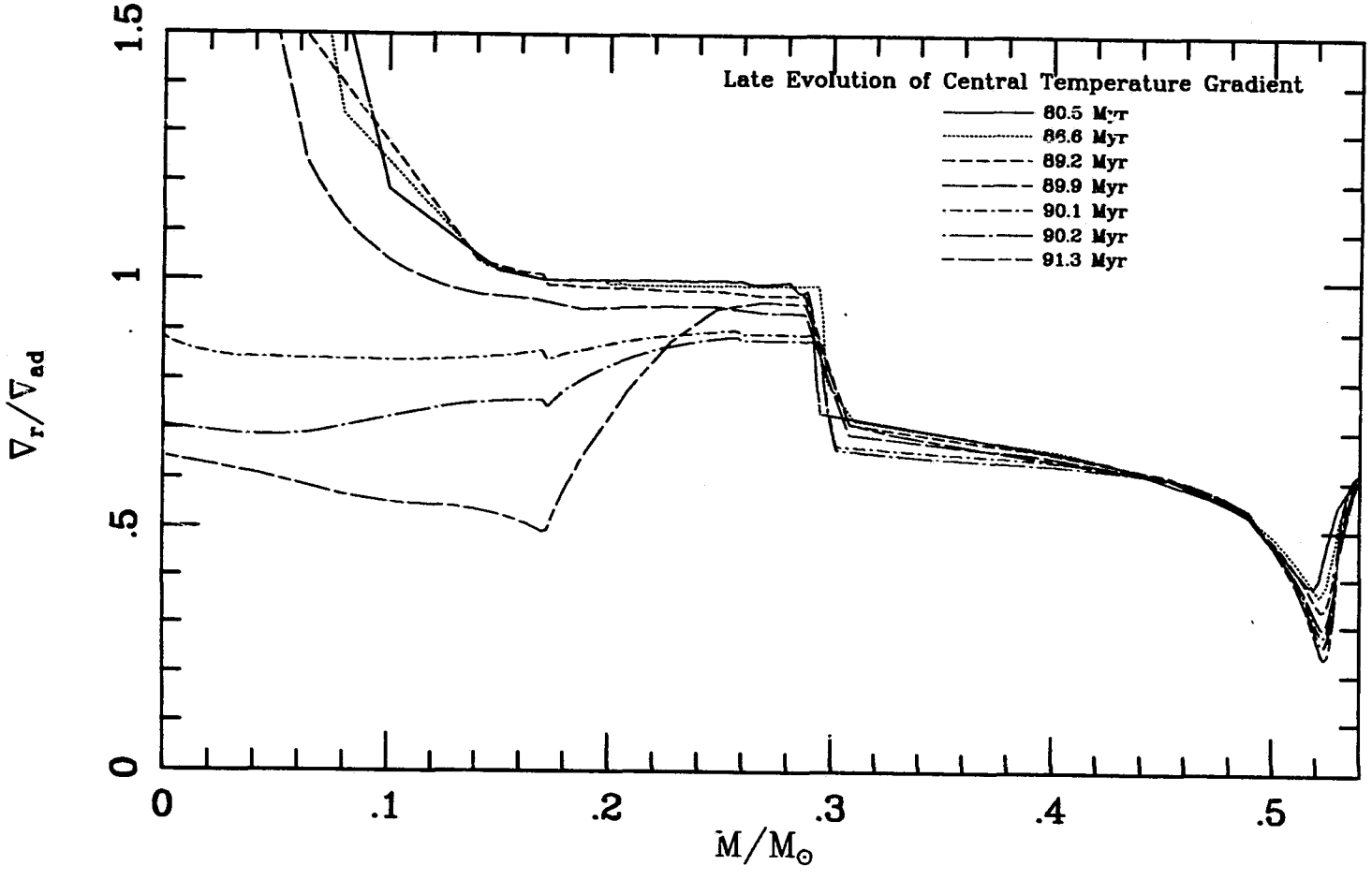

Fig 3–2–8: As for 3–2–6, but for the evolution of the temperature gradient.

in the opacity of the convective core during this phase; the opacity begins to rise again later when the core becomes quite degenerate. The accompanying Figure 3-2-8 appears to indicate that the numerical difficulties arise because the semiconvective instability is, in fact receding at this stage. If the opacity is not to decrease as shown in this plot, the escalating temperature rise must be dampened. This can only be done by an infusion of fuel into the centre (a 'breathing pulse'), and the shrinking of the convective/semiconvective region can only be delayed. Further, the region well inside the semiconvection zone has a slightly greater tendency to become radiative with increasing temperature than its outer edge. This behaviour would imply a termination of the mixing instability, so that fresh helium can no longer reach the burning region. If the outer layers of the semiconvection zone are still convectively unstable (an instance which does not arise in the calculations presented here, unless breathing pulses occur), a detached convective zone will form. However, since the temperature continues to rise even this region becomes less susceptible to convection as time progresses. Occasionally, the programme is able to converge on a 'breathing pulse'; in these cases, generally the entire semiconvective region becomes homogenized.

It seems apparent from these diagrams that the instability will eventually disappear altogether, as noted by Gingold (1974) in a study of AGB evolution. Certainly, the convective core itself must shrink, because the exhausted carbon-oxygen core of the star will be roughly isothermal ($\nabla \lesssim 0$) at central helium exhaustion. Thus, it was decided to remove the call to the semiconvection routine altogether at some arbitrary small value of the helium abundance, taken as $Y_c = 0.035$. In the diagrams one can see that this procedure leads to a small discontinuity in κ and in ∇_r. Quite possibly, this problem could be removed by utilizing a similar scheme to that employed during the core expansion phase. In the sequence illustrated here, the age at which this criterion was reached was 87.2 Myr. The convective core started contracting when $Y_c \sim 0.003$, at age 89.7 Myr.

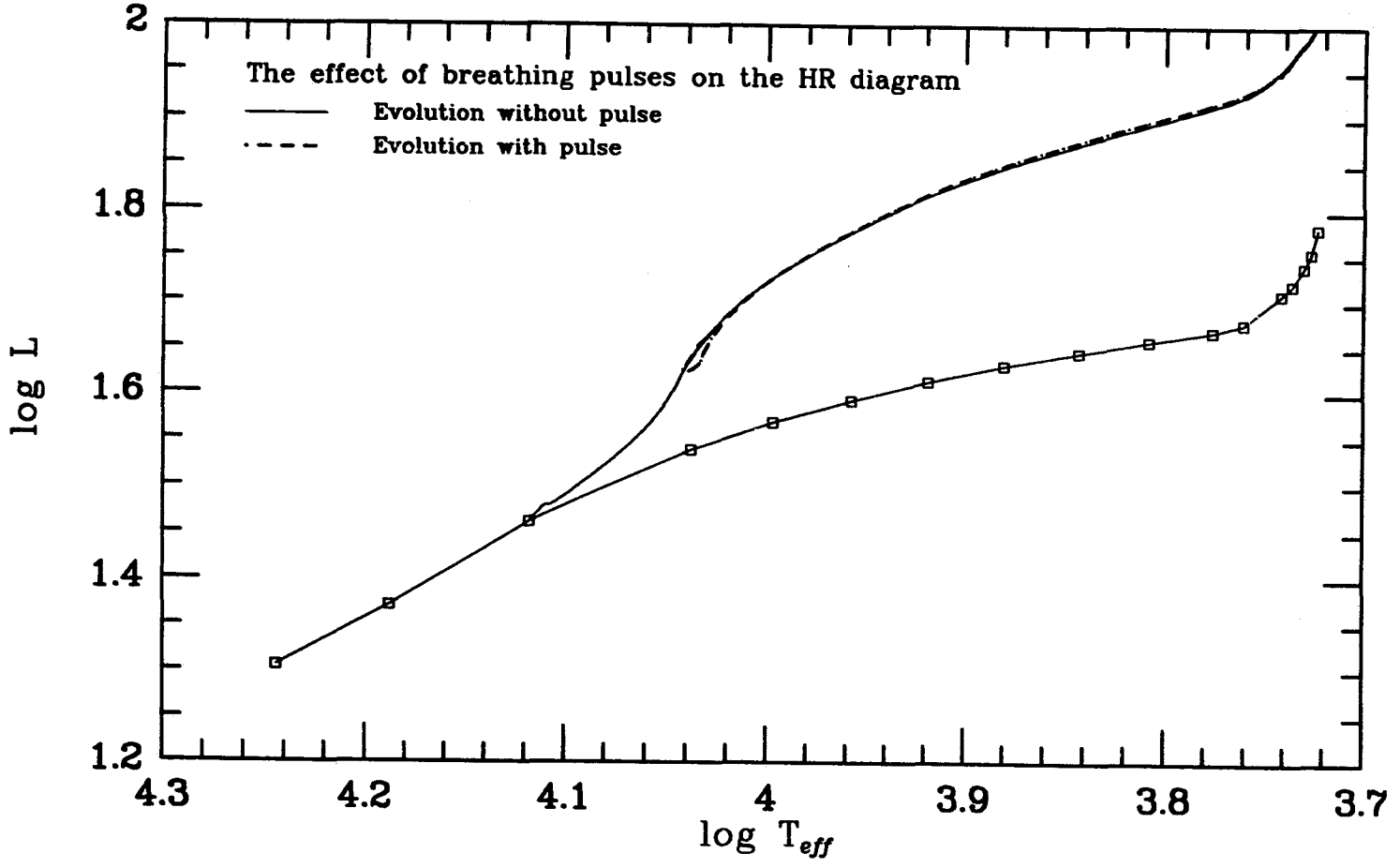

Fig 3–2–9: An illustration of the effect of a small breathing pulse on the theoretical HR diagram.

Figure 3-2-9 illustrates the effect of a breathing pulse on the HR diagram behaviour of a model sequence. In the diagram, the original track (solid line) contained a pulse when Y_c was about 0.02, raising the central helium abundance by a factor of 3. This sequence was later restarted from a model calculated before the pulse occurred, and the resulting track (dotted line) did not contain the pulse. The sequence with the breathing pulse took 4 million years longer to reach a luminosity $\log L/L_\odot = 2$.

The fact that two parallel runs of the stellar evolution code did not produce the breathing pulse suggests strongly that at least some pulse events produced by the code are numerical artefacts. In addition, the discussion above regarding the response of the star to the rapid temperature rise at late times suggests that the 'instability' of the convective core size that gives rise to semiconvection may disappear, and the extended mixing zone diminishes in size smoothly.

It must be remembered that 'semiconvection' itself is the result of a hypothesis about the way the star adjusts itself to the core conditions, rather than modelling a particular physical process. However, the model calculations resulting from its inclusion give timescales for HB evolution in good agreement with comparative star counts of red giant and HB stars in globular clusters (Buzzoni *et al.* 1983). Further, the models with a partial mixing zone may reproduce another feature of globular cluster colour-magnitude diagrams, namely the excess of stars at the base of the AGB. It must be said, however, that the length of this phase, in which the evolutionary tracks reverse direction, is sensitive to the abundance in the old semiconvective layers, but the observations need to be highly complete in order to test the various mixing hypotheses.

It has been claimed previously that the existence of breathing pulses, which would reduce the lifetimes of AGB stars, is disfavoured by the measured values of $R2 = N(AGB)/N(HB)$ in globular clusters (Renzini and Fusi Pecci 1988). On

the other hand, some clusters contain RR Lyrae variables which have apparently suffered significant shortening of their periods, which would be one consequence of a breathing pulse (see Lee 1990, and references therein). In conclusion, it is unlikely that the behaviour of the cores of Horizontal Branch stars will be understood without an enormous increase in the complexity of models, and the number of observational tests available for this understanding are unlikely to increase. More attention is likely to be given to improvements in determinations of cluster abundances, and the application of this new information to the models.

Chapter 4 Notes on Selected Numerical Procedures

4.1 Scope of this Chapter

The object of this section is to explain some of the techniques used in this study. Most of the basic numerical procedures, as well as the implementation of the physical inputs to the programme, have been discussed in detail elsewhere (see *e.g.*, Kippenhahn, Weigert and Hofmeister 1967; VandenBerg 1983; Dorman 1986), and extensive discussions of those which are common to previous studies will not be repeated. A brief summary of these will be contained in the fourth section of this chapter. There are two major areas which have received attention (in addition to the core evolution problem discussed in the last chapter), which are the initialization programme used for constructing ZAHB models, and the equation of state (hereafter EOS) routines. In the latter case, two topics have been investigated during the course of this study; firstly, the effect of alternative numerical procedures for the calculation of ionization equilibrium (particularly for $\log T \lesssim 6$) and secondly the effect of non-ideal corrections in the core, where electrostatic effects on the EOS for carbon and oxygen may be non-negligible.

The fourth section also contains a brief summary of the implementation of the programme. Some of the details provided here may seem superfluous in this context, but this implementation has proved to be very efficient, and has aided this project significantly by allowing new sequences to be calculated with very little human intervention. In addition, it has enabled variants of the main calculation grid (for some of the test sequences used for illustration in Chapter 2) to be computed almost without effort. This information is therefore provided to document the existing routines and in the spirit of sharing useful techniques.

4.2 Initialization: the production of ZAHB models at fixed composition

The importance of the initial location in mass of the hydrogen shell source in relation to the edge of the helium-rich core has been discussed in detail by a number of authors (Gross 1973; Lauterborn, Refsdal, and Stabell 1972; Fricke and Strittmatter 1972). The zero-age location and the subsequent initial evolutionary behaviour is sensitively affected by the hydrogen profile in the 'shell relaxation phase', but, as one expects from intuition, it does not affect the later evolution (*i.e.*, for $t - t_{ZAHB} \gtrsim 3 \times 10^7$). However, in order to comment usefully on the masses of stars in the instability strip, the consistency of initial model chemical composition profiles with their precursors has been treated carefully. Note that the arguments presented in §2.5 for the direction of evolution for different masses depend on the initial shell temperature rather than the adopted composition.

If the 'Zero-Age' model is not the result of an evolutionary calculation through the Helium Flash, then its initial entropy is indeterminate. Therefore, the 'Zero-Age' thermal equilibrium configuration was found by evolving an initial structure over a number of short (100,000 year) timesteps until the interior structure became stable. Generally, the composition of the relaxed model was then reinitialized and the evolution again followed using small timesteps until an age of 10^6 years was reached. The initial structure is generated as follows. A set of physical variables is taken from a previously generated ZAHB model [1], and the composition profile in the hydrogen shell is drawn from red-giant tip models of the same composition as that assumed for the HB calculation. About 40 mass shells from the red-giant precursor are included in the initial HB model profile between the edge of the He-rich zone (at mass coordinate M_c, as derived from the giant-branch

[1] *The first Horizontal Branch model used in the Victoria code (or its ancestor) was computed by Laskarides (1972); the model used as the 'seed' for the current set of calculations was supplied to the author by D.A. VandenBerg.*

model) and the base of the envelope, defined at the point where X, the mass fractional abundance of hydrogen, satisfies $|1-X/X_{surface}| < 0.00001$. The region where the composition changes rapidly generally corresponds to a mass range $M_c < M_r \lesssim M_c + 4 \times 10^{-4}$ in solar units. The hydrogen composition of the new shells was derived by interpolation using the Hermite spline subroutine introduced into the literature by Hill (1986). The adopted abundances of the CNO elements were taken from the convective envelope of the red giant tip model. Thus, CNO equilibrium in the H-burning shell was not originally assumed; however, it was generally achieved by the end of the initialization procedure described below.

In order to account for carbon production during the Helium Flash, the core helium abundance Y was taken to be $Y = 1 - Z - 0.029$, where Z is the total mass fraction of elements with nuclei heavier than that of helium. The abundances of the elements carbon, nitrogen and oxygen were taken to be approximately equal to their values at CNO equilibrium in the core of the giant star, with the carbon abundance enriched by the amount that Y is reduced. This estimate for the enrichment is justified to within a factor of order unity by an argument in IR70 for the energy required to lift the degeneracy in the core of a red giant; the number adopted here was that used by SG76. As also found by Rood (1970), small changes in the central abundances of helium and carbon produce very small changes in the initial location of the model on the HR diagram. Since no reactants, apart from helium, are involved in the triple-α process, and reactions involving the other elements followed in detail here are unimportant because of their relatively low abundance at this stage of evolution, the main effect of inaccuracies in the assumed initial core composition is a small uncertainty in the total lifetime of the star.

Once a model for a relatively high-mass HB star ($M_* = 0.90\ M_\odot$) has been created, models of lower mass were found from it by imposing the same hydrogen-burning zone composition profile, scaling the envelope by an appropriate amount, and again performing ten short timesteps on the resulting structure. The initial

models used for calculating evolution had a central helium content of about $Y = 0.94 - 0.95$, depending on Z.

There are two implicit assumptions in this method. The first, as referred to in §2.5, is that large-scale mixing between the core and the envelope does not occur during the helium flash, as hypothesised by F66. The second is that the structure, which is likely to be severely disrupted by the helium flash, relaxes to the same thermal equilibrium configuration that is found by this method. It is necessary to assume that mass is lost from the outer envelope before the horizontal branch is reached, as it is impossible to explain the observed horizontal branch morphology in globular clusters using models with the masses of the red giants. That is, using canonical main-sequence stellar evolution to provide estimates of the ages of the globulars, the masses of stars approaching the tip of the giant branch are approximately $0.85 - 0.90\ M_{\odot}$. Models of this mass do not evolve very far to the blue, and certainly do not populate the extreme blue 'vertical' sequence on the colour magnitude plane, contrary to observation. On the other hand, a spread in core masses at fixed total stellar mass would also not provide a solution, since then the slope of the ZAHB would be different from observation. However, the models generated with these assumptions show a high level of consistency with the observations. In addition, the code used here produces results which agree very well with the Sweigart (1987) ZAHB models, if similar physics is assumed. In turn, the Sweigart calculations show good consistency with model calculations with a hydrostatic code taken through the helium flash (Mengel and Sweigart 1981).

However, the implication is that, during the late part of giant branch evolution, or during the helium flash era and the descent to the horizontal branch, a large fraction (up to $\sim 25\%$) of the envelope may be expelled owing to events happening deep in the interior, whilst the hydrogen-shell-burning region of the star is not severely mixed with either the core or the envelope. It seems feasible, however, that small degrees of mixing could take place without producing a

significant discrepancy with the observations.

According to the theory of Chapter 2, the enhancement of helium would shift the models to higher luminosity at fixed mass, and enhancements in carbon should alter the energy balance in the model, so that lower masses occupy redder positions in the CM diagram. It must be stressed that unless mass-loss processes are very different for different metallicity, the existing calculations would fail to explain blue horizontal branches if the amount of carbon added to the shell burning layers were a significant fraction of its observed value in metal-poor clusters. In addition, significant helium enhancement appears to be excluded by the 'morphological' arguments such as those presented in Chapter 6 (see also Buonanno, Corsi, and Fusi Pecci 1985, hereafter BCF; S87). These show how the luminosity width of the HB is a function of Y, and therefore the latter can be constrained by observation; according to Chapter 2, this width appears to be a function of Y *in the hydrogen shell-burning layers.* Since Helium Flash calculations are still somewhat uncertain (see *e.g.,* Dupree 1986), the hypothesis of no core-envelope mixing has been adopted strictly. The sequences computed with this assumption are demonstrably able to reproduce the observations to a fair degree of accuracy.

4.3 On the Equation of State for Horizontal Branch Stellar Interiors

The Equation of State adopted by VandenBerg (1983) is originally due to Eggleton, Faulkner and Flannery (1973), hereafter EFF. The formulation differs from others used in stellar structure calculations in its treatment of partial ionization. The transition from a partially ionized (or neutral) gas in the atmosphere to what is assumed to be a fully ionized gas in the interior presents very difficult problem, particularly at densities which are high relative to atmospheric values. In the tenous outer layers of the star where hydrogen and helium undergo ionization, the Saha equation is used to calculate the ionization equilibrium. The Saha equation is derived from the Boltzmann equation applied to ionization processes (*i.e.*, $Z^i \rightleftharpoons Z^{i+1} + e^-$, where Z^k represents a nucleus of charge Z in its k^{th} ionization stage), and often under the assumption of negligible interparticle interactions. However, in this form, the equilibrium cannot be calculated at high density, since at high pressure it would yield a solution with many neutral atoms. Eddington (1926) argued that the centres of very dense objects could not be neutral, and indeed, the assumption that full ionization takes place is necessary to avoid the embarrassment of a theory which implies that electron orbital radii are greater than the average interparticle distance. Hence the term pressure ionization was coined to represent the physical processes by which matter at intermediate to high densities remained ionized.

A thorough review of the question of ionization equilibrium has recently been presented by Hummer and Mihalas (1988), which additionally contains many references, including another very readable account by Fontaine, Graboske and Van Horn (1977, hereafter FGH). In this latter paper, the Free Energy Minimization technique is used to derived thermodynamic quantities, and this requires that the canonical partition function of the various species in the gas (*i.e.*, the ions at their different ionization stages) is separable into kinetic, interaction, and configurational parts. The work of Hummer and Mihalas (1988) concentrated on the

internal configurational free energy, and indicates that the presence of other elements alters the partition function of incompletely ionized atoms. Their formalism is based on 'occupational probabilities': in contrast to other techniques (such as that of EFF) they state that pressure ionization is largely the result of alterations in the effective statistical weight of electron levels rather than a change in the effective ionization potential. That is, the occupation probability for energy levels with large values of the quantum number n is zero, so that these electrons are free rather than bound; the non-ideal effects cause a truncation of the partition function. The key point here is that the regime of partial ionization requires complex calculations. In other treatments, full ionization is assumed beyond a given value of the local temperature, and the Saha equation, with or without a correction term to the effective ionization potential, is used to calculate the ionization equilibrium at lower temperatures. The EFF method, in contrast, assumes a schematic correction to the ionization potential which is intended to ensure a transition to full ionization at high temperature. There is some agreement at present that the size of the correction originally suggested in the 1973 paper is too small to produce full ionization at a low enough temperature (*e.g.,* Proffitt and Michaud 1991). As well as increasing the size of this correction, therefore, other methods of representing the region of transition to full ionization were considered. Since a fair proportion of the calculation time of the evolution code is taken up with iteration for EOS variables, it is not necessarily desirable to incorporate too intensive an approach to the problem.

An approach often taken (Dorman, Nelson and Chau 1989; D'Antona and Mazzitelli 1985; see also Chieffi and Straniero 1989), and seriously considered for this study, is to use a more complex equation of state in tabular form, as is done with complex opacity calculations. This method has various pitfalls, the most serious of which is the non-linearity of the adiabatic gradient in the hydrogen and helium ionization zones. The technique of choice for composition interpolation

of EOS data are usually known as the 'additive volume method'. Under the assumption that different elements represented by different EOS tables *do not interact*, and that the first law of thermodynamics can be written simply as

$$dU = TdS - PdV \tag{4.1}$$

it is trivial to show (Dorman 1986) that the density of a mixture is given by

$$\frac{1}{\rho(P,T)} = \sum_i \frac{X^i}{\rho^i(P,T)} \tag{4.2}$$

where the summation runs over the tables used to interpolate the result. X^i represents the fractional contribution of each separate table, indexed by i. In the particular case of tables for data constructed using pure elements (as in the FGH or the Straniero 1988 data), the X^i are simply the mass fraction abundance of the element in question. The other quantities of interest which are generally just C_P, the specific heat at constant pressure, and ∇_{ad}, can be found using the formulae

$$C_P = \sum_i X^i C_P^i \tag{4.3}$$

and

$$\nabla_{ad} = \sum_i \frac{X^i \nabla_{ad}^i C_P^i}{C_P}. \tag{4.4}$$

However, while ionization is taking place, the equilibrium is dependent upon the density of free electrons, and this is in general a function of the entire mixture. Despite the fact that the density is quite well represented, the errors resulting from adoption of a tabulation which represents a different element mix may well cause errors which are of the same magnitude as the problems resulting from inadequate representation of the pressure ionization processes. Therefore, this method was rejected.

A second approach would be to use a tabulated equation of state which is generated with a composition very close to that required. During the HB phase of evolution, in canonical stellar evolution models, the envelope does not change its composition. Thus it should be possible to incorporate complex EOS calculations for a specific composition into the evolutionary computations by simply generating the correct table. This approach was considered in the following way. Irwin (1989) has generalised the EFF EOS to include the detailed ionization equilibrium of carbon, nitrogen, oxygen and iron, as well as the first ionization stage of some of the less abundant elements. It was decided, as a first attempt, to replace the EFF pressure ionization technique in this version of the EOS with one based directly upon the Static Screened Coulomb Potential (a modified Debye-Hückel approximation), as used by Straniero (1988) for low densities. Following the calculation of tables of EOS quantities at a set of values for P and T, the interpolation was tested by comparing the results obtained by interpolating the table, and by direct calculation of the equilibrium using the Saha formulation, for a typical stellar interior.

In this test, the Straniero (1988) data were used for $\log T > 6.25$. The results of this test are given in Figure 4-3-1 , which shows the run of adiabatic gradient against $\log P$. The solid curve represents the direct calculations, whilst the dotted curve is its interpolated representation. The $HII/HeII$ and $HeIII$ ionization zones are clearly visible, and the interpolant takes a clearly different path through the $HeIII$ zone than does the direct calculation. This particular set of coordinates were picked to highlight problems caused by interpolation; in fact, the interpolant in density (against either T or P) is indistinguishable from the result of direct calculation. In the table used for this diagram, isotherms were calculated at intervals of 0.1 in $\log T$, and defined at pressure points spaced by $\Delta \log P = 0.2$. The interpolation was carried out using the four-point Lagrange formula. Whilst the differences between the interpolant and the direct calculation

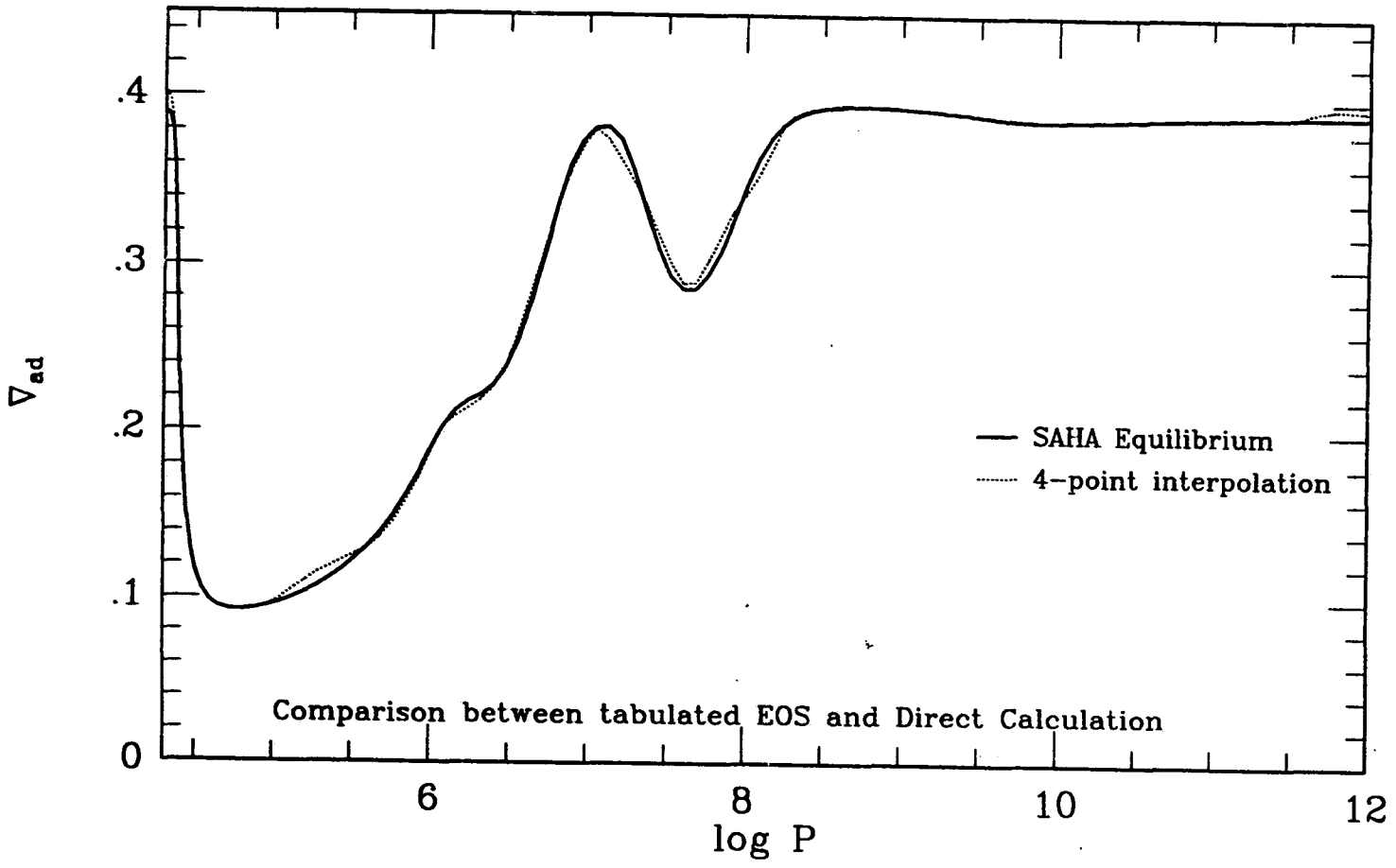

Fig. 4–3–1: Direct comparison between adiabatic gradients derived by direct calculation and interpolated from a table.

do not seem large here, they have been minimized somewhat by using a much finer grid than, say, that of the tabulation of Magni and Mazzitelli (1979). Clearly, a still finer grid is required for material undergoing ionization. Also the errors that arise appear in zones which are likely to be convective, and therefore could become important in defining the equilibrium surface temperature and radius of the star.

A recent study (Chieffi and Straniero 1989) of main sequence and giant evolution showed that incorporation of the tabulated equations of state of FGH and Magni and Mazzitelli (1979) produced evolutionary tracks which differed significantly from those generated using direct calculation, and more importantly, differed from the observations. They were able to offer no explanation for the fact that 'improved equation of state calculations give poorer evolutionary calculations'. It is speculated here that the answer to this problem lies in the numerical techniques used for interpolation. Firstly, both of the tabulations they used require interpolations in composition, which is itself a significant source of error. Secondly, even if no composition interpolation is required, the spacing of the table used is extremely important if ionization is taking place. A more detailed study of this question is in preparation (Dorman, Irwin and Pedersen 1991).

The other issue raised by consideration of the EOS is the effect of interactions, chiefly by the electrostatic forces, at high density. The magnitude of the Coulomb correction is often represented by the plasma parameter Γ, which is the ratio of the Coulomb potential energy to the thermal energy of an ion. For sufficiently high densities (or smaller interatomic distances) the Free Energy Minimization technique breaks down because the partition functions for individual particles are not separable in the sense described earlier. This also implies a breakdown of the ideal gas approximation, and indeed Γ becomes of order unity or much greater. The high density regime is dealt with by a number of techniques, such as the Thomas-Fermi model adopted by FGH and with slight variation by Magni and Mazzitelli (1979). Straniero (1988) adopts an 'expansion' approach, and uses a formula for

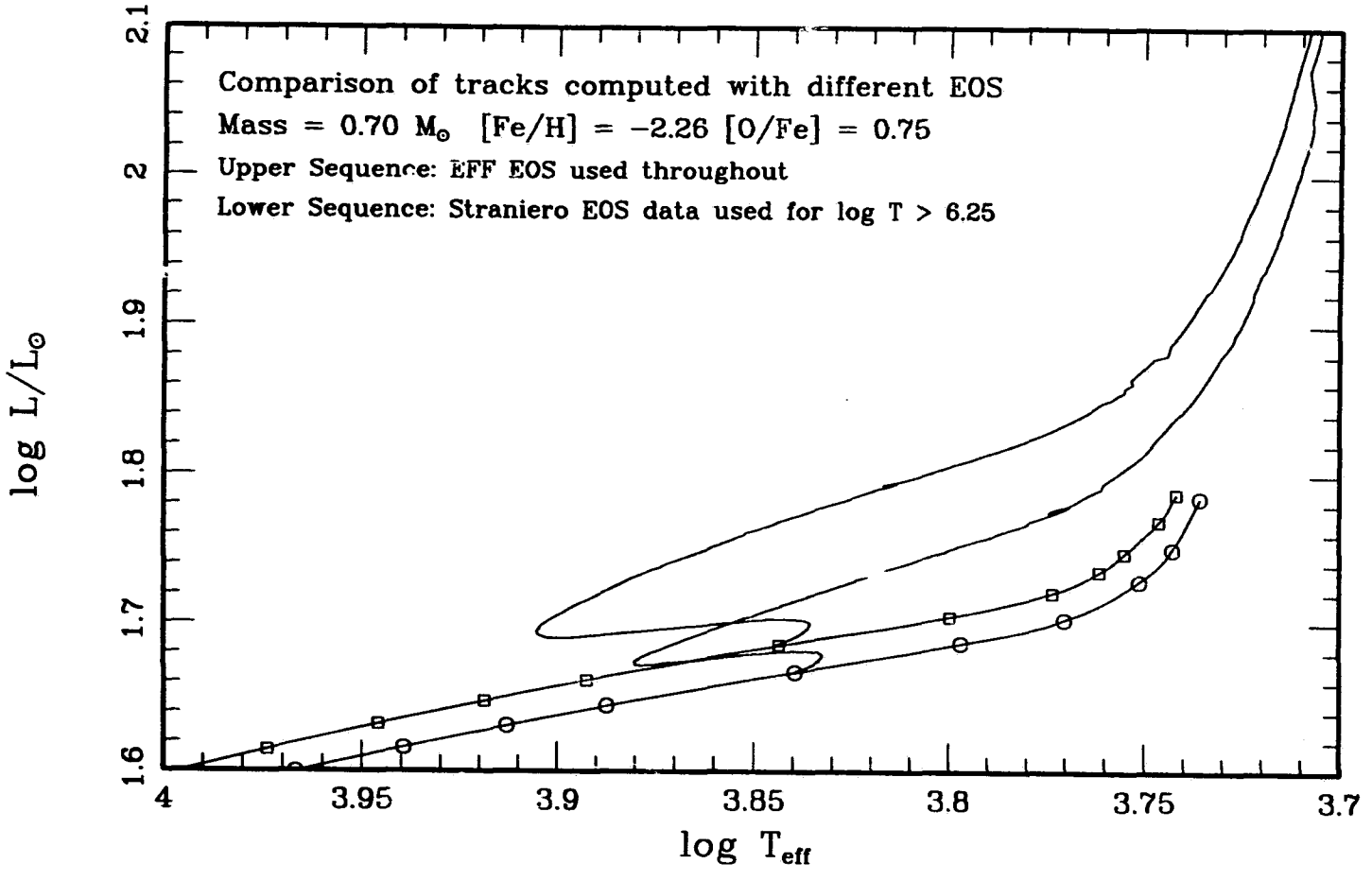

Fig. 4–3–2: Illustration of the changes in HB evolutionary tracks resulting from the assumption of EFF and Straniero (1988) equations of state in the core.

the correction to the pressure and the internal energy derived from Monte-Carlo simulations. According to the data he provided, the plasma parameter is of order unity for carbon and oxygen for the range of densities and pressures appropriate to the centres of HB stars. It was therefore decided to use his calculations for this study, for $\log T > 6.25$ [2], to see the effect on HB morphology of variations in the equation of state at high densities. One product of this decision was that full ionization was assumed in the calculations, as it is in the Straniero data, for all values of the temperature greater than 6.25. This has the effect of depressing the ZAHB luminosity compared to the results obtained by using the EFF equation of state throughout the star. The difference between the evolutionary tracks so caused is illustrated in Figure 4-3-2 . The upper ZAHB and evolutionary track is the result of an earlier calculation with the same input physics apart from the adoption of a different equation of state. The lower sequence is taken from the main set of evolutionary calculations listed in the Appendix. The ZAHB core masses are very slightly different (the upper sequence has an initial core mass which is 0.0004 $M_{\odot}$ greater), but insufficiently so to explain the differences between the tracks. It appears that the difference in the adopted equation of state produces a significant effect on the length of the blueward loop (affecting HB stellar distributions synthesised from these calculations), and, importantly, in the luminosity width of the sequence. Also, an uncertainty results in estimates of the cluster distance moduli when these are derived using the apparent visual magnitude of the horizontal branch. Clearly, these preliminary findings for the

---

[2] *It is possible that this data set also has some problems. In tests performed with a very similar EOS at low density for hydrogen, it was possible to reproduce the density values given in Straniero's tabulations only if the mass of hydrogen was set equal to unity, rather than its correct value of 1.00783 amu. Of course, the discrepancy caused by adopting integer values for the atomic weights is most severe for hydrogen, and does not affect* ^{12}C.

effect of the EOS on HB interiors require further investigation.

4.4 Summary of other numerical procedures

4.4.i Physical Inputs for Stellar Interiors

The computer code used for these calculations is substantially that developed by VandenBerg (1983) with modifications required to model accurately the behaviour of the helium core. The physical inputs into the programme were as previously recorded (VandenBerg & Bell 1985), apart from a revision of the nuclear reaction and neutrino loss rates. For the former, the rates listed by Caughlan and Fowler (1988) have been used. Since the previous publication of nuclear reaction rates published by Caughlan *et al.* (1985) (see also Harris *et al.* 1983; Fowler, Caughlan and Zimmerman 1975), the rate for the $^{12}C(\alpha,\gamma)^{16}O$ reaction has been revised back downward, close to the value tabulated in the 1983 paper of this series. Caughlan *et al.* (1985) consider that this reaction is still uncertain by a factor of two. The adoption of the 1985 or the 1988 values produces significant differences in the length of the blueward loops of evolutionary sequences. Figure 4-4-1 shows evolutionary sequences computed with these two reaction rate determinations. The curve referred to in the figure as the 'outer curve' reaches about 0.02 in $\log T_{eff}$ further to the blue, and was computed with the larger 1985 rate. In addition, the ratio of carbon to oxygen produced in the core after helium exhaustion is 4:1 rather than about 3:2 for the lower rate. Also, the time taken to evolve through the portions of the track shown in this diagram is different, being about 12 Myr longer with the 1985 rate. This fact has implications for star counts and also for the R-method (Buzzoni *et al.* 1983) used to determine the helium content of globular clusters. It may be possible with suitable observational data to constrain the rate of the $^{12}C(\alpha,\gamma)^{16}O$ reaction, but this obviously cannot be done without another method for determining cluster helium abundance, such as that used in Chapter 6.

The neutrino energy loss rates resulting from plasma, pair creation and pho-

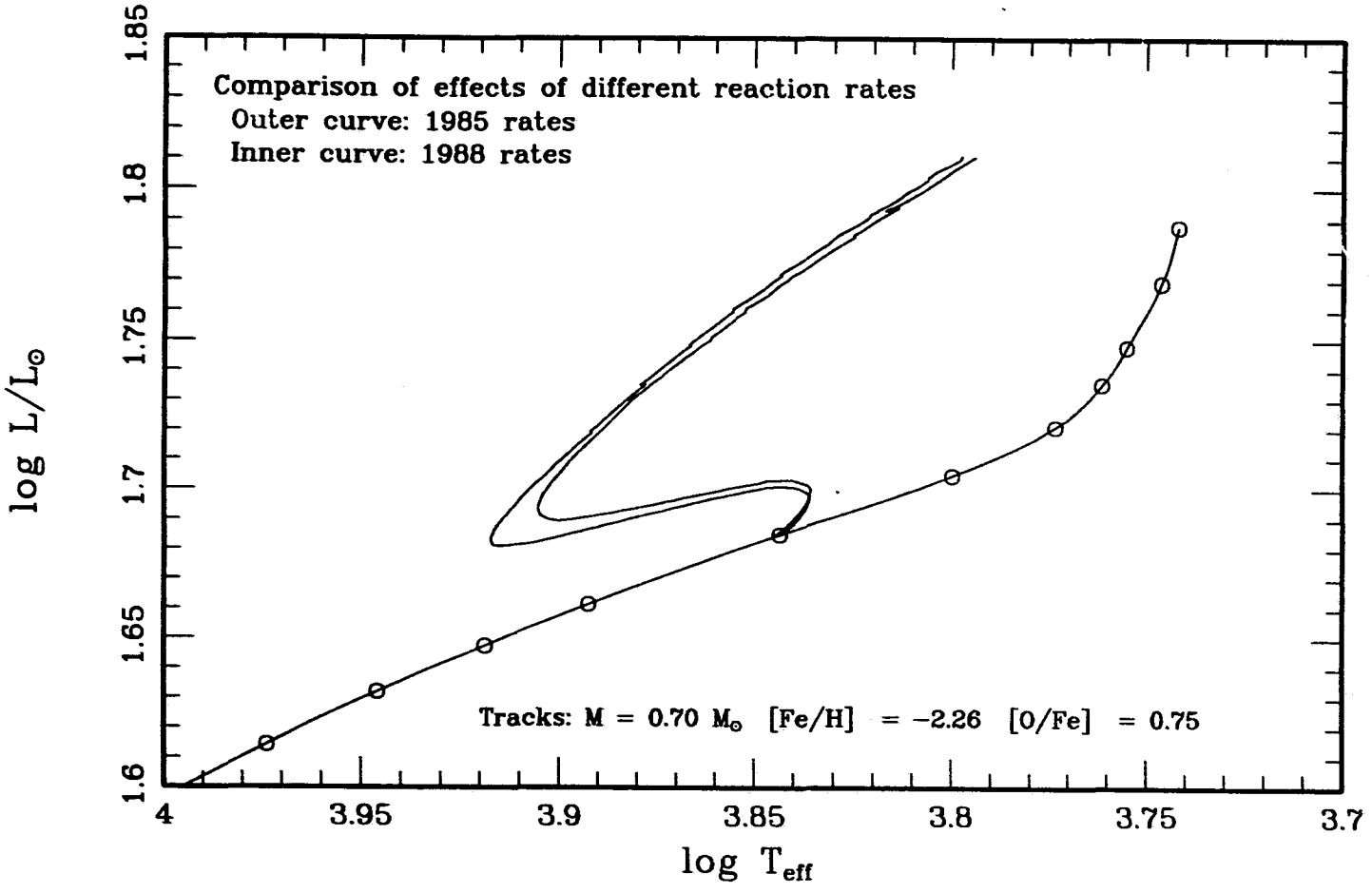

Fig. 4–4–1: Illustration of the changes in HB evolutionary tracks caused by adopting the 1985 or 1988 reaction rate tabulations.

todisintegration processes were those derived under Weinberg-Salam theory by Munakata *et al.* (1985, 1986a,b), although their effects during HB evolution are virtually imperceptible.

The helium core masses and envelope abundances were taken from appropriate RGB models at the onset of the helium flash. New calculations of the neutrino energy loss rates by Itoh *et al.* (1989) have been incorporated into the giant branch calculations used to derive the core masses for the zero age models. The core masses so calculated differ from a previous set (used in the study DLV reproduced in §6.3) by a few ten-thousandths of a solar mass. Such a small shift in core masses produces almost negligible effect on the ZAHB colour and luminosity. These later determinations have not been included in the *HB* and early AGB calculations, but the differences which would have resulted are expected to be of similar small consequence. The values of M_c were assumed to be constant for each unique composition considered. Thus, for each initial composition, a series of ZAHB models was computed for fixed helium core mass, abundances appropriate to a representative red giant precursor, and a range in total mass.

Because observed metallicities are generally expressed in terms of the logarithm of the metals-to-hydrogen number abundance ratio relative to that of the sun, the values of $[m/H]$ for the assumed element mixtures have also been tabulated. These were calculated accurately using a slightly modified routine from the Los Alamos Astrophysical Opacity Library software package (Huebner *et al.* 1977) which takes into account the twenty most abundant elements. In addition, since enhanced oxygen abundances have been adopted for the vast majority of the calculations in the study, metallicity is parametrized here by [Fe/H], and by [O/Fe], the ratio of oxygen to iron relative to solar abundances.

4.4.ii Code Implementation

All of the calculations were performed in the months of June, July and August

1990 on the University of Victoria Astronomy Group Sun Network[3]. Some effort was expended early in the project to minimize the amount of human intervention needed to produce a large set of calculations. The initialization routine **SCALE** reads the composition vector for the exterior envelope and the core, the evolutionary phase to be calculated (*e.g.*, 'hb', 'ms' or 'rg' for horizontal branch, main sequence or giant branch) the core mass, and a set of mass values to be calculated from an input file. The name of this file (the 'mass input file') has the form **mas<x><yy><zz>** which has the following significance: **yy** represents the first two significant digits of the $ZAMS$ helium abundance of the models to be calculated, neglecting enhancements due to dredge-up on the giant branch. **zz** represents Z', which is the value of the heavy element abundance fraction by mass, neglecting the effect of oxygen enhancement; the first digit is the mantissa, and the second the exponent. For example, for [Fe/H] $= -2.26$, $Z' = 0.0001$, but the actual mass fraction of elements heavier than helium, Z is 0.000323. Thus, for this value of Z', **zz** $= 14$. **x** is a single character which allows the storage of composition vectors for differing values of [O/Fe] (for example) at the same value of Y and Z'.

The other input arguments to the programme are a two character opacity table code, which selects the opacity table with the correct value of [O/Fe] at a given metallicity. The first character is used to differentiate between opacity calculations from different sources, such as Cox and Stewart (1970) opacities, and Los Alamos (Huebner *et al.* 1977) calculations. The second character is **z** for scaled-solar opacities, and a letter, **<op>** which indicates the value of [O/Fe] used if this is desired. Also supplied are an input string **<in>** and an output **<out>** identification letter, which tell the programme whence to read the input model and how to define the output filenames. This input string can be a single character, if the input and output models have precisely the same composition

[3] *Special thanks are due to Dr. C. J. Pritchet and Dr. F. D. A. Hartwick for allowing the use of their personal Workstations for some of the computations.*

(*e.g.*, when producing an evolutionary track from an initialized model) or the filename of an existing model (*e.g.*, when producing a calculations for a new set of composition parameters). This information is parsed to select the opacity table and atmospheric pressure grids, and this information is also used to define the output filenames of for the calculated models. The main programme **STEV**, used to run the evolutionary tracks and the short initialization sequences, uses the same input files, but needs to know the evolutionary phase to be calculated, the mass to be calculated and the information coded into the filename of the mass input file, and the opacity code.

A short programme called **PROCESS** has been written to read each mass in turn from the mass input file, and call the other programmes sequentially for each separate value of the mass. **PROCESS** reads the input arguments, and passes the appropriate ones to **SCALE**. After the programme completes, **PROCESS** calls **STEV** to run the 10-model initialization sequences. **PROCESS** also calls **STEV** directly to calculate a set of evolutionary sequences.

Each model calculation produces six output files. These are:

(1) The last model calculated, with name **<out><yy><op><zz><mm>.<ev>**, where **mm** represents the first two decimal place in the value of the mass in solar units, and **ev** represents a code for the evolutionary phase. For example, **h24a1490.hb** represents an horizontal-branch model with mass 0.90 $M_{\odot}$, composition $Z' = 0.0001$, $Y_{MS} = 0.24$, and with oxygen enhancement code **a**, which corresponds to [O/Fe] = 0.75. The **h** is selected arbitrarily to distinguish it from calculations with similar parameters. Its scaled-solar counterpart could be named **h24z1490.hb**. This file is dumped to disk without format. This filename, excluding the suffix, is the stem used to create all the other filenames produced by the calculation.

(2) A file containing unformatted models, dumped to disk at regular intervals defined by an integer variable supplied to the main programme **STEV**. The

name of this file is the letter m, followed by the name defined above, *e.g.*, **mh24a1490.hb**.

(3) A listing file, containing a brief summary of each model and a detailed listing of the models dumped to the file described in (2). This file has the suffix **ls**.

(4) A file containing various pieces of diagnostic information about the convergence of the physical variables and the composition. It has suffix **out**.

(5) A file containing single line summaries of each model for use in plotting colour-magnitude diagrams etc. This has suffix **pl**. An auxiliary programme, **COLTRAN** reads these files and produces a table of synthetic colours for the sequence in question.

(6) An unformatted file containing information about 12 interior variables, which is again supplemented occasionally rather than at every model. These files (with suffix **pf**) produce the profile plots extensively utilized in Chapters 2 and 3.

The fact that each run of the programme **PROCESS** can produce unique filenames facilitates the parallel calculation of several different sets of sequences where more than one CPU is available. Producing different calculations involves simply giving **PROCESS** a set of up to four arguments plus the name of the operation to be performed (usually **SCALE** or **STEV**). The average computation time from the ZAHB to the cut-off luminosity chosen for the end of the calculations is four to six hours on a Sun SparcStation 1+, and consists of about 120 models up to late HB evolution, about 50 close to helium exhaustion, and between 50 and 250 models to the cut-off luminosity, depending on whether the point where the evolution reverses direction is reached after or before the cut-off. Where a large number of early AGB models is calculated, the programme run is extended by having to produce a large number of models (taking ~ 20 seconds each) with small timesteps.

In the case of convergence failure during execution, the computation may be

restarted from a point 20-30 models back from the point of failure, with a reduction in the timestep. In practically all cases, computation was successfully restarted and completed. In addition, in the region of overlap between the successful and unsuccessful sequences, the calculations generally agreed to within a few thousandths in $\log L$ and $\log T_{eff}$.

Chapter 5 Presentation of the Calculations

5.1 Introduction

The purpose of this chapter is to present the entire set of computations derived for this study, and to summarize some of their observational consequences. Zero-age sequences have been calculated for a set of metallicities for both scaled-solar and for oxygen enhanced compositions. In addition, a number of ZAHBs have been computed with variations in the envelope helium abundance. In each case, the composition and the core mass is derived from a giant branch tip model provided by VandenBerg (1990). The evolutionary sequences to be presented have been computed for a selected range of masses ($M_* < 0.90\,M_\odot$), for all of the enhanced oxygen compositions.

The first section of this chapter lists the composition parameters used for the calculations and states the choices made for the oxygen enhancement and the helium abundance. The zero age sequences are used to define the relation between luminosity and metallicity over a range of temperature corresponding closely to the values expected in the instability strip. This relationship has received much attention recently for several reasons. The absolute luminosity of the globular cluster horizontal branch stars, including their RR Lyrae variables, are at the core of two of the most widely used methods for determining cluster ages.

In principle, the distance to globular clusters may be found by fitting the lower envelope of the observed cluster horizontal branch to theoretical ZAHBs. Together with a knowledge of the bolometric corrections for stars at the main sequence turnoff, the age of the cluster may be determined. The level of the HB through the instability strip is used for distance calibration purposes because, as will be seen later, the horizontal branch is observed to be nearly 'horizontal' in

the colour-magnitude plane for this range in temperature or colour. Of course, this method works directly only if the strip is populated; if the theoretical ZAHB luminosity is known at the appropriate metallicity, it may be extended to other cases.

A second method for cluster ages uses the difference in luminosity between the ZAHB (denoted $M_V(HB)$) and the main sequence turnoff ($M_V(TO)$), which is often given the symbol ΔV_{TO}^{HB}. The main sequence turnoff becomes fainter as stars of lower mass evolve off the main sequence, whereas the horizontal branch luminosity remains fixed with age. This latter phenomenon is explained by the observations that (a) the HB is a sequence of *low mass* stars in an advanced stage of evolution, and (b) the mass distribution of stars on the HB implied by the observations is often somewhat less, presumably owing to mass loss, than the mass of the stars at the tip of the giant branch. Provided, therefore, that the stars arriving on the HB are of sufficiently low mass to populate the 'horizontal' part of the sequence the magnitude of its lower envelope will be constant in time. However, as seen earlier, the ZAHB luminosity is a function of metallicity, as is the value of $M_V(TO)$. Sandage (1982b) has argued that if the slope of the ZAHB luminosity-metallicity relationship is sufficiently large, then the observed near-constancy of ΔV_{TO}^{HB} among clusters implies that they are coeval. As a third point, a great deal of controversy has been raised by the Sandage period shift effect (Sandage 1982a). Sandage and others (*e.g.*, Caputo *et al.* 1987) have claimed that the difference in RR Lyrae periods amongst clusters is a steeper function of metallicity than that predicted by stellar evolution theory, unless the cluster helium abundances are anti-correlated with metallicity (see also Sweigart, Renzini and Tornambè 1987). The periods of the variables (at a given temperature) are strongly affected by the luminosity since the fundamental mode of pulsation depends on the radius and the mass of the variable.

Appendix A tabulates the observable quantities M_V and $(B-V)$, as well as the

the theoretical values ($\log L$, $\log T_{eff}$ and $\log g_s$) used to derive them. Commonly used colour transformations are those of Kurucz (1979) for higher temperatures, and those derived by Bell for the VB85 set of isochrones for lower temperatures. Unfortunately, the blue end of the range of synthetic colours computed by Bell lies approximately at the location of the red end of the instability strip for the range of surface gravities appropriate to horizontal branch stars. While the existing colour transformations are in excellent agreement here, the bolometric corrections derived by these two authors are quite different, and are difficult to match smoothly in this region (see §6.2). This source of uncertainty gives rise to very important difficulties for the comparison of theory with observation.

The second section of the chapter deals with the evolutionary sequences. Its purposes are to provide illustrations of these calculations on both the theoretical and observer's planes, to mention some of the important differences between these computations and previously published evolutionary tracks, and to state some of the limitations of the current work. Selected results are tabulated in Appendix B.

5.2 Basic Parameters for Zero Age Sequences

Tables 5-2-1 and 5-2-2 list some fundamental parameters for the calculations of oxygen enhanced and scaled solar ZAHBs. In the first of these tables, the first column gives the value of [Fe/H] derived from the opacity table calculation as explained in §4.4. The second column lists the value of the helium abundance Y_{MS} used in the corresponding main sequence model. The variation of Y_{MS} with Z has been derived using a linear relationship between the lowest values of Y found to date (*e.g.*, Pagel, Terlevich and Melnick 1986) and a value derived for the solar helium abundance by VandenBerg (1990) by calibrating a solar model. The third column lists the actual helium abundance Y_{HB} in the envelope during the horizontal branch phase. This includes the helium enrichment which occurs during the 'first dredge-up' phase on the red giant branch. The fourth column represents the core mass M_c in solar units. The definition adopted here is the value of the mass coordinate at which the hydrogen shell energy generation rate is at its peak, for compatibility with the definition used for the evolutionary sequences. The difference between these definitions is constant on the ZAHB, and is less than 0.001 $M_\odot$. The fifth column gives the value of [O/Fe], using a linear relationship between [Fe/H] and [O/Fe] derived by VandenBerg (1989), based on his consideration of dwarf abundances available up until 1987. The slope turns out to be approximately the mean of the latest observational estimates by Barbuy (1990) and Abia and Rebolo (1989). Column six lists the value of Z, the total fraction by mass of elements heavier than helium. The number in brackets denotes the base ten exponent of Z. The final column gives the Table in the Appendix where the model properties for each ZAHB are tabulated.

The ZAHB calculations listed in Table A-1 have been extended to a relatively high mass (1.5 $M_\odot$) in order to show clearly the location in colour and temperature of the red end of the horizontal branch. Otherwise, apart from the models

Table 5-2-1: Parameters for Oxygen-Enhanced Calculations						
[Fe/H]	Y_{MS}	Y_{HB}	$M_c/M_\odot$	[O/Fe]	Z	Table
−2.26	0.2352	0.2460	0.4926	0.75	3.23(-4)	A-1
−2.03	0.2353	0.2467	0.4904	0.70	4.97(-4)	A-1
−1.78	0.2356	0.2478	0.4881	0.66	8.16(-4)	A-1
−1.66	0.2358	0.2477	0.4866	0.63	1.03(-3)	A-1
−1.48	0.2362	0.2489	0.4852	0.60	1.46(-3)	A-1
−1.26	0.2370	0.2499	0.4835	0.55	2.23(-3)	A-1
−1.03	0.2385	0.2520	0.4815	0.50	3.47(-3)	A-1
−0.78	0.2412	0.2565	0.4792	0.39	5.10(-3)	A-1
−0.65	0.2433	0.2589	0.4776	0.30	6.02(-3)	A-1
−0.47	0.2474	0.2660	0.4757	0.23	8.00(-3)	A-1
−2.26	0.2352	0.2456	0.4958	0.50	2.04(-4)	A-2
−2.26	0.2352	0.2466	0.4900	1.00	5.34(-4)	A-2

with solar composition, the most massive ZAHB models are for 0.90 $M_\odot$. For the extreme blue end of the HB, the mass range is constrained by the use of atmospheric pressure grids for the surface boundary condition in the models. Currently, these are only available for $\log g_s > 5$, and this limits the models which can be computed to $M_* \geq 0.51$ to $0.54\,M_\odot$, depending on the metallicity. For all of the models, outer boundary conditions are provided by tables of model atmospheres compiled by VandenBerg (1990). The value of $l/\mathcal{H}_P$, the mixing length parameter, was taken to be 1.5.

Table 5-2-2 contains similar information for the scaled-solar sequences ([O/Fe] = 0); the first five columns list [Fe/H], Y_{MS}, Y_{HB}, $M_c/M_\odot$, Z, and, lastly, the Appendix table where the model properties may be found. For these sequences, the surface pressures are again supplied by tabulated model atmospheres except for the case of solar composition, where the scaled-solar $T-\tau$ relationship of Krishna-Swamy (1967) is used. The use of the $T-\tau$ relationship for the outer boundary condition allows the extension of these calculations to lower mass values (0.48 $M_\odot$). In addition, $l/\mathcal{H}_P$ was taken to be 1.58; this is the value used to calibrate the solar model at about 4.6 Gyr. Because of the difference in the mixing length

and the definition of the outer boundary conditions, these models have not been included in the luminosity-metallicity curves described in the next section.

Table 5-2-2: Parameters for Scaled-Solar Sequences

[Fe/H]	Y_{MS}	Y_{HB}	$M_c/M_\odot$	Z	Table
−2.23	0.2000	0.2094	0.5097	1.00(-4)	A-3
−1.23	0.2000	0.2134	0.4966	1.00(-3)	A-3
−2.26	0.2700	0.2787	0.4923	1.00(-4)	A-4
−1.26	0.2700	0.2824	0.4810	1.00(-3)	A-4
−2.26	0.2352	0.2447	0.5003	1.00(-4)	A-5
−1.78	0.2356	0.2466	0.4945	3.00(-4)	A-5
−1.48	0.2362	0.2480	0.4909	6.00(-4)	A-5
−1.26	0.2370	0.2500	0.4883	1.00(-3)	A-5
−0.78	0.2412	0.2579	0.4820	3.00(-3)	A-5
−0.47	0.2474	0.2675	0.4766	6.00(-3)	A-5
0.00	0.2676	0.2896	0.4689	1.69(-2)	A-5

5.3 The Dependence of Observable Quantities on Parameters

In this section, the effects of variations in [Fe/H], [O/Fe] and Y are explored graphically. The results presented are slightly different from those in §2.4, as the calculations presented here have been derived with initial conditions which are consistent with earlier phases of evolution. The main difference is in the adopted core mass[1]. The illustration of the entire oxygen-enhanced ZAHB grid is delayed until the later section of this chapter where they are presented (for $M < 0.90 M_\odot$) together with the evolutionary tracks.

[1] *Small variations in M_c which have not been accounted for here can result from the variation of red-giant tip masses with age. Despite the fact that the age of clusters is rather uncertain, the variations of core mass with total mass, and mass with age, are minor although not completely negligible (see, e.g., Sweigart and Gross 1978). However, the differences in M_c caused by variations in cluster age are well below the resolution of the observations, and is in any case smaller than the effects of variations in metallicity.*

The following set of figures illustrates the effect of oxygen enhancement on the morphology of the ZAHB and its mass distribution. In each of them, the mass value used at fixed [Fe/H] is the same. At low metallicities, the result of oxygen enrichment is especially interesting. There is a wide variation in observationally determined values of the ratio $[O/Fe]$ in globular cluster and field stars (Pilachowski 1988; Abia and Rebolo 1989; Barbuy 1990), ranging from almost zero to values which exceed unity.

Theoretically, the differences caused by high [O/Fe] are much greater for lower metallicity, and this is easily seen in the figures. Since the relationship between ZAHB mass and temperature is a function of $[O/H]$ rather than [Fe/H], it follows that models with much lower mass will lie at a given colour when oxygen is enhanced. But this also implies that the model luminosity, which has its greatest sensitivity to the mass of the stellar envelope, decreases at fixed colour with increasing [O/Fe]. At the low end of the metallicity range, the models with scaled-solar abundance are radiative, which implies a much steeper ZAHB mass-surface temperature relationship, whilst increasing [O/Fe] forces a outer convective zone in the more massive models. As noted earlier, this structural difference can cause a change in ZAHB morphology which also exaggerates the effects on ZAHB luminosities through the instability strip. To summarize, the more convective the reddest HB models are, the less massive will be the models at a fixed colour within the instability strip. The dependence of the hydrogen shell luminosity on envelope mass is an important factor determining the ZAHB luminosity-metallicity relationship, and is additional to the phenomena studied earlier in chapter 2. The discussion presented there indicated that this relation will be quite different at opposite ends of the globular cluster metallicity range.

Figures 5-3-1 and 5-3-2 depict the ZAHB morphology for four values of [O/Fe] and for [Fe/H] = −2.26, appropriate to the most metal-poor globular clusters. The models which comprise these sequences have the masses listed in

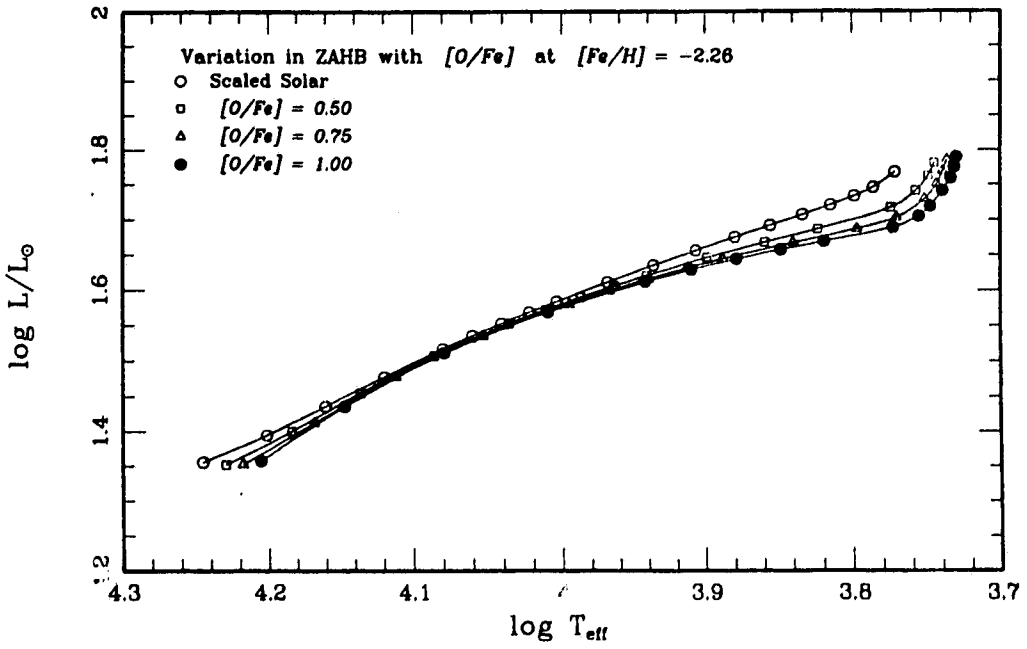

Fig. 5–3–1: Theoretical–plane illustration of the ZAHB sequences for models with [Fe/H] = –2.26 and with [O/Fe] = 0, 0.5, 0.75, 1.0.

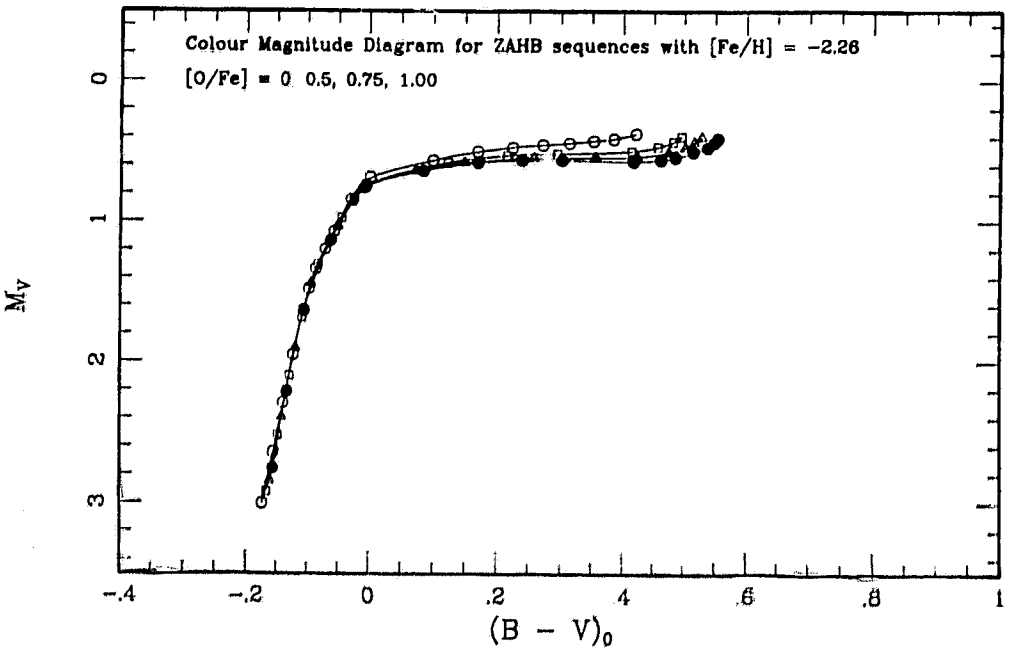

Fig. 5–3–2: Colour–Magnitude Diagram for sequences shown in Figure 5–3–1.

Tables A-2, apart from the exclusion of the lowest mass value, which would have had $\log g_s > 5$, and therefore could not be computed with the adopted atmospheric pressure grids. The first of these figures shows the theoretical plane, and the second shows the morphology predicted in the $(V, (B-V))$ colour magnitude plane. The most obvious feature of these sequences has been stressed earlier, namely, the change in morphology caused by the transition from radiative to convective envelopes in the most massive models (see also VandenBerg 1988b). The redistribution of mass points toward the red end with increasing [O/Fe] is also very striking; spline-interpolated estimates for the ZAHB mass at a representative instability strip temperature $\log T_{eff} = 3.84$ are 0.79, 0.73, 0.70 and 0.67 $M_\odot$ for the values of [O/Fe] equal to 0, 0.5, 0.75 and 1.0 respectively.

The next sets of figures show the same comparisons, for the single value of [O/Fe] adopted in the corresponding evolutionary tracks, at progressively higher metallicity. Again, the sequences are illustrated in the theoretical and observed planes. The sequences shown are (a) Figures 5-3-3 and 5-3-4 , for [Fe/H] = −1.78: (b) 5-3-5 and 5-3-6 , for [Fe/H] = −1.48: (c) 5-3-7 and 5-3-8 , for [Fe/H] = −1.26: (d) 5-3-9 and 5-3-10 , for [Fe/H] = −0.78: (e) 5-3-11 and 5-3-12 , for [Fe/H] = −0.47. Finally, Figures 5-3-13 and 5-3-14 show the Zero Age sequence for solar composition. As the metallicity increases, the differences between the ZAHB morphology between the high-oxygen and scaled solar calculations on both theoretical and observational planes decreases; however, the mass distribution along the sequences is quite different. This increasing similarity is due in large part to the choice of parameters; the enhancement factor is about 1.7 for [Fe/H] = −0.47, as compared to 5.6 for the most metal poor composition. Note that the intention here is to illustrate the effect of the incorporation of a 'realistic' [O/Fe] *vs* [Fe/H] relationship.

A feature of the colour-magnitude diagrams is a slight increase in M_V as the models move blueward; this is caused by the behaviour of the bolometric

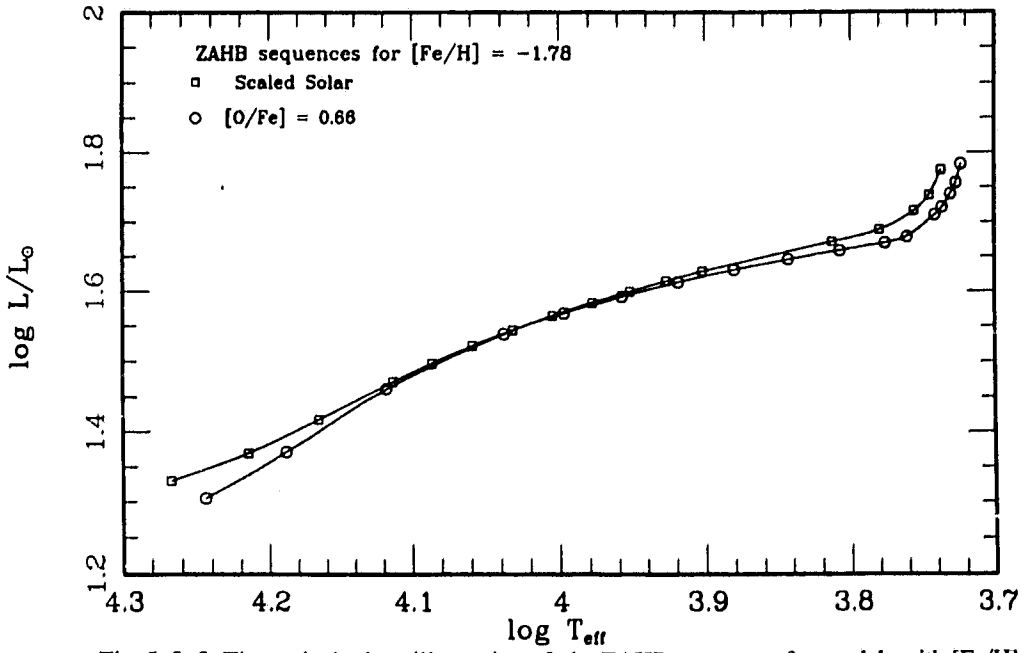

Fig. 5–3–3: Theoretical–plane illustration of the ZAHB sequences for models with [Fe/H] = −1.78 and with [O/Fe] = 0, 0.66.

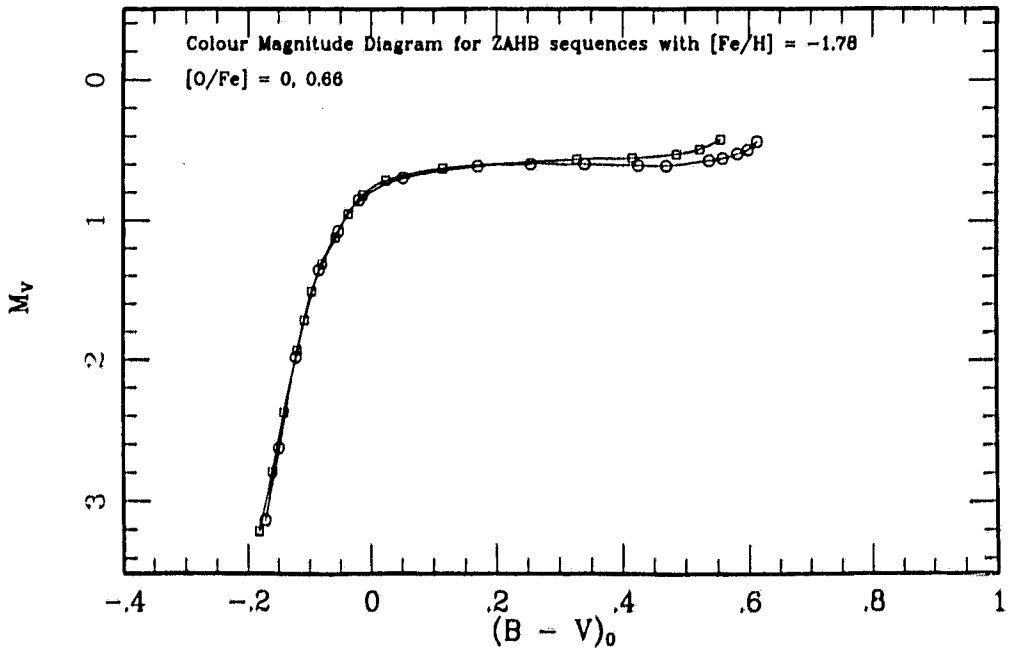

Fig. 5–3–4: Colour–Magnitude diagram for sequences shown in Figure 5–3–3.

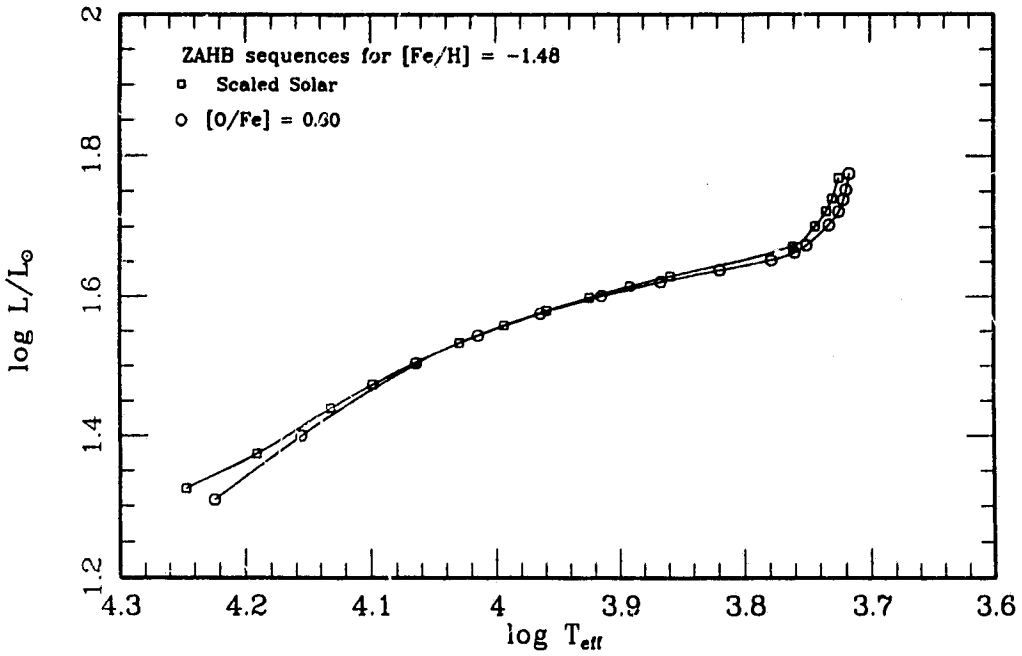

Fig. 5–3–5: Theoretical–plane illustration of the ZAHB sequences for models with [Fe/H] = –1.48 and with [O/Fe] = 0, 0.60.

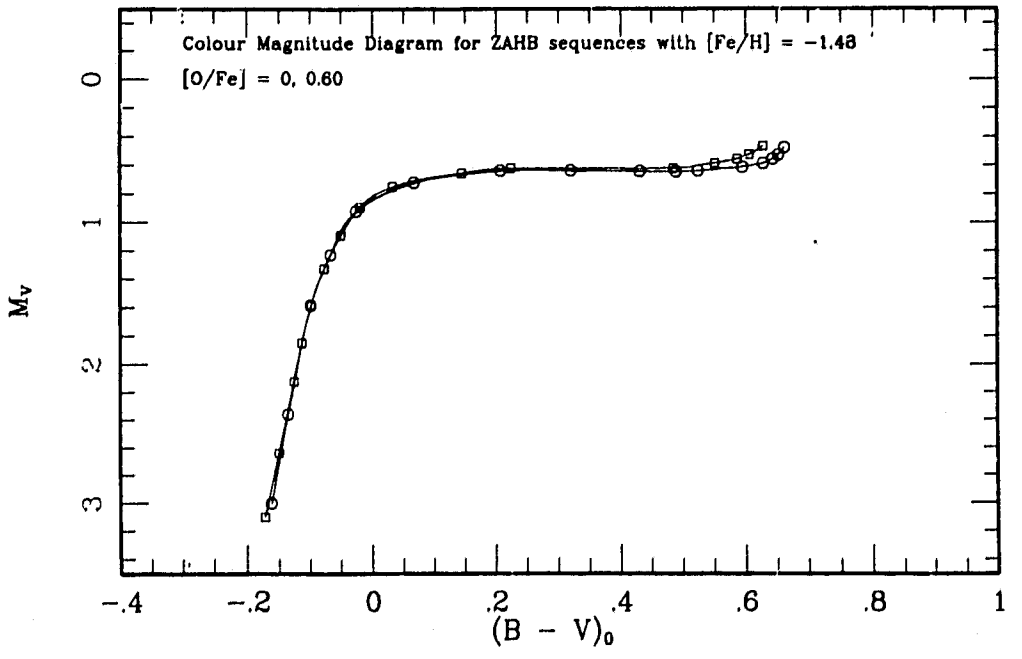

Fig. 5–3–6: Colour–Magnitude diagram for sequences shown in Fig. 5–3–5.

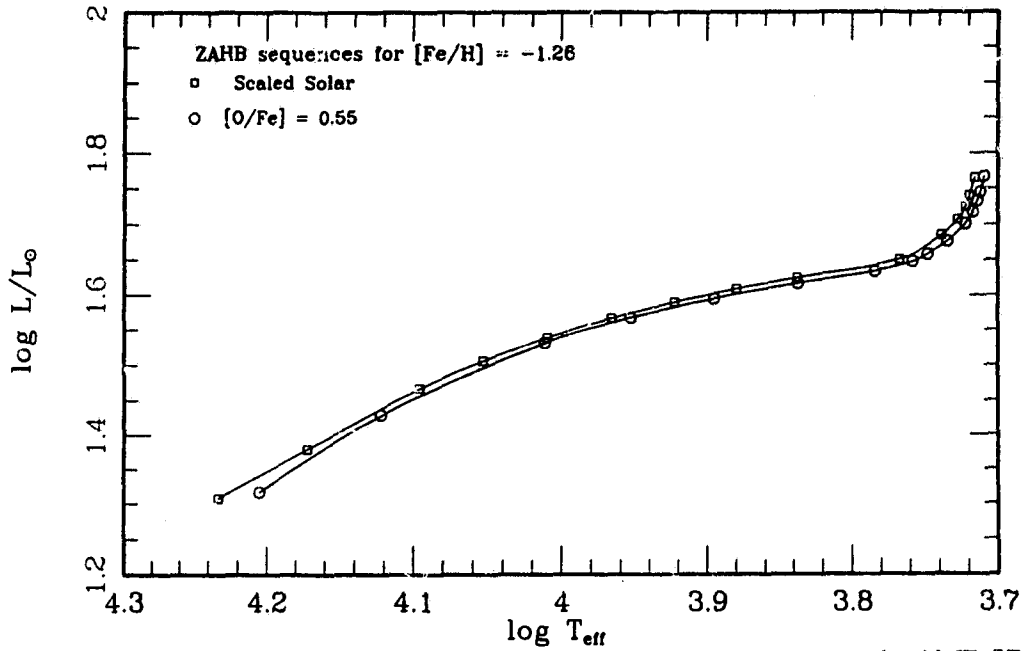

Fig. 5–3–7: Theoretical–plane illustration of the ZAHB sequences for models with [Fe/H] = −1.26 and with [O/Fe] = 0, 0.55.

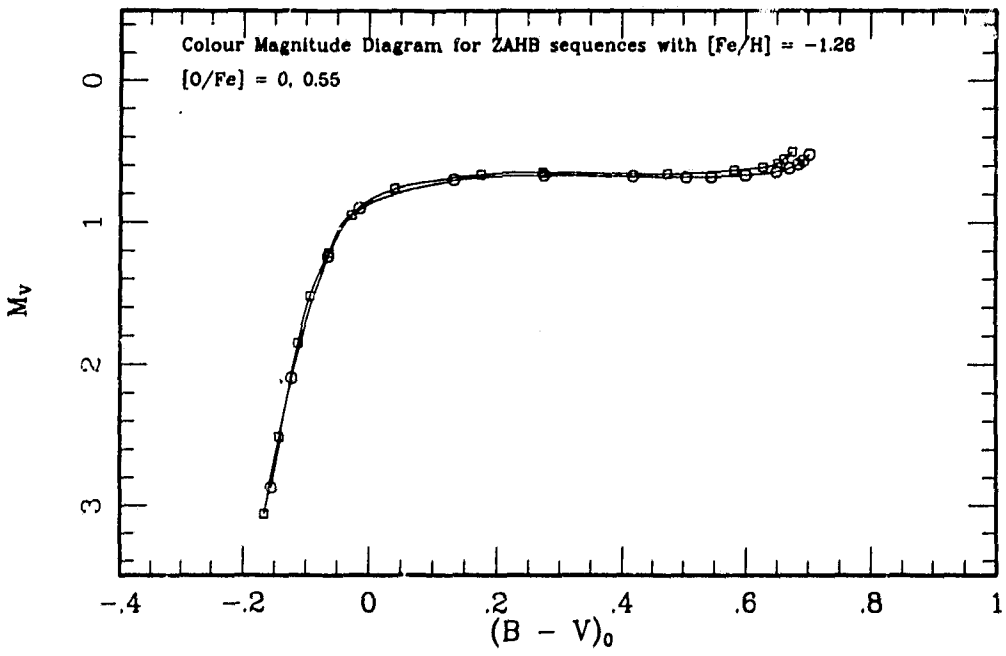

Fig. 5–3–8: Colour–Magnitude diagram for sequences shown in Figure 5–3–7.

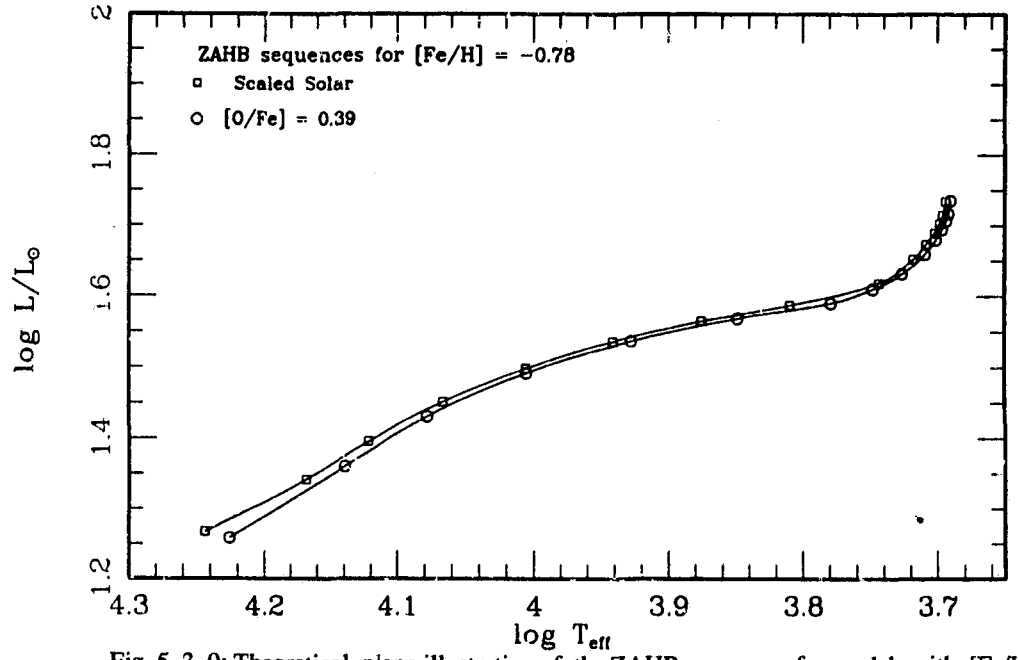

Fig. 5–3–9: Theoretical–plane illustration of the ZAHB sequences for models with [Fe/H] = –0.78 and with [O/Fe] = 0, 0.39.

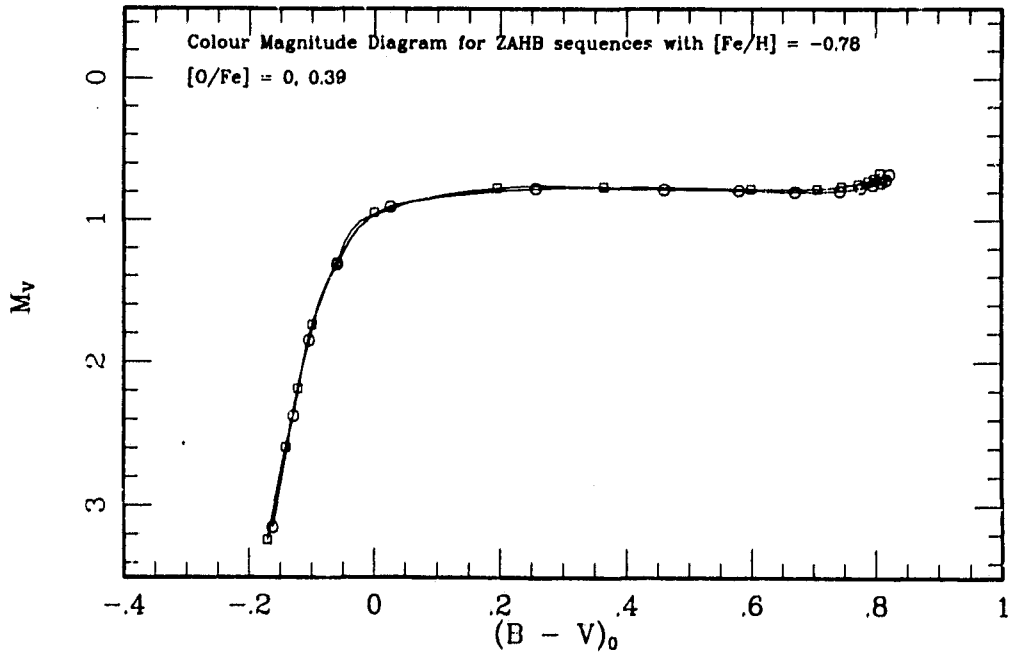

Fig. 5–3–10: Colour–Magnitude diagram for sequences shown in Figure 5–3–9.

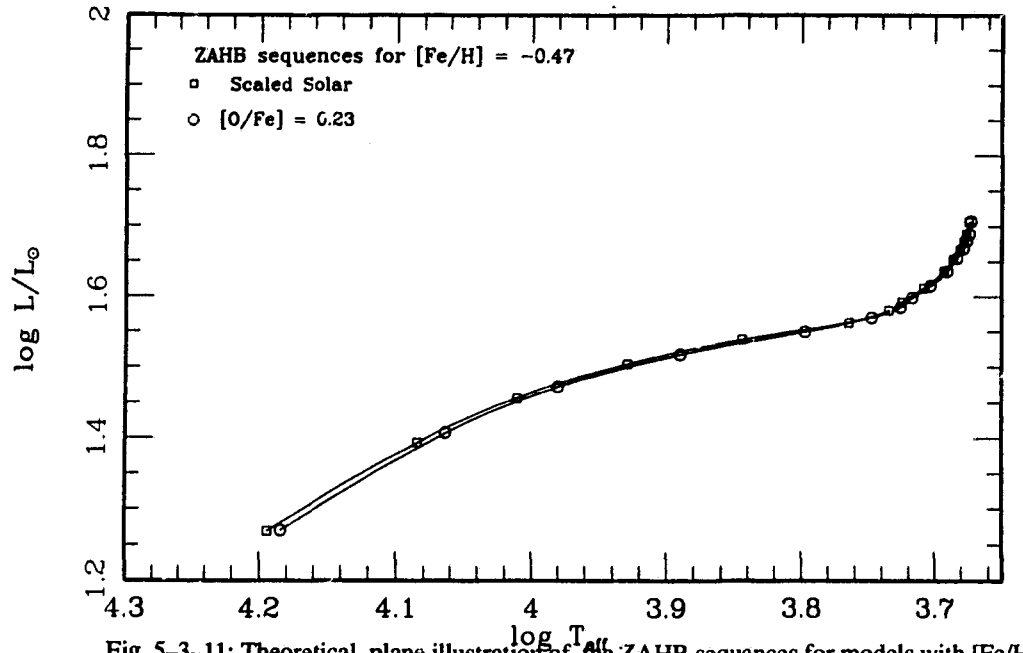

Fig. 5–3–11: Theoretical–plane illustration of the ZAHB sequences for models with [Fe/H] = –0.47 and with [O/Fe] = 0, 0.23.

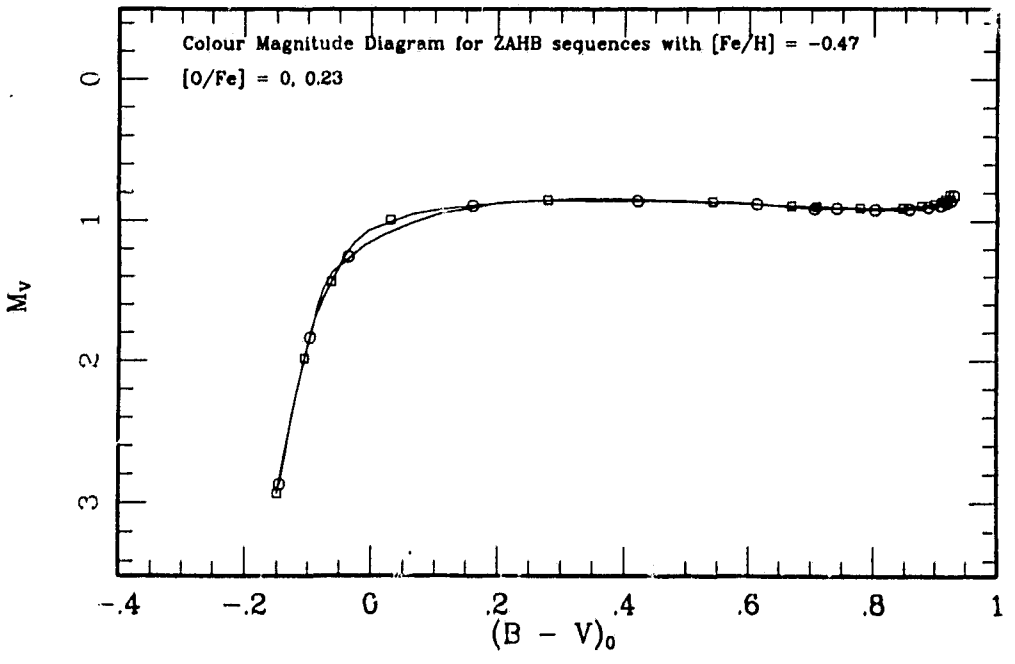

Fig. 5–3–12: Colour–Magnitude diagram for sequences shown in Figure 5–3–11.

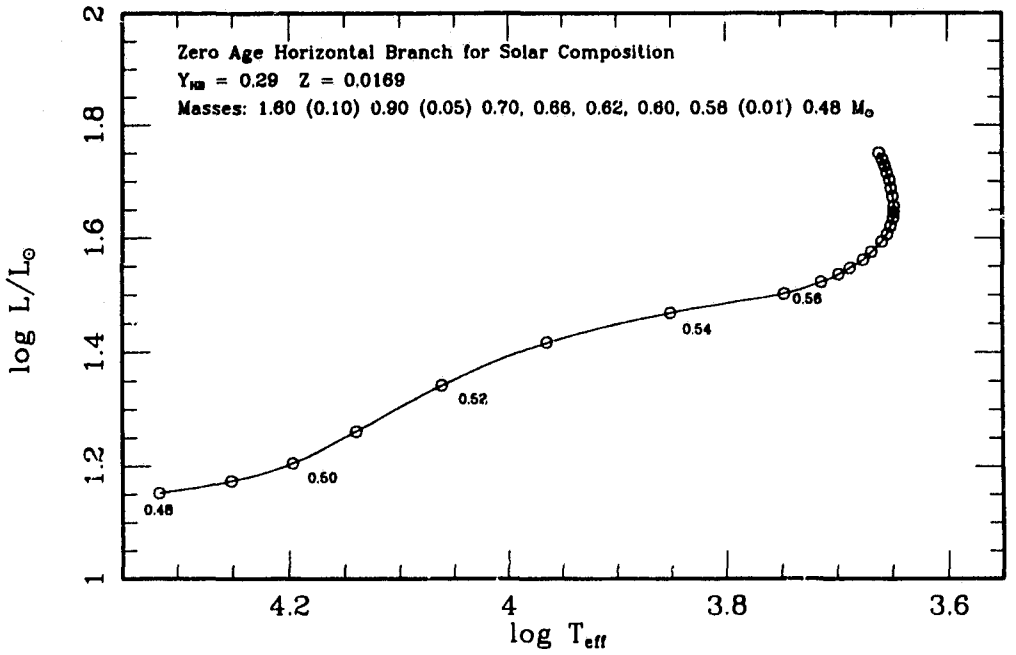

Fig. 5–3–13: Theoretical–plane illustration of the ZAHB sequence for models with solar composition, for masses 0.48 3 M* 3 1.60 $M_\odot$.

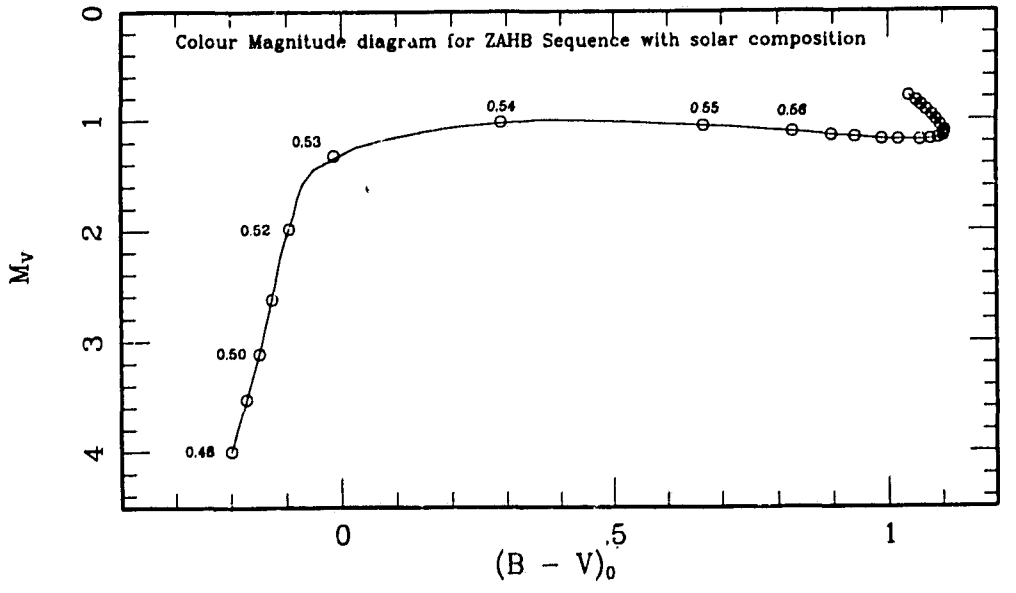

Fig. 5–3–14: Colour–Magnitude diagram for sequences shown in Figure 5–3–13.

corrections, which decreases slightly in this temperature range [2], but faster than the accompanying decrease in luminosity. This is most noticeable for the sequences with higher metallicity. As a result, the sequences are quite 'horizontal' in the colour-magnitude plane; in addition, this effect almost removes the temperature dependence of the M_{bol} – [Fe/H] relation. The sharp decrease in M_V at the near-vertical low-mass tail of the sequences is a consequence of both the decline in luminosity with mass and the fact that the peak of the stellar radiation curve moves out of the optical range of frequency. The bolometric corrections become very large (> 2.0 mag at the base of the computed sequences) and the colour index $(B - V)$ becomes much less sensitive to increases in the temperature.

The sequence with solar composition also illustrates the ZAHB model location for masses greater than 1 $M_\odot$. The relocation of the models to the blue with increasing mass is much more evident in the colour-magnitude diagram as a result of the increase in the surface gravity. The more massive models are actually smaller in radius as the mass contained in their outer convection zones is reduced.

Luminosity versus metallicity curves are plotted in Figures 5-3-15 and 5-3-16 , derived using the enhanced-oxygen and scaled-solar models respectively. The upper panel shows the relationship between M_V and [Fe/H], and the lower shows M_{bol} against [Fe/H]. There has been some debate recently concerning the most useful temperature to adopt for the comparison of RR Lyrae pulsational properties. Many authors (Sandage 1982b; Rood and Crocker 1989) have used $\log T_{eff} = 3.85$. Recently, Lee, Demarque and Zinn (1990) (see also Chapter 6) have argued convincingly that this temperature is too high for use with the pulsation equations for fundamental mode (RRab) variables, since with the Kurucz (1979)

---

[2] *The effect of this is to increase M_V. This observation may help to clarify the following statement, which looks confusing because it is much more common to add bolometric corrections to observed magnitudes!*

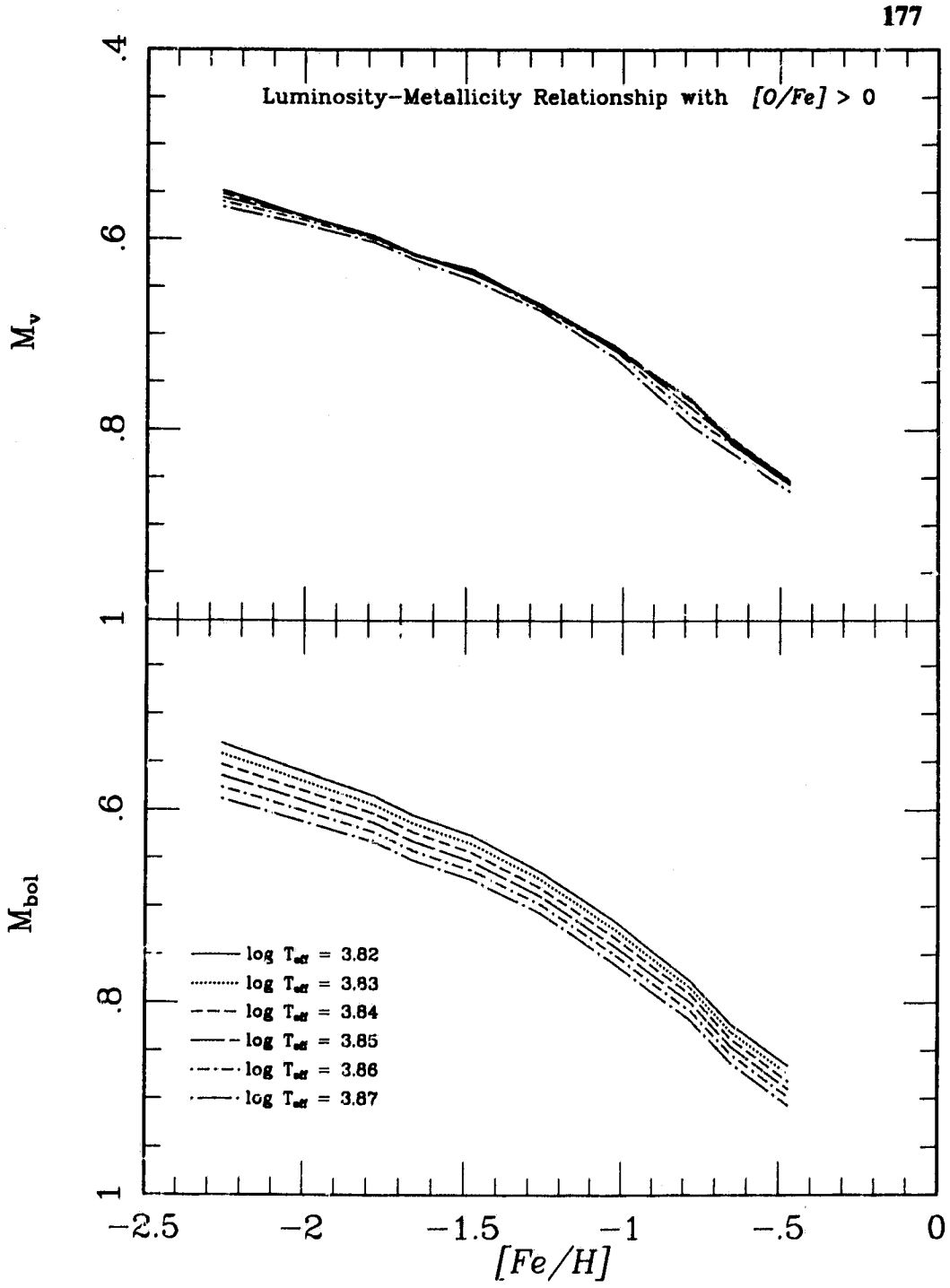

Fig. 5–3–15: Luminosity–Metallicity relationship (M_V and M_{bol} vs [Fe/H]) derived from oxygen–enhanced sequences.

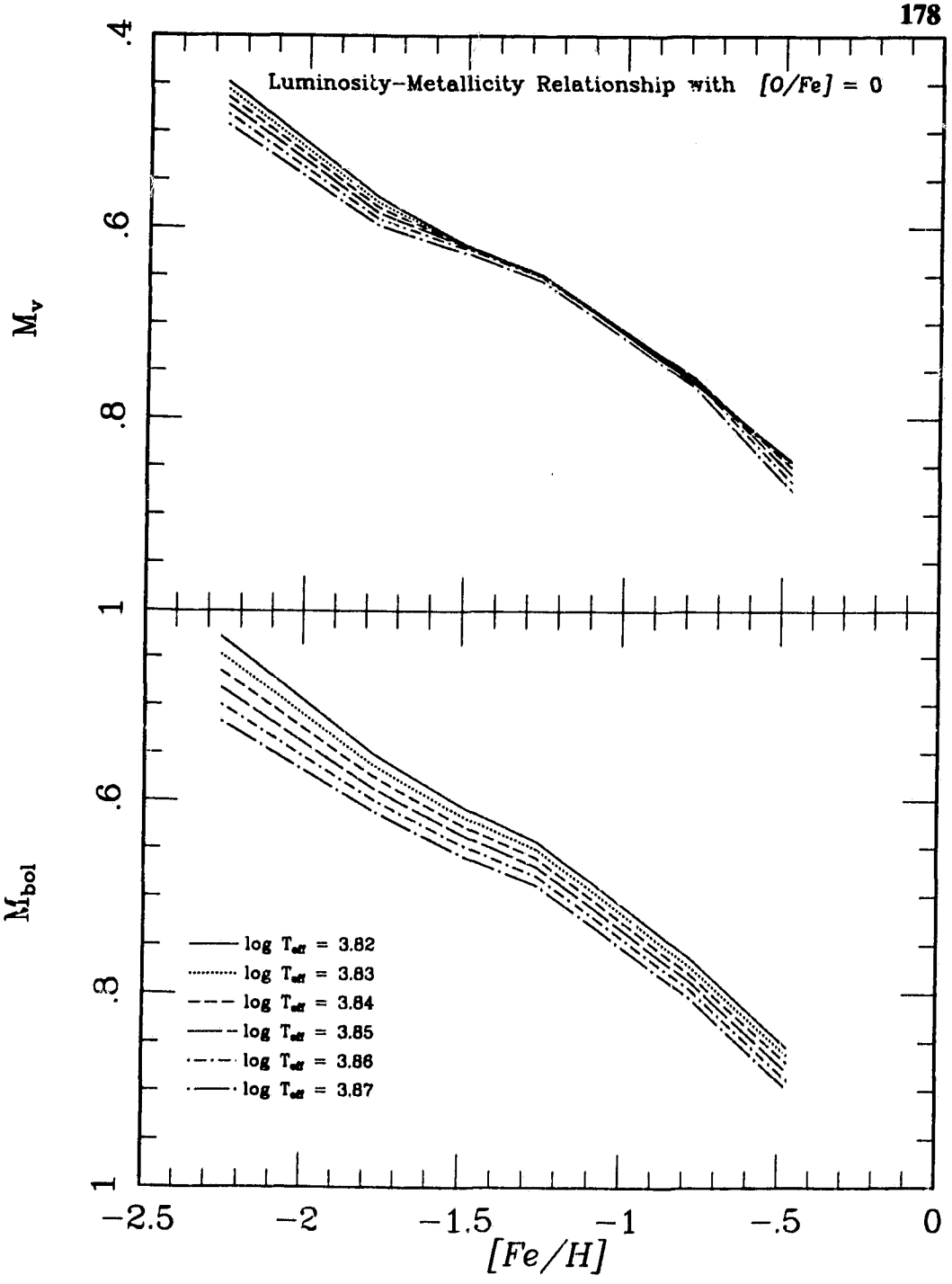

Fig. 5–3–16: As for Fig. 5–3–15, but relationships are derived from the scaled–solar sequences.

temperature-colour calibrations this temperature corresponds to the Fundamental Blue Edge. In order to provide the most satisfactory theoretical relationship, the data for these curves are given in Tables 5-3-1 and 5-3-2, which contain, as a function of [Fe/H], values for M_V and M_{bol} for the assumptions of [O/Fe] > 0 and [O/Fe] $= 0$. These are tabulated for temperatures between $3.82 < \log T_{eff} < 3.87$ at intervals of 0.01 in $\log T_{eff}$. The data in these tables were compiled from the ZAHBs using Hermite spline interpolation with the mass as the independent variable. To give an example of the character of these relationships (which appear to be clearly quadratic or cubic), the data for $\log T_{eff} = 3.84$ were fitted to polynomials of degrees 1 to 4. As expected, the best fits for the [O/Fe] relationship were quadratic polynomials (but in the case of visual magnitude, only marginally to be preferred over a cubic), as follows:

$$M_{bol} = (0.068 \pm 0.005)[\mathrm{Fe/H}]^2 + (0.367 \pm 0.015)[\mathrm{Fe/H}] + (1.040 \pm 0.009) \tag{5.1}$$

$$M_V = (0.063 \pm 0.004)[\mathrm{Fe/H}]^2 + (0.338 \pm 0.012)[\mathrm{Fe/H}] + (0.998 \pm 0.007) \tag{5.2}$$

The fitting formulae derived from the scaled-solar sequences are:

$$M_{bol} = (0.056 \pm 0.019)[\mathrm{Fe/H}]^3 + (0.258 \pm 0.077)[\mathrm{Fe/H}]^2 + (0.572 \pm 0.096)[\mathrm{Fe/H}] + (1.090 \pm 0.034) \tag{5.3}$$

$$M_V = (0.080 \pm 0.018)[\mathrm{Fe/H}]^3 + (0.350 \pm 0.074)[\mathrm{Fe/H}]^2 + (0.664 \pm 0.093)[\mathrm{Fe/H}] + (1.095 \pm 0.033) \tag{5.4}$$

As can be seen from the uncertainties in the coefficients, these latter relationships are not very well determined, being derived from only six data points. However,

the character of the solution is quite clear from the figure. It must be stressed, however, that both the data presented in the tables and the above fitting formulae are strictly ZAHB relations; the effects of evolution on the mean luminosity have not been considered.

The ZAHB sequences illustrated above show clearly the differences between the two sets of relationships, for models with and without oxygen enrichment, at the metal-poor end. The most metal-poor scaled solar ZAHBs are significantly brighter than their oxygen-rich counterparts (*cf.* Fig. 5-3-2). The flattening of the relation for [O/Fe] > 0 at low metallicity is also a consequence of the dependence of the mass-temperature relation on [O/H]. At the metal rich end, however, the difference between the relations is a change in the zero-point luminosity, rather than a change in slope.

The final set of figures to be presented in this section show the variation in the ZAHB luminosity with envelope helium abundance. Figure 5-3-17 and 5-3-18 show the ZAHBs at $Z = 0.0001$, [Fe/H] $= -2.2$, for $Y_{HB} \sim 0.21$, 0.25 and 0.28, and Figures 5-3-19 and 5-3-20 show the equivalent calculations for $Z = 0.001$, [Fe/H] ~ -1.2[3]. All of these sequences have scaled-solar composition. The changes in 'evolutionary' core masses adopted in these models is sufficient to change the direction of the small temperature differences at fixed mass (recall from §2.4 that at fixed core mass, the models with higher Y are always very slightly hotter). The sequences cross each other at very low masses because of the increase in core temperature with decreasing Y.

According to the theoretical discussion presented earlier, the variation in stellar luminosity with helium content should be almost linear where the hydrogen shell luminosity is significant. This is because the change in Y produces little

[3] *The value of* [Fe/H] *varies slightly with* Y *because of the changing hydrogen abundance.*

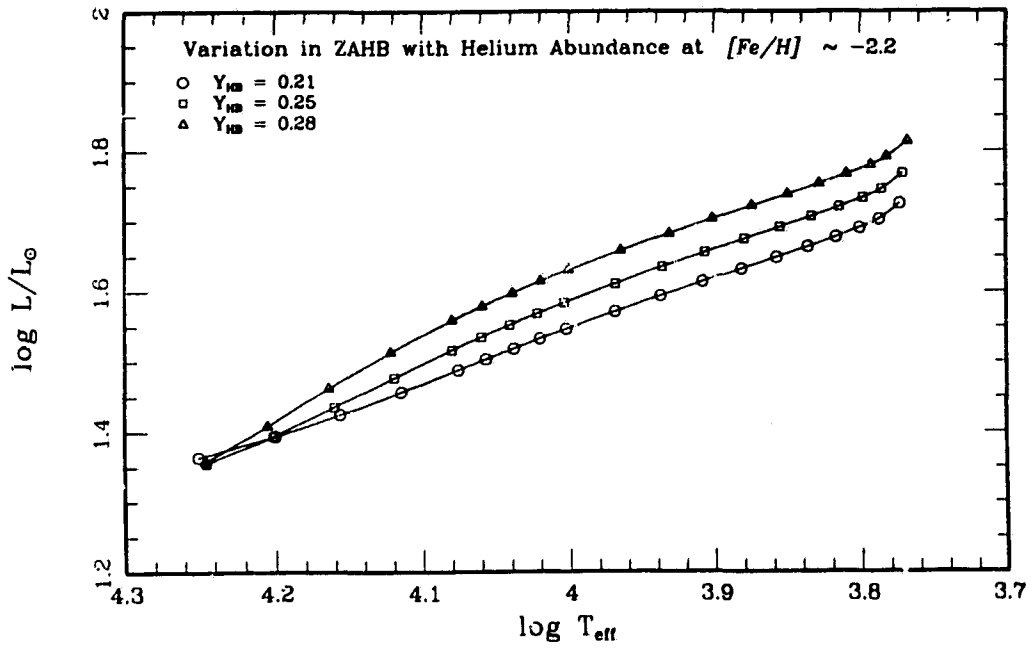

Fig. 5–3–17: Theoretical–plane illustration of the ZAHB sequences for models with [Fe/H] ~ –2.2 , and with Y_{HB} ~ 0.21, 0.25, and 0.28.

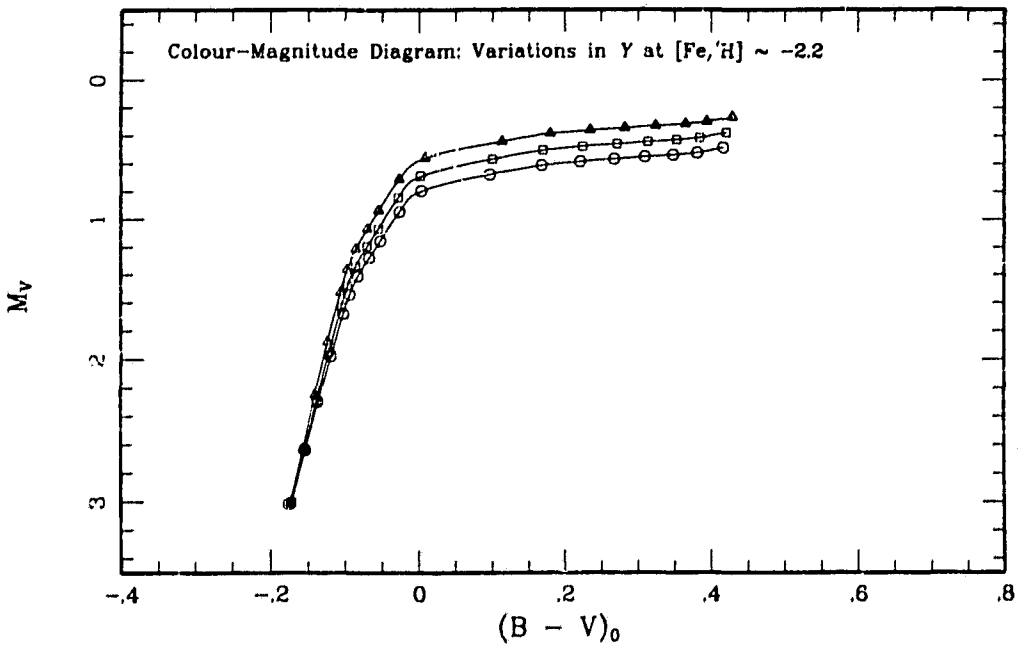

Fig. 5–3–18: Colour–Magnitude diagram for sequences shown in Figure 5–3–17.

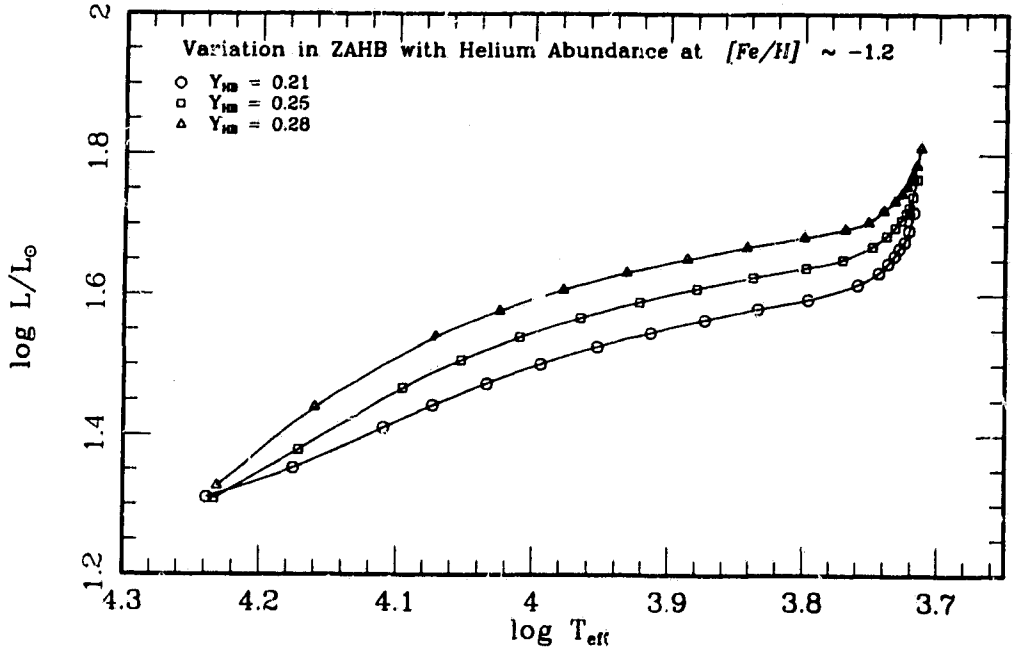

Fig. 5–3–19: Theoretical–plane illustration of the ZAHB sequences for models with [Fe/H] ~ –1.2, and with Y_{HB} ~ 0.21, 0.25, and 0.28.

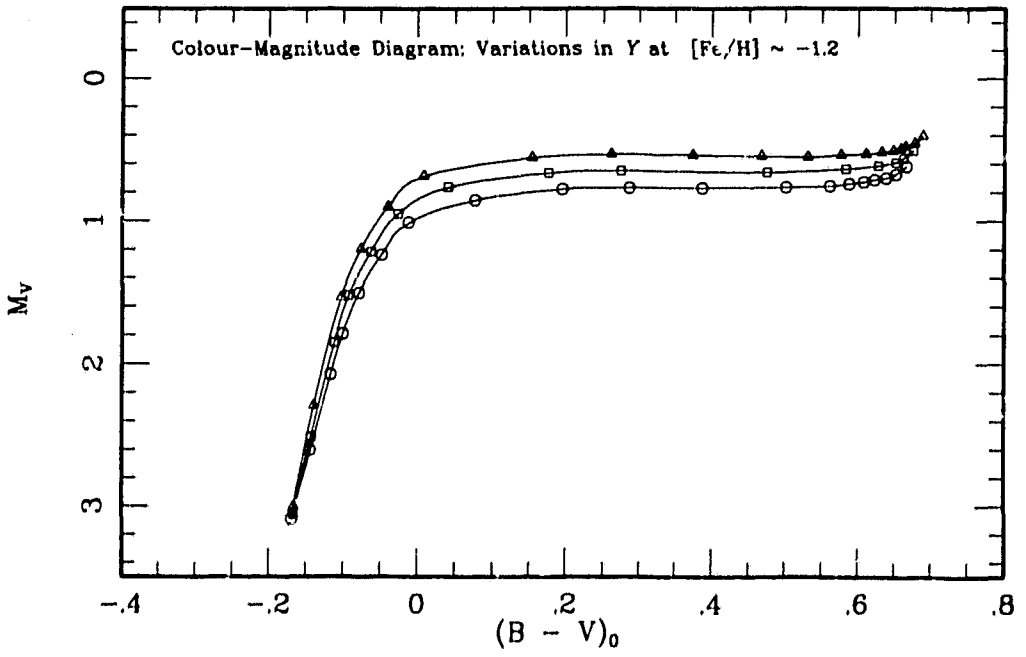

Fig. 5–3–20: Colour–Magnitude diagram for sequences shown in Figure 5–3–19.

Table 5-3-1: Luminosity vs [Fe/H] for sequences with [O/Fe] > 0

	(a) M_V at $\log T_{eff}$					
[Fe/H]	3.82	3.83	3.84	3.85	3.86	3.87
-2.26	0.5484	0.5493	0.5520	0.5558	0.5601	0.5659
-2.03	0.5728	0.5725	0.5724	0.5736	0.5773	0.5821
-1.78	0.5977	0.5968	0.5973	0.5986	0.5998	0.6037
-1.66	0.6161	0.6153	0.6160	0.6164	0.6173	0.6214
-1.48	0.6364	0.6347	0.6326	0.6320	0.6348	0.6426
-1.26	0.6690	0.6689	0.6707	0.6718	0.6730	0.6760
-1.03	0.7154	0.7127	0.7108	0.7111	0.7147	0.7229
-0.78	0.7691	0.7682	0.7706	0.7774	0.7860	0.7955
-0.65	0.8142	0.8111	0.8094	0.8103	0.8149	0.8242
-0.47	0.8560	0.8538	0.8525	0.8531	0.8566	0.8641
	(b) M_{bol} at $\log T_{eff}$					
	3.82	3.83	3.84	3.85	3.86	3.87
−2.26	0.5308	0.5415	0.5528	0.5644	0.5762	0.5880
−2.03	0.5567	0.5666	0.5769	0.5873	0.5981	0.6091
−1.78	0.5852	0.5943	0.6036	0.6133	0.6232	0.6334
−1.66	0.6056	0.6141	0.6231	0.6325	0.6422	0.6522
−1.48	0.6262	0.6351	0.6440	0.6531	0.6625	0.6722
−1.26	0.6643	0.6722	0.6808	0.6896	0.6984	0.7075
−1.03	0.7130	0.7217	0.7303	0.7389	0.7479	0.7572
−0.78	0.7766	0.7833	0.7907	0.7991	0.8082	0.8175
−0.65	0.8225	0.8301	0.8377	0.8455	0.8537	0.8626
−0.47	0.8657	0.8737	0.8815	0.8895	0.8977	0.9064

change in the envelope structure; therefore, the envelope transmits to the surface temperature any change in the shell temperature. But the shell temperature decreases very slightly with decreasing helium abundance. The variations in nuclear energy generation in the shell which are clearly the dominant consequence of the changes should therefore act linearly for small changes in Y. The sequences, which are evenly spaced in L (until the Hydrogen burning luminosity begins to decline rapidly at the blue end), are also evenly spaced in Y; however there is insufficient evidence here to provide a complete confirmation of this prediction.

Table 5-3-2: Luminosity vs [Fe/H] for Sequences with [O/Fe] = 0

(a) M_V at $\log T_{eff}$

[Fe/H]	3.82	3.83	3.84	3.85	3.86	3.87
−2.26	0.4488	0.4568	0.4647	0.4726	0.4823	0.4929
−1.78	0.5674	0.5729	0.5783	0.5839	0.5902	0.5973
−1.48	0.6225	0.6218	0.6217	0.6225	0.6246	0.6294
−1.26	0.6498	0.6493	0.6502	0.6507	0.6518	0.6562
−0.78	0.7632	0.7603	0.7577	0.7569	0.7596	0.7671
−0.47	0.8442	0.8456	0.8502	0.8577	0.8658	0.8749

(b) M_{bol} at $\log T_{eff}$

	3.82	3.83	3.84	3.85	3.86	3.87
−2.26	0.4285	0.4468	0.4647	0.4823	0.4997	0.5169
−1.78	0.5499	0.5621	0.5742	0.5863	0.5984	0.6105
−1.48	0.6094	0.6189	0.6285	0.6385	0.6493	0.6602
−1.26	0.6429	0.6511	0.6599	0.6692	0.6787	0.6886
−0.78	0.7624	0.7709	0.7789	0.7866	0.7946	0.8033
−0.47	0.8550	0.8624	0.8704	0.8792	0.8882	0.8974

5.4 Presentation of the Evolutionary Sequences

Many of the theoretical features of HB evolution have been treated in detail in §2.5, and some of the observational consequences of these phenomena will be revisited in Chapter 6, where evolutionary sequences are used to interpret cluster data. The object of this section, therefore, is to provide a bridge between theory and observation, by contrasting the behaviour of the sequences in the theoretical and observational planes. In addition, the illustrations of the sequences are indexed, and a few brief comments concerning the calculations will be made.

Evolutionary sequences have been calculated for ten to twelve masses for each of the compositions listed in Table 5-2-1. The full grid of calculations comprises a total of 108 sequences containing about 38,000 stellar models. The tracks are displayed here on both the theoretical and observational planes, as listed below in Table 5-4-1. For the metallicity given in the first column, the masses for which

evolutionary tracks have been computed are listed in the second column. Following the usage of SG76, the notation x (y) z means that masses between the values x and z are calculated at mass intervals of y. The column marked 'L,T' gives the figure number of this section in which the tracks are illustrated in the theoretical ($\log L$, $\log T_{eff}$) plane, while that marked '*CM*' gives the number of the corresponding Colour-Magnitude diagram.

Table 5-4-1: Index for the Evolutionary Tracks

[Fe/H]	**Track Masses Computed** ($M_*/M_\odot$)	**Shown in Fig. 5-4-**	
		L, T	*CM*
−2.26	0.54 (0.04) 0.62 (0.02) 0.70, 0.74, 0.82, 0.90	1	11
−2.03	0.54 (0.04) 0.62 (0.02) 0.70, 0.74, 0.82, 0.90	2	12
−1.78	0.54 (0.02) 0.68, 0.74, 0.82, 0.90	3	13
−1.66	0.54 (0.02) 0.68, 0.72, 0.78, 0.82, 0.90	4	14
−1.48	0.54, 0.58 (0.02) 0.66 (0.04) 0.78, 0.82, 0.90	5	15
−1.26	0.52, 0.56 (0.02) 0.62 (0.04) 0.78, 0.82, 0.90	6	16
−1.03	0.52 (0.02) 0.62 (0.04) 0.70, 0.78, 0.82, 0.90	7	17
−0.78	0.56 (0.02) 0.66 (0.04) 0.78, 0.82, 0.90	8	18
−0.65	0.57, 0.58, 0.60 (0.02) 0.66 (0.04) 0.78, 0.82, 0.90	9	19
−0.47	0.58 (0.01) 0.60, 0.62 (0.04) 0.78, 0.82, 0.90	10	20

For each of the diagrams, dots along the tracks mark off 5 million year intervals during the evolution. For clarity, the mass of the sequence is shown close to the ZAHB point, where this is possible given the density of points on the figure. It should be noted that in some areas of the section of the colour magnitude plane shown in the diagrams, the colour transformations are close to or exceed their range of validity. This is true for the bluer low-gravity paths which are taken by the very low mass models at late times.

Apart from the adopted compositions, the major differences between these calculations and those of SG76 and S87 are the extension of the sequences beyond

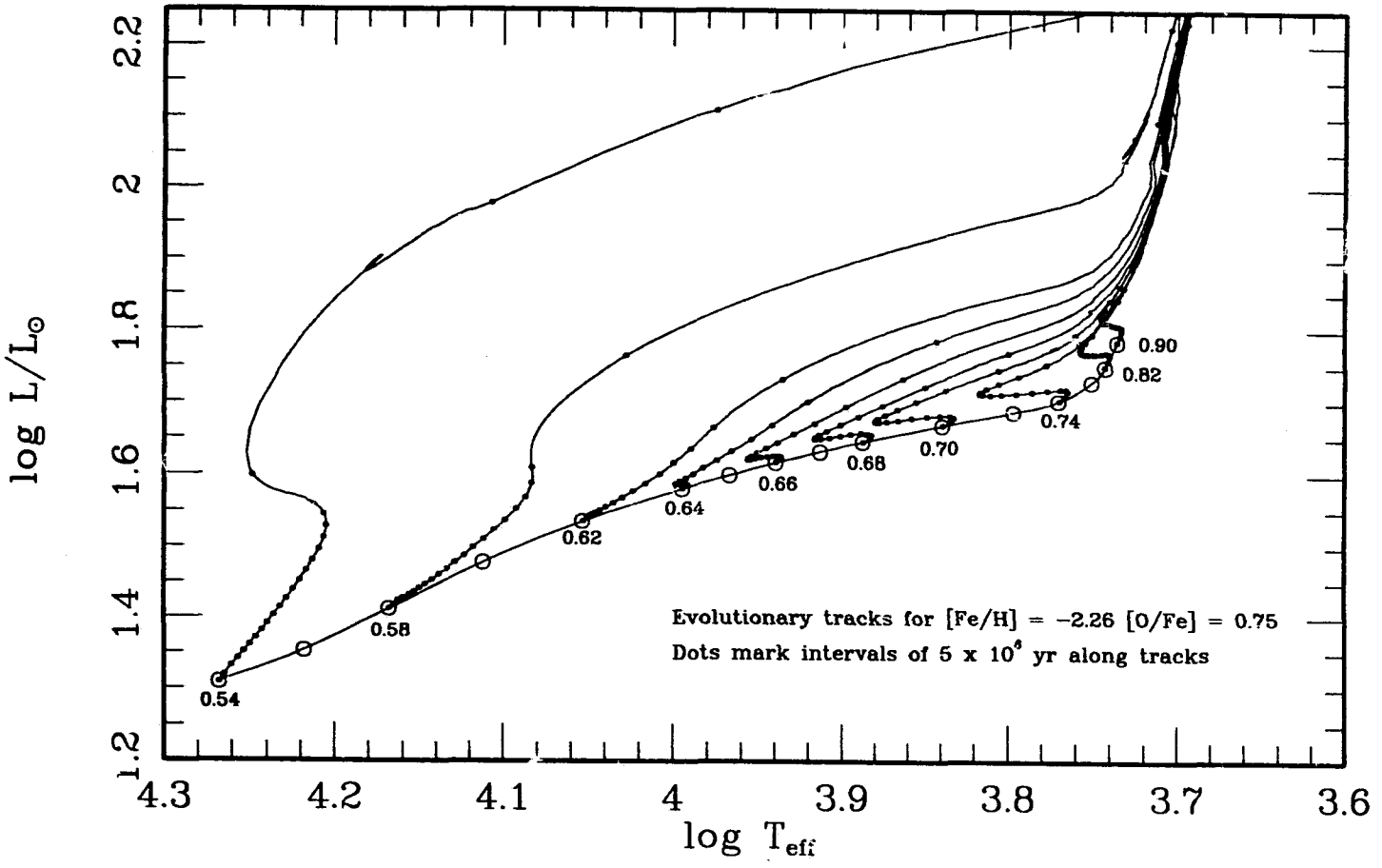

Fig. 5–4–1: Theoretical plane illustration of evolutionary tracks for models with [Fe/H] = –2.26, [O/Fe] = 0.75. In this and the figures to 5–4–20, selected individual tracks are labelled by their total masses in solar units.

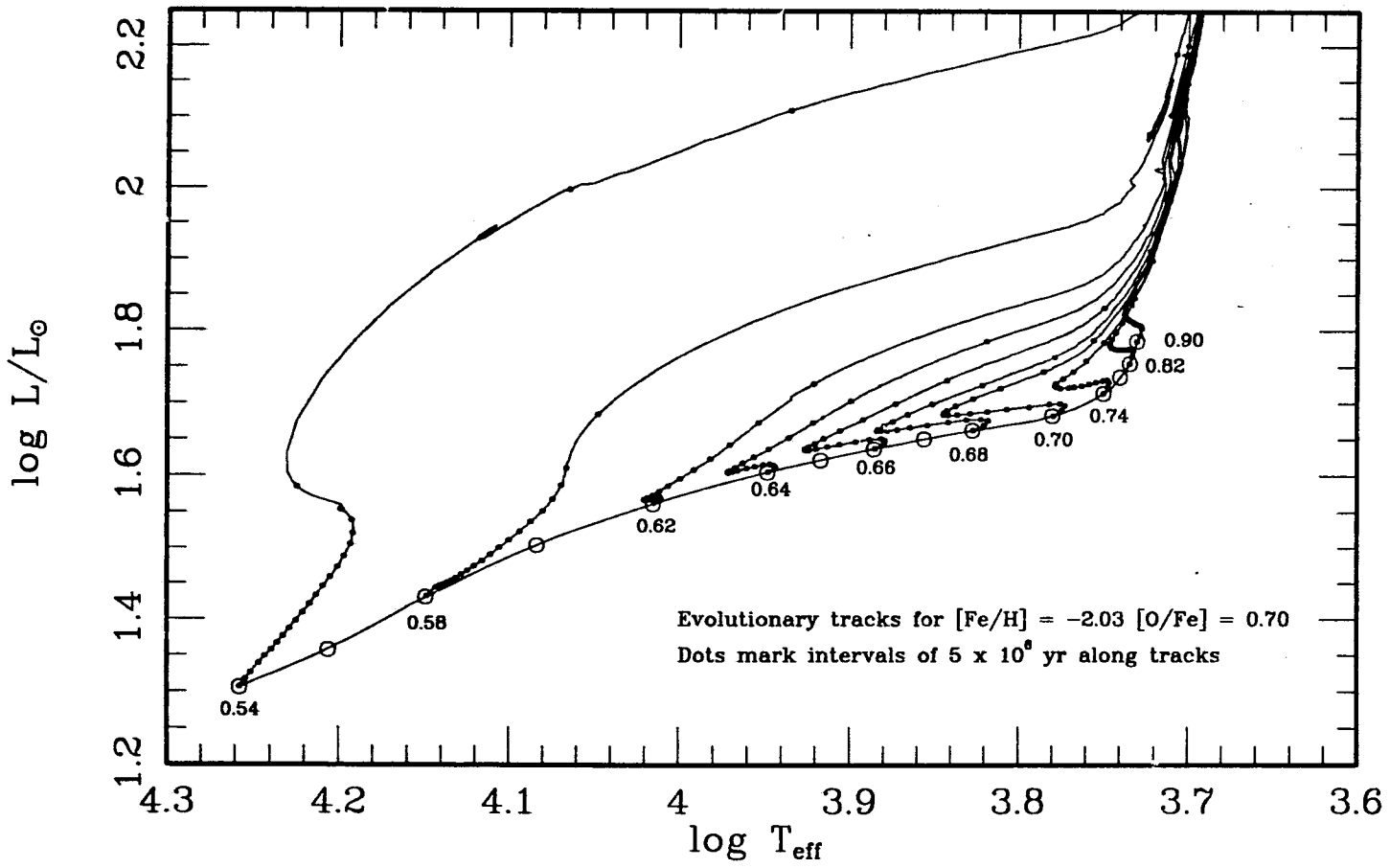

Fig. 5–4–2: Theoretical plane illustration of evolutionary tracks for models with [Fe/H] = –2.03, [O/Fe] = 0.70.

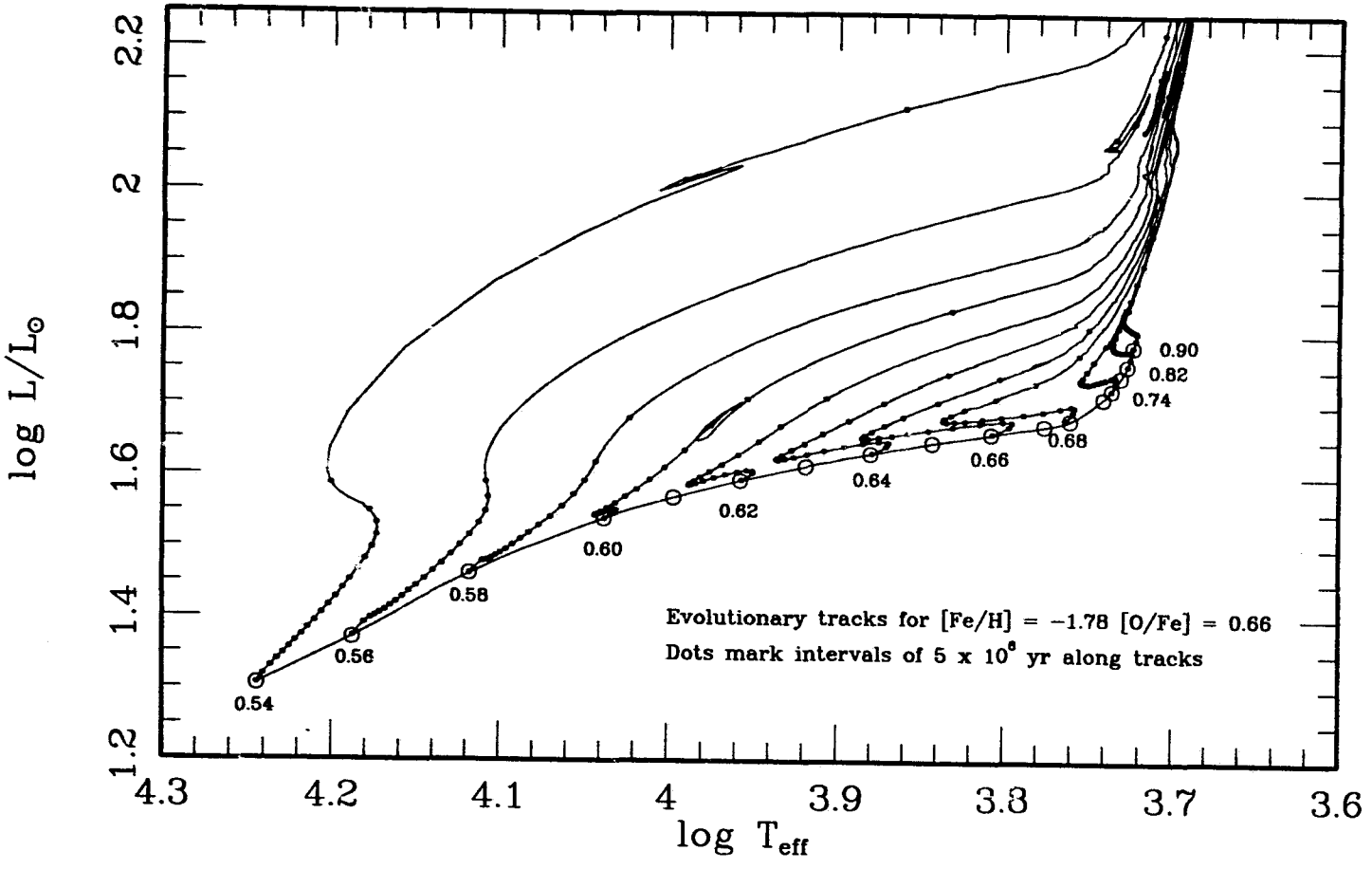

Fig. 5–4–3: Theoretical plane illustration of evolutionary tracks for models with [Fe/H] = –1.78, [O/Fe] = 0.66.

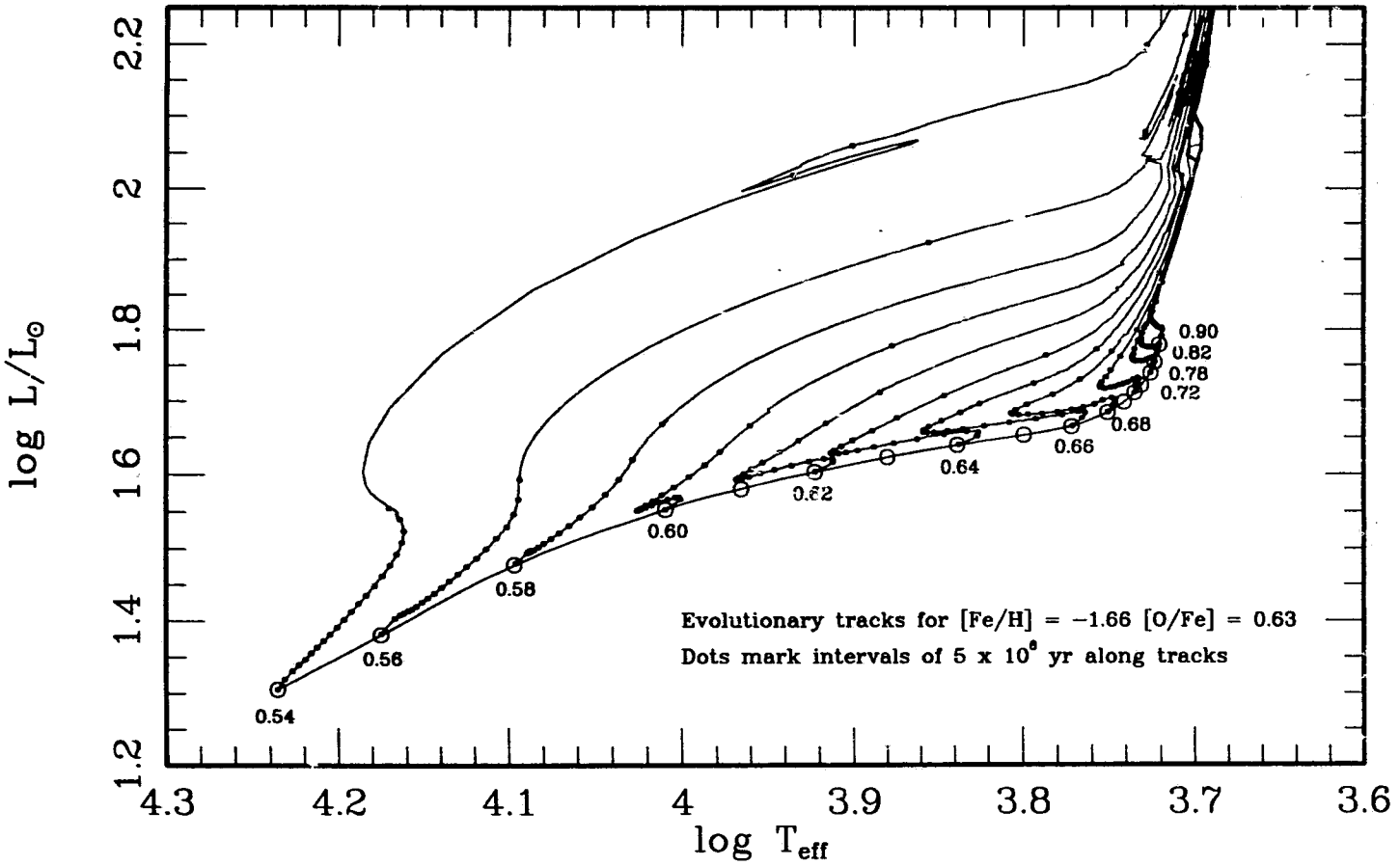

Fig. 5–4–4: Theoretical plane illustration of evolutionary tracks for models with [Fe/H] = –1.66, [O/Fe] = 0.63.

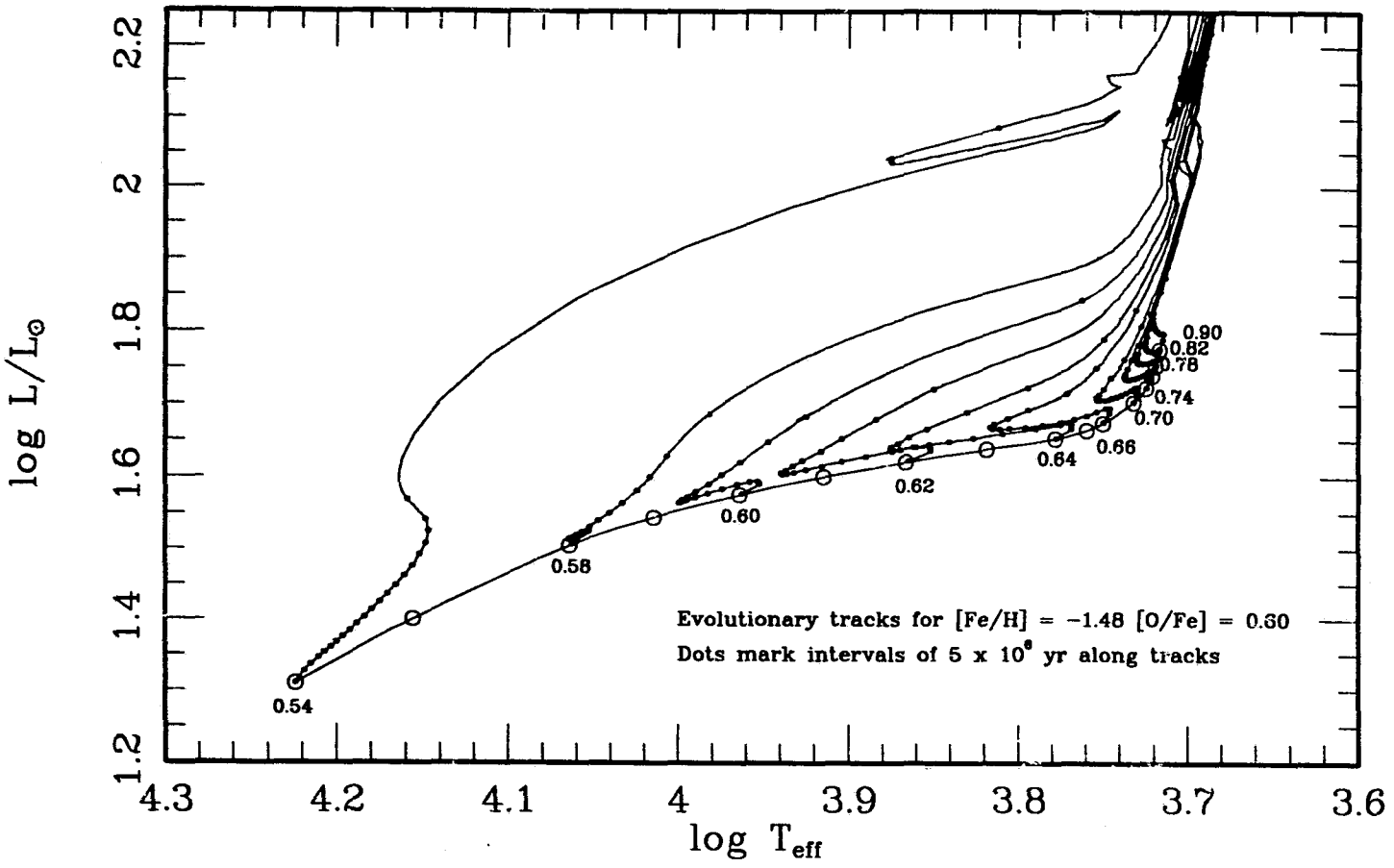

Fig. 5–4–5: Theoretical plane illustration of evolutionary tracks for models with [Fe/H] = –1.48, [O/Fe] = 0.60.

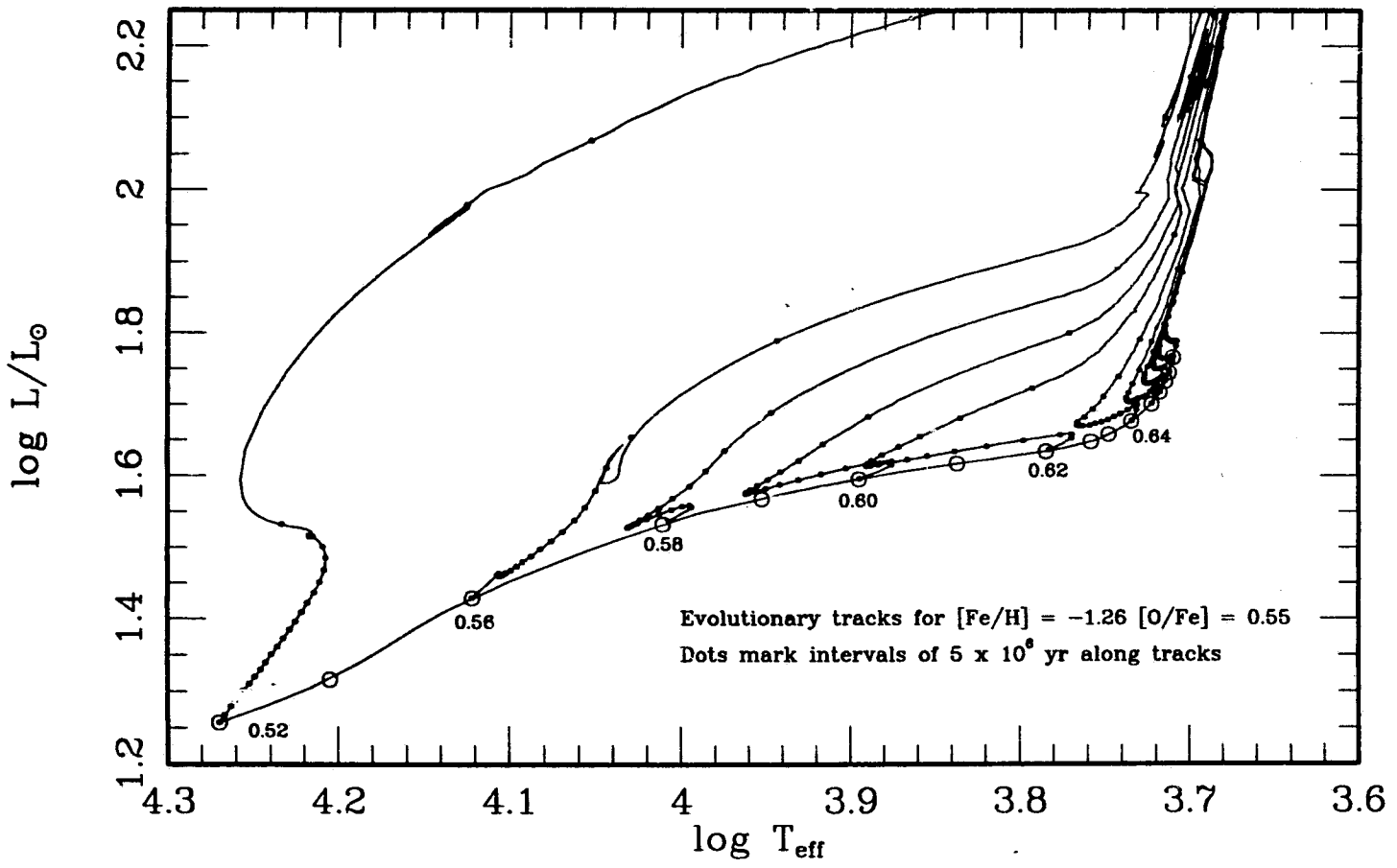

Fig. 5–4–6: Theoretical plane illustration of evolutionary tracks for models with [Fe/H] = –1.26, [O/Fe] = 0.55.

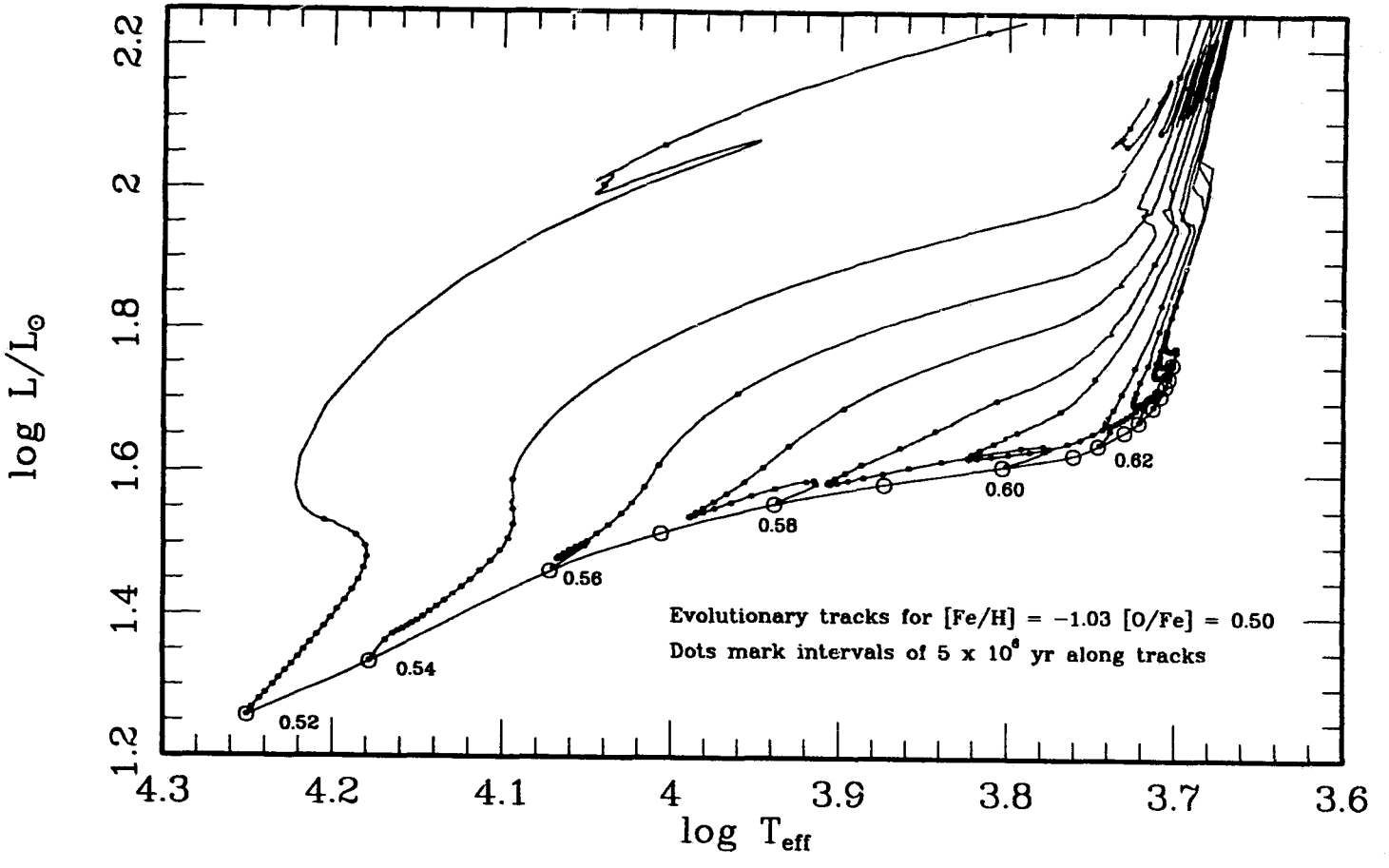

Fig. 5–4–7: Theoretical plane illustration of evolutionary tracks for models with [Fe/H] = –1.03, [O/Fe] = 0.50.

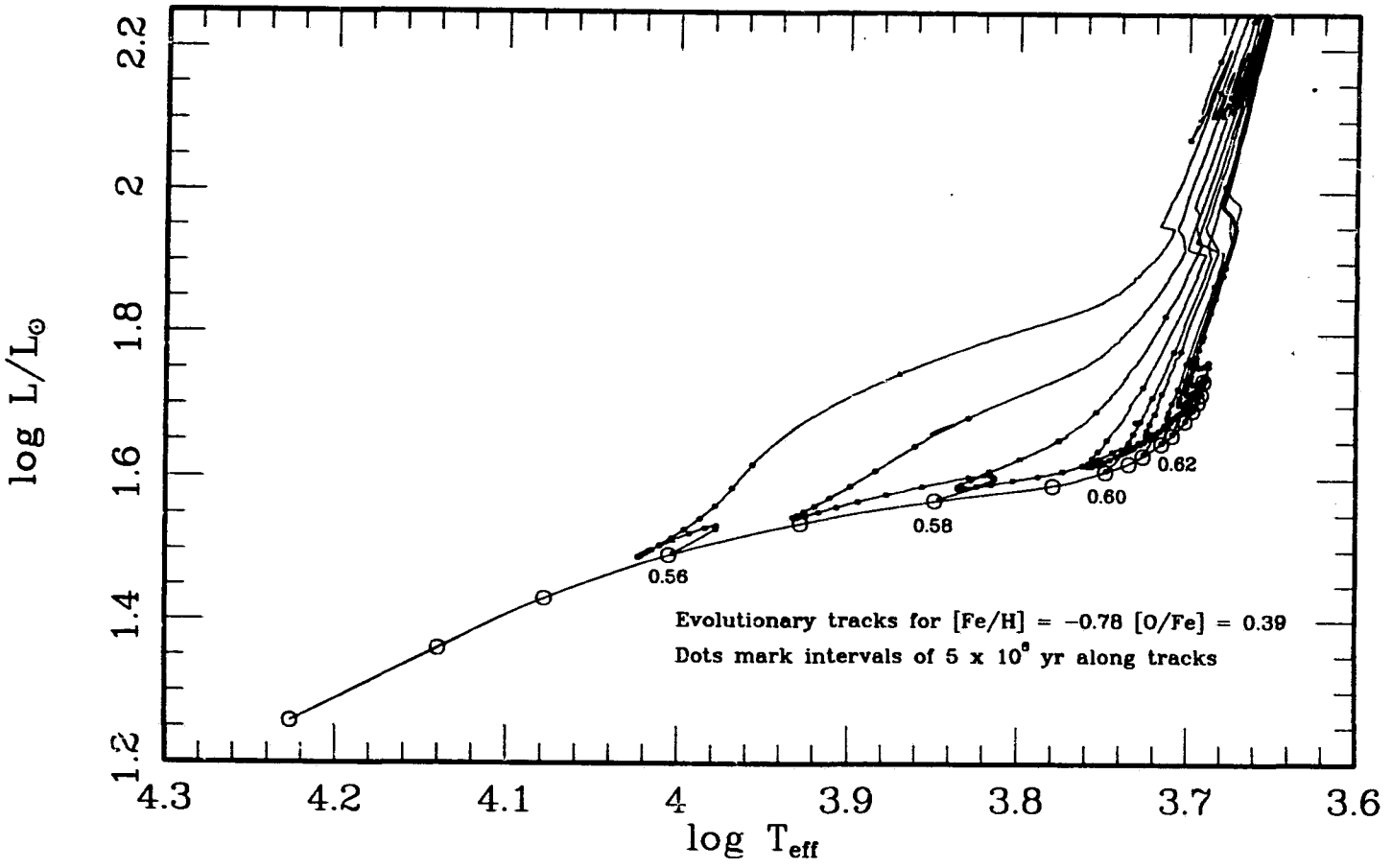

Fig. 5–4–8: Theoretical plane illustration of evolutionary tracks for models with [Fe/H] = –0.78, [O/Fe] = 0.39.

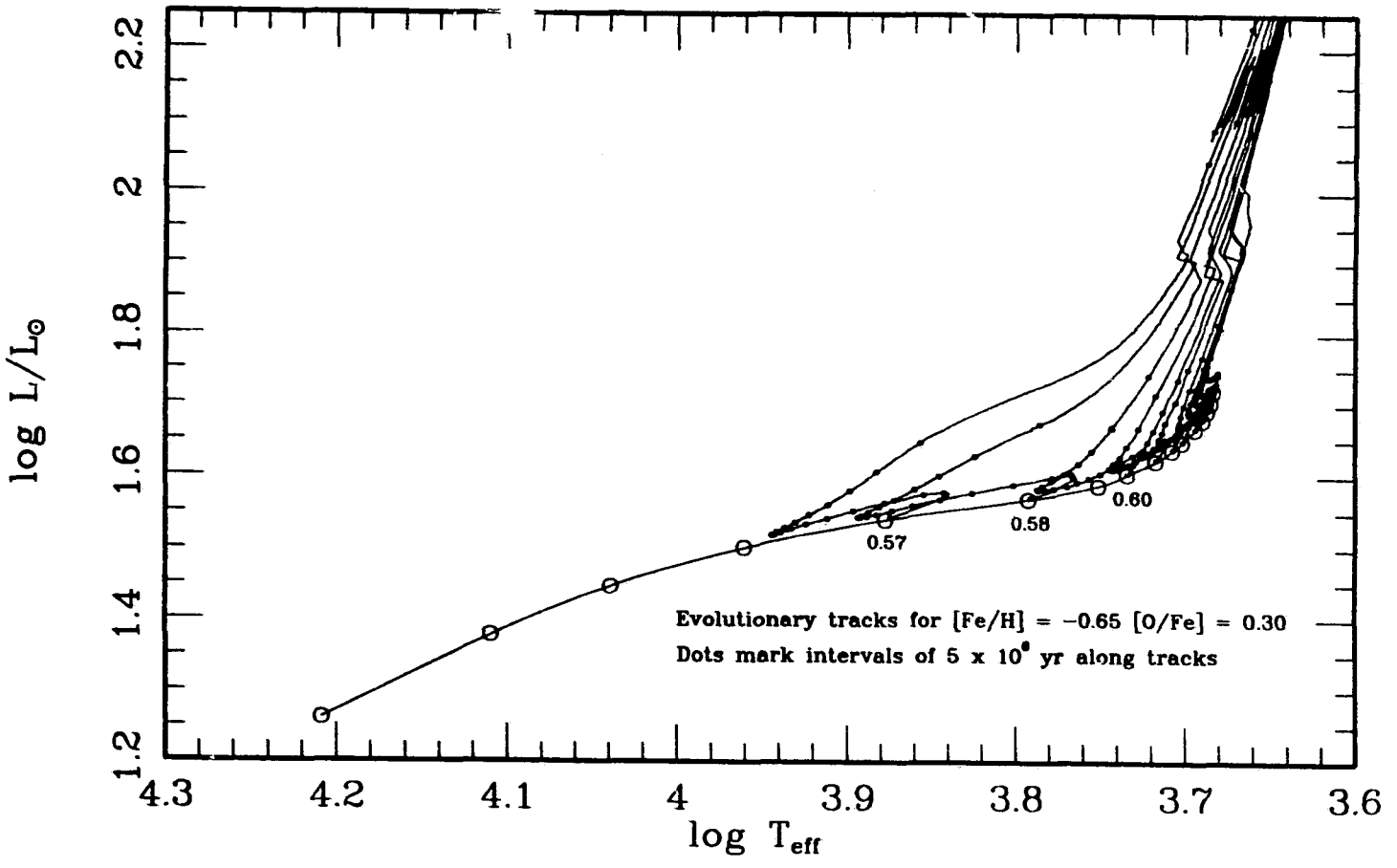

Fig. 5–4–9: Theoretical plane illustration of evolutionary tracks for models with [Fe/H] = –0.65, [O/Fe] = 0.30.

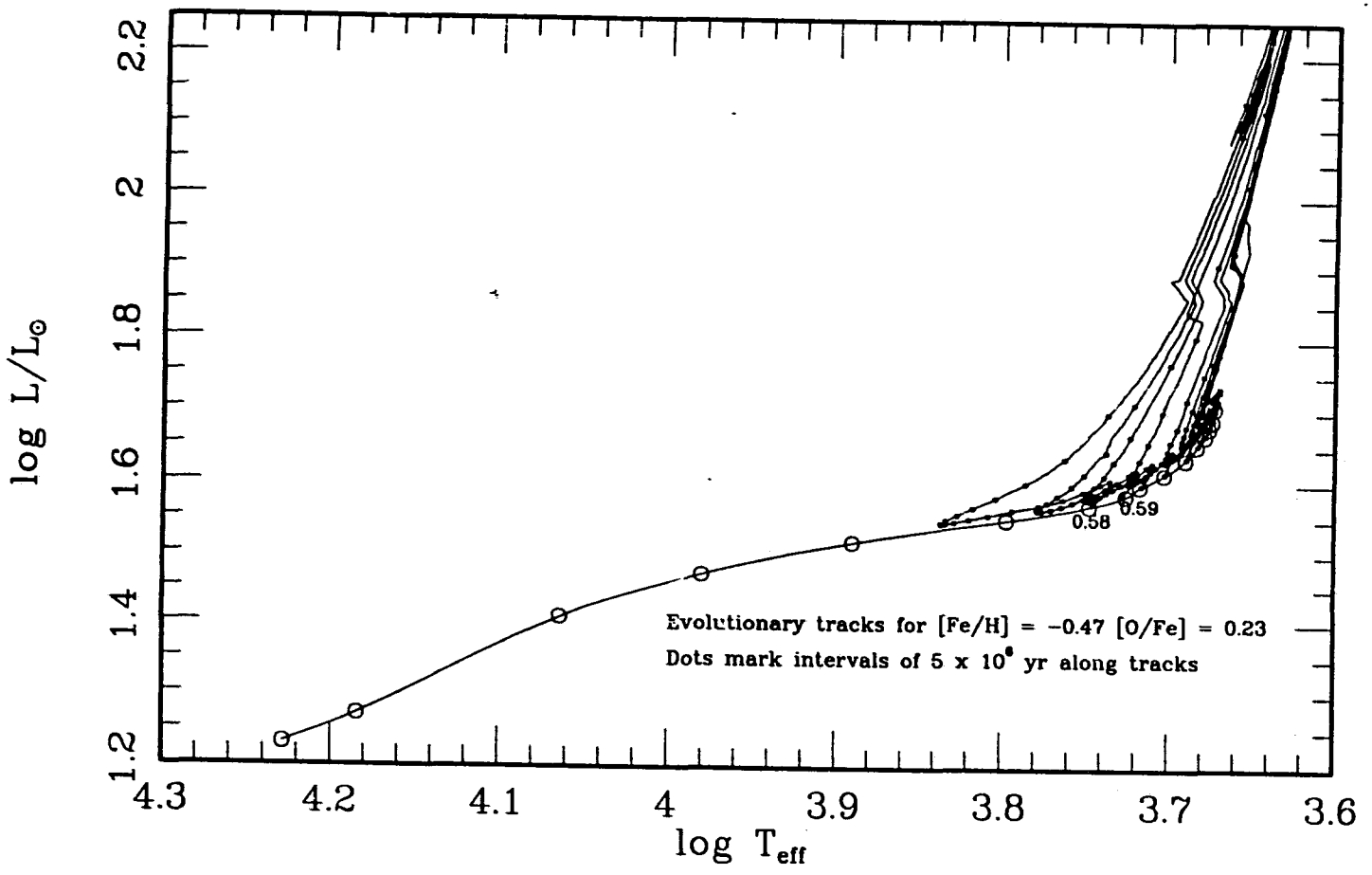

Fig. 5–4–10: Theoretical plane illustration of evolutionary tracks for models with [Fe/H] = –0.47, [O/Fe] = 0.23.

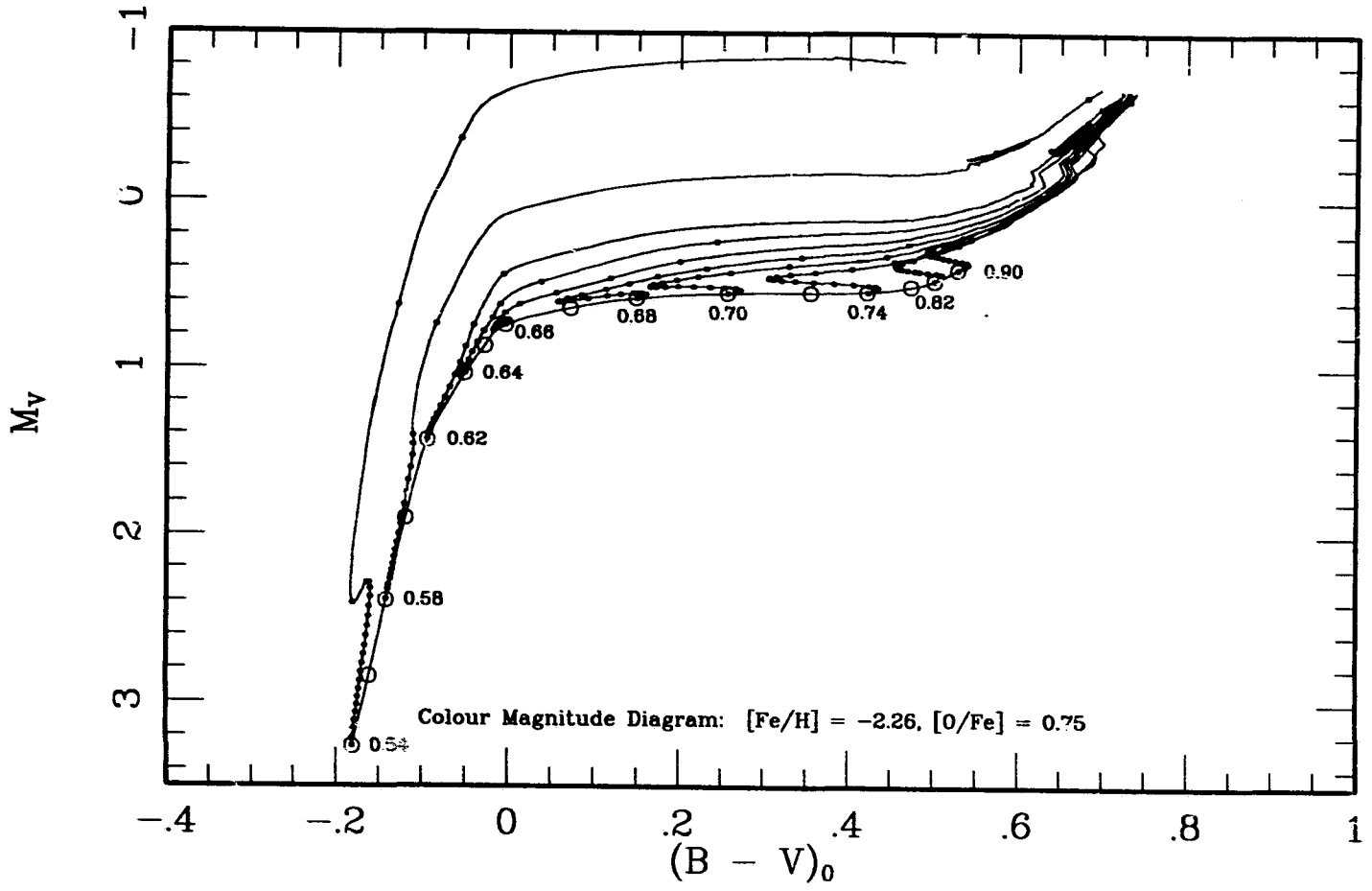

Fig. 5–4–11: Colour Magnitude diagram for evolutionary tracks shown in Figure 5–4–1.

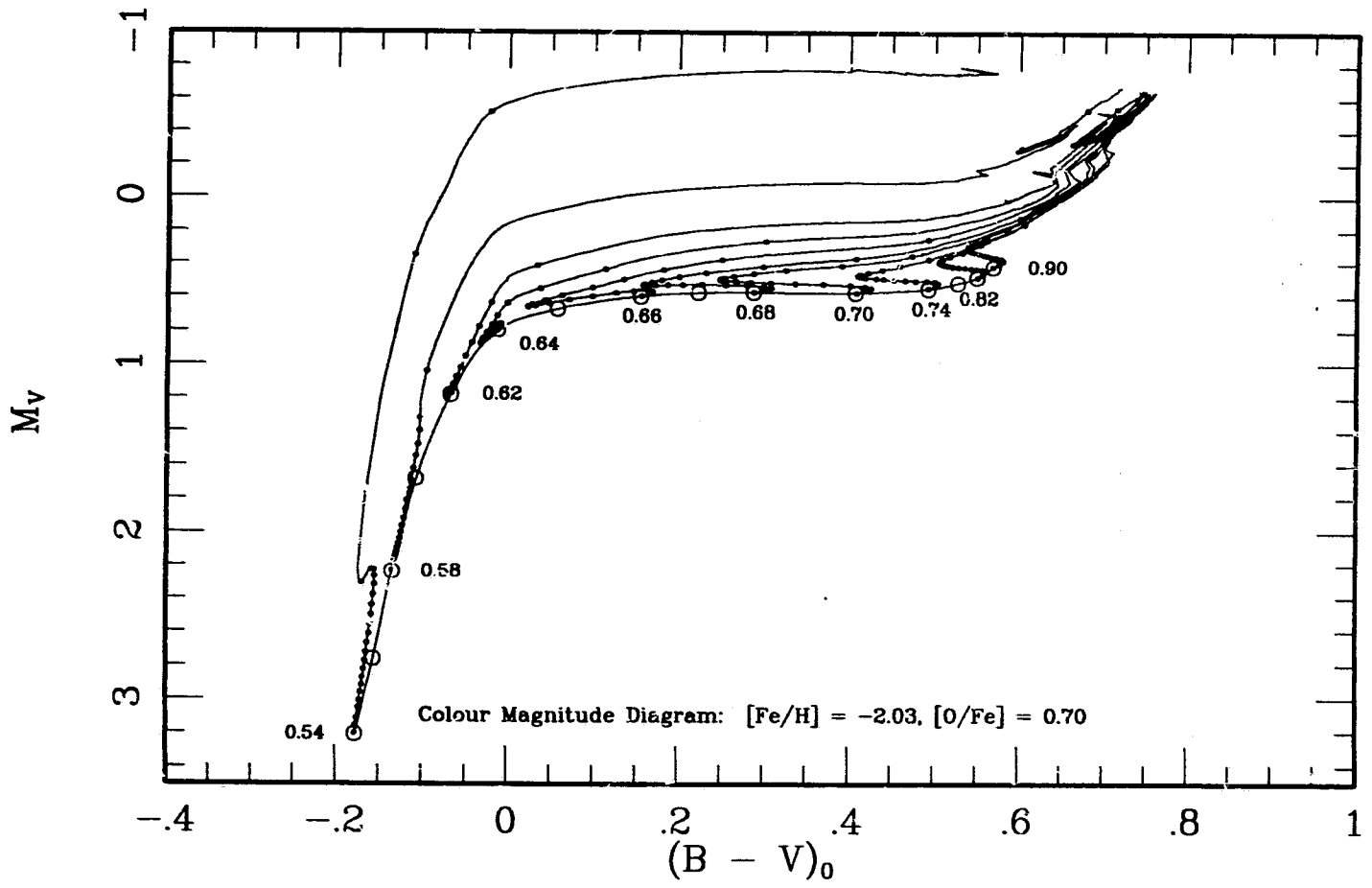

Fig. 5–4–12: Colour Magnitude diagram for evolutionary tracks shown in Figure 5–4–2.

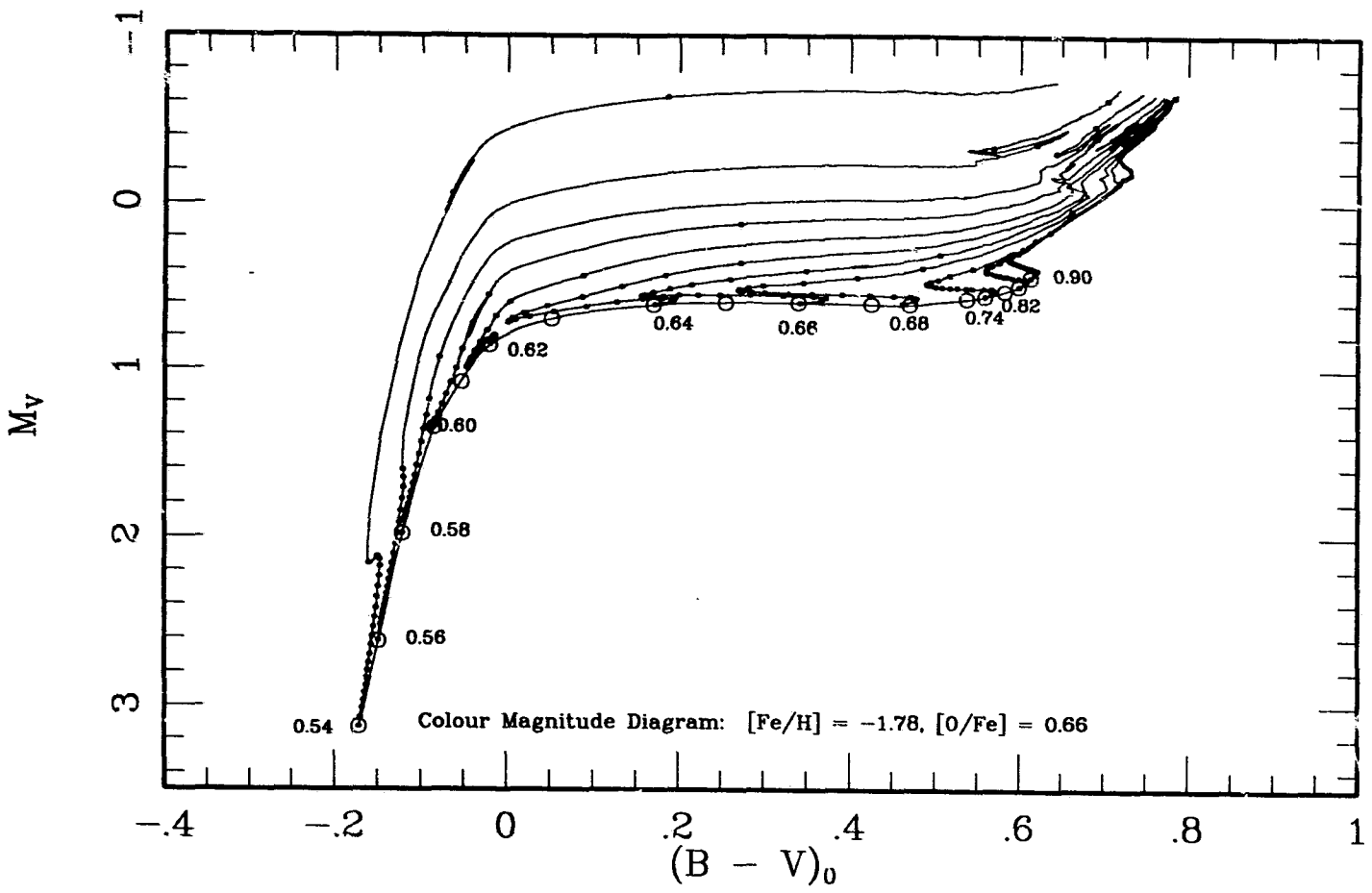

Fig. 5–4–13: Colour Magnitude diagram for evolutionary tracks shown in Figure 5–4–3.

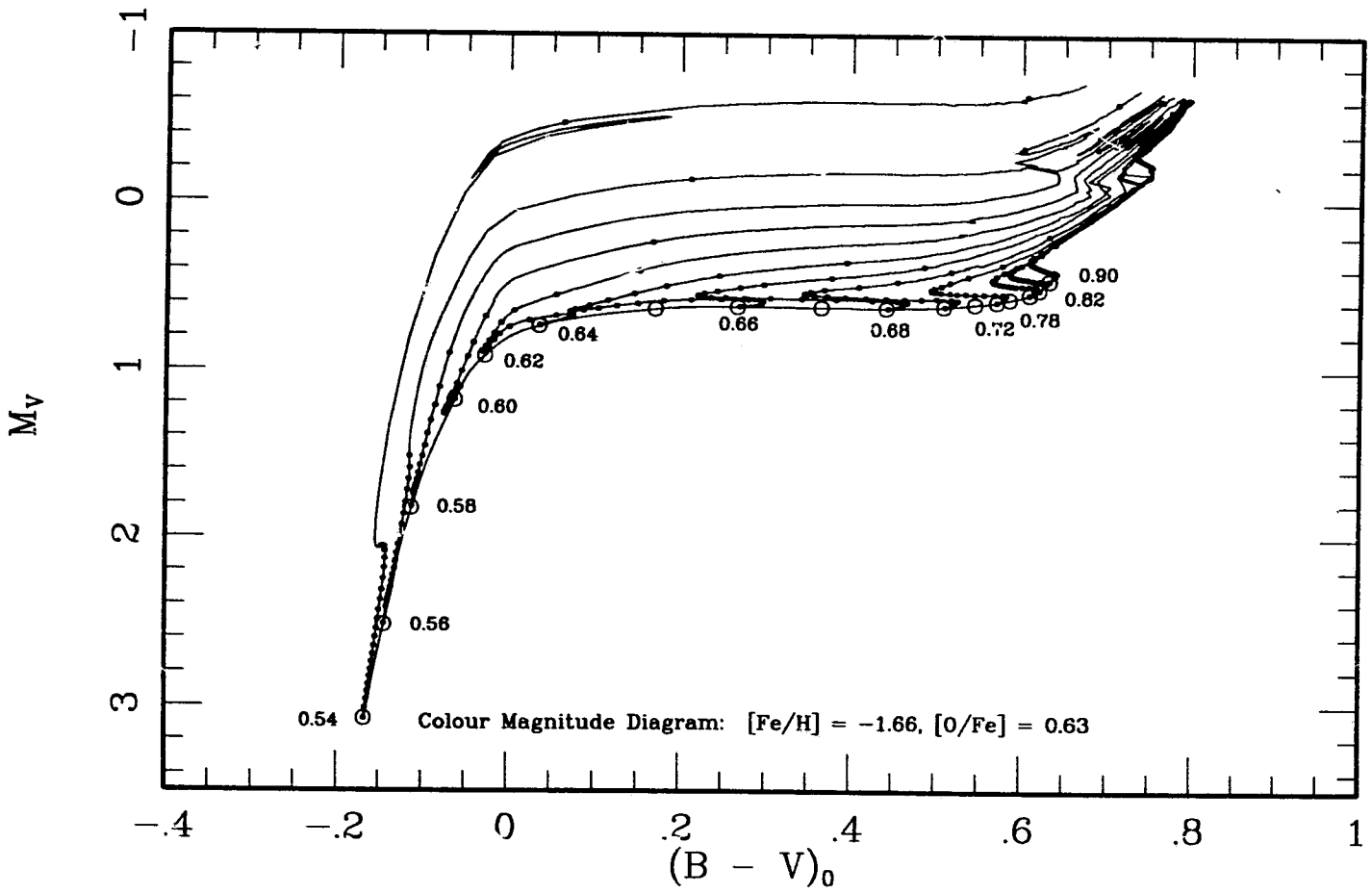

Fig. 5–4–14: Colour Magnitude diagram for evolutionary tracks shown in Figure 5–4–4.

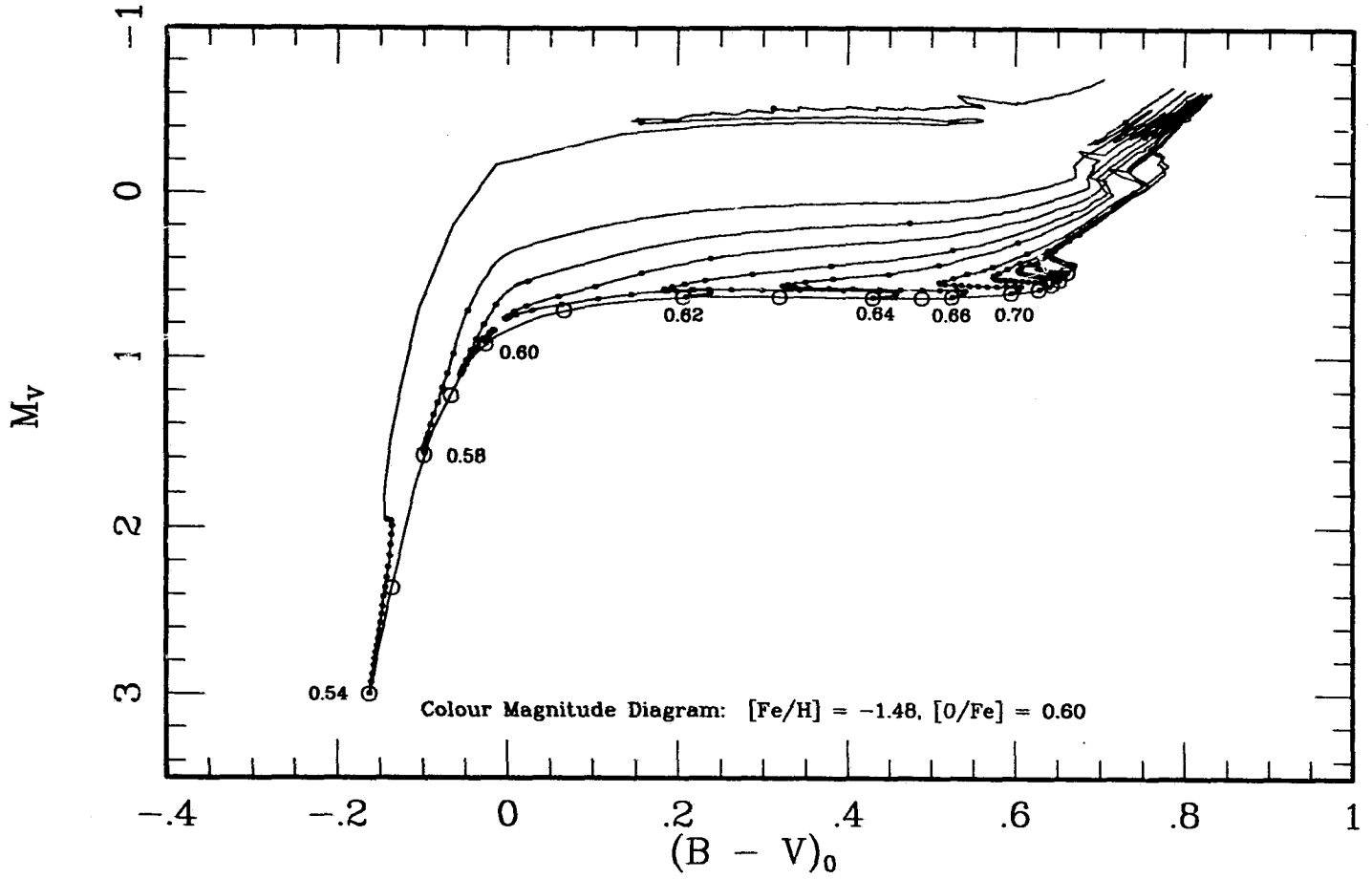

Fig. 5–4–15: Colour Magnitude diagram for evolutionary tracks shown in Figure 5–4–5.

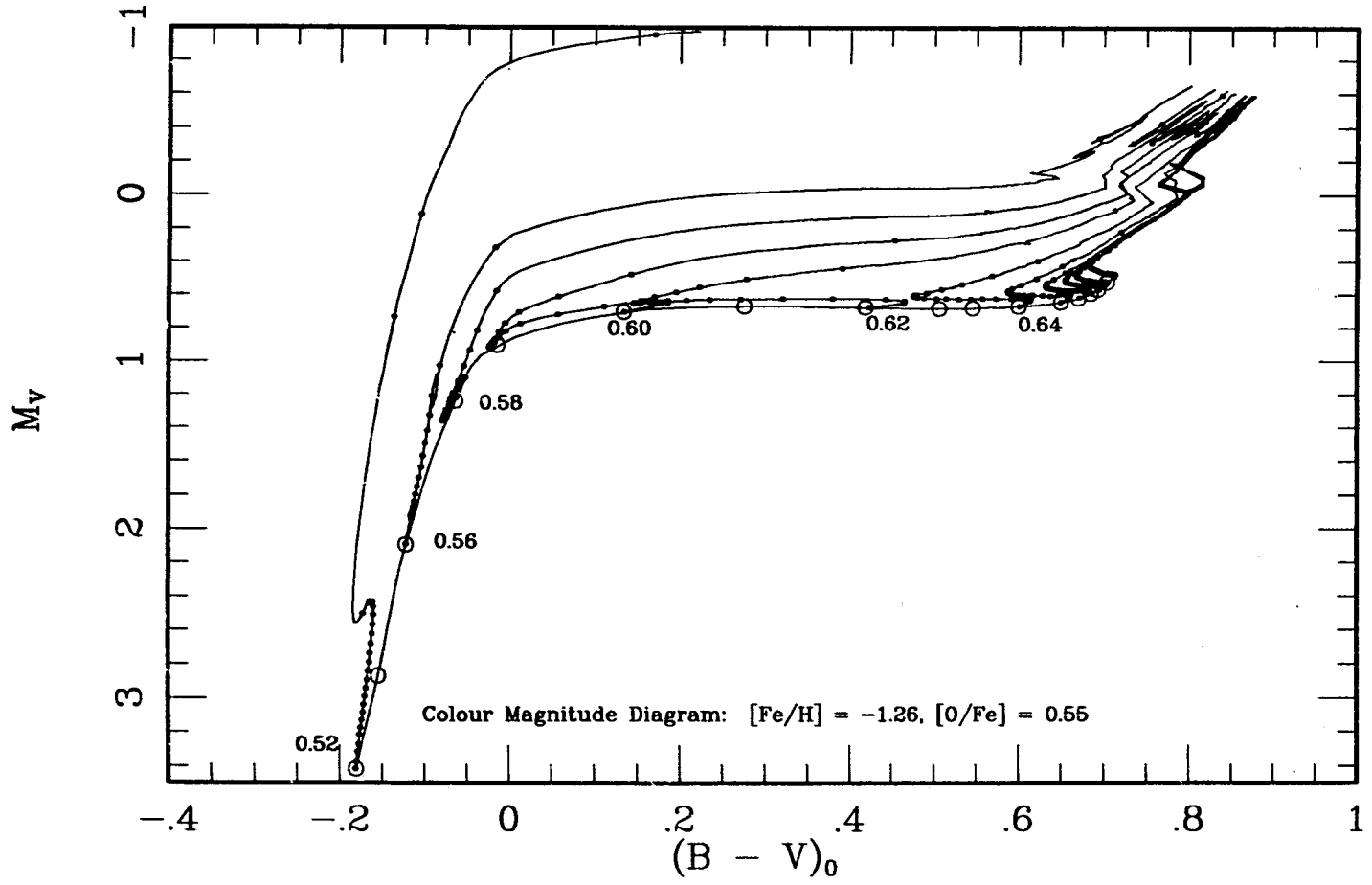

Fig. 5–4–16: Colour Magnitude diagram for evolutionary tracks shown in Figure 5–4–6.

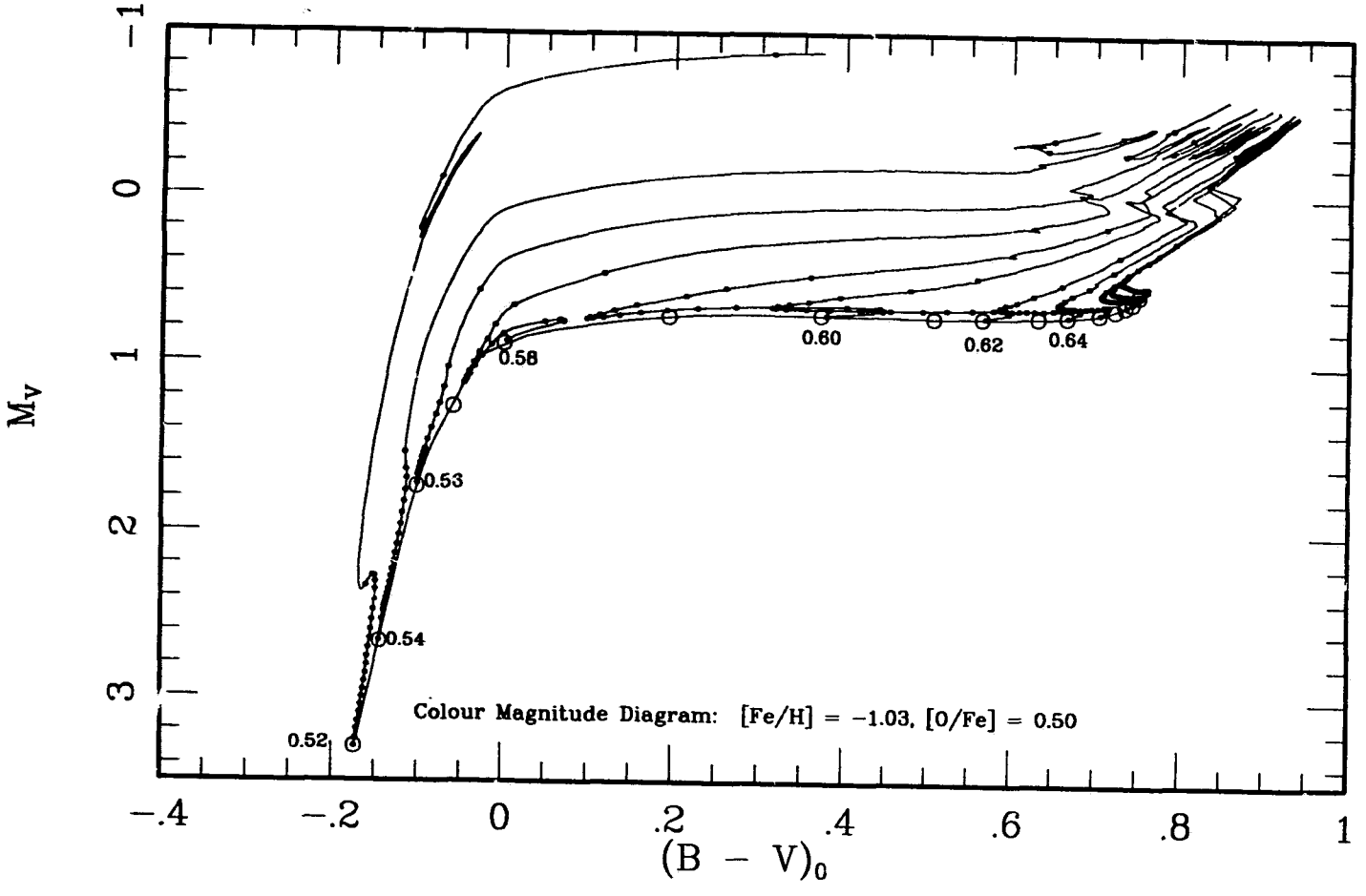

Fig. 5–4–17: Colour Magnitude diagram for evolutionary tracks shown in Figure 5–4–7.

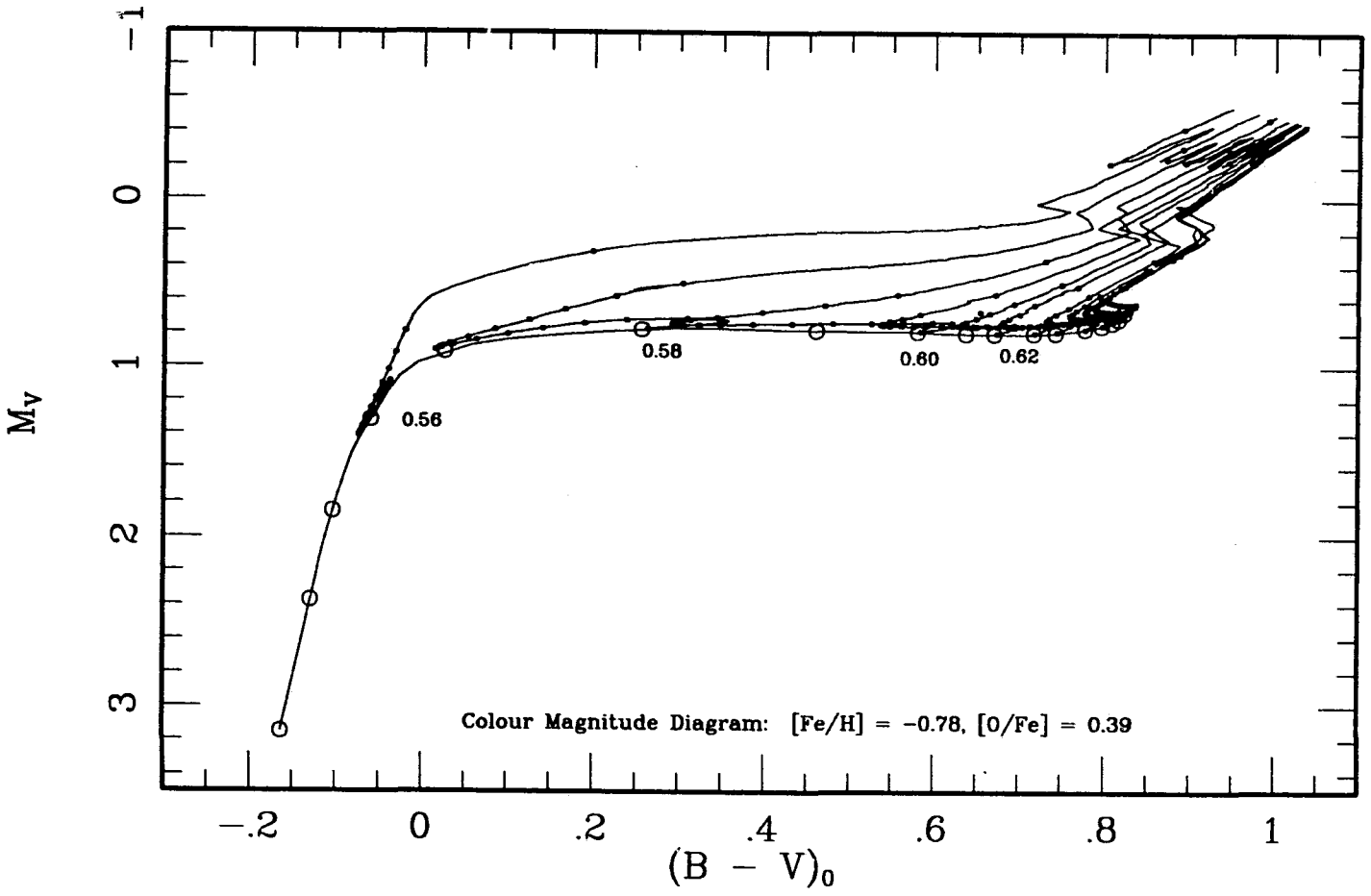

Fig. 5–4–18: Colour Magnitude diagram for evolutionary tracks shown in Figure 5–4–8.

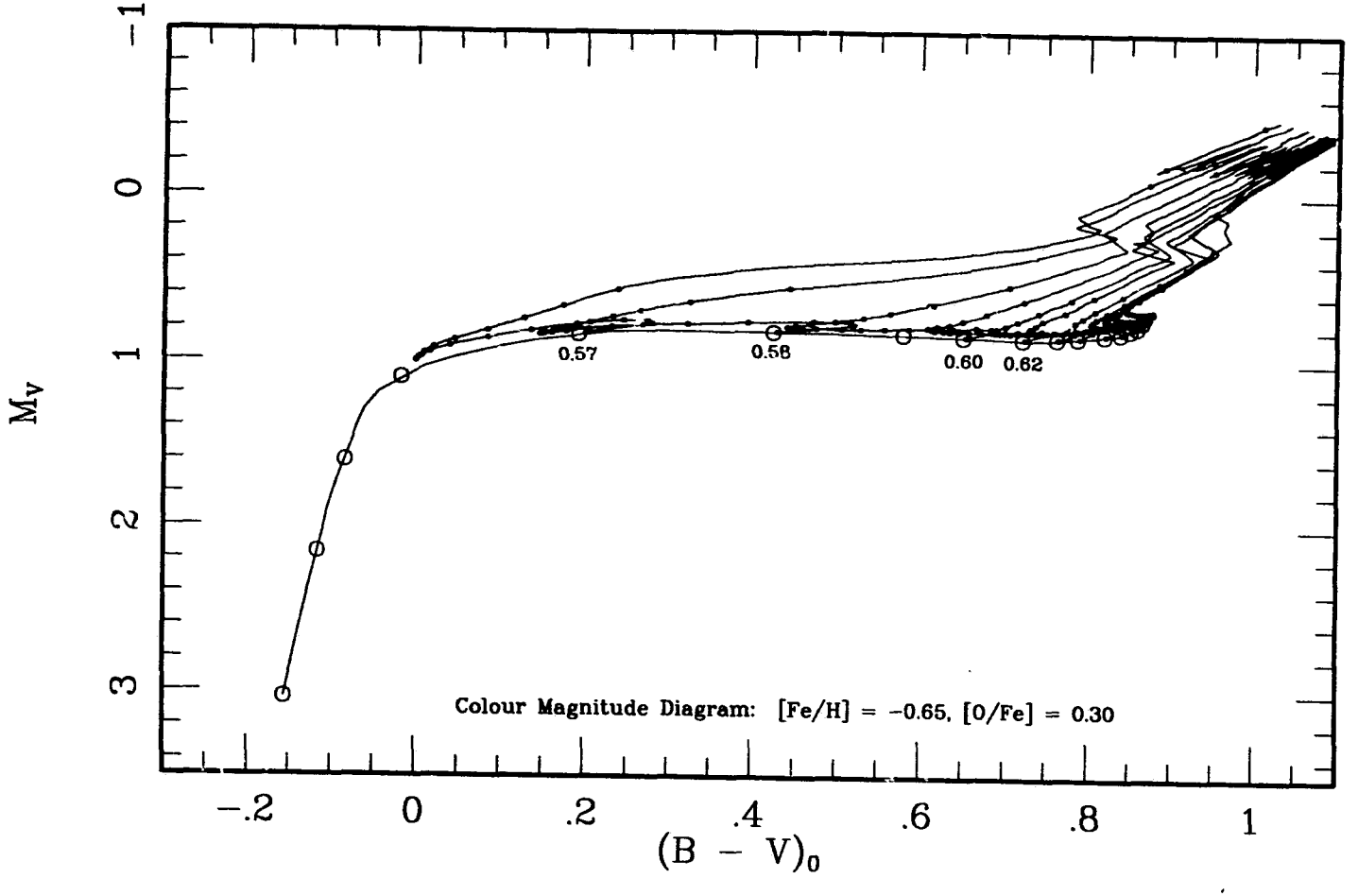

Fig. 5–4–19: Colour Magnitude diagram for evolutionary tracks shown in Figure 5–4–9.

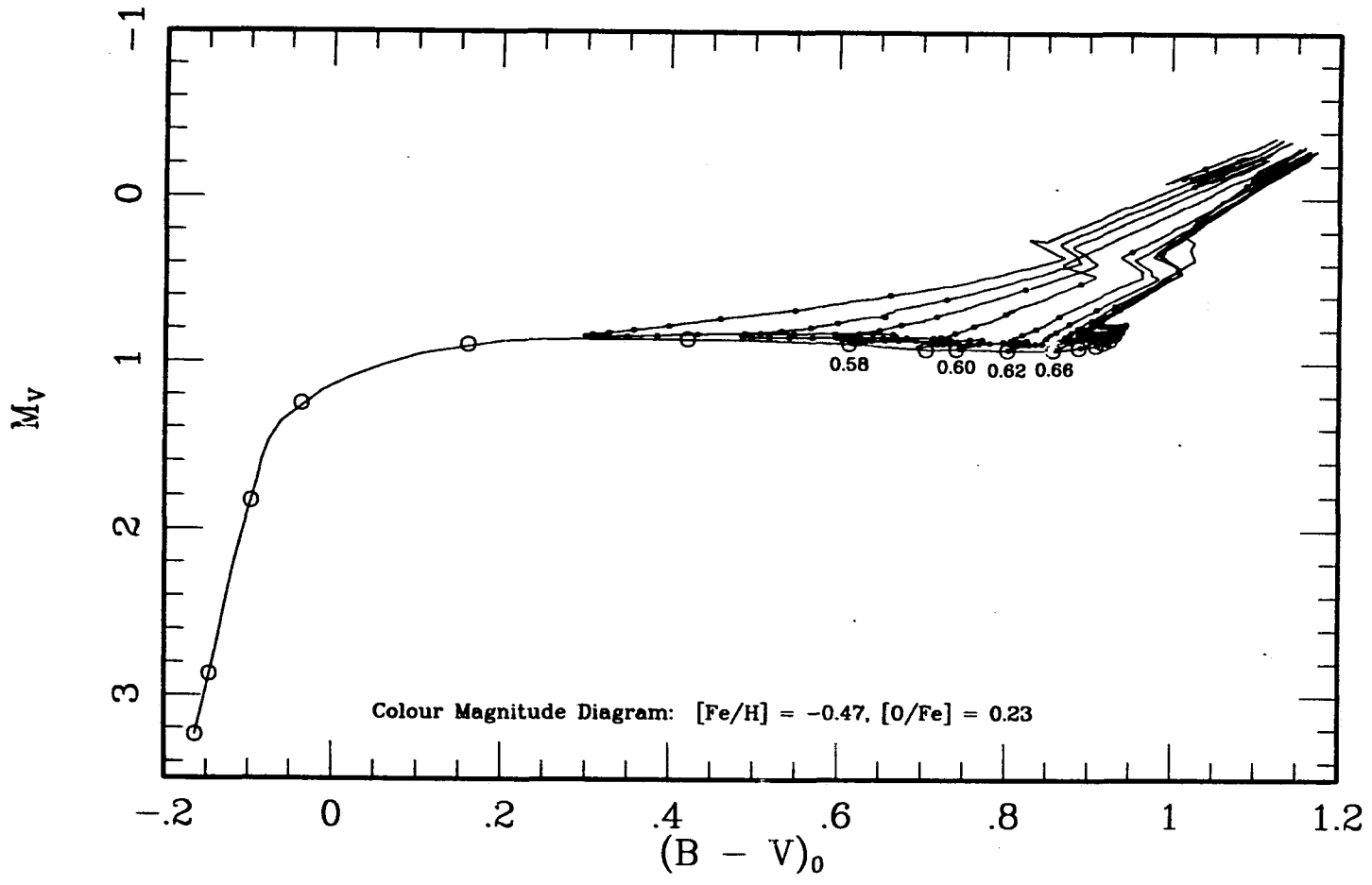

Fig. 5–4–20: Colour Magnitude diagram for evolutionary tracks shown in Figure 5–4–10.

helium exhaustion and the incorporation of non-ideal corrections to the equation of state. The first of these, it must be said, has been achieved by making simplifications at a late stage in the HB evolution which are somewhat unsatisfactory. Despite this problem, it is highly likely that the gross features of stellar evolution to core exhaustion are quite well represented by these sequences. This is because the core must eventually contract rapidly, exhaust itself, and the envelope must grow to giant proportions. As it does so, the stars must evolve redward and to higher luminosities. The details of the core behaviour can, of course, complicate the path actually taken to the AGB; if, for example, the breathing pulse phenomenon is not an artefact, then the direction of evolution will occasionally be reversed. The observable consequence of this would be the existence of higher number of stars in the appropriate region of the colour-magnitude plane for a cluster, than would be present if the luminosity and colour were strictly monotonic. Thus, star counts can, in principle, give indirect evidence for the assumptions made about the core behaviour (recall the lengthier discussion on this point given in chapter 3). The observations are, however, still somewhat ambiguous at present. The last stages of this evolution are useful for the modelling of more complete synthetic horizontal branches, as exemplified by Lee, Demarque and Zinn (1990), who use sequences computed by Lee and Demarque (1990) which are evolved to a point close to central helium exhaustion. In several of the tracks (*e.g.*, [Fe/H] = -1.78 $M_* = 0.60\,M_\odot$), the models develop small 'breathing pulses' during the evolution[4]. These have been incorporated into the figures; clearly, they do not produce an observable effect on the track morphology.

The phase slightly beyond central helium exhaustion is also very interesting, because the evolutionary tracks, reverse direction (growing dimmer for a time)

[4] *Recall the statement in Chapter 3 that the programme failed where it attempted to converge on a model with a large central helium change. The pulses depicted here therefore do not reflect their possible size, if they are not entirely numerical in origin.*

before proceeding to higher magnitudes on the AGB. As has been explained earlier, this is a result of the transition to helium shell burning after core exhaustion, at which point the model is largely held in equilibrium by gravitational and hydrogen burning energy sources. However, this transition is not made fully until the helium burning shell is established above the old convective core boundary, where the fuel supply is much more plentiful. The time take to regain the maximum luminosity reached earlier is affected by the helium abundance in the semiconvective zone. As a consequence, these calculations predict that post-exhaustion stars spend between half and two thirds of their total lifetime on the AGB below this 'luminosity maximum'. This prediction can be checked, again with the use of star counts, provided that the AGB populations can be properly differentiated from the first giant branch population, and provided that samples are sufficiently large and complete.

As for differences caused by the equation of state, it is rather surprising that the morphology of the evolutionary sequences are significantly altered by such a change in the basic physics. The effect, as was seen in Chapter 4, is to reduce the 'luminosity width' of the tracks at given Y. Unlike the problems noted in Chieffi and Straniero (1989) the equation of state in the interior (below the ionization zones) is not affected by the same problems of interpolation in composition. These calculations demonstrate the effect on evolution which results if the non-ideal effects are as significant as the Straniero (1988) data implies. As will be seen in Chapter 6, a reduction in the sequence width would very much help to reconcile the optimal value of the helium abundance determined for M15 with the commonly accepted primordial values. On the other hand, the track shapes obtained with the Straniero (1988) data apparently run contrary to the findings of §6.2 concerning the helium abundance of 47 Tucanae. Hence either the helium abundance was underestimated in this study, or the equation of state data does not properly represent the behaviour of the matter in the stellar interior. Very probably, this

question could be resolved by adopting other 'reliable' EOS data in the deep interior.

The close similarity between the synthetic colour-magnitude diagrams presented here and their globular cluster counterparts is very encouraging (although far from being a new discovery); indeed, it can been seen as a confirmation of the predictions of the theories of both stellar evolution and stellar atmospheres. In turn, these rely on fundamental principles of physics. One example is the behaviour of the bolometric corrections at high temperature. Another is the difference between the theoretical and observational planes in the slope of the sequences as they tend toward the AGB. This is caused by the dependence of the colour index on the surface gravity.

In nature, however, the dispersion in HB masses in real stellar systems is insufficient to populate the full extent of colour and luminosity which is possible during the HB phase of evolution. For this reason, the choice of mass values used for the evolutionary tracks is designed to cover the regions of the HB which are likely to be populated at each metallicity. However, because of the Second Parameter Effect, this requires a fairly extensive range of calculations. Erring on the side of producing too many sequences, tracks have been computed which cover the entire colour range for $[Fe/H] < -1$. For higher metallicities, the model sequence with the lowest mass covers most of the range in colour spanned by the 'horizontal' part of the HB.

The comparison of tracks at different metallicity shows several interesting features. Since the colour of the 'blue tail' is almost fixed, the colour range of the horizontal branch is stretched by the redward extension caused by both the higher envelope opacity and the enhanced line-blanketing in their atmospheres. The 'clump' distribution seen in metal-rich clusters such as 47 Tucanae is the result of the concentration of evolutionary sequences at the red end of the HB.

In contrast, metal weak clusters such as M3, in which the red end of the HB is populated, show the curve of the HB as it descends and continues blueward at approximately constant visual magnitude.

Most importantly, the slope of the late, redward evolving parts of the sequences steepens considerably with metallicity. For [Fe/H] ~ -2, the tracks evolve almost parallel to the ZAHB, and at a luminosity which increases slowly with decreasing mass. This is the 'confluence' effect referred to below in §6.3, and it implies an observable enhancement of the density of stars lying above the ZAHB in the colour range of the instability strip, if the bluer portions of the HB are populated. In contrast, the more metal-rich model tracks are steeper, and should distribute the redward evolving stars over a wider area in the colour-magnitude plane. As a final note, the very low mass stars cross the instability strip very rapidly at relatively high luminosities (up to -1 in M_V). These models have been associated with the BL Herculis type variables, with periods of about a day (see Gingold 1974 and references therein).

This completes a very brief review of the properties of the evolutionary sequences. The next chapter contains detailed studies of two globular clusters at opposite ends of the metallicity scale, and deals more extensively with the behaviour of evolutionary sequences as they apply to observations.

Chapter 6 The Comparison of Theory with Observation

6.1 Introduction

The bulk of this chapter reproduces material which has previously been accepted for the *Astrophysical Journal*. §6.1 discusses the nearby globular cluster 47 Tucanae (Dorman, VandenBerg and Laskarides 1989), and the second deals with M15 (Dorman, Lee and VandenBerg 1991). The sequences which were used for both of these studies were generated with earlier versions of the programme than that used to calculate the main grid of models which are described earlier and tabulated in the Appendix. In both cases, different physical inputs were utilized for the reaction rates and the equation of state, as detailed in each section. Because of this, a third section of this chapter briefly revisits each study and shows the effect of adopting the new calculations on the conclusions of each paper.

6.2 On the Helium Content of 47 Tucanae

6.2.i Foreword

In this study, written in the fall of 1988, the basic semiconvection algorithm described in detail in Chapter 3 was used to perform the computations, with the exception of the simplifications introduced into the routine in order to extend the sequences to the helium exhaustion stage and beyond, and some minor revisions of the code. The differences between these models and those presented in the Appendix are fourfold. Firstly, the initialization programme for the Zero Age models had not yet been developed, and the initial models used were provided by D.A. VandenBerg from previous unpublished calculations. The main difference between the earlier and later initial models was in the hydrogen abundance profile

just above the core. The profile was somewhat less steep, with a value of the hydrogen abundance $X \sim 10^{-4}$ at the energy generation peak of the shell. The resulting models do not have the 'relaxation phase' motion, in which the models become slightly brighter and cooler. Secondly, the nuclear reaction rates used were those tabulated by Caughlan *et al.* (1985), which, as noted in Chapter 4, contain a much higher estimate for the $^{12}C(\alpha,\gamma)^{16}O$ rate, and tend to produce sequences which extend further to the blue. Thirdly, the equation of state used was that of Eggleton, Faulkner and Flannery (1973) throughout the stellar interior. This results in tracks whose Zero Age luminosity is greater, and again, have larger colour range. Finally, as implied above, the model sequences were truncated when the central helium content reached a value $Y_c \sim 0.10 - 0.15$. The ramifications for the study in this section arising from these differences is explored in the afterword in the last section of this chapter.

6.2.ii Introduction

47 Tucanae has been one of the most extensively studied of the Galactic globular clusters (GCs), in part because it is one of the nearest and most massive such systems with little foreground reddening, but also because it is relatively abundant in the heavy elements. Indeed 47 Tuc has become the archetype of the metal-rich group of GCs – those with $[m/H] \sim -0.7$ – and consequently it plays a pivotal role in, for instance, assessing the age-metallicity relation encompassed by these objects.

In the latest photometric study of 47 Tuc, Hesser *et al.* (1987; hereafter HHVASS) estimated the cluster age to be about 13.5 Gyr using theoretical isochrones for metal abundance $[m/H] = -0.65$, an oxygen enhancement $[O/Fe] = 0.3$, and a helium content $Y = 0.24$. In support of their age determination, HHVASS noted that: (1) The current best estimates of the observed (or inferred) abundances in the cluster stars were assumed in the model computations so as to make the latter

as realistic as possible. In particular, an oxygen enhancement was adopted which is consistent both with the field-star relation between $[O/Fe]$ and $[Fe/H]$ (*e.g.*, see Sneden 1985) and with spectroscopic results for 47 Tuc giants (Gratton 1985). (2) The distance modulus which is obtained by matching a computed zero-age horizontal branch (ZAHB) with its observational counterpart agrees well with that implied by the local Population *II* subdwarf standards. (3) The isochrones for the assumed composition and an age of 13-14 Gyr provide a superb match to the shape of the entire colour-magnitude (C-M) diagram from $M_V \approx 7$ to $M_V \lesssim 0$, and accurately reproduce the luminosity function data over that magnitude range.

Because there is no obvious conflict between the assumptions made in the HHVASS study and available observational constraints (see the recent summary by VandenBerg 1988a), it is tempting to conclude that the age of 47 Tuc has been particularly well determined. On the other hand, only when all of the observations are explained in a self-consistent way will it be possible to ascribe an uncertainty of less than 1 Gyr to a particular age estimate. Accordingly, this next step in the continuing process extends the comparison of theory with observation to include the post-ZAHB evolutionary phase.

However, some aspects of HB observations, such as the presence of gaps in the stellar distributions in a few systems (*e.g.*, M15), have resisted interpretation by standard models and may be indicating the existence of distinct HB populations within a given cluster (see Crocker, Rood, and O'Connell 1988). An essential part of this suggestion is that all of the member stars do not, perhaps as a consequence of proposed differences in rotational properties, have the same core mass. The envelope abundances of HB stars can also be subject to considerable uncertainty. For example, the metal-poor clusters M15 and M92 show clear evidence that giants undergo deep mixing at much fainter magnitudes than are indicated by current predictions of the first dredge-up (Carbon *et al.* 1982, Trefzger *et al.* 1982, Langer *et al.* 1986). As described by VandenBerg and Smith (1988), one ramification

of such mixing would be a significant enhancement of the helium abundance in the envelopes of the bright giants and HB stars. Thus, for some systems, it may well be necessary to explore more widely the parameter space of M_c and envelope composition in order to explain the cluster properties adequately. Fortunately, 47 Tuc does not appear to show such anomalies (see the relevant discussion by HHVASS and by VandenBerg and Smith 1988), and this investigation will show that the cluster HB can be readily matched by canonical stellar models.

6.2.iii Results

Horizontal Branch evolutionary sequences have been computed, for the choices of Y, Z and $[O/Fe]$ which are listed in Table 6-2-1, in order to show clearly the dependence of the morphology and luminosity of the models on composition and to provide limits on the uncertainties of our conclusions. Also given is the helium enhancement ΔY resulting from the dredge-up during the red giant phase: these agree well with the similar calculations made by Sweigart and Gross (1978). The sixth column of Table 6-2-1 contains the helium core mass value for which HB models have been constructed. The final column gives a reference to the figure in which the ZAHB and selected evolutionary tracks have been plotted.

The locations of the ZAHB models on both the theoretical and the observed planes are listed in Table 6-2-2 for all the compositions which we have considered. Note the high sensitivity of the ZAHB luminosity to the envelope helium abundance, especially in view of the fact that stars with larger cores are predicted to have higher luminosities. The computations have been referred to the C-M diagram using the bolometric corrections and temperature-colour calibrations of VB85, and Bell and Gustafsson (1978). It should be appreciated, of course, that such transformations are open to uncertainties arising from the atmosphere models which are used to derive emergent fluxes and colour indices, while the effective temperatures of the interior models are themselves subject to theoretical problems.

Table 6-2-1: Model Parameters						
Y	ΔY	$[Fe/H]$	$[O/Fe]$	Z	M_c	Figure
0.20	0.0171	− 0.79	0	0.003	0.486	6-2-2a
0.20	0.0200	− 0.49	0	0.006	0.484	6-2-2b
0.30	0.0119	− 0.73	0	0.003	0.469	6-2-3a
0.30	0.0142	− 0.43	0	0.006	0.466	6-2-3b
0.24	0.0173	− 0.65	0	0.004	0.477	6-2-4a
0.24	0.0177	− 0.65	0.3	0.006*	0.477	6-2-4b

* *The excess in Z over 0.004 is solely the effect of enhanced oxygen*

These arise, for example, in the use of standard mixing-length theory to estimate the temperature gradient in an outer convective zone.

Figure 6-2-1 a illustrates the data for 47 Tuc which are the basis for this investigation. They include all of the stars having $13.6 < V < 14.2$ from the HHVASS composite C-M diagram (see their Fig. 15). The sample of CCD photometry includes 78 stars identified as horizontal branch objects. Although the density of points along the RGB is not indicative of the cluster luminosity function, the *HB* stars which have been plotted do represent a complete sample of data obtained by reliable CCD photometry. It is readily apparent that the majority of *HB* stars have intrinsic $B-V$ colours in the range $0.72 \leq (B-V)_0 \leq 0.82$ on the standard assumption that the foreground reddening amounts to $E(B-V) = 0.04$ mag, and that the mean visual magnitude is approximately 14.06.

Figures 6-2-1 b and c display the ZAHB (crosses) and evolutionary sequences which have been computed for a metal abundance $Z = 0.003$ and helium contents $Y = 0.3$ and $Y = 0.2$ respectively. The tracks have been marked at approximately ten million year intervals in order to show the expected observable density of stars on the C-M diagram.

Distance moduli to clusters are often derived by assuming a value for the magnitude of the ZAHB; the horizontal branch is observed to be truly 'horizontal' for a large number of clusters. This phenomenon can be related to the theory by

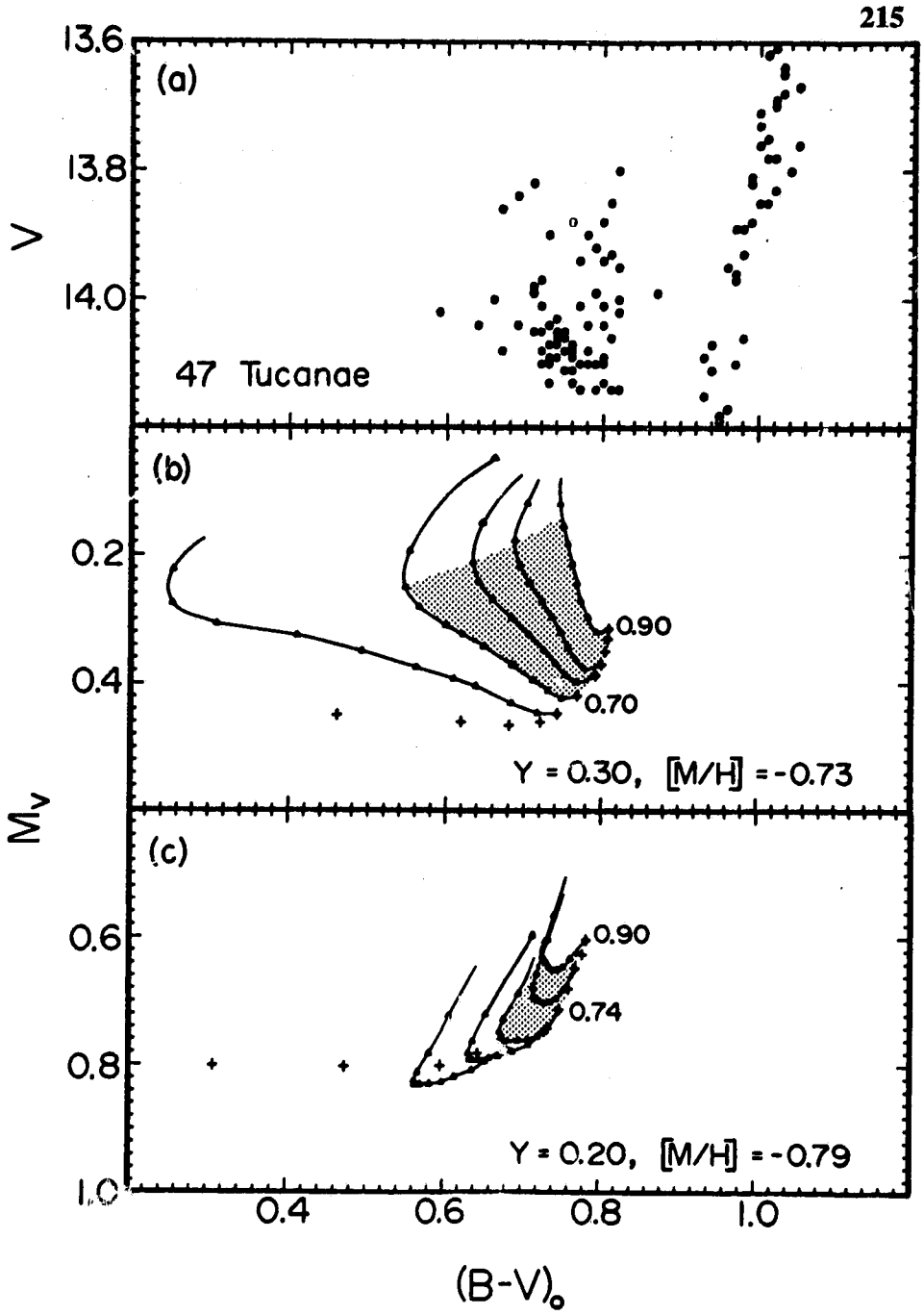

Fig. 6–2–1 (a) Data for 47 Tuc from the HHVASS composite color–magnitude diagram. (b) Evolutionary tracks for Y = 0.30 , Z = 0.003. Locations of ZAHB models are marked with crosses. Triangles mark intervals of 10^7 years of elapsed time from the ZAHB position. The shaded region indicates where the majority of horizontal branch stars should be found if if the masses of the stars lie between 0.70 and 0.90 Mo . (c): As for (b), but assuming Y=0.20 . The shaded region here indicates the expected HB shape for masses distributed between M/Mo = 0.74 and 0.90 .

Table 6-2-2: Zero Age Horizontal Branches[a]

$M/M_\odot$	M_{bol}	$\log T_e$	$\log g_s$	$(B-V)$	M_V
		(a) $Y = 0.20$, $Z = 0.003$ *models*			
0.90*	0.335	3.693	2.356	0.786	0.605
0.86	0.363	3.694	2.352	0.781	0.627
0.82*	0.394	3.696	2.353	0.772	0.649
0.78	0.434	3.698	2.356	0.763	0.681
0.74*	0.478	3.701	2.361	0.751	0.714
0.70*	0.530	3.706	2.376	0.731	0.749
0.66*	0.596	3.717	2.424	0.682	0.774
0.64	0.629	3.726	2.457	0.646	0.783
0.62	0.679	3.737	2.508	0.597	0.802
0.60	0.748	3.769	2.649	0.476	0.805
0.58	0.871	3.895	3.189	0.137	0.875
0.56	1.073	4.037	3.822	− 0.081	1.585
0.54	1.364	4.155	4.394	− 0.134	2.524
		(b) $Y = 0.30$, $Z = 0.003$ *models*			
0.90*	0.030	3.688	2.215	0.812	0.316
0.86	0.048	3.689	2.204	0.811	0.333
0.82	0.071	3.689	2.196	0.808	0.352
0.78*	0.097	3.691	2.190	0.803	0.372
0.74*	0.121	3.693	2.184	0.795	0.389
0.70*	0.175	3.698	2.203	0.772	0.419
0.66*	0.226	3.704	2.222	0.745	0.448
0.62	0.295	3.718	2.279	0.683	0.466
0.60	0.329	3.746	2.388	0.566	0.424
0.58	0.415	3.771	2.509	0.470	0.460
0.56	0.541	3.927	3.169	0.023	0.593
0.54	0.779	4.084	3.877	− 0.109	1.537

[a] *Masses with depicted evolutionary sequences are asterisked*

noting that for fixed values of the metal abundance, the zero-age models, for a range in M_*, form a sequence with nearly constant luminosity. In contrast, for metal-rich models with relatively high mass, the red end of the ZAHB is more vertical than horizontal. Indeed, for 47 Tuc and other clusters with red horizontal branches, the horizontal blueward extension of the *HB* is not populated: the observed stellar distribution has a large vertical spread, and the ZAHB luminosity is

Table 6-2-2: (continued)

$M/M_\odot$	M_{bol}	$\log T_e$	$\log g_s$	$(B-V)$	M_V
		(c) $Y = 0.20$, $Z = 0.006$ *models*			
0.90*	0.392	3.675	2.308	0.879	0.743
0.86	0.418	3.676	2.301	0.877	0.765
0.82*	0.448	3.677	2.298	0.871	0.788
0.78	0.487	3.679	2.299	0.863	0.818
0.74*	0.523	3.682	2.302	0.851	0.842
0.70*	0.573	3.687	2.318	0.830	0.869
0.66*	0.624	3.695	2.345	0.797	0.885
0.64	0.662	3.701	2.370	0.773	0.899
0.62	0.707	3.709	2.408	0.737	0.912
0.60	0.759	3.728	2.491	0.660	0.901
0.58	0.841	3.760	2.637	0.532	0.908
0.56	0.983	3.912	3.287	0.089	0.997
0.54	1.265	4.085	4.073	− 0.105	2.014
		(d) $Y = 0.30$, $Z = 0.006$ *models*			
0.90*	0.100	3.671	2.172	0.910	0.473
0.86	0.113	3.670	2.157	0.911	0.487
0.82*	0.133	3.671	2.146	0.910	0.504
0.78	0.154	3.672	2.146	0.905	0.519
0.74*	0.184	3.674	2.135	0.896	0.538
0.70*	0.219	3.678	2.139	0.881	0.554
0.66*	0.261	3.682	2.148	0.862	0.576
0.64	0.296	3.686	2.164	0.845	0.593
0.62	0.335	3.693	2.195	0.814	0.601
0.60	0.371	3.702	2.232	0.775	0.598
0.58	0.421	3.717	2.296	0.713	0.592
0.56	0.497	3.756	2.468	0.551	0.564
0.54	0.656	3.945	3.272	− 0.001	0.747
0.52	1.022	4.137	4.169	− 0.131	2.063

poorly defined. A real uncertainty also arises in matching the observed luminosity of horizontal branch stars to theoretical models because the zero-age sequence (formed from models of progressively lower masses) may approximately coincide with the evolutionary track of a single star. For instance, the seven faintest points in the 47 Tuc horizontal branch data (see Fig. 6-2-1a) are either all approximately

Table 6-2-2: (continued)

$M/M_\odot$	M_{bol}	$\log T_e$	$\log g_s$	$(B-V)$	M_V
		(e) $Y = 0.24$, $Z = 0.004$ *models*, $[O/Fe] = 0$			
0.90*	0.297	3.684	2.307	0.831	0.604
0.86	0.325	3.685	2.300	0.829	0.630
0.82	0.353	3.686	2.295	0.825	0.652
0.78*	0.381	3.687	2.290	0.819	0.675
0.74*	0.415	3.690	2.290	0.809	0.698
0.70*	0.452	3.693	2.294	0.795	0.720
0.66	0.495	3.699	2.311	0.768	0.736
0.62	0.561	3.720	2.394	0.680	0.726
0.60	0.599	3.740	2.475	0.595	0.708
0.58	0.684	3.785	2.674	0.426	0.711
		(f) $Y = 0.24$, $Z = 0.004$ *models*, $[O/Fe] = 0.3$			
0.90*	0.251	3.682	2.278	0.842	0.568
0.86	0.283	3.683	2.274	0.840	0.597
0.82	0.314	3.683	2.269	0.836	0.625
0.78	0.346	3.685	2.265	0.831	0.651
0.76*	0.366	3.686	2.266	0.827	0.667
0.70*	0.420	3.690	2.269	0.808	0.701
0.66*	0.461	3.695	2.281	0.786	0.719
0.62	0.523	3.707	2.327	0.735	0.735
0.60	0.539	3.724	2.384	0.666	0.694
0.58	0.611	3.751	2.509	0.552	0.697

at the zero-age locations appropriate to varying masses, or represent a set of stars of about the same mass at slightly different stages of life. The difference in luminosity between the evolved and unevolved stars, and the corresponding distance estimates, tends to grow as hotter stars are considered. Certainly the lower bound of the 47 Tuc data sample, which is quite steeply sloped from upper left to lower right, is not reproducible using zero-age models. That is, the observed morphology can be explained by adducing only evolution (*cf.* Lee, Demarque and Zinn 1987).

In order to model the shape of the observed distribution of stars on the horizontal branch, we require that *(i)* the theoretical calculations reproduce the sharp

cut-off in the data at $(B - V)_0 = 0.82$, *(ii)* the evolution proceed, essentially, to higher visual magnitudes, and *(iii)* the predicted magnitude spread, or the *luminosity width* of the sequences, mimic that of the observations. To these, we can add the 'external' constraint that *(iv)* the observed gap between the giant branch and the horizontal branch should be reproduced by the theoretical sequences (allowing for some uncertainty due to photometric scatter). While the breadth of the gap depends to some extent on age and metal abundance, the main usefulness of this feature is to provide some needed guidance as regards the probable size of temperature and/or colour errors of the models. The difference in T_{eff} or colour of two models having comparable luminosities is much more likely to be correct than the predicted absolute values of either of these quantities – especially if the models are located fairly close to each other on the HR diagram. Thus, if the absolute magnitude scale of the observations is set, the colour shift which must be applied to the theoretical calculations in order to achieve a simultaneous coincidence with the observed *HB* and RGB locations provides a reasonable estimate of the errors in the model colours, if, in all other respects (*e.g.*, the assumed composition), the properties of the latter match those of the real stars. Furthermore, by bridging the comparison between theory and observation from the *HB* to the RGB, the interpretation of the the horizontal branch data is not made in isolation from the rest of the C-M diagram.

Before discussing the detailed fits of the evolutionary computations to the 47 Tuc photometry, further comments about Figure 6-2-1 are in order, especially since the main result of this study can be anticipated from the comparison presented therein. Consider first the middle panel and recall that symbols have been located on each track to mark every interval of 10^7 years of elapsed time from the ZAHB position. Something which is true of all evolutionary sequences, but shown most clearly in the case of the $0.7\,M_\odot$ track, is that the rate of evolution is fairly uniform from the ZAHB to the blueward 'nose', and thereafter increases

rapidly as the model evolves back to the red. Since the most blueward point is reached between 80 and 90 million years beyond the zero-age location, while the total lifetime before the rapid ascent to the AGB is about 105 to 115 million years (the timescales depending on the envelope helium abundance), approximately 80 percent of the stars should be found between the ZAHB and the locus connecting the bluest points of each track. So, for instance, if the masses of the *HB* stars lie in the range $0.7 \leq M/M_{\odot} \leq 0.9$, the majority of the stars should be found in the shaded region shown in Figure 6-2-1b. A visual intercomparison of the middle with the uppermost panel suggests that, if these particular models apply, then the masses of the 47 Tuc horizontal branch stars tend to be concentrated towards the lower end of the aforementioned range. However, one has the distinct impression that the observed density of stars at higher luminosities and temperatures (*i.e.*, in a later evolutionary stage) is too low. In other words, the region on the observed $C - M$ diagram where the stars give the impression of a roughly uniform distribution is much smaller than that predicted by the $Y = 0.30$ sequences.

The case of $Y = 0.20$ given in Figure 6-2-1c is even more problematical. Again, the density of points along the tracks indicates where the stars will spend most of their lifetimes, and it is clear that the region on the C-M plane that is expected to be most heavily populated must curve from lower left to upper right – quite unlike what is seen in the case of 47 Tuc. As an illustrative example, if the *HB* stars had masses between 0.74 and $0.90\,M_{\odot}$, then nearly all of the stars should be found in the shaded region in Fig. 6-2-1c. Obviously, it does not matter what assumption is made about the masses of 47 Tuc stars as it is simply not possible to obtain a predicted *HB* morphology that looks like that observed from this choice of Y.

As we will now show, this impression is confirmed by the detailed matching of the evolutionary tracks to the photometry of 47 Tuc. Illustrated in Figure 6-2-2 are our 'best fits' of the models for $Z = 0.003$ and $Z = 0.006$, on the assumption of

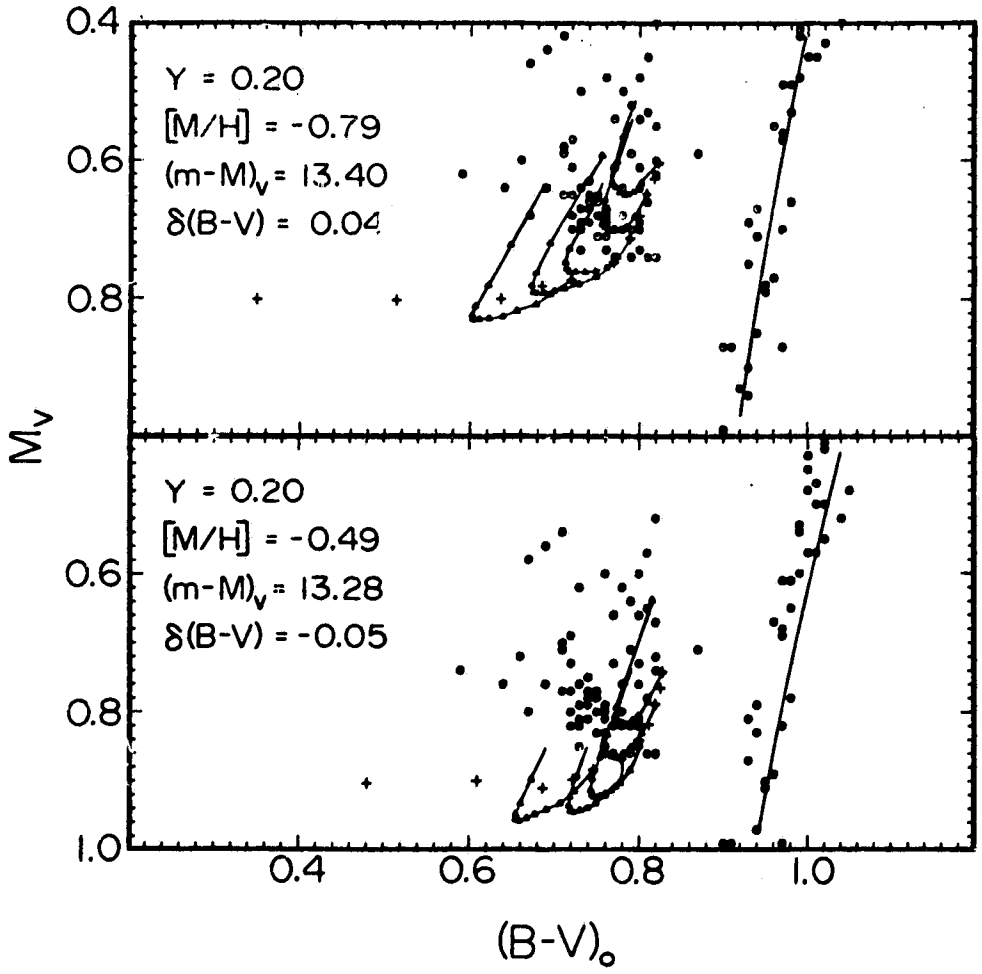

Fig. 6–2–2. Fits to HB data of evolutionary sequences for Y = 0.20 and metallicities (a) Z = 0.003 and (b) Z = 0.006 . The ZAHB models are indicated by crosses. Tracks are plotted for masses M/Mo = 0.90, 0.82, 0.74, 0.70, and 0.66.

$Y = 0.20$, to the cluster data. In these and the following plots, we have attempted to find the best possible coincidence of the predicted and observed HBs, subject to the constraint that the apparent gap between the horizontal branch and the red giant branch be reasonably well-matched by the model sequences. Note that age differences of a few billions of years do not significantly affect the giant branch location, so that our conclusions are not sensitive to our choice of giant evolutionary tracks for mass $0.9\,M_{\odot}$, which we have assumed throughout. Obviously, the fitting involves a certain amount of subjectivity; however, note that the magnitude scale has been considerably expanded and we would argue that the fits which we have adopted would deteriorate noticeably were our derived distance moduli or colour shifts altered by more than a few hundredths of a magnitude.

The quantity $\delta(B-V)$ given on the diagrams specifies the colour corrections which have been applied to the models in order to obtain the comparisons which are illustrated, given the value of $(m-M)_V$. Whereas the $Z = 0.003$ computations had to be shifted by 0.04 mag. to the red, those for $Z = 0.006$ were adjusted by 0.05 mag. to the blue. These colour adjustments should be interpreted in the following way. If, for instance, $Y = 0.2$ and $[m/H] = -0.79$ does accurately represent the chemical makeup of the cluster stars, then we would infer from the upper panel in Fig. 3 that the colours of the respective models tend to be too blue, for whatever reason, (*e.g.*, see VB85) by 0.04 mag. (Actually, we had initially applied shifts in T_{eff} to the models, but subsequently found that the temperature-independent colour corrections gave marginally better fits.)

However, it is clear from Fig. 3 that the models for $Y = 0.2$ fail to explain the morphology of the 47 Tuc horizontal branch. Because the stars are predicted to evolve downwards and to the blue in the C-M plane, the comparison between theory and observation leads to major inconsistencies. For example, in the lower panel, the dense grouping of stars at $M_V \approx 0.8$ and $(B-V)_0 \approx 0.74$ can only be matched by the extension of the least massive tracks to higher luminosities. But

this would mean that many stars are found where the evolution is particularly rapid, whilst no stars whatsoever are found where the rate of evolution is slowest (near the luminosity minimum of these sequences). Interestingly, the sensitivity of these arguments to metal abundance is very slight: the overall evolutionary behaviour is clearly very similar for models having the same Y but a factor of two difference in Z. In fact, it is an important result of this study that the conclusions which are reached concerning the cluster helium abundance are really quite independent of the controversy which has been surrounding the metallicity of 47 Tuc for some time (*e.g.*, Geisler 1986). Two points deserve particular emphasis. First, Figure 6-2-2 provides a persuasive argument that the initial helium abundance of 47 Tuc stars must have been greater than 20 percent by mass. Second, the apparent distance modulus of 47 Tuc is constrained to be greater than about 13.3 mag. This assumes, of course, that our adopted core masses are not substantially in error.

Figure 6-2-3 illustrates completely analogous comparisons, but for an assumed helium abundance $Y = 0.3$. The morphology of these computations, which tend to evolve upward and to the blue, is much closer in appearance to the observed distribution. Note that, in order to provide a simultaneous match of the *HB* and RGB, the higher metallicity sequences require a large blueward shift, which most probably indicates that a metal abundance $Z = 0.006$ is not appropriate for 47 Tuc. In addition, note that the assumption of high helium leads to a bright horizontal branch ($M_V = 0.4$ at $(B-V)_0 \approx 0.76$ in the $[m/H] = -0.73$ case) and consequently a large distance modulus. While such magnitudes conflict with the results of recent Baade-Wesselink studies of metal-rich RR Lyrae stars (*e.g.*, Jones *et al.*1988, Cacciari *et al.* 1989), the most compelling argument against the adoption of such a high value of the cluster helium content is that the colour and more importantly the luminosity spread of the observed *HB* is much smaller than that of the models. That is to say, the observations do not conform to the

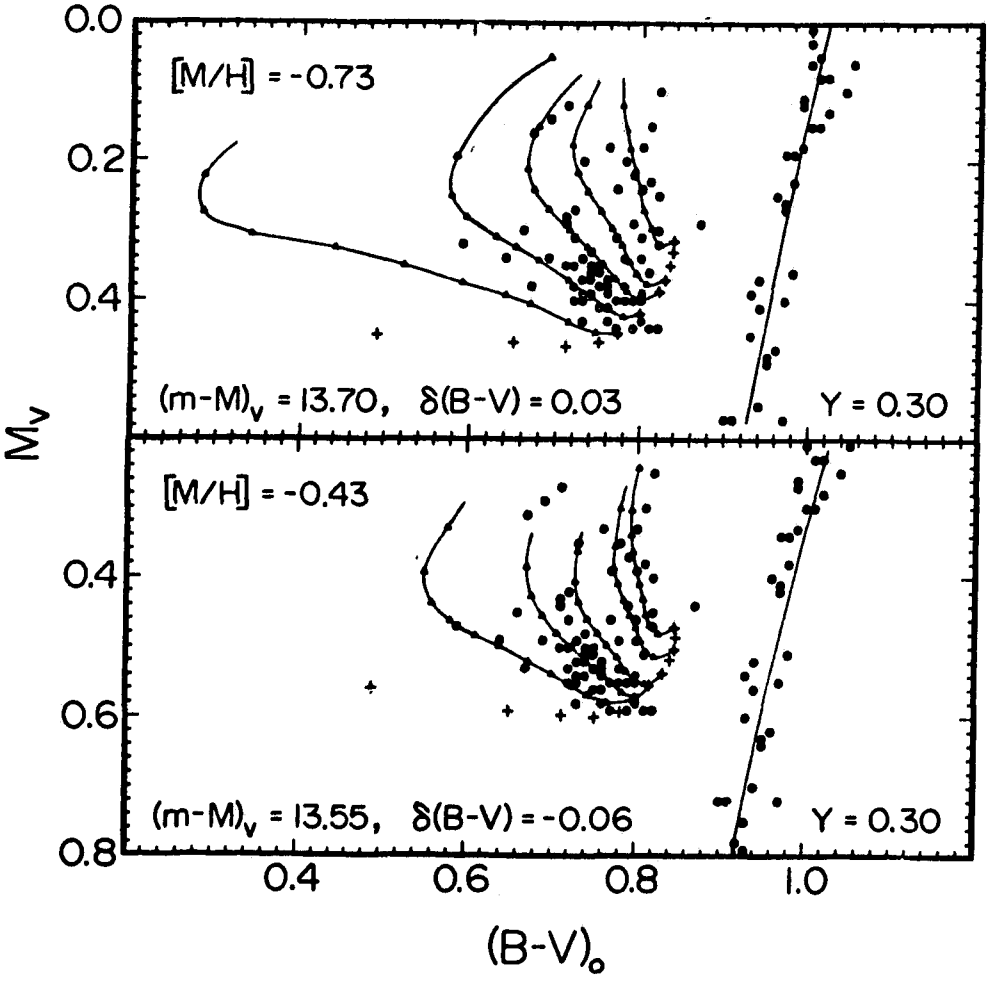

Fig. 6–2–3. As for Fig. 6–2–2, but with Y = 0.30 . In the upper panel, the tracks plotted are for M/Mo = 0.90 , 0.78 , 0.74 , 0.70 and 0.66 . In the lower panel, the track plotted are for M/Mo = 0.90, 0.82, 0.74, 0.70, and 0.66 .

prediction that they should be fairly uniformly distributed between the ZAHB and the curve connecting the bluest point of the tracks, over some appropriate mass range.

A natural conclusion from the above analyses is that a median value of the initial helium abundance should be selected. We have therefore chosen the composition parameters adopted by HHVASS in their study, namely $Y = 0.24$ and $[m/H] = -0.65$. Two cases are considered – one where all of the heavy elements have scaled-solar number abundance ratios, the other where only oxygen is enhanced above its scaled-solar value, by an amount corresponding to $[O/Fe] = 0.3$. The comparisons that result are presented in Figure 6-2-4 . Very encouragingly, the models now appear to be able to reproduce the observed C-M diagram rather well, as the quality of the fits is noticeably improved over those previously depicted. The thin scatter to the blue is to be expected: for lower mass models, the rate of blueward evolution is much higher and the relevant tracks span a larger range in luminosity. To be sure, a few stars – *e.g.*, those redder than the $0.9M_{\odot}$ tracks – may pose some problems in interpretation, but, on the whole, the morphology and the luminosity width of the observed data is well approximated by either set of models in this diagram.

In very good agreement with the findings of HHVASS, the derived distance modulus is $(m - M)_V = 13.44$ (independent of $[O/Fe]$). Our work therefore strengthens the case made by HHVASS that the age of 47 Tuc lies somewhere in the range of 13 – 14 Gyr. (It could be argued that there is a slight preference for a number near the lower end of this range as our distance is slightly higher than the 13.40 proposed in that study, but the uncertainties in the fit and the choice of Y, Z clearly encompass such a small difference in $(m - M)_V$.) Of some interest is the fact that the $[m/H] = -0.65$ models provide a fine match of the data without the need for any adjustment of the synthetic colours. On the basis of the most recent assessment of the Population II subdwarf standards (van Altena

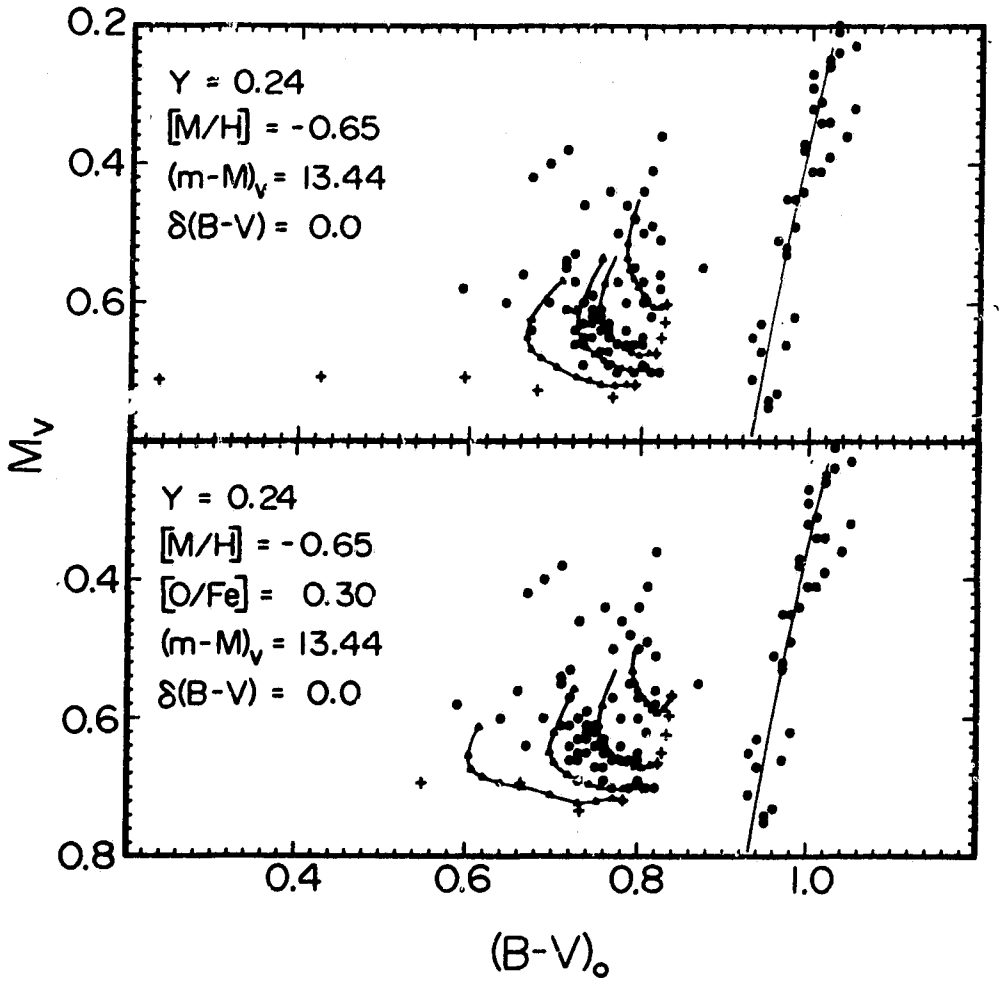

Fig. 6–2–4. Fits to HB data for Y = 0.24 , [Fe/H] = –0.65 , with (a) scaled–solar metal abundance and (b) [O/Fe] = 0.3 . In the upper panel, tracks plotted are for masses M/Mo = 0.90, 0.78, 0.74, and 0.70 : the bulk of the sample stars lie between the tracks for 0.74 and 0.78 Mo . In the lower panel, the tracks plotted are for masses M/Mo = 0.90, 0.76, 0.70, and 0.66 : the sample stars lie between the tracks for 0.70 and 0.76 Mo . Note the coincidence of the 0.78 Mo scaled solar calculation with the oxygen–enhanced 0.76 Mo track.

et al. 1988), VandenBerg (1988c) has suggested that the VB85 isochrones, computed using basically the same physics as the present models, are too blue by 0.02 mag. If a correction of this amount were applied to the theoretical calculations discussed here, then a metal abundance slightly lower than $[m/H] = -0.65$ would be indicated. But again, such small differences are within the uncertainties of the kinds of comparisons that we have made in this investigation.

The major difference between the models computed using scaled solar and enhanced oxygen abundances is a shift in the derived mass of the bulk of the sample stars. The higher oxygen abundance allows the hydrogen shell to burn at lower temperatures, and the blueward motion is damped. Thus the oxygen-enhanced models tend to act like scaled-solar models of slightly higher mass. Indeed, it is a real advantage of our fitting procedure that fairly precise estimates can be made of the masses of *HB* stars. For example, according to Figure 6-2-4a and Table 6-1-2, the majority of the stars in the sample have masses predicted to be in the range $0.74 \leq M/M_{\odot} \leq 0.78$ if $[O/Fe] = 0$. The comparisons also suggest that some stars undergo little, if any, mass loss.

6.2.iv Summary and Discussion

New theoretical sequences for horizontal branch evolution, in which canonical semiconvection is treated to high accuracy, have been computed for the ranges in Y, Z and [O/Fe] that are believed to bracket the composition of 47 Tuc stars. On the basis of morphology and timescale arguments, it has been possible to rule out the assumptions that the initial helium content of the cluster was as low as twenty percent (provided that the only change in the envelope abundance of member stars occurred during the first dredge-up on the RGB), or as high as $Y = 0.3$. Indeed, the comparisons that have been made indicate that the gas out of which the stars formed must have contained about 24% helium by mass. This estimate is made precise by the high sensitivity of the predicted *HB* morphology to helium abundance. (Although this is readily apparent from the SG76, S87 calculations, it has not, to our knowledge, previously been used to determine cluster compositions.) Also worth reiterating is the fact that the value of Y derived from the horizontal branch appears to be insensitive to the choice of Z or oxygen abundance, at least to within a factor of two. Interestingly, Sandage (1987) has suggested, from a careful study of a number of globular cluster $C - M$ diagrams and from period-luminosity-amplitude data for member *RR* Lyrae stars, that the vertical width of the *HB* varies directly with metal abundance. Clearly, similar studies should be undertaken of GCs with different metallicities since, if the suggestion from this work is correct (that Y may be determined to within $0.01 - 0.02$), it should be possible to ascertain if, and how, Y varies with Z among the globulars.

Of course, the conclusion that $Y \approx 0.24$ in 47 Tuc is not entirely unexpected. As is well known, this result is fully consistent with current estimates of the primordial helium abundance (*e.g.,* Boesgaard and Steigman 1985, Yang *et al.* 1985) and with the results of the R-method analyses of many other Galactic GCs (Buzzoni *et al.* 1985, Caputo *et al.* 1987). But what this investigation has done is to

show that not only the star counts, but also the distribution of the stars on the C-M diagram can be explained by theoretical models *only* if the helium abundances is close to our derived value. The fine overall consistency which has been obtained could be viewed, alternatively, as evidence that modern evolutionary theory with semiconvection provides a plausible description of how stars evolve.

Since the abundance parameters of the models which best reproduce the 47 Tuc horizontal branch data are the same as those adopted by HHVASS, and additionally the distance modulus ($(m-M)_V = 13.4$) found in that study is very similar to ours, their derived age of ≈ 13.5 Gyr has been given added weight. This age is probably one of the most reliable such estimates yet made for any GC, simply for the reason that there is no clear conflict between any of the observed properties of 47 Tuc and the predictions of standard stellar evolutionary theory. At the same time, it should be appreciated that the present results depend strongly on the accuracy and comprehensiveness of the observations. Some concern may be raised, for example, by the fact that the Lee (1977) data, containing 365 *HB* stars, suggest that the horizontal branch spans a wider colour range and is more uniformly populated both in colour and luminosity. We expect, though, that our conclusions would be very similar, and perhaps the matching even more convincing, if the Lee dataset in fact *does* accurately reflect the cluster *HB* morphology. For example, the slight gap between the redder horizontal branch stars and the main clump of the distribution would be filled, so that a small redward shift of our models, in line with other findings about our adopted temperature-colour calibration, would be necessary. However, the photographic photometry available at the time was incapable of producing the high internal precision now possible with CCDs, and we have chosen instead to assume that the differences between the samples might only be a reflection of the relative accuracy of the detectors. Fortunately, extensive new datasets for the bright stars in several GCs will soon be made available by Bergbusch (1989). When compared with modern computations in the way that

has been done here, these data can be expected to have a significant impact on our understanding of the globular clusters in our Galaxy.

6.3 On the Helium Abundance of M15 and the Sandage Effect

6.3.i Foreword

This study was carried out in the Fall of 1989, again before the final choice of physical inputs for the major part of the calculations was made. Here, the differences in the interior physics are the adoption of the 1985 (Caughlan *et al.* 1985) tabulation of nuclear reaction rates, and again, the use of the EFF equation of state through to the centre of the star. Since Synthetic Horizontal Branch calculations using the new set of evolutionary tracks have not yet been derived, in this case the afterword on this study will show the fit to the data, and the implied distance modulus, which follow from the new sequences. The location in the period-colour diagram of the RR Lyrae variables will also be demonstrated.

6.3.ii Introduction

For objects in an advanced stage of evolution such as the horizontal branch, analyses of surface abundances and their implications for evolution are complicated by the fact that modification of CNO elemental abundances may have taken place earlier on in their history, rather than being 'primordial', *i.e.*, reflecting the material out of which the stars formed. There is evidence, for example, suggesting convective dredge-up of nuclear-processed material to the stellar surface during the red-giant phase (*e.g.*, see Smith 1987; Sneden, Pilachowski, and VandenBerg 1986). These mixing phenomena are not explained by canonical assumptions about stellar evolution (but see Sweigart and Mengel 1979; for other implications of deep mixing, see VandenBerg and Smith 1988). However, recent work, (Abia and Rebolo 1989) indicates that even unevolved halo stars show a rising, nearly linear trend of oxygen overabundance with decreasing metallicity. According to their results, stars with [Fe/H] ~ -2.2 have [O/Fe] values near 1.1. Although it is controversial that globular cluster stars have such high oxygen contents (Pilachowski 1988), it is

possible that accurate fits of stellar evolutionary calculations to cluster data may be obtained only if this factor is taken into account.

A major part of the fundamental question of galactic chemical evolution is the study of the halo field and cluster populations. There is mounting evidence in support of the possibility that the metal-poor stars of the outer halo are composed of material in which oxygen is observed to be 'overabundant' with respect to iron ($[O/Fe] > 0$). For instance, spectroscopic analyses of cluster giants show oxygen to iron ratios which are much greater than the solar value (Kraft 1985 and references therein). According to current theories for massive star evolution (Maeder 1985), a large quantity of oxygen is produced in and liberated by the more massive type II supernovae (along with the so-called α-nuclei elements), while the enrichment of iron results from less massive objects which detonate later in galactic history (Matteucci 1987). The relative enhancement of these elements over solar ratios would therefore be consistent with the hypothesis that the halo stars formed at an earlier epoch in galactic history than the disk, and this must be related to current pictures of galactic formation (*e.g.*, Eggen, Lynden-Bell, and Sandage 1962; Searle and Zinn 1978). With the availability of more sensitive electronic detectors, high-resolution spectroscopic techniques have been used to derive abundances for both highly evolved and unevolved objects, and the science of abundance determinations has become the subject of numerous studies over the last ten years (*e.g.*, Gehren 1988; Wheeler, Sneden, and Truran 1989, and references therein).

The purposes of this study are threefold: (i) to demonstrate that the dominant effect on HB morphology arising from heavy-element abundance is, in fact, the enhancement of nuclear reaction rates, especially for very low metallicities, (ii) to comment on the possible implications of our evolutionary calculations for the helium abundance of M15, and (iii) to compare our theoretical predictions for the properties of RR Lyrae variables with those observed, to try to resolve the apparent discrepancies between observed and predicted period shifts among

globular clusters.

6.3.iii Method and Data

Before presenting the evolutionary calculations and fits to the cluster data, we pause to summarize the method and to discuss the data and their limitations for this purpose. It is our central hypothesis that horizontal branches have finite intrinsic widths which are a reflection of the envelope helium content (Y_{HB}) of stars evolving onto the ZAHB, the post-helium-flash stellar sequence. In principle, the lower bound of the observed HB distribution on the colour-magnitude diagram is associated with the ZAHB, while the upper envelope of the observations is represented by the late stages of HB evolution. A population of HB stars arriving on the zero-age sequence at random points in time, after having suffered variable amounts of mass loss, will 'fill in' the region of the HR diagram spanned by the evolutionary tracks of appropriate masses. The reality of the width of HB sequences was long suspected but could not be conclusively shown until CCD photometry and sophisticated computer-assisted photometric analysis became possible. Accurately fitting the observed HB morphology enables us to find the envelope helium abundance – since the luminosity width of evolutionary tracks is an increasing function of Y_{HB} – and to derive values for the absolute magnitudes of the stars. This, in turn, allows us to determine the cluster distance modulus from the horizontal branch visual magnitude, even in the case (as for 47 Tuc) that the 'horizontal' part of the HB is not populated. However, for clusters with blue horizontal branches, a problem of identification arises because of the similarity of the evolutionary tracks towards core helium exhaustion to the shape of the zero-age sequence. Within the level of both theoretical and observational uncertainties which are still prevalent, it is possible to associate data points within the instability strip with either the ZAHB or with the models close to core helium exhaustion. This problem is at the heart of the controversy surrounding the Sandage Period-Shift effect (Sandage

1982a; Lee, Demarque and Zinn 1990, hereafter LDZ).

Additional evidence for the nature of M15 horizontal-branch stars is provided by a relatively large population of RR Lyrae variables. These have been particularly well-studied, and both Bingham *et al.* (1984, hereafter BCDF) and more recently Sandage (1990b) have claimed that the luminosity to mass ratio for the fundamental-mode, RR ab-type variables – or more precisely the parameter $A = \log(L/M^{0.81})$ – is much greater for this cluster than for Oosterhoff group I clusters like M3. In other words, the observations predict a different sensitivity of this quantity to metallicities than the theoretical models. This is the basis of the Sandage Period-Shift Effect (Sandage 1982a) as derived from the 'observed' period-temperature relationship. Recently, LDZ have suggested that the fundamental mode pulsators in the Oosterhoff group II clusters (*e.g,* M15 and M92) are, in the main, evolving redward during late evolution, thus increasing the theoretical period shift between these clusters and systems such as M3. That is, in the group II clusters, the variables are suggested to be brighter and less massive than newly formed HB stars at the same mean effective temperature, and so have longer periods than would be predicted from the ZAHB models. The fact that there is no significant HB population redward of the instability strip is taken as support for this suggestion. In contrast, the cluster M3 has a large number of red HB stars, implying that all phases of HB evolution should be represented in the instability strip.

The subject of RR Lyrae masses has also been a matter of considerable debate. The period ratio (first-overtone to fundamental) for double-mode pulsators allow us to determine the mass using the theoretical Petersen (1973) diagram. According to Cox, Hodson, and Clancy (1983), the masses of these variables are substantially smaller than those predicted from evolutionary tracks which pass through the instability strip; but the size of the apparent discrepancy has been questioned by Kovács (1985). The existence of the double mode pulsators apparently places

constraints on Y_{HB}, or at least on the helium abundance in the pulsational-driving helium ionization zones. Cox (1987) maintains that a large upper envelope helium content ($Y \gtrsim 0.29$) is necessary for stable double-mode pulsations.

As well as the helium abundance, the other composition parameters referred to in the previous section, *viz.* CNO and heavy-element abundance, can affect the appearance of the HB. As far as pulsation is concerned, we have shown how the oxygen abundance affects the masses of stars in the instability strip. In this section, we examine the morphology of the HB and discuss the evidence we can bring in favor of, or contrary to, the above suggestions.

The ideal dataset for this method would, of course, be large, complete samples of HB stars, with high photometric accuracy. However, probably the most complete sample available to us for the cluster in question is the photographic data of Buonanno *et al.* (1983, our Figure 6-3-1 a). The giant branch of these observations, however, has a width of 0.1 – 0.2 mag in colour which, if real, would require that the cluster population contains significant inhomogeneity in chemical composition. Since there is no other observational evidence for this, we assume that the giant branch is intrinsically fine. This places limits on the precision to which we may draw conclusions from these data either about the stellar distribution in colour or about the luminosity width.

An alternative data sample for the non-variable stars is provided by the recent work of Sandage (1990a; our Figure 6-3-1b), which contains previously unpublished results from a survey that was also used for the Sandage, Katem, and Kristian (1968) study. These data include a number of horizontal-branch objects above V $\sim$ 16 which is similar in size to that of the Buonanno *et al.* HB sample. The two figures incorporate the careful treatments of the location of RR Lyrae variables, given by BCDF (their Table 8) and by the Sandage paper referred to above, respectively. Different methods have been used to define the colour of the 'equivalent

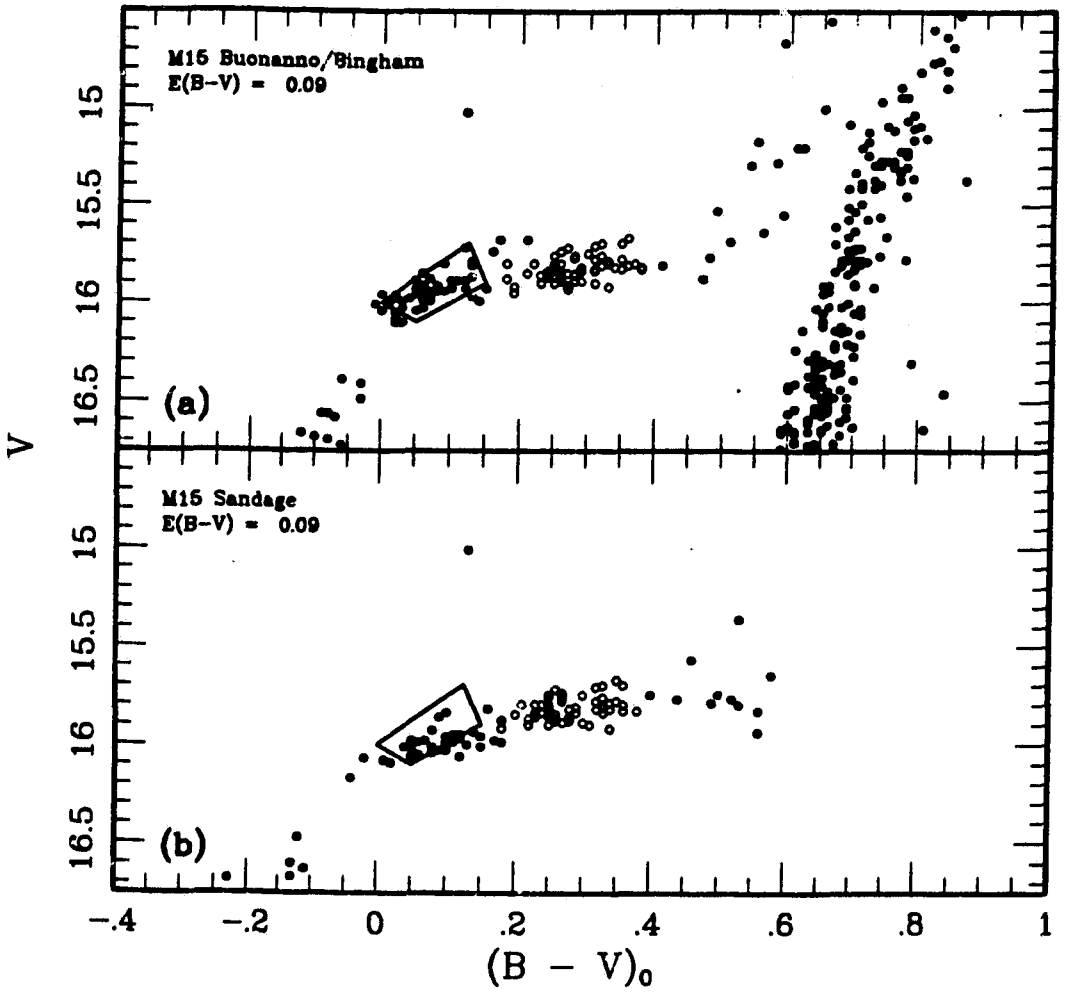

Figure 6–3–1: Photographic data for M15 from two different studies. (a) Buonanno *et. al.* 1983 with RR Lyrae data from Bingham *et. al.* 1984, (b) Sandage 1990a. In these and all subsequent diagrams, open circles denote RR Lyrae variables. The frame was drawn to enclose the blue star distribution of the data in (a); it is reproduced in (b)

static star', $(B-V)_{eq}$ (see Preston 1961), but their resulting distributions of variables, which appear in the range $0.27 < (B-V)_{eq} < 0.47$, are very similar. This is due in part to the fact that the selections of RR Lyraes are not independent; both papers draw data from the Sandage, Katem, and Sandage (1981) study.

The observations are concentrated in two main 'clumps': the variable stars, and the distribution lying beyond the blue end of the instability strip. In Figures 6-3-1a and b, all the variables listed by BCDF and Sandage are plotted, comprising 62 and 55 stars respectively. In all subsequent diagrams, only the variables taken from the same fields as the non-variable stars are shown, containing 30 and 23 data points. In the upper panel, the apparent width of the blue non-variable distribution appears much greater, and the brightness of its lower envelope is a few hundredths of a magnitude higher in the V-band. In contrast, the lower panel seems to contain a larger number of objects close to the ZAHB. To emphasize the differences between the two samples, we have framed the distribution of blue stars in the upper panel, and plotted the same frame in the lower panel.

6.3.iv Results

We have computed a number of horizontal-branch tracks for selected values of Y_{HB} and [O/Fe] for the heavy-element abundance $Z = 10^{-4}$. Zero-age sequences for these calculations are listed in Table 6-3-1.

Our computations are referred to the observational plane using bolometric correction and temperature colour calibrations given by Kurucz (1979). As for the reddening to M15, commonly adopted values are in the range 0.10 ± 0.02. Comparisons of observed to theoretical HB morphology are not seriously affected by uncertainties in reddening of this order. However, this is far from being the case with pulsational properties: differences in the derived temperature cause the radius estimate for a given model to vary strongly with the adopted intrinsic colour. Since the periods are well-determined, the resultant uncertainty falls to the luminosity-

Table 6-3-1: Zero Age Horizontal Branches

$M/M_\odot$	$\log L/L_\odot$	$\log T_e$	M_V	$(B-V)$	$\log g_s$
(a) $Y = 0.208$, $Z = 0.0001$, [O/Fe] $= 0$ *models*					
0.560	1.3399	4.2369	3.0574	−0.1684	4.7401
0.580	1.3747	4.1909	2.6913	−0.1495	4.5365
0.600	1.4105	4.1490	2.3532	−0.1326	4.3481
0.620	1.4476	4.1084	2.0276	−0.1156	4.1627
0.640	1.4835	4.0690	1.7232	−0.0989	3.9828
0.660	1.5167	4.0306	1.4391	−0.0758	3.8094
0.680	1.5464	3.9939	1.1840	−0.0468	3.6459
0.700	1.5727	3.9595	0.9773	−0.0178	3.4948
0.720	1.5960	3.9275	0.8346	0.0220	3.3558
0.740	1.6163	3.8982	0.7256	0.1287	3.2298
0.760	1.6348	3.8714	0.6774	0.1902	3.1160
0.780	1.6515	3.8473	0.6537	0.2429	3.0140
0.820	1.6809	3.8074	0.6311	0.3318	2.8466
0.860	1.7061	3.7832	0.6032	0.3925	2.7455
0.900	1.7284	3.7719	0.5714	0.4198	2.6978
(b) $Y = 0.211$, $Z = 0.0001$, [O/Fe] $= 0.75$ *models*					
0.540	1.3120	4.2976	3.5044	−0.1934	4.9953
0.560	1.3455	4.2410	3.0684	−0.1703	4.7510
0.580	1.3845	4.1924	2.6759	−0.1504	4.5331
0.600	1.4353	4.1434	2.2584	−0.1309	4.3011
0.620	1.4897	4.0905	1.8235	−0.1090	4.0494
0.640	1.5390	4.0356	1.4096	−0.0813	3.7943
0.660	1.5797	3.9811	1.0436	−0.0393	3.5488
0.680	1.6123	3.9296	0.7978	0.0131	3.3233
0.700	1.6390	3.8807	0.6622	0.1668	3.1135
0.720	1.6604	3.8368	0.6406	0.2643	2.9285
0.740	1.6791	3.7974	0.6473	0.3546	2.7642
0.760	1.6951	3.7721	0.6527	0.4183	2.6587
0.780	1.7091	3.7634	0.6391	0.4395	2.6210
0.820	1.7326	3.7519	0.6028	0.4714	2.5734
0.860	1.7527	3.7456	0.5599	0.4915	2.5489
0.900	1.7699	3.7422	0.5190	0.5033	2.5378

to-mass ratio. We choose the value 0.09, for the reason that, as discussed below, it leads to a nice consistency between the evolutionary and pulsational properties of M15 horizontal branch stars (see also Caputo, Castellani, and Quarta 1984; LDZ).

Table 6-3-1 (continued)

$M/M_\odot$	$\log L/L_\odot$	$\log T_e$	M_V	$(B-V)$	$\log g_s$
		(c) $Y = 0.246$, $Z = 0.0001$, [O/Fe] $= 0$ *models*			
0.560	1.3436	4.2487	3.1199	−0.1736	4.7838
0.580	1.3875	4.2071	2.7572	−0.1563	4.5888
0.600	1.4347	4.1670	2.3983	−0.1409	4.3959
0.620	1.4825	4.1264	2.0420	−0.1245	4.2000
0.640	1.5267	4.0855	1.7036	−0.1074	4.0061
0.660	1.5654	4.0456	1.3957	−0.0889	3.8210
0.680	1.5988	4.0071	1.1162	−0.0591	3.6466
0.700	1.6275	3.9713	0.8834	−0.0317	3.4876
0.720	1.6522	3.9383	0.7176	−0.0019	3.3430
0.740	1.6737	3.9079	0.5921	0.0924	3.2117
0.760	1.6929	3.8802	0.5262	0.1668	3.0934
0.780	1.7100	3.8554	0.4952	0.2229	2.9884
0.820	1.7398	3.8142	0.4708	0.3134	2.8155
0.900	1.7876	3.7729	0.4184	0.4162	2.6429
		(d) $Y = 0.249$, $Z = 0.0001$, [O/Fe] $= 0.50$ *models*			
0.540	1.2960	4.2779	3.4217	−0.1851	4.9324
0.560	1.3416	4.2317	3.0214	−0.1661	4.7181
0.580	1.3996	4.1863	2.6011	−0.1483	4.4936
0.600	1.4646	4.1369	2.1472	−0.1289	4.2458
0.620	1.5230	4.0848	1.7090	−0.1074	3.9932
0.640	1.5707	4.0326	1.3147	−0.0799	3.7506
0.660	1.6093	3.9823	0.9748	−0.0415	3.5241
0.680	1.6404	3.9355	0.7399	0.0013	3.3185
0.700	1.6661	3.8915	0.5946	0.1392	3.1296
0.720	1.6875	3.8516	0.5543	0.2308	2.9607
0.740	1.7060	3.8158	0.5523	0.3094	2.8110
0.760	1.7221	3.7862	0.5551	0.3824	2.6879
0.780	1.7363	3.7714	0.5502	0.4195	2.6260
0.820	1.7608	3.7580	0.5205	0.4537	2.5695
0.860	1.7816	3.7510	0.4807	0.4743	2.5416
0.900	1.7999	3.7466	0.4402	0.4884	2.5253

We concentrate here on the morphology of the extended 'horizontal' sequence, but note in passing that the location of theoretical calculations for the faint blue tail of the HB on the colour-magnitude diagram is almost completely insensitive

Table 6-3-1 (continued)

$M/M_\odot$	$\log L/L_\odot$	$\log T_e$	M_V	$(B-V)$	$\log g_s$
		(e) $Y = 0.247$, $Z = 0.0001$, [O/Fe] $= 0.75$ *models*			
0.540	1.2965	4.2758	3.4073	−0.1842	4.9238
0.560	1.3444	4.2279	2.9913	−0.1645	4.7001
0.580	1.4114	4.1784	2.5242	−0.1454	4.4502
0.600	1.4851	4.1218	2.0092	−0.1229	4.1648
0.620	1.5468	4.0620	1.5277	−0.0978	3.8780
0.640	1.5946	4.0026	1.1054	−0.0566	3.6064
0.650	1.6143	3.9738	0.9265	−0.0348	3.4784
0.660	1.6319	3.9459	0.7870	−0.0108	3.3556
0.670	1.6473	3.9188	0.6806	0.0488	3.2387
0.680	1.6613	3.8925	0.6068	0.1361	3.1257
0.700	1.6849	3.8435	0.5690	0.2481	2.9186
0.720	1.7044	3.7997	0.5784	0.3476	2.7365
0.740	1.7209	3.7733	0.5835	0.4148	2.6261
0.760	1.7353	3.7614	0.5767	0.4444	2.5759
0.780	1.7478	3.7551	0.5583	0.4619	2.5492
0.820	1.7693	3.7462	0.5168	0.4896	2.5137
0.860	1.7878	3.7418	0.4733	0.5048	2.4987
0.900	1.8042	3.7394	0.4307	0.5140	2.4924
		(f) $Y = 0.252$, $Z = 0.0001$, [O/Fe] $= 1.00$ *models*			
0.540	1.2902	4.2514	3.2706	−0.1739	4.8321
0.580	1.4631	4.1336	2.1318	−0.1278	4.2193
0.600	1.5425	4.0603	1.5295	−0.0973	3.8616
0.620	1.5982	3.9871	1.0240	−0.0460	3.5269
0.630	1.6196	3.9521	0.8347	−0.0158	3.3725
0.640	1.6382	3.9177	0.7003	0.0522	3.2232
0.650	1.6541	3.8843	0.6218	0.1551	3.0806
0.660	1.6678	3.8525	0.6014	0.2281	2.9464
0.670	1.6803	3.8216	0.6073	0.2958	2.8166
0.680	1.6909	3.7940	0.6201	0.3616	2.7023
0.700	1.7094	3.7631	0.6373	0.4397	2.5726
0.720	1.7246	3.7549	0.6163	0.4623	2.5369
0.740	1.7374	3.7474	0.5951	0.4856	2.5062
0.780	1.7588	3.7402	0.5455	0.5106	2.4788
0.820	1.7764	3.7357	0.4918	0.5290	2.4645
0.860	1.7918	3.7333	0.4483	0.5392	2.4603
0.900	1.8058	3.7317	0.4101	0.5461	2.4600

Table 6-3-1 (continued)

$M/M_\odot$	$\log L/L_\odot$	$\log T_e$	M_V	$(B-V)$	$\log g_s$
		(g) $Y = 0.242$, $Z = 0.0004$, [O/Fe] = 0 *models*			
0.560	1.3496	4.2358	3.0142	−0.1681	4.7261
0.580	1.4123	4.1858	2.5543	−0.1484	4.4788
0.600	1.4845	4.1290	2.0398	−0.1260	4.1941
0.620	1.5484	4.0671	1.5387	−0.1002	3.8970
0.640	1.5979	4.0049	1.0952	−0.0592	3.6124
0.660	1.6364	3.9447	0.7577	−0.0091	3.3465
0.680	1.6666	3.8872	0.5745	0.1517	3.0993
0.700	1.6905	3.8344	0.5455	0.2760	2.8766
0.720	1.7099	3.7877	0.5618	0.3959	2.6826
0.740	1.7264	3.7650	0.5693	0.4621	2.5874
0.760	1.7405	3.7568	0.5524	0.4889	2.5523
0.780	1.7529	3.7497	0.5341	0.5138	2.5226
0.820	1.7738	3.7419	0.4907	0.5431	2.4923
0.900	1.8075	3.7345	0.3992	0.5732	2.4694
		(h) $Y = 0.281$, $Z = 0.0001$, [O/Fe] = 0.75 *models*			
0.540	1.2982	4.2627	3.3203	−0.1789	4.8696
0.580	1.4823	4.1538	2.2009	−0.1369	4.2811
0.600	1.5593	4.0887	1.6390	−0.1105	3.9582
0.640	1.6575	3.9611	0.7691	−0.0255	3.3776
0.650	1.6745	3.9314	0.6425	0.0054	3.2487
0.660	1.6895	3.9027	0.5421	0.1055	3.1256
0.670	1.7028	3.8751	0.4975	0.1752	3.0081
0.680	1.7146	3.8488	0.4855	0.2351	2.8977
0.700	1.7349	3.8003	0.4982	0.3449	2.6961
0.720	1.7520	3.7709	0.5096	0.4202	2.5737
0.740	1.7663	3.7583	0.5039	0.4532	2.5206
0.780	1.7903	3.7468	0.4620	0.4885	2.4735
0.820	1.8076	3.7407	0.4226	0.5099	2.4536
0.900	1.8423	3.7358	0.3262	0.5297	2.4397

to the parameters we discuss below. That is, all computed low-mass HB model sequences are able to reproduce its location, given the uncertainties in the photometry of the intrinsically faint blue stars. The apparently real gap just below the knee of the M15 HB at $V \approx 16.25$ (BCF) cannot be explained by models cal-

culated with a homogeneous set of parameters and a unimodal mass distribution as is assumed here – one can either reproduce the tail, and not the break in the HB sequence, or vice versa. The apparent coincidence of the position of the gap in M15 with the blueward edge of the HB's of NGC 5466 and M53 suggests that the horizontal branches of these clusters would be identical if it were not for some mechanism working in M15 that produces the blue tail (see BCF; LDZ). We have taken this view in the synthetic calculations, and adopt a small mass dispersion ($\sigma_M \approx 0.01$). Consequently, the populations of blue HB, RR Lyrae and red HB stars ($B : V : R$) in the present synthetic models are $B : V : R \approx 0.68 : 0.27 : 0.05$, in contrast to the observations ($B : V : R \approx 0.76 : 0.20 : 0.04$; see BCF)[1].

Figure 6-3-2 a shows the ZAHB locations for HB phase helium abundances Y_{HB} =0.208 and 0.246, for scaled-solar composition models. In Figure 6-3-2b, we show the ZAHB locations assuming $Y_{HB} \sim 0.246$, with [O/Fe] = 0, 0.50, 0.75 and 1.0 and scaled-solar abundances for all other metals. In both of these figures, the distance modulus has been chosen so as to fit the lower envelope of the Buonanno *et al.* data to the scaled solar sequence with $Y_{HB} \sim 0.246$. The value of the distance modulus required to reconcile the $Y_{HB} \sim 0.21$ set of models with the observed horizontal branch would be closer to 15.25 mag (but see the comment in §III concerning this set of calculations), and slightly less than 15.40 for the enhanced oxygen sequences in Figure 6-3-2b.

Note that the shape of the ZAHB does not change with helium abundance, whilst increasing the oxygen abundance draws the red end of the ZAHB to progressively lower temperatures, and the horizontal sequence to slightly lower luminosities, so that the most massive unevolved stars occupy a position close to the base of the AGB.

These diagrams show some evidence for a population of such stars in M15,

[1] *The Synthetic Horizontal Branch models presented here were computed by Young-Wook Lee.*

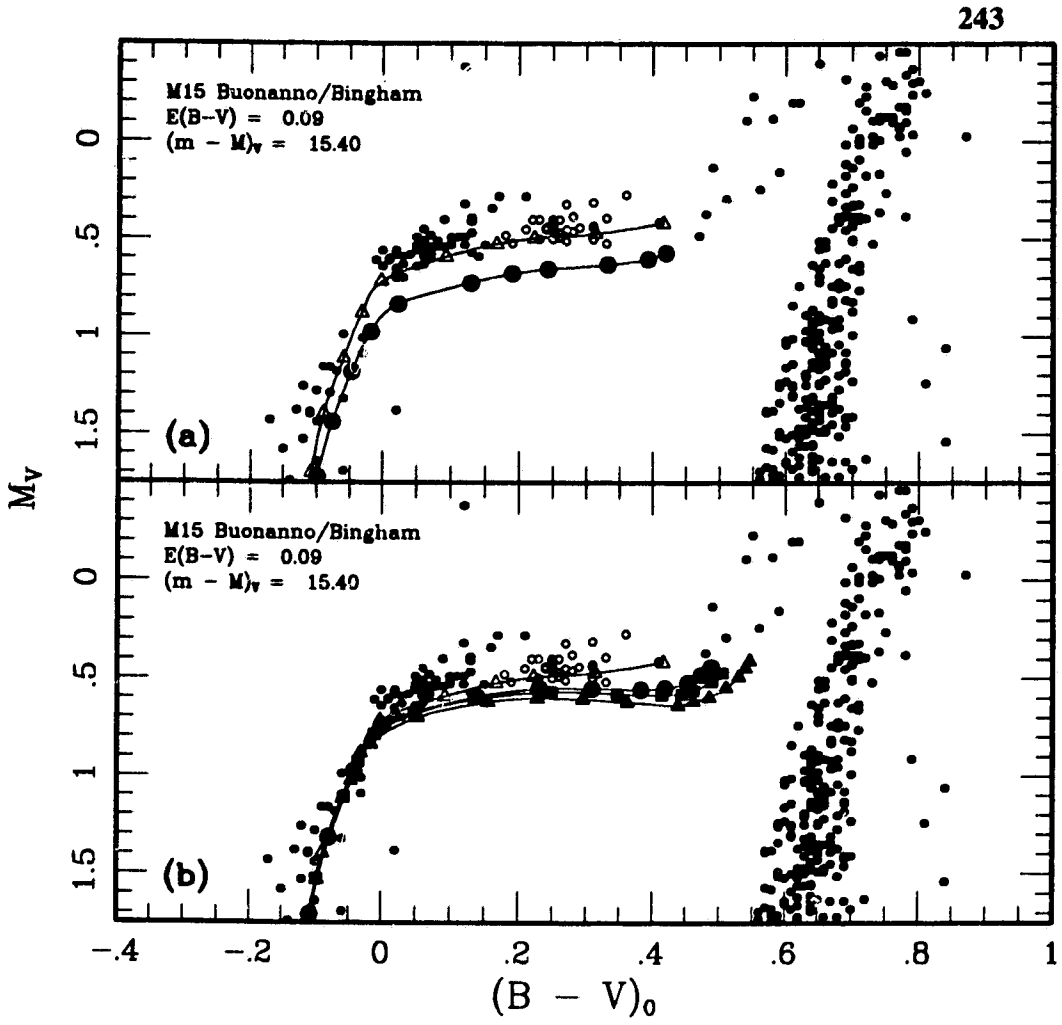

Fig. 6–3–2. ZAHB sequences superimposed upon Buonanno *et. al.* /Bingham *et. al.* observations (a) [O/Fe] = 0, Y_{HB} = 0.21 (circles), 0.25 (triangles) (b) Y_{HB} ~ 0.25 [O/Fe] = 0 (open triangles), 0.50 (squares), 0.75 (filled triangles), and 1.0 (circles). The distance modulus has been chosen in these figures so that the scaled–solar ZAHB for Y_{HB} ~ 0.25 fits the lower envelope of the data.

in view of a few data points which fall on the red ends of the oxygen-enhanced ZAHBs (assuming, of course, that they are cluster members). However, it is difficult to make a strong case, on this basis alone, for high oxygen content in these stars. The most obvious counter-argument (apart from non-membership) is that the fainter red points are highly evolved HB stars that are subject to some degree of photometric scatter. If this be the case, then either a scaled-solar or an oxygen-enhanced composition may provide acceptable matches to the observed shape of the stellar distribution [2].

Figures 6-3-3 and 6-3-4 show the results of scaled-solar evolutionary calcu-

[2] *This result is at odds with the conclusion reached by VandenBerg (1988b) who suggested that satisfactory fits of computed ZAHBs to the M15 horizontal branch could be achieved only if high* [O/Fe] *values were assumed. Notwithstanding some differences in the data and the fitting procedure, we have found that his conclusion is largely due to the scale of bolometric corrections employed in that study. For stars cooler than* $T_{eff} = 7000K$, *he used the relations given by Bell and Gustafsson (1978) and VandenBerg and Bell (1985), while those given by Kurucz (1979) were employed for hotter stars. Although zero-point adjustments were made so that all three scales were consistent with* $B.C._{\odot} = -0.12$ *mag, some systematic differences (i.e., as a function of* $[m/H]$*) remain. In particular, the Kurucz B.C.'s are smaller than those of Bell and Gustafsson/VandenBerg and Bell by about 0.06 mag at* $T_{eff} = 7000K$ *and* $[m/H] = -2$, *even when they have first been corrected to give essentially identical bolometric corrections for solar abundances. Based on interpolations between the available B.C.'s in the range* $6000 \leq T_{eff} \leq 8000K$, *VandenBerg (1988b) produced a ZAHB for scaled-solar abundances for which the appearance on the colour-magnitude diagram was much steeper than for the corresponding oxygen-rich sequence. This arose from a greater sensitivity of the bolometric corrections to changes in the surface temperature at the slightly higher surface gravities of these models. This highlights the critical importance of the bolometric corrections and colours to the type of analysis we have undertaken.*

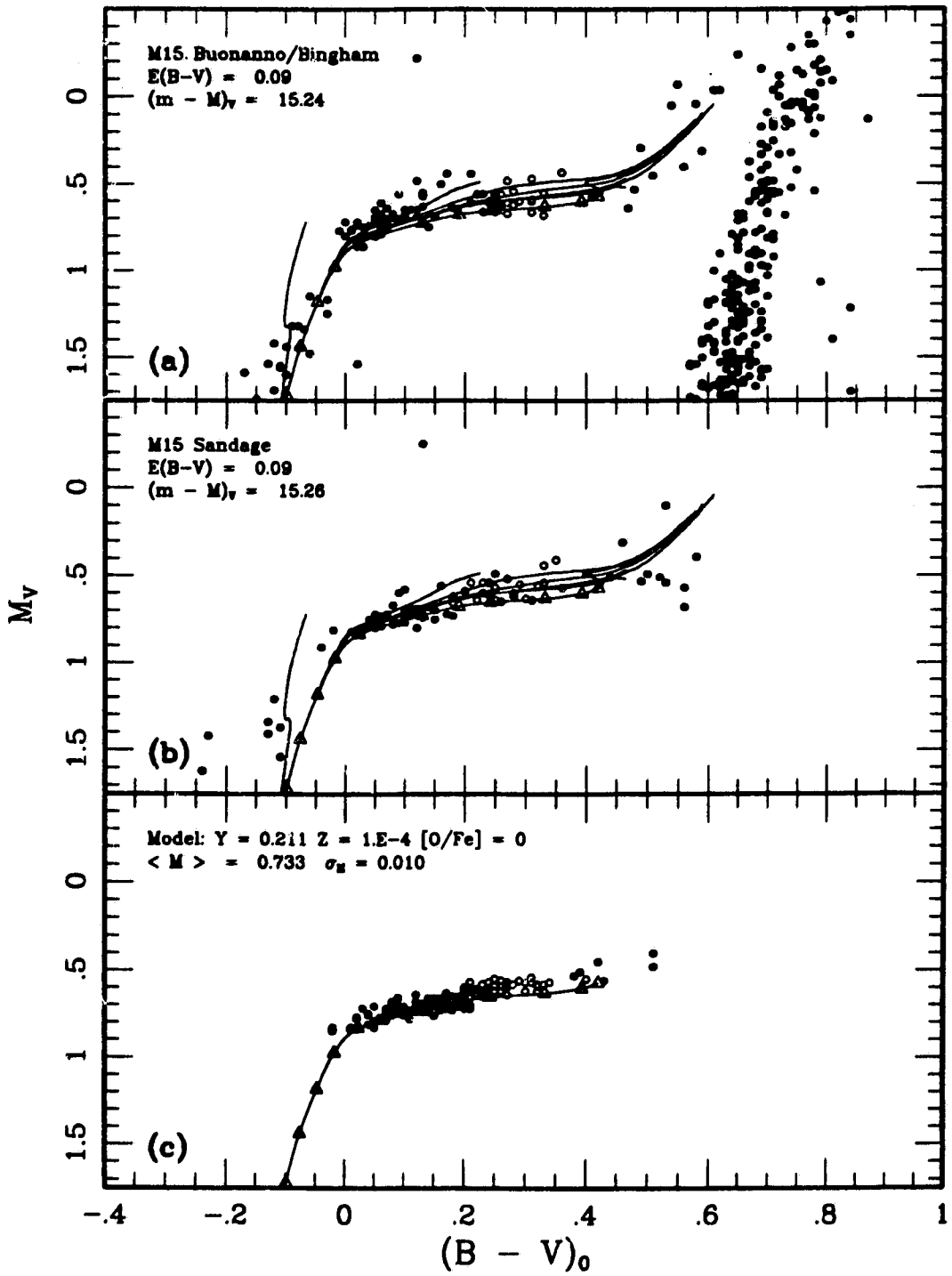

Fig. 6–3–3: a) Comparison of theoretical models for scaled-solar abundance and $Y_{HB} \sim 0.21$, with the Buonanno *et. al.* /Bingham *et. al.* observations. b) As (a), but with observations by Sandage. c) Synthetic model for M15 horizontal branch using theoretical sequences plotted in a and b. The adopted mean mass is $\langle M \rangle \sim 0.73$, with dispersion $\sigma_M \sim 0.010$. Open triangles show the location of the corresponding theoretical ZAHB.

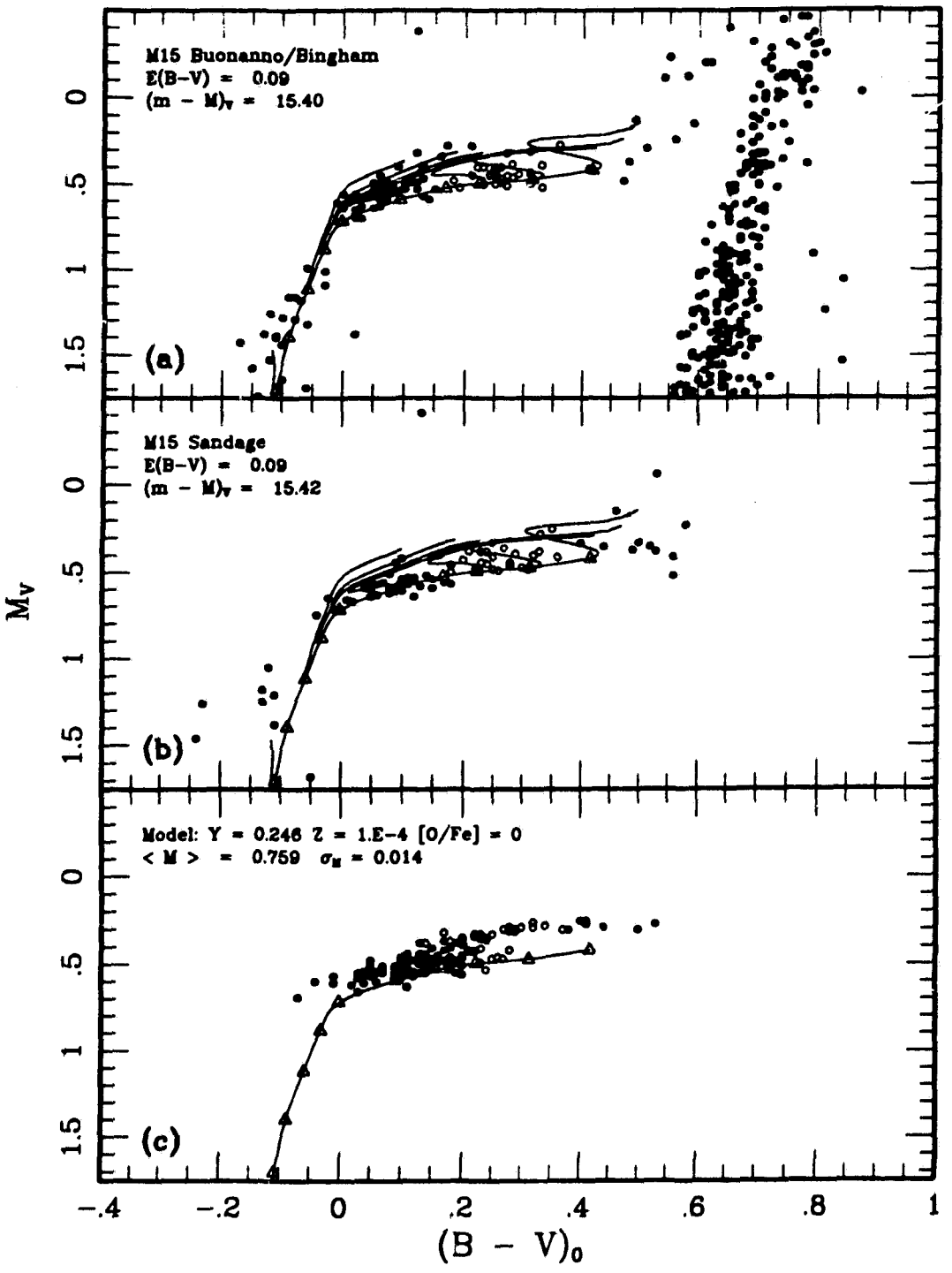

Fig. 6-3-4. a) Comparison of theoretical models for scaled solar abundances and $Y_{IIB} \sim 0.25$ with the Buonanno/Bingham observations. b) As a, but with observations by Sandage. c) Synthetic model for M15 horizontal branch using calculations depicted in (a). For this model, <M> ~ 0.76, σ_M ~0.014. The location of the theoretical ZAHB is marked by the solid curve with individual models indicated by open triangles.

lations with two different values of Y_{HB}, approximately 0.21 and 0.25 respectively, appropriate to primordial helium abundances of 0.20 and 0.235. In panels (a) and (b) of each figure, we produce fits of our evolutionary sequences to the Buonanno *et al.*/BCDF and Sandage data, while panels (c) show the synthetic horizontal branches based on the calculations. The synthetic models include random photometric errors based upon the observers' estimates ($\sigma_V \sim 0.02, \sigma_{B-V} \sim 0.03$).

According to Figure 6-3-3a, if the Buonanno *et al.* blue star data reliably represent the cluster population, then the luminosity width predicted by the models (*cf.* Fig. 6-3-3c) is small. However, the expected width of the evolutionary sequences is marginally consistent with the Sandage data, as seen in Fig. 6-3-3b. In contrast, the higher value of Y_{HB} illustrated in Figure 6-3-4 matches the width of the data distribution in the uppermost panel. In the middle panel, the smaller luminosity range of the data seems to indicate the the bulk of the blue stars are in an earlier phase of evolution than the previous diagram. The synthetic model (Fig. 6-3-4c) appears to be almost a combination of the two.

Thus, if the small, relatively faint population of red HB stars not matched by scaled solar models can be disregarded, it appears that the sequences of Fig. 6-3-3 may represent a lower bound to the acceptable range of the helium abundance, whilst those in Figure 6-3-4 may be close to the upper bound of that range. Nevertheless, the apparent conflict with masses derived from pulsational calculations motivates us to look at CNO enhanced sequences, which would also explain quite naturally the existence of the red, fainter stars. It is, of course, not possible to make any statement about the degree of oxygen enhancement present with the available data. We cannot, for instance, exclude either [O/Fe] = 0.5 or 1.0, but we have adopted the value 0.75, because it is roughly the mean of available estimates of the value of [O/Fe] at [Fe/H] = −2.2 (*e.g.*, Abia and Rebolo 1989; but see Barbuy 1990).

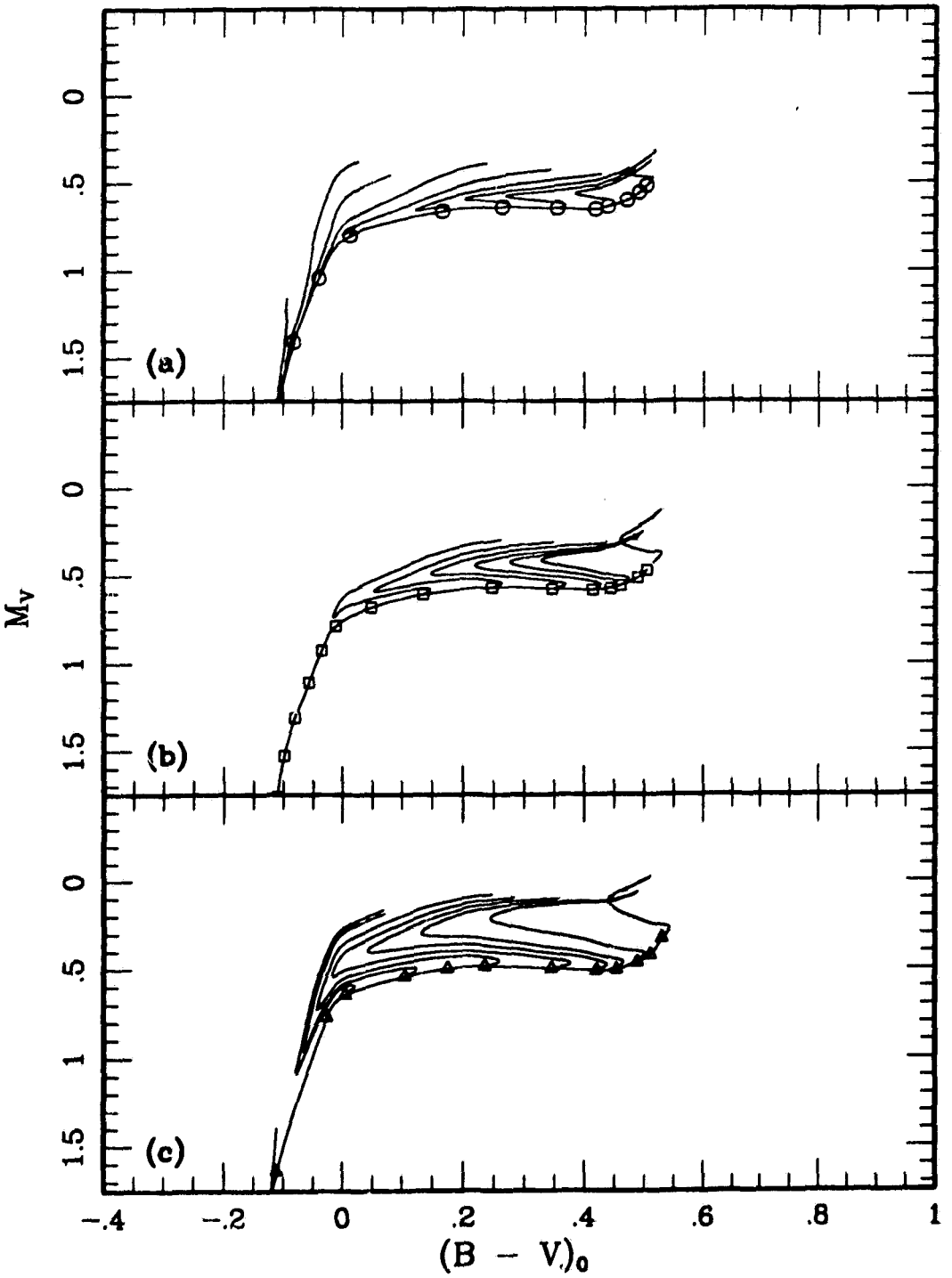

Fig. 6–3–5: Theoretical models for different helium abundances, with [O/Fe] = 0.75. ZAHB models are indicated by circles, squares and triangles in (a), (b) and (c) respectively. (a) $Y_{HB} \sim 0.21$ tracks, for masses 0.90, 0.78, 0.74, 0.72, 0.70, 0.68, 0.66, 0.64 and 0.62 Mo. (b) $Y_{HB} \sim 0.25$ tracks, for masses 0.90, 0.78, 0.76, 0.74, 0.72, 0.70, and 0.68 Mo. (c) Tracks for $Y_{HB} \sim 0.28$ for masses 0.90, 0.78, 0.74, 0.72 0.70, 0.68, 0.66, 0.65 and 0.60 M_o.

Figures 6-3-5 (a) through (c) show zero-age sequences and evolutionary tracks for the helium abundances Y_{HB} approximately equal to 0.21, 0.25, and 0.28 respectively. The 'luminosity width' of the blue loops increases strongly with the helium abundance. For the lowest value of Y adopted here, this width is about 0.1-0.2 mag, while the highest helium abundance used has a luminosity spread close to 0.5 mag. Note that only for the lowest value of Y presented here is there a significant difference in the sequence width as a result of oxygen enhancement. However, since the initial evolution of the sequences to the blue is of greater duration and length for the high oxygen than for the scaled solar sequences, the predicted stellar distributions are therefore somewhat different. The confluence of model sequences in their later phases leads us to predict an enhanced density of objects lying significantly above the ZAHB. The redward extreme of the instability strip has long been associated with the onset of convection in the pulsational driving zones. As the base of the AGB is marked by the development of extensive convective envelopes associated with a giant phase, it follows that the more luminous RR Lyrae variables, lying just blueward of the region of ascent to the AGB, should be represented by highly evolved HB models. Further, brighter variables (with longer periods) must be present in clusters where AGB stars are in evidence, whereas variables lying close to the ZAHB need be present only if the red horizontal branch is fully populated at the zero-age level.

Figures 6-3-6 a, b and c illustrate the result of adopting a low estimate for the helium abundance $Y_{HB} = 0.211$ ($Y_{MS} = 0.20$). In Figures 6-3-6a and b, we show fits of the evolutionary sequences to the Buonanno/Bingham and Sandage cluster data respectively, while Figure 6-3-6c shows a synthetic HB based on these calculations. The optimal value of the distance modulus appears to be about 15.30; we have derived $(m - M)_V = 15.28$ and 15.30 for the Buonanno *et al.* and Sandage data respectively. Note that the difference in the mean magnitude of the blue non-variable stars in the two datasets has important ramifications for

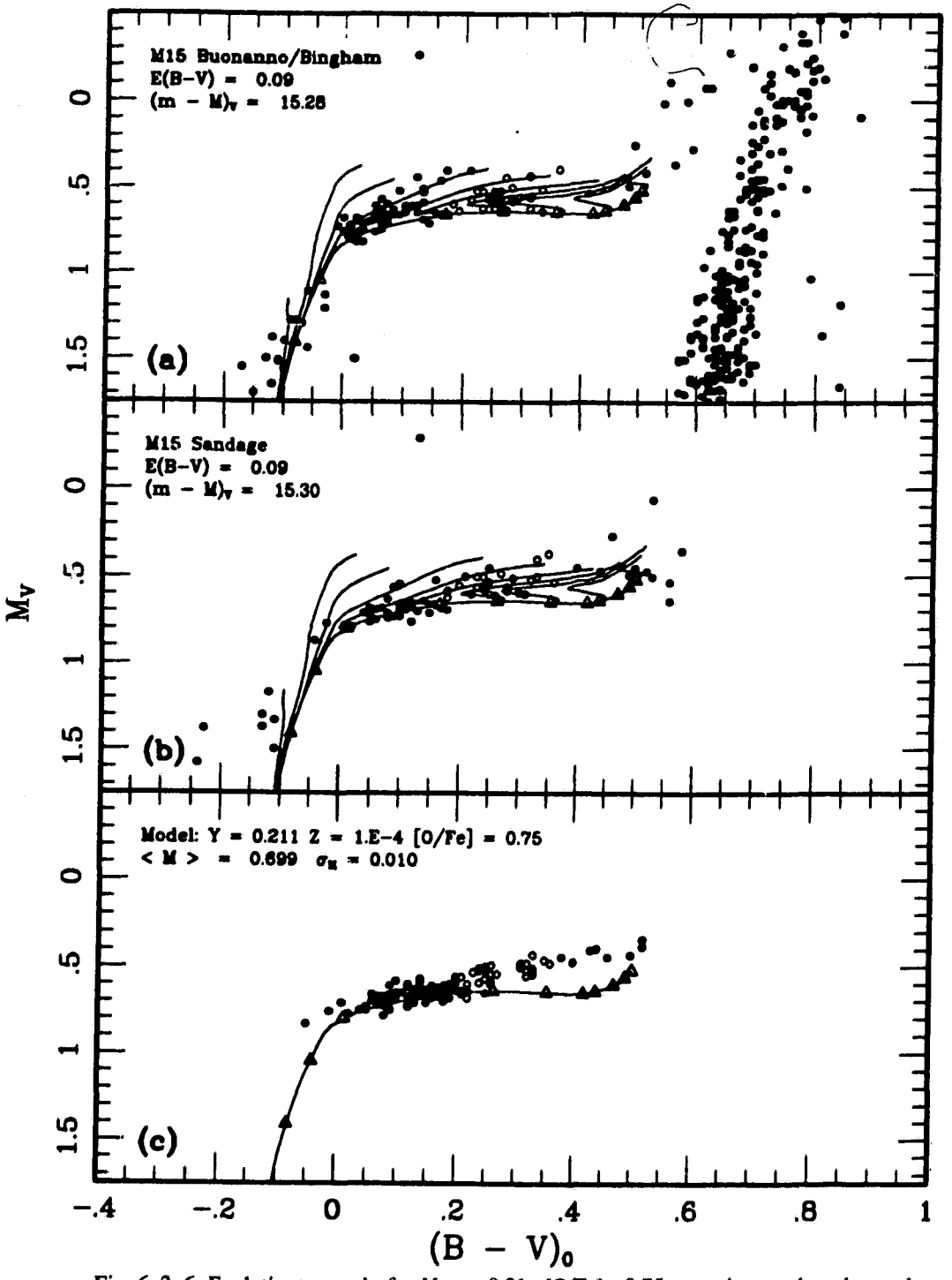

Fig. 6–3–6. Evolutionary tracks for $Y_{HB} \sim 0.21$, [O/Fe] = 0.75, superimposed on cluster data. (a) Buonanno/Bingham data. (b) Sandage data. A synthetic horizontal branch with <M> ~ 0.70 M_o, $\sigma_M \sim 0.01$ is shown in panc' (c).

the evolutionary status of the RR Lyraes. In the top panel, the computed ZAHB provides a good match to the observed lower envelope of the entire HB, including the variables, while in the middle panel, the blue stars constrain the ZAHB in such a way as to imply that the variables are brighter than the zero-age sequence. With this dataset and these evolutionary models, it is natural to conclude that the majority of the variables are evolved objects, in accordance with the LDZ hypothesis. The corresponding pulsational masses would be in the range 0.68 to $0.72 M_{\odot}$, with the brighter objects being associated with the lower end of the mass range. Arguably, these diagrams represent our most visually appealing matches to the data.

In the next figure, comparisons are made with the evolutionary tracks for $Y_{HB} = 0.281$. This large value of the helium fraction is appropriate either to large primordial abundance, or an enhancement from standard universal helium fractions following the prediction of VandenBerg and Smith (1988); it is also similar to the predicted difference in this parameter between the clusters M15 and M3 suggested by Sandage, Katem, and Sandage (1982). For this abundance, we compare with the Buonanno *et al.* data only, since their observations have greater width in luminosity, but our comments apply to the Sandage data with perhaps greater force. These wider HB sequences are populated towards the early phase of evolution, assuming a distance modulus of about 15.45 (see Figure 6-3-7 a). The bluer RR Lyrae stars are clustered around the tracks for 0.68 $M_{\odot}$, and the blue stars appear to represent the later phase of evolution for these objects. However, if this value for the helium abundance were appropriate for M15, the brighter RR Lyrae stars would be relatively young stars. The synthesized distribution of Figure 6-3-7b shows that the higher concentration of the evolved objects at luminosities greater than that of the ZAHB, gives rise to a stellar distribution which is bimodal in luminosity at the colour of the instability strip. Such a distribution *must* arise in this case if the blue end of the horizontal branch is populated; however, the bright

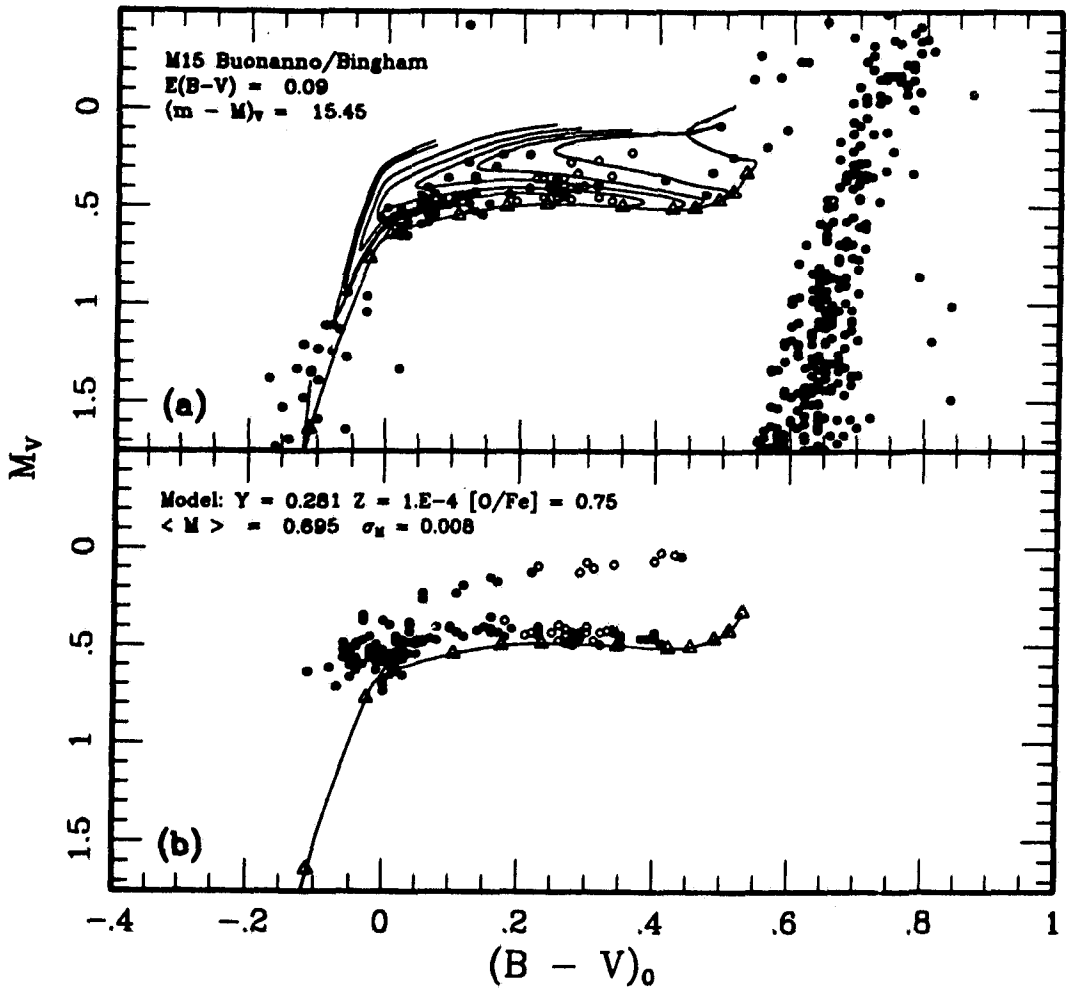

Fig. 6–3–7. Evolutionary tracks for helium abundance $Y_{HB} \sim 0.28$, [O/Fe] = 0.75, superimposed on cluster data. (a) Buonanno/Bingham data from Fig. 6–3–1a. (b) Synthetic distribution derived from tracks in (a), with $\langle M \rangle \sim 0.70$, $\sigma_M \sim 0.01$.

stars in late evolutionary phases as illustrated by this model are totally absent in the data. This suggests very strongly that a high envelope helium abundance is simply not appropriate.

Next, we consider a value of Y that is close to the currently accepted primordial abundance prediction. Figures 6-3-8 a through c show evolutionary sequences for $Y_{HB} = 0.247$ and [O/Fe] $= 0.75$ superposed on the Buonanno *et al.* data in Fig. 6-3-8a, and the Sandage data in Fig. 6-3-8b. Figure 6-3-8c shows a synthetic HB model computed from these sequences. The brighter blue stars in the Buonanno data can be explained as low-mass, highly evolved HB stars. However, these stars are absent in the Sandage data, which implies that more of these blue stars are in early evolutionary phases. The disparity between the two samples emphasizes the need for large, complete sets of data for this cluster. The synthetic model indicates that, even for this value of Y, the evolved models start to form a group distinct in location from the ZAHB, so that the enhanced oxygen models favor values of Y which are smaller than those arising from scaled-solar fits to the data. Since the data for RR Lyraes in both panels (a) and (b) do not show this bimodality, this conclusion is not affected by the choice of data.

6.3.v RR Lyrae Variables and the Sandage Period-Shift Effect

We next discuss the implications of our findings for the Period-Shift Effect. Having chosen a set of models which matches the observed HB stellar distribution, we may then use the fundamental-mode pulsation equation, which can be written in the form

$$A = \log L - p \log M = (q + \log P - r \log T_{eff})/s, \tag{6.1}$$

where p, q, r, s are constants, to predict periods for the cluster variables: note that all of the available determinations of the coefficients in this equation (Cox

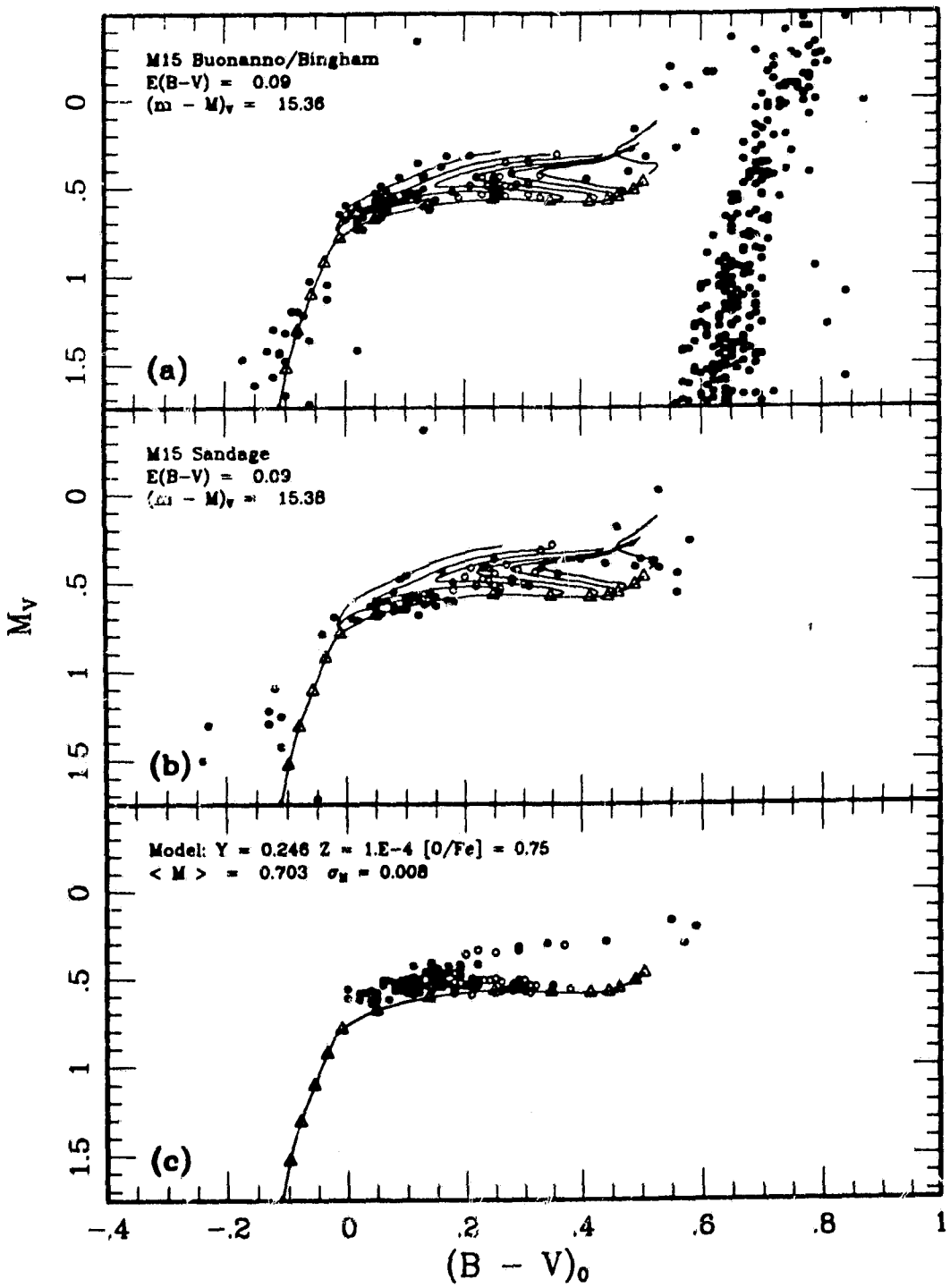

Fig. 6–3–8. Evolutionary sequences for intermediate helium composition $Y_{HB} \sim 0.25$, [O/Fe]= 0.75. (a) Sequences superimposed on Buonanno/Bingham data. (b) As (a), but superimposed upon Sandage (1990a) data. (c) Synthetic distribution derived from evolutionary tracks plotted in (a) and (b), assuming $\langle M \rangle \sim 0.70$, $\sigma_M \sim 0.01$.

1987) give very similar periods. We can then plot a period-colour diagram for the models using the adopted synthetic temperature-colour relations, and superimpose on them the de-reddened data. We believe that this is preferable to matching the data and theory in the period-temperature plane, as it is important to recognize that the properties of the variable stars must also be reconciled with their location on the colour-magnitude diagram. We can more easily ensure that the colour determined for a model is consistent on both diagrams than we can be certain that the temperature assigned to a pulsator is consistent with its mean CM diagram location. This period-colour plane has the important advantage (over the colour-magnitude diagram) of being distance-independent. Also, our derived colours are sensitive to the surface gravity, which can vary enough during evolution or along the ZAHB sequence to produce noticeable changes in log T_{eff} at given colour.

Figure 6-3-9 a illustrates that the effect of oxygen enhancement on RR Lyrae periods through the fundamental mode region of the instability strip is almost negligible. The sequences for values of [O/Fe] equal to 0, 0.5, 0.75 and 1.00 are close to coincident. This close agreement is, in part, due to the compensating effect of differing core masses for each value of [O/Fe]. If the core mass were held fixed as the oxygen abundance was varied, a small but noticeable shift would be present, with the increased oxygen content implying longer periods. In other words, the effect of oxygen enhancement on the period predictions for zero-age models is of the same order as uncertainties produced by small variations in the core mass. Figure 6-3-9b shows the models for $Y_{HB} \sim 0.25$ at [O/Fe] = 0, and 14c for $Y = 0.21$ at [O/Fe] = 0.75. The M15 RR ab-type period-mean colour data have been taken from BCDF, with a 'static' colour derived using the relation

$$(B-V)_{eq} = 2/3 < B-V > +1/3(< B > - < V >). \qquad (6.2)$$

For the larger value of the helium abundance, the theoretical ZAHB produces an acceptable fit to the lower envelope of the variable distribution, as is the case

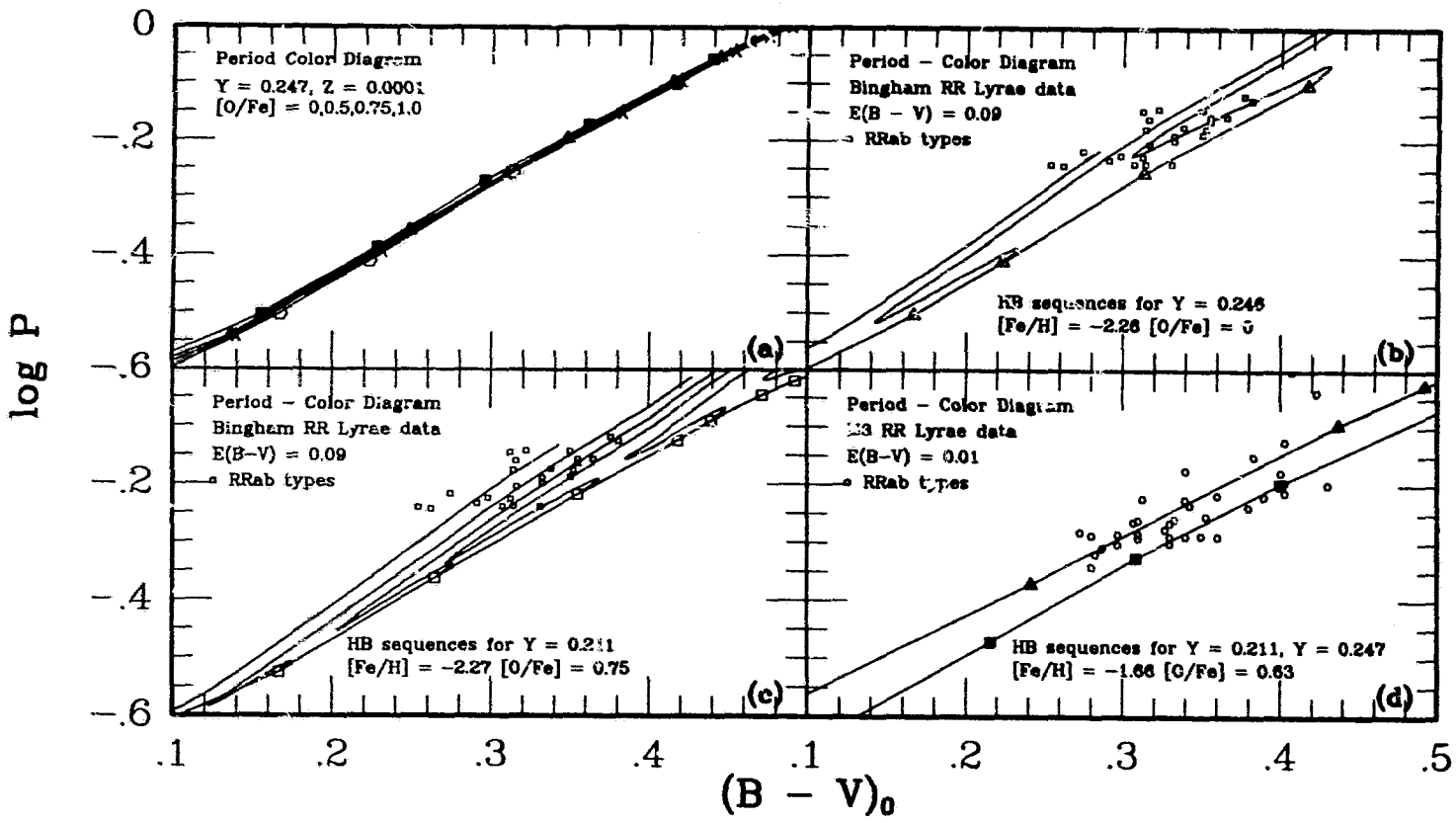

Fig 6–3–9. Period–color diagrams for theoretical and observational results. (a) ZAHB sequences at approximately fixed helium abundance. Hexagons: Scaled–solar calculations. Asterisks: models with [O/Fe] = 0.50. Triangles: [O/Fe] = 0.75. Filled squares: [C/Fe] = 1.0. (b) Evolutionary tracks for $Y_{HB} \sim 0.25$, [O/Fe] = 0. Masses for the tracks are 0.90, 0.78, and 0.74 Mo. The RR Lyrae ab–type data from BCDF are marked with open squares. (c) As for (b), but with evolutionary tracks for $Y_{HB} \sim 0.21$. ZAHB points are marked with large squares. Masses for the tracks are 0.90, 0.78, 0.74, 0.72, 0.70, and 0.68 Mo. (d) M3 RR Lyrae data with zero–age HB sequences for $Y_{HB} \sim 0.21$ (lower) and 0.25 (upper). For these models, $Z = 4 \times 10^{-4}$ ([Fe/H] = –1.66) and [O/Fe] = 0.63.

with Fig 6-3-4b. However, adopting a larger value for the reddening to M15 would move more of the points to later evolutionary phases. If the adopted value of Y is smaller (Fig. 6-3-8c), then nearly all of the RR Lyrae star locations on this figure fall on the late parts of the evolutionary tracks, consistent with Figures 6-3-6b and c. If, however, the realistic value for the reddening to M15 is much above 0.10, then the pulsation equation will predict periods which are too short for the observations at their given colour. It is also worth noting that the scatter in the observed data comes almost entirely from that in $(B-V)$ rather than in the period. In fact, if $\sigma_{B-V} \sim 0.03$ one can easily have a range in colour greater than 0.06. Note also that in this case, high oxygen abundance is required so that the evolutionary tracks reproduce the observed sequence width in the period-colour plane.

We are thus in a position to show that it is possible to attain agreement between theory and observation for the variables in M15. However, we must also be able to explain the apparently large period difference between M15 and M3. Fig. 6-3-9d shows data from M3 with ZAHB sequences for the two values of the helium abundance used above, but with $Z = 0.0004$ ([Fe/H] $= -1.66$), and [O/Fe] $= 0.63$. The photometry of the M3 variables was taken from Sandage (1981), and the 'equivalent static' colour was calculated according to the relation used by BCDF. In this diagram, we have used a reddening to M3 of 0.01 mag. The oxygen enhancement is taken from VandenBerg's (1990) adopted relationship between [O/Fe] and [Fe/H]; of course, according to Fig. 6-3-9a, the location of the ZAHB on the period-colour diagram is unlikely to be affected by this choice. For $Y_{HB} \sim 0.25$ the ZAHB models predict periods which are too long for large number of the variables, while the fainter sequences for lower Y are much closer to the observations. We have not studied the evolutionary sequences for the lower helium abundance at this metallicity, but their luminosity width is likely to be greater than that for the lower Z illustrated in Fig. 6-3-9c, encompassing the range of colours

and periods occupied by the variables. Thus, for both clusters, oxygen enhanced *low-helium* models can satisfactorily explain the period distribution, provided that the majority of the type ab variables in M15 are bright, evolved stars as suggested by LDZ. However, the uncertainties in this analysis warrant a careful discussion, which we attempt to provide in the concluding section of this paper.

6.3.vi Summary and Discussion

Comparisons of our theoretical horizontal-branch sequences, for a range in Y and [O/Fe], to data for M15 have shown that our calculations can reproduce, in part at least, the observed morphology. It is obvious that the current uncertainties involved in both theory and observation limit the definiteness of our findings. For the sake of clarity, we start by assuming that the pulsation formulae so far derived are accurate, and that our model core masses, input physics, *etc.* are reliable, and summarize our results as follows:

(i) The observed horizontal branch morphology indicates that the value of Y in the envelopes of HB stars is $\lesssim 0.25$. Larger values conflict with the observations, as they predict the existence of variables which are separated from and considerably brighter than the ZAHB.

(ii) Our models favor values of the envelope helium abundance in the range $0.21 < Y \lesssim 0.25$ if [O/Fe] $= 0$, with the lower bound consistent with only one of the two sets of data we have utilized. However, if [O/Fe] is as high as 0.75 in M15, the helium content satisfies $0.21 \lesssim Y_{HB} < 0.24$, with the upper bound excluded by the bimodality in variable luminosities shown by the synthetic models. For the case $Y_{HB} \sim 0.21$, [O/Fe] $= 0.75$, the derived mean magnitudes of the RR Lyrae stars imply that they are evolving to the red towards the end of their lifetimes, as suggested by LDZ. The recently published Sandage (1990a) data are more supportive of this possibility than the Buonanno *et al.* (1983) data, because of very different photometry at the blue end of the horizontal sequence.

(iii) The scaled-solar models predict masses which are near the upper bound of the values expected from the Petersen diagram, while the oxygen-rich sequences give masses close to the middle of the expected range. For the low Y sequences for low metallicity, the mean RR Lyrae mass should be approx-

imately 0.70 $M_\odot$. Approximately the same mass is required for the higher helium oxygen-rich sequences, but this value rises to 0.75 $M_\odot$ for the scaled-solar models. If our adopted metallicity is an underestimate, then our mass estimates would, of course, be decreased further. For the higher metallicity appropriate to M3, the masses of stars in the instability strip lie between 0.63 and 0.66 $M_\odot$ (for the adopted value of [O/Fe]). The expected mean mass would be somewhere toward the lower end of this range, since we expect lower mass stars evolving from the blu to be present also within the instability strip. Evolutionary sequences are necessary to make a more precise statement here. For the observed period ratio for double-mode pulsators in M15 ($P_1/P_0 = 0.746$), the Kovács Petersen diagram gives $0.75M_\odot$, while the Cox calculations give $0.65M_\odot$ (Kovács 1985). In M3, there are only two positive identifications of double-mode pulsators, with somewhat smaller period ratios (Nemec and Clement 1989).

(iv) The period-colour diagram for M15 shows that theoretical period determinations are consistent with those observed, provided that the true reddening value is less than 0.10. This conclusion holds for the full range of Y values adopted here; however, the period shift between M15 and M3 tends to exclude the higher values of Y.

(v) In order to fit the period-colour distribution for M15 and M3 simultaneously with our models, we require low Y (~ 0.21) in M3. For models with $Y = 0.24, Z = 4 \text{ x } 10^{-4}$ ([Fe/H] $= -1.66$), theoretical periods are too long compared with the observations. The mean period difference between the two clusters is explained satisfactorily only if M15, too, has low Y. As is the case for the colour-magnitude diagram fit, the lower estimate for Y puts the variables at highly evolved stages relative to the ZAHB, supporting the LDZ hypothesis.

(vi) A major difference in calculated luminosity-to-mass ratios between previous

determinations (BCDF, Sandage 1990a) arises. This is due to the adoption of different temperature-colour relations, as well as differing reddening assumptions. By searching our theoretical grids for models appropriate to the colour-magnitude diagram locations of the variable stars, we can derive temperatures for 'equivalent static stars'. For M15, we can reproduce the temperatures derived by BCDF only if a reddening of 0.12 is used, compared with the value 0.10 that they adopt. It is also unlikely that the final word has been written on the reduction of RR Lyrae light curves to an equivalent static star location on the colour-magnitude plane.

The first source of uncertainty we discuss is in the apparent morphology itself. Because of difficulties in deriving correct mean locations for the variable stars, the most reliable evidence for the helium content should come from the large distribution of stars blueward of the instability strip. (The extreme blue tail does not provide any constraint since the colour-temperature relationship here is very weak, although theoretically its absolute colour should be independent of cluster composition). The two sets of data that we have used for comparison are quite different precisely in this region of the colour-magnitude diagram, with the Buonanno *et al.* data being much more scattered in V, while the Sandage (1990a) data have smaller luminosity width which leads us to prefer lower helium abundances. The scarcity of suitable standards in this region of the HR diagram should also be mentioned as a source of photometric uncertainty. It seems important to attempt to resolve this problem by collecting CCD data for M15, so that photometric uncertainties may be fully quantified.

In the period-colour diagram, the observational uncertainty is in the dereddened, equivalent static colour, $(B-V)_{eq,0}$, while the theoretical uncertainty lies in the pulsation equation, as well in as the temperature-colour relations. A revision downward of order 0.05 in the zero-point of the pulsation relations (*i.e.*, in the constant term) is sufficient to match the M3 period data with the theo-

retical models for $Y = 0.246, [Fe/H] = -1.66$. Applying the same revision to corresponding models for M15 would shift the observed points to the later phases of the evolutionary sequences: however, this is not consistent with the synthetic calculations. It also appears that the high values of helium abundance which are both widely used and preferred by researchers into RR Lyrae pulsation are difficult to reconcile with the observed stellar distribution. We note, however, that the pulsational evidence does not of itself imply a high helium abundance in the entire envelope region, *i.e.*, extending down into the hydrogen shell burning zone.

Finally, we recall the factors that may enter into our analysis of the apparent discrepancy between pulsational and evolutionary masses, which cause severe difficulties if the lower estimates for RR Lyrae masses are valid. The stars which lie at the red extremity of the HB require relatively bright hydrogen burning shells. Phenomena that may cause an increase in the core mass (such as core rotation) would imply larger masses for pulsating variables, since the shell brightness must be maintained. This is particularly true at low metallicity, and both theoretical and observational considerations support this.

Uncertainties in the input physics may be particularly crucial to the theoretical predictions. Importantly, we comment on changes which may arises owing to the adopted of a more comprehensive treatment of the equation of state. Straniero (1988) estimates that, at the central conditions prevailing throughout the horizontal branch phase, the plasma parameter Γ for oxygen is greater than unity, and close to unity for carbon. Preliminary results we have obtained using the Straniero equation of state table indicate that the width of the blue loops is reduced at a given value of Y. Calculations by Castellani, Chieffi, and Puloné (1990) appear to show the same effect, although their core masses are somewhat larger than ours, a factor which would also decrease the luminosity width of the sequences. Recently, Iglesias, Rogers, and Wilson (1990) have stated that their more detailed treatment of atomic line structure implies that a revision of stellar envelope opacities

is necessary. Their conclusions, which apply to metal opacities, would imply an enhancement of opacity which is progressively larger for higher metallicities, albeit at a temperature range appropriate to the region well below the photosphere. While it is not possible to say, without detailed modelling, how these results would affect the properties of the stars within the instability strip, perhaps Figure 2-4-2 of this study provides a clue to the effect of a localized change in the opacity. The change in κ due to the presence of oxygen is at most 15% here, but this is sufficient to reduce the luminosity (compared to the test sequence, with lower κ) and very slightly reduce the mass at a given colour (see Fig. 2-4-5). If much greater metal opacities do, in fact, obtain at temperatures of a few hundred thousand degrees, the changes in pulsation properties may well be in the direction of larger theoretical period shifts.

Currently, however, there are few models for pulsating stellar envelopes in the mass range predicted by evolutionary calculations, and little consistency between input physics used in pulsational and evolutionary calculations. A possible approach to the problem would be to follow the evolution of the variables, using, for example, the linear adiabatic wave equation with the static solution known from the evolutionary calculation. The success or failure of this exercise in the reconciliation of the period-colour and the colour-magnitude diagram locations of variables may pinpoint the remaining uncertainties in the structure of model envelopes. A similar exercise was carried out by Jorgensen and Petersen (1967), before the nature of horizontal branch evolution was properly understood.

In conclusion, despite some of the uncertainties involved in our analysis, our models provide some important constraints on the cluster helium content and the properties of the RR Lyrae stars in M15.

6.4 A Brief Re-Examination of the Cluster Studies

6.4.i 47 Tucanae

It has been seen in Chapter 4 how changes in the adopted nuclear reaction rates and equation of state shorten the blueward motion of the evolutionary tracks in the HR diagram. In addition, the adoption of the new equation of state has the effect of displacing, the ZAHB location downward by about 0.05 mag in the colour-magnitude plane. For the composition approriate for modelling the HB of 47 Tucanae, the newer evolutionary sequences have a morphology which is distinct from the older; the blueward-evolving stage in the sequences is significantly flatter than those presented in Figure 6-2-4, and the subsequent turnoff back to the red is sharper. Figure 6-4-1 (a) shows the cluster data superposed upon the sequences for the 'best fit' to the data, the apparent distance modulus being about 13.3 mag. The tracks shown are for masses between 0.90 and 0.60 $M_{\odot}$, and thus span a range which is significantly wider than previously found. The data points at the base of the AGB $M_V \gtrsim 0.2$ mag are reasonably well-matched in colour and brightness by the extension of the sequences to late evolutionary phases, but it should be pointed out that this agreement is very sensitive to both the adopted bolometric correction scale and the choice of distance modulus. In addition, there are similar numbers of stars in the range $0.2 < M_V < 0$ as there are above $M_V = 0$, while the evolutionary timescale of the tracks would seem to predict very few stars below this luminosity.

One of the appealing features of the results of the original study was the fact that the distribution of the data appears to slope upward toward the blue, and this is matched very well by the shape of the evolutionary tracks presented earlier, for sufficiently large values of Y. However, this highly desirable agreement is lost with the new sequences, which have a morphology which is closer to that of the low helium sequences shown in Figure 6-2-2, although the evolution to lower

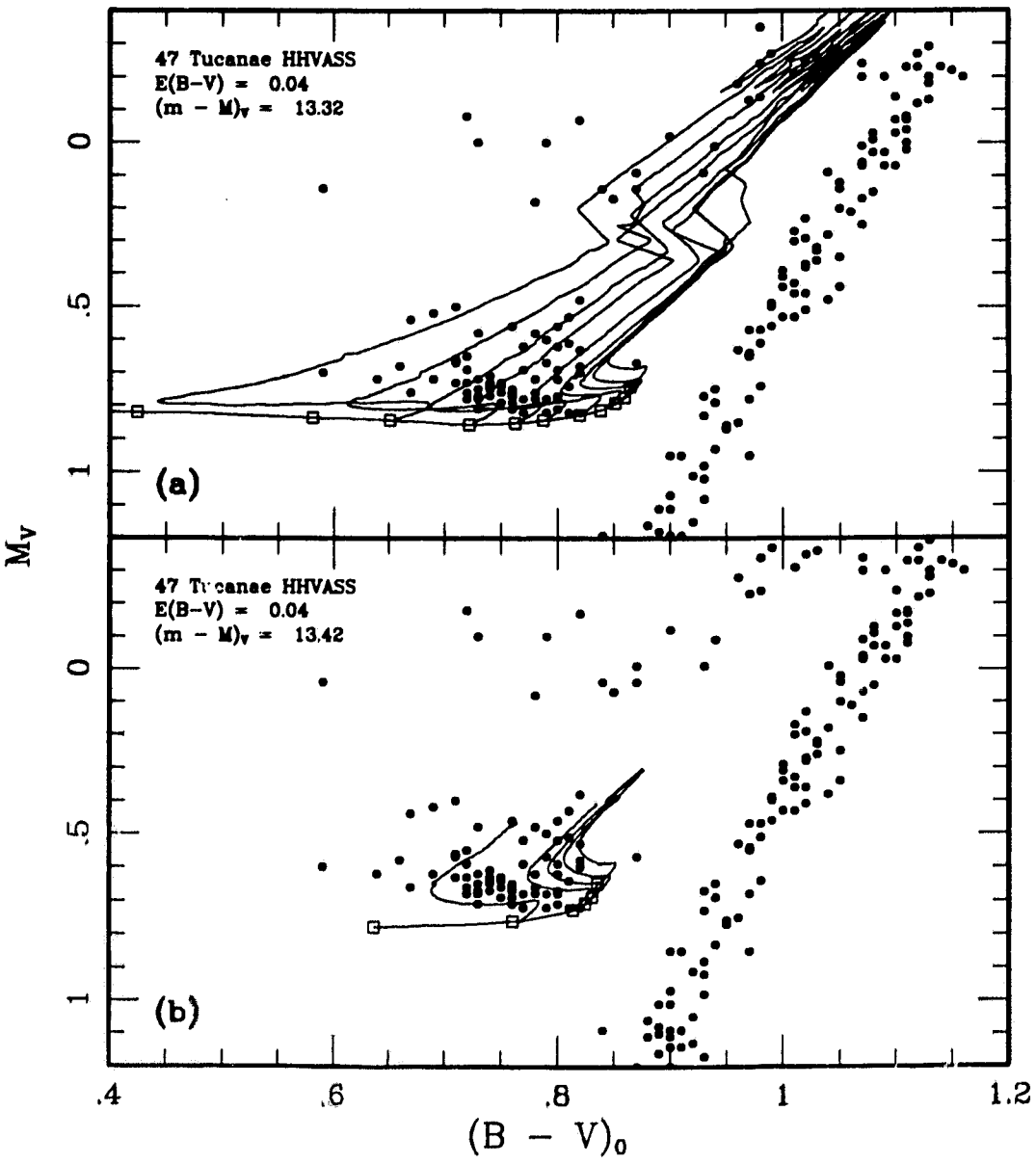

Fig. 6-4-1: Data for 47 Tucanae from the HHVASS study superposed on evolutionary sequences. (a) Evolutionary tracks are from the set depicted in Figure 5-4-19. (b) Evolutionary tracks calculated with similar input physics, except that the EFF equation of state has been used for the entire stellar interior.

luminosities is much less pronounced. It is important to locate the source of the discrepancy, since the earlier sequences, gave the best fit at $(m - M)_V = 13.44$ mag, which was consistent with the fit found by HHVASS to the rest of the cluster CM diagram. In particular, the general impression obtained from the data itself — that evolutionary sequences should become slightly brighter in M_V after the relaxation phase — was properly simulated. In order to study this, a small number of sequences have been calculated with the new choice of input physics, apart from the adoption of the EFF equation of state in the entire stellar interior. These sequences are illustrated in Figure 6-4-1b. Apart from the relaxation phase which is restore to the sequences with the use of the later version of the initialization programme, the track shape is very close to those used in the 1989 study. The luminosity of the blueward phase of evolution is also very similar, and the best visual comparison fits the data with a distance modulus $(m-M)_V \sim 13.42$. Thus, the major difference between the new and the old evolutionary sequences is due to the equation of state assumption, rather than the initialization procedure.

The conclusions to be drawn here either can be taken either as a comment upon the accuracy of the new EOS data (see §4.3), or alternatively on the determination of the helium abundance. There is some evidence that other metal-rich globular clusters have horizontal branches whose mean luminosity increases toward the blue, at least using the $(V - I)$ colour index (Friel 1990). If this is generally true, and the Straniero EOS reflects properly the behaviour of the material in the star, then it is possible that cluster helium abundances are somewhat greater than previously suspected. However, further theoretical study is required in order to determine whether the original sequence morphology may indeed be recovered by increasing the value of Y.

6.4.ii M15 and the Sandage Effect

The earlier study of M15 was unable to put very tight constraints on its

helium abundance, except to suggest that the HB morphology is inconsistent with the high values of Y preferred by some stellar pulsation theorists. In this section, it is assumed that Y is consistent with current primordial estimates in M15 and M3, and the conclusions for the pulsational properties for the two clusters are re-examined.

The first task is to establish that a helium abundance $Y_{HB} \sim 0.245$ is consistent with the HB morphology. Figures 6-4-2 and 6-4-3 show the observations, superposed on evolutionary sequences from the main set of calculations, for [Fe/H] $= -2.26$ and -2.03 respectively. As previously, the upper panel shows the Buonanno *et al.* (1983)/BCDF data, and the lower panel shows the Sandage (1990) data. The difference caused by the change in the ZAHB luminosity tends to be offset by a change of similar magnitude in the luminosity width of the sequences, with the result that the visual estimates for of the distance modulus to M15 are unchanged. Because of the lack of observations populating the red end of the HB in these samples, and perhaps also because synthetic HBs derived from these calculations are not yet available, it is difficult to choose between the fits illustrated in Figures 6-4-2 and 6-4-3. The more metal-rich sequences appear to associate the data points with the later phase of evolution, whilst the other set put these points closer to the ZAHB. However, new observations by Stetson (1990) seem to indicate that the red HB population in M15 is in fact quite significant, so that this question may soon be resolved. It should be noted that if, indeed, the red HB is populated in M15, a severe difficulty arises for the LDZ hypothesis (that Oosterhoff group II clusters are populated, in the main, by low-mass HB stars), since it would be then be hard to explain a gap in the distribution of young HB stars in the region of the instability strip.

Before demonstrating the pulsational properties implied by the new sequences, several comments are in order regarding the fits of the evolutionary sequences to the blue tail stellar distribution. Recall that the models which evolve redward

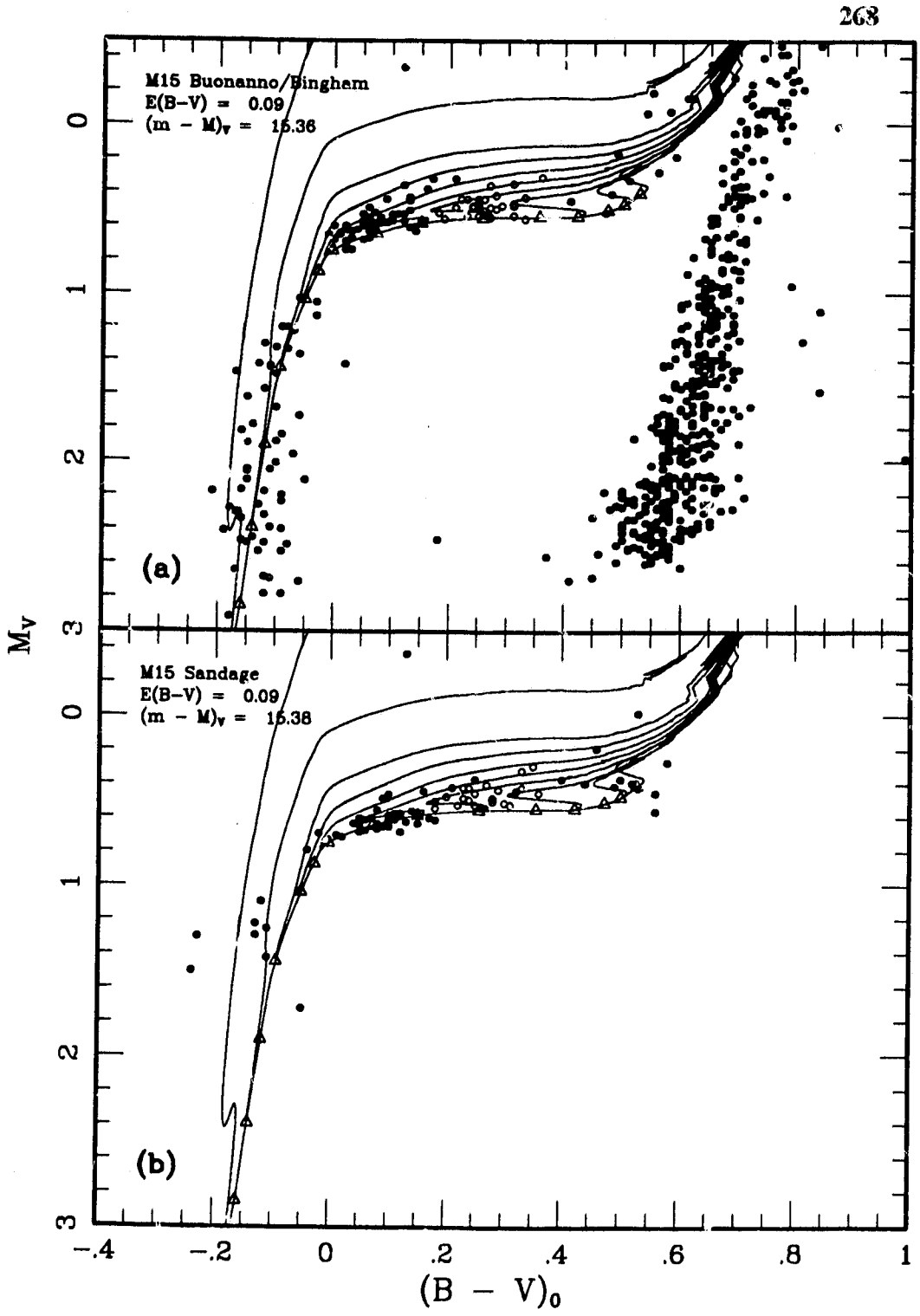

Fig. 6–4–2. Data from Figure 6–3–1 superposed on evolutionary sequences from Figure 5–4–11. (a) Buonanno *et al.* (1983)/ BCDF data. (b) Sandage (1990a) data.

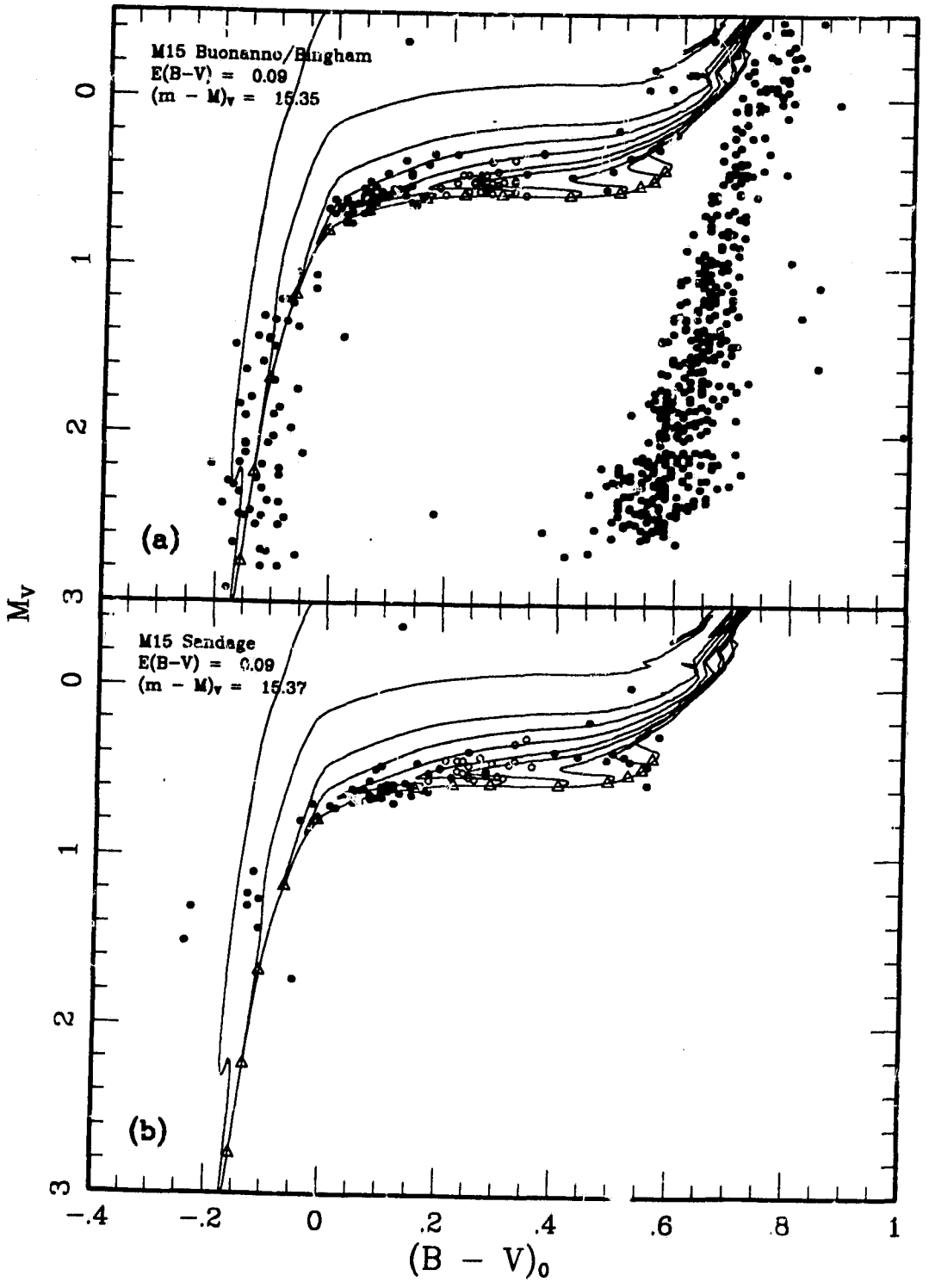

Fig. 6–4–3. Data from Figure 6–3–1 superposed on evolutionary sequences from Figure 5–4–12. (a) Buonanno *et al.* (1983)/ BCDF data. (b) Sandage (1990a) data.

throughout their entire lifetime move slowly and almost vertically on the HR diagram. For example, the sequences with the lowest mass illustrated in these diagrams reach the point where their evolution changes direction (at $M_V \sim 2.3$) after about 100 Myr; at this point, $Y_c \sim 0.02$. In addition, the sequences which evolve to the blue but marginally spend most of their lifetime very close to the ZAHB point. Since the change from blueward to redward evolution occurs very close to the blue end of the 'horizontal' part of the HB, one expects the population at the 'knee' of the horizontal branch to be thinner than elsewhere. That is, fewer evolutionary sequences pass through this region of the CM diagram. This cannot on its own explain gaps in cluster horizontal branches, since they do not occur in all clusters.

The appearance of the HB data for M3 of Sandage (1981) on the colour-magnitude diagram is itself very difficult to reconcile with the theoretical models. Figure 6-4-4 illustrates these data, again with the variables shown as open circles. Models from this current study with [Fe/H] $= -1.66$, [O/Fe] $= 0.63$ are superposed upon the data. It is not the intention here to produce a detailed match to the M3 data: it should be noted that the evidence from the red part of the HB dataset seems to indicate that the cluster metallicity, or its oxygen abundance, may be overestimated by these particular calculations. Clearly, however, various criteria for fitting the data are possible, based on producing the best match to different features of the observations.

In the upper panel, the distance modulus has been chosen to match the lower envelope of the ZAHB at both the red and blue 'horizontal' parts of the HB. It is immediately apparent that the lower bound of the calculated mean visual magnitude distribution for the RR Lyrae stars is significantly less than for the non-variables. As in §6.3, the 'equivalent static colour' for these points has been defined using Equation 6.2. The discrepancy between the variable and the non-variable data is of the order of 0.1 mag. This inconsistency — which is very large

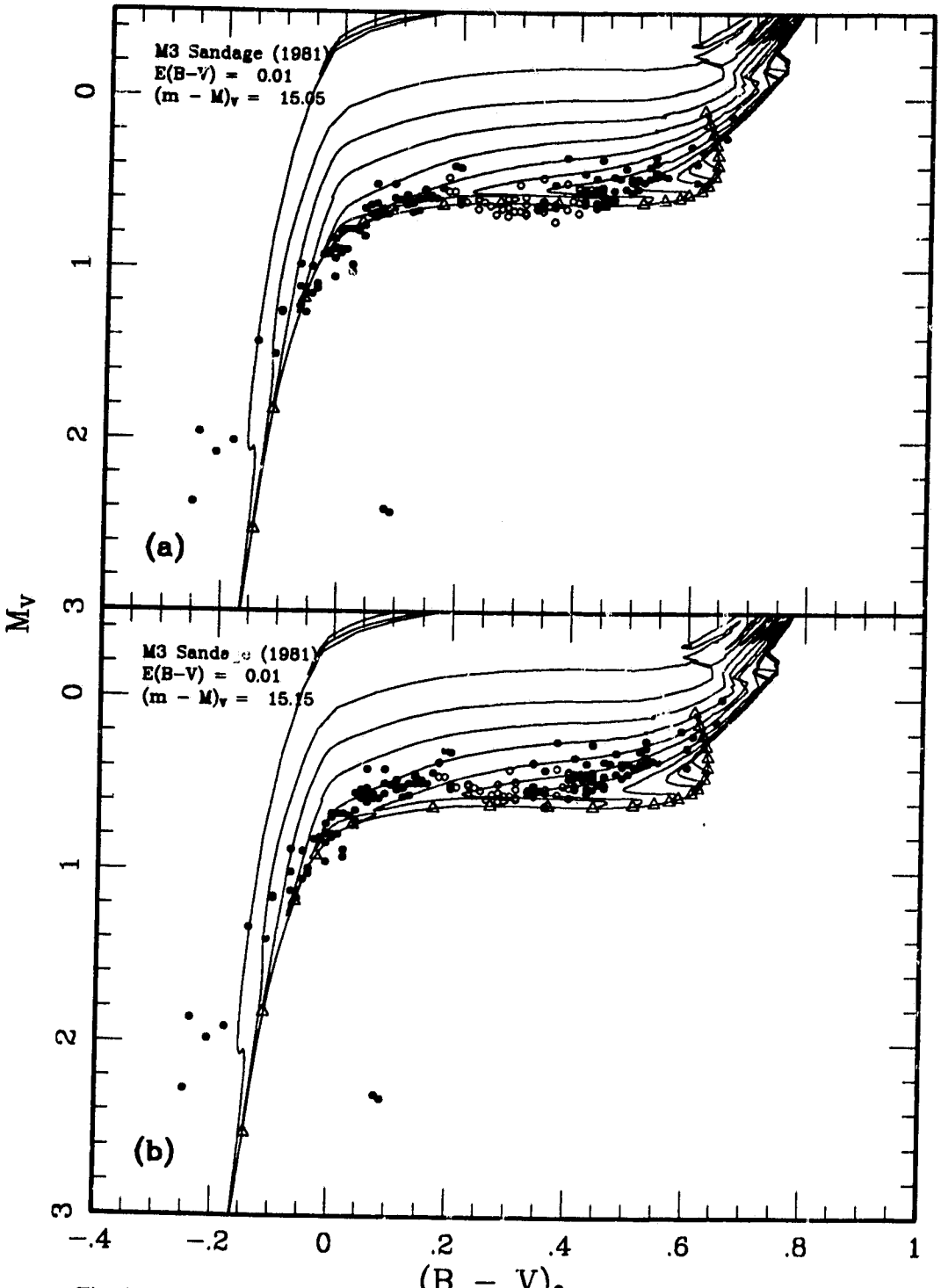

Fig. 6–4–4: Data for M3 from Buonanno *et. al.* (1986) / Sandage (1981) superposed upon data from Figure 5–4–14. (a) Fit of sequences to data with $(m-M)_V = 15.05$. (b) Fit with $(m-M)_V = 15.15$.

when one is concerned with the level of accuracy appropriate here — makes it difficult to use M3 as a 'reference cluster' for the period-shift effect, as has been done by Sandage (1990b). Since there is no possible theoretical explanation for a 'dip' in the ZAHB luminosity *only* in the instability strip, the diagram is highly suggestive of calibration problems with the variable star photometry. If this is the case, then the difficulty with the pulsational properties discussed below may not actually arise; for example, if the calibration error is very slightly different in each filter, shifting the B magnitudes slightly more than the V. In the lower panel, a higher value of the distance modulus is used, which fits the lower bound of the variable data, and places the blue tail of the data distribution above the ZAHB. If this fit is adopted then the stellar distribution appears very strongly bimodal in mass. Note that the recent value for $(m - M)_V$ derived by Sandage and Cacciari (1990) is a full 0.25 mag less than the lower value derived here, given that the reddening to M3 is almost negligible.

The final figure, Figure 6-4-5 , shows the period-colour diagrams for M15 and M3 plotted with the new sequences. Evolutionary tracks are shown for all masses which cross the instability strip before the very rapid 'thermal' evolutionary phase which occurs at helium exhaustion. For the lower metallicity sequences which are superposed on the M15 RR Lyrae data in the upper panel, the sequences have $M_* \geq 0.66\,M_\odot$. In the lower panel, the tracks superposed on the M3 data satisfy $M_* \geq 0.62\,M_\odot$. The first-harmonic RR Lyrae c-type data have been 'fundamentalized' as suggested by BCDF; this is an approximation to the formulae for the period ratio P_1/P_0 derived from pulsation calculations (*e.g.*, van Albada and Baker 1971) which contains a term in the (unknown) mass. It is clear from the upper panel of this figure that the theoretical calculations are completely consistent with the M15 RR Lyrae data, assuming that the observational scatter and the derivation of mean colours will not significantly alter the location of the main ab-type variable distribution. However, with the adopted value for Y, the sequences used

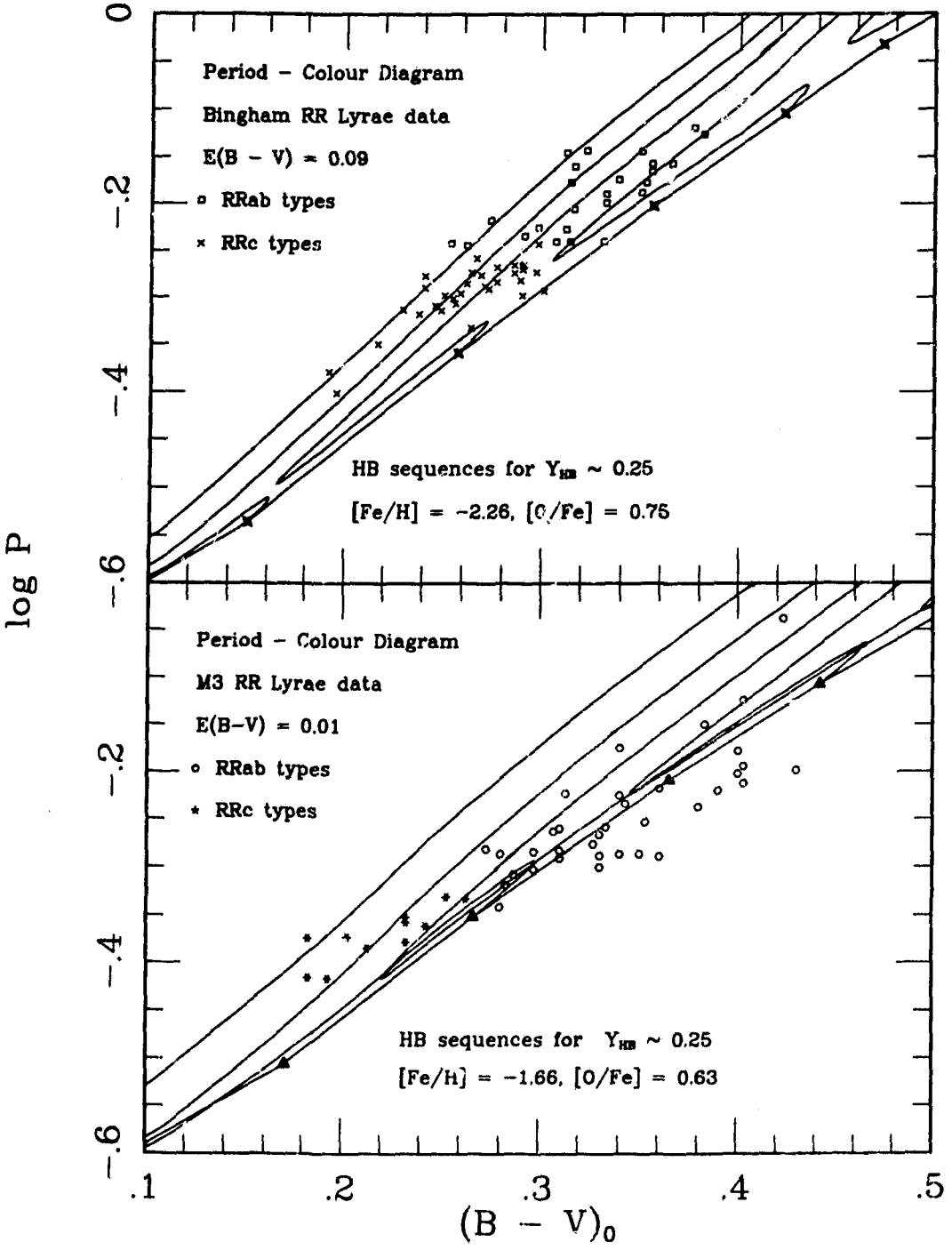

Fig. 6–4–5: Period–Colour diagrams for the clusters M15 and M3 using the data shown in Figure 6–3–1a for M15 and 6–4–4 for M3. Upper panel: Pulsational properties calculated from sequences depicted in Figure 5–4–11 with M15 data from BCDF. Lower panel Pulsational properties from sequences depicted in Figure 5–4–14 with M3 data from Sandage (1981).

to model the M3 pulsators clearly overestimate the periods at present (assuming that the mean colours are correct), although the disagreement is not quite as severe as that shown in §6.3 for the ZAHB with $Y_{HB} \sim 0.24$. In order to reconcile the calculations with the M3 data, it appears necessary to adopt a higher opacity in the models, for example, by the inclusion of enhanced α elements or by the upward revision of opacity calculations.

As a final note, it is claimed that the techniques used here, when combined with the resolution of certain issues affecting stellar interior physics, may provide very important constraints on globular cluster parameters. Sufficiently well-defined data samples for use with these methods are now becoming available, and may well serve to remove many of the problems in stellar astronomy which have arisen in the last decade of heightened interest in Galactic Chemical Evolution.

References

Abia, C., and Rebolo, R. 1989, *Ap. J.* **347** 186.

Applegate, J.H. 1988, *Ap. J.* **329** 803.

Barbuy, B. 1990 in *Proceedings of the Sixth Cambridge Conference on Cool Stars, Stellar Systems, and the Sun*, ed. G. Wallerstein, ASP Conference Proceedings No. 9 (BYU Press:Utah) p.328.

Bell, R.A. and Gustafsson, B. 1978, *Astr. Ap. Suppl.* **34** 229.

Bencivenni, D., Castellani, V., Tornambè, A. and Weiss, A. 1989, *Ap. J. Suppl.* **71** 109.

Bertelli, G., Bressan, A., Chiosi, C., and Angerer, K. 1986, *Astr. Ap. Suppl.* **66** 191.

Bergbusch, P.A. 1989, *in preparation*

Bergbusch, P.A. and VandenBerg, D.A., 1990, *in preparation*

Bingham, E., Cacciari, C., Dickens, R.J. and Fusi Pecci, F. 1984, *M.N.R.A.S.* **209** 765.

Boesgaard, A., and Steigman, G. 1985, *Ann. Rev. Astr. Ap* **23** 319.

Bressan, A.G. Bertelli, G. and Chiosi, C. 1981, *Astr. Ap.* **102** 25.

Buonanno, R., Buscema, G., Corsi, C.E., Iannicola, G., and Fusi Pecci, F. 1983, *Astr. Ap. Suppl.* **51** 83.

Buonanno, R., Corsi, C., and Fusi Pecci, F. 1985 (BCF), *Astr. Ap.* **145** 97.

Buonanno, R., Cacciari, C., Corsi, C.E., and Fusi Pecci, F. 1990, *Astr. Ap.* **230** 315.

Buzzoni, A., Fusi Pecci, F., Buonanno, R. and Corsi, C.E. 1983, *Astr. Ap.* **128** 94.

Cacciari, C., Clementini, G., and Buser, R. 1989, *Astr. Ap.* **209** 154.

Caloi, V. 1972, *Astr. Ap.* **20** 357.

Caputo, F., Castellani, V., and Quarta, M.L. 1984, *Astr. Ap.* **138** 457.

Caputo, F., Martinez Roger, C., and Paez, E. 1987, *Astr. Ap.* **183** 228.

Caputo, F., De Stefanis, P., Paez, E., and Quarta, M.L. 1987, *Astr. Ap. Suppl.* **68** 119.

Carbon, D.F., Langer, G.E., Butler, D., Kraft, R.P., Suntzeff, N.B, Kemper, E., Trefzger, C., and Romainshin W. 1982 , *Ap. J. Suppl.* **49** 207.

Castellani, V., Giannone, R., and Renzini, A. 1971a, *Ap. Sp. Sci.* **10**, 340.

Castellani, V., Giannone, R., and Renzini, A. 1971b, *Ap. Sp. Sci.* **10**, 355.

Castellani, V., and Tornambè, A. 1977, *Astr. Ap.* **61** 427. (CT)

Castellani, V., Chieffi, A., Puloné, L. and Tornambè 1985, *Ap. J.* **296** 204.

Castellani, V., Chieffi, A., and Puloné, L. 1990 *preprint, Universita di Pisa.*

Caughlan, G.R., Fowler, W.A., Harris, M.J., and Zimmerman, B.A. 1985, *Atomic and Nuclear Data Tables* **32** 192..

Caughlan, G.R., and Fowler, W.A. 1988, *Atomic and Nuclear Data Tables* **40** 283.

Chandrasekhar, S. 1939 *An Introduction to the Study of Stellar Structure* (Dover: New York)

Chieffi, A. and Straniero, O. 1989, *Ap. J. Suppl.* **71** 47.

Cloutman 1987, *Ap. J.* **313** 699.

Cogan, B.G. 1975, *Ap. J.* **201** 637.

Cox, A.N. 1987 in *IAU Colloquium 95: The Second Conference on Faint Stars*, ed. A.G. Davis Philip, D.S. Hayes, and J.W. Leibert (L. Davis Press: Schenectady) p. 161.

Cox, A.N., and Stewart, J.N. 1970, *Ap. J. Suppl.* **19** 243.

Cox, A.N., Hodson, S.W. and Clancy, S.P. 1983, *Ap. J.* **266** 94.

Cox, J.P. 1963, *Ap. J.* **138** 487.

Cox, J.P. and Giuli, R. 1968 in *Principles of Stellar Structure* (Gordon and Breach: New York)

Crocker, D.A., Rood, R.T., and O'Connell, R.W. 1988, *Ap. J.* **332** 236.

D'Antona, F. and Mazzitelli, I. 1985, *Ap. J.* **296** 502.

Demarque, P., and Mengel, J.G. 1972 , *Ap. J.* **171** 583.

Deupree, R.G. 1986, *Ap. J.* **303** 649.

Dickens, R.J. 1972, *M.N.R.A.S.* **157** 281.

Dorman, B. 1986 *M. Sc. thesis, Queen's University at Kingston.*

Dorman, B. 1990 in *The Confrontation Between Stellar Evolution and Pulsation*, ed. C. Cacciari, ASP Conference Proceedings No. 10 (BYU Press: Utah), in press.

Dorman, B., Irwin, A.W., and Pedersen, B.B. 1991 *in preparation*

Dorman, B., Nelson, L.A., and Chau, W-Y. 1989, *Ap. J.* **342** 1003.

Dorman, B., Lee, Y-W., and VandenBerg D.A. 1991, *Ap. J.* **366** *in press* (DLV).

Dorman, B., VandenBerg, D.A., and Laskarides P.G. 1989, *Ap. J.* **343** 750 (DVL).

Eddington, A.S. 1926 in *The Internal Constitution of the Stars* (Dover: New York), p 172

Eggen, O.J., Lynden-Bell, D., and Sandage, A.R. 1962, *Ap. J.* **136** 748.

Eggleton, P.P., and Faulkner, J. 1981 in *Physical Processes in Red Giants*, eds. I. Iben Jr. and A. Renzini (Dordrecht: Reidel), p.179

Eggleton, P.P., Faulkner, J., and Flannery, B.F. 1973, *Astr. Ap.* **23** 325.

Emden, V.R. 1907 *Gaskugeln* (Teuber: Leipzig)

Faulkner, D.J. 1971, *Proc. A.S.A.* **2** 26.

Faulkner, J. 1966, *Ap. J.* **144** 978 (F66).

Faulkner, J. 1972, *Ap. J.* **173** 401.

Faulkner, J. and Gilliland 1985, *Ap. J.* **299** 994.

Fontaine, G.F., Graboske, H.C., and van Horn, H.M. 1977, *Ap. J. Suppl.* **35** 293 (FGH).

Fowler, R.H. 1930, *M.N.R.A.S.* **91** 63.

Fowler, W.A., Caughlan, G.R., and Zimmermann. B.A. 1975, *Ann. Rev. Astr. Ap.*

13 69.

Fricke, K.J. and Strittmatter, P.A. 1972, *M.N.R.A.S.* **156** 129.

Friel, E. 1990 *private communication.*

Gehren, T., 1988 *Reviews in Modern Astronomy* **1**, 52.

Geisler, D. 1986, *Pub. A.S.P.,* **98** 762.

Gingold, R.A. 1974, *Ap. J.* **193** 177.

Gratton, R.G. 1985, *Astr. Ap.* **147** 169.

Green, E.M., Demarque, P., and King, C.R. 1987 *The Revised Yale Isochrones* (Yale University Observatory: New Haven)

Gross, P.G. 1973, *M.N.R.A.S.* **164** 65.

Harris, M.J., Fowler, W.A., Caughlan, G.R., and Zimmermann, B.A. 1983, *Ann. Rev. Astr. Ap.* **21** 165.

Hartwick, F.D.A. 1968, *Ap. J.* **154** 475.

Hartwick, F.D.A., and VandenBerg, D.A.1973a, *Pub. A.S.P.,* **85** 355.

Hartwick, F.D.A., and VandenBerg, D.A.1973b *unpublished*

Hayashi, C. 1966a in *Stellar Evolution*, eds. R.F. Stein and A.G.W. Cameron (Plenum Press: New York), p. 193

Hayashi, C. 1966b *ibid.*, p. 263

Hesser, J.E., Harris, W.E., VandenBerg, D.A., Allwright, J.W.B., Shott, P., and Stetson, P.B. 1987, *Pub. A.S.P.,* **99** 739 (HHVASS).

Hill, G., 1986, *Pub. D.A.O.* **16** 67.

Hofmeister, E., Kippenhahn, R., and Weigert, A. 1966 in *Stellar Evolution*, eds. R.F. Stein and A.G.W. Cameron (Plenum Press: New York), p. 263

Hopf, E. 1931, *M.N.R.A.S.* **91** 653.

Huebner, W.F., Merts, A.L., Magee, N.H., and Argo M.F. 1977 *Los Alamos Sci. Lab. Rep.* No. LA-6760-M

Hummer, D.G. and Mihalas, D. 1988, *Ap. J.* **331** 794.

Huppert, H.E. 1979 in *Problems of Stellar Convection Lecture Notes in Physics* **71** (Springer-Verlag:Berlin) p.239

Iben, I. 1968, *Nature* **220** 143.

Iben, I. and Faulkner, J. 1968, *Ap. J.* **153** 101.

Iben, I. and Renzini, A. 1984, *Phys. Rep.* **105** 329.

Iben, I. and Rood, R.T. 1970, *Ap. J.* **161** 587.

Iglesias, C.A. Rogers, F.C. and Wilson 1990, *Ap. J.* **360** 22[illegible]

Irwin, A.W. 1990, *in preparation*

Itoh, N., Adachi, T., Nakagawa, M., Kohyama, Y., and Munakata, H. 1989, *Ap. J.* **339** 354.

Jones, R.V., Carney, B.W., and Latham, D.W. 1988, *Ap. J.* **332** 206.

Jorgensen, H.E. and Petersen, J.O. 1967, *Z. Ap* **67** 377.

Kippenhahn, R., Weigert, A., and Hofmeister, E. 1967, *Meth. Comp. Phys.* **7** 129.

Kovács, G. 1985, *Acta Astr.* **35** 37.

Kraft, R.P. 1985 in *The Production and Distribution of C, N, and O elements* ed. I.J. Danziger, F. Matteucci, and K. Kjär (Garching bei Munchen: ESO), p.21.

Krishna-Swamy, K.S. 1966, *Ap. J.* **145** 174.

Kurucz, R. 1979, *Ap. J. Suppl.* **40** 1.

Lane, J. Homer, 1869, *Am. J. Sci.* 2^{nd} ser. **50** 57.

Langer, G.E., Kraft, R.P., Carbon, D.F., Friel E., and Oke, J.B. 1986, *Pub. A.S.P.*, **98** 473.

Laskarides, P.G. 1972 *Ph.D. thesis, University of Victoria*

Lattanzio, J. 1986 *Ph. D. thesis, Monash University*

Lauterborn, D., Refsdal, S., and Weigert, A. 1971a, *Astr. Ap.* **10** 97.

Lauterborn, D., Refsdal, S., and Stabell, R. 1972, *Astr. Ap.* **17** 113.

Lauterborn, D. 1973, *Astr. Ap.* **24** 421.

Ledoux, P. 1947, *Ap. J.* **105** 305.

Lee, S-W. 1977, *Astr. Ap. Suppl.* **27** 381.

Lee, Y-W. 1989 *Ph.D. thesis, Yale University*

Lee, Y-W. 1990, *Ap. J.* **367** *in press.*

Lee, Y-W., Demarque, P., and Zinn, R.A. 1987 in *I.A.U. Colloquium 95: The Second Conference on Faint Blue Stars* ed. A.G.D. Philip, D.S. Hayes, and J. Liebert. (L. Davis Press: Schenectady), p.137

Lee, Y-W., Demarque, P., and Zinn, R.A. 1990, *Ap. J.* **350** 155.

Lee, Y-W. and Demarque, P. 1990, *Ap. J.* in press.

Liu, T. and Janes, K. 1990, *Ap. J.* **354** 273.

Maeder, A. 1985 in *The Production and Distribution of C, N, and O elements* ed. I.J. Danziger, F. Matteucci, and K. Kjär (ESO: Munchen), p.187.

Maeder, A. 1975, *Astr. Ap.* **40** 303.

Magni, G., and Mazzitelli I. 1979, *Astr. Ap.* **72** 134.

Mengel, J. and Sweigart, A.V. 1981 in *Astrophysical Parameters for Globular Clusters*, I.A.U. Coll. 68 eds. A.G. Davis Philip and D.S. Hayes (L. Davis Press: Schenectady) p. 277

Milne, E.A. 1931, *M.N.R.A.S.* **91** 751.

Milne, E.A. 1932, *M.N.R.A.S.* **92** 610.

Mironov, A.V. 1972, *Soviet Astron.* **17** 16.

Munakata, H., Kohyama, Y., and Itoh, N. 1985, *Ap. J.* **296** 197.

Munakata, H., Kohyama, Y., and Itoh, N. 1986, *Ap. J.* **304** 580.

Munakata, H., Kohyama, Y., and Itoh, N. 1986, *Ap. J.* **310** 815.

Nemec, J. and Clement, C. 1989, *A.J.* **98** 860.

Matteucci, F. 1987 in *Stellar Evolution and Dynamics in the Outer Halo of the Galaxy* ed. M. Azzopardi and F. Matteucci (ESO: Munchen), p.609

Oosterhoff, P. Th. 1939 *Observatory* **62** 104

Paczyński, B. 1970, *Acta Astr.* **20** 195.

Pagel, B.E.J., Terlevich, R.J., and Melnick, J. 1986, *Pub. A.S.P.*, **98** 1005.

Petersen, J.O., 1973, *Astr. Ap.* **27** 89.

Pilachowski, C.A. 1988, *Ap. J. Lett.* **326** L57.

Preston, G.W. 1961, *Ap. J.* **133** 29.

Profitt, C.A. and Michaud, G. 1991, *Ap. J.* in press.

Refsdal, S. and Weigert, A. 1970, *Astr. Ap.* **6** 426.

Renzini, A. 1977, in *Advanced Stages of Stellar Evolution*, ed. P. Bouvier and A. Maeder (Geneva Observatory), p.149.

Renzini, A. 1984 in *I.A.U. Symposium 105: Observational Tests of the Stellar Evolution Theory* ed. Maeder, A. and Renzini, A. (Reidel: Dordrecht) p.21

Renzini, A. 1987, *Astr. Ap.* **188** 49.

Renzini, A. and Fusi Pecci F. 1988, *Ann. Rev. Astr. Ap.* **26** 199.

Robertson, J.W., and Faulkner, D.J. 1972 , *Ap. J.* **171** 309.

Ross, J.E. and Aller, L.H. 1976, *Science*, **191** 1223.

Rood, R.T. 1970, *Ap. J.* **161** 145.

Rood, R.T. 1973, *Ap. J.* **184** 815.

Rood, R.T. and Crocker, D. A. 1989 in *The Use of Pulsating Stars in Fundamental Problems of Astronomy* I.A.U. Colloquium No. 111 ed. E.G. Schmidt (CUP: Cambridge) p.xxx

Rood, R.T. and Iben, I. 1968, *Ap. J.* **154** 215.

Rood, R.T.. and Seitzer, P.E. 1981, in *Astrophysical Parameters for Globular Clusters*, I.A.U. Coll. 68 eds. A.G. Davis Philip and D.S. Hayes (L. Davis Press: Schenectady) p. 36

Russell, H.N. 1931, *M.N.R.A.S.* **91** 739.

Sandage, A. 1970, *Ap. J.* **162** 841.

Sandage, A. 1981, *Ap. J.* **248** 161.

Sandage, A. 1982a, *Ap. J.* **252** 553.

Sandage, A. 1982b, *Ap. J.* **252** 574.

Sandage, A. 1987 in *I.A.U. Colloquium 95: The Second Conference on Faint Blue Stars* ed. A.G.D. Philip, D.S. Hayes J.W. Liebert (L. Davis Press: Schenectady), p.41

Sandage, A. 1990a, *Ap. J.* **350** 603.

Sandage, A. 1990b, *Ap. J.* **350** 631.

Sandage, A., and Cacciari, C. 1990, *Ap. J.* **350** 645.

Sandage, A., Katem, B., and Kristian, J. 1968, *Ap. J. Lett.* **153** L129.

Sandage, A., Katem, B., and Sandage, M. 1981, *Ap. J. Suppl.* **46** 41.

Saslaw, W.C. and Schwarzschild, M. 1965, *Ap. J.* **142** 1468.

Schönberg, M. and Chandrasekhar, S. 1942, *Ap. J.* **96** 161.

Schwarzschild, K. 1906, *Gott. Nach.* **1** 41.

Schwarzschild, M. 1958 *Structure and Evolution of the Stars* (Dover: New York)

Schwarzschild, M. 1970, *Q.J.R.A.S.* **11** 12.

Schwarzschild, M. and Härm, K. 1958, *Ap. J.* **128** 348.

Schwarzschild, M., Howard, R. and Härm, K. 1957, *Ap. J.* **125** 233.

Searle, L., and Zinn, R. 1978, *Ap. J.* **225** 357.

Shaviv, G and Salpeter E.E. 1973, *Ap. J.* **184** 191.

Smith, G.H. 1987, *Pub. A.S.P.*, **99** 67.

Sneden, C. 1985 in *The Production and Distribution of C, N and O elements* ed. I.J. Danziger, F. Matteuci, and K. Kjär (Garching bei München: ESO), p.1

Sneden, C., Pilachowski, C.A., and VandenBerg, D.A. 1986, *Ap. J.* **311** 826.

Spiegel, E. 1969, *Comm. Ap. Sp. Phys.* **1** 57.

Spiegel, E. 1979 in *Problems of Stellar Convection Lecture Notes in Physics* **71** (Springer-Verlag:Berlin) p.1

Stetson, P.B. 1990 *private communication.*

Stothers, R. 1970, *M.N.R.A.S.* **151** 65.

Straniero, O. 1988, *Astr. Ap. Suppl.* **76** 157.

Stein, R.F. 1966 in *Stellar Evolution* eds. R.F. Stein and A.G.W. Cameron (Plenum Press: New York), p.3

Sweigart, A.V. 1987, *Ap. J. Suppl.* **65** 95. (S87)

Sweigart, A.V. 1990 in *The Confrontation Between Stellar Evolution and Pulsation*, ed. C. Cacciari, ASP Conference Proceedings No. 10 (BYU Press: Utah), in press.

Sweigart, A.V., and Gross, P.G. 1974, *Ap. J.* **190** 101. (SG74)

Sweigart, A.V., and Gross, P.G. 1976, *Ap. J. Suppl.* **32** 367. (SG76)

Sweigart, A.V., and Gross, P.G. 1978, *Ap. J. Suppl.* **36** 405.

Sweigart, A.V., and Demarque, P. 1972, *Ap. J.* **20** 445.

Sweigart, A.V., and Mengel, J. 1979, *Ap. J.* **229** 624.

Sweigart, A.V., Renzini, A., and Tornambè 1987, *Ap. J.* **312** 762.

Tornambè, A., 1987, in *Stellar Evolution and Dynamics in the Outer Halo of the Galaxy* ed. M. Azzopardi and F. Matteucci (ESO: Munchen), p.307.

Trefzger, C. Carbon, D.F., Langer, G.E., Suntzeff, N.B., and Kraft, R. 1983, *Astr. Ap.* **166** 144.

Turner, J.S. 1974, *Ann. Rev. Fl. Mechs.* **6** 37.

Upton, E.K.L., Little, S.J., and Dworetsky, M.M. 1968, *Ap. J.* **154** 597.

van Altena, W.F., Lee, J.T., Hanson, R.B. and Lutz, T.E. 1988 in *The Calibration of Stellar Ages* ed. A.G.D. Philip (Davis Press: Schenectady), p.175

van Albada, T.S. and Baker, N. 1971, *Ap. J.* **169** 311.

VandenBerg, D.A.1983, *Ap. J. Suppl.* **51** 29.

VandenBerg, D.A. 1984 in *I.A.U. Symposium 105: Observational Tests of the Stellar Evolution Theory* ed. Maeder, A. and Renzini, A. (Reidel: Dordrecht)

p.143

VandenBerg, D.A. 1988a in *The Extragalactic Distance Scale* ed. S. Van den bergh and C.J. Pritchet, A.S.P. Conference series (BYU Press: Utah) p.187

VandenBerg, D.A. 1988b in *Globular Cluster Systems in Galaxies*, ed. J.E. Grindlay and A.G.D. Philip (Kluwer: Dordrecht) p.107.

VandenBerg, D.A. 1988c in *The Calibration of Stellar Ages* ed. A.G.D. Philip (Davis Press: Schenectady), p.117

VandenBerg, D.A. 1990, *in preparation*

VandenBerg, D.A. and Bell, R.A. 1985, *Ap. J. Suppl.* **58** 561 (VB85).

VandenBerg, D.A. and Smith, G.H. 1988, *Pub. A.S.P.*, **100** 314.

Weiss, A. 1989, *Astr. Ap.* **209** 135.

Wheeler, J.C., Sneden, C., and Truran, J.W. 1989, *Ann. Rev. Astr. Ap.* **27** 279.

Xiong, Da-run 1981 *Sci. Sin.* **24** 1406

Xiong, Da-run 1986, *Astr. Ap.* **167** 239.

Yahil, A. and van den Horn, L. 1985, *Ap. J.* **296** 554.

Yang, J., Turner, M.S., Schramm, D.N., and Olive, K.A. 1985, *Ap. J.* **281** 493.

Zhevakin, S.A. 1953, *Russian A.J.* **30** 161.

Appendices

This appendix contains tabulations of the Zero Age Horizontal Branch Sequences computed for this study. The first table, Table A-1, gives the set of ZAHBs used as initial models for the evolutionary tracks which are partially tabulated in Appendix B. The other four tables contain sequences which are used to demonstrate the effects of variations in parameters (Tables A-2 to A-4) and to provide results for scaled solar sequences for comparison with those used for the main grid of calculations (Table A-5).

Appendix B contains tabulations of the evolutionary tracks. For each composition, four or five sequences have been selected to illustrate the run of surface and core properties through evolution. These tables have been obtained from the original calculations using Hermite spline interpolation with the central helium abundance as independent variable for $Y_c > 0$, and thereafter, with the time coordinate as independent variable, at intervals of 750,000 years. The data listed in the colums are as follows. The first column (t_6) gives the age since the initial model in units of 10^6 years. Note that the ZAHB models tabulated in Appendix A have age 1 Myr, and this is reflected in these tabulations. The second column gives Y_c, the central helium abundance. The third, fourth, and fifth column contain the logarithms respectively of the luminosity, $\log L$, in solar units, the effective temperature $\log T_{eff}$, and the surface gravity, $\log g_s$. The next two columns give the logarithms of the cen the mass contained in the convective core. M_{sc}, the mass coordinate at ..e outer edge of the semiconvection zone (or the symbol 'N/A' if this is not applicable) and M_{sh}, the mass coordinate at the peak of the hydrogen-burning shell. These latter quantities are in solar units.

Table A-1: Zero Age Sequences with $[O/Fe] > 0$

$M/M_\odot$	$\log L$	$\log T_{eff}$	M_V	$(B-V)$	$\log g_s$
(a) [Fe/H] = −2.26 [O/Fe] = 0.75 $M_c = 0.493$ $Y_{HB} = 0.245$					
0.540	1.3081	4.2677	3.2635	−0.1812	4.8797
0.560	1.3524	4.2180	2.8475	−0.1604	4.6522
0.580	1.4121	4.1678	2.3944	−0.1410	4.4070
0.600	1.4780	4.1119	1.9037	−0.1184	4.1323
0.620	1.5352	4.0530	1.4414	−0.0930	3.8535
0.640	1.5805	3.9947	1.0353	−0.0502	3.5890
0.650	1.5992	3.9667	0.8691	−0.0277	3.4653
0.660	1.6159	3.9394	0.7443	−0.0034	3.3457
0.670	1.6308	3.9130	0.6430	0.0725	3.2320
0.680	1.6443	3.8874	0.5822	0.1498	3.1223
0.700	1.6671	3.8395	0.5519	0.2576	2.9204
0.720	1.6864	3.7967	0.5476	0.3556	2.7424
0.740	1.7025	3.7702	0.5425	0.4222	2.6320
0.780	1.7290	3.7513	0.5104	0.4729	2.5530
0.820	1.7504	3.7429	0.4752	0.5004	2.5197
0.900	1.7850	3.7358	0.4058	0.5283	2.4971
1.000	1.8213	3.7326	0.3234	0.5419	2.4938
1.100	1.8545	3.7325	0.2408	0.5424	2.5014
1.200	1.8871	3.7334	0.1572	0.5387	2.5103
1.300	1.9204	3.7358	0.0680	0.5286	2.5214
1.400	1.9552	3.7399	−0.0291	0.5116	2.5350
1.500	1.9916	3.7453	−0.1326	0.4924	2.5502
(b) [Fe/H] = −2.03 [O/Fe] = 0.70 $M_c = 0.490$ $Y_{HB} = 0.247$					
0.540	1.3060	4.2575	3.2079	−0.1769	4.8409
0.560	1.3575	4.2059	2.7641	−0.1554	4.5989
0.580	1.4306	4.1487	2.2378	−0.1334	4.3121
0.600	1.5040	4.0831	1.6818	−0.1065	3.9910
0.620	1.5614	4.0150	1.1825	−0.0658	3.6756
0.640	1.6050	3.9481	0.7943	−0.0117	3.3780
0.650	1.6219	3.9167	0.6728	0.0581	3.2423
0.660	1.6373	3.8853	0.5980	0.1558	3.1082
0.670	1.6506	3.8558	0.5755	0.2239	2.9832
0.680	1.6625	3.8272	0.5725	0.2882	2.8633
0.700	1.6826	3.7795	0.5742	0.4078	2.6652
0.740	1.7134	3.7493	0.5495	0.4933	2.5378
0.780	1.7361	3.7397	0.5149	0.5277	2.4993
0.820	1.7548	3.7341	0.4826	0.5509	2.4799
0.900	1.7853	3.7298	0.4182	0.5692	2.4728
1.000	1.8178	3.7276	0.3433	0.5788	2.4772
1.100	1.8473	3.7274	0.2704	0.5798	2.4884
1.200	1.8765	3.7284	0.1949	0.5756	2.5007
1.300	1.9061	3.7300	0.1167	0.5687	2.5125
1.400	1.9377	3.7320	0.0323	0.5602	2.5211
1.500	1.9718	3.7356	−0.0625	0.5449	2.5314

Table A-1 (continued)

$M/M_\odot$	$\log L$	$\log T_{eff}$	M_V	$(B-V)$	$\log g_s$
(c) [Fe/H] = −1.78 [O/Fe] = 0.66 $M_c = 0.488$ $Y_{HB} = 0.248$					
0.540	1.3051	4.2440	3.1303	−0.1710	4.7878
0.560	1.3708	4.1877	2.6231	−0.1485	4.5126
0.580	1.4617	4.1177	1.9830	−0.1209	4.1571
0.600	1.5386	4.0376	1.3577	−0.0839	3.7746
0.610	1.5682	3.9968	1.0795	−0.0525	3.5890
0.620	1.5923	3.9573	0.8552	−0.0192	3.4139
0.630	1.6130	3.9183	0.6981	0.0522	3.2440
0.640	1.6305	3.8798	0.6130	0.1706	3.0795
0.650	1.6455	3.8427	0.5977	0.2552	2.9227
0.660	1.6584	3.8076	0.5994	0.3403	2.7762
0.670	1.6697	3.7760	0.6068	0.4254	2.6451
0.680	1.6784	3.7607	0.6100	0.4701	2.5813
0.720	1.7099	3.7413	0.5726	0.5377	2.4970
0.740	1.7214	3.7361	0.5575	0.5587	2.4770
0.780	1.7406	3.7304	0.5255	0.5826	2.4575
0.820	1.7566	3.7266	0.4966	0.5988	2.4481
0.900	1.7834	3.7233	0.4397	0.6131	2.4484
1.000	1.8117	3.7221	0.3730	0.6184	2.4614
1.100	1.8377	3.7221	0.3083	0.6185	2.4767
1.200	1.8627	3.7230	0.2434	0.6147	2.4929
1.300	1.8881	3.7242	0.1766	0.6096	2.5073
1.400	1.9147	3.7259	0.1053	0.6023	2.5196
1.500	1.9433	3.7281	0.0275	0.5929	2.5298
(d) [Fe/H] = −1.66 [O/Fe] = 0.63 $M_c = 0.487$ $Y_{HB} = 0.248$					
0.540	1.3055	4.2354	3.0783	−0.1672	4.7529
0.560	1.3806	4.1751	2.5242	−0.1437	4.4524
0.580	1.4782	4.0967	1.8251	−0.1122	4.0568
0.600	1.5530	4.0095	1.1793	−0.0621	3.6478
0.610	1.5808	3.9656	0.9147	−0.0271	3.4517
0.620	1.6032	3.9227	0.7333	0.0363	3.2645
0.630	1.6229	3.8800	0.6314	0.1710	3.0811
0.640	1.6394	3.8383	0.6158	0.2670	2.9047
0.650	1.6530	3.7992	0.6194	0.3652	2.7413
0.660	1.6647	3.7718	0.6234	0.4417	2.6264
0.680	1.6837	3.7509	0.6141	0.5095	2.5370
0.700	1.6985	3.7411	0.5999	0.5462	2.4954
0.720	1.7109	3.7350	0.5854	0.5711	2.4711
0.740	1.7214	3.7313	0.5697	0.5865	2.4575
0.780	1.7391	3.7258	0.5418	0.6098	2.4407
0.820	1.7540	3.7233	0.5122	0.6205	2.4376
0.900	1.7792	3.7206	0.4579	0.6322	2.4421
1.000	1.8060	3.7195	0.3947	0.6370	2.4566
1.100	1.8303	3.7196	0.3340	0.6367	2.4739
1.200	1.8537	3.7203	0.2737	0.6337	2.4914
1.300	1.8771	3.7216	0.2115	0.6282	2.5078
1.400	1.9010	3.7232	0.1471	0.6214	2.5224
1.500	1.9275	3.7251	0.0753	0.6132	2.5336

Table A-1 (continued)

$M/M_\odot$	$\log L$	$\log T_{eff}$	M_V	$(B-V)$	$\log g_s$
(e) [Fe/H] = −1.48 [O/Fe] = 0.60 $M_c = 0.485$ $Y_{HB} = 0.249$					
0.540	1.3089	4.2237	3.0008	−0.1622	4.7030
0.560	1.4000	4.1553	2.3599	−0.1358	4.3539
0.580	1.5039	4.0636	1.5835	−0.0981	3.8986
0.590	1.5434	4.0143	1.2284	−0.0661	3.6690
0.600	1.5754	3.9639	0.9228	−0.0256	3.4429
0.610	1.6004	3.9144	0.7202	0.0675	3.2270
0.620	1.6207	3.8659	0.6389	0.2063	3.0198
0.630	1.6381	3.8183	0.6365	0.3197	2.8190
0.640	1.6521	3.7778	0.6430	0.4304	2.6497
0.650	1.6636	3.7595	0.6439	0.4891	2.5719
0.660	1.6737	3.7497	0.6388	0.5245	2.5290
0.700	1.7026	3.7320	0.6127	0.5952	2.4550
0.740	1.7217	3.7242	0.5888	0.6280	2.4291
0.780	1.7387	3.7208	0.5572	0.6425	2.4210
0.820	1.7524	3.7187	0.5297	0.6514	2.4208
0.900	1.7754	3.7164	0.4798	0.6612	2.4288
1.100	1.8227	3.7154	0.3656	0.6654	2.4650
1.200	1.8437	3.7163	0.3107	0.6616	2.4852
1.300	1.8644	3.7174	0.2558	0.6569	2.5036
1.400	1.8856	3.7188	0.1987	0.6510	2.5202
1.500	1.9079	3.7205	0.1379	0.6438	2.5347
(f) [Fe/H] = −1.26 [O/Fe] = 0.55 $M_c = 0.484$ $Y_{HB} = 0.250$					
0.520	1.2571	4.2697	3.4163	−0.1812	4.9224
0.540	1.3167	4.2050	2.8703	−0.1544	4.6202
0.560	1.4289	4.1215	2.0929	−0.1221	4.1899
0.580	1.5322	4.0108	1.2407	−0.0634	3.6590
0.590	1.5676	3.9522	0.9025	−0.0142	3.3967
0.600	1.5953	3.8946	0.7042	0.1346	3.1457
0.610	1.6168	3.8368	0.6700	0.2757	2.9002
0.620	1.6341	3.7842	0.6765	0.4185	2.6796
0.630	1.6477	3.7580	0.6829	0.5058	2.5682
0.640	1.6580	3.7476	0.6794	0.5459	2.5231
0.660	1.6765	3.7343	0.6687	0.6000	2.4647
0.700	1.7007	3.7224	0.6458	0.6495	2.4188
0.740	1.7174	3.7174	0.6204	0.6704	2.4058
0.780	1.7330	3.7140	0.5926	0.6848	2.3996
0.820	1.7455	3.7120	0.5681	0.6932	2.4007
0.900	1.7665	3.7096	0.5240	0.7032	2.4109
1.000	1.7893	3.7089	0.4698	0.7059	2.4307
1.100	1.8095	3.7093	0.4184	0.7040	2.4538
1.200	1.8284	3.7104	0.3679	0.6992	2.4769
1.300	1.8467	3.7117	0.3182	0.6936	2.4985
1.400	1.8649	3.7131	0.2685	0.6876	2.5183
1.500	1.8836	3.7147	0.2168	0.6809	2.5360

Table A-1 (continued)

$M/M_\odot$	$\log L$	$\log T_{eff}$	M_V	$(B-V)$	$\log g_s$
(g) [Fe/H] = −1.03 [O/Fe] = 0.50 $M_c = 0.482$ $Y_{HB} = 0.252$					
0.520	1.2568	4.2506	3.3009	−0.1731	4.8460
0.540	1.3331	4.1781	2.6688	−0.1441	4.4965
0.560	1.4626	4.0719	1.7359	−0.1012	3.9576
0.570	1.5159	4.0061	1.2600	−0.0596	3.6491
0.580	1.5563	3.9380	0.8901	0.0013	3.3436
0.590	1.5840	3.8729	0.7263	0.1950	3.0630
0.600	1.6090	3.8027	0.7186	0.3727	2.7644
0.610	1.6257	3.7607	0.7292	0.5074	2.5870
0.620	1.6390	3.7461	0.7272	0.5661	2.5225
0.640	1.6586	3.7301	0.7243	0.6322	2.4524
0.660	1.6729	3.7216	0.7168	0.6672	2.4174
0.700	1.6933	3.7125	0.6964	0.7048	2.3864
0.740	1.7097	3.7081	0.6705	0.7232	2.3766
0.780	1.7230	3.7053	0.6471	0.7348	2.3748
0.820	1.7345	3.7033	0.6255	0.7430	2.3770
0.900	1.7542	3.7014	0.5834	0.7506	2.3901
1.000	1.7740	3.7010	0.5358	0.7518	2.4146
1.100	1.7936	3.7014	0.4858	0.7496	2.4380
1.200	1.8106	3.7026	0.4395	0.7442	2.4634
1.300	1.8270	3.7039	0.3944	0.7385	2.4873
1.400	1.8430	3.7054	0.3495	0.7320	2.5094
1.500	1.8589	3.7072	0.3039	0.7244	2.5306
(h) [Fe/H] = −0.78 [O/Fe] = 0.39 $M_c = 0.479$ $Y_{HB} = 0.256$					
0.520	1.2583	4.2260	3.1500	−0.1624	4.7462
0.540	1.3601	4.1391	2.3725	−0.1282	4.3133
0.550	1.4310	4.0776	1.8474	−0.1030	4.0042
0.560	1.4920	4.0050	1.3159	−0.0586	3.6607
0.570	1.5366	3.9274	0.9100	0.0272	3.3133
0.580	1.5689	3.8484	0.7760	0.2573	2.9725
0.590	1.5900	3.7788	0.7828	0.4608	2.6804
0.600	1.6099	3.7480	0.7891	0.5809	2.5448
0.610	1.6212	3.7344	0.7994	0.6375	2.4861
0.620	1.6314	3.7261	0.8017	0.6716	2.4501
0.640	1.6486	3.7149	0.7974	0.7183	2.4017
0.660	1.6592	3.7089	0.7919	0.7435	2.3805
0.700	1.6794	3.7009	0.7702	0.7775	2.3540
0.740	1.6941	3.6965	0.7500	0.7968	2.3456
0.780	1.7063	3.6935	0.7310	0.8095	2.3443
0.820	1.7171	3.6917	0.7110	0.8170	2.3479
0.900	1.7356	3.6902	0.6709	0.8229	2.3639
1.000	1.7537	3.6901	0.6266	0.8224	2.3911
1.100	1.7716	3.6910	0.5788	0.8177	2.4183
1.200	1.7885	3.6920	0.5331	0.8127	2.4433
1.300	1.8031	3.6938	0.4902	0.8044	2.4705
1.400	1.8170	3.6955	0.4495	0.7966	2.4959
1.500	1.8311	3.6976	0.4069	0.7873	2.5199

Table A-1 (continued)

$M/M_\odot$	$\log L$	$\log T_{eff}$	M_V	$(B-V)$	$\log g_s$
(i) [Fe/H] = −0.65 [O/Fe] = 0.30 $M_c = 0.478$ $Y_{HB} = 0.259$					
0.520	1.2605	4.2088	3.0413	−0.1550	4.6752
0.540	1.3773	4.1098	2.1615	−0.1159	4.1790
0.550	1.4462	4.0390	1.6055	−0.0835	3.8347
0.560	1.5009	3.9603	1.0996	−0.0173	3.4729
0.570	1.5402	3.8771	0.8344	0.1936	3.1086
0.580	1.5682	3.7923	0.8211	0.4252	2.7490
0.590	1.5868	3.7511	0.8362	0.5803	2.5729
0.600	1.6027	3.7340	0.8444	0.6515	2.4958
0.620	1.6213	3.7170	0.8571	0.7220	2.4235
0.640	1.6367	3.7074	0.8525	0.7627	2.3837
0.660	1.6484	3.7016	0.8445	0.7876	2.3619
0.700	1.6665	3.6942	0.8272	0.8198	2.3400
0.740	1.6792	3.6898	0.8128	0.8386	2.3340
0.780	1.6920	3.6868	0.7929	0.8515	2.3317
0.820	1.7028	3.6848	0.7743	0.8598	2.3347
0.900	1.7191	3.6834	0.7398	0.8651	2.3534
1.000	1.7400	3.6831	0.6893	0.8656	2.3770
1.100	1.7570	3.6842	0.6427	0.8600	2.4057
1.200	1.7714	3.6860	0.5998	0.8514	2.4363
1.300	1.7871	3.6874	0.5553	0.8447	2.4610
1.400	1.8001	3.6900	0.5129	0.8329	2.4905
1.500	1.8147	3.6917	0.4702	0.8252	2.5126
(j) [Fe/H] = −0.47 [O/Fe] = 0.23 $M_c = 0.476$ $Y_{HB} = 0.266$					
0.510	1.2298	4.2282	3.2381	−0.1628	4.7751
0.520	1.2699	4.1842	2.8695	−0.1454	4.5676
0.540	1.4074	4.0634	1.8316	−0.0961	3.9631
0.550	1.4717	3.9799	1.2526	−0.0362	3.5729
0.560	1.5173	3.8895	0.8944	0.1608	3.1727
0.570	1.5496	3.7969	0.8601	0.4214	2.7784
0.580	1.5700	3.7474	0.8829	0.6133	2.5676
0.590	1.5845	3.7255	0.9163	0.7050	2.4727
0.600	1.5982	3.7170	0.9126	0.7410	2.4325
0.620	1.6153	3.7028	0.9216	0.8022	2.3729
0.660	1.6364	3.6901	0.9183	0.8573	2.3279
0.700	1.6545	3.6830	0.9027	0.8880	2.3072
0.740	1.6682	3.6782	0.8897	0.9085	2.2984
0.780	1.6796	3.6759	0.8718	0.9181	2.3008
0.820	1.6895	3.6740	0.8562	0.9260	2.3050
0.900	1.7069	3.6726	0.8198	0.9312	2.3224
1.000	1.7245	3.6728	0.7754	0.9294	2.3512
1.100	1.7393	3.6741	0.7329	0.9229	2.3830
1.200	1.7559	3.6755	0.6853	0.9162	2.4098
1.300	1.7698	3.6781	0.6392	0.9043	2.4411
1.400	1.7836	3.6802	0.5958	0.8947	2.4678
1.500	1.7968	3.6821	0.5549	0.8860	2.4924

Table A-2: Additional ZAHB sequences for low Z

$M/M_\odot$	$\log L$	$\log T$	M_V	$(B-V)$	$\log g_s$
(a) [Fe/H] = −2.27 [O/Fe] = 0.50 $M_c = 0.496$ $Y_{HB} = 0.246$					
0.540	1.3122	4.2794	3.3264	−0.1861	4.9222
0.560	1.3518	4.2297	2.9201	−0.1655	4.6998
0.580	1.4000	4.1837	2.5200	−0.1473	4.4829
0.600	1.4550	4.1360	2.0996	−0.1282	4.2516
0.620	1.5075	4.0859	1.6857	−0.1074	4.0130
0.640	1.5526	4.0356	1.3074	−0.0817	3.7807
0.650	1.5723	4.0110	1.1335	−0.0619	3.6690
0.660	1.5900	3.9869	0.9757	−0.0443	3.5617
0.670	1.6060	3.9636	0.8407	−0.0244	3.4589
0.680	1.6206	3.9411	0.7369	−0.0049	3.3609
0.700	1.6461	3.8984	0.5831	0.1235	3.1769
0.720	1.6678	3.8586	0.5330	0.2160	3.0085
0.740	1.6864	3.8230	0.5204	0.2940	2.8593
0.780	1.7167	3.7739	0.5017	0.4137	2.6554
0.820	1.7414	3.7570	0.4685	0.4563	2.5851
0.860	1.7623	3.7486	0.4331	0.4814	2.5512
0.900	1.7809	3.7445	0.3956	0.4950	2.5357
(a) [Fe/H] = −2.27 [O/Fe] = 1.00 $M_c = 0.490$ $Y_{HB} = 0.247$					
0.540	1.3042	4.2571	3.2070	−0.1767	4.8410
0.560	1.3578	4.2056	2.7586	−0.1553	4.5974
0.580	1.4359	4.1469	2.2111	−0.1328	4.2997
0.600	1.5117	4.0793	1.6393	−0.1049	3.9681
0.620	1.5694	4.0097	1.1347	−0.0616	3.6464
0.640	1.6121	3.9421	0.7602	−0.0069	3.3469
0.650	1.6292	3.9097	0.6401	0.0845	3.2071
0.660	1.6440	3.8783	0.5819	0.1704	3.0733
0.670	1.6573	3.8478	0.5679	0.2390	2.9447
0.680	1.6689	3.8190	0.5670	0.3021	2.8243
0.700	1.6888	3.7724	0.5728	0.4167	2.6306
0.720	1.7049	3.7552	0.5624	0.4612	2.5579
0.740	1.7185	3.7474	0.5445	0.4851	2.5251
0.780	1.7408	3.7391	0.5077	0.5145	2.4920
0.820	1.7592	3.7336	0.4755	0.5374	2.4736
0.860	1.7749	3.7312	0.4425	0.5477	2.4691
0.900	1.7893	3.7298	0.4102	0.5538	2.4685

Table A-3: Scaled-solar sequences with Low Y

$M/M_\odot$	$\log L$	$\log T$	M_V	$(B-V)$	$\log g$
(a) [Fe/H] = −2.27 M_c = 0.510 Y_{HB} = 0.209					
0.560	1.3641	4.2504	3.0153	−0.1748	4.7704
0.580	1.3942	4.2002	2.6345	−0.1537	4.5548
0.600	1.4252	4.1562	2.2929	−0.1361	4.3623
0.620	1.4572	4.1152	1.9747	−0.1188	4.1807
0.640	1.4889	4.0760	1.6788	−0.1021	4.0060
0.650	1.5042	4.0570	1.5398	−0.0936	3.9214
0.660	1.5189	4.0384	1.4062	−0.0825	3.8387
0.670	1.5330	4.0202	1.2768	−0.0673	3.7583
0.680	1.5466	4.0024	1.1557	−0.0529	3.6801
0.700	1.5715	3.9687	0.9460	−0.0267	3.5328
0.720	1.5939	3.9372	0.7959	0.0025	3.3967
0.740	1.6140	3.9082	0.6773	0.0963	3.2727
0.760	1.6322	3.8813	0.6153	0.1681	3.1584
0.780	1.6487	3.8573	0.5856	0.2214	3.0569
0.800	1.6637	3.8359	0.5680	0.2678	2.9677
0.820	1.6776	3.8170	0.5523	0.3095	2.8889
0.840	1.6906	3.8007	0.5366	0.3481	2.8210
0.860	1.7027	3.7875	0.5214	0.3813	2.7665
0.900	1.7249	3.7732	0.4850	0.4168	2.7066
(b) [Fe/H] = −1.27 M_c = 0.497 Y_{HB} = 0.213					
0.540	1.3099	4.2385	3.0909	−0.1687	4.7612
0.560	1.3524	4.1753	2.6009	−0.1430	4.4818
0.580	1.4104	4.1097	2.0724	−0.1160	4.1764
0.590	1.4424	4.0731	1.7906	−0.1005	4.0053
0.600	1.4734	4.0341	1.5072	−0.0792	3.8259
0.610	1.5012	3.9941	1.2377	−0.0480	3.6451
0.620	1.5257	3.9534	1.0122	−0.0120	3.4647
0.630	1.5461	3.9136	0.8562	0.0764	3.2920
0.640	1.5645	3.8731	0.7801	0.1952	3.1186
0.650	1.5800	3.8337	0.7693	0.2861	2.9522
0.660	1.5934	3.7963	0.7698	0.3867	2.7960
0.680	1.6150	3.7594	0.7649	0.5013	2.6396
0.700	1.6318	3.7438	0.7566	0.5605	2.5731
0.720	1.6455	3.7372	0.7400	0.5872	2.5452
0.740	1.6564	3.7323	0.7272	0.6073	2.5266
0.760	1.6671	3.7288	0.7112	0.6218	2.5133
0.780	1.6761	3.7250	0.7008	0.6376	2.5004
0.820	1.6920	3.7217	0.6718	0.6514	2.4930
0.900	1.7181	3.7181	0.6184	0.6664	2.4931

Table A-4: ZAHB sequences with high Y and low Z

$M/M_\odot$	$\log L$	$\log T$	M_V	$(B-V)$	$\log g_s$
(a) [Fe/H] = −2.23 [O/Fe] = 0 $M_c = 0.492$ $Y_{HB} = 0.279$					
0.560	1.3578	4.2459	3.0041	−0.1727	4.7585
0.580	1.4087	4.2052	2.6289	−0.1560	4.5602
0.600	1.4626	4.1642	2.2468	−0.1404	4.3568
0.620	1.5137	4.1223	1.8738	−0.1235	4.1525
0.640	1.5592	4.0801	1.5253	−0.1058	3.9520
0.650	1.5793	4.0595	1.3655	−0.0969	3.8564
0.660	1.5978	4.0393	1.2144	−0.0857	3.7634
0.670	1.6149	4.0196	1.0702	−0.0702	3.6741
0.680	1.6306	4.0005	0.9382	−0.0554	3.5883
0.700	1.6584	3.9646	0.7135	−0.0270	3.4295
0.720	1.6826	3.9311	0.5569	0.0079	3.2838
0.740	1.7034	3.9012	0.4412	0.1130	3.1552
0.760	1.7218	3.8740	0.3869	0.1799	3.0394
0.780	1.7383	3.8496	0.3622	0.2348	2.9366
0.800	1.7533	3.8281	0.3452	0.2821	2.8466
0.820	1.7670	3.8095	0.3303	0.3240	2.7694
0.840	1.7798	3.7930	0.3162	0.3651	2.7011
0.860	1.7915	3.7820	0.3007	0.3940	2.6557
0.900	1.8134	3.7678	0.2672	0.4291	2.5968
(b) [Fe/H] = −1.23 [O/Fe] = 0 $M_c = 0.481$ $Y_{HB} = 0.282$					
0.540	1.3259	4.2307	3.0036	−0.1657	4.7140
0.560	1.4392	4.1597	2.2904	−0.1387	4.3325
0.580	1.5394	4.0711	1.5371	−0.1025	3.8931
0.590	1.5766	4.0245	1.1995	−0.0755	3.6769
0.600	1.6064	3.9780	0.9035	−0.0397	3.4682
0.610	1.6308	3.9320	0.6865	0.0080	3.2671
0.620	1.6508	3.8867	0.5592	0.1333	3.0727
0.630	1.6676	3.8422	0.5353	0.2608	2.8850
0.640	1.6816	3.7997	0.5395	0.3737	2.7079
0.650	1.6935	3.7689	0.5469	0.4671	2.5796
0.660	1.7041	3.7518	0.5528	0.5308	2.5072
0.680	1.7207	3.7407	0.5391	0.5758	2.4592
0.700	1.7339	3.7324	0.5297	0.6100	2.4255
0.720	1.7446	3.7271	0.5197	0.6319	2.4058
0.740	1.7546	3.7233	0.5071	0.6478	2.3924
0.760	1.7632	3.7209	0.4936	0.6579	2.3858
0.780	1.7712	3.7193	0.4789	0.6646	2.3826
0.820	1.7847	3.7163	0.4551	0.6772	2.3789
0.900	1.8091	3.7136	0.4033	0.6884	2.3839

Table A-5: Scaled-solar ZAHB sequences

(a) [Fe/H] $= -2.26$ $M_c = 0.500$ $Y_{HB} = 0.245$

$M/M_\odot$	$\log L$	$\log T$	M_V	$(B-V)$	$\log g_s$
0.560	1.3557	4.2452	3.0047	−0.1724	4.7578
0.580	1.3944	4.2014	2.6412	−0.1542	4.5590
0.600	1.4359	4.1603	2.2903	−0.1381	4.3682
0.620	1.4778	4.1199	1.9498	−0.1215	4.1787
0.640	1.5172	4.0800	1.6294	−0.1047	3.9934
0.650	1.5356	4.0602	1.4780	−0.0961	3.9028
0.660	1.5527	4.0410	1.3355	−0.0857	3.8155
0.670	1.5689	4.0220	1.1966	−0.0703	3.7299
0.680	1.5841	4.0036	1.0682	−0.0556	3.6475
0.700	1.6113	3.9685	0.8457	−0.0284	3.4924
0.720	1.6352	3.9362	0.6890	0.0018	3.3517
0.740	1.6561	3.9064	0.5677	0.0997	3.2234
0.760	1.6749	3.8792	0.5063	0.1702	3.1072
0.780	1.6916	3.8550	0.4774	0.2244	3.0050
0.800	1.7069	3.8333	0.4596	0.2719	2.9138
0.820	1.7208	3.8144	0.4442	0.3136	2.8352
0.840	1.7338	3.7982	0.4286	0.3526	2.7677
0.860	1.7459	3.7856	0.4133	0.3848	2.7157
0.900	1.7681	3.7712	0.3779	0.4203	2.6555
[Fe/H] $= -1.78$ $M_c = 0.495$ $Y_{HB} = 0.247$					
0.540	1.3300	4.2669	3.2092	−0.1814	4.8547
0.560	1.3692	4.2147	2.7911	−0.1594	4.6225
0.580	1.4174	4.1654	2.3727	−0.1401	4.3920
0.600	1.4713	4.1134	1.9346	−0.1188	4.1451
0.610	1.4975	4.0863	1.7183	−0.1075	4.0177
0.620	1.5219	4.0590	1.5112	−0.0956	3.8909
0.630	1.5443	4.0315	1.3114	−0.0785	3.7658
0.640	1.5646	4.0044	1.1245	−0.0572	3.6436
0.650	1.5830	3.9777	0.9569	−0.0369	3.5250
0.660	1.5996	3.9518	0.8195	−0.0133	3.4117
0.670	1.6147	3.9263	0.7149	0.0247	3.3013
0.680	1.6282	3.9017	0.6298	0.1157	3.1955
0.720	1.6716	3.8128	0.5632	0.3282	2.8216
0.740	1.6885	3.7797	0.5559	0.4160	2.6842
0.780	1.7161	3.7556	0.5264	0.4869	2.5830
0.820	1.7385	3.7451	0.4930	0.5235	2.5404
0.900	1.7747	3.7369	0.4231	0.5555	2.5119

Table A-5 (continued)

(c) [Fe/H] = −1.48 $M_c = 0.491$ $Y_{HB} = 0.248$					
0.540	1.3248	4.2464	3.0990	−0.1725	4.7776
0.560	1.3741	4.1910	2.6384	−0.1499	4.5227
0.580	1.4393	4.1313	2.1209	−0.1262	4.2340
0.590	1.4732	4.0984	1.8491	−0.1126	4.0758
0.600	1.5048	4.0640	1.5835	−0.0980	3.9138
0.610	1.5331	4.0289	1.3287	−0.0767	3.7525
0.620	1.5579	3.9936	1.0923	−0.0497	3.5934
0.630	1.5795	3.9588	0.8942	−0.0197	3.4395
0.640	1.5984	3.9243	0.7497	0.0322	3.2895
0.650	1.6145	3.8911	0.6555	0.1448	3.1474
0.660	1.6290	3.8584	0.6242	0.2240	3.0089
0.700	1.6719	3.7608	0.6217	0.4850	2.6008
0.740	1.7008	3.7428	0.5881	0.5511	2.5241
0.780	1.7224	3.7340	0.5581	0.5869	2.4901
0.820	1.7401	3.7295	0.5273	0.6057	2.4764
0.900	1.7695	3.7242	0.4703	0.6280	2.4662
(d) [Fe/H] = −1.26 $M_c = 0.488$ $Y_{HB} = 0.250$					
0.540	1.3083	4.2330	3.0615	−0.1662	4.7408
0.560	1.3791	4.1714	2.5106	−0.1421	4.4391
0.580	1.4668	4.0955	1.8515	−0.1114	4.0631
0.590	1.5063	4.0527	1.5226	−0.0925	3.8598
0.600	1.5390	4.0093	1.2163	−0.0619	3.6610
0.610	1.5668	3.9653	0.9511	−0.0262	3.4643
0.620	1.5896	3.9221	0.7655	0.0404	3.2759
0.630	1.6087	3.8794	0.6657	0.1765	3.0928
0.640	1.6249	3.8376	0.6499	0.2742	2.9161
0.650	1.6384	3.7980	0.6525	0.3799	2.7509
0.660	1.6506	3.7706	0.6543	0.4617	2.6357
0.680	1.6698	3.7484	0.6486	0.5428	2.5408
0.700	1.6847	3.7385	0.6364	0.5827	2.4990
0.720	1.6969	3.7321	0.6249	0.6090	2.4733
0.740	1.7070	3.7276	0.6137	0.6276	2.4573
0.760	1.7167	3.7241	0.6007	0.6422	2.4451
0.780	1.7248	3.7219	0.5877	0.6514	2.4396
0.820	1.7403	3.7193	0.5576	0.6623	2.4355
0.900	1.7654	3.7160	0.5058	0.6760	2.4374
1.000	1.7921	3.7146	0.4440	0.6818	2.4508

Table A-5 (continued)

$M/M_\odot$	$\log L$	$\log T$	M_V	$(B-V)$	$\log g_s$
(e) [Fe/H] $= -0.78$ $M_c = 0.482$ $Y_{HB} = 0.258$					
0.520	1.2680	4.2439	3.2290	−0.1705	4.8082
0.540	1.3414	4.1682	2.5861	−0.1402	4.4482
0.550	1.3954	4.1217	2.1781	−0.1214	4.2163
0.560	1.4509	4.0663	1.7329	−0.0983	3.9468
0.570	1.4981	4.0054	1.2993	−0.0579	3.6638
0.580	1.5359	3.9410	0.9498	−0.0022	3.3760
0.590	1.5647	3.8752	0.7768	0.1884	3.0917
0.600	1.5870	3.8095	0.7722	0.3493	2.8139
0.620	1.6181	3.7434	0.7903	0.5627	2.5323
0.660	1.6521	3.7175	0.7837	0.6699	2.4219
0.700	1.6734	3.7081	0.7614	0.7099	2.3885
0.740	1.6894	3.7018	0.7431	0.7371	2.3717
0.780	1.7028	3.6981	0.7228	0.7536	2.3661
0.820	1.7144	3.6959	0.7016	0.7632	2.3677
0.900	1.7341	3.6936	0.6608	0.7720	2.3792
(f) [Fe/H] $= -0.47$ $M_c = 0.477$ $Y_{HB} = 0.268$					
0.520	1.2690	4.1942	2.9296	−0.1494	4.6082
0.540	1.3935	4.0844	1.9786	−0.1051	4.0611
0.550	1.4562	4.0103	1.4314	−0.0616	3.7098
0.560	1.5041	3.9289	0.9962	0.0238	3.3441
0.570	1.5385	3.8438	0.8575	0.2692	2.9773
0.580	1.5627	3.7643	0.8742	0.5152	2.6424
0.590	1.5802	3.7344	0.9028	0.6372	2.5127
0.600	1.5922	3.7246	0.9056	0.6775	2.4690
0.620	1.6115	3.7084	0.9134	0.7452	2.3990
0.660	1.6361	3.6927	0.9094	0.8131	2.3388
0.700	1.6533	3.6856	0.8943	0.8440	2.3189
0.740	1.6670	3.6807	0.8804	0.8653	2.3098
0.780	1.6786	3.6777	0.8644	0.8781	2.3090
0.820	1.6887	3.6761	0.8463	0.8847	2.3140
0.900	1.7062	3.6742	0.8114	0.8922	2.3293

Table A-5 (continued)

(g) [Fe/H] = 0 $M_c = 0.469$ $Y_{HB} = 0.290$

$M/M_\odot$	$\log L$	$\log T$	M_V	$(B-V)$	$\log g_s$
0.480	1.1520	4.3172	3.9939	−0.1983	5.1824
0.490	1.1736	4.2510	3.5204	−0.1719	4.9053
0.500	1.2050	4.1965	3.1066	−0.1491	4.6645
0.510	1.2617	4.1393	2.6205	−0.1263	4.3875
0.520	1.3425	4.0616	1.9800	−0.0936	4.0046
0.530	1.4166	3.9640	1.3222	−0.0119	3.5481
0.540	1.4687	3.8504	1.0151	0.2912	3.0499
0.550	1.5015	3.7469	1.0503	0.6686	2.6110
0.560	1.5221	3.7136	1.1086	0.8275	2.4651
0.570	1.5363	3.6974	1.1382	0.8988	2.3937
0.580	1.5470	3.6875	1.1548	0.9408	2.3511
0.600	1.5615	3.6759	1.1742	0.9894	2.3047
0.620	1.5751	3.6687	1.1777	1.0194	2.2765
0.660	1.5936	3.6592	1.1853	1.0593	2.2472
0.700	1.6072	3.6546	1.1795	1.0786	2.2408
0.750	1.6218	3.6511	1.1656	1.0933	2.2423
0.800	1.6351	3.6488	1.1478	1.1028	2.2477
0.850	1.6462	3.6486	1.1218	1.1028	2.2621
0.900	1.6560	3.6480	1.1016	1.1047	2.2748
1.000	1.6735	3.6492	1.0506	1.0975	2.3078
1.100	1.6886	3.6507	1.0037	1.0892	2.3402
1.200	1.7030	3.6522	0.9586	1.0811	2.3694
1.300	1.7158	3.6543	0.9139	1.0707	2.4000
1.400	1.7281	3.6565	0.8701	1.0604	2.4286
1.500	1.7394	3.6583	0.8315	1.0519	2.4544
1.600	1.7508	3.6616	0.7841	1.0376	2.4843

Table B-1: Evolutionary Tracks for $Y_{HB} = 0.246$ [Fe/H] $= -2.26$ [O/Fe] $= 0.75$
(a) $M_* = 0.90\,M_\odot$

t_6	Y_c	$\log L$	$\log T_{eff}$	$\log g_s$	$\log T_c$	$\log \rho_c$	M_{cc}	M_{sc}	M_{sh}
1.10	0.95	1.785	3.736	2.497	8.073	4.268	0.125	N/A	0.493
4.36	0.90	1.793	3.734	2.483	8.076	4.266	0.136	N/A	0.493
8.05	0.85	1.799	3.733	2.473	8.078	4.262	0.147	N/A	0.493
12.31	0.80	1.804	3.733	2.467	8.081	4.255	0.161	N/A	0.496
17.14	0.75	1.807	3.734	2.468	8.085	4.245	0.177	N/A	0.499
22.17	0.70	1.807	3.736	2.474	8.089	4.233	0.179	0.193	0.502
27.26	0.65	1.808	3.737	2.480	8.092	4.223	0.179	0.204	0.504
32.64	0.60	1.810	3.739	2.486	8.097	4.213	0.179	0.217	0.507
37.95	0.55	1.811	3.741	2.492	8.101	4.205	0.179	0.228	0.509
43.08	0.50	1.813	3.742	2.496	8.106	4.198	0.181	0.239	0.512
47.98	0.45	1.814	3.744	2.499	8.111	4.192	0.181	0.247	0.514
52.88	0.40	1.816	3.745	2.501	8.116	4.189	0.181	0.255	0.516
57.57	0.35	1.819	3.745	2.501	8.122	4.187	0.181	0.261	0.518
62.28	0.30	1.822	3.745	2.497	8.128	4.189	0.181	0.269	0.519
66.71	0.25	1.827	3.744	2.489	8.136	4.193	0.181	0.274	0.520
71.17	0.20	1.833	3.743	2.478	8.144	4.203	0.181	0.280	0.522
74.97	0.15	1.843	3.740	2.456	8.155	4.220	0.180	0.287	0.523
79.00	0.10	1.858	3.736	2.423	8.169	4.249	0.177	0.292	0.524
82.74	5.00E-02	1.884	3.729	2.373	8.191	4.306	0.177	0.293	0.525
83.64	4.00E-02	1.892	3.728	2.358	8.197	4.322	0.179	0.295	0.525
84.32	3.00E-02	1.902	3.725	2.337	8.204	4.347	0.181	N/A	0.526
85.12	2.00E-02	1.916	3.723	2.313	8.214	4.381	0.181	N/A	0.526
86.04	1.00E-02	1.940	3.719	2.276	8.230	4.435	0.181	N/A	0.526
87.02	1.00E-03	2.006	3.710	2.173	8.267	4.587	0.110	N/A	0.527
87.17	1.00E-04	2.064	3.704	2.090	8.279	4.722	0.019	N/A	0.526
87.20	0.00	2.079	3.703	2.070	8.280	4.753	0.000	N/A	0.526
Post Helium Exhaustion Phase									
87.95	0.00	2.193	3.700	1.946	8.252	5.053	0.000	N/A	0.529
88.70	0.00	2.176	3.701	1.967	8.226	5.149	0.000	N/A	0.530
89.45	0.00	2.177	3.701	1.966	8.212	5.212	0.000	N/A	0.531
90.20	0.00	2.184	3.701	1.957	8.202	5.257	0.000	N/A	0.531
90.95	0.00	2.203	3.699	1.933	8.194	5.295	0.000	N/A	0.531
91.70	0.00	2.229	3.697	1.897	8.189	5.332	0.000	N/A	0.531
92.20	0.00	2.250	3.695	1.870	8.188	5.359	0.000	N/A	0.531

Table B-1 (continued)
(b) $M_* = 0.74M_\odot$

t_6	Y_c	$\log L$	$\log T_{eff}$	$\log g_s$	$\log T_c$	$\log \rho_c$	M_{cc}	M_{sc}	M_{sh}
1.10	0.95	1.703	3.770	2.630	8.074	4.266	0.126	N/A	0.493
4.31	0.90	1.709	3.767	2.613	8.076	4.264	0.136	N/A	0.493
7.98	0.85	1.714	3.765	2.601	8.079	4.260	0.148	N/A	0.493
12.24	0.80	1.718	3.765	2.598	8.082	4.254	0.162	N/A	0.493
17.11	0.75	1.720	3.767	2.604	8.085	4.246	0.178	N/A	0.496
22.24	0.70	1.718	3.773	2.628	8.088	4.236	0.177	0.193	0.499
27.40	0.65	1.716	3.781	2.660	8.092	4.228	0.177	0.204	0.500
33.02	0.60	1.714	3.791	2.706	8.096	4.219	0.178	0.218	0.502
38.44	0.55	1.712	3.801	2.746	8.100	4.212	0.178	0.228	0.504
43.54	0.50	1.711	3.809	2.779	8.105	4.206	0.178	0.237	0.505
48.77	0.45	1.711	3.814	2.799	8.109	4.202	0.179	0.245	0.506
53.75	0.40	1.712	3.817	2.809	8.114	4.199	0.179	0.252	0.507
58.75	0.35	1.714	3.817	2.808	8.120	4.199	0.179	0.258	0.508
63.29	0.30	1.718	3.814	2.794	8.126	4.201	0.176	0.264	0.509
68.41	0.25	1.724	3.809	2.765	8.133	4.206	0.178	0.270	0.510
73.40	0.20	1.732	3.799	2.719	8.142	4.216	0.178	0.276	0.510
77.93	0.15	1.745	3.785	2.649	8.153	4.235	0.175	0.283	0.511
82.01	0.10	1.763	3.769	2.566	8.167	4.264	0.175	0.285	0.512
86.44	5.00E-02	1.797	3.751	2.462	8.188	4.322	0.174	0.286	0.513
87.33	4.00E-02	1.807	3.748	2.437	8.194	4.339	0.176	0.288	0.513
88.44	3.00E-02	1.820	3.743	2.406	8.202	4.362	0.175	0.270	0.513
89.21	2.00E-02	1.838	3.737	2.365	8.212	4.396	0.167	N/A	0.513
90.18	1.00E-02	1.869	3.730	2.306	8.227	4.451	0.167	N/A	0.514
91.19	1.00E-03	1.955	3.716	2.161	8.265	4.607	0.106	N/A	0.514
91.30	1.00E-04	1.994	3.710	2.101	8.276	4.693	0.034	N/A	0.514
91.40	0.00	2.060	3.706	2.019	8.276	4.806	0.000	N/A	0.514
Post Helium Exhaustion Phase									
92.15	0.00	2.155	3.701	1.904	8.241	5.082	0.000	N/A	0.516
92.90	0.00	2.140	3.702	1.922	8.216	5.164	0.000	N/A	0.517
93.65	0.00	2.140	3.702	1.922	8.205	5.217	0.000	N/A	0.518
94.40	0.00	2.140	3.702	1.922	8.196	5.258	0.000	N/A	0.518
95.15	0.00	2.154	3.701	1.905	8.187	5.294	0.000	N/A	0.519
95.90	0.00	2.173	3.700	1.881	8.181	5.325	0.000	N/A	0.519
96.65	0.00	2.196	3.698	1.848	8.178	5.356	0.000	N/A	0.519
97.40	0.00	2.226	3.695	1.808	8.177	5.393	0.000	N/A	0.519
98.00	0.00	2.251	3.694	1.778	8.177	5.420	0.000	N/A	0.519

Table B-1 (continued)
(c) $M_* = 0.68\,M_\odot$

t_6	Y_c	$\log L$	$\log T_{eff}$	$\log g_s$	$\log T_c$	$\log \rho_c$	M_{cc}	M_{sc}	M_{sh}
1.10	0.95	1.645	3.887	3.121	8.074	4.264	0.126	N/A	0.493
4.35	0.90	1.650	3.883	3.101	8.076	4.263	0.137	N/A	0.493
8.01	0.85	1.653	3.882	3.094	8.079	4.259	0.148	N/A	0.493
12.25	0.80	1.655	3.883	3.094	8.082	4.254	0.162	N/A	0.493
17.03	0.75	1.656	3.886	3.105	8.085	4.247	0.179	N/A	0.494
22.13	0.70	1.656	3.891	3.126	8.088	4.238	0.178	0.193	0.496
27.60	0.65	1.654	3.898	3.155	8.092	4.230	0.178	0.205	0.497
32.99	0.60	1.651	3.905	3.185	8.096	4.223	0.178	0.217	0.499
38.61	0.55	1.649	3.911	3.213	8.099	4.216	0.178	0.226	0.500
43.89	0.50	1.648	3.915	3.230	8.104	4.211	0.178	0.235	0.501
49.09	0.45	1.648	3.916	3.234	8.109	4.208	0.178	0.243	0.502
54.20	0.40	1.650	3.916	3.233	8.113	4.206	0.175	0.249	0.503
59.47	0.35	1.653	3.914	3.220	8.119	4.206	0.175	0.257	0.503
64.64	0.30	1.659	3.910	3.197	8.125	4.208	0.175	0.263	0.504
69.29	0.25	1.666	3.902	3.161	8.132	4.215	0.175	0.266	0.504
74.04	0.20	1.677	3.893	3.112	8.141	4.226	0.173	0.274	0.505
79.04	0.15	1.692	3.879	3.040	8.152	4.244	0.173	0.281	0.505
83.42	0.10	1.712	3.860	2.945	8.166	4.274	0.171	0.282	0.506
87.96	5.00E-02	1.746	3.825	2.772	8.187	4.329	0.173	0.283	0.506
89.31	4.00E-02	1.760	3.810	2.699	8.194	4.350	0.173	0.286	0.506
90.17	3.00E-02	1.772	3.795	2.627	8.200	4.371	0.167	N/A	0.506
91.06	2.00E-02	1.793	3.773	2.517	8.210	4.405	0.166	N/A	0.507
92.02	1.00E-02	1.828	3.750	2.390	8.226	4.460	0.166	N/A	0.507
93.10	1.00E-03	1.926	3.722	2.180	8.263	4.615	0.103	N/A	0.507
93.24	1.00E-04	1.984	3.714	2.088	8.273	4.723	0.029	N/A	0.507
93.30	0.00	2.020	3.710	2.035	8.273	4.787	0.000	N/A	0.507
Post Helium Exhaustion Phase									
94.05	0.00	2.131	3.704	1.902	8.237	5.084	0.000	N/A	0.509
94.80	0.00	2.117	3.705	1.921	8.212	5.158	0.000	N/A	0.510
95.55	0.00	2.120	3.705	1.918	8.201	5.211	0.000	N/A	0.511
96.30	0.00	2.119	3.705	1.919	8.194	5.253	0.000	N/A	0.512
97.05	0.00	2.125	3.704	1.909	8.185	5.286	0.000	N/A	0.512
97.80	0.00	2.143	3.703	1.886	8.178	5.318	0.000	N/A	0.512
98.55	0.00	2.162	3.702	1.861	8.174	5.346	0.000	N/A	0.512
99.30	0.00	2.186	3.699	1.829	8.172	5.376	0.000	N/A	0.512
100.05	0.00	2.212	3.697	1.791	8.171	5.407	0.000	N/A	0.512
100.80	0.00	2.245	3.694	1.748	8.171	5.442	0.000	N/A	0.513
101.00	0.00	2.253	3.693	1.738	8.171	5.451	0.000	N/A	0.513

Table B-1 (continued)
(d) $M_* = 0.64\,M_\odot$

t_6	Y_c	$\log L$	$\log T_{eff}$	$\log g_s$	$\log T_c$	$\log \rho_c$	M_{cc}	M_{sc}	M_{sh}
1.10	0.95	1.581	3.994	3.586	8.074	4.263	0.126	N/A	0.493
4.30	0.90	1.585	3.992	3.572	8.076	4.262	0.137	N/A	0.493
7.97	0.85	1.587	3.992	3.571	8.079	4.259	0.148	N/A	0.492
12.22	0.80	1.587	3.993	3.574	8.082	4.254	0.162	N/A	0.493
17.02	0.75	1.587	3.994	3.579	8.085	4.247	0.178	N/A	0.493
22.09	0.70	1.587	3.995	3.585	8.088	4.240	0.178	0.192	0.494
27.57	0.65	1.587	3.997	3.591	8.091	4.232	0.176	0.205	0.495
33.03	0.60	1.587	3.998	3.596	8.095	4.226	0.176	0.216	0.495
38.46	0.55	1.587	3.999	3.598	8.099	4.221	0.176	0.225	0.496
43.88	0.50	1.588	3.998	3.596	8.103	4.217	0.176	0.234	0.497
49.20	0.45	1.590	3.996	3.586	8.108	4.214	0.176	0.241	0.498
54.41	0.40	1.595	3.993	3.569	8.113	4.213	0.175	0.248	0.498
59.64	0.35	1.601	3.989	3.545	8.118	4.213	0.173	0.255	0.499
64.78	0.30	1.608	3.983	3.513	8.124	4.216	0.173	0.259	0.499
69.56	0.25	1.618	3.975	3.473	8.131	4.223	0.170	0.264	0.500
74.63	0.20	1.630	3.966	3.425	8.139	4.233	0.172	0.270	0.500
79.82	0.15	1.646	3.955	3.363	8.150	4.252	0.170	0.277	0.500
84.93	0.10	1.667	3.942	3.291	8.165	4.282	0.169	0.283	0.500
90.99	5.00E-02	1.702	3.919	3.166	8.185	4.334	0.173	0.290	0.501
91.98	4.00E-02	1.713	3.911	3.120	8.192	4.353	0.173	0.291	0.501
93.22	3.00E-02	1.728	3.900	3.061	8.200	4.377	0.162	N/A	0.501
94.04	2.00E-02	1.750	3.880	2.961	8.210	4.412	0.163	N/A	0.501
95.07	1.00E-02	1.788	3.840	2.761	8.225	4.467	0.163	N/A	0.501
96.14	1.00E-03	1.901	3.735	2.232	8.262	4.622	0.098	N/A	0.502
96.28	1.00E-04	1.954	3.722	2.127	8.272	4.715	0.019	N/A	0.502
96.30	0.00	1.962	3.721	2.112	8.273	4.729	0.005	N/A	0.502
Post Helium Exhaustion Phase									
97.05	0.00	2.105	3.709	1.919	8.237	5.065	0.000	N/A	0.503
97.80	0.00	2.088	3.711	1.946	8.212	5.134	0.000	N/A	0.504
98.55	0.00	2.092	3.710	1.940	8.198	5.189	0.000	N/A	0.505
99.30	0.00	2.103	3.709	1.925	8.192	5.231	0.000	N/A	0.506
100.05	0.00	2.113	3.708	1.910	8.189	5.268	0.000	N/A	0.506
100.80	0.00	2.123	3.707	1.897	8.186	5.305	0.000	N/A	0.507
101.55	0.00	2.137	3.706	1.876	8.181	5.335	0.000	N/A	0.507
102.30	0.00	2.159	3.704	1.846	8.177	5.366	0.000	N/A	0.507
103.05	0.00	2.185	3.701	1.811	8.173	5.399	0.000	N/A	0.508
103.80	0.00	2.211	3.699	1.774	8.171	5.429	0.000	N/A	0.508
104.55	0.00	2.242	3.695	1.730	8.170	5.462	0.000	N/A	0.508
104.70	0.00	2.248	3.695	1.723	8.170	5.469	0.000	N/A	0.508

Table B-1 (continued)
(e) $M_* = 0.54\,M_\odot$

t_6	Y_c	$\log L$	$\log T_{eff}$	$\log g_s$	$\log T_c$	$\log \rho_c$	M_{cc}	M_{sc}	M_{sh}
1.10	0.95	1.308	4.268	4.879	8.073	4.274	0.125	N/A	0.493
4.62	0.90	1.318	4.265	4.858	8.075	4.274	0.135	N/A	0.493
8.45	0.85	1.327	4.262	4.836	8.077	4.272	0.146	N/A	0.493
13.00	0.80	1.337	4.258	4.814	8.080	4.269	0.160	N/A	0.492
18.32	0.75	1.348	4.254	4.787	8.083	4.263	0.176	0.177	0.493
23.82	0.70	1.359	4.250	4.760	8.086	4.257	0.172	0.190	0.492
29.78	0.65	1.370	4.247	4.733	8.089	4.252	0.170	0.201	0.493
35.74	0.60	1.383	4.242	4.704	8.092	4.248	0.170	0.211	0.493
41.72	0.55	1.396	4.238	4.674	8.096	4.244	0.170	0.221	0.493
47.58	0.50	1.409	4.234	4.643	8.100	4.241	0.167	0.227	0.493
53.48	0.45	1.423	4.229	4.612	8.105	4.239	0.167	0.234	0.493
59.27	0.40	1.437	4.225	4.579	8.109	4.239	0.167	0.242	0.493
64.88	0.35	1.452	4.221	4.547	8.115	4.240	0.165	0.247	0.493
70.63	0.30	1.467	4.216	4.513	8.121	4.244	0.165	0.253	0.493
76.03	0.25	1.484	4.212	4.481	8.128	4.250	0.163	0.258	0.493
81.25	0.20	1.500	4.208	4.450	8.136	4.261	0.162	0.261	0.493
87.19	0.15	1.518	4.205	4.420	8.147	4.279	0.162	0.270	0.493
92.42	0.10	1.536	4.205	4.401	8.160	4.307	0.162	0.272	0.493
98.74	5.00E-02	1.555	4.210	4.402	8.183	4.363	0.165	0.276	0.493
100.22	4.00E-02	1.559	4.212	4.407	8.189	4.379	0.165	0.276	0.493
101.95	3.00E-02	1.563	4.216	4.416	8.196	4.399	0.164	0.267	0.493
102.91	2.00E-02	1.568	4.221	4.432	8.206	4.433	0.157	N/A	0.493
103.92	1.00E-02	1.574	4.231	4.468	8.222	4.487	0.157	N/A	0.493
105.17	1.00E-03	1.619	4.251	4.503	8.263	4.649	0.134	N/A	0.493
105.40	1.00E-04	1.696	4.244	4.396	8.283	4.780	0.067	N/A	0.493
105.50	0.00	1.696	4.244	4.397	8.283	4.780	0.024	N/A	0.493
Post Helium Exhaustion Phase									
106.25	0.00	1.884	4.182	3.960	8.251	5.061	0.000	N/A	0.493
107.00	0.00	1.899	4.170	3.898	8.234	5.120	0.000	N/A	0.493
107.75	0.00	1.921	4.156	3.819	8.222	5.171	0.000	N/A	0.493
108.50	0.00	1.945	4.140	3.733	8.216	5.211	0.000	N/A	0.493
109.25	0.00	1.959	4.129	3.674	8.212	5.236	0.000	N/A	0.493
110.00	0.00	1.978	4.107	3.566	8.203	5.273	0.000	N/A	0.493
110.75	0.00	1.991	4.094	3.504	8.201	5.287	0.000	N/A	0.493
111.50	0.00	2.012	4.075	3.405	8.198	5.310	0.000	N/A	0.493
112.25	0.00	2.034	4.055	3.303	8.196	5.333	0.000	N/A	0.493
113.00	0.00	2.050	4.041	3.230	8.196	5.350	0.000	N/A	0.493
113.75	0.00	2.066	4.024	3.146	8.194	5.367	0.000	N/A	0.493
114.50	0.00	2.093	3.996	3.007	8.195	5.394	0.000	N/A	0.494
115.25	0.00	2.117	3.966	2.863	8.194	5.418	0.000	N/A	0.494
116.00	0.00	2.150	3.920	2.647	8.192	5.452	0.000	N/A	0.494
116.75	0.00	2.176	3.883	2.475	8.193	5.478	0.000	N/A	0.494
117.50	0.00	2.208	3.827	2.217	8.192	5.509	0.000	N/A	0.494
118.25	0.00	2.241	3.767	1.943	8.192	5.541	0.000	N/A	0.495
118.40	0.00	2.249	3.755	1.889	8.192	5.549	0.000	N/A	0.495

Table B-2: Evolutionary Tracks for $Y_{HB} = 0.247$ [Fe/H] $= -2.03$ [O/Fe] $= 0.70$
(a) $M_* = 0.90\,M_\odot$

t_6	Y_c	$\log L$	$\log T_{eff}$	$\log g_s$	$\log T_c$	$\log \rho_c$	M_{cc}	M_{sc}	M_{sh}
1.10	0.95	1.786	3.730	2.472	8.073	4.274	0.124	N/A	0.491
4.51	0.90	1.793	3.728	2.458	8.075	4.272	0.135	N/A	0.491
8.27	0.85	1.801	3.727	2.447	8.078	4.267	0.146	N/A	0.491
12.77	0.80	1.806	3.727	2.442	8.081	4.260	0.160	N/A	0.495
17.84	0.75	1.808	3.728	2.445	8.084	4.249	0.176	N/A	0.498
23.01	0.70	1.809	3.730	2.451	8.088	4.237	0.178	0.194	0.501
28.21	0.65	1.810	3.731	2.453	8.092	4.227	0.178	0.205	0.503
33.44	0.60	1.812	3.732	2.456	8.096	4.217	0.177	0.217	0.506
38.79	0.55	1.813	3.733	2.459	8.101	4.208	0.178	0.228	0.509
43.93	0.50	1.815	3.735	2.462	8.105	4.201	0.180	0.237	0.511
49.01	0.45	1.817	3.736	2.464	8.110	4.196	0.179	0.245	0.513
54.06	0.40	1.819	3.736	2.465	8.116	4.192	0.179	0.254	0.515
58.88	0.35	1.822	3.737	2.464	8.121	4.190	0.179	0.262	0.517
63.37	0.30	1.825	3.737	2.461	8.128	4.191	0.180	0.267	0.518
68.00	0.25	1.830	3.737	2.455	8.135	4.196	0.180	0.273	0.520
72.40	0.20	1.836	3.736	2.446	8.144	4.205	0.179	0.279	0.522
77.55	0.15	1.848	3.733	2.423	8.158	4.228	0.177	0.290	0.523
81.49	0.10	1.861	3.731	2.401	8.169	4.250	0.179	0.291	0.524
85.78	5.00E-02	1.887	3.725	2.351	8.191	4.307	0.178	0.292	0.526
86.42	4.00E-02	1.896	3.724	2.337	8.197	4.323	0.178	0.294	0.528
87.46	3.00E-02	1.908	3.722	2.317	8.205	4.347	0.176	0.227	0.528
88.18	2.00E-02	1.923	3.720	2.294	8.215	4.381	0.170	N/A	0.528
89.09	1.00E-02	1.949	3.716	2.255	8.230	4.436	0.170	N/A	0.528
89.99	1.00E-03	2.021	3.706	2.143	8.268	4.589	0.113	N/A	0.528
90.14	1.00E-04	2.082	3.703	2.069	8.281	4.721	0.027	N/A	0.528
90.20	0.00	2.122	3.703	2.028	8.281	4.794	0.000	N/A	0.528
Post Helium Exhaustion Phase									
90.40	0.00	2.250	3.694	1.865	8.287	4.959	0.000	N/A	0.529

Table B-2 (continued)
(b) $M_* = 0.74\,M_\odot$

t_6	Y_c	$\log L$	$\log T_{eff}$	$\log g_s$	$\log T_c$	$\log \rho_c$	M_{cc}	M_{sc}	M_{sh}
1.10	0.95	1.714	3.749	2.537	8.073	4.272	0.125	N/A	0.490
4.39	0.90	1.721	3.747	2.522	8.075	4.270	0.135	N/A	0.490
8.12	0.85	1.727	3.746	2.512	8.078	4.266	0.147	N/A	0.491
12.49	0.80	1.731	3.746	2.508	8.081	4.260	0.160	N/A	0.492
17.58	0.75	1.732	3.748	2.515	8.084	4.251	0.176	N/A	0.495
22.98	0.70	1.730	3.752	2.533	8.088	4.240	0.176	0.194	0.498
28.12	0.65	1.727	3.757	2.553	8.092	4.231	0.176	0.205	0.500
33.78	0.60	1.725	3.761	2.573	8.096	4.222	0.178	0.218	0.502
39.01	0.55	1.723	3.766	2.594	8.100	4.215	0.178	0.227	0.503
44.24	0.50	1.722	3.769	2.610	8.104	4.209	0.178	0.235	0.505
49.49	0.45	1.721	3.775	2.631	8.109	4.204	0.178	0.244	0.506
54.74	0.40	1.722	3.777	2.640	8.114	4.201	0.178	0.251	0.507
59.66	0.35	1.724	3.778	2.643	8.120	4.201	0.178	0.258	0.508
64.29	0.30	1.727	3.778	2.637	8.126	4.203	0.176	0.263	0.509
69.13	0.25	1.733	3.774	2.619	8.133	4.208	0.176	0.270	0.510
73.82	0.20	1.741	3.769	2.588	8.142	4.218	0.176	0.276	0.511
78.88	0.15	1.756	3.760	2.538	8.155	4.240	0.173	0.286	0.512
83.06	0.10	1.771	3.754	2.499	8.167	4.266	0.173	0.285	0.513
87.23	5.00E-02	1.805	3.742	2.418	8.188	4.323	0.175	0.287	0.513
88.33	4.00E-02	1.818	3.738	2.389	8.195	4.343	0.176	0.288	0.514
89.22	3.00E-02	1.829	3.735	2.367	8.202	4.363	0.176	0.223	0.514
90.05	2.00E-02	1.847	3.731	2.332	8.212	4.397	0.176	N/A	0.514
91.06	1.00E-02	1.879	3.725	2.274	8.227	4.452	0.176	N/A	0.515
92.08	1.00E-03	1.965	3.712	2.139	8.264	4.603	0.108	N/A	0.515
92.24	1.00E-04	2.031	3.707	2.050	8.276	4.731	0.023	N/A	0.515
92.30	0.00	2.070	3.706	2.007	8.276	4.800	0.000	N/A	0.515
Post Helium Exhaustion Phase									
93.05	0.00	2.160	3.700	1.892	8.240	5.085	0.000	N/A	0.516
93.80	0.00	2.148	3.701	1.909	8.217	5.161	0.000	N/A	0.518
94.55	0.00	2.148	3.701	1.909	8.205	5.219	0.000	N/A	0.519
95.30	0.00	2.147	3.701	1.909	8.195	5.260	0.000	N/A	0.520
96.05	0.00	2.160	3.699	1.892	8.187	5.294	0.000	N/A	0.520
96.80	0.00	2.180	3.697	1.863	8.181	5.327	0.000	N/A	0.520
97.55	0.00	2.202	3.696	1.835	8.178	5.357	0.000	N/A	0.520
98.30	0.00	2.232	3.693	1.794	8.177	5.393	0.000	N/A	0.520
98.80	0.00	2.253	3.692	1.769	8.177	5.416	0.000	N/A	0.520

Table B-2 (continued)
(c) $M_* = 0.68\,M_\odot$

t_6	Y_c	$\log L$	$\log T_{eff}$	$\log g_s$	$\log T_c$	$\log \rho_c$	M_{cc}	M_{sc}	M_{sh}
1.10	0.95	1.663	3.827	2.861	8.073	4.271	0.125	N/A	0.490
4.42	0.90	1.670	3.820	2.828	8.075	4.269	0.135	N/A	0.490
8.21	0.85	1.675	3.818	2.814	8.078	4.265	0.147	N/A	0.490
12.56	0.80	1.678	3.819	2.817	8.081	4.260	0.160	N/A	0.491
17.59	0.75	1.678	3.826	2.842	8.084	4.251	0.177	N/A	0.493
22.91	0.70	1.676	3.837	2.889	8.087	4.242	0.176	0.192	0.496
28.15	0.65	1.671	3.850	2.944	8.091	4.234	0.176	0.202	0.497
33.85	0.60	1.667	3.862	2.998	8.095	4.225	0.176	0.216	0.499
39.49	0.55	1.664	3.871	3.037	8.099	4.219	0.176	0.225	0.500
44.84	0.50	1.662	3.878	3.066	8.104	4.213	0.176	0.234	0.501
50.17	0.45	1.662	3.882	3.082	8.108	4.210	0.176	0.242	0.502
55.39	0.40	1.662	3.884	3.090	8.113	4.207	0.176	0.250	0.503
60.52	0.35	1.665	3.883	3.083	8.119	4.208	0.174	0.256	0.504
65.45	0.30	1.670	3.879	3.064	8.125	4.210	0.174	0.260	0.505
71.08	0.25	1.676	3.873	3.035	8.132	4.214	0.176	0.268	0.505
75.32	0.20	1.686	3.865	2.991	8.140	4.226	0.174	0.272	0.506
80.45	0.15	1.701	3.848	2.909	8.151	4.243	0.173	0.279	0.506
84.83	0.10	1.724	3.823	2.786	8.165	4.273	0.170	0.285	0.507
89.95	5.00E-02	1.764	3.779	2.568	8.187	4.331	0.174	0.288	0.507
91.15	4.00E-02	1.775	3.770	2.522	8.193	4.347	0.174	0.288	0.507
92.28	3.00E-02	1.789	3.760	2.470	8.200	4.371	0.162	N/A	0.507
93.18	2.00E-02	1.809	3.751	2.411	8.210	4.405	0.162	N/A	0.507
94.14	1.00E-02	1.845	3.739	2.327	8.226	4.460	0.162	N/A	0.508
95.17	1.00E-03	1.944	3.717	2.142	8.263	4.616	0.101	N/A	0.508
95.30	1.00E-04	1.991	3.711	2.070	8.275	4.704	0.031	N/A	0.508
95.40	0.00	2.058	3.709	1.996	8.274	4.813	0.000	N/A	0.508
Post Helium Exhaustion Phase									
96.15	0.00	2.146	3.701	1.876	8.237	5.082	0.000	N/A	0.510
96.90	0.00	2.128	3.703	1.902	8.214	5.155	0.000	N/A	0.511
97.65	0.00	2.127	3.703	1.903	8.202	5.210	0.000	N/A	0.512
98.40	0.00	2.128	3.703	1.902	8.194	5.252	0.000	N/A	0.513
99.15	0.00	2.134	3.703	1.895	8.186	5.285	0.000	N/A	0.513
99.90	0.00	2.148	3.701	1.874	8.180	5.313	0.000	N/A	0.513
100.65	0.00	2.168	3.700	1.848	8.175	5.345	0.000	N/A	0.514
101.40	0.00	2.191	3.698	1.818	8.173	5.374	0.000	N/A	0.514
102.15	0.00	2.220	3.695	1.777	8.172	5.409	0.000	N/A	0.514
102.90	0.00	2.250	3.692	1.736	8.172	5.441	0.000	N/A	0.514

Table B-2 (continued)

(d) $M_* = 0.64\,M_\odot$

t_6	Y_c	$\log L$	$\log T_{eff}$	$\log g_s$	$\log T_c$	$\log \rho_c$	M_{cc}	M_{sc}	M_{sh}
1.10	0.95	1.606	3.947	3.375	8.073	4.269	0.125	N/A	0.490
4.36	0.90	1.612	3.944	3.354	8.076	4.268	0.136	N/A	0.490
8.08	0.85	1.614	3.944	3.351	8.078	4.265	0.147	N/A	0.490
12.41	0.80	1.615	3.945	3.355	8.081	4.260	0.161	N/A	0.491
17.50	0.75	1.615	3.948	3.368	8.084	4.252	0.177	N/A	0.491
22.85	0.70	1.614	3.953	3.389	8.087	4.244	0.177	0.192	0.493
28.20	0.65	1.611	3.958	3.413	8.091	4.236	0.176	0.203	0.494
33.85	0.60	1.608	3.964	3.440	8.095	4.229	0.176	0.214	0.495
39.47	0.55	1.605	3.968	3.459	8.099	4.223	0.176	0.225	0.497
44.86	0.50	1.604	3.971	3.470	8.103	4.218	0.175	0.232	0.497
50.22	0.45	1.605	3.971	3.470	8.108	4.215	0.173	0.241	0.500
55.53	0.40	1.608	3.970	3.462	8.113	4.214	0.173	0.248	0.499
60.84	0.35	1.612	3.966	3.444	8.118	4.214	0.173	0.255	0.499
65.72	0.30	1.618	3.962	3.419	8.124	4.217	0.171	0.259	0.499
70.85	0.25	1.627	3.954	3.381	8.131	4.224	0.171	0.265	0.500
75.65	0.20	1.638	3.946	3.336	8.140	4.234	0.171	0.271	0.500
80.74	0.15	1.655	3.934	3.270	8.151	4.253	0.169	0.279	0.501
85.28	0.10	1.675	3.920	3.195	8.164	4.281	0.168	0.278	0.501
91.03	5.00E-02	1.713	3.892	3.046	8.186	4.337	0.171	0.285	0.502
92.59	4.00E-02	1.725	3.882	2.994	8.192	4.353	0.171	0.285	0.502
93.46	3.00E-02	1.741	3.865	2.911	8.199	4.379	0.169	N/A	0.502
94.39	2.00E-02	1.764	3.843	2.799	8.209	4.413	0.171	N/A	0.503
95.42	1.00E-02	1.803	3.795	2.569	8.225	4.468	0.171	N/A	0.503
96.54	1.00E-03	1.914	3.728	2.191	8.262	4.621	0.099	N/A	0.503
96.68	1.00E-04	1.969	3.717	2.091	8.272	4.717	0.019	N/A	0.503
96.70	0.00	1.977	3.716	2.077	8.273	4.731	0.007	N/A	0.503
Post Helium Exhaustion Phase									
97.45	0.00	2.129	3.705	1.883	8.239	5.074	0.000	N/A	0.504
98.20	0.00	2.108	3.708	1.915	8.210	5.156	0.000	N/A	0.505
98.95	0.00	2.112	3.708	1.909	8.200	5.206	0.000	N/A	0.507
99.70	0.00	2.114	3.708	1.907	8.193	5.249	0.000	N/A	0.507
100.45	0.00	2.114	3.707	1.906	8.186	5.282	0.000	N/A	0.507
101.20	0.00	2.126	3.705	1.887	8.179	5.312	0.000	N/A	0.508
101.95	0.00	2.142	3.704	1.865	8.173	5.339	0.000	N/A	0.508
102.70	0.00	2.164	3.702	1.832	8.170	5.370	0.000	N/A	0.508
103.45	0.00	2.188	3.699	1.801	8.168	5.398	0.000	N/A	0.508
104.20	0.00	2.216	3.697	1.762	8.167	5.430	0.000	N/A	0.508
104.95	0.00	2.247	3.695	1.722	8.167	5.464	0.000	N/A	0.509
105.10	0.00	2.253	3.694	1.715	8.167	5.469	0.000	N/A	0.509

Table B-2 (continued)
(e) $M_* = 0.54\,M_\odot$

t_6	Y_c	$\log L$	$\log T_{eff}$	$\log g_s$	$\log T_c$	$\log \rho_c$	M_{cc}	M_{sc}	M_{sh}
1.10	0.95	1.306	4.257	4.840	8.072	4.276	0.124	N/A	0.490
4.62	0.90	1.316	4.254	4.818	8.075	4.276	0.134	N/A	0.490
8.57	0.85	1.323	4.252	4.801	8.077	4.276	0.146	N/A	0.490
13.13	0.80	1.335	4.248	4.771	8.080	4.271	0.160	N/A	0.490
18.43	0.75	1.346	4.244	4.746	8.082	4.266	0.175	0.176	0.490
23.93	0.70	1.356	4.240	4.721	8.085	4.260	0.172	0.188	0.490
29.99	0.65	1.367	4.235	4.691	8.089	4.255	0.169	0.200	0.490
36.13	0.60	1.379	4.231	4.662	8.092	4.250	0.169	0.210	0.490
42.12	0.55	1.392	4.227	4.632	8.096	4.246	0.169	0.219	0.490
48.03	0.50	1.405	4.222	4.601	8.100	4.243	0.167	0.228	0.490
54.00	0.45	1.419	4.218	4.569	8.104	4.241	0.167	0.235	0.490
59.86	0.40	1.433	4.213	4.535	8.109	4.241	0.167	0.241	0.490
65.55	0.35	1.447	4.208	4.502	8.114	4.242	0.165	0.246	0.490
71.22	0.30	1.463	4.203	4.468	8.120	4.246	0.165	0.251	0.490
76.81	0.25	1.479	4.199	4.434	8.127	4.252	0.162	0.257	0.490
81.97	0.20	1.495	4.195	4.402	8.135	4.263	0.162	0.260	0.490
87.69	0.15	1.513	4.192	4.373	8.146	4.280	0.162	0.266	0.490
92.80	0.10	1.531	4.191	4.351	8.160	4.308	0.160	0.272	0.490
98.85	5.00E-02	1.551	4.196	4.351	8.182	4.364	0.163	0.273	0.490
100.30	4.00E-02	1.554	4.198	4.356	8.187	4.378	0.163	0.277	0.490
102.37	3.00E-02	1.562	4.201	4.360	8.195	4.401	0.147	N/A	0.490
103.32	2.00E-02	1.566	4.207	4.379	8.206	4.435	0.148	N/A	0.490
104.39	1.00E-02	1.574	4.217	4.410	8.221	4.489	0.148	N/A	0.490
105.63	1.00E-03	1.639	4.230	4.397	8.263	4.652	0.140	N/A	0.490
105.80	1.00E-04	1.733	4.209	4.220	8.282	4.773	0.085	N/A	0.490
105.90	0.00	1.788	4.190	4.087	8.283	4.839	0.037	N/A	0.490
Post Helium Exhaustion Phase									
106.65	0.00	1.942	4.110	3.613	8.271	5.002	0.000	N/A	0.490
107.40	0.00	1.929	4.116	3.553	8.219	5.121	0.000	N/A	0.490
108.15	0.00	1.950	4.101	3.569	8.208	5.168	0.000	N/A	0.490
108.90	0.00	1.978	4.081	3.463	8.206	5.204	0.000	N/A	0.491
109.65	0.00	1.997	4.066	3.382	8.203	5.243	0.000	N/A	0.491
110.40	0.00	2.005	4.055	3.332	8.197	5.274	0.000	N/A	0.492
111.15	0.00	2.013	4.044	3.279	8.194	5.292	0.000	N/A	0.492
111.90	0.00	2.032	4.020	3.165	8.188	5.320	0.000	N/A	0.492
112.65	0.00	2.048	4.003	3.081	8.185	5.339	0.000	N/A	0.492
113.40	0.00	2.069	3.982	2.974	8.184	5.362	0.000	N/A	0.492
114.15	0.00	2.085	3.963	2.883	8.183	5.379	0.000	N/A	0.493
114.90	0.00	2.109	3.935	2.748	8.184	5.404	0.000	N/A	0.493
115.65	0.00	2.132	3.902	2.592	8.184	5.428	0.000	N/A	0.493
116.40	0.00	2.160	3.856	2.383	8.183	5.457	0.000	N/A	0.493
117.15	0.00	2.184	3.815	2.192	8.183	5.482	0.000	N/A	0.493
117.90	0.00	2.215	3.760	1.943	8.182	5.513	0.000	N/A	0.494
118.60	0.00	2.251	3.730	1.785	8.179	5.548	0.000	N/A	0.494

Table B-3: Evolutionary Tracks for $\mathbf{Y_{HB} = 0.248}$ **[Fe/H]** $= -1.78$ **[O/Fe]** $= 0.66$

(a) $M_* = 0.90\,M_\odot$

t_6	Y_c	$\log L$	$\log T_{eff}$	$\log g_s$	$\log T_c$	$\log \rho_c$	M_{cc}	M_{sc}	M_{sh}
1.10	0.95	1.784	3.723	2.448	8.072	4.280	0.123	N/A	0.488
4.62	0.90	1.794	3.722	2.433	8.074	4.278	0.133	N/A	0.488
8.56	0.85	1.802	3.721	2.423	8.077	4.273	0.145	N/A	0.490
13.01	0.80	1.805	3.722	2.420	8.080	4.266	0.159	N/A	0.493
18.06	0.75	1.806	3.723	2.423	8.084	4.254	0.176	N/A	0.496
23.25	0.70	1.807	3.724	2.427	8.088	4.242	0.174	0.193	0.499
28.42	0.65	1.808	3.725	2.429	8.091	4.232	0.176	0.203	0.502
34.03	0.60	1.810	3.726	2.431	8.096	4.222	0.176	0.216	0.505
39.40	0.55	1.812	3.727	2.433	8.100	4.213	0.176	0.225	0.507
44.62	0.50	1.814	3.727	2.435	8.105	4.206	0.178	0.236	0.510
49.71	0.45	1.816	3.728	2.436	8.110	4.200	0.178	0.245	0.512
54.69	0.40	1.818	3.729	2.436	8.115	4.196	0.178	0.253	0.514
59.63	0.35	1.821	3.729	2.436	8.121	4.194	0.178	0.259	0.516
64.51	0.30	1.825	3.730	2.433	8.127	4.195	0.178	0.266	0.518
69.17	0.25	1.829	3.729	2.426	8.135	4.200	0.178	0.273	0.520
73.63	0.20	1.836	3.728	2.416	8.143	4.209	0.178	0.278	0.521
78.52	0.15	1.846	3.726	2.397	8.155	4.226	0.178	0.286	0.522
82.40	0.10	1.861	3.724	2.374	8.169	4.256	0.177	0.289	0.524
86.64	5.00E-02	1.887	3.720	2.332	8.191	4.313	0.177	0.290	0.525
87.55	4.00E-02	1.897	3.719	2.317	8.198	4.333	0.179	0.291	0.525
88.56	3.00E-02	1.905	3.718	2.304	8.204	4.351	0.176	0.261	0.526
89.28	2.00E-02	1.920	3.715	2.280	8.214	4.385	0.171	N/A	0.526
90.18	1.00E-02	1.947	3.712	2.239	8.229	4.440	0.171	N/A	0.527
91.15	1.00E-03	2.023	3.702	2.126	8.268	4.593	0.112	N/A	0.527
91.28	1.00E-04	2.077	3.701	2.064	8.279	4.708	0.016	N/A	0.527
91.30	0.00	2.086	3.700	2.055	8.280	4.726	0.000	N/A	0.527
Post Helium Exhaustion Phase									
91.50	0.00	2.222	3.693	1.888	8.288	4.924	0.000	N/A	0.527

Table B-3 (continued)
(b) $M_* = 0.74\,M_\odot$

t_6	Y_c	$\log L$	$\log T_{eff}$	$\log g_s$	$\log T_c$	$\log \rho_c$	M_{cc}	M_{sc}	M_{sh}
1.10	0.95	1.722	3.736	2.476	8.072	4.279	0.123	N/A	0.488
4.53	0.90	1.731	3.734	2.459	8.075	4.277	0.134	N/A	0.488
8.46	0.85	1.739	3.733	2.448	8.077	4.273	0.145	N/A	0.488
12.97	0.80	1.742	3.734	2.446	8.080	4.266	0.159	N/A	0.491
18.12	0.75	1.742	3.736	2.454	8.084	4.256	0.175	N/A	0.494
23.49	0.70	1.739	3.739	2.471	8.087	4.244	0.175	0.193	0.497
28.69	0.65	1.737	3.741	2.482	8.091	4.235	0.175	0.202	0.498
34.38	0.60	1.734	3.744	2.495	8.095	4.226	0.175	0.215	0.501
39.90	0.55	1.733	3.747	2.508	8.099	4.218	0.175	0.224	0.503
45.21	0.50	1.732	3.749	2.520	8.104	4.212	0.177	0.235	0.504
50.49	0.45	1.731	3.752	2.529	8.109	4.207	0.177	0.243	0.505
55.65	0.40	1.732	3.753	2.534	8.114	4.204	0.177	0.250	0.507
60.75	0.35	1.734	3.754	2.537	8.119	4.203	0.177	0.257	0.508
65.75	0.30	1.737	3.754	2.535	8.126	4.205	0.174	0.263	0.510
70.61	0.25	1.741	3.753	2.525	8.133	4.209	0.175	0.269	0.511
75.12	0.20	1.749	3.751	2.507	8.142	4.220	0.173	0.274	0.512
79.83	0.15	1.762	3.747	2.478	8.153	4.238	0.173	0.283	0.513
83.92	0.10	1.779	3.742	2.441	8.166	4.266	0.172	0.282	0.513
88.29	5.00E-02	1.814	3.733	2.370	8.188	4.324	0.174	0.286	0.514
89.36	4.00E-02	1.825	3.731	2.351	8.194	4.341	0.175	0.286	0.515
90.28	3.00E-02	1.839	3.727	2.325	8.201	4.364	0.173	0.240	0.515
91.17	2.00E-02	1.857	3.724	2.293	8.211	4.398	0.169	N/A	0.515
92.11	1.00E-02	1.889	3.719	2.243	8.227	4.453	0.169	N/A	0.515
93.14	1.00E-03	1.980	3.707	2.101	8.265	4.607	0.105	N/A	0.516
93.28	1.00E-04	2.038	3.703	2.029	8.275	4.716	0.018	N/A	0.516
93.30	0.00	2.048	3.703	2.017	8.277	4.735	0.000	N/A	0.516
Post Helium Exhaustion Phase									
94.05	0.00	2.175	3.695	1.859	8.241	5.078	0.000	N/A	0.518
94.80	0.00	2.160	3.697	1.881	8.218	5.157	0.000	N/A	0.519
95.55	0.00	2.157	3.697	1.885	8.206	5.210	0.000	N/A	0.520
96.30	0.00	2.152	3.697	1.891	8.196	5.252	0.000	N/A	0.520
97.05	0.00	2.162	3.697	1.881	8.187	5.288	0.000	N/A	0.520
97.80	0.00	2.179	3.695	1.853	8.181	5.319	0.000	N/A	0.520
98.55	0.00	2.201	3.693	1.826	8.178	5.349	0.000	N/A	0.521
99.30	0.00	2.227	3.691	1.793	8.177	5.383	0.000	N/A	0.521
100.05	0.00	2.259	3.690	1.754	8.177	5.420	0.000	N/A	0.521
100.10	0.00	2.263	3.690	1.749	8.177	5.423	0.000	N/A	0.521

Table B-3 (continued)

(c) $M_* = 0.68\,M_\odot$

t_6	Y_c	$\log L$	$\log T_{eff}$	$\log g_s$	$\log T_c$	$\log \rho_c$	M_{cc}	M_{sc}	M_{sh}
1.10	0.95	1.680	3.763	2.590	8.072	4.278	0.124	N/A	0.488
4.53	0.90	1.690	3.759	2.564	8.075	4.276	0.134	N/A	0.488
8.45	0.85	1.696	3.758	2.554	8.077	4.272	0.145	N/A	0.488
12.90	0.80	1.699	3.759	2.554	8.080	4.266	0.159	N/A	0.490
18.06	0.75	1.698	3.763	2.573	8.084	4.257	0.175	0.175	0.493
23.35	0.70	1.693	3.773	2.616	8.087	4.247	0.174	0.191	0.494
28.70	0.65	1.688	3.785	2.669	8.091	4.238	0.175	0.202	0.496
34.70	0.60	1.683	3.801	2.736	8.095	4.229	0.175	0.215	0.498
40.14	0.55	1.680	3.813	2.788	8.099	4.222	0.175	0.223	0.500
45.50	0.50	1.677	3.824	2.836	8.103	4.216	0.175	0.232	0.501
51.10	0.45	1.676	3.830	2.862	8.108	4.212	0.175	0.242	0.502
56.33	0.40	1.676	3.835	2.881	8.113	4.210	0.175	0.248	0.503
61.47	0.35	1.678	3.836	2.884	8.119	4.209	0.175	0.255	0.504
66.38	0.30	1.681	3.835	2.876	8.125	4.211	0.174	0.261	0.505
71.41	0.25	1.688	3.830	2.847	8.132	4.217	0.174	0.267	0.506
76.11	0.20	1.697	3.821	2.803	8.141	4.227	0.172	0.272	0.507
81.40	0.15	1.712	3.802	2.714	8.151	4.243	0.175	0.284	0.507
85.16	0.10	1.732	3.780	2.605	8.165	4.275	0.171	0.283	0.507
90.00	5.00E-02	1.771	3.755	2.468	8.187	4.332	0.173	0.283	0.508
91.30	4.00E-02	1.784	3.750	2.432	8.193	4.350	0.173	0.282	0.508
92.06	3.00E-02	1.798	3.745	2.400	8.200	4.372	0.165	N/A	0.508
92.96	2.00E-02	1.819	3.738	2.352	8.210	4.406	0.165	N/A	0.508
93.95	1.00E-02	1.855	3.730	2.282	8.225	4.461	0.165	N/A	0.509
95.00	1.00E-03	1.954	3.713	2.114	8.262	4.613	0.104	N/A	0.509
95.16	1.00E-04	2.026	3.707	2.018	8.273	4.739	0.020	N/A	0.509
95.20	0.00	2.047	3.706	1.993	8.273	4.777	0.000	N/A	0.509
Post Helium Exhaustion Phase									
95.95	0.00	2.155	3.699	1.859	8.237	5.076	0.000	N/A	0.511
96.70	0.00	2.138	3.700	1.881	8.211	5.156	0.000	N/A	0.512
97.45	0.00	2.139	3.700	1.879	8.201	5.207	0.000	N/A	0.513
98.20	0.00	2.137	3.701	1.883	8.193	5.249	0.000	N/A	0.513
98.95	0.00	2.140	3.700	1.879	8.186	5.280	0.000	N/A	0.514
99.70	0.00	2.153	3.699	1.859	8.179	5.311	0.000	N/A	0.514
100.45	0.00	2.172	3.696	1.831	8.175	5.342	0.000	N/A	0.514
101.20	0.00	2.193	3.695	1.805	8.173	5.370	0.000	N/A	0.515
101.95	0.00	2.219	3.693	1.768	8.173	5.401	0.000	N/A	0.515
102.70	0.00	2.249	3.691	1.732	8.173	5.435	0.000	N/A	0.515

Table B-3 (continued)
(d) $M_* = 0.64\,M_\odot$

t_6	Y_c	$\log L$	$\log T_{eff}$	$\log g_s$	$\log T_c$	$\log \rho_c$	M_{cc}	M_{sc}	M_{sh}
1.10	0.95	1.631	3.879	3.075	8.072	4.276	0.124	N/A	0.488
4.52	0.90	1.640	3.871	3.035	8.075	4.275	0.134	N/A	0.488
8.50	0.85	1.644	3.870	3.026	8.077	4.273	0.146	N/A	0.488
13.00	0.80	1.647	3.872	3.033	8.080	4.266	0.160	N/A	0.489
18.12	0.75	1.646	3.881	3.067	8.083	4.257	0.175	N/A	0.491
23.63	0.70	1.642	3.893	3.119	8.087	4.248	0.175	0.191	0.493
29.27	0.65	1.635	3.906	3.179	8.091	4.240	0.175	0.203	0.494
34.92	0.60	1.630	3.917	3.231	8.094	4.232	0.175	0.214	0.496
40.54	0.55	1.625	3.926	3.271	8.098	4.226	0.175	0.224	0.497
46.19	0.50	1.622	3.932	3.296	8.102	4.220	0.175	0.233	0.498
51.54	0.45	1.622	3.935	3.310	8.107	4.217	0.175	0.240	0.498
56.92	0.40	1.623	3.936	3.311	8.112	4.215	0.172	0.248	0.499
62.07	0.35	1.626	3.934	3.301	8.118	4.215	0.172	0.253	0.500
67.17	0.30	1.631	3.931	3.283	8.124	4.218	0.170	0.260	0.500
72.13	0.25	1.639	3.924	3.248	8.131	4.224	0.170	0.266	0.501
76.91	0.20	1.649	3.915	3.203	8.140	4.235	0.169	0.269	0.502
82.08	0.15	1.664	3.903	3.139	8.150	4.251	0.169	0.275	0.502
87.07	0.10	1.687	3.885	3.043	8.164	4.281	0.169	0.280	0.503
92.85	5.00E-02	1.726	3.851	2.869	8.185	4.336	0.171	0.286	0.503
94.80	4.00E-02	1.739	3.838	2.804	8.192	4.353	0.173	0.286	0.503
95.68	3.00E-02	1.756	3.819	2.709	8.199	4.378	0.159	N/A	0.503
96.54	2.00E-02	1.780	3.792	2.581	8.210	4.412	0.164	N/A	0.504
97.54	1.00E-02	1.820	3.757	2.398	8.225	4.467	0.164	N/A	0.504
98.64	1.00E-03	1.931	3.721	2.145	8.262	4.621	0.102	N/A	0.504
98.78	1.00E-04	1.993	3.711	2.043	8.272	4.728	0.016	N/A	0.504
98.80	0.00	2.004	3.710	2.026	8.273	4.747	0.000	N/A	0.504
Post Helium Exhaustion Phase									
99.55	0.00	2.138	3.702	1.862	8.237	5.072	0.000	N/A	0.506
100.30	0.00	2.120	3.704	1.888	8.210	5.154	0.000	N/A	0.507
101.05	0.00	2.124	3.704	1.883	8.201	5.200	0.000	N/A	0.507
101.80	0.00	2.127	3.704	1.880	8.194	5.246	0.000	N/A	0.508
102.55	0.00	2.127	3.704	1.879	8.188	5.279	0.000	N/A	0.509
103.30	0.00	2.137	3.703	1.866	8.181	5.310	0.000	N/A	0.509
104.05	0.00	2.152	3.701	1.845	8.176	5.338	0.000	N/A	0.509
104.80	0.00	2.174	3.699	1.812	8.173	5.370	0.000	N/A	0.510
105.55	0.00	2.198	3.696	1.779	8.171	5.400	0.000	N/A	0.510
106.30	0.00	2.226	3.694	1.739	8.170	5.433	0.000	N/A	0.510
106.90	0.00	2.252	3.692	1.708	8.170	5.460	0.000	N/A	0.510

Table B-3 (continued)

(e) $M_* = 0.54\,M_\odot$

t_6	Y_c	$\log L$	$\log T_{eff}$	$\log g_s$	$\log T_c$	$\log \rho_c$	M_{cc}	M_{sc}	M_{sh}
1.10	0.95	1.306	4.244	4.787	8.072	4.279	0.123	N/A	0.488
4.66	0.90	1.317	4.240	4.762	8.074	4.279	0.134	N/A	0.488
8.63	0.85	1.326	4.237	4.738	8.077	4.278	0.145	N/A	0.488
13.34	0.80	1.334	4.234	4.718	8.079	4.275	0.159	N/A	0.488
18.73	0.75	1.345	4.229	4.689	8.082	4.269	0.175	N/A	0.488
24.53	0.70	1.355	4.225	4.663	8.085	4.263	0.171	0.188	0.488
30.35	0.65	1.365	4.221	4.636	8.088	4.257	0.169	0.198	0.488
36.65	0.60	1.377	4.217	4.606	8.092	4.252	0.169	0.210	0.488
42.65	0.55	1.389	4.212	4.576	8.096	4.249	0.169	0.218	0.488
48.71	0.50	1.401	4.207	4.544	8.100	4.246	0.166	0.226	0.488
54.64	0.45	1.415	4.202	4.511	8.104	4.244	0.166	0.234	0.488
60.55	0.40	1.429	4.197	4.477	8.109	4.243	0.167	0.240	0.488
66.33	0.35	1.443	4.192	4.442	8.114	4.245	0.164	0.245	0.488
71.91	0.30	1.458	4.187	4.407	8.120	4.248	0.164	0.250	0.488
77.68	0.25	1.474	4.182	4.371	8.127	4.254	0.162	0.256	0.488
82.70	0.20	1.490	4.178	4.338	8.135	4.265	0.162	0.260	0.488
88.24	0.15	1.508	4.174	4.306	8.146	4.283	0.161	0.267	0.488
93.48	0.10	1.526	4.173	4.284	8.160	4.312	0.161	0.269	0.488
99.69	5.00E-02	1.545	4.177	4.281	8.181	4.363	0.162	0.273	0.488
101.36	4.00E-02	1.551	4.180	4.287	8.188	4.383	0.162	0.275	0.488
102.31	3.00E-02	1.557	4.183	4.291	8.195	4.405	0.162	N/A	0.488
103.30	2.00E-02	1.562	4.188	4.307	8.205	4.438	0.162	N/A	0.488
104.48	1.00E-02	1.574	4.197	4.329	8.220	4.492	0.162	N/A	0.488
105.85	1.00E-03	1.671	4.195	4.225	8.261	4.651	0.166	N/A	0.488
106.08	1.00E-04	1.818	4.134	3.837	8.284	4.798	0.092	N/A	0.488
106.20	0.00	1.872	4.104	3.661	8.287	4.853	0.064	N/A	0.488
Post Helium Exhaustion Phase									
106.95	0.00	2.031	3.966	2.951	8.261	5.058	0.000	N/A	0.488
107.70	0.00	2.005	3.999	3.107	8.229	5.134	0.000	N/A	0.489
108.45	0.00	2.000	4.005	3.136	8.205	5.191	0.000	N/A	0.489
109.20	0.00	2.017	3.991	3.063	8.198	5.231	0.000	N/A	0.490
109.95	0.00	2.015	3.991	3.064	8.187	5.267	0.000	N/A	0.490
110.70	0.00	2.023	3.982	3.021	8.183	5.288	0.000	N/A	0.491
111.45	0.00	2.033	3.969	2.962	8.179	5.307	0.000	N/A	0.491
112.20	0.00	2.047	3.952	2.878	8.175	5.329	0.000	N/A	0.491
112.95	0.00	2.063	3.930	2.776	8.168	5.353	0.000	N/A	0.491
113.70	0.00	2.079	3.910	2.677	8.165	5.371	0.000	N/A	0.492
114.45	0.00	2.098	3.884	2.554	8.165	5.392	0.000	N/A	0.492
115.20	0.00	2.121	3.850	2.398	8.166	5.416	0.000	N/A	0.492
115.95	0.00	2.143	3.815	2.233	8.168	5.437	0.000	N/A	0.492
116.70	0.00	2.171	3.767	2.013	8.170	5.465	0.000	N/A	0.492
117.45	0.00	2.197	3.740	1.879	8.171	5.492	0.000	N/A	0.492
118.20	0.00	2.230	3.725	1.788	8.167	5.527	0.000	N/A	0.492
118.60	0.00	2.250	3.719	1.743	8.164	5.547	0.000	N/A	0.492

Table B-4: Evolutionary Tracks for $Y_{HB} = 0.248$ [Fe/H] $= -1.66$ [O/Fe] $= 0.63$
(a) $M_* = 0.90\,M_\odot$

t_6	Y_c	$\log L$	$\log T_{eff}$	$\log g_s$	$\log T_c$	$\log \rho_c$	M_{cc}	M_{sc}	M_{sh}
1.10	0.95	1.780	3.721	2.441	8.072	4.284	0.122	N/A	0.487
4.64	0.90	1.790	3.719	2.426	8.074	4.281	0.133	N/A	0.487
8.63	0.85	1.798	3.719	2.415	8.077	4.278	0.144	N/A	0.489
13.22	0.80	1.802	3.719	2.413	8.080	4.268	0.158	N/A	0.492
18.46	0.75	1.802	3.720	2.416	8.083	4.257	0.175	N/A	0.495
23.70	0.70	1.803	3.721	2.419	8.087	4.245	0.174	0.191	0.498
29.03	0.65	1.805	3.722	2.421	8.091	4.234	0.176	0.202	0.501
34.61	0.60	1.806	3.723	2.423	8.095	4.224	0.176	0.215	0.504
40.11	0.55	1.808	3.723	2.424	8.100	4.215	0.176	0.224	0.506
45.39	0.50	1.810	3.724	2.425	8.104	4.208	0.176	0.235	0.508
50.55	0.45	1.812	3.725	2.426	8.109	4.202	0.178	0.244	0.511
55.56	0.40	1.814	3.725	2.426	8.115	4.198	0.178	0.252	0.513
60.42	0.35	1.817	3.726	2.425	8.121	4.196	0.178	0.258	0.515
65.08	0.30	1.820	3.726	2.421	8.127	4.197	0.178	0.264	0.517
69.88	0.25	1.825	3.725	2.415	8.135	4.202	0.178	0.272	0.519
74.41	0.20	1.831	3.725	2.408	8.143	4.211	0.178	0.277	0.520
78.93	0.15	1.841	3.723	2.391	8.154	4.227	0.178	0.284	0.522
82.66	0.10	1.856	3.721	2.367	8.168	4.256	0.177	0.287	0.522
86.75	5.00E-02	1.883	3.718	2.326	8.189	4.311	0.176	0.290	0.524
87.58	4.00E-02	1.891	3.717	2.315	8.196	4.328	0.180	0.292	0.526
88.68	3.00E-02	1.903	3.715	2.296	8.204	4.351	0.169	0.178	0.526
89.40	2.00E-02	1.919	3.713	2.271	8.214	4.385	0.168	N/A	0.526
90.27	1.00E-02	1.946	3.709	2.229	8.229	4.440	0.168	N/A	0.526
91.25	1.00E-03	2.025	3.700	2.113	8.267	4.592	0.108	N/A	0.527
91.38	1.00E-04	2.078	3.698	2.054	8.279	4.700	0.018	N/A	0.526
91.40	0.00	2.089	3.698	2.043	8.280	4.720	0.000	N/A	0.526
Post Helium Exhaustion Phase									
91.60	0.00	2.226	3.691	1.878	8.287	4.920	0.000	N/A	0.526

Table B-4 (continued)
(b) $M_* = 0.72\,M_\odot$

t_6	Y_{c_c}	$\log L$	$\log T_{eff}$	$\log g_s$	$\log T_c$	$\log \rho_c$	M_{cc}	M_{sc}	M_{sh}
1.10	0.95	1.712	3.735	2.470	8.072	4.282	0.123	N/A	0.487
4.65	0.90	1.722	3.733	2.452	8.074	4.280	0.133	N/A	0.487
8.60	0.85	1.729	3.732	2.442	8.077	4.276	0.145	N/A	0.487
13.17	0.80	1.732	3.733	2.441	8.080	4.269	0.158	N/A	0.490
18.40	0.75	1.731	3.735	2.450	8.083	4.259	0.175	N/A	0.493
23.34	0.70	1.727	3.738	2.466	8.087	4.248	0.174	0.188	0.495
28.98	0.65	1.724	3.741	2.481	8.091	4.238	0.174	0.202	0.497
34.77	0.60	1.722	3.744	2.496	8.095	4.229	0.174	0.214	0.499
40.10	0.55	1.720	3.747	2.509	8.099	4.222	0.174	0.224	0.501
45.56	0.50	1.718	3.749	2.521	8.104	4.215	0.174	0.233	0.503
50.92	0.45	1.717	3.752	2.534	8.108	4.210	0.174	0.242	0.504
56.09	0.40	1.718	3.754	2.541	8.113	4.208	0.176	0.249	0.505
61.19	0.35	1.719	3.755	2.543	8.119	4.207	0.174	0.255	0.507
66.18	0.30	1.722	3.755	2.541	8.126	4.209	0.173	0.262	0.508
70.94	0.25	1.727	3.754	2.531	8.133	4.214	0.173	0.267	0.509
75.79	0.20	1.735	3.751	2.512	8.141	4.224	0.173	0.273	0.510
81.12	0.15	1.748	3.747	2.484	8.153	4.243	0.173	0.282	0.511
85.54	0.10	1.766	3.742	2.446	8.167	4.271	0.173	0.283	0.511
90.07	5.00E-02	1.800	3.733	2.375	8.188	4.326	0.174	0.284	0.513
91.21	4.00E-02	1.811	3.731	2.356	8.194	4.343	0.176	0.286	0.513
92.49	3.00E-02	1.825	3.729	2.332	8.202	4.366	0.169	0.174	0.513
93.31	2.00E-02	1.844	3.724	2.295	8.211	4.400	0.162	N/A	0.513
94.21	1.00E-02	1.878	3.719	2.241	8.227	4.455	0.162	N/A	0.513
95.23	1.00E-03	1.972	3.706	2.094	8.264	4.608	0.098	N/A	0.514
95.37	1.00E-04	2.036	3.704	2.022	8.274	4.724	0.020	N/A	0.514
95.40	0.00	2.051	3.704	2.008	8.275	4.752	0.000	N/A	0.514
Post Helium Exhaustion Phase									
96.15	0.00	2.173	3.694	1.843	8.239	5.078	0.000	N/A	0.516
96.90	0.00	2.157	3.697	1.871	8.216	5.154	0.000	N/A	0.517
97.65	0.00	2.156	3.697	1.872	8.205	5.213	0.000	N/A	0.518
98.40	0.00	2.152	3.697	1.877	8.196	5.255	0.000	N/A	0.518
99.15	0.00	2.158	3.696	1.870	8.189	5.285	0.000	N/A	0.519
99.90	0.00	2.174	3.694	1.843	8.182	5.318	0.000	N/A	0.519
100.65	0.00	2.195	3.692	1.817	8.179	5.349	0.000	N/A	0.519
101.40	0.00	2.222	3.691	1.782	8.177	5.384	0.000	N/A	0.519
102.10	0.00	2.251	3.688	1.744	8.177	5.418	0.000	N/A	0.520

Table B-4 (continued)
(c) $M_* = 0.66\,M_\odot$

t_6	Y_c	$\log L$	$\log T_{eff}$	$\log g_s$	$\log T_c$	$\log \rho_c$	M_{cc}	M_{sc}	M_{sh}
1.10	0.95	1.666	3.771	2.623	8.072	4.280	0.123	N/A	0.487
4.53	0.90	1.676	3.766	2.592	8.074	4.279	0.133	N/A	0.487
8.53	0.85	1.681	3.764	2.578	8.076	4.277	0.146	N/A	0.487
13.04	0.80	1.685	3.766	2.582	8.080	4.269	0.158	N/A	0.489
18.10	0.75	1.682	3.773	2.615	8.083	4.260	0.175	N/A	0.491
23.99	0.70	1.676	3.789	2.682	8.087	4.250	0.174	0.191	0.493
29.32	0.65	1.671	3.806	2.757	8.090	4.241	0.174	0.201	0.495
35.18	0.60	1.665	3.823	2.832	8.094	4.232	0.174	0.213	0.497
40.86	0.55	1.661	3.837	2.889	8.098	4.225	0.174	0.223	0.498
46.41	0.50	1.658	3.847	2.934	8.103	4.220	0.174	0.232	0.499
51.83	0.45	1.656	3.854	2.964	8.107	4.216	0.174	0.240	0.500
57.28	0.40	1.656	3.858	2.979	8.113	4.213	0.174	0.247	0.502
62.56	0.35	1.658	3.859	2.981	8.118	4.213	0.174	0.254	0.502
67.55	0.30	1.662	3.857	2.971	8.124	4.215	0.172	0.258	0.503
72.53	0.25	1.668	3.852	2.943	8.132	4.221	0.172	0.266	0.503
77.49	0.20	1.678	3.843	2.899	8.140	4.231	0.172	0.270	0.504
84.44	0.15	1.693	3.828	2.824	8.151	4.247	0.171	0.287	0.505
88.84	0.10	1.716	3.804	2.703	8.165	4.278	0.168	0.287	0.505
93.59	5.00E-02	1.755	3.767	2.516	8.186	4.333	0.172	0.286	0.506
94.65	4.00E-02	1.768	3.760	2.475	8.192	4.351	0.172	0.286	0.506
95.86	3.00E-02	1.784	3.752	2.428	8.200	4.375	0.160	N/A	0.506
96.75	2.00E-02	1.806	3.744	2.374	8.210	4.409	0.160	N/A	0.506
97.68	1.00E-02	1.844	3.733	2.293	8.225	4.465	0.160	N/A	0.507
98.74	1.00E-03	1.948	3.713	2.108	8.262	4.616	0.098	N/A	0.507
98.88	1.00E-04	2.006	3.709	2.034	8.273	4.716	0.017	N/A	0.507
98.90	0.00	2.016	3.709	2.023	8.274	4.734	0.000	N/A	0.507
Post Helium Exhaustion Phase									
99.65	0.00	2.159	3.697	1.834	8.239	5.072	0.000	N/A	0.509
100.40	0.00	2.134	3.699	1.868	8.212	5.152	0.000	N/A	0.510
101.15	0.00	2.131	3.700	1.873	8.200	5.206	0.000	N/A	0.511
101.90	0.00	2.131	3.700	1.872	8.192	5.245	0.000	N/A	0.512
102.65	0.00	2.135	3.699	1.867	8.186	5.276	0.000	N/A	0.512
103.40	0.00	2.146	3.698	1.852	8.180	5.307	0.000	N/A	0.512
104.15	0.00	2.162	3.697	1.832	8.176	5.335	0.000	N/A	0.512
104.90	0.00	2.191	3.695	1.793	8.172	5.372	0.000	N/A	0.512
105.65	0.00	2.218	3.692	1.755	8.172	5.403	0.000	N/A	0.513
106.40	0.00	2.249	3.690	1.715	8.172	5.438	0.000	N/A	0.513
106.50	0.00	2.253	3.690	1.710	8.172	5.442	0.000	N/A	0.513

Table B-4 (continued)
(d) $M_* = 0.60\,M_\odot$

t_6	Y_c	$\log L$	$\log T_{eff}$	$\log g_s$	$\log T_c$	$\log \rho_c$	M_{cc}	M_{sc}	M_{sh}
1.00	0.95	1.553	4.009	3.647	8.072	4.278	0.123	N/A	0.487
4.57	0.90	1.566	4.001	3.600	8.074	4.277	0.134	N/A	0.487
8.50	0.85	1.569	4.001	3.597	8.077	4.274	0.145	N/A	0.487
13.07	0.80	1.569	4.003	3.605	8.080	4.269	0.159	N/A	0.487
18.12	0.75	1.567	4.006	3.620	8.083	4.262	0.175	0.175	0.488
23.53	0.70	1.564	4.011	3.645	8.086	4.253	0.172	0.189	0.489
29.31	0.65	1.559	4.017	3.670	8.090	4.246	0.172	0.200	0.490
35.30	0.60	1.555	4.021	3.694	8.094	4.239	0.172	0.212	0.491
41.04	0.55	1.552	4.024	3.709	8.097	4.233	0.172	0.222	0.492
46.63	0.50	1.551	4.026	3.714	8.102	4.229	0.172	0.229	0.493
52.31	0.45	1.553	4.025	3.708	8.106	4.226	0.172	0.238	0.494
57.79	0.40	1.556	4.022	3.695	8.111	4.225	0.169	0.243	0.493
63.42	0.35	1.562	4.018	3.672	8.116	4.226	0.170	0.251	0.494
68.94	0.30	1.570	4.013	3.643	8.122	4.228	0.170	0.257	0.494
73.82	0.25	1.580	4.006	3.609	8.130	4.235	0.167	0.261	0.495
79.01	0.20	1.593	3.998	3.563	8.138	4.245	0.167	0.265	0.495
84.07	0.15	1.609	3.989	3.510	8.148	4.262	0.167	0.274	0.495
90.07	0.10	1.631	3.978	3.442	8.162	4.291	0.166	0.278	0.495
95.56	5.00E-02	1.670	3.958	3.324	8.185	4.349	0.168	0.279	0.496
96.84	4.00E-02	1.684	3.950	3.278	8.191	4.368	0.168	0.280	0.496
97.87	3.00E-02	1.698	3.944	3.242	8.198	4.387	0.166	0.248	0.496
98.78	2.00E-02	1.722	3.927	3.148	8.208	4.422	0.161	N/A	0.496
99.83	1.00E-02	1.767	3.888	2.945	8.223	4.477	0.161	N/A	0.497
100.95	1.00E-03	1.896	3.743	2.239	8.259	4.628	0.102	N/A	0.497
101.10	1.00E-04	1.956	3.723	2.100	8.271	4.719	0.025	N/A	0.496
101.20	0.00	2.024	3.716	2.000	8.269	4.822	0.000	N/A	0.496
Post Helium Exhaustion Phase									
101.95	0.00	2.132	3.705	1.853	8.237	5.088	0.000	N/A	0.499
102.70	0.00	2.106	3.709	1.893	8.209	5.162	0.000	N/A	0.500
103.45	0.00	2.106	3.709	1.894	8.198	5.211	0.000	N/A	0.501
104.20	0.00	2.104	3.710	1.897	8.189	5.254	0.000	N/A	0.501
104.95	0.00	2.101	3.710	1.901	8.182	5.282	0.000	N/A	0.502
105.70	0.00	2.109	3.709	1.890	8.175	5.309	0.000	N/A	0.503
106.45	0.00	2.123	3.707	1.870	8.169	5.335	0.000	N/A	0.503
107.20	0.00	2.141	3.705	1.843	8.166	5.362	0.000	N/A	0.503
107.95	0.00	2.160	3.703	1.815	8.164	5.388	0.000	N/A	0.503
108.70	0.00	2.185	3.700	1.779	8.163	5.418	0.000	N/A	0.503
109.45	0.00	2.212	3.698	1.742	8.162	5.448	0.000	N/A	0.503
110.20	0.00	2.241	3.695	1.702	8.161	5.479	0.000	N/A	0.503
110.40	0.00	2.251	3.694	1.685	8.161	5.490	0.000	N/A	0.503

Table B-4 (continued)
(e) $M_* = 0.54\,M_\odot$

t_6	Y_c	$\log L$	$\log T_{eff}$	$\log g_s$	$\log T_c$	$\log \rho_c$	M_{cc}	M_{sc}	M_{sh}
1.10	0.95	1.306	4.235	4.752	8.072	4.281	0.123	N/A	0.487
4.67	0.90	1.319	4.231	4.724	8.074	4.281	0.133	N/A	0.487
8.64	0.85	1.328	4.228	4.700	8.076	4.279	0.145	N/A	0.487
13.36	0.80	1.336	4.225	4.680	8.079	4.277	0.159	N/A	0.487
18.97	0.75	1.345	4.221	4.654	8.082	4.271	0.175	N/A	0.487
24.54	0.70	1.355	4.216	4.626	8.085	4.264	0.171	0.187	0.487
30.50	0.65	1.365	4.212	4.600	8.088	4.259	0.163	0.197	0.487
36.71	0.60	1.376	4.207	4.570	8.092	4.254	0.168	0.208	0.487
42.85	0.55	1.387	4.203	4.540	8.095	4.250	0.168	0.218	0.487
48.87	0.50	1.400	4.198	4.507	8.100	4.247	0.166	0.226	0.487
54.96	0.45	1.413	4.192	4.474	8.104	4.245	0.166	0.232	0.487
60.85	0.40	1.426	4.187	4.439	8.109	4.245	0.164	0.238	0.487
66.93	0.35	1.441	4.182	4.404	8.114	4.246	0.163	0.246	0.487
72.57	0.30	1.456	4.177	4.368	8.120	4.250	0.163	0.249	0.487
78.19	0.25	1.471	4.171	4.332	8.127	4.256	0.161	0.255	0.487
83.44	0.20	1.487	4.167	4.297	8.135	4.266	0.161	0.259	0.487
89.24	0.15	1.506	4.163	4.264	8.146	4.284	0.161	0.267	0.487
95.01	0.10	1.524	4.162	4.240	8.160	4.314	0.159	0.269	0.487
101.64	5.00E-02	1.545	4.166	4.234	8.181	4.367	0.163	0.275	0.487
103.89	4.00E-02	1.552	4.167	4.231	8.187	4.382	0.164	0.280	0.487
105.43	3.00E-02	1.556	4.171	4.244	8.195	4.406	0.162	0.288	0.487
106.50	2.00E-02	1.565	4.175	4.253	8.205	4.439	0.162	N/A	0.487
107.68	1.00E-02	1.580	4.182	4.267	8.221	4.493	0.162	N/A	0.487
108.94	1.00E-03	1.703	4.165	4.075	8.263	4.660	0.156	N/A	0.487
109.20	1.00E-04	1.857	4.086	3.603	8.285	4.810	0.080	N/A	0.487
109.30	0.00	1.930	4.027	3.294	8.285	4.887	0.028	N/A	0.487
Post Helium Exhaustion Phase									
110.05	0.00	2.017	3.938	2.851	8.244	5.085	0.000	N/A	0.487
110.80	0.00	1.996	3.965	2.981	8.207	5.161	0.000	N/A	0.488
111.55	0.00	2.009	3.953	2.921	8.198	5.194	0.000	N/A	0.488
112.30	0.00	2.033	3.930	2.804	8.196	5.232	0.000	N/A	0.489
113.05	0.00	2.039	3.927	2.785	8.187	5.271	0.000	N/A	0.489
113.80	0.00	2.041	3.924	2.772	8.182	5.290	0.000	N/A	0.490
114.55	0.00	2.054	3.908	2.693	8.181	5.318	0.000	N/A	0.490
115.30	0.00	2.065	3.891	2.615	8.178	5.341	0.000	N/A	0.490
116.05	0.00	2.078	3.869	2.517	8.172	5.362	0.000	N/A	0.490
116.80	0.00	2.097	3.843	2.394	8.172	5.383	0.000	N/A	0.491
117.55	0.00	2.117	3.811	2.245	8.172	5.405	0.000	N/A	0.491
118.30	0.00	2.139	3.773	2.071	8.171	5.429	0.000	N/A	0.491
119.05	0.00	2.165	3.745	1.931	8.170	5.457	0.000	N/A	0.491
119.80	0.00	2.189	3.729	1.842	8.167	5.484	0.000	N/A	0.491
120.55	0.00	2.223	3.720	1.774	8.163	5.519	0.000	N/A	0.492
121.20	0.00	2.252	3.714	1.722	8.158	5.550	0.000	N/A	0.492

Table B-5: Evolutionary Tracks for $Y_{HB} = 0.249$ [Fe/H] $= -1.48$ [O/Fe] $= 0.60$
(a) $M_* = 0.90\,M_\odot$

t_6	Y_c	$\log L$	$\log T_{eff}$	$\log g_s$	$\log T_c$	$\log \rho_c$	M_{cc}	M_{sc}	M_{sh}
1.10	0.95	1.776	3.716	2.428	8.071	4.287	0.121	N/A	0.485
4.57	0.90	1.788	3.715	2.410	8.074	4.285	0.132	N/A	0.485
8.34	0.85	1.796	3.714	2.401	8.076	4.280	0.143	N/A	0.488
12.71	0.80	1.798	3.715	2.400	8.080	4.272	0.157	N/A	0.491
17.44	0.75	1.798	3.716	2.404	8.083	4.261	0.173	N/A	0.493
22.73	0.70	1.798	3.717	2.408	8.087	4.249	0.173	0.189	0.496
28.34	0.65	1.799	3.717	2.410	8.091	4.238	0.173	0.201	0.499
33.95	0.60	1.801	3.718	2.410	8.095	4.228	0.174	0.214	0.502
39.58	0.55	1.803	3.719	2.411	8.099	4.219	0.175	0.223	0.505
44.90	0.50	1.804	3.719	2.412	8.104	4.212	0.175	0.234	0.507
50.12	0.45	1.806	3.720	2.412	8.109	4.206	0.175	0.243	0.510
55.25	0.40	1.808	3.720	2.412	8.114	4.202	0.175	0.251	0.511
60.20	0.35	1.811	3.721	2.411	8.120	4.200	0.177	0.257	0.514
65.19	0.30	1.815	3.721	2.408	8.127	4.200	0.177	0.264	0.516
69.91	0.25	1.819	3.721	2.402	8.134	4.205	0.175	0.269	0.517
74.51	0.20	1.826	3.720	2.394	8.143	4.214	0.177	0.276	0.519
79.67	0.15	1.837	3.719	2.377	8.155	4.233	0.176	0.287	0.520
83.14	0.10	1.851	3.717	2.358	8.167	4.256	0.177	0.288	0.522
87.68	5.00E-02	1.881	3.713	2.312	8.190	4.315	0.175	0.289	0.524
88.80	4.00E-02	1.890	3.712	2.299	8.196	4.328	0.179	0.291	0.525
89.86	3.00E-02	1.902	3.710	2.279	8.204	4.352	0.179	0.193	0.525
90.68	2.00E-02	1.919	3.708	2.254	8.214	4.386	0.172	N/A	0.525
91.58	1.00E-02	1.948	3.705	2.211	8.229	4.441	0.172	N/A	0.526
92.52	1.00E-03	2.031	3.695	2.088	8.268	4.596	0.108	N/A	0.527
92.66	1.00E-04	2.095	3.694	2.021	8.279	4.720	0.026	N/A	0.527
92.70	0.00	2.118	3.695	2.002	8.280	4.763	0.000	N/A	0.527
Post Helium Exhaustion Phase									
92.80	0.00	2.193	3.690	1.907	8.285	4.870	0.000	N/A	0.527

Table B-5 (continued)
(b) $M_* = 0.70\,M_\odot$

t_6	Y_c	$\log L$	$\log T_{eff}$	$\log g_s$	$\log T_c$	$\log \rho_c$	M_{cc}	M_{sc}	M_{sh}
1.10	0.95	1.703	3.732	2.454	8.071	4.285	0.122	N/A	0.485
4.53	0.90	1.715	3.730	2.435	8.074	4.283	0.132	N/A	0.485
8.28	0.85	1.721	3.729	2.425	8.076	4.279	0.143	N/A	0.486
12.65	0.80	1.724	3.730	2.425	8.079	4.272	0.157	N/A	0.489
17.78	0.75	1.721	3.732	2.437	8.083	4.262	0.174	N/A	0.491
22.75	0.70	1.717	3.735	2.452	8.086	4.252	0.173	0.187	0.493
28.61	0.65	1.714	3.738	2.468	8.090	4.242	0.173	0.201	0.495
34.52	0.60	1.711	3.741	2.484	8.094	4.233	0.173	0.214	0.497
40.06	0.55	1.708	3.744	2.498	8.099	4.225	0.173	0.222	0.499
45.41	0.50	1.707	3.747	2.510	8.103	4.219	0.173	0.231	0.501
50.92	0.45	1.706	3.749	2.520	8.108	4.214	0.173	0.240	0.503
56.31	0.40	1.705	3.752	2.533	8.113	4.211	0.173	0.247	0.504
61.48	0.35	1.707	3.753	2.536	8.119	4.211	0.173	0.253	0.505
66.46	0.30	1.709	3.754	2.535	8.125	4.212	0.173	0.261	0.506
71.21	0.25	1.714	3.751	2.521	8.132	4.218	0.173	0.265	0.507
75.58	0.20	1.722	3.749	2.503	8.141	4.228	0.173	0.271	0.508
79.85	0.15	1.735	3.745	2.474	8.151	4.245	0.172	0.278	0.508
83.96	0.10	1.756	3.739	2.429	8.165	4.275	0.169	0.279	0.509
88.26	5.00E-02	1.791	3.731	2.363	8.186	4.329	0.172	0.282	0.509
89.68	4.00E-02	1.802	3.728	2.341	8.192	4.347	0.172	0.284	0.510
90.80	3.00E-02	1.816	3.726	2.316	8.200	4.370	0.163	N/A	0.511
91.63	2.00E-02	1.837	3.722	2.281	8.210	4.405	0.163	N/A	0.511
92.57	1.00E-02	1.872	3.716	2.223	8.226	4.459	0.163	N/A	0.511
93.63	1.00E-03	1.972	3.703	2.070	8.263	4.611	0.107	N/A	0.512
93.78	1.00E-04	2.034	3.702	2.004	8.274	4.721	0.016	N/A	0.512
93.80	0.00	2.044	3.702	1.995	8.275	4.740	0.000	N/A	0.512
Post Helium Exhaustion Phase									
94.55	0.00	2.172	3.691	1.823	8.238	5.075	0.000	N/A	0.513
95.30	0.00	2.163	3.692	1.834	8.225	5.134	0.000	N/A	0.514
96.05	0.00	2.155	3.693	1.848	8.210	5.196	0.000	N/A	0.515
96.80	0.00	2.146	3.694	1.858	8.199	5.243	0.000	N/A	0.516
97.55	0.00	2.148	3.694	1.856	8.189	5.277	0.000	N/A	0.517
98.30	0.00	2.161	3.692	1.838	8.181	5.308	0.000	N/A	0.516
99.05	0.00	2.181	3.691	1.812	8.176	5.340	0.000	N/A	0.516
99.80	0.00	2.205	3.689	1.781	8.174	5.372	0.000	N/A	0.517
100.55	0.00	2.232	3.686	1.744	8.173	5.405	0.000	N/A	0.517
101.10	0.00	2.251	3.685	1.718	8.174	5.427	0.000	N/A	0.517

Table B-5 (continued)
(c) $M_* = 0.64\,M_\odot$

t_6	Y_c	$\log L$	$\log T_{eff}$	$\log g_s$	$\log T_c$	$\log \rho_c$	M_{cc}	M_{sc}	M_{sh}
1.10	0.95	1.653	3.777	2.647	8.071	4.284	0.122	N/A	0.485
4.58	0.90	1.665	3.769	2.601	8.074	4.282	0.132	N/A	0.485
8.38	0.85	1.671	3.768	2.593	8.076	4.279	0.144	N/A	0.485
12.73	0.80	1.673	3.771	2.601	8.079	4.273	0.157	N/A	0.487
17.55	0.75	1.669	3.781	2.647	8.083	4.264	0.173	N/A	0.490
22.92	0.70	1.662	3.801	2.732	8.086	4.254	0.174	0.187	0.491
28.59	0.65	1.655	3.822	2.823	8.090	4.245	0.173	0.200	0.493
34.50	0.60	1.648	3.839	2.899	8.094	4.236	0.173	0.211	0.495
40.41	0.55	1.644	3.853	2.958	8.098	4.229	0.173	0.222	0.496
45.98	0.50	1.640	3.863	3.004	8.102	4.224	0.173	0.231	0.497
51.49	0.45	1.638	3.871	3.035	8.107	4.220	0.173	0.238	0.498
56.98	0.40	1.637	3.875	3.052	8.112	4.218	0.173	0.245	0.499
62.27	0.35	1.639	3.875	3.053	8.118	4.218	0.171	0.252	0.500
67.51	0.30	1.643	3.873	3.041	8.124	4.220	0.171	0.257	0.500
72.58	0.25	1.650	3.868	3.011	8.131	4.226	0.171	0.264	0.501
77.59	0.20	1.659	3.860	2.970	8.139	4.236	0.169	0.269	0.502
82.26	0.15	1.674	3.845	2.898	8.150	4.253	0.169	0.274	0.502
86.97	0.10	1.699	3.819	2.767	8.164	4.283	0.169	0.278	0.503
91.93	5.00E-02	1.740	3.778	2.564	8.186	4.340	0.170	0.277	0.503
93.09	4.00E-02	1.752	3.769	2.513	8.192	4.356	0.169	0.277	0.504
94.23	3.00E-02	1.768	3.759	2.458	8.199	4.379	0.161	N/A	0.503
95.08	2.00E-02	1.791	3.749	2.394	8.209	4.413	0.162	N/A	0.504
96.11	1.00E-02	1.831	3.736	2.302	8.224	4.468	0.162	N/A	0.504
97.19	1.00E-03	1.942	3.712	2.097	8.261	4.619	0.108	N/A	0.505
97.36	1.00E-04	2.020	3.707	1.999	8.271	4.746	0.020	N/A	0.505
97.40	0.00	2.042	3.707	1.976	8.271	4.784	0.000	N/A	0.505
Post Helium Exhaustion Phase									
98.15	0.00	2.155	3.696	1.820	8.237	5.083	0.000	N/A	0.507
98.90	0.00	2.139	3.697	1.842	8.219	5.146	0.000	N/A	0.507
99.65	0.00	2.131	3.699	1.854	8.203	5.203	0.000	N/A	0.508
100.40	0.00	2.125	3.699	1.863	8.193	5.249	0.000	N/A	0.509
101.15	0.00	2.126	3.699	1.861	8.184	5.281	0.000	N/A	0.510
101.90	0.00	2.137	3.698	1.846	8.177	5.309	0.000	N/A	0.510
102.65	0.00	2.152	3.696	1.823	8.172	5.336	0.000	N/A	0.510
103.40	0.00	2.172	3.694	1.795	8.169	5.364	0.000	N/A	0.510
104.15	0.00	2.195	3.693	1.766	8.168	5.393	0.000	N/A	0.511
104.90	0.00	2.223	3.690	1.728	8.168	5.425	0.000	N/A	0.511
105.60	0.00	2.251	3.687	1.688	8.168	5.455	0.000	N/A	0.511

Table B-5 (continued)
(d) $M_* = 0.58\,M_\odot$

t_6	Y_c	$\log L$	$\log T_{eff}$	$\log g_s$	$\log T_c$	$\log \rho_c$	M_{cc}	M_{sc}	M_{sh}
1.10	0.95	1.506	4.062	3.889	8.072	4.281	0.123	N/A	0.485
4.48	0.90	1.524	4.052	3.834	8.074	4.280	0.133	N/A	0.485
8.28	0.85	1.525	4.052	3.831	8.077	4.277	0.144	N/A	0.485
12.72	0.80	1.525	4.053	3.837	8.079	4.273	0.158	N/A	0.485
17.80	0.75	1.523	4.056	3.848	8.082	4.265	0.174	N/A	0.485
23.54	0.70	1.520	4.059	3.863	8.086	4.258	0.172	0.189	0.487
29.01	0.65	1.517	4.061	3.876	8.089	4.251	0.172	0.198	0.488
35.20	0.60	1.514	4.063	3.887	8.093	4.244	0.169	0.210	0.488
41.07	0.55	1.513	4.064	3.892	8.097	4.239	0.170	0.220	0.489
46.85	0.50	1.513	4.063	3.888	8.101	4.235	0.169	0.227	0.490
52.51	0.45	1.516	4.061	3.877	8.105	4.233	0.169	0.235	0.490
58.35	0.40	1.522	4.058	3.857	8.110	4.231	0.168	0.242	0.490
63.89	0.35	1.528	4.053	3.833	8.116	4.232	0.167	0.247	0.491
69.47	0.30	1.538	4.047	3.799	8.122	4.236	0.167	0.253	0.491
74.69	0.25	1.549	4.041	3.761	8.129	4.242	0.165	0.259	0.491
79.81	0.20	1.563	4.033	3.718	8.137	4.252	0.166	0.262	0.491
85.24	0.15	1.581	4.024	3.663	8.148	4.271	0.164	0.272	0.492
90.33	0.10	1.602	4.015	3.606	8.161	4.297	0.164	0.276	0.492
96.62	5.00E-02	1.640	4.002	3.515	8.184	4.356	0.165	0.276	0.492
97.92	4.00E-02	1.654	3.997	3.481	8.190	4.375	0.165	0.276	0.492
99.20	3.00E-02	1.668	3.991	3.444	8.197	4.394	0.165	0.276	0.493
100.13	2.00E-02	1.692	3.978	3.367	8.207	4.428	0.165	N/A	0.493
101.32	1.00E-02	1.739	3.946	3.194	8.222	4.483	0.165	N/A	0.493
102.51	1.00E-03	1.870	3.792	2.446	8.256	4.631	0.089	N/A	0.493
102.67	1.00E-04	1.929	3.739	2.177	8.263	4.720	0.014	N/A	0.493
102.70	0.00	1.942	3.732	2.135	8.263	4.741	0.000	N/A	0.493
Post Helium Exhaustion Phase									
103.45	0.00	2.139	3.705	1.829	8.243	5.086	0.000	N/A	0.495
104.20	0.00	2.101	3.710	1.888	8.212	5.162	0.000	N/A	0.496
104.95	0.00	2.099	3.711	1.893	8.197	5.215	0.000	N/A	0.497
105.70	0.00	2.097	3.712	1.898	8.188	5.254	0.000	N/A	0.497
106.45	0.00	2.091	3.713	1.910	8.180	5.284	0.000	N/A	0.498
107.20	0.00	2.095	3.712	1.901	8.172	5.309	0.000	N/A	0.498
107.95	0.00	2.108	3.710	1.880	8.166	5.334	0.000	N/A	0.499
108.70	0.00	2.124	3.708	1.857	8.162	5.359	0.000	N/A	0.499
109.45	0.00	2.142	3.706	1.829	8.159	5.383	0.000	N/A	0.499
110.20	0.00	2.164	3.704	1.798	8.160	5.409	0.000	N/A	0.499
110.95	0.00	2.188	3.701	1.764	8.159	5.438	0.000	N/A	0.500
111.70	0.00	2.214	3.698	1.727	8.158	5.466	0.000	N/A	0.500
112.45	0.00	2.245	3.695	1.682	8.158	5.498	0.000	N/A	0.500
112.60	0.00	2.251	3.694	1.672	8.158	5.505	0.000	N/A	0.500

Table B-5 (continued)

(e) $M_* = 0.54\,M_\odot$

t_6	Y_c	$\log L$	$\log T_{eff}$	$\log g_s$	$\log T_c$	$\log \rho_c$	M_{cc}	M_{sc}	M_{sh}
1.10	0.95	1.310	4.224	4.702	8.072	4.283	0.123	N/A	0.485
4.57	0.90	1.325	4.219	4.669	8.074	4.283	0.133	N/A	0.485
8.51	0.85	1.334	4.216	4.647	8.076	4.282	0.144	N/A	0.485
13.11	0.80	1.342	4.212	4.622	8.079	4.278	0.157	N/A	0.485
18.42	0.75	1.350	4.208	4.598	8.082	4.272	0.173	N/A	0.485
24.24	0.70	1.358	4.204	4.573	8.085	4.266	0.170	0.187	0.485
30.15	0.65	1.367	4.200	4.548	8.088	4.260	0.168	0.197	0.485
36.33	0.60	1.377	4.195	4.519	8.092	4.255	0.168	0.208	0.485
42.46	0.55	1.388	4.190	4.489	8.095	4.251	0.166	0.217	0.485
48.60	0.50	1.400	4.185	4.456	8.099	4.248	0.166	0.225	0.485
54.73	0.45	1.412	4.180	4.424	8.103	4.246	0.166	0.231	0.485
60.67	0.40	1.426	4.174	4.388	8.108	4.246	0.163	0.237	0.485
66.73	0.35	1.440	4.169	4.352	8.113	4.247	0.163	0.243	0.485
72.45	0.30	1.455	4.163	4.315	8.120	4.251	0.161	0.249	0.485
78.12	0.25	1.470	4.158	4.277	8.127	4.257	0.161	0.253	0.485
83.41	0.20	1.486	4.153	4.242	8.135	4.268	0.161	0.257	0.485
89.22	0.15	1.505	4.148	4.206	8.146	4.286	0.159	0.265	0.485
94.46	0.10	1.523	4.147	4.181	8.159	4.315	0.158	0.269	0.485
101.23	5.00E-02	1.545	4.150	4.172	8.181	4.367	0.163	0.274	0.485
102.81	4.00E-02	1.551	4.152	4.174	8.187	4.385	0.162	0.274	0.485
103.86	3.00E-02	1.558	4.154	4.177	8.195	4.407	0.162	0.258	0.485
104.91	2.00E-02	1.567	4.159	4.184	8.205	4.441	0.162	N/A	0.485
106.10	1.00E-02	1.589	4.163	4.181	8.220	4.495	0.162	N/A	0.485
107.42	1.00E-03	1.734	4.127	3.891	8.261	4.657	0.146	N/A	0.485
107.65	1.00E-04	1.879	4.029	3.356	8.281	4.796	0.076	N/A	0.485
107.70	0.00	1.918	3.994	3.177	8.283	4.837	0.052	N/A	0.485
Post Helium Exhaustion Phase									
108.45	0.00	2.080	3.781	2.162	8.253	5.069	0.000	N/A	0.486
109.20	0.00	2.037	3.864	2.536	8.215	5.152	0.000	N/A	0.487
109.95	0.00	2.036	3.875	2.581	8.196	5.203	0.000	N/A	0.488
110.70	0.00	2.041	3.874	2.571	8.186	5.241	0.000	N/A	0.488
111.45	0.00	2.040	3.878	2.590	8.180	5.266	0.000	N/A	0.489
112.20	0.00	2.042	3.876	2.580	8.176	5.294	0.000	N/A	0.489
112.95	0.00	2.044	3.871	2.559	8.170	5.309	0.000	N/A	0.489
113.70	0.00	2.062	3.847	2.443	8.165	5.336	0.000	N/A	0.490
114.45	0.00	2.077	3.825	2.339	8.163	5.356	0.000	N/A	0.490
115.20	0.00	2.094	3.800	2.225	8.163	5.374	0.000	N/A	0.490
115.95	0.00	2.113	3.770	2.085	8.163	5.396	0.000	N/A	0.490
116.70	0.00	2.134	3.748	1.974	8.164	5.420	0.000	N/A	0.491
117.45	0.00	2.156	3.747	1.948	8.163	5.445	0.000	N/A	0.491
118.20	0.00	2.181	3.726	1.841	8.162	5.472	0.000	N/A	0.491
118.95	0.00	2.209	3.718	1.780	8.158	5.503	0.000	N/A	0.491
119.70	0.00	2.240	3.712	1.725	8.153	5.536	0.000	N/A	0.492
119.90	0.00	2.249	3.711	1.709	8.151	5.545	0.000	N/A	0.492

Table B-6: Evolutionary Tracks for $Y_{HB} = 0.250$ $[Fe/H] = -1.26$ $[O/Fe] = 0.55$

(a) $M_* = 0.90\,M_\odot$

t_6	Y_c	$\log L$	$\log T_{eff}$	$\log g_s$	$\log T_c$	$\log \rho_c$	M_{cc}	M_{sc}	M_{sh}
1.10	0.95	1.768	3.710	2.409	8.071	4.291	0.120	N/A	0.484
4.61	0.90	1.781	3.708	2.389	8.073	4.289	0.131	N/A	0.484
8.48	0.85	1.789	3.707	2.380	8.076	4.284	0.142	N/A	0.486
12.86	0.80	1.790	3.708	2.381	8.079	4.276	0.156	N/A	0.489
17.98	0.75	1.789	3.709	2.386	8.083	4.265	0.172	N/A	0.492
23.55	0.70	1.787	3.710	2.392	8.087	4.253	0.172	0.189	0.494
28.81	0.65	1.789	3.711	2.394	8.090	4.242	0.172	0.200	0.497
34.66	0.60	1.790	3.712	2.396	8.094	4.232	0.172	0.211	0.500
40.33	0.55	1.791	3.712	2.397	8.099	4.223	0.174	0.223	0.503
45.75	0.50	1.793	3.713	2.399	8.103	4.216	0.174	0.232	0.505
51.06	0.45	1.795	3.714	2.399	8.108	4.210	0.174	0.241	0.507
56.13	0.40	1.796	3.714	2.399	8.114	4.206	0.174	0.248	0.510
61.26	0.35	1.799	3.714	2.398	8.119	4.204	0.174	0.256	0.512
66.38	0.30	1.802	3.714	2.394	8.126	4.204	0.176	0.262	0.513
71.25	0.25	1.807	3.714	2.389	8.133	4.208	0.176	0.268	0.515
75.87	0.20	1.813	3.714	2.381	8.142	4.217	0.176	0.274	0.516
80.07	0.15	1.824	3.712	2.364	8.153	4.235	0.173	0.279	0.519
83.87	0.10	1.839	3.710	2.341	8.167	4.263	0.174	0.282	0.519
88.25	5.00E-02	1.869	3.706	2.295	8.189	4.320	0.174	0.286	0.520
89.49	4.00E-02	1.880	3.705	2.279	8.195	4.337	0.178	0.290	0.521
90.38	3.00E-02	1.892	3.704	2.262	8.203	4.357	0.177	0.293	0.521
91.11	2.00E-02	1.909	3.702	2.236	8.213	4.391	0.158	N/A	0.522
91.99	1.00E-02	1.939	3.698	2.190	8.228	4.446	0.159	N/A	0.522
92.94	1.00E-03	2.028	3.689	2.065	8.266	4.599	0.109	N/A	0.522
93.08	1.00E-04	2.095	3.690	2.004	8.277	4.722	0.017	N/A	0.522
93.10	0.00	2.108	3.691	1.993	8.278	4.744	0.000	N/A	0.522
Post Helium Exhaustion Phase									
93.30	0.00	2.244	3.680	1.814	8.284	4.928	0.000	N/A	0.523

Table B-6 (continued)

(b) $M_* = 0.66\,M_\odot$

t_6	Y_c	$\log L$	$\log T_{eff}$	$\log g_s$	$\log T_c$	$\log \rho_c$	M_{cc}	M_{sc}	M_{sh}
1.10	0.95	1.678	3.734	2.462	8.071	4.289	0.121	N/A	0.484
4.59	0.90	1.692	3.731	2.437	8.073	4.287	0.131	N/A	0.484
8.46	0.85	1.698	3.731	2.428	8.076	4.283	0.142	N/A	0.484
12.80	0.80	1.699	3.732	2.431	8.079	4.276	0.156	N/A	0.487
17.87	0.75	1.695	3.735	2.447	8.082	4.267	0.171	N/A	0.489
23.07	0.70	1.689	3.739	2.471	8.086	4.257	0.170	0.185	0.491
28.90	0.65	1.684	3.744	2.495	8.090	4.247	0.172	0.198	0.493
34.56	0.60	1.679	3.748	2.516	8.095	4.238	0.172	0.209	0.495
40.60	0.55	1.675	3.752	2.538	8.098	4.230	0.172	0.222	0.496
46.13	0.50	1.672	3.756	2.558	8.102	4.225	0.172	0.228	0.498
51.72	0.45	1.670	3.760	2.572	8.107	4.220	0.172	0.238	0.499
57.27	0.40	1.669	3.764	2.590	8.112	4.217	0.172	0.245	0.500
62.43	0.35	1.670	3.766	2.597	8.118	4.217	0.172	0.252	0.502
67.65	0.30	1.673	3.766	2.596	8.124	4.219	0.170	0.257	0.502
72.75	0.25	1.679	3.765	2.584	8.131	4.225	0.170	0.264	0.503
77.44	0.20	1.687	3.760	2.558	8.140	4.234	0.170	0.268	0.504
82.46	0.15	1.702	3.754	2.518	8.151	4.252	0.170	0.275	0.505
87.40	0.10	1.723	3.747	2.471	8.165	4.282	0.167	0.279	0.505
92.37	5.00E-02	1.760	3.737	2.392	8.186	4.336	0.171	0.281	0.506
93.51	4.00E-02	1.771	3.734	2.370	8.192	4.353	0.171	0.281	0.506
94.81	3.00E-02	1.786	3.730	2.340	8.200	4.376	0.161	0.194	0.506
95.58	2.00E-02	1.808	3.726	2.298	8.210	4.410	0.157	N/A	0.507
96.60	1.00E-02	1.847	3.718	2.227	8.225	4.465	0.157	N/A	0.507
97.62	1.00E-03	1.959	3.702	2.053	8.263	4.620	0.096	N/A	0.508
97.77	1.00E-04	2.027	3.700	1.978	8.272	4.735	0.020	N/A	0.508
97.80	0.00	2.043	3.700	1.959	8.273	4.762	0.000	N/A	0.508
Post Helium Exhaustion Phase									
98.55	0.00	2.167	3.687	1.786	8.237	5.073	0.000	N/A	0.509
99.30	0.00	2.146	3.690	1.819	8.212	5.155	0.000	N/A	0.511
100.05	0.00	2.146	3.691	1.820	8.201	5.209	0.000	N/A	0.512
100.80	0.00	2.142	3.691	1.826	8.194	5.248	0.000	N/A	0.512
101.55	0.00	2.141	3.691	1.827	8.186	5.282	0.000	N/A	0.513
102.30	0.00	2.152	3.690	1.811	8.179	5.310	0.000	N/A	0.513
103.05	0.00	2.169	3.687	1.784	8.175	5.339	0.000	N/A	0.513
103.80	0.00	2.190	3.686	1.757	8.173	5.369	0.000	N/A	0.513
104.55	0.00	2.215	3.683	1.722	8.172	5.400	0.000	N/A	0.513
105.30	0.00	2.246	3.681	1.681	8.172	5.436	0.000	N/A	0.513
105.40	0.00	2.250	3.680	1.675	8.172	5.441	0.000	N/A	0.514

Table B-6 (continued)
(c) $M_* = 0.62\,M_\odot$

t_6	Y_c	$\log L$	$\log T_{eff}$	$\log g_s$	$\log T_c$	$\log \rho_c$	M_{cc}	M_{sc}	M_{sh}
1.10	0.95	1.636	3.782	2.671	8.071	4.288	0.121	N/A	0.484
4.55	0.90	1.651	3.770	2.605	8.073	4.287	0.131	N/A	0.484
8.37	0.85	1.657	3.770	2.599	8.076	4.283	0.142	N/A	0.484
12.86	0.80	1.658	3.774	2.615	8.079	4.277	0.155	N/A	0.486
18.09	0.75	1.653	3.789	2.680	8.082	4.268	0.172	N/A	0.488
23.29	0.70	1.644	3.811	2.779	8.085	4.259	0.173	0.183	0.490
29.20	0.65	1.635	3.835	2.884	8.089	4.248	0.170	0.198	0.491
35.06	0.60	1.627	3.854	2.967	8.093	4.240	0.172	0.211	0.493
40.87	0.55	1.621	3.868	3.027	8.097	4.234	0.172	0.219	0.494
46.75	0.50	1.617	3.879	3.076	8.102	4.228	0.172	0.228	0.495
52.34	0.45	1.615	3.885	3.103	8.106	4.225	0.172	0.236	0.496
58.01	0.40	1.614	3.890	3.122	8.112	4.222	0.172	0.243	0.497
63.39	0.35	1.616	3.890	3.122	8.117	4.222	0.169	0.250	0.498
68.77	0.30	1.620	3.888	3.109	8.123	4.225	0.169	0.255	0.498
73.90	0.25	1.626	3.883	3.081	8.130	4.230	0.169	0.260	0.499
79.02	0.20	1.637	3.874	3.035	8.139	4.241	0.168	0.266	0.499
83.83	0.15	1.652	3.860	2.964	8.150	4.259	0.166	0.271	0.500
89.11	0.10	1.675	3.840	2.861	8.163	4.287	0.167	0.277	0.500
94.41	5.00E-02	1.718	3.798	2.651	8.185	4.343	0.168	0.276	0.501
95.77	4.00E-02	1.731	3.785	2.586	8.191	4.359	0.170	0.276	0.501
97.05	3.00E-02	1.750	3.768	2.500	8.198	4.383	0.156	N/A	0.501
97.90	2.00E-02	1.774	3.754	2.418	8.208	4.417	0.156	N/A	0.502
98.91	1.00E-02	1.817	3.738	2.313	8.224	4.473	0.156	N/A	0.502
100.00	1.00E-03	1.937	3.709	2.077	8.261	4.628	0.098	N/A	0.502
100.16	1.00E-04	2.014	3.705	1.982	8.271	4.748	0.020	N/A	0.502
100.20	0.00	2.036	3.705	1.959	8.270	4.784	0.000	N/A	0.502
Post Helium Exhaustion Phase									
100.95	0.00	2.148	3.693	1.800	8.234	5.072	0.000	N/A	0.504
101.70	0.00	2.129	3.696	1.831	8.209	5.152	0.000	N/A	0.505
102.45	0.00	2.130	3.696	1.830	8.199	5.202	0.000	N/A	0.506
103.20	0.00	2.1	3.696	1.835	8.192	5.244	0.000	N/A	0.506
103.95	0.00	2.124	3.697	1.840	8.185	5.274	0.000	N/A	0.507
104.70	0.00	2.131	3.696	1.829	8.178	5.304	0.000	N/A	0.507
105.45	0.00	2.144	3.694	1.810	8.173	5.331	0.000	N/A	0.508
106.20	0.00	2.161	3.692	1.784	8.170	5.358	0.000	N/A	0.508
106.95	0.00	2.183	3.690	1.752	8.168	5.387	0.000	N/A	0.508
107.70	0.00	2.211	3.687	1.713	8.167	5.420	0.000	N/A	0.508
108.45	0.00	2.239	3.685	1.677	8.167	5.451	0.000	N/A	0.508
108.70	0.00	2.250	3.683	1.658	8.167	5.464	0.000	N/A	0.508

Table B-6 (continued)

(d) $M_* = 0.58\,M_\odot$

t_6	Y_c	$\log L$	$\log T_{eff}$	$\log g_s$	$\log T_c$	$\log \rho_c$	M_{cc}	M_{sc}	M_{sh}
1.10	0.95	1.535	4.009	3.647	8.071	4.285	0.121	N/A	0.484
4.56	0.90	1.555	3.994	3.570	8.074	4.285	0.132	N/A	0.484
8.38	0.85	1.559	3.994	3.566	8.076	4.282	0.143	N/A	0.484
12.81	0.80	1.558	3.997	3.579	8.079	4.277	0.156	N/A	0.484
17.93	0.75	1.555	4.003	3.605	8.082	4.270	0.172	N/A	0.485
23.55	0.70	1.548	4.011	3.642	8.085	4.261	0.171	0.186	0.487
29.48	0.65	1.540	4.019	3.685	8.089	4.253	0.171	0.198	0.488
35.55	0.60	1.533	4.026	3.719	8.093	4.246	0.171	0.209	0.488
41.51	0.55	1.529	4.030	3.738	8.097	4.241	0.169	0.218	0.489
47.42	0.50	1.527	4.031	3.746	8.101	4.236	0.168	0.228	0.490
53.08	0.45	1.528	4.031	3.745	8.105	4.234	0.168	0.233	0.490
58.87	0.40	1.531	4.028	3.731	8.110	4.232	0.168	0.240	0.491
64.50	0.35	1.537	4.025	3.709	8.116	4.233	0.166	0.248	0.491
70.01	0.30	1.545	4.019	3.680	8.122	4.236	0.166	0.252	0.492
75.11	0.25	1.555	4.013	3.644	8.129	4.242	0.166	0.256	0.492
80.21	0.20	1.569	4.004	3.597	8.137	4.253	0.163	0.261	0.492
85.70	0.15	1.587	3.994	3.537	8.148	4.272	0.165	0.269	0.492
90.51	0.10	1.609	3.984	3.477	8.162	4.300	0.164	0.270	0.493
96.66	5.00E-02	1.648	3.968	3.371	8.184	4.356	0.165	0.276	0.493
98.22	4.00E-02	1.661	3.962	3.336	8.190	4.373	0.165	0.278	0.493
99.04	3.00E-02	1.676	3.954	3.287	8.197	4.395	0.165	0.191	0.493
100.45	2.00E-02	1.701	3.939	3.202	8.207	4.428	0.191	N/A	0.493
101.70	1.00E-02	1.749	3.901	3.001	8.222	4.482	0.191	N/A	0.494
103.07	1.00E-03	1.884	3.746	2.248	8.258	4.630	0.097	N/A	0.494
103.24	1.00E-04	1.962	3.720	2.065	8.267	4.745	0.021	N/A	0.494
103.30	0.00	2.001	3.713	1.998	8.266	4.802	0.000	N/A	0.494
Post Helium Exhaustion Phase									
104.05	0.00	2.139	3.700	1.810	8.243	5.107	0.000	N/A	0.496
104.80	0.00	2.102	3.706	1.869	8.210	5.186	0.000	N/A	0.497
105.55	0.00	2.100	3.706	1.873	8.196	5.233	0.000	N/A	0.497
106.30	0.00	2.095	3.707	1.882	8.186	5.269	0.000	N/A	0.498
107.05	0.00	2.096	3.707	1.880	8.177	5.296	0.000	N/A	0.499
107.80	0.00	2.106	3.706	1.865	8.169	5.322	0.000	N/A	0.498
108.55	0.00	2.121	3.704	1.843	8.163	5.347	0.000	N/A	0.499
109.30	0.00	2.139	3.701	1.815	8.160	5.373	0.000	N/A	0.499
110.05	0.00	2.158	3.699	1.787	8.158	5.397	0.000	N/A	0.499
110.80	0.00	2.181	3.697	1.754	8.157	5.425	0.000	N/A	0.500
111.55	0.00	2.205	3.694	1.717	8.157	5.453	0.000	N/A	0.500
112.30	0.00	2.236	3.690	1.672	8.156	5.486	0.000	N/A	0.500
112.70	0.00	2.254	3.688	1.646	8.156	5.504	0.000	N/A	0.500

Table B-6 (continued)
(e) $M_* = 0.52\,M_\odot$

t_6	Y_c	$\log L$	$\log T_{eff}$	$\log g_s$	$\log T_c$	$\log \rho_c$	M_{cc}	M_{sc}	M_{sh}
1.00	0.95	1.257	4.270	4.923	8.071	4.292	0.120	N/A	0.484
4.68	0.90	1.267	4.267	4.901	8.073	4.292	0.131	N/A	0.483
8.79	0.85	1.277	4.264	4.878	8.075	4.291	0.142	N/A	0.483
13.56	0.80	1.287	4.261	4.856	8.077	4.288	0.155	N/A	0.483
19.04	0.75	1.299	4.256	4.827	8.081	4.282	0.170	N/A	0.483
25.25	0.70	1.311	4.252	4.799	8.084	4.276	0.165	0.184	0.483
31.83	0.65	1.324	4.248	4.769	8.087	4.270	0.165	0.197	0.483
38.08	0.60	1.336	4.244	4.740	8.090	4.265	0.165	0.205	0.483
44.43	0.55	1.349	4.240	4.709	8.094	4.261	0.163	0.213	0.483
50.86	0.50	1.363	4.235	4.678	8.098	4.258	0.163	0.221	0.483
57.19	0.45	1.378	4.231	4.645	8.102	4.256	0.163	0.229	0.483
63.40	0.40	1.393	4.226	4.613	8.107	4.255	0.161	0.235	0.483
69.58	0.35	1.408	4.222	4.580	8.112	4.257	0.161	0.241	0.484
75.59	0.30	1.424	4.217	4.546	8.119	4.260	0.160	0.245	0.484
81.31	0.25	1.440	4.213	4.514	8.125	4.266	0.159	0.251	0.484
87.02	0.20	1.457	4.210	4.482	8.133	4.276	0.159	0.255	0.484
92.14	0.15	1.475	4.208	4.455	8.144	4.293	0.157	0.263	0.484
97.72	0.10	1.494	4.208	4.438	8.158	4.322	0.159	0.263	0.484
104.20	5.00E-02	1.513	4.214	4.442	8.179	4.374	0.159	0.269	0.484
105.78	4.00E-02	1.517	4.217	4.449	8.185	4.391	0.161	0.271	0.484
108.20	3.00E-02	1.526	4.220	4.453	8.193	4.413	0.145	N/A	0.483
109.30	2.00E-02	1.528	4.227	4.479	8.204	4.447	0.150	N/A	0.484
110.40	1.00E-02	1.534	4.238	4.518	8.219	4.501	0.150	N/A	0.484
111.71	1.00E-03	1.598	4.257	4.532	8.260	4.663	0.128	N/A	0.484
111.90	1.00E-04	1.692	4.244	4.386	8.277	4.769	0.079	N/A	0.483
112.00	0.00	1.747	4.230	4.272	8.280	4.824	0.044	N/A	0.484
Post Helium Exhaustion Phase									
112.75	0.00	1.952	4.140	3.708	8.245	5.054	0.000	N/A	0.484
113.50	0.00	1.939	4.146	3.747	8.210	5.135	0.000	N/A	0.484
114.25	0.00	1.957	4.136	3.688	8.195	5.185	0.000	N/A	0.484
115.00	0.00	1.978	4.125	3.622	8.187	5.225	0.000	N/A	0.484
115.75	0.00	1.994	4.116	3.572	8.181	5.261	0.000	N/A	0.485
116.50	0.00	2.001	4.111	3.543	8.177	5.290	0.000	N/A	0.485
117.25	0.00	2.008	4.103	3.505	8.170	5.316	0.000	N/A	0.486
118.00	0.00	2.020	4.091	3.446	8.164	5.337	0.000	N/A	0.486
118.75	0.00	2.038	4.080	3.381	8.163	5.356	0.000	N/A	0.486
119.50	0.00	2.055	4.064	3.303	8.158	5.377	0.000	N/A	0.486
120.25	0.00	2.073	4.049	3.222	8.155	5.397	0.000	N/A	0.486
121.00	0.00	2.095	4.032	3.133	8.155	5.418	0.000	N/A	0.486
121.75	0.00	2.116	4.012	3.033	8.154	5.438	0.000	N/A	0.486
122.50	0.00	2.142	3.986	2.903	8.156	5.463	0.000	N/A	0.487
123.25	0.00	2.168	3.959	2.767	8.157	5.486	0.000	N/A	0.487
124.00	0.00	2.198	3.921	2.584	8.157	5.515	0.000	N/A	0.487
124.75	0.00	2.229	3.880	2.391	8.157	5.542	0.000	N/A	0.487
125.20	0.00	2.252	3.844	2.226	8.155	5.564	0.000	N/A	0.488

Table B-7: Evolutionary Tracks for $Y_{HB} = 0.252$ [Fe/H] $= -1.03$ [O/Fe] $= 0.50$
(d) $M_* = 0.90\,M_\odot$

t_6	Y_c	$\log L$	$\log T_{eff}$	$\log g_s$	$\log T_c$	$\log \rho_c$	M_{cc}	M_{sc}	M_{sh}
1.10	0.95	1.755	3.701	2.388	8.070	4.295	0.119	N/A	0.482
4.55	0.90	1.771	3.699	2.365	8.073	4.293	0.129	N/A	0.482
8.35	0.85	1.778	3.699	2.357	8.075	4.288	0.140	N/A	0.485
12.78	0.80	1.778	3.700	2.359	8.079	4.280	0.154	N/A	0.487
17.91	0.75	1.776	3.701	2.365	8.082	4.268	0.169	N/A	0.490
22.98	0.70	1.773	3.702	2.372	8.086	4.258	0.170	0.183	0.492
28.58	0.65	1.773	3.702	2.375	8.090	4.247	0.170	0.196	0.495
34.42	0.60	1.774	3.703	2.378	8.094	4.237	0.170	0.209	0.498
40.30	0.55	1.775	3.704	2.380	8.098	4.228	0.172	0.219	0.500
45.97	0.50	1.776	3.705	2.382	8.103	4.221	0.172	0.228	0.503
51.48	0.45	1.777	3.705	2.383	8.108	4.215	0.172	0.237	0.505
56.81	0.40	1.779	3.706	2.383	8.113	4.211	0.172	0.244	0.507
62.04	0.35	1.782	3.706	2.381	8.119	4.209	0.172	0.252	0.509
67.09	0.30	1.785	3.706	2.378	8.126	4.210	0.172	0.258	0.511
71.97	0.25	1.789	3.706	2.374	8.133	4.214	0.172	0.264	0.512
76.73	0.20	1.795	3.705	2.365	8.142	4.223	0.172	0.270	0.514
80.91	0.15	1.805	3.704	2.351	8.153	4.239	0.172	0.276	0.515
84.81	0.10	1.822	3.702	2.326	8.167	4.268	0.173	0.279	0.516
88.98	5.00E-02	1.851	3.698	2.282	8.188	4.321	0.173	0.282	0.518
90.00	4.00E-02	1.862	3.697	2.264	8.194	4.341	0.174	0.282	0.518
91.11	3.00E-02	1.876	3.695	2.243	8.202	4.363	0.164	N/A	0.518
91.85	2.00E-02	1.894	3.693	2.217	8.212	4.397	0.164	N/A	0.519
92.75	1.00E-02	1.926	3.689	2.170	8.227	4.451	0.164	N/A	0.519
93.79	1.00E-03	2.020	3.679	2.033	8.265	4.603	0.105	N/A	0.520
93.96	1.00E-04	2.098	3.682	1.970	8.277	4.739	0.023	N/A	0.520
94.00	0.00	2.121	3.680	1.938	8.278	4.780	0.000	N/A	0.520
Post Helium Exhaustion Phase									
94.10	0.00	2.196	3.674	1.837	8.283	4.881	0.000	N/A	0.520

Table B-7 (continued)
(b) $M_* = 0.66\,M_\odot$

t_6	Y_c	$\log L$	$\log T_{eff}$	$\log g_s$	$\log T_c$	$\log \rho_c$	M_{cc}	M_{sc}	M_{sh}
1.10	0.95	1.674	3.721	2.415	8.071	4.293	0.120	N/A	0.481
4.57	0.90	1.691	3.718	2.387	8.073	4.291	0.129	N/A	0.481
8.40	0.85	1.697	3.718	2.378	8.076	4.287	0.141	N/A	0.483
12.84	0.80	1.698	3.719	2.383	8.079	4.281	0.154	N/A	0.485
17.80	0.75	1.692	3.722	2.399	8.082	4.271	0.169	N/A	0.488
23.23	0.70	1.686	3.725	2.417	8.085	4.260	0.171	0.183	0.490
28.77	0.65	1.681	3.728	2.434	8.089	4.251	0.171	0.195	0.491
34.48	0.60	1.677	3.731	2.451	8.093	4.242	0.171	0.209	0.493
40.32	0.55	1.673	3.734	2.465	8.097	4.234	0.171	0.218	0.495
45.97	0.50	1.671	3.736	2.478	8.102	4.228	0.171	0.228	0.496
51.57	0.45	1.669	3.738	2.489	8.107	4.223	0.171	0.235	0.498
57.16	0.40	1.668	3.741	2.501	8.111	4.220	0.171	0.242	0.499
62.41	0.35	1.669	3.741	2.500	8.117	4.220	0.171	0.249	0.500
67.58	0.30	1.672	3.741	2.498	8.124	4.222	0.169	0.254	0.501
72.66	0.25	1.676	3.741	2.491	8.131	4.227	0.168	0.260	0.502
77.96	0.20	1.685	3.738	2.471	8.140	4.237	0.170	0.266	0.501
82.08	0.15	1.698	3.735	2.444	8.150	4.255	0.168	0.269	0.503
86.32	0.10	1.721	3.729	2.401	8.164	4.285	0.168	0.272	0.504
90.87	5.00E-02	1.757	3.722	2.336	8.185	4.338	0.170	0.277	0.504
92.00	4.00E-02	1.769	3.720	2.316	8.191	4.357	0.169	0.277	0.505
93.25	3.00E-02	1.785	3.717	2.286	8.199	4.379	0.163	0.184	0.505
94.11	2.00E-02	1.807	3.713	2.249	8.209	4.413	0.162	N/A	0.505
95.14	1.00E-02	1.845	3.707	2.187	8.224	4.468	0.161	N/A	0.506
96.21	1.00E-03	1.958	3.693	2.019	8.262	4.620	0.108	N/A	0.507
96.37	1.00E-04	2.032	3.692	1.942	8.272	4.738	0.020	N/A	0.506
96.40	0.00	2.048	3.690	1.918	8.273	4.765	0.000	N/A	0.506
Post Helium Exhaustion Phase									
97.15	0.00	2.169	3.678	1.746	8.238	5.077	0.000	N/A	0.508
97.90	0.00	2.150	3.680	1.775	8.214	5.152	0.000	N/A	0.509
98.65	0.00	2.147	3.681	1.781	8.202	5.204	0.000	N/A	0.510
99.40	0.00	2.138	3.682	1.792	8.193	5.245	0.000	N/A	0.510
100.15	0.00	2.135	3.682	1.796	8.184	5.277	0.000	N/A	0.511
100.90	0.00	2.146	3.681	1.781	8.176	5.309	0.000	N/A	0.511
101.65	0.00	2.161	3.679	1.761	8.172	5.334	0.000	N/A	0.511
102.40	0.00	2.182	3.677	1.729	8.169	5.363	0.000	N/A	0.511
103.15	0.00	2.205	3.674	1.696	8.168	5.393	0.000	N/A	0.512
103.90	0.00	2.232	3.672	1.659	8.169	5.424	0.000	N/A	0.512
104.40	0.00	2.254	3.670	1.630	8.169	5.450	0.000	N/A	0.512

Table B-7 (continued)
(c) $M_* = 0.62\,M_\odot$

t_6	Y_c	$\log L$	$\log T_{eff}$	$\log g_s$	$\log T_c$	$\log \rho_c$	M_{cc}	M_{sc}	M_{sh}
1.10	0.95	1.641	3.745	2.516	8.071	4.292	0.120	N/A	0.482
4.57	0.90	1.659	3.739	2.474	8.073	4.291	0.128	N/A	0.482
8.50	0.85	1.666	3.738	2.465	8.076	4.287	0.141	N/A	0.482
13.12	0.80	1.666	3.741	2.476	8.079	4.281	0.154	N/A	0.485
18.25	0.75	1.659	3.747	2.508	8.082	4.271	0.169	N/A	0.487
23.06	0.70	1.651	3.754	2.542	8.085	4.262	0.171	0.180	0.488
29.21	0.65	1.643	3.763	2.585	8.089	4.252	0.170	0.196	0.490
35.20	0.60	1.635	3.776	2.644	8.093	4.243	0.170	0.207	0.492
41.17	0.55	1.630	3.789	2.703	8.097	4.237	0.170	0.217	0.493
47.08	0.50	1.625	3.803	2.766	8.101	4.231	0.170	0.227	0.494
52.78	0.45	1.621	3.814	2.813	8.106	4.227	0.170	0.234	0.496
58.38	0.40	1.620	3.821	2.840	8.111	4.224	0.170	0.242	0.496
63.71	0.35	1.621	3.823	2.849	8.117	4.225	0.170	0.248	0.497
68.97	0.30	1.625	3.822	2.840	8.123	4.227	0.168	0.254	0.498
74.10	0.25	1.631	3.817	2.814	8.130	4.233	0.168	0.258	0.498
79.66	0.20	1.640	3.809	2.774	8.138	4.241	0.168	0.264	0.499
84.22	0.15	1.653	3.798	2.716	8.149	4.259	0.167	0.273	0.499
88.78	0.10	1.678	3.776	2.602	8.163	4.289	0.167	0.273	0.500
93.82	5.00E-02	1.722	3.751	2.459	8.185	4.345	0.169	0.275	0.501
95.07	4.00E-02	1.734	3.748	2.433	8.191	4.360	0.169	0.275	0.501
96.31	3.00E-02	1.751	3.742	2.393	8.198	4.384	0.158	N/A	0.501
97.22	2.00E-02	1.775	3.734	2.340	8.208	4.418	0.158	N/A	0.501
98.18	1.00E-02	1.817	3.723	2.254	8.224	4.473	0.158	N/A	0.502
99.29	1.00E-03	1.938	3.700	2.037	8.261	4.626	0.103	N/A	0.502
99.44	1.00E-04	2.010	3.701	1.970	8.271	4.735	0.026	N/A	0.502
99.50	0.00	2.046	3.696	1.913	8.271	4.792	0.000	N/A	0.502
Post Helium Exhaustion Phase									
100.25	0.00	2.160	3.683	1.748	8.236	5.084	0.000	N/A	0.504
101.00	0.00	2.134	3.686	1.787	8.210	5.160	0.000	N/A	0.505
101.75	0.00	2.130	3.688	1.798	8.199	5.210	0.000	N/A	0.506
102.50	0.00	2.122	3.689	1.810	8.190	5.250	0.000	N/A	0.507
103.25	0.00	2.120	3.689	1.812	8.182	5.281	0.000	N/A	0.507
104.00	0.00	2.130	3.688	1.797	8.175	5.308	0.000	N/A	0.507
104.75	0.00	2.146	3.685	1.771	8.170	5.336	0.000	N/A	0.507
105.50	0.00	2.163	3.683	1.746	8.167	5.362	0.000	N/A	0.507
106.25	0.00	2.186	3.681	1.714	8.166	5.391	0.000	N/A	0.507
107.00	0.00	2.211	3.678	1.677	8.165	5.421	0.000	N/A	0.507
107.75	0.00	2.242	3.674	1.630	8.166	5.455	0.000	N/A	0.508
108.00	0.00	2.252	3.674	1.620	8.166	5.465	0.000	N/A	0.508

Table B-7 (continued)
(d) $M_* = 0.56\,M_\odot$

t_6	Y_c	$\log L$	$\log T_{eff}$	$\log g_s$	$\log T_c$	$\log \rho_c$	M_{cc}	M_{sc}	M_{sh}
1.10	0.95	1.466	4.070	3.946	8.071	4.288	0.120	N/A	0.481
4.50	0.90	1.497	4.052	3.844	8.073	4.288	0.130	N/A	0.482
8.38	0.85	1.501	4.051	3.834	8.075	4.288	0.142	N/A	0.482
12.96	0.80	1.501	4.052	3.839	8.078	4.281	0.154	N/A	0.482
18.31	0.75	1.498	4.055	3.856	8.082	4.274	0.169	N/A	0.482
24.06	0.70	1.493	4.060	3.878	8.085	4.267	0.170	0.184	0.484
30.11	0.65	1.487	4.064	3.900	8.088	4.259	0.167	0.195	0.484
35.94	0.60	1.482	4.067	3.918	8.092	4.253	0.168	0.205	0.485
42.16	0.55	1.479	4.068	3.924	8.096	4.248	0.168	0.215	0.486
48.09	0.50	1.480	4.067	3.919	8.100	4.244	0.168	0.223	0.486
54.12	0.45	1.483	4.064	3.906	8.104	4.241	0.165	0.231	0.486
60.02	0.40	1.489	4.060	3.884	8.109	4.240	0.165	0.237	0.487
65.75	0.35	1.497	4.055	3.856	8.115	4.241	0.165	0.243	0.487
71.20	0.30	1.507	4.049	3.821	8.121	4.244	0.163	0.249	0.487
76.61	0.25	1.519	4.042	3.782	8.128	4.251	0.163	0.253	0.488
82.13	0.20	1.533	4.034	3.736	8.136	4.261	0.163	0.259	0.487
88.19	0.15	1.552	4.026	3.683	8.146	4.277	0.161	0.273	0.488
93.90	0.10	1.574	4.017	3.628	8.160	4.308	0.159	0.276	0.488
100.32	5.00E-02	1.612	4.007	3.547	8.183	4.364	0.163	0.275	0.488
101.83	4.00E-02	1.626	4.002	3.515	8.190	4.383	0.163	0.275	0.488
102.93	3.00E-02	1.640	3.997	3.481	8.196	4.402	0.163	0.269	0.488
103.88	2.00E-02	1.666	3.985	3.408	8.206	4.436	0.163	N/A	0.489
105.07	1.00E-02	1.716	3.955	3.239	8.221	4.491	0.163	N/A	0.489
106.33	1.00E-03	1.856	3.803	2.489	8.255	4.636	0.087	N/A	0.489
106.48	1.00E-04	1.911	3.743	2.194	8.262	4.714	0.016	N/A	0.489
106.50	0.00	1.920	3.736	2.156	8.263	4.727	0.003	N/A	0.489
Post Helium Exhaustion Phase									
107.25	0.00	2.137	3.699	1.791	8.242	5.077	0.000	N/A	0.490
108.00	0.00	2.092	3.706	1.863	8.209	5.157	0.000	N/A	0.492
108.75	0.00	2.089	3.707	1.873	8.194	5.207	0.000	N/A	0.493
109.50	0.00	2.088	3.708	1.878	8.185	5.246	0.000	N/A	0.493
110.25	0.00	2.084	3.709	1.885	8.179	5.270	0.000	N/A	0.494
111.00	0.00	2.088	3.710	1.884	8.179	5.286	0.000	N/A	0.494
111.75	0.00	2.094	3.708	1.870	8.175	5.316	0.000	N/A	0.495
112.50	0.00	2.105	3.706	1.851	8.168	5.342	0.000	N/A	0.495
113.25	0.00	2.119	3.704	1.828	8.163	5.365	0.000	N/A	0.495
114.00	0.00	2.137	3.701	1.801	8.160	5.389	0.000	N/A	0.495
114.75	0.00	2.157	3.700	1.774	8.158	5.415	0.000	N/A	0.496
115.50	0.00	2.181	3.696	1.735	8.158	5.442	0.000	N/A	0.496
116.25	0.00	2.209	3.692	1.691	8.156	5.473	0.000	N/A	0.496
117.00	0.00	2.241	3.687	1.641	8.155	5.507	0.000	N/A	0.496
117.30	0.00	2.251	3.686	1.625	8.154	5.517	0.000	N/A	0.496

Table B-7 (continued)
(e) $M_* = 0.52\,M_\odot$

t_6	Y_c	$\log L$	$\log T_{eff}$	$\log g_s$	$\log T_c$	$\log \rho_c$	M_{cc}	M_{sc}	M_{sh}
1.10	0.95	1.257	4.251	4.846	8.070	4.294	0.120	N/A	0.481
4.67	0.90	1.267	4.248	4.824	8.073	4.294	0.129	N/A	0.481
8.75	0.85	1.277	4.244	4.800	8.075	4.292	0.141	N/A	0.481
13.57	0.80	1.286	4.241	4.777	8.077	4.290	0.154	N/A	0.481
18.95	0.75	1.298	4.236	4.746	8.080	4.283	0.168	N/A	0.481
25.11	0.70	1.310	4.231	4.717	8.084	4.277	0.166	0.182	0.481
31.18	0.65	1.322	4.227	4.687	8.087	4.272	0.166	0.192	0.481
37.63	0.60	1.334	4.222	4.655	8.090	4.267	0.163	0.203	0.481
44.10	0.55	1.347	4.217	4.623	8.094	4.263	0.163	0.212	0.482
50.43	0.50	1.361	4.212	4.590	8.098	4.260	0.163	0.219	0.481
56.97	0.45	1.375	4.207	4.555	8.102	4.258	0.161	0.227	0.482
63.01	0.40	1.390	4.202	4.520	8.107	4.257	0.161	0.233	0.481
69.38	0.35	1.405	4.197	4.485	8.112	4.258	0.161	0.239	0.481
75.35	0.30	1.421	4.192	4.449	8.118	4.262	0.159	0.244	0.481
81.10	0.25	1.437	4.188	4.414	8.125	4.268	0.159	0.249	0.481
86.45	0.20	1.454	4.184	4.381	8.133	4.278	0.156	0.252	0.481
92.38	0.15	1.472	4.181	4.350	8.144	4.294	0.156	0.258	0.482
98.18	0.10	1.491	4.180	4.330	8.158	4.324	0.159	0.258	0.481
105.32	5.00E-02	1.511	4.186	4.335	8.180	4.378	0.158	0.268	0.481
107.03	4.00E-02	1.515	4.189	4.343	8.186	4.394	0.158	0.271	0.481
108.07	3.00E-02	1.520	4.193	4.351	8.193	4.416	0.160	0.204	0.482
109.17	2.00E-02	1.525	4.197	4.364	8.201	4.441	0.160	N/A	0.482
110.51	1.00E-02	1.536	4.210	4.404	8.219	4.503	0.160	N/A	0.482
111.87	1.00E-03	1.636	4.216	4.329	8.260	4.666	0.151	N/A	0.481
112.10	1.00E-04	1.786	4.168	3.988	8.281	4.795	0.090	N/A	0.481
112.20	0.00	1.873	4.122	3.717	8.283	4.872	0.039	N/A	0.481
Post Helium Exhaustion Phase									
112.95	0.00	2.050	3.977	2.958	8.256	5.072	0.000	N/A	0.482
113.70	0.00	1.994	4.042	3.273	8.214	5.153	0.000	N/A	0.483
114.45	0.00	2.005	4.039	3.251	8.199	5.202	0.000	N/A	0.483
115.20	0.00	2.013	4.037	3.236	8.192	5.233	0.000	N/A	0.484
115.95	0.00	2.021	4.037	3.225	8.190	5.261	0.000	N/A	0.484
116.70	0.00	2.010	4.046	3.273	8.183	5.281	0.000	N/A	0.484
117.45	0.00	2.014	4.042	3.255	8.177	5.304	0.000	N/A	0.485
118.20	0.00	2.027	4.032	3.203	8.173	5.325	0.000	N/A	0.485
118.95	0.00	2.040	4.023	3.151	8.171	5.340	0.000	N/A	0.485
119.70	0.00	2.059	4.008	3.074	8.170	5.361	0.000	N/A	0.485
120.45	0.00	2.076	3.992	2.992	8.167	5.383	0.000	N/A	0.486
121.20	0.00	2.097	3.972	2.893	8.167	5.404	0.000	N/A	0.486
121.95	0.00	2.117	3.952	2.793	8.167	5.424	0.000	N/A	0.486
122.70	0.00	2.140	3.928	2.671	8.167	5.446	0.000	N/A	0.486
123.45	0.00	2.165	3.896	2.519	8.166	5.471	0.000	N/A	0.486
124.20	0.00	2.194	3.857	2.336	8.166	5.499	0.000	N/A	0.487
124.95	0.00	2.221	3.818	2.151	8.166	5.524	0.000	N/A	0.487
125.30	0.00	2.238	3.791	2.025	8.167	5.540	0.000	N/A	0.487

Table B-8: Evolutionary Tracks for $Y_{HB} = 0.257$ [Fe/H] $= -0.78$ [O/Fe] $= 0.39$
(a) $M_* = 0.90\,M_\odot$

t_6	Y_c	$\log L$	$\log T_{eff}$	$\log g_s$	$\log T_c$	$\log \rho_c$	M_{cc}	M_{sc}	M_{sh}
1.10	0.95	1.737	3.690	2.361	8.070	4.299	0.118	N/A	0.479
4.52	0.90	1.755	3.687	2.334	8.072	4.297	0.127	N/A	0.479
8.47	0.85	1.761	3.687	2.325	8.075	4.292	0.136	N/A	0.482
12.93	0.80	1.760	3.688	2.330	8.078	4.284	0.152	N/A	0.485
17.86	0.75	1.758	3.689	2.337	8.082	4.273	0.166	N/A	0.488
23.42	0.70	1.756	3.690	2.344	8.086	4.261	0.169	0.183	0.490
28.89	0.65	1.755	3.691	2.348	8.089	4.251	0.169	0.194	0.493
34.48	0.60	1.755	3.692	2.351	8.093	4.241	0.169	0.206	0.495
40.24	0.55	1.755	3.693	2.355	8.098	4.232	0.169	0.216	0.498
46.03	0.50	1.755	3.693	2.357	8.102	4.225	0.171	0.225	0.500
51.58	0.45	1.756	3.694	2.359	8.107	4.219	0.171	0.235	0.502
56.94	0.40	1.757	3.694	2.359	8.113	4.216	0.171	0.242	0.505
62.20	0.35	1.759	3.695	2.359	8.118	4.214	0.171	0.248	0.506
67.30	0.30	1.762	3.695	2.356	8.125	4.215	0.171	0.255	0.508
72.27	0.25	1.766	3.695	2.351	8.132	4.219	0.171	0.261	0.509
76.83	0.20	1.773	3.694	2.342	8.141	4.228	0.171	0.266	0.511
81.55	0.15	1.784	3.693	2.326	8.152	4.245	0.171	0.273	0.512
85.58	0.10	1.799	3.691	2.303	8.165	4.272	0.171	0.277	0.513
90.49	5.00E-02	1.834	3.686	2.248	8.187	4.327	0.172	0.278	0.515
91.64	4.00E-02	1.848	3.684	2.228	8.194	4.345	0.173	0.280	0.515
98.49	3.00E-02	1.858	3.683	2.214	8.204	4.367	0.274	N/A	0.518
99.74	2.00E-02	1.877	3.681	2.186	8.215	4.400	0.274	N/A	0.518
101.14	1.00E-02	1.911	3.677	2.135	8.231	4.454	0.274	N/A	0.518
102.60	1.00E-03	2.012	3.676	2.032	8.270	4.603	0.118	N/A	0.519
102.76	1.00E-04	2.086	3.669	1.929	8.282	4.737	0.024	N/A	0.519
102.80	0.00	2.111	3.667	1.895	8.283	4.780	0.000	N/A	0.519
Post Helium Exhaustion Phase									
102.90	0.00	2.193	3.659	1.783	8.290	4.886	0.000	N/A	0.519

Table B-8 (continued)
(b) $M_* = 0.62\,M_\odot$

t_6	Y_c	$\log L$	$\log T_{eff}$	$\log g_s$	$\log T_c$	$\log \rho_c$	M_{cc}	M_{sc}	M_{sh}
1.10	0.95	1.634	3.725	2.444	8.070	4.296	0.118	N/A	0.479
4.44	0.90	1.655	3.721	2.405	8.072	4.295	0.128	N/A	0.479
8.41	0.85	1.662	3.720	2.396	8.075	4.291	0.139	N/A	0.480
12.91	0.80	1.661	3.722	2.404	8.078	4.285	0.151	N/A	0.483
17.84	0.75	1.653	3.726	2.428	8.081	4.276	0.165	N/A	0.484
23.74	0.70	1.645	3.731	2.457	8.085	4.266	0.167	0.183	0.486
29.30	0.65	1.638	3.736	2.482	8.089	4.257	0.167	0.193	0.488
34.95	0.60	1.631	3.741	2.511	8.093	4.248	0.167	0.204	0.490
41.04	0.55	1.626	3.746	2.537	8.097	4.241	0.167	0.215	0.491
46.89	0.50	1.622	3.750	2.556	8.101	4.235	0.167	0.222	0.492
52.68	0.45	1.619	3.755	2.576	8.106	4.231	0.169	0.230	0.493
58.29	0.40	1.617	3.757	2.589	8.111	4.229	0.167	0.237	0.494
63.90	0.35	1.618	3.759	2.594	8.116	4.229	0.167	0.244	0.495
69.28	0.30	1.621	3.758	2.588	8.123	4.231	0.167	0.250	0.496
74.38	0.25	1.627	3.756	2.576	8.130	4.236	0.167	0.255	0.497
79.19	0.20	1.636	3.753	2.554	8.138	4.247	0.164	0.260	0.497
84.68	0.15	1.652	3.747	2.514	8.150	4.267	0.165	0.269	0.498
89.17	0.10	1.672	3.741	2.467	8.163	4.293	0.163	0.269	0.498
94.13	5.00E-02	1.710	3.732	2.393	8.184	4.345	0.169	0.277	0.500
94.62	4.00E-02	1.720	3.728	2.370	8.191	4.362	0.167	0.276	0.500
95.58	3.00E-02	1.738	3.724	2.333	8.198	4.386	0.166	N/A	0.500
96.54	2.00E-02	1.762	3.718	2.288	8.208	4.420	0.166	N/A	0.500
97.62	1.00E-02	1.804	3.710	2.212	8.224	4.475	0.167	N/A	0.500
98.74	1.00E-03	1.926	3.693	2.021	8.262	4.628	0.101	N/A	0.500
98.88	1.00E-04	1.991	3.690	1.946	8.272	4.726	0.018	N/A	0.500
98.90	0.00	2.002	3.688	1.927	8.274	4.744	0.003	N/A	0.500
Post Helium Exhaustion Phase									
99.65	0.00	2.128	3.672	1.738	8.233	5.071	0.000	N/A	0.502
100.40	0.00	2.115	3.674	1.757	8.212	5.141	0.000	N/A	0.503
101.15	0.00	2.118	3.674	1.755	8.198	5.200	0.000	N/A	0.504
101.90	0.00	2.118	3.674	1.756	8.191	5.243	0.000	N/A	0.505
102.65	0.00	2.112	3.675	1.764	8.184	5.277	0.000	N/A	0.505
103.40	0.00	2.118	3.674	1.754	8.177	5.306	0.000	N/A	0.505
104.15	0.00	2.133	3.672	1.734	8.172	5.333	0.000	N/A	0.505
104.90	0.00	2.153	3.670	1.705	8.168	5.362	0.000	N/A	0.506
105.65	0.00	2.175	3.667	1.670	8.166	5.390	0.000	N/A	0.506
106.40	0.00	2.201	3.663	1.629	8.166	5.420	0.000	N/A	0.506
107.15	0.00	2.232	3.660	1.586	8.166	5.454	0.000	N/A	0.506
107.70	0.00	2.250	3.658	1.559	8.167	5.472	0.000	N/A	0.506

Table B-8 (continued)
(c) $M_* = 0.58\,M_\odot$

t_6	Y_c	$\log L$	$\log T_{eff}$	$\log g_s$	$\log T_c$	$\log \rho_c$	M_{cc}	M_{sc}	M_{sh}
1.10	0.95	1.572	3.845	2.958	8.070	4.294	0.119	N/A	0.479
4.46	0.90	1.598	3.815	2.809	8.072	4.294	0.128	N/A	0.479
8.36	0.85	1.604	3.813	2.796	8.075	4.291	0.139	N/A	0.480
12.86	0.80	1.603	3.823	2.837	8.078	4.286	0.151	N/A	0.481
17.93	0.75	1.593	3.846	2.941	8.081	4.277	0.165	N/A	0.483
23.09	0.70	1.582	3.868	3.038	8.084	4.269	0.168	0.178	0.484
29.26	0.65	1.569	3.891	3.144	8.088	4.259	0.168	0.192	0.486
35.27	0.60	1.559	3.907	3.217	8.092	4.252	0.168	0.205	0.487
41.30	0.55	1.552	3.919	3.272	8.096	4.245	0.168	0.213	0.488
47.41	0.50	1.547	3.927	3.308	8.100	4.241	0.165	0.223	0.489
53.20	0.45	1.545	3.931	3.326	8.105	4.237	0.168	0.228	0.489
58.99	0.40	1.545	3.932	3.330	8.110	4.236	0.165	0.235	0.490
64.79	0.35	1.548	3.930	3.318	8.115	4.236	0.165	0.243	0.490
70.16	0.30	1.554	3.925	3.294	8.122	4.239	0.165	0.247	0.491
75.49	0.25	1.563	3.918	3.258	8.128	4.245	0.165	0.253	0.491
80.70	0.20	1.574	3.909	3.209	8.136	4.255	0.164	0.257	0.491
86.02	0.15	1.592	3.896	3.139	8.148	4.273	0.162	0.263	0.492
90.91	0.10	1.615	3.880	3.053	8.162	4.303	0.163	0.267	0.492
96.65	5.00E-02	1.655	3.852	2.903	8.182	4.354	0.165	0.273	0.492
97.90	4.00E-02	1.669	3.841	2.842	8.189	4.373	0.163	0.273	0.493
100.27	3.00E-02	1.691	3.821	2.743	8.197	4.395	0.147	N/A	0.493
101.19	2.00E-02	1.718	3.796	2.614	8.207	4.429	0.147	N/A	0.493
102.23	1.00E-02	1.765	3.755	2.403	8.222	4.484	0.147	N/A	0.493
103.32	1.00E-03	1.904	3.706	2.066	8.260	4.640	0.093	N/A	0.494
103.47	1.00E-04	1.980	3.700	1.969	8.269	4.747	0.017	N/A	0.494
103.50	0.00	1.996	3.699	1.949	8.269	4.772	0.000	N/A	0.494
Post Helium Exhaustion Phase									
104.25	0.00	2.124	3.682	1.751	8.230	5.063	0.000	N/A	0.495
105.00	0.00	2.108	3.685	1.779	8.207	5.139	0.000	N/A	0.496
105.75	0.00	2.112	3.685	1.776	8.197	5.193	0.000	N/A	0.497
106.50	0.00	2.115	3.685	1.772	8.191	5.236	0.000	N/A	0.498
107.25	0.00	2.109	3.686	1.784	8.187	5.270	0.000	N/A	0.499
108.00	0.00	2.105	3.687	1.791	8.180	5.298	0.000	N/A	0.499
108.75	0.00	2.112	3.686	1.778	8.173	5.325	0.000	N/A	0.499
109.50	0.00	2.128	3.683	1.753	8.168	5.352	0.000	N/A	0.499
110.25	0.00	2.146	3.680	1.723	8.164	5.378	0.000	N/A	0.499
111.00	0.00	2.171	3.677	1.684	8.162	5.408	0.000	N/A	0.500
111.75	0.00	2.195	3.673	1.647	8.161	5.436	0.000	N/A	0.500
112.50	0.00	2.224	3.670	1.602	8.160	5.468	0.000	N/A	0.500
113.10	0.00	2.246	3.666	1.565	8.160	5.491	0.000	N/A	0.500

Table B-8 (continued)
(d) $M_* = 0.56\,M_\odot$

t_6	Y_c	$\log L$	$\log T_{eff}$	$\log g_s$	$\log T_c$	$\log \rho_c$	M_{cc}	M_{sc}	M_{sh}
1.10	0.95	1.495	4.002	3.647	8.071	4.293	0.119	N/A	0.479
4.40	0.90	1.527	3.979	3.520	8.073	4.293	0.128	N/A	0.479
8.33	0.85	1.533	3.976	3.504	8.075	4.291	0.139	N/A	0.480
12.88	0.80	1.533	3.980	3.518	8.078	4.287	0.152	N/A	0.480
18.01	0.75	1.526	3.989	3.561	8.081	4.279	0.166	N/A	0.481
24.01	0.70	1.516	4.000	3.617	8.084	4.270	0.168	0.182	0.482
29.75	0.65	1.506	4.010	3.667	8.088	4.263	0.168	0.191	0.484
35.93	0.60	1.497	4.018	3.707	8.092	4.256	0.166	0.204	0.484
41.98	0.55	1.491	4.022	3.729	8.096	4.250	0.166	0.212	0.485
48.08	0.50	1.490	4.023	3.735	8.100	4.246	0.166	0.220	0.486
54.11	0.45	1.491	4.022	3.730	8.104	4.243	0.166	0.223	0.486
60.10	0.40	1.495	4.019	3.713	8.109	4.242	0.163	0.234	0.486
66.02	0.35	1.501	4.014	3.689	8.114	4.242	0.163	0.239	0.487
71.73	0.30	1.509	4.008	3.655	8.121	4.246	0.163	0.246	0.487
77.08	0.25	1.521	4.000	3.614	8.127	4.252	0.161	0.251	0.487
82.45	0.20	1.534	3.992	3.566	8.136	4.262	0.161	0.255	0.487
88.02	0.15	1.554	3.981	3.504	8.147	4.281	0.160	0.263	0.487
93.38	0.10	1.575	3.971	3.443	8.160	4.307	0.161	0.269	0.488
99.76	5.00E-02	1.616	3.956	3.342	8.183	4.365	0.162	0.269	0.488
101.29	4.00E-02	1.630	3.950	3.303	8.190	4.384	0.162	0.271	0.488
102.46	3.00E-02	1.645	3.943	3.261	8.196	4.403	0.163	0.280	0.488
103.45	2.00E-02	1.671	3.929	3.176	8.206	4.436	0.162	N/A	0.488
104.65	1.00E-02	1.721	3.891	2.976	8.221	4.491	0.162	N/A	0.488
105.89	1.00E-03	1.864	3.739	2.224	8.256	4.641	0.088	N/A	0.489
106.04	1.00E-04	1.936	3.716	2.060	8.264	4.740	0.021	N/A	0.489
106.10	0.00	1.974	3.712	2.007	8.263	4.793	0.000	N/A	0.489
Post Helium Exhaustion Phase									
106.85	0.00	2.135	3.687	1.745	8.239	5.096	0.000	N/A	0.491
107.60	0.00	2.094	3.694	1.814	8.207	5.170	0.000	N/A	0.492
108.35	0.00	2.091	3.695	1.823	8.194	5.215	0.000	N/A	0.492
109.10	0.00	2.084	3.697	1.836	8.185	5.251	0.000	N/A	0.493
109.85	0.00	2.075	3.699	1.853	8.176	5.281	0.000	N/A	0.493
110.60	0.00	2.079	3.698	1.846	8.168	5.306	0.000	N/A	0.494
111.35	0.00	2.090	3.696	1.827	8.161	5.328	0.000	N/A	0.494
112.10	0.00	2.106	3.694	1.800	8.157	5.352	0.000	N/A	0.494
112.85	0.00	2.123	3.691	1.774	8.155	5.375	0.000	N/A	0.494
113.60	0.00	2.142	3.689	1.745	8.154	5.398	0.000	N/A	0.495
114.35	0.00	2.165	3.685	1.708	8.153	5.426	0.000	N/A	0.495
115.10	0.00	2.188	3.681	1.670	8.153	5.451	0.000	N/A	0.495
115.85	0.00	2.218	3.677	1.621	8.152	5.483	0.000	N/A	0.495
116.60	0.00	2.249	3.672	1.573	8.151	5.515	0.000	N/A	0.496
116.70	0.00	2.252	3.672	1.567	8.151	5.518	0.000	N/A	0.496

Table B-9: Evolutionary Tracks for $Y_{HB} = 0.259$ [Fe/H] $= -0.65$ [O/Fe] $= 0.30$
(a) $M_* = 0.90\,M_\odot$

t_6	Y_c	$\log L$	$\log T_{eff}$	$\log g_s$	$\log T_c$	$\log \rho_c$	M_{cc}	M_{sc}	M_{sh}
1.10	0.95	1.721	3.683	2.350	8.070	4.301	0.117	N/A	0.478
4.53	0.90	1.741	3.681	2.321	8.072	4.300	0.126	N/A	0.478
8.46	0.85	1.748	3.680	2.313	8.075	4.295	0.137	N/A	0.480
12.86	0.80	1.746	3.681	2.317	8.078	4.287	0.150	N/A	0.483
17.95	0.75	1.743	3.682	2.326	8.081	4.277	0.165	N/A	0.486
23.24	0.70	1.740	3.683	2.332	8.085	4.266	0.168	0.179	0.488
28.97	0.65	1.740	3.684	2.336	8.089	4.255	0.168	0.192	0.491
34.95	0.60	1.738	3.685	2.341	8.093	4.246	0.168	0.202	0.493
40.89	0.55	1.737	3.686	2.345	8.097	4.237	0.168	0.214	0.495
46.53	0.50	1.737	3.687	2.348	8.102	4.230	0.168	0.224	0.498
51.96	0.45	1.737	3.687	2.350	8.107	4.224	0.170	0.231	0.499
57.45	0.40	1.738	3.688	2.351	8.112	4.221	0.170	0.238	0.501
62.88	0.35	1.740	3.688	2.351	8.118	4.219	0.170	0.246	0.503
68.26	0.30	1.743	3.688	2.348	8.124	4.220	0.170	0.252	0.505
73.21	0.25	1.747	3.688	2.343	8.131	4.224	0.170	0.258	0.506
78.34	0.20	1.754	3.687	2.334	8.140	4.233	0.170	0.263	0.508
83.07	0.15	1.763	3.686	2.320	8.151	4.249	0.170	0.270	0.509
87.42	0.10	1.781	3.684	2.293	8.165	4.278	0.168	0.273	0.510
91.99	5.00E-02	1.811	3.680	2.249	8.186	4.330	0.172	0.280	0.512
93.07	4.00E-02	1.822	3.678	2.231	8.193	4.349	0.171	0.279	0.512
93.86	3.00E-02	1.838	3.677	2.207	8.201	4.371	0.163	0.180	0.512
94.73	2.00E-02	1.858	3.674	2.176	8.211	4.405	0.162	N/A	0.512
95.65	1.00E-02	1.893	3.670	2.125	8.226	4.460	0.162	N/A	0.513
96.69	1.00E-03	1.999	3.664	1.995	8.264	4.613	0.106	N/A	0.513
96.80	1.00E-04	2.046	3.663	1.946	8.276	4.695	0.039	N/A	0.513
96.90	0.00	2.114	3.657	1.853	8.276	4.804	0.000	N/A	0.513
Post Helium Exhaustion Phase									
97.10	0.00	2.249	3.645	1.669	8.281	4.964	0.000	N/A	0.515

Table B-9 (continued)
(b) $M_* = 0.62\,M_\odot$

t_6	Y_c	$\log L$	$\log T_{eff}$	$\log g_s$	$\log T_c$	$\log \rho_c$	M_{cc}	M_{sc}	M_{sh}
1.10	0.95	1.624	3.716	2.418	8.070	4.299	0.117	N/A	0.478
4.46	0.90	1.645	3.712	2.379	8.072	4.298	0.127	N/A	0.478
8.32	0.85	1.652	3.711	2.371	8.075	4.294	0.137	N/A	0.479
12.80	0.80	1.651	3.713	2.377	8.078	4.288	0.149	N/A	0.481
17.83	0.75	1.644	3.716	2.399	8.081	4.279	0.164	N/A	0.483
23.66	0.70	1.635	3.721	2.426	8.085	4.269	0.167	0.179	0.485
29.38	0.65	1.628	3.725	2.449	8.088	4.260	0.167	0.191	0.486
34.83	0.60	1.623	3.729	2.471	8.092	4.252	0.167	0.201	0.488
40.69	0.55	1.617	3.733	2.492	8.096	4.245	0.167	0.211	0.489
46.72	0.50	1.613	3.736	2.509	8.101	4.239	0.167	0.221	0.491
52.44	0.45	1.611	3.739	2.522	8.105	4.235	0.167	0.229	0.492
58.08	0.40	1.609	3.742	2.534	8.110	4.232	0.167	0.236	0.493
63.66	0.35	1.610	3.743	2.540	8.116	4.232	0.167	0.241	0.493
69.07	0.30	1.612	3.743	2.536	8.122	4.234	0.165	0.247	0.494
74.28	0.25	1.617	3.742	2.527	8.129	4.240	0.165	0.253	0.495
79.44	0.20	1.626	3.739	2.505	8.138	4.250	0.165	0.257	0.495
84.64	0.15	1.641	3.735	2.474	8.149	4.267	0.163	0.265	0.496
89.24	0.10	1.663	3.728	2.426	8.162	4.296	0.163	0.267	0.497
93.94	5.00E-02	1.702	3.720	2.353	8.183	4.349	0.166	0.272	0.497
95.10	4.00E-02	1.717	3.716	2.325	8.190	4.368	0.166	0.272	0.498
95.99	3.00E-02	1.736	3.712	2.289	8.197	4.390	0.157	N/A	0.497
96.85	2.00E-02	1.760	3.707	2.245	8.207	4.424	0.157	N/A	0.498
97.95	1.00E-02	1.802	3.699	2.171	8.223	4.478	0.157	N/A	0.498
99.07	1.00E-03	1.928	3.685	1.988	8.260	4.632	0.105	N/A	0.499
99.24	1.00E-04	2.010	3.678	1.878	8.271	4.752	0.023	N/A	0.499
99.30	0.00	2.049	3.672	1.816	8.270	4.812	0.000	N/A	0.499
Post Helium Exhaustion Phase									
100.05	0.00	2.144	3.660	1.675	8.232	5.083	0.000	N/A	0.501
100.80	0.00	2.122	3.664	1.709	8.207	5.154	0.000	N/A	0.502
101.55	0.00	2.121	3.664	1.712	8.195	5.208	0.000	N/A	0.502
102.30	0.00	2.117	3.665	1.719	8.190	5.236	0.000	N/A	0.503
103.05	0.00	2.112	3.666	1.727	8.185	5.270	0.000	N/A	0.503
103.80	0.00	2.115	3.665	1.722	8.177	5.298	0.000	N/A	0.503
104.55	0.00	2.127	3.663	1.703	8.171	5.323	0.000	N/A	0.504
105.30	0.00	2.144	3.661	1.678	8.167	5.350	0.000	N/A	0.504
106.05	0.00	2.165	3.659	1.647	8.165	5.378	0.000	N/A	0.504
106.80	0.00	2.189	3.655	1.610	8.164	5.406	0.000	N/A	0.505
107.55	0.00	2.214	3.653	1.573	8.164	5.436	0.000	N/A	0.505
108.30	0.00	2.247	3.649	1.527	8.164	5.470	0.000	N/A	0.505
108.40	0.00	2.247	3.649	1.527	8.164	5.470	0.000	N/A	0.505

Table B-8 (continued)
(c) $M_* = 0.58\,M_\odot$

t_6	Y_c	$\log L$	$\log T_{eff}$	$\log g_s$	$\log T_c$	$\log \rho_c$	M_{cc}	M_{sc}	M_{sh}
1.10	0.95	1.571	3.791	2.740	8.070	4.298	0.117	N/A	0.478
4.46	0.90	1.597	3.766	2.617	8.072	4.297	0.127	N/A	0.478
8.51	0.85	1.603	3.765	2.606	8.075	4.294	0.137	N/A	0.478
13.01	0.80	1.602	3.772	2.635	8.077	4.289	0.150	N/A	0.480
18.27	0.75	1.594	3.788	2.707	8.080	4.282	0.165	N/A	0.482
23.65	0.70	1.580	3.819	2.844	8.084	4.271	0.167	0.177	0.483
29.78	0.65	1.568	3.844	2.957	8.088	4.262	0.167	0.191	0.484
35.53	0.60	1.559	3.862	3.039	8.092	4.255	0.167	0.202	0.485
41.40	0.55	1.551	3.876	3.102	8.096	4.249	0.167	0.211	0.487
47.39	0.50	1.546	3.886	3.145	8.100	4.243	0.167	0.221	0.487
53.44	0.45	1.543	3.891	3.167	8.104	4.240	0.165	0.229	0.488
59.06	0.40	1.543	3.893	3.177	8.109	4.238	0.165	0.234	0.489
64.75	0.35	1.546	3.891	3.168	8.115	4.239	0.165	0.241	0.489
70.40	0.30	1.551	3.887	3.145	8.121	4.242	0.163	0.247	0.490
75.81	0.25	1.559	3.879	3.106	8.128	4.247	0.164	0.250	0.490
80.93	0.20	1.571	3.870	3.056	8.137	4.258	0.162	0.255	0.490
86.58	0.15	1.587	3.856	2.985	8.147	4.275	0.162	0.262	0.491
92.25	0.10	1.611	3.837	2.886	8.161	4.304	0.162	0.268	0.491
97.73	5.00E-02	1.653	3.803	2.706	8.183	4.359	0.163	0.269	0.491
99.35	4.00E-02	1.668	3.790	2.642	8.189	4.374	0.164	0.272	0.492
100.68	3.00E-02	1.687	3.772	2.550	8.196	4.398	0.164	0.271	0.492
101.70	2.00E-02	1.714	3.756	2.456	8.206	4.432	0.158	N/A	0.492
102.76	1.00E-02	1.760	3.735	2.326	8.222	4.487	0.158	N/A	0.492
103.94	1.00E-03	1.896	3.701	2.055	8.259	4.641	0.095	N/A	0.492
104.08	1.00E-04	1.961	3.696	1.972	8.269	4.731	0.018	N/A	0.492
104.10	0.00	1.970	3.694	1.956	8.270	4.744	0.007	N/A	0.492
Post Helium Exhaustion Phase									
104.85	0.00	2.137	3.670	1.690	8.238	5.079	0.000	N/A	0.494
105.60	0.00	2.105	3.676	1.746	8.208	5.158	0.000	N/A	0.496
106.35	0.00	2.103	3.676	1.750	8.196	5.205	0.000	N/A	0.496
107.10	0.00	2.097	3.678	1.762	8.188	5.245	0.000	N/A	0.497
107.85	0.00	2.087	3.679	1.779	8.180	5.277	0.000	N/A	0.497
108.60	0.00	2.091	3.679	1.772	8.172	5.302	0.000	N/A	0.497
109.35	0.00	2.102	3.677	1.754	8.166	5.325	0.000	N/A	0.497
110.10	0.00	2.119	3.674	1.727	8.161	5.350	0.000	N/A	0.498
110.85	0.00	2.137	3.672	1.698	8.159	5.375	0.000	N/A	0.498
111.60	0.00	2.159	3.668	1.662	8.158	5.402	0.000	N/A	0.499
112.35	0.00	2.181	3.665	1.628	8.158	5.428	0.000	N/A	0.499
113.10	0.00	2.208	3.661	1.585	8.158	5.457	0.000	N/A	0.499
113.85	0.00	2.241	3.656	1.532	8.157	5.491	0.000	N/A	0.499
114.10	0.00	2.251	3.655	1.517	8.157	5.502	0.000	N/A	0.499

Table B-9 (continued)

(d) $M_* = 0.57\,M_\odot$

t_6	Y_c	$\log L$	$\log T_{eff}$	$\log g_s$	$\log T_c$	$\log \rho_c$	M_{cc}	M_{sc}	M_{sh}
1.10	0.95	1.543	3.874	3.094	8.070	4.297	0.118	N/A	0.478
4.45	0.90	1.571	3.843	2.942	8.072	4.297	0.127	N/A	0.478
8.41	0.85	1.578	3.841	2.925	8.075	4.294	0.137	N/A	0.478
12.99	0.80	1.577	3.848	2.954	8.077	4.290	0.150	N/A	0.479
18.22	0.75	1.568	3.870	3.051	8.081	4.281	0.165	N/A	0.481
23.75	0.70	1.555	3.892	3.153	8.084	4.272	0.167	0.177	0.482
29.88	0.65	1.542	3.911	3.243	8.088	4.264	0.167	0.191	0.483
35.82	0.60	1.532	3.926	3.311	8.091	4.256	0.167	0.200	0.484
42.11	0.55	1.524	3.936	3.359	8.095	4.250	0.167	0.212	0.485
48.09	0.50	1.520	3.941	3.385	8.099	4.245	0.165	0.220	0.487
54.18	0.45	1.519	3.944	3.396	8.104	4.242	0.165	0.227	0.487
59.93	0.40	1.519	3.944	3.397	8.109	4.241	0.165	0.233	0.487
65.69	0.35	1.523	3.940	3.379	8.115	4.241	0.163	0.239	0.488
71.27	0.30	1.530	3.935	3.349	8.121	4.244	0.162	0.244	0.488
76.77	0.25	1.539	3.928	3.311	8.127	4.250	0.162	0.250	0.488
82.06	0.20	1.552	3.918	3.259	8.136	4.261	0.162	0.254	0.488
87.80	0.15	1.570	3.904	3.188	8.147	4.279	0.162	0.262	0.489
92.78	0.10	1.593	3.890	3.105	8.161	4.308	0.160	0.263	0.489
98.76	5.00E-02	1.634	3.865	2.965	8.183	4.364	0.163	0.269	0.490
99.96	4.00E-02	1.647	3.857	2.920	8.189	4.380	0.163	0.271	0.490
101.40	3.00E-02	1.663	3.845	2.856	8.196	4.401	0.160	0.211	0.490
102.39	2.00E-02	1.690	3.822	2.737	8.206	4.435	0.156	N/A	0.490
103.51	1.00E-02	1.739	3.772	2.488	8.221	4.490	0.156	N/A	0.490
104.71	1.00E-03	1.880	3.706	2.086	8.258	4.641	0.095	N/A	0.490
104.87	1.00E-04	1.957	3.698	1.976	8.268	4.747	0.017	N/A	0.490
104.90	0.00	1.973	3.698	1.960	8.269	4.769	0.000	N/A	0.490
Post Helium Exhaustion Phase									
105.65	0.00	2.129	3.674	1.708	8.237	5.083	0.000	N/A	0.492
106.40	0.00	2.098	3.679	1.758	8.211	5.148	0.000	N/A	0.493
107.15	0.00	2.095	3.682	1.772	8.197	5.202	0.000	N/A	0.494
107.90	0.00	2.088	3.683	1.786	8.188	5.243	0.000	N/A	0.494
108.65	0.00	2.076	3.685	1.806	8.179	5.274	0.000	N/A	0.495
109.40	0.00	2.079	3.685	1.801	8.171	5.298	0.000	N/A	0.495
110.15	0.00	2.093	3.683	1.778	8.163	5.323	0.000	N/A	0.496
110.90	0.00	2.108	3.680	1.752	8.160	5.346	0.000	N/A	0.496
111.65	0.00	2.124	3.677	1.726	8.157	5.370	0.000	N/A	0.496
112.40	0.00	2.143	3.675	1.696	8.158	5.393	0.000	N/A	0.496
113.15	0.00	2.164	3.671	1.661	8.157	5.419	0.000	N/A	0.497
113.90	0.00	2.191	3.667	1.617	8.157	5.450	0.000	N/A	0.497
114.65	0.00	2.220	3.663	1.572	8.158	5.479	0.000	N/A	0.497
115.40	0.00	2.251	3.658	1.521	8.156	5.511	0.000	N/A	0.497

Table B-10: Evolutionary Tracks for $Y_{HB} = 0.266$ [Fe/H] $= -0.47$ [O/Fe] $= 0.23$
(a) $M_* = 0.90\,M_\odot$

t_6	Y_c	$\log L$	$\log T_{eff}$	$\log g_s$	$\log T_c$	$\log \rho_c$	M_{cc}	M_{sc}	M_{sh}
1.10	0.95	1.708	3.672	2.320	8.069	4.304	0.116	N/A	0.476
4.43	0.90	1.729	3.670	2.290	8.071	4.303	0.124	N/A	0.476
8.44	0.85	1.736	3.669	2.281	8.074	4.298	0.135	N/A	0.479
12.94	0.80	1.733	3.670	2.287	8.077	4.290	0.147	N/A	0.481
17.72	0.75	1.729	3.672	2.297	8.081	4.280	0.160	N/A	0.484
23.07	0.70	1.724	3.673	2.306	8.084	4.270	0.167	0.175	0.486
29.07	0.65	1.724	3.673	2.309	8.088	4.259	0.167	0.189	0.489
34.41	0.60	1.723	3.674	2.313	8.092	4.250	0.167	0.196	0.490
40.22	0.55	1.721	3.675	2.318	8.097	4.241	0.167	0.210	0.493
45.84	0.50	1.720	3.676	2.322	8.101	4.234	0.167	0.220	0.495
51.42	0.45	1.720	3.677	2.325	8.106	4.229	0.167	0.227	0.497
56.93	0.40	1.721	3.677	2.326	8.111	4.225	0.167	0.234	0.499
62.46	0.35	1.722	3.677	2.326	8.117	4.224	0.167	0.241	0.501
67.72	0.30	1.724	3.677	2.324	8.124	4.225	0.167	0.249	0.502
72.41	0.25	1.729	3.677	2.319	8.131	4.229	0.167	0.255	0.503
76.57	0.20	1.735	3.676	2.310	8.139	4.239	0.167	0.259	0.504
80.83	0.15	1.745	3.675	2.295	8.150	4.255	0.167	0.265	0.505
84.86	0.10	1.762	3.673	2.268	8.164	4.283	0.167	0.269	0.506
89.55	5.00E-02	1.796	3.669	2.217	8.186	4.340	0.169	0.273	0.507
90.87	4.00E-02	1.808	3.667	2.199	8.193	4.358	0.168	0.273	0.508
92.08	3.00E-02	1.820	3.666	2.182	8.200	4.377	0.155	N/A	0.508
92.96	2.00E-02	1.840	3.663	2.151	8.210	4.411	0.156	N/A	0.509
93.87	1.00E-02	1.876	3.659	2.099	8.225	4.465	0.156	N/A	0.509
94.90	1.00E-03	1.986	3.657	1.980	8.263	4.619	0.108	N/A	0.510
95.06	1.00E-04	2.058	3.650	1.879	8.274	4.737	0.024	N/A	0.510
95.10	0.00	2.080	3.648	1.848	8.275	4.774	0.000	N/A	0.510
Post Helium Exhaustion Phase									
95.85	0.00	2.190	3.638	1.699	8.238	5.068	0.000	N/A	0.511
96.60	0.00	2.170	3.640	1.728	8.216	5.145	0.000	N/A	0.513
97.35	0.00	2.162	3.641	1.739	8.203	5.199	0.000	N/A	0.513
98.10	0.00	2.153	3.641	1.751	8.198	5.237	0.000	N/A	0.514
98.85	0.00	2.149	3.642	1.756	8.188	5.271	0.000	N/A	0.515
99.60	0.00	2.161	3.641	1.740	8.180	5.302	0.000	N/A	0.515
100.35	0.00	2.178	3.639	1.717	8.175	5.331	0.000	N/A	0.515
101.10	0.00	2.201	3.637	1.685	8.173	5.364	0.000	N/A	0.515
101.85	0.00	2.225	3.634	1.652	8.173	5.395	0.000	N/A	0.516
102.60	0.00	2.254	3.632	1.612	8.174	5.428	0.000	N/A	0.516

Table B-10 (continued)
(b) $M_* = 0.70\,M_\odot$

t_6	Y_c	$\log L$	$\log T_{eff}$	$\log g_s$	$\log T_c$	$\log \rho_c$	M_{cc}	M_{sc}	M_{sh}
1.10	0.94	1.656	3.682	2.302	8.069	4.302	0.116	N/A	0.476
4.41	0.90	1.678	3.679	2.267	8.071	4.302	0.124	N/A	0.476
8.42	0.85	1.685	3.678	2.258	8.074	4.298	0.135	N/A	0.478
12.89	0.80	1.683	3.680	2.265	8.077	4.291	0.147	N/A	0.480
17.84	0.75	1.677	3.682	2.280	8.081	4.282	0.161	N/A	0.482
24.20	0.70	1.671	3.684	2.294	8.084	4.271	0.166	0.176	0.484
29.93	0.65	1.668	3.686	2.304	8.088	4.261	0.166	0.188	0.486
35.51	0.60	1.664	3.687	2.314	8.092	4.253	0.166	0.198	0.488
41.23	0.55	1.661	3.689	2.323	8.096	4.245	0.166	0.209	0.490
46.90	0.50	1.658	3.690	2.331	8.101	4.239	0.166	0.218	0.491
52.50	0.45	1.656	3.691	2.337	8.105	4.234	0.166	0.225	0.493
58.14	0.40	1.655	3.692	2.341	8.111	4.231	0.166	0.233	0.494
63.66	0.35	1.656	3.692	2.343	8.116	4.230	0.166	0.240	0.495
68.92	0.30	1.658	3.692	2.340	8.123	4.232	0.166	0.246	0.497
74.12	0.25	1.662	3.692	2.335	8.130	4.237	0.166	0.252	0.497
79.06	0.20	1.669	3.691	2.325	8.138	4.247	0.166	0.256	0.498
84.83	0.15	1.682	3.690	2.306	8.149	4.263	0.165	0.263	0.499
89.16	0.10	1.701	3.687	2.275	8.162	4.291	0.164	0.264	0.500
93.75	5.00E-02	1.738	3.681	2.217	8.184	4.344	0.166	0.270	0.502
94.89	4.00E-02	1.751	3.679	2.195	8.191	4.363	0.166	0.270	0.502
96.06	3.00E-02	1.769	3.676	2.166	8.198	4.386	0.156	N/A	0.502
96.99	2.00E-02	1.792	3.673	2.130	8.208	4.420	0.157	N/A	0.502
98.01	1.00E-02	1.832	3.667	2.065	8.224	4.475	0.157	N/A	0.502
99.10	1.00E-03	1.955	3.662	1.920	8.262	4.630	0.106	N/A	0.503
99.26	1.00E-04	2.037	3.652	1.801	8.272	4.754	0.020	N/A	0.503
99.30	0.00	2.061	3.649	1.766	8.272	4.792	0.000	N/A	0.503
Post Helium Exhaustion Phase									
100.05	0.00	2.167	3.639	1.618	8.234	5.081	0.000	N/A	0.504
100.80	0.00	2.141	3.641	1.654	8.208	5.160	0.000	N/A	0.506
101.55	0.00	2.138	3.642	1.659	8.201	5.193	0.000	N/A	0.507
102.30	0.00	2.131	3.643	1.669	8.196	5.227	0.000	N/A	0.507
103.05	0.00	2.121	3.644	1.683	8.187	5.266	0.000	N/A	0.507
103.80	0.00	2.129	3.643	1.673	8.178	5.294	0.000	N/A	0.508
104.55	0.00	2.144	3.641	1.651	8.172	5.323	0.000	N/A	0.508
105.30	0.00	2.162	3.640	1.627	8.168	5.349	0.000	N/A	0.508
106.05	0.00	2.184	3.637	1.594	8.167	5.379	0.000	N/A	0.509
106.80	0.00	2.209	3.635	1.559	8.167	5.409	0.000	N/A	0.509
107.55	0.00	2.240	3.631	1.515	8.168	5.443	0.000	N/A	0.509
107.80	0.00	2.251	3.630	1.499	8.168	5.455	0.000	N/A	0.509

Table B-10 (continued)
(c) $M_* = 0.60\,M_\odot$

t_6	Y_c	$\log L$	$\log T_{eff}$	$\log g_s$	$\log T_c$	$\log \rho_c$	M_{cc}	M_{sc}	M_{sh}
1.10	0.94	1.600	3.716	2.427	8.069	4.301	0.116	N/A	0.476
4.49	0.90	1.624	3.710	2.379	8.072	4.301	0.125	N/A	0.476
8.45	0.85	1.631	3.709	2.370	8.074	4.297	0.135	N/A	0.477
12.94	0.80	1.629	3.712	2.380	8.077	4.292	0.147	N/A	0.479
17.94	0.75	1.621	3.716	2.407	8.080	4.283	0.161	N/A	0.481
23.48	0.70	1.611	3.722	2.440	8.084	4.273	0.166	0.176	0.482
29.28	0.65	1.602	3.728	2.471	8.088	4.264	0.166	0.188	0.484
34.86	0.60	1.595	3.733	2.501	8.092	4.257	0.166	0.199	0.485
40.70	0.55	1.589	3.738	2.526	8.096	4.250	0.166	0.206	0.487
46.63	0.50	1.584	3.743	2.549	8.100	4.244	0.166	0.216	0.487
52.50	0.45	1.580	3.747	2.569	8.104	4.240	0.166	0.224	0.489
58.31	0.40	1.579	3.749	2.578	8.110	4.238	0.163	0.232	0.489
64.09	0.35	1.580	3.750	2.582	8.115	4.238	0.163	0.237	0.490
69.54	0.30	1.583	3.749	2.576	8.121	4.240	0.163	0.243	0.491
74.73	0.25	1.589	3.748	2.564	8.128	4.246	0.163	0.248	0.492
80.01	0.20	1.598	3.744	2.543	8.137	4.256	0.163	0.253	0.492
85.58	0.15	1.615	3.738	2.501	8.149	4.276	0.161	0.261	0.492
90.29	0.10	1.635	3.732	2.457	8.161	4.302	0.161	0.262	0.493
95.73	5.00E-02	1.676	3.721	2.370	8.183	4.354	0.166	0.270	0.493
96.77	4.00E-02	1.691	3.717	2.339	8.189	4.372	0.163	0.269	0.493
98.34	3.00E-02	1.710	3.712	2.303	8.197	4.396	0.150	N/A	0.494
99.17	2.00E-02	1.735	3.706	2.253	8.207	4.430	0.150	N/A	0.494
100.24	1.00E-02	1.780	3.697	2.169	8.222	4.485	0.150	N/A	0.494
101.35	1.00E-03	1.912	3.684	1.987	8.259	4.637	0.095	N/A	0.495
101.50	1.00E-04	1.980	3.672	1.872	8.272	4.734	0.022	N/A	0.495
101.60	0.00	2.053	3.661	1.755	8.269	4.835	0.000	N/A	0.495
Post Helium Exhaustion Phase									
102.35	0.00	2.140	3.650	1.623	8.232	5.080	0.000	N/A	0.496
103.10	0.00	2.115	3.654	1.663	8.207	5.155	0.000	N/A	0.498
103.85	0.00	2.111	3.655	1.670	8.196	5.204	0.000	N/A	0.498
104.60	0.00	2.100	3.657	1.691	8.188	5.243	0.000	N/A	0.499
105.35	0.00	2.090	3.658	1.706	8.179	5.273	0.000	N/A	0.499
106.10	0.00	2.097	3.657	1.695	8.170	5.301	0.000	N/A	0.500
106.85	0.00	2.111	3.655	1.673	8.165	5.325	0.000	N/A	0.500
107.60	0.00	2.128	3.653	1.646	8.161	5.350	0.000	N/A	0.500
108.35	0.00	2.146	3.651	1.619	8.160	5.374	0.000	N/A	0.500
109.10	0.00	2.168	3.648	1.585	8.159	5.401	0.000	N/A	0.501
109.85	0.00	2.191	3.645	1.550	8.160	5.428	0.000	N/A	0.501
110.60	0.00	2.219	3.641	1.509	8.160	5.458	0.000	N/A	0.501
111.30	0.00	2.251	3.638	1.463	8.163	5.489	0.000	N/A	0.501

Table B-10 (continued)

(d) $M_* = 0.58\,M_\odot$

t_6	Y_c	$\log L$	$\log T_{eff}$	$\log g_s$	$\log T_c$	$\log \rho_c$	M_{cc}	M_{sc}	M_{sh}
1.10	0.95	1.573	3.746	2.560	8.070	4.301	0.116	N/A	0.476
4.35	0.90	1.599	3.735	2.490	8.072	4.301	0.124	N/A	0.476
8.34	0.85	1.607	3.734	2.477	8.074	4.297	0.135	N/A	0.476
13.06	0.80	1.605	3.738	2.493	8.077	4.292	0.147	N/A	0.478
18.01	0.75	1.595	3.747	2.541	8.080	4.284	0.161	N/A	0.480
23.48	0.70	1.583	3.759	2.602	8.084	4.274	0.166	0.175	0.482
29.52	0.65	1.572	3.776	2.681	8.088	4.266	0.166	0.188	0.483
35.43	0.60	1.563	3.795	2.764	8.091	4.258	0.163	0.197	0.484
41.28	0.55	1.555	3.810	2.835	8.095	4.252	0.165	0.206	0.485
47.29	0.50	1.549	3.823	2.892	8.100	4.247	0.165	0.216	0.486
53.25	0.45	1.546	3.832	2.931	8.104	4.243	0.165	0.224	0.487
59.12	0.40	1.545	3.836	2.946	8.109	4.241	0.163	0.230	0.487
64.82	0.35	1.546	3.836	2.948	8.115	4.241	0.163	0.237	0.488
70.31	0.30	1.550	3.833	2.929	8.120	4.244	0.163	0.241	0.489
75.85	0.25	1.558	3.825	2.891	8.128	4.250	0.161	0.248	0.489
80.75	0.20	1.569	3.815	2.837	8.136	4.260	0.160	0.252	0.489
86.39	0.15	1.586	3.799	2.757	8.147	4.278	0.161	0.257	0.490
91.19	0.10	1.608	3.780	2.660	8.161	4.306	0.161	0.261	0.490
96.80	5.00E-02	1.652	3.755	2.516	8.183	4.362	0.163	0.268	0.490
97.98	4.00E-02	1.664	3.749	2.480	8.189	4.379	0.163	0.269	0.491
99.36	3.00E-02	1.681	3.742	2.435	8.196	4.400	0.157	0.174	0.491
100.34	2.00E-02	1.708	3.733	2.371	8.206	4.434	0.156	N/A	0.491
101.44	1.00E-02	1.755	3.717	2.260	8.221	4.489	0.156	N/A	0.491
102.60	1.00E-03	1.892	3.695	2.035	8.258	4.641	0.100	N/A	0.492
102.77	1.00E-04	1.976	3.680	1.893	8.268	4.757	0.018	N/A	0.492
102.80	0.00	1.992	3.677	1.865	8.269	4.781	0.000	N/A	0.492
Post Helium Exhaustion Phase									
103.55	0.00	2.134	3.656	1.637	8.236	5.085	0.000	N/A	0.493
104.30	0.00	2.101	3.661	1.694	8.207	5.158	0.000	N/A	0.494
105.05	0.00	2.104	3.662	1.690	8.202	5.190	0.000	N/A	0.495
105.80	0.00	2.089	3.664	1.716	8.192	5.240	0.000	N/A	0.496
106.55	0.00	2.081	3.666	1.730	8.184	5.267	0.000	N/A	0.496
107.30	0.00	2.084	3.665	1.724	8.174	5.292	0.000	N/A	0.496
108.05	0.00	2.095	3.664	1.708	8.167	5.317	0.000	N/A	0.497
108.80	0.00	2.109	3.661	1.685	8.162	5.341	0.000	N/A	0.497
109.55	0.00	2.127	3.659	1.655	8.159	5.367	0.000	N/A	0.498
110.30	0.00	2.146	3.656	1.625	8.158	5.391	0.000	N/A	0.498
111.05	0.00	2.171	3.652	1.585	8.157	5.420	0.000	N/A	0.498
111.80	0.00	2.197	3.648	1.543	8.157	5.449	0.000	N/A	0.498
112.55	0.00	2.225	3.644	1.500	8.157	5.478	0.000	N/A	0.498
113.10	0.00	2.248	3.642	1.466	8.158	5.501	0.000	N/A	0.498